NASA Conference Publication 3020—Vol. I
Part 2

Transonic Symposium: Theory, Application, and Experiment

Jerome T. Foughner, Jr., *Compiler*
Langley Research Center
Hampton, Virginia

Proceedings of a symposium sponsored by the
National Aeronautics and Space Administration,
Washington, D.C., and held at
NASA Langley Research Center
Hampton, Virginia
April 19–21, 1988

ORIGINAL CONTAINS
COLOR ILLUSTRATIONS

NASA
National Aeronautics
and Space Administration

Scientific and Technical
Information Division

1989

PREFACE

The last major Transonic Symposium was held at NASA Ames Research Center in February 1981. Since then, significant advances have been made in computer hardware, theoretical and computational methods, applications, experimental facilities, and testing techniques. Although much research remains to be done, these advances now provide us with capabilities in the transonic regime which we hardly envisioned 7 years ago. In order to assess the state of the art in transonic flow disciplines and to glimpse at future directions, the NASA Langley Research Center held a Transonic Symposium on April 19-21, 1988. Emphasis was placed on steady, three-dimensional external, transonic flow and its simulation, both numerically and experimentally.

Papers were presented by researchers from NASA, industry, and universities. The symposium included technical sessions on wind tunnel and flight experiments; computational fluid dynamics applications (industry overviews and configuration analysis design); inviscid methods and grid generation; viscous methods and boundary-layer stability; and wind tunnel techniques and wall interference.

The proceedings are published in two volumes as follows because of the range of classifications:

Volume I, Unclassified (Parts 1 and 2)
Volume II, Unclassified, FEDD Restricted

A list of attendees is included in this document.

General Chairman:	P. J. Bobbitt
Organizing Committee:	M. D. Salas
	L. E. Putnam
	J. T. Foughner
Technical Committee Chairman:	
Theory and Computational	J. L. Thomas
Applications	E. G. Waggoner
Experiments	L. W. McKinney

PRECEDING PAGE BLANK NOT FILMED

CONTENTS

PREFACE iii

ATTENDEES ix

Volume I - Part 1*

SESSION 1: WIND TUNNEL AND FLIGHT EXPERIMENTS
Chairman: P. J. Bobbitt

AIRFRAME/PROPULSION INTEGRATION CHARACTERISTICS AT TRANSONIC SPEEDS 1
William P. Henderson and Bobby L. Berrier

FLIGHT RESEARCH AND TESTING 33
Terrill W. Putnam and Theodore G. Ayers

SHOCK-BOUNDARY-LAYER INTERACTION IN FLIGHT 61
Arild Bertelrud

SESSION 2: CFD APPLICATIONS, INDUSTRY OVERVIEWS
Chairman: E. G. Waggoner

TRANSONIC CFD APPLICATIONS AT BOEING 79
E. N. Tinoco

THE APPLICATION OF CFD FOR MILITARY AIRCRAFT DESIGN AT TRANSONIC SPEEDS 109
C. W. Smith, W. W. Braymen, I. C. Bhateley, and W. K. Londenberg

APPLIED TRANSONICS AT GRUMMAN 133
W. H. Davis

TRANSONICS AND FIGHTER AIRCRAFT: CHALLENGES AND OPPORTUNITIES FOR CFD 153
Luis R. Miranda

COMPUTATION OF AIRCRAFT COMPONENT FLOW FIELDS AT TRANSONIC MACH NUMBERS USING A THREE-DIMENSIONAL NAVIER-STOKES ALGORITHM 175
George D. Shrewsbury, Joseph Vadyak, David M. Schuster, and Marilyn J. Smith

TRANSONIC AERODYNAMIC DESIGN EXPERIENCE 195
E. Bonner

SESSION 3: INVISCID METHODS AND GRID GENERATION
Chairman: J. L. Thomas

EULER SOLVERS FOR TRANSONIC APPLICATIONS 217
Bram van Leer

*Part 1 is presented under separate cover.

PRECEDING PAGE BLANK NOT FILMED

AN EMBEDDED MESH PROCEDURE FOR LEADING-EDGE VORTEX FLOWS 231
Kenneth G. Powell and Earll M. Murman

ASYMPTOTIC METHODS FOR INTERNAL TRANSONIC FLOWS 261
T. C. Adamson, Jr., and A. F. Messiter

WAVE DRAG DUE TO LIFT FOR TRANSONIC AIRPLANES 293
Julian D. Cole and Norman D. Malmuth

VECTOR POTENTIAL METHODS 309
M. Hafez

DEVELOPMENTS AND TRENDS IN THREE-DIMENSIONAL MESH GENERATION 341
Timothy J. Baker

GENERATION OF UNSTRUCTURED GRIDS AND EULER SOLUTIONS FOR COMPLEX GEOMETRIES ... 377
Rainald Löhner, Paresh Parikh, and Manuel D. Salas

Volume I - Part 2

SESSION 4: CFD APPLICATIONS, CONFIGURATION ANALYSIS AND DESIGN
Chairman: L. E. Putnam

TRANSONIC PROPULSION SYSTEM INTEGRATION ANALYSIS AT MCDONNELL AIRCRAFT COMPANY 409
Raymond R. Cosner

AERODYNAMIC ANALYSIS OF THREE ADVANCED CONFIGURATIONS USING THE TRANAIR FULL-POTENTIAL CODE 437
M. D. Madson, R. L. Carmichael, and J. P. Mendoza

METHOD TO PREDICT EXTERNAL STORE CARRIAGE LOADS AT TRANSONIC SPEEDS 453
Bruce S. Rosen

STEADY AND UNSTEADY TRANSONIC SMALL DISTURBANCE ANALYSIS OF REALISTIC AIRCRAFT CONFIGURATIONS 467
John T. Batina, David A. Seidel, Robert M. Bennett,
Herbert J. Cunningham, and Samuel R. Bland

INVERSE WING DESIGN IN TRANSONIC FLOW INCLUDING VISCOUS INTERACTION 497
Leland A. Carlson, Robert R. Ratcliff, and Thomas A. Gally

EULER/NAVIER-STOKES CALCULATIONS OF TRANSONIC FLOW PAST FIXED- AND ROTARY-WING AIRCRAFT CONFIGURATIONS 521
J. E. Deese and R. K. Agarwal

SESSION 5: VISCOUS METHODS AND BOUNDARY-LAYER STABILITY
Chairman: M. D. Salas

NAVIER-STOKES AND VISCOUS-INVISCID INTERACTION 547
Joseph L. Steger and William R. Van Dalsem

3-D EULER AND NAVIER-STOKES CALCULATIONS FOR AIRCRAFT COMPONENTS 571
Veer N. Vatsa, Bruce W. Wedan, and Eli Turkel

TURBULENCE AND MODELING IN TRANSONIC FLOW 581
Morris W. Rubesin and John R. Viegas

TURBULENT EDDY VISCOSITY MODELING IN TRANSONIC SHOCK/BOUNDARY-LAYER INTERACTIONS 611
G. R. Inger

STABILITY OF COMPRESSIBLE BOUNDARY LAYERS 629
Ali H. Nayfeh

SECONDARY THREE-DIMENSIONAL INSTABILITY IN COMPRESSIBLE BOUNDARY LAYERS 691
Nabil M. El-Hady

SESSION 6: WIND TUNNEL TECHNIQUES AND WALL INTERFERENCE
Chairman: L. W. McKinney

TEST TECHNIQUES - A SURVEY PAPER ON CRYOGENIC TUNNELS, ADAPTIVE WALL TEST SECTIONS, AND MAGNETIC SUSPENSION AND BALANCE SYSTEMS 705
Robert A. Kilgore, David A. Dress, Stephen W. D. Wolf, and Colin P. Britcher

AN LDA INVESTIGATION OF THREE-DIMENSIONAL NORMAL SHOCK WAVE BOUNDARY-LAYER INTERACTIONS 741
R. M. Chriss, W. R. Hingst, A. J. Strazisar, and T. G. Keith, Jr.

INSTRUMENTATION ADVANCES FOR TRANSONIC TESTING 765
Percy J. Bobbitt

WALL INTERFERENCE ASSESSMENT AND CORRECTIONS 817
P. A. Newman, W. B. Kemp, Jr., and J. A. Garriz

TWO-MEASURED VARIABLE METHOD FOR WALL INTERFERENCE ASSESSMENT/CORRECTION 853
C. F. Lo and W. L. Sickles

COMPARISON OF AIRFOIL RESULTS FROM AN ADAPTIVE WALL TEST SECTION AND A POROUS WALL TEST SECTION 867
Raymond E. Mineck

CAPABILITIES OF WIND TUNNELS WITH TWO ADAPTIVE WALLS TO MINIMIZE BOUNDARY INTERFERENCE IN 3-D MODEL TESTING 891
Rainer Rebstock and Edwin E. Lee, Jr.

Volume II*

NATIONAL TRANSONIC FACILITY STATUS
L. W. McKinney, W. E. Bruce, Jr., and B. B. Gloss..... 1

*Volume II is presented under separate cover.

REYNOLDS NUMBER EFFECTS ON THE TRANSONIC AERODYNAMICS OF A SLENDER WING-BODY CONFIGURATION..... 41
James M. Luckring, Charles H. Fox, Jr., and Jeffrey S. Cundiff

LAMINAR-FLOW FLIGHT EXPERIMENTS..... 59
R. D. Wagner, D. V. Maddalon, D. W. Bartlett, F. S. Collier, Jr., and A. L. Braslow

LAMINAR-FLOW WIND TUNNEL EXPERIMENTS..... 105
William D. Harvey, Charles D. Harris, William G. Sewall, and John P. Stack

COMPUTATIONAL SUPPORT OF THE X-29A ADVANCED TECHNOLOGY DEMONSTRATOR FLIGHT EXPERIMENT..... 147
E. G. Waggoner and B. L. Bates

RESULTS OF CORRELATIONS FOR TRANSITION LOCATION ON A CLEAN-UP GLOVE INSTALLED ON AN F14 AIRCRAFT AND DESIGN STUDIES FOR A LAMINAR GLOVE FOR THE X-29 AIRCRAFT ACCOUNTING FOR SPANWISE PRESSURE GRADIENT..... 167
S. H. Goradia

ATTENDEES

NASA LANGLEY

ABEYOUNIS, W. K.
Mail Stop 280

ABDOL-HAMID, K
Analytical Services & Materials
Mail Stop 280

ADCOCK, J.
Mail Stop 267

AL-SAADI, J.
N. C. State University
Mail Stop 267

ALLISON, D. O.
Mail Stop 294

ANDERSON, C.
Mail Stop 159

ATKINS, H.
Mail Stop 159

BANGERT, L.
Mail Stop 280

BARE, E. A.
Mail Stop 280

BARNWELL, R.
Mail Stop 105A

BARTLETT, D.
Mail Stop 261

BATES, B. L.
Vigyan Research Associates, Inc.
Mail Stop 294

BATINA, J. T.
Mail Stop 173

BENNETT, B. B.
Mail Stop 280

BERRIER, B. L.
Mail Stop 280

BERTELRUD, A.
High Technology Corporation
Mail Stop 163

BIEDRON, R. T.
Mail Stop 128

BLAND, S. R.
Mail Stop 173

BOBBITT, P. J.
Mail Stop 285

BOYDEN, R.
Mail Stop 267

BOYLES, G.
Mail Stop 267

BRASLOW, A.
Analytical Services & Materials
Mail Stop 261

BROOKS, C. W., Jr.
Mail Stop 359

BRUCE, W. E.
Mail Stop 267

CAMPBELL, D.
Mail Stop 294

CANNIZZARO, F. E.
Old Dominion University
Mail Stop 159

CARLSON, J. R.
Mail Stop 280

CARPENTER, M. H.
Mail Stop 156

CARRAWAY, D. L.
Mail Stop 238

CARSON, G. T., Jr.
Mail Stop 280

CHU, Julio
Mail Stop 267

CLUKEY, P.
Mail Stop 359

CLUKEY, S.
Mail Stop 359

COMPTON, W. B.,
Mail Stop 280

COVELL, P.
Mail Stop 413

CUNDIFF, J. S.
Mail Stop 294

DAGENHART, J. R.
Mail Stop 339

DAVIS, R. E.
Mail Stop 474

DESMARAIS, R.
Planning Research Corporation
Mail Stop 246

DODBELE, S.
Vigyan Research Associates, Inc.
Mail Stop 247

DRESS, D. A.
Mail Stop 267

EL-HADY, N. M.
Old Dominion University
Mail Stop 359

EVANGELISTA, R.
Analytical Services & Materials
Mail Stop 359

FAULKNER, J.
Mail Stop 390

FERRIS, J.
Mail Stop 294

FLECHNER, S.
Mail Stop 267

FOSS, W.
Mail Stop 431

FOSTER, J.
Mail Stop 294

FOUGHNER, J. T., Jr.
Mail Stop 285

FOX, C. H., Jr.
Mail Stop 295

FULLER, D.
Mail Stop 267

GAINER, T.
Mail Stop 359

GARRIZ, J.
Vigyan Research Associates , Inc.
Mail Stop 159

GATLIN, G. M.
Mail Stop 286

GHAFFARI, F.
Vigyan Research Associates, Inc.
Mail Stop 294

GLOSS, B. B.
Mail Stop 267

GORADIA, S. H.
Vigyan Research Associates, Inc.
Mail Stop 359

GREEN, L. L.
Mail Stop 159

GUMBERT, C. R.
Mail Stop 159

HALL, R. M.
Mail Stop 294

HALLISSY, J. B.
Mail Stop 294

HARRIS, C. D.
Mail Stop 359

HARRIS, R. V., Jr.
Mail Stop 116

HARVEY, W. D.
Mail Stop 359

HEMSCH, M. J.
Planning Research Corporation
Mail Stop 294

HENDERSON, W. P.
Mail Stop 280

HODGE, S.
Mail Stop 159

JONES, G.
Mail Stop 359

KALBURGI, V.
Analytical Services & Materials
Mail Stop 359

KAMEMOTO, D.
Mail Stop 359

KEMP, W. B.
LRC
Mail Stop 267

KURUVILLA, G.
Vigyan Research Associates, Inc.
Mail Stop 159

LEE, E.
Mail Stop 173

IGOE, W.
Mail Stop 267

INGRALDI, A.
Mail Stop 280

JACOBS, P.
Mail Stop 294

JENKINS, R. V.
Mail Stop 359

JOHNSON, C. B.
Mail Stop 359

JOHNSON, T.
Planning Research Corporation
Mail Stop 294

JOHNSON, W. G., Jr.
Mail Stop 267

LADSON, C. L.
Mail Stop 285

LAMAR, J.
Mail Stop 294

LEAVITT, L.
Mail Stop 280

LUCKRING, J. M.
Mail Stop 294

MADDALON, D
Mail Stop 261

MANGALAM, S.
Analytical Services & Materials
Mail Stop 915

MANN, M
Mail Stop 411

MAVRIPLIS, D.
ICASE
Mail Stop 132C

MCKINNEY, L. W.
Mail Stop 285

MCGHEE, R.
Mail Stop 339

MEHROTRA, S. C.
Vigyan Research Associates, Inc.
Mail Stop 912

MELSON, D.
Mail Stop 159

MERCER, C.
Mail Stop 280

MINECK, R.
Mail Stop 294

MOLLOY, J. K.
Mail Stop 116

MORGAN, H. L.
Mail Stop 359

MURTHY, A.
Vigyan Research Associates, Inc.
Mail Stop 287

NAIK, D.
Vigyan Research Associates, Inc.
Mail Stop 280

NEELY, R. W.
Mail Stop 173

NEWMAN, P. A.
Mail Stop 159

PARIKH, P.
Vigyan Research Associates, Inc.
Mail Stop 159

PASCHAL, K.
Mail Stop 359

PATTERSON, J. C., Jr.
Mail Stop 246A

PENDERGRAFT, O. C.
Mail Stop 280

PETERSON, J. B.
Mail Stop 267

PFENNINGER, W.
Analytical Services & Materials
Mail Stop 261

PHILLIPS, P.
Mail Stop 294

POPERNACK, T. G., Jr.
Mail Stop 267

PUTNAM, L. E.
Mail Stop 294

RADESPIEL, R.
Mail Stop 287

RE, R.
Mail Stop 280

REBSTOCK, R.
National Research Council
Mail Stop 287

ROSE, L. J.
Mail Stop 139A

RUMSEY, C
Mail Stop 128

SALAS, M. D.
Mail Stop 159

SCHOONOVER, E.
Mail Stop 294

SEIDEL, D. A.
Mail Stop 173

SEKAR, B.
Vigyan Research Associates, Inc.
Mail Stop 156

SEWALL, W. G.
Mail Stop 339

SMITH, L. A
Mail Stop 294

SOMERS, D. M.
Mail Stop 294

SOUTH, J. C.
Mail Stop 128

STACK, J. P.
Mail Stop 359

STAINBACK, P. C.
Mail Stop 359

STRGANAC, T.
Mail Stop 431

SWANSON, R. C.
Mail Stop 159

SWITZER, G.
Analytical Services & Materials
Mail Stop 156

TAYLOR, J.
Mail Stop 280

THAMES, F.
Mail Stop 159

THIBODEAUX, J. J.
Mail Stop 267

THOMAS, J. L.
Mail Stop 128

TURKEL, E.
ICASE
Mail Stop 132C

VATSA, V. N.
Mail Stop 159

VEMURU, C. S.
Mail Stop 159

VENKATAKRISHNAN, V.
Analytical Services & Materials
Mail Stop 159

VIJGEN, P.
High Technology Corporation
Mail Stop 247

VRETAKIS, N. G.
AFSCLO
Mail Stop 221

WAGGONER, E. G.
Mail Stop 294

WAGNER, R. D.
Mail Stop 261

WAHLS, R. A.
N. C. State University
Mail Stop 156

WALKER, B.
Mail Stop 359

WARREN, G. P
Mail Stop 128

WATSON, R.
Mail Stop 163

WHITCOMB, R. T.
Mail Stop 188E

WHITESIDES, J.
George Wasnington University
Mail Stop 269

WIESEMAN, C. D.
Mail Stop 243

WILLIAMS, M. S.
Mail Stop 267

WOLF, S.
Vigyan Research Associates, Inc.
Mail Stop 287

WOODSON, S.
Mail Stop 294

WORNOM, S. F.
Mail Stop 159

YAROS, S. F.
Mail Stop 280

YATES, C.
Mail Stop 246

ATTENDEES

NON-LANGLEY

ADAMSON, Thomas C., Jr.
The University of Michigan

AGARWAL, Ramesh K.
McDonnell Douglas Research Labs.

AYERS, Theodore G.
NASA Ames Research Center

BAKER, T. J.
Princeton University

BENGELINK, Ronald L.
Boeing Commercial Airplane Company

BHARADVAJ, Bala K., Dr.
Douglas Aircraft Company

BONNER, Ellwood
Rockwell International Corporation

BRAYMEN, William
General Dynamics

CARLSON, Leland A.
Texas A&M University

CHAN, Y. Y.
National Aeronautical Establishment

CHEN, Lee T.
McDonnell Douglas Corporation

CHRISS, Randall
NASA Lewis Research Center

COLE, Julian D.
Rensselaer Polytechnic

COLEHOUR, Jeffery L.
Boeing Commercial Airplane Company

CONNELL, Stuart
General Electric

COSNER, Ray R.
McDonnell Douglas

DA COSTA, A. L.
Boeing Advanced Systems

DANG, Thong
Douglas Aircraft Company

DAVIS, Warren H., Jr.
Grumman Corporation

DEESE, E. Jerry
McDonnell Dougals Research Labs.

DIRLIK, Steven P.
David Taylor Research Center

DOUGHERTY, F. Carroll
University of Colorado

DRIVER, Cornelius
Eagle Engineering, Incorporated

DUQUE, Earl P. N.
NASA Ames Research Center

GEORGE, Mike
Northrop Corporation

GOLDHAMMER, Mark I.
Boeing

GORDNIER, Raymond E.
University of Cincinnati

GREGOREK, Gerald M.
Ohio State University

GROSSMAN, B.
Virginia Polytechnic Institute
and State University

GRUBER, Glenn J.
Pratt & Whitney

HAFEZ, D. D.
University of California-Davis

HASSAN, H. A.
North Carolina State University

IDE, Hiroshi
Rockwell International

INGER, George R.
Iowa State University

ISHIMITSU, K. K.
Boeing Advanced Systems

JAMESON, Antony
Princeton University

KHOSLA, Prem K.
University of Cincinnati

LAN, C. Edward
University of Kansas

LEVINE, Mark
Rockwell International

LO, Ching F.
Calspan Corporation

LOFTIN, Laurence K., Jr.
Self Employed

LORD, Wesley
Pratt & Whitney

LYNCH, Frank T.
Douglas Aircraft Company

MACWILKINSON, Derek G.
McDonnell Douglas

MADSON, Mike
NASA Ames Research Center

MAGUIRE, William B.
David Taylor Research Center

MALMUTH, Norman D., Dr.
Rockwell International Science Center

MASIELLO, Matthew
Grumman Aerospace Corporation

MAYER, David
Boeing Military Airplane Company

MIDDLETON, Wilbur D.
Boeing Company

MIRANDA, L. R.
Lockheed-California Company

MUELLER, Thomas J., Dr.
University of Notre Dame

NACHMAN, Arje
U. S. Air Force

NAYFEH, Ali H.
Virginia Polytechnic Institute
and State University

NIETUBILZ, Charles J.
Ballistic Research Laboratory

POWELL, Ken
University of Michigan

PUTNAM, Terry
NASA Dryden Flight Research Facility

RATCLIFF, Robert
Texas A&M University

ROSEN, Bruce S.
Grumman Corporation

RUBESIN, M. W.
NASA Ames Research Center

RUBIN, Stanley G.
University of Cincinnati

SCHLEINIGER, Gilberto
University of Delaware

SHREWSBURY, G. D.
Lockheed-Georgia Company

SMITH, Charles
General Dynamics

SMITH, Norbert F.
McDonnell Douglas

SNYDER, James
Wright Patterson Air Force Base

SORRELLS, Russell B.
U. S. Air Force

STEGER, J. L.
NASA Ames Research Center

TINOCO, E. N.
Boeing Commercial Airplane Company

TSENG, Wei W.
Naval Air Development Center

VAN LEER, Bram
University of Michigan

VERHOFF, August Dr.
McDonnell Aircraft Company

VOLPE, Giuseepe
Grumman Aerospace Corporation

WEBBER, Geoff W.
Lockheed Aeronautical Systems Company

WIGTON, Larry
Boeing Aerospace Corporation

WILCOX, Peter
Douglas Aircraft Company

WYCKOFF, John C.
AMETEK

ZICKUHR, Tom
Beech Aircraft Corporation

N89-20943

TRANSONIC PROPULSION SYSTEM INTEGRATION ANALYSIS AT MCDONNELL AIRCRAFT COMPANY

Raymond R. Cosner
Computational Fluid Dynamics
Propulsion/Thermodynamics Dept.
McDonnell Aircraft Company
McDonnell Douglas
St. Louis, Missouri

INTRODUCTION

The technology of Computational Fluid Dynamics (CFD) is becoming an important tool in the development of aircraft propulsion systems. This is largely because CFD analysis methods are gaining the versatility and reliability needed for engineering applications. Two of the most valuable features of CFD are:

- Acquisition of flowfield data in days rather than months.
- Complete description of flowfields, allowing detailed investigation of interactions.

Current analysis methods complement wind tunnel testing by:

- Screening proposed test parametrics, increasing the productivity of wind tunnel programs.
- Assisting in determining the type and location of wind tunnel instrumentation.
- Providing means to assess wind tunnel wall and support interference.
- Helping to interpret wind tunnel data and analyze problems.

This discussion is focused on CFD methods. However, aircraft design studies need data from both CFD analysis and wind tunnel testing. Each approach complements the other.

NOMENCLATURE

BL	Buttline
CAD	Computer-Aided Design
CFD	Computational Fluid Dynamics
Cp	Pressure Coefficient $(P-P_\infty)/q_\infty$
FS	Fuselage Station
MCAIR	McDonnell Aircraft Company
P	Pressure
q	Dynamic pressure
WL	Waterline
α	Angle of Attack
β	Angle of Sideslip, Yaw

Subscripts

t	Total (stagnation) state
∞	Freestream state

GOALS

Several characteristics of an ideal engineering CFD capability can be identified:

- A set of grid generation and flowfield prediction codes applicable to the full range of geometry and flow conditions.

- A database of validated predictions, compared with wind tunnel or flight data, demonstrating that the attainable results are satisfactory for engineering studies and how the results should be adjusted (if appropriate).

- An experience base, defining the steps to be followed in obtaining best results.

- An affordable cost of obtaining solutions -- in terms of both computing resources and engineering labor.

- A system that is easy to learn.

- Rapid turnaround of geometric or flowfield parametric variations.

- Suitable tools to assist the user in preparing and verifying geometric and flowfield input data.

- Suitable tools to assist the user in examining results, and extracting engineering data from CFD results.

- Communication interfaces to reformulate CFD results for input to other codes (e.g., structural, loads, or thermal analyses).

Omission of any of these characteristics can reduce the usefulness of a CFD system for engineering analysis. These items are a statement of objectives rather than a description of our current methods. Improvement is needed. Our efforts have been guided by several general policies. We have chosen to:

- Develop methods to be used by engineers without special training in CFD.

- Develop a limited number of multi-purpose codes, rather than a large number of specialized codes.

- Use a common database format for CFD results.

These objectives represent our interpretation of the best manner to inject CFD into the engineering environment. These goals will be discussed later in this section.

Most engineers and scientists who develop CFD methods are amazed at the reductions in computing costs which have occurred over the past decade, and are continuing to occur. At the same time, however, there has been a sharp increase in the quantity and complexity of CFD analyses. The computer time per job which marks the limit of engineering capability is, in our experience, on the order of 30 minutes to two hours on whatever computers are available. However, the capability that a CFD engineer considers attractive and inexpensive today is usually seen as extremely expensive by a project engineer.

A key consideration at MCAIR has been the need to streamline the operation of CFD codes to the point where non-CFD engineers can use these methods effectively with minimal support from specialists. This approach has, in a sense, been forced by the lack of adequate numbers of CFD specialists. Also, this situation has occurred because some classified projects require a dedicated engineering staff.

The application of new CFD capability passes through several evolutionary stages at MCAIR:

1) Initial development and validation, up to the point where the CFD engineer believes the code can be used for an engineering purpose by someone else.

2) Application by other technology engineers to problems of interest, with continuous support by the original code developer. In parallel, a more thorough validation is performed. The code is modified as a result of this initial experience.

3) After successful application has been demonstrated, engineers on various projects start using the new capabilities with consulting support from CFD specialists.

4) Eventually, project engineers develop enough experience and confidence that they need little support from the CFD specialist.

The key to effective engineering application is to build a high level of versatility into the CFD procedures. This is done in several ways.

At MCAIR, several different Computer-Aided Design (CAD) systems are used, depending on the application, to generate geometric data. Automated tools have been developed to access and translate these different geometric data systems. Improvement of these tools is continuing. The product of these interfaces is a common geometric data format for CFD analysis.

A 3D multiple zone mesh generator has been developed based on this standard geometry format. It serves several different flowfield codes.

The flowfield codes must be applicable to a range of configurations and should not require tuning of non-physical input parameters to obtain results. This goal, for example, favors upwind codes rather than central difference codes which require specification of artificial viscosity parameters or smoothing coefficients.

With a high versatility in each code, the total number of codes can be minimized. This leads to advantages in training engineers, and in maintaining and upgrading the CFD capability.

Common post-processing tools are used so that all CFD data are processed consistently. These tools are supported by a common CFD data file structure. With this common data structure, only a modest number of interface procedures are needed to communicate CFD results to other codes for additional processing.

The project engineer needs tools to assist in preparing CFD input data - both geometric and flowfield data. These include graphics tools to display and verify the input geometry prior to the expense of a 3D mesh generation job.

A set of validation comparisons with test data must be provided. These check cases should be extensive, since they will have maximum value if some of the cases are close to the desired engineering application.

PRE-PROCESSORS

CFD pre-processors assist the user in preparing and verifying input data for the grid and flowfield codes. They are used for:

- Accessing and reformatting data from CAD data bases.
- Displaying and verifying the geometric data.
- Modifying the geometric data.
- Preparing input data files.

Several different systems are used to generate and store geometric data at MCAIR. The most commonly used are the loft data base and the Unigraphics system. Loft data are accessed interactively, with the engineer selecting section cuts and individual points on a workstation. As the points are picked, the coordinates are written to a file. This file is reformatted for input to the CFD procedures. Efforts are in progress to eliminate the man-in-loop process by generating input data from a batch procedure. Batch setup procedures are already in use for Unigraphics data. Interactive interfaces have been prepared for the less commonly used geometric systems.

The product of these interface procedures is a standard geometric definition file. This is a formatted file; the geometry is defined by a sequence of cuts. Each cut is defined by a string of points. For simple geometries, the input data can be set up or modified manually, using a text editor.

Several features have been built into the geometry description method to improve user friendliness. Chief among these is an approach where each cut is defined independently of the other cuts. For example, successive cuts need not have the same number of points. The points within a cut, and the cuts themselves, need not be spaced uniformly. The geometry description is independent of the grid to be constructed.

An interactive procedure has been prepared to display the geometric data prior to executing the grid generator. This verification tool is hosted on a VAX computer and provides displays on Tektronix terminals. The user can examine all or part of the geometry from any viewing angle.

The geometric data file can be modified readily by the user. Several simplified procedures have been written to assist basic propulsion studies, such as changing the compression angles on an inlet ramp. Further efforts in this area are in progress.

GRID GENERATION

Grid generation is often the bottleneck in providing CFD support for engineering studies. One of our top priorities is to improve the application of CFD by developing improved grid generation methods. We need to generate grids quickly and reliably for a range of complex, realistic flight vehicle geometries.

Many approaches are available to meet these needs. We have chosen to develop the approach of dividing a complex solution domain into several sub-domains. Each of these sub-domains, or zones, is geometrically simple and spans a unique region of space. Grid and flowfield algorithms have been developed to provide continuous solutions across the non-physical boundaries between zones.

Two grid generators have been developed for 2D applications. The primary focus of these methods has been inlet configuration modeling, although nozzle applications also have been examined.

The INLETG grid generator was developed for a range of 2D inlet applications. This method has been used for all published applications of our FANSI inlet code, as discussed in the next section and also in References 1 and 2.

Recently, a new 2D grid generator, Program INOZG, has been developed. This method extends the multiple zone method to an arbitrary set of 2D bodies in a flowfield, with arbitrary inflow/outflow boundary conditions as appropriate. The primary advance in this new method is the modeling of multiple inlet and nozzle flow passages.

Three-dimensional multi-zone grids are provided by Program ZGRID. This code supports three full Navier-Stokes methods: X3D, NASTD, and CFL3D (single zones only). ZGRID is applicable to partial or full configurations (fuselage with optional addition of inlet, wings, and tails) and to selected components (isolated inlets, isolated ducts).

FLOWFIELD PREDICTION CODES

A wide range of flowfield prediction codes are used in transonic propulsion integration studies at MCAIR. These range from 2D integral boundary layer methods to 3D zonal time-marching Navier-Stokes codes. Only codes based on the Navier-Stokes equations will be discussed in detail.

Velocity-Split Navier-Stokes Methods - Three analysis methods have been developed at MCAIR based on the velocity-splitting method. The first procedure (Ref. 3) was developed as a testbed for axisymmetric afterbody-plume combinations and is not an engineering tool. The second procedure, Program AFTEND, applies to analysis of 3D forebody-afterbody combinations. Several results from AFTEND have been published (Refs. 4, 5, and 6).

The same methodology was implemented in Program X3D, with improvements for multiple zone analysis and improved vector processing efficiency. This code uses our ZGRID grid generator. X3D is currently considered our most sophisticated engineering tool for 3D transonic viscous analysis.

Time-Dependent Navier-Stokes Methods - Two time-dependent analysis codes are in use or under development. Both are based on non-overlapping multi-zone grid methods to achieve maximum geometric capability.

A two-dimensional code, Program FANSI, was developed for inlet flowfield analysis (Refs. 1 and 2). This code has gained wide application at all speeds of interest, and is the most-used Navier-Stokes code at MCAIR.

A three-dimensional code using the same methodology as FANSI is under development. This program (NASTD) is an implicit, upwind, finite-volume code based on the approximate factorization method. NASTD also uses the ZGRID grid generator, and therefore has the same geometric applicability as Program X3D. Due to the higher solution cost of this time-marching methodology, NASTD is generally used on a limited basis to check results from X3D. At this time, the primary applications of NASTD are at higher speeds.

In summary, analysis of propulsion integration flowfields is based on a family of analysis methods of varying sophistication and cost. Several methods have been developed based on the Navier-Stokes equations. Results from these methods will be presented below. Initial inlet and nozzle trade studies often are based on the 2D Navier-Stokes code, FANSI. Transonic trade studies and integration analyses are performed by X3D, with selective use of NASTD.

POST-PROCESSING

Post-processing provides the tools for the project engineer to extract needed information from CFD results. To simplify post-processing, we have defined a Common Data File for CFD results. All codes used for propulsion analysis enter their results into this file structure for post-processing and for long-term storage. Currently, 26 CFD codes are integrated into this system. These include 2D (planar, axisymmetric) and 3D codes using Euler, PNS, and full Navier-Stokes methodologies. Codes using both perfect and real gas models are supported, along with combustion analysis programs.

This structure is a random-access file, storing the data in binary form. This format provides rapid input/output (I/O) and avoids the need to read and store a full flowfield file in order to use the post-processors. Binary-to-binary conversion routines have been prepared to transfer data between dissimilar computers. Currently, these common data files are created on Cray, VAX, and Convex computers; they are generally moved to a VAX computer for post-processing.

All propulsion post-processing packages access this Common Data File. Thus, our engineers only need to learn to use one set of graphics software. Full graphics support can be provided quickly for a newly received code simply by inserting interface subroutines that write the data into the common format. This interface task typically requires about one day. Another advantage is that a single set of post-processing software is used. Therefore, all CFD results are processed consistently regardless of their source.

At MCAIR, CFD graphics are supported using Tektronix terminals (both black/white and color displays) and the Silicon Graphics IRIS Workstation. Several software packages are in use:

PLTTR - This package, which was developed at MCAIR, is hosted on a VAX or Convex computer and presents displays on Tektronix 40xx and 41xx terminals. Several functions are available. The most commonly used are contour plots, vector plots, surface function plots (Cp vs. x, etc.) and boundary layer profiles. These plots are not restricted to grid surfaces; linear interpolation is performed as required. Experimental data and more than one set of CFD data can be presented on the same plot for comparison.

Other functions include a force/moment integration, printout of various properties, and integration of flow properties in an arbitrary closed contour in the flowfield.

MOVIE.BYU - This is a program developed at Brigham Young University for displaying 3D geometries and flowfield properties. At MCAIR, it operates on VAX computers with the displays presented on Tektronix terminals. An interactive interface program has been written to extract data from the Common Data File along selected grid surfaces for display by MOVIE.BYU.

PLOT3D - PLOT3D is a software package developed at NASA Ames Research Center which runs interactively on the Silicon Graphics IRIS Workstation. This system has a tremendous range of capabilities and in most respects is our most powerful graphics tool. We have written a menu driver for PLOT3D, to facilitate its use by inexperienced engineers. This package is described in Reference 7.

TRACE - This is a program developed at MCAIR to compute and display off-body or surface streamlines. It runs on a VAX computer, and provides displays on a Tektronix terminal. Recently, we have used the surface streamline capability to define flow properties along an Euler streamline at a wall, providing data for subsequent strip analysis using 2D boundary layer codes.

ARTIS - ARTIS is a software set developed at Douglas Aircraft Co. for interactive displays on the IRIS Workstation. Its display capabilities, which are discussed in Reference 8, are generally similar to MOVIE.BYU. ARTIS is a menu-driven package. Our engineers generally need less than 30 minutes of instruction to become self-sufficient. This is the most commonly used graphics package at MCAIR, for engineers who have access to an IRIS Workstation.

APPLICATIONS

Several representative applications of CFD in transonic propulsion system integration are discussed below. Many of these results have been published previously.

Forebody Flowfield - Accurate prediction of forebody flowfields is important to selecting candidate inlet concepts and integration locations. In particular, the engineer needs accurate data on flow angularity, local Mach number, and local total pressure recovery.

The flowfield for an isolated forebody, depicted in Figure 1 was computed with Program X3D. The flow condition is Mach 0.9, 10° angle of attack (α). This calculation, which was previously presented in Reference 4, was validated with experimental data acquired under MCAIR IRAD funding. The computed flow angularity is in good agreement with test data. Typically, the mismatch is less than one degree.

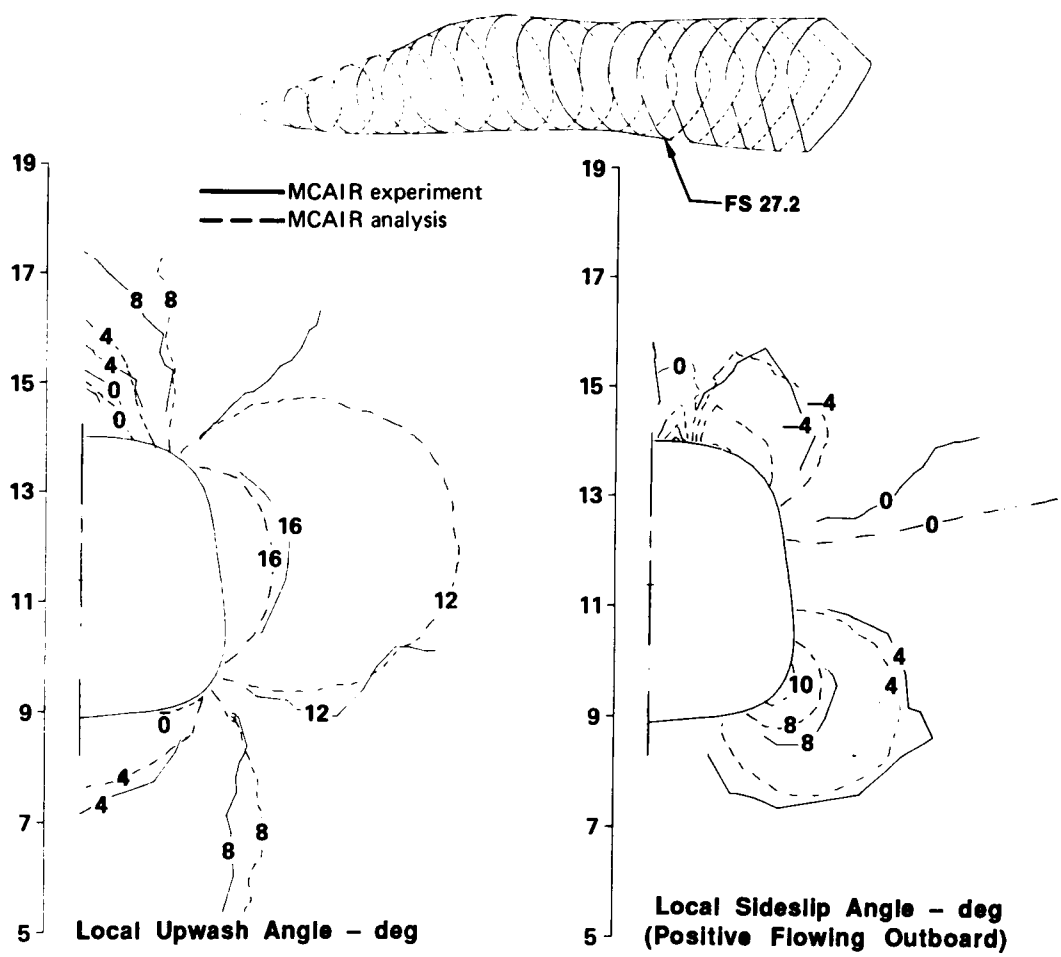

Figure 1. Flow Angularity
Forebody Flowfield
Mach 0.9 $\alpha = 10°$ FS 27.2

ORIGINAL PAGE IS
OF POOR QUALITY

Similar results for the Project Tailor-Mate A-1 forebody (Ref. 9) are presented in Figure 2. For this case, Mach 0.9 at high angle of attack, the level of agreement in angularity is 1° to 2°, satisfactory for most inlet integration studies.

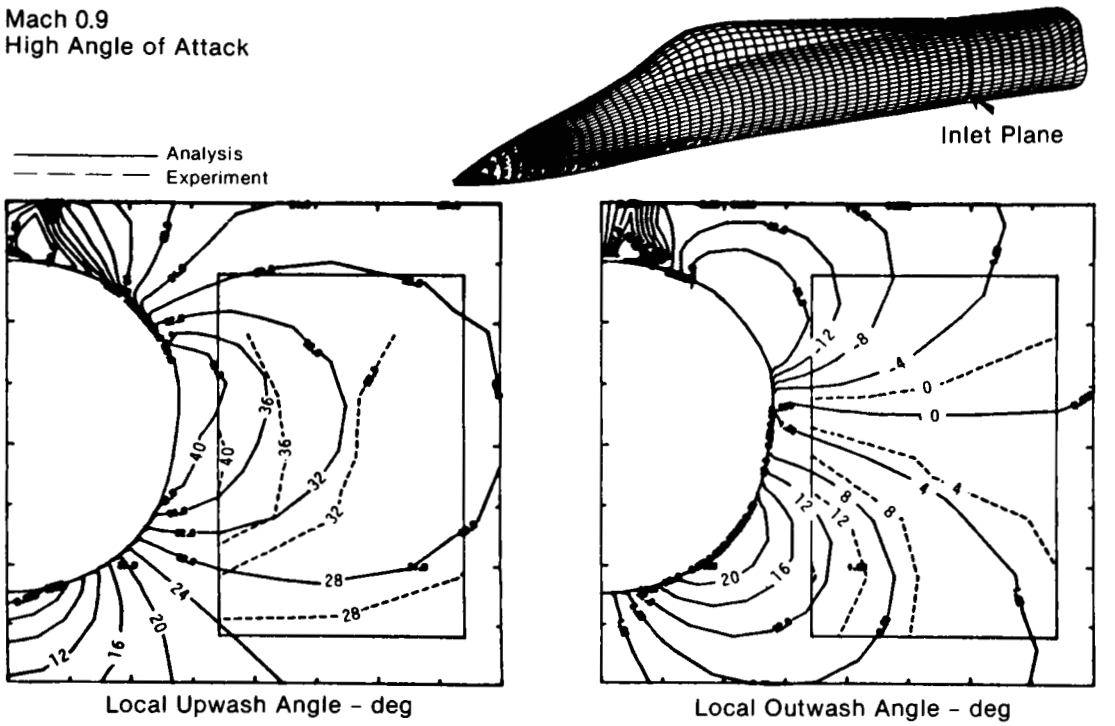

Figure 2. Flow Angularity Comparison
Tailor-Mate A-1 Forebody

Specialized post-processing capability can greatly enhance the value of CFD analysis. One example is shown in Figure 3, presenting data from an inviscid solution of the F-18 forebody at Mach 0.8, a=0°, 7.5° yaw angle (β). For this condition, some distortion was observed in the lee-side engine face flowfield. We defined the streamtube captured by the inlet on the lee side of the yawed forebody, using a predecessor of the program TRACE, described earlier.

These results showed that the captured streamtube is initially speared by the nosetip. The streamtube falls off to the lower surface of the fuselage, then sweeps around to the lee side as it moves aft. During this process, air from the boundary layer is entrained in the streamtube, leading to flow distortion in the inlet. These results were subsequently validated by a wind tunnel study using smoke to visualize this streamtube.

Program NASTD has been used to analyze vortex flowfields over various highly swept wing-body configurations. One such configuration was taken from the Cooperative Propulsion Integration Program (Reference 10). This is a joint MCAIR/USAF/NASA study. Representative results are presented in Figure 4. At Mach 0.9, α=18°, the CFD analysis has predicted the vortex location to good accuracy. However, for supersonic flow - Mach 2.0, α=12° - the predicted vortex is too high, and too far inboard. Investigations are in progress to improve this type of prediction.

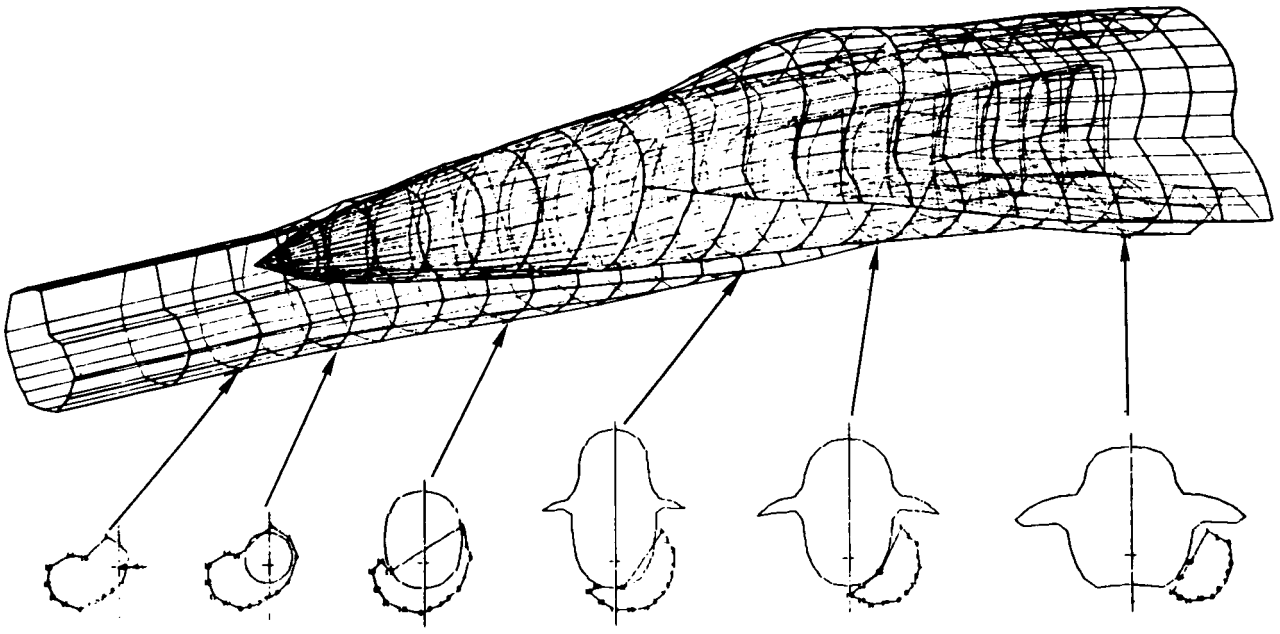

Figure 3. Forebody Flowfield Capture Streamtube Tracing
Forebody/Strake Configuration
$M_\infty = 0.8 \quad \alpha = 0° \quad \beta = 7.5°$

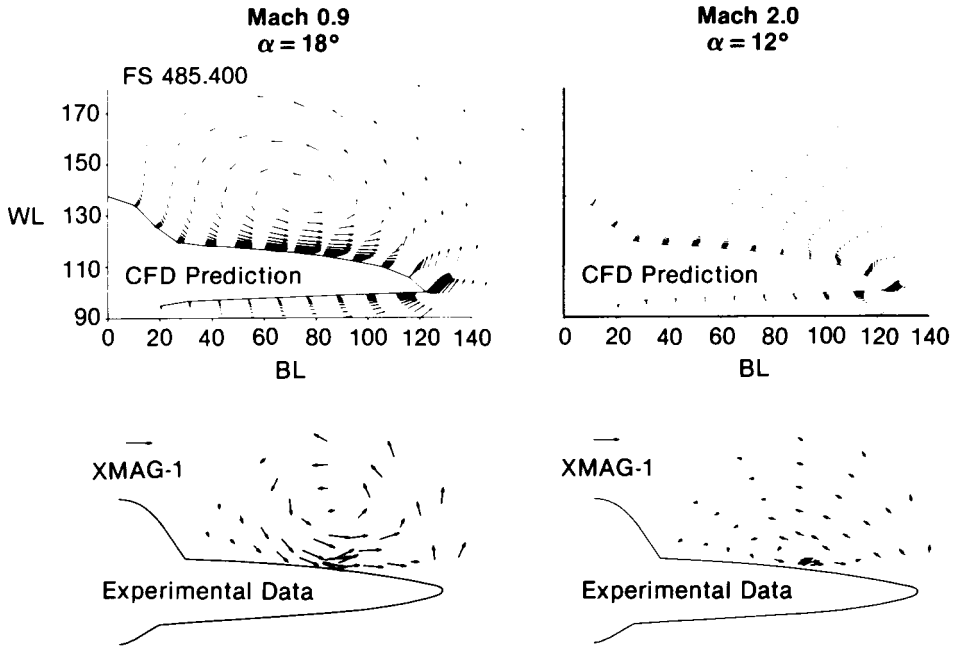

Figure 4. CFD Comparison With Test Data
Wing-Body Vortex Flowfield
Program NASTD

ORIGINAL PAGE IS
OF POOR QUALITY

ORIGINAL PAGE IS
OF POOR QUALITY

Isolated Inlet - Our primary tool for analysis of isolated inlets is Program FANSI. This 2D code has high geometric flexibility and a short run time for parametric investigations. Details of this method have been presented in References 1 and 2. This code has been validated for recovery predictions in 2-D inlets.

Initial validation of the FANSI code focused on total pressure recovery predictions. Sample results for several different mass flow rates are presented in Figure 5. The effect of different flow rates on shock locations is readily depicted. In the lower left portion of the figure, the dependence of recovery on mass flow is presented. These data include CFD analysis, test data, and simple estimates based on oblique shock theory. In general, the computed recovery agrees well with test data, although the accuracy falls off somewhat at the lower mass flow rates. This is attributed to spill over the sidewalls, which is not modeled in the 2D analysis.

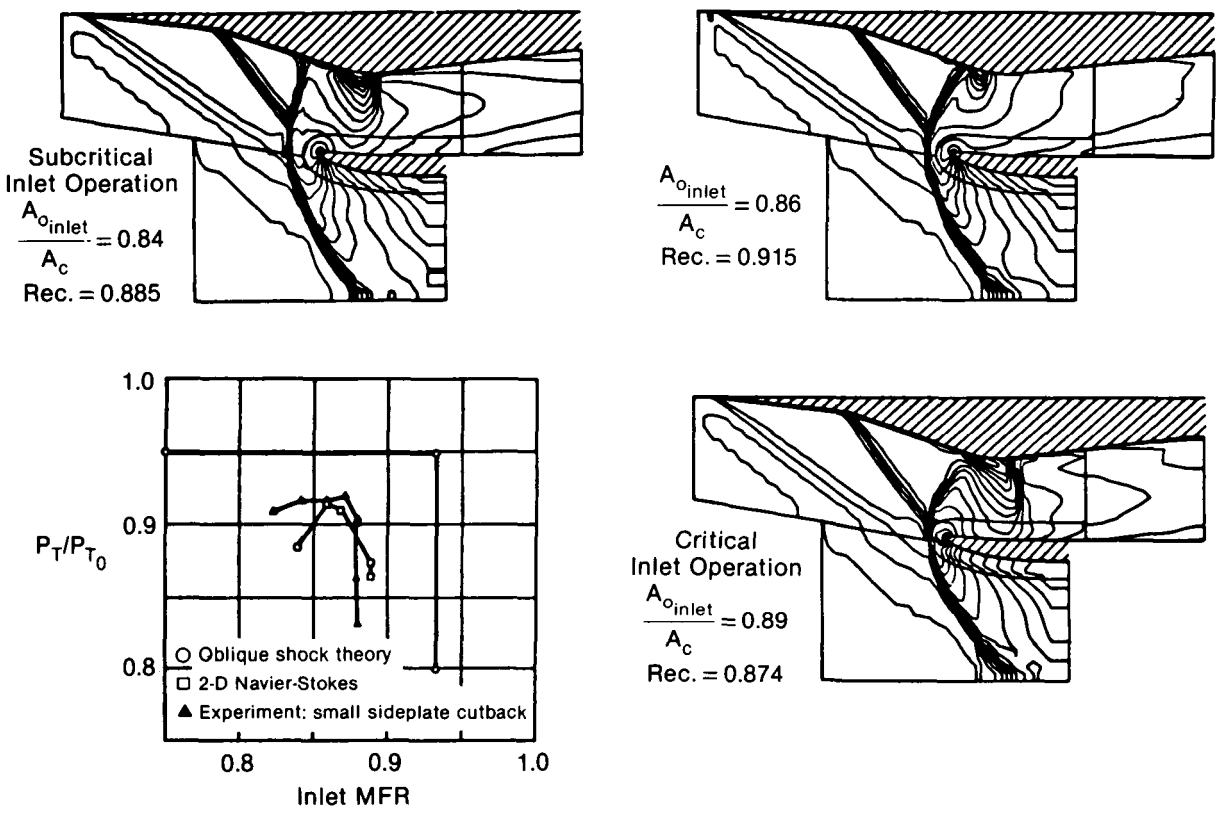

Figure 5. Effect of Mass Flow Variation on Supersonic Inlet Flowfield

With these tools, CFD results also can be used to determine the amount of bleed required to control boundary layer behavior. The results shown in Figure 6 describe the impact of different ramp bleed rates on boundary layer displacement thickness. For this example, a ramp bleed of 1% removes about two-thirds of the boundary layer, while 2% bleed completely eliminates the viscous layer.

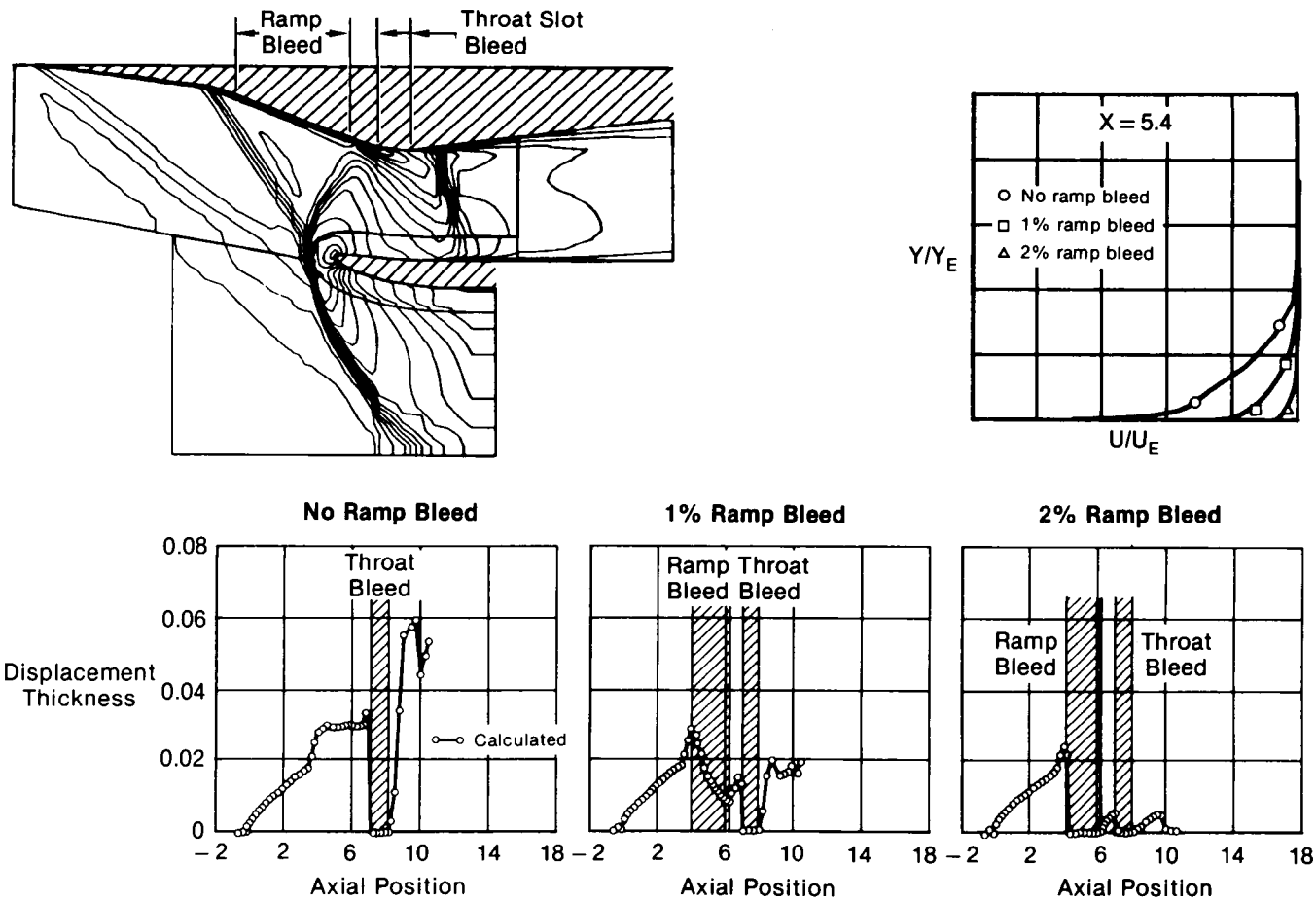

Figure 6. Effect of Inlet Bleed on Boundary Layer Thickness

Another key issue in inlet design is the selection of the proper lip contour. The FANSI code can be used with a C-grid about the inlet lip for accurate results in lip contour evaluation. Sample results are shown for a supersonic inlet in Figure 7. This inlet was designed for low supersonic drag and consequently features a sharp lip.

An analysis of this same configuration was done at takeoff conditions, where sharp lips often create flow quality problems. The stagnation point for the captured flow is on the lower surface of the cowl. The flow runs forward along the outside surface of the cowl, then attempts to turn sharply at the lip. The flow cannot follow this sharp contour, and separates from the inside of the lip. This separation extends downstream for about two duct heights. The analysis code also has captured a secondary vortex under the large separated zone.

The FANSI code was used to examine alternate lip designs. One concept is an actuated, drooped lip. Such a design can be used for improving low speed, high mass flow performance as well as for high a flight at higher speeds. This concept was tested recently at NASA Lewis Research Center (Ref. 11). The CFD results agree with test data in showing that a 20° lip droop provides high recovery for this inlet at high angle of attack, as shown in Figure 8.

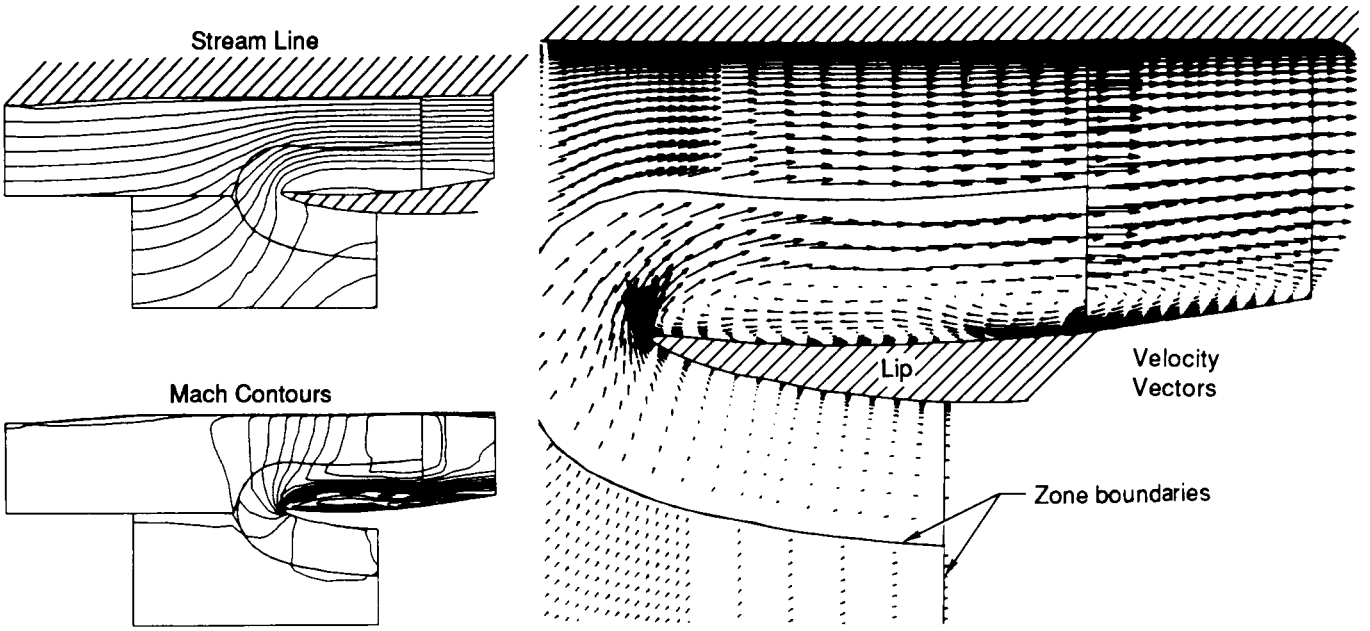

Figure 7. Cowl Lip Flow at Takeoff

Mach 0.1 $\left.\frac{A_o}{A_c}\right|_{inlet} = 4.5$ No Bleed

20° Rotated Cowl Lip Configuration

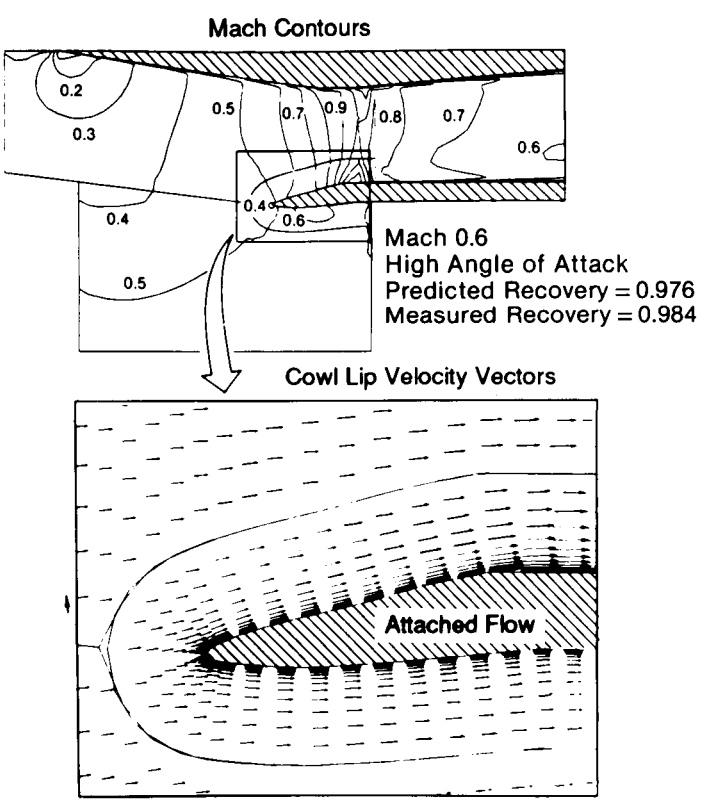

Comparison of 2-D Flowfield Analysis Code Predictions With Experimental Total Pressure Recoveries

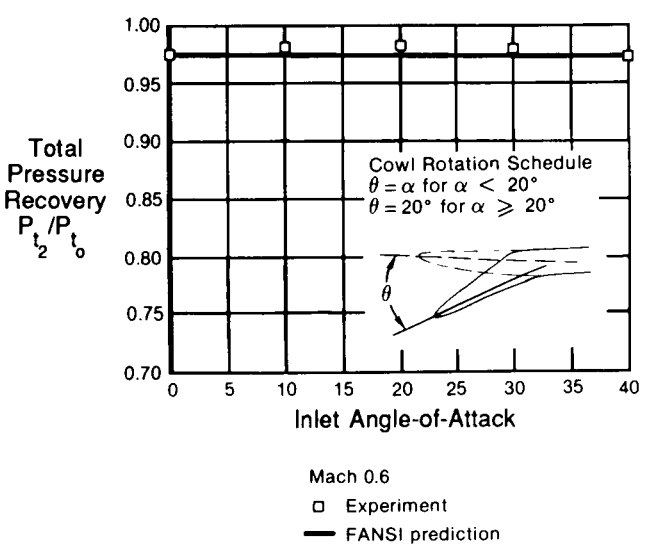

Figure 8. Rotated Cowl Performance
Prediction vs Experiment

The flowfield about an undrooped cowl lip at Mach 0.6, high α is presented in Figure 9. The flow separation inside the lip is clearly revealed. The predicted pressures agree very well with experimental data. With the lip drooped 20° the flow remains attached, as shown in Figure 8. The predicted inlet recovery is nearly constant over a range of α in agreement with test data. A comparison of lip surface pressures, CFD versus test data, is presented in Figure 9. The predictions show acceptable accuracy for engineering studies.

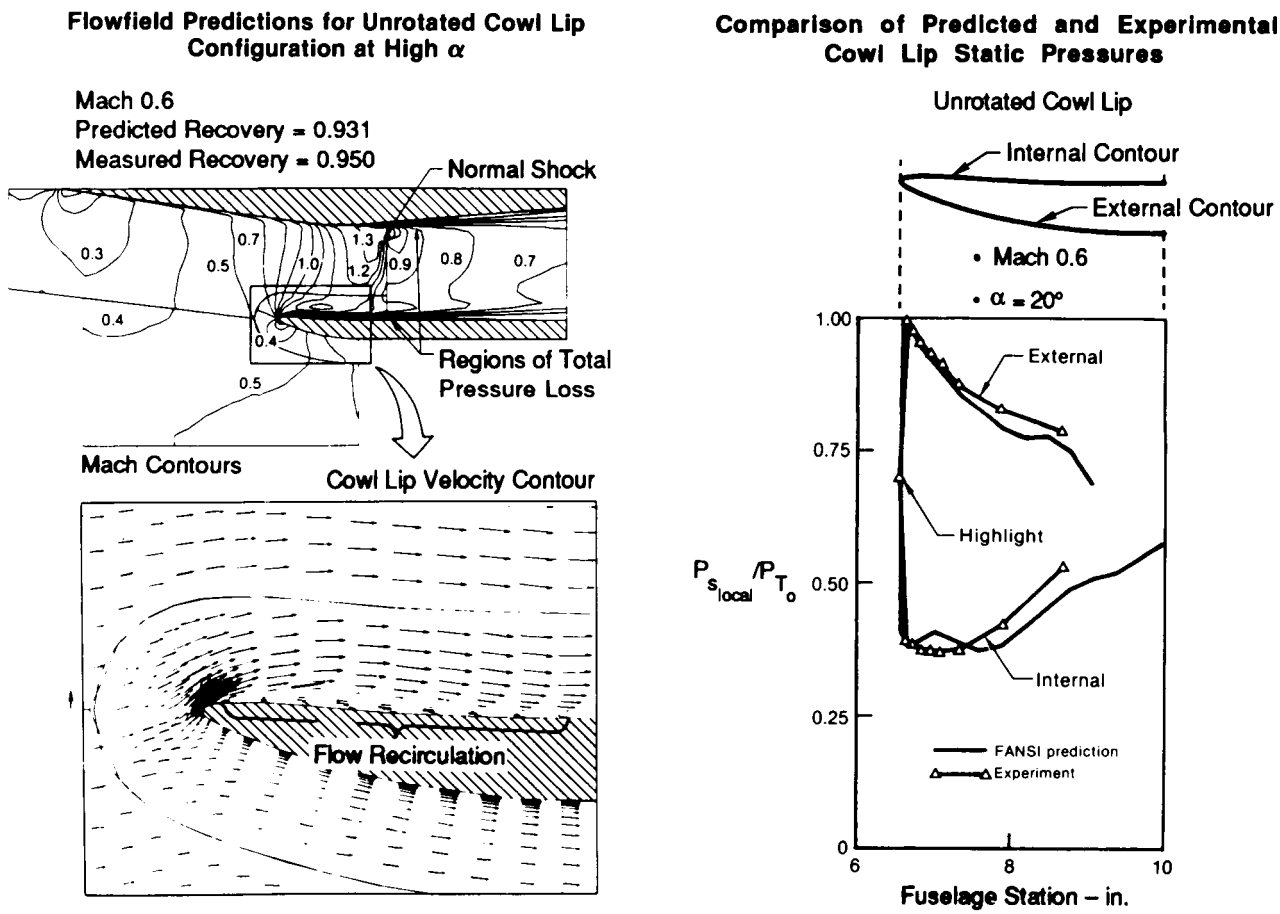

Figure 9. CFD Predictions Compare Favorably With Experimental Results

The 3D codes X3D and NASTD have been used to predict flow over 3D isolated inlets. An inviscid solution from X3D is presented in Figure 10. This example presents flow at Mach 2.0 through the A-1 inlet from the Tailor-Mate program. This test was conducted by General Dynamics, under contract to the Air Force. An inviscid NASTD solution is presented in Figure 11, for an inlet tested by MCAIR at NASA Lewis Research Center (Ref. 11). Both these isolated inlet solutions used a two-zone mesh from ZGRID. The boundary between zones extends forward from the inlet highlight, and can be seen in these two figures. The oblique and normal shocks pass cleanly through the zone boundary, and the spill over the inlet lip and sidewalls is captured.

ORIGINAL PAGE IS
OF POOR QUALITY

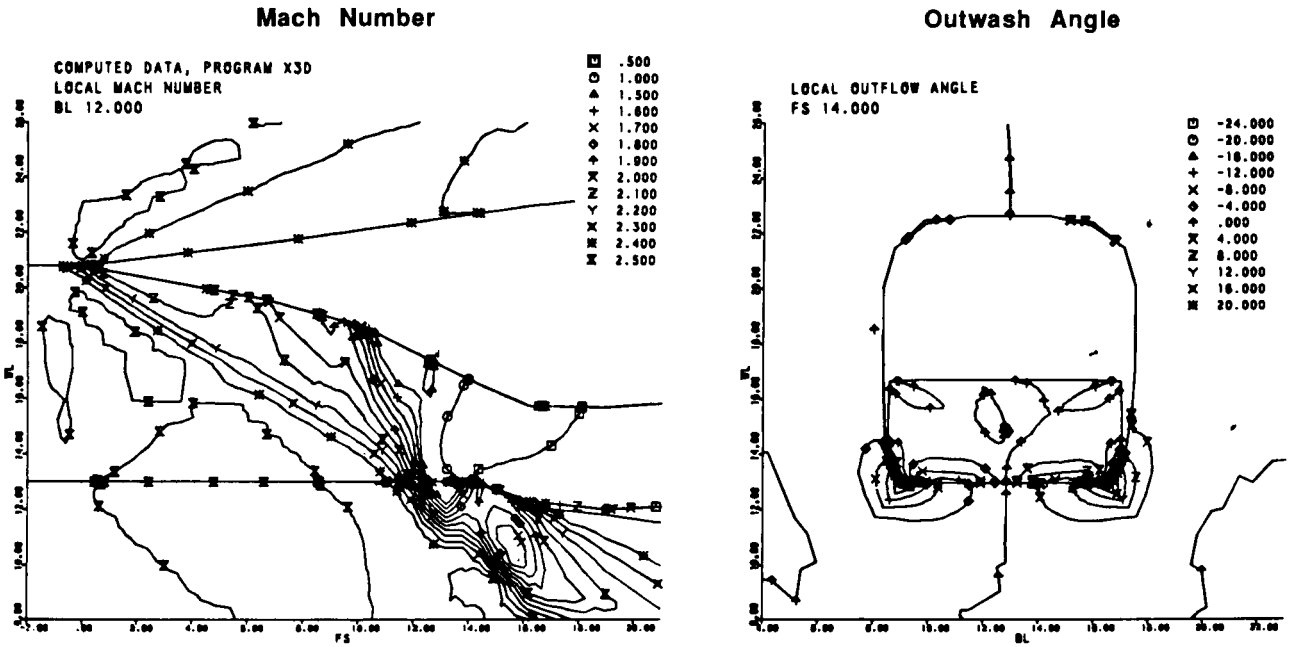

Figure 10. Tailor-Mate A-1 Inlet
Mach 2.5, With Bleed
X3D Inviscid Solution

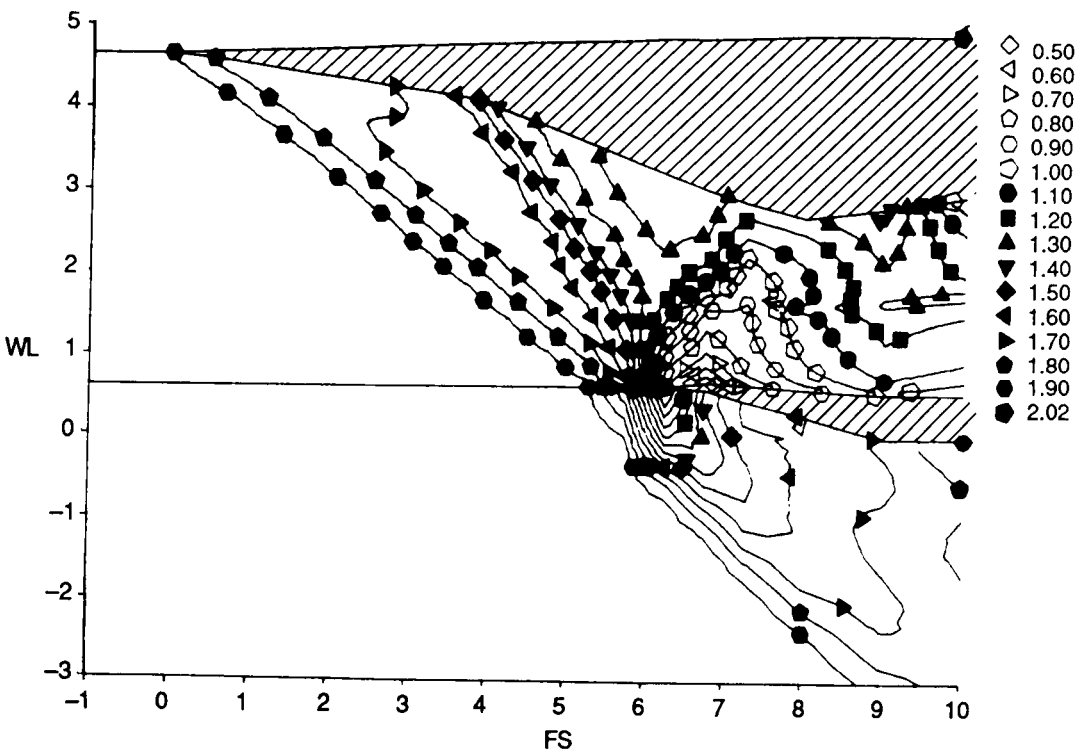

Figure 11. Supercruise Inlet Analysis, Mach 2.0
Program NASTD

Isolated diffuser - Another key element of the propulsion system is the inlet diffuser. Detailed analysis of diffuser flowfields can be a critical concern in aircraft design. Sample analysis results are presented for several cases.

ORIGINAL PAGE IS
OF POOR QUALITY

As part of the Ref. 12 study, MCAIR designed and tested several concepts for compact, highly offset diffusers. Many of these concepts were analyzed using Program X3D. One result, for the so-called B19 diffuser, is presented in Figure 12. Strong viscous interactions are present as a result of a high rate of diffusion and a high offset. The boundary layer is completely separated from the upper wall for about half the diffuser length, as seen in the total pressure contour plots. The predicted area-averaged total pressure recovery is in reasonable agreement with the test data, as seen in Figure 13.

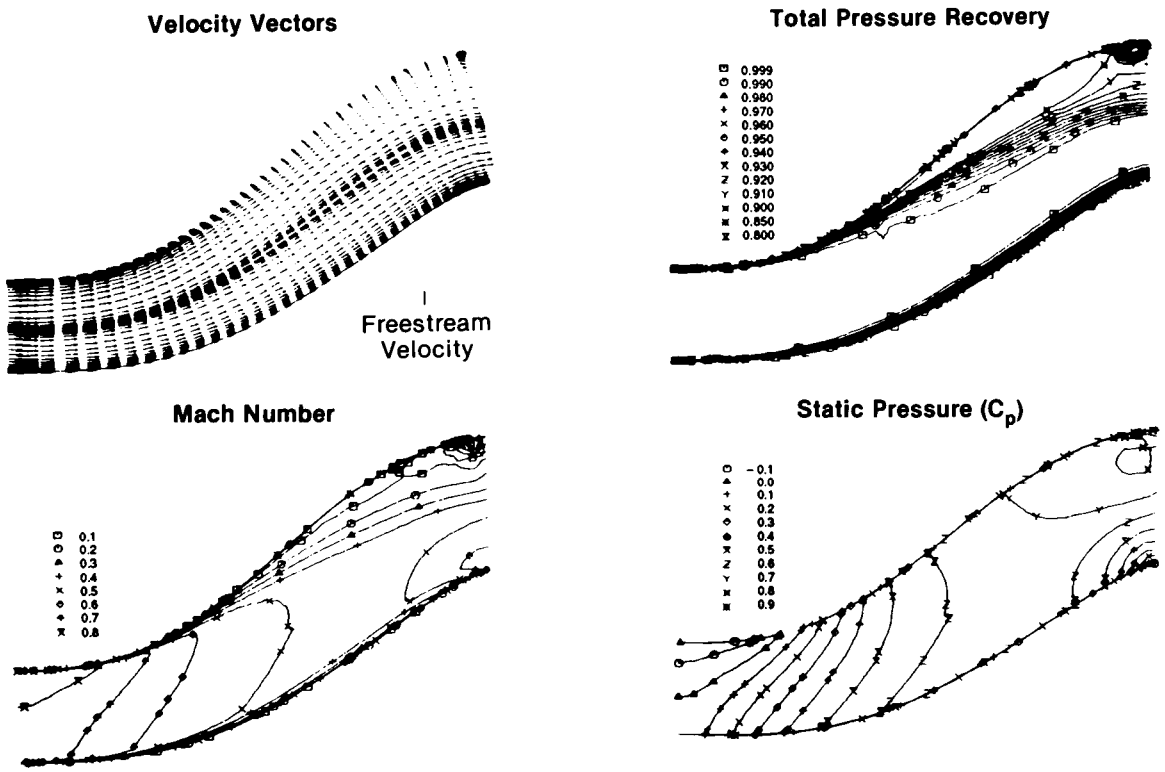

Figure 12. B19 Diffuser Flowfield
Uniform Inflow Mach 0.777

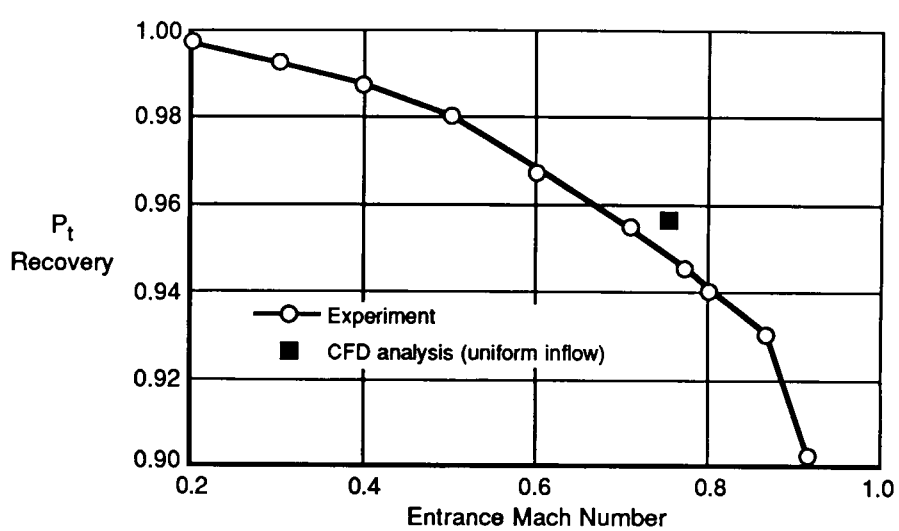

Figure 13. Recovery Prediction
B19 Diffuser

ORIGINAL PAGE IS
OF POOR QUALITY

ORIGINAL PAGE IS
OF POOR QUALITY

ORIGINAL PAGE IS
OF POOR QUALITY

In the same study, the X3D code was used to assess the impact of diffuser entrance conditions on exit properties. Predictions were made for cases with uniform inflow, and with measured inflow data taken from entrance flowfield surveys. The predicted total pressure profiles for these two cases are presented in Figure 14. These results show that the exit total pressure distribution is significantly affected, even though the core entrance Mach number is practically the same (0.005 difference).

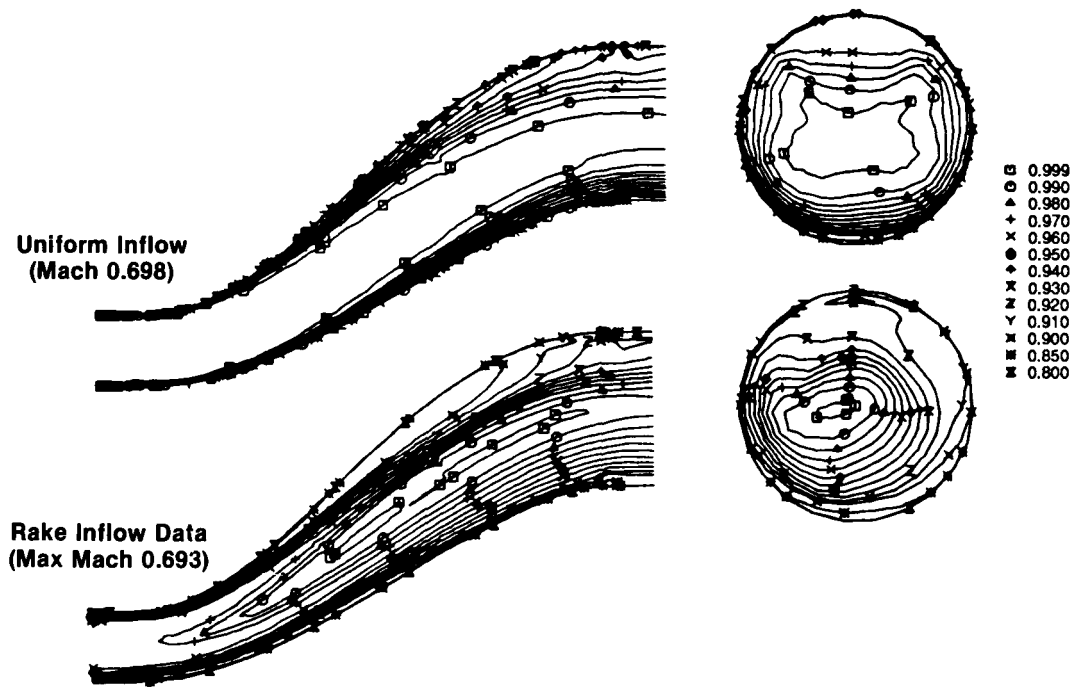

Figure 14. Effect of Inflow Condition
ADII Diffuser
Total Pressure Recovery
CFD Analysis

The diffuser exit area-averaged recovery for these two inflow conditions is presented in Figure 15. The recovery predictions with uniform inflow are unacceptably high compared with test data. By recognizing the proper inflow, but otherwise performing the same analysis, the recovery prediction error is reduced considerably.

Integrated Forebody-Inlet - The X3D code is used extensively for analysis of integrated forebody-inlet combinations. Some results have been presented in Ref. 13. The initial application was for a representative fighter geometry. Predictions were validated by comparison with wind tunnel data for Mach 0.8, a=0°. These results are presented in Figure 16. The comparison is made for pressures on the inside of the lower inlet lip. Good accuracy is demonstrated at both a flight idle mass flow rate (116 lb/sec) and near-maximum mass flow (155 lb/sec).

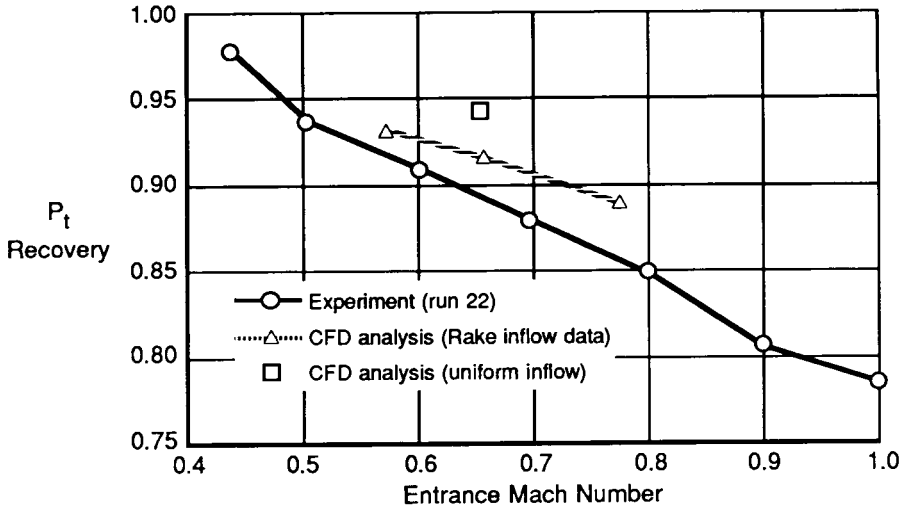

Figure 15. Recovery Prediction
ADII Diffuser

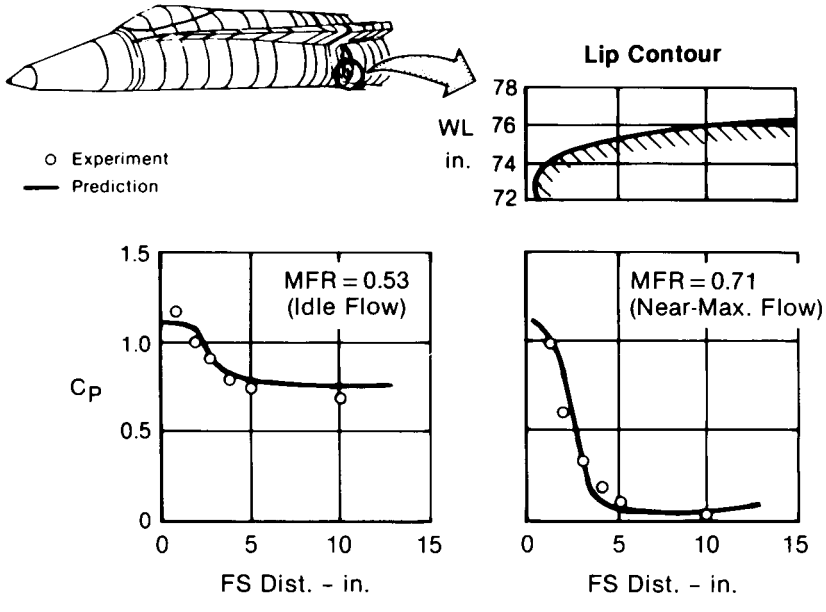

Figure 16. Inlet Internal Pressure
Bottom Lip Static Pressure Mach 0.8 $\alpha = 0°$

ORIGINAL PAGE IS
OF POOR QUALITY

The analysis code also provides valuable information which was not acquired in the wind tunnel program. In one example, CFD was used to investigate the effect of engine airflow rate on forebody pressures, as shown in Figure 17. Predicted data are shown for the two mass flow rates presented previously and also for zero net mass flow through the inlet. The integrated mass flow is zero, but the method allows local flow into or out of various portions of the inlet entrance plane. These results show a forebody pressure impact which extends upstream more than 100 inches from the inlet entrance.

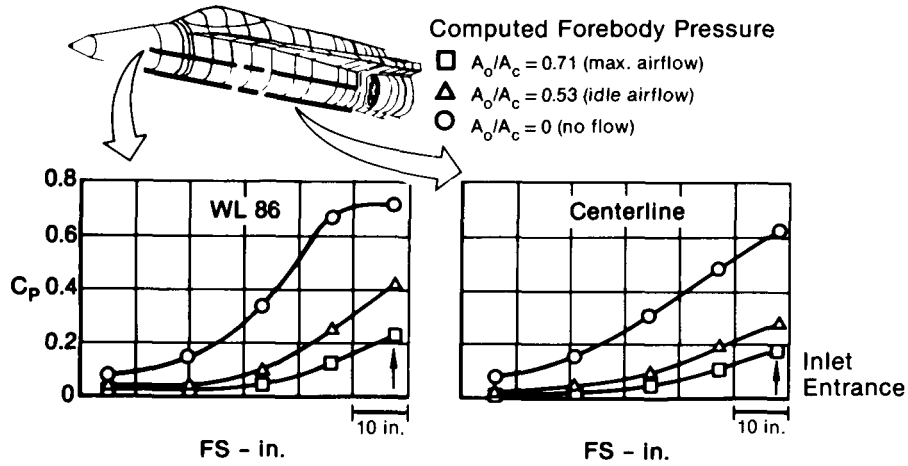

Figure 17. Effect of Engine Airflow on Fighter Forebody Pressure
Mach 0.8 $\alpha = 0°$

Similar analysis has been conducted for other inlet ducts. As seen in Figure 18, the analytical data agree well with test data for the inside of the lower lip at Mach 0.67, a=10°. The extensive data provided by CFD analysis also allowed detailed examination of additional flow properties, such as surface static pressure (right side of Figure 18).

The development of the total pressure field in an inlet duct is presented in Figure 19. At Fuselage Station (FS) 225, which is about five inches inside the inlet, the viscous layer is very thin and behaves as a simple boundary layer. In the middle of the duct (FS 245), the viscous layer is much thicker and is not behaving as a simple boundary layer on the inboard wall: the total pressure contours are not parallel to the wall. Three inches in front of the engine face (FS 260), a complex pattern of total pressure loss is predicted. A more detailed examination of this and other solutions was used by engineers to suggest duct modifications which were incorporated into production AV-8B's.

Nozzle Internal Flow - All three zonal Navier-Stokes codes (FANSI, NASTD, X3D) have been applied to nozzle internal flow. The objectives have been to predict effective vector angles, nozzle internal losses, wall heating distributions, and the overall development of flow properties in the duct. Sample results are presented in Figure 20 for the throat region of a 3D nozzle analyzed using NASTD.

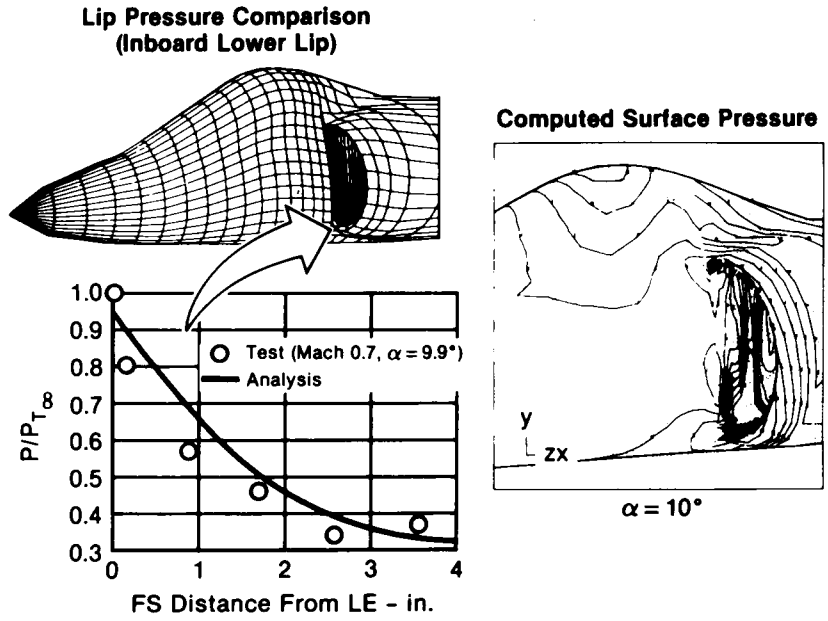

Figure 18. Forebody-Inlet Viscous Analysis
Mach 0.67 $\alpha = 10°$ Cruise Airflow

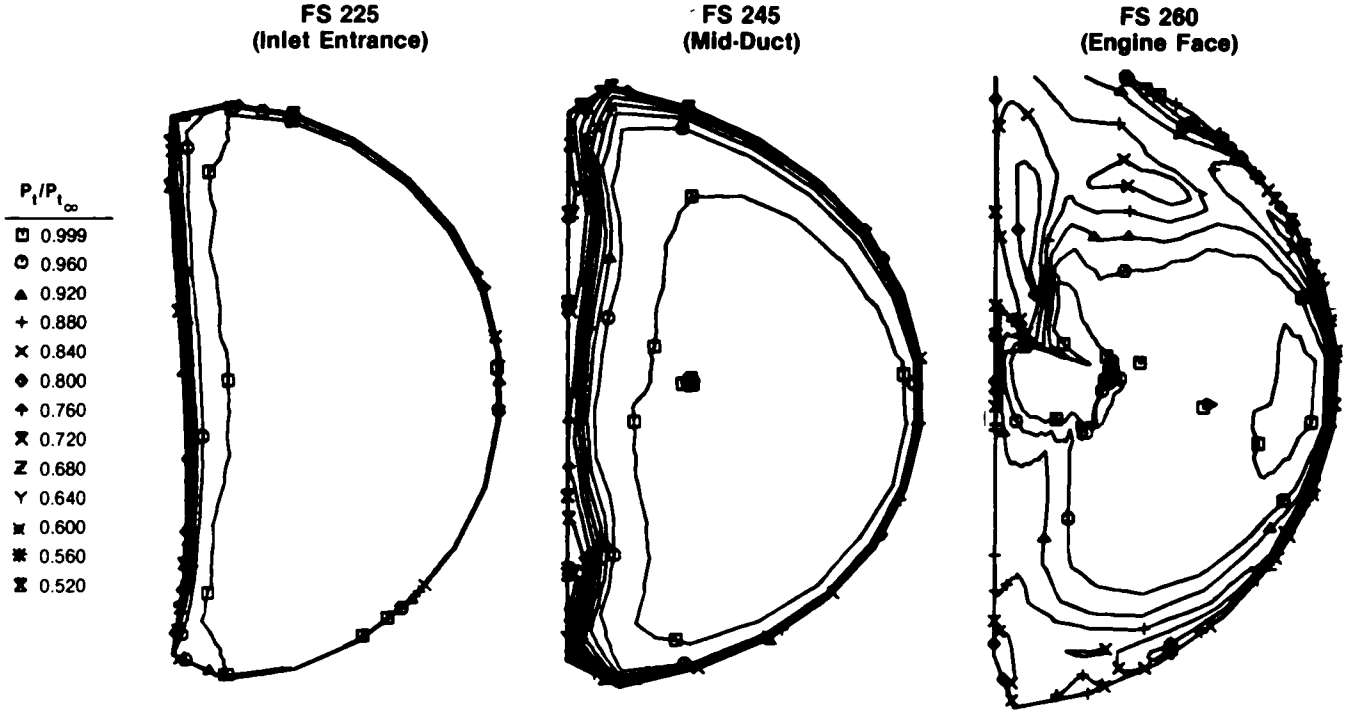

Figure 19. Computed Total Pressure Distribution
Fighter Diffuser Mach 0.67 α 0.67 Cruise Airflow

ORIGINAL PAGE IS
OF POOR QUALITY

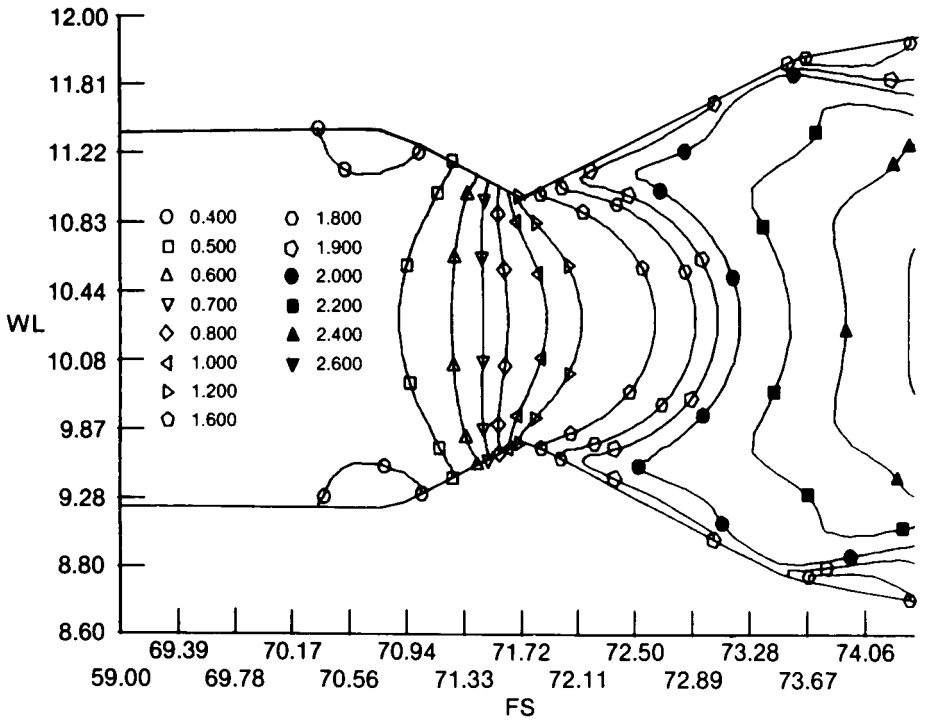

Figure 20. Mach Contours for 3D Nozzle Internal Flow

Nozzle External Flow - The initial development of the velocity-splitting method was aimed at analysis of nozzle-afterbody configurations at transonic speeds. Several applications have been published in past years (Refs. 4 and 5). Most of our validation efforts for afterbody-nozzle external flow have been based on the test data from the Advanced Nozzle Concepts (ANC) Program, Ref. 14.

A comparison between test and analysis for the baseline axisymmetric nozzle from the ANC program is presented in Figure 21. This case is for a dry power (non-afterburning) nozzle setting at Mach 0.9, $\alpha=0°$. At the time this analysis was performed (1983), we could not represent the vertical tail. Omission of this component did affect the prediction accuracy somewhat over the upper surface behind the vertical tail, but the agreement was good elsewhere. The most important figure of merit for afterbody flowfield prediction is the drag accuracy. For this case, our analysis agreed with test data, with a one count (0.0001) error in drag coefficient.

Similar results for Mach 2.0 are presented in Figure 22. Again, excellent agreement is obtained for the baseline axisymmetric nozzle - one count error in pressure drag. For the 2D nozzle, the pressure drag error is not as good - seven counts.

ORIGINAL PAGE IS
OF POOR QUALITY

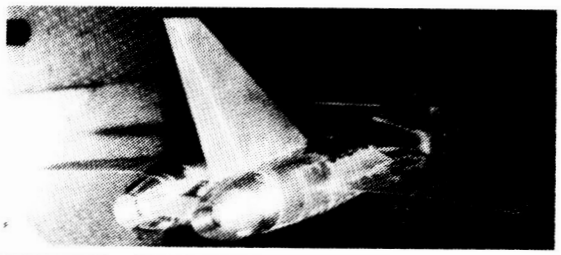

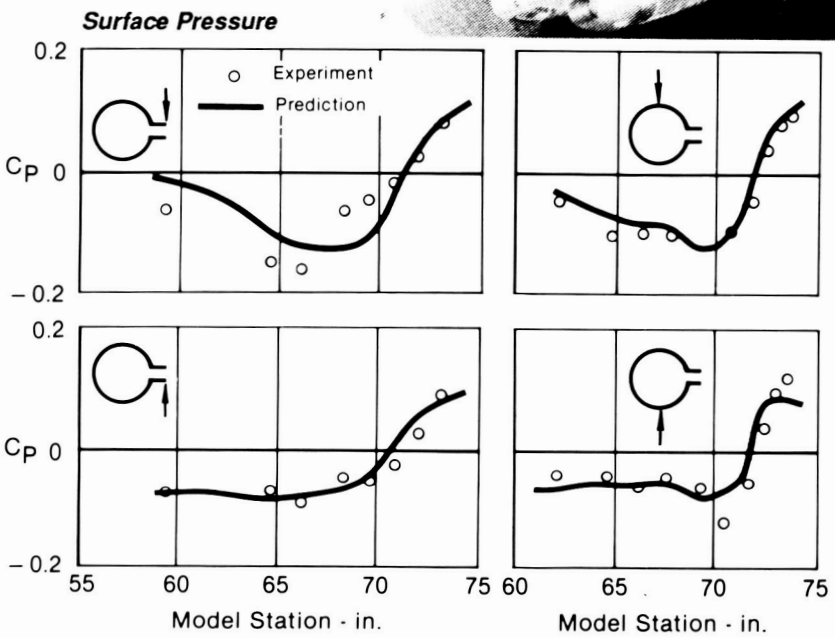

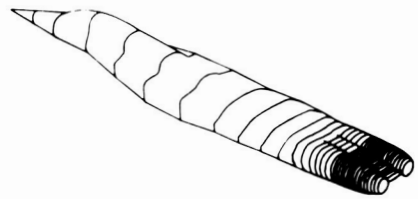

Pressure Drag Coefficient (Based on Wing Area)

	Experiment	Prediction
Afterbody	0.0018	0.0016
Nozzle	− 0.0009	− 0.0008
Net	0.0009	0.0008

Figure 21. Pressure and Drag Prediction
ANC Air-to-Surface Model
Baseline Axi Nozzle
Dry Power Mach 0.9 $\alpha = 0°$

More recently, NASTD has been used to analyze external flow over nozzles tested in the USAF/MCAIR program "High Performance Supercruise Nozzles" (Contract F33615-84-C-3003). Comparisons between CFD and test data at Mach 0.9 are presented for the Pratt and Whitney Tandem Disk 2D C-D Nozzle in Figure 23. These comparisons present the longitudinal variation of surface pressure on the upper surface nozzle centerline, and also the boundary layer profile at the start of the nozzle. These data show generally good agreement in the surface pressure and excellent agreement in the approach boundary layer profile. The afterbody pressure drag is predicted to about 10% accuracy; the CFD drag coefficient based on wing area is 0.0056; the coefficient computed from measured data is 0.0050.

Our prediction accuracy for 3D afterbody drag is not consistent however. It is excellent for some cases, disappointing for others. Current usage therefore is generally restricted to examination of flowfield features and relative variations in drag due to moldline changes.

ORIGINAL PAGE IS
OF POOR QUALITY

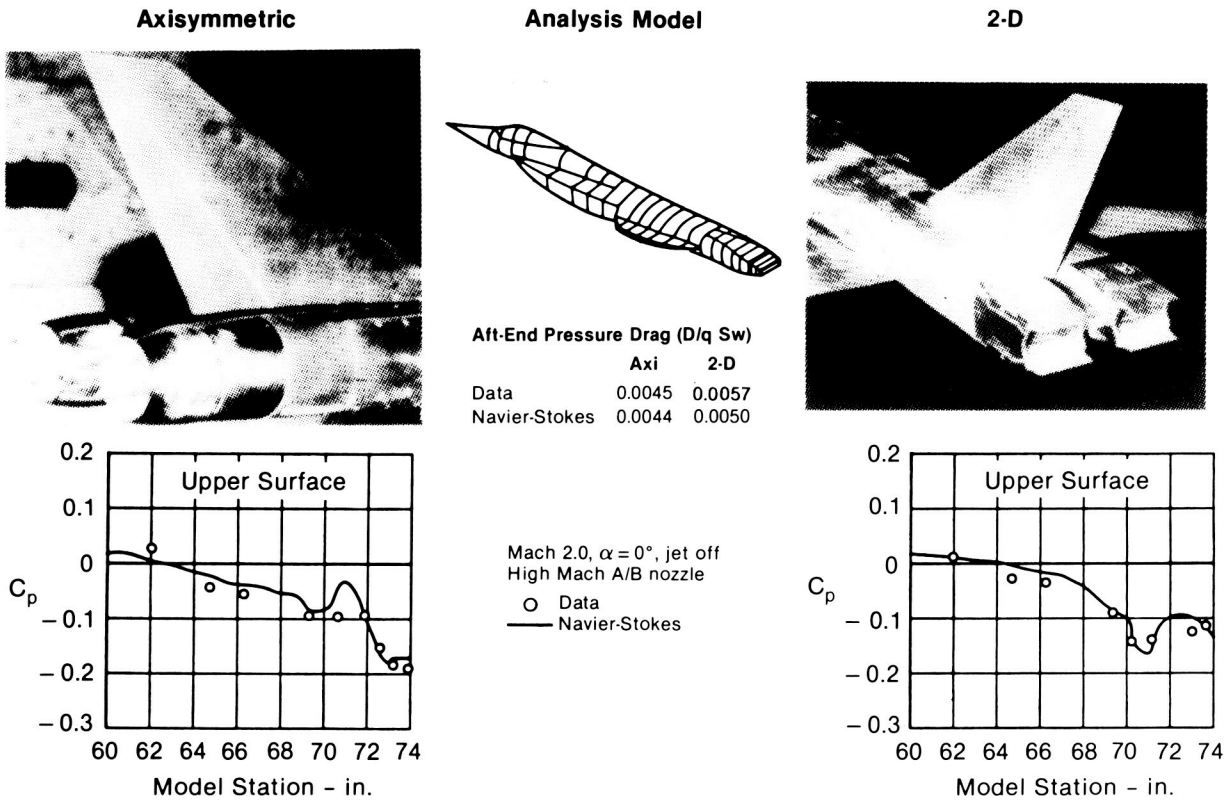

Figure 22. Code Verification for Supercruise Nozzle Integration

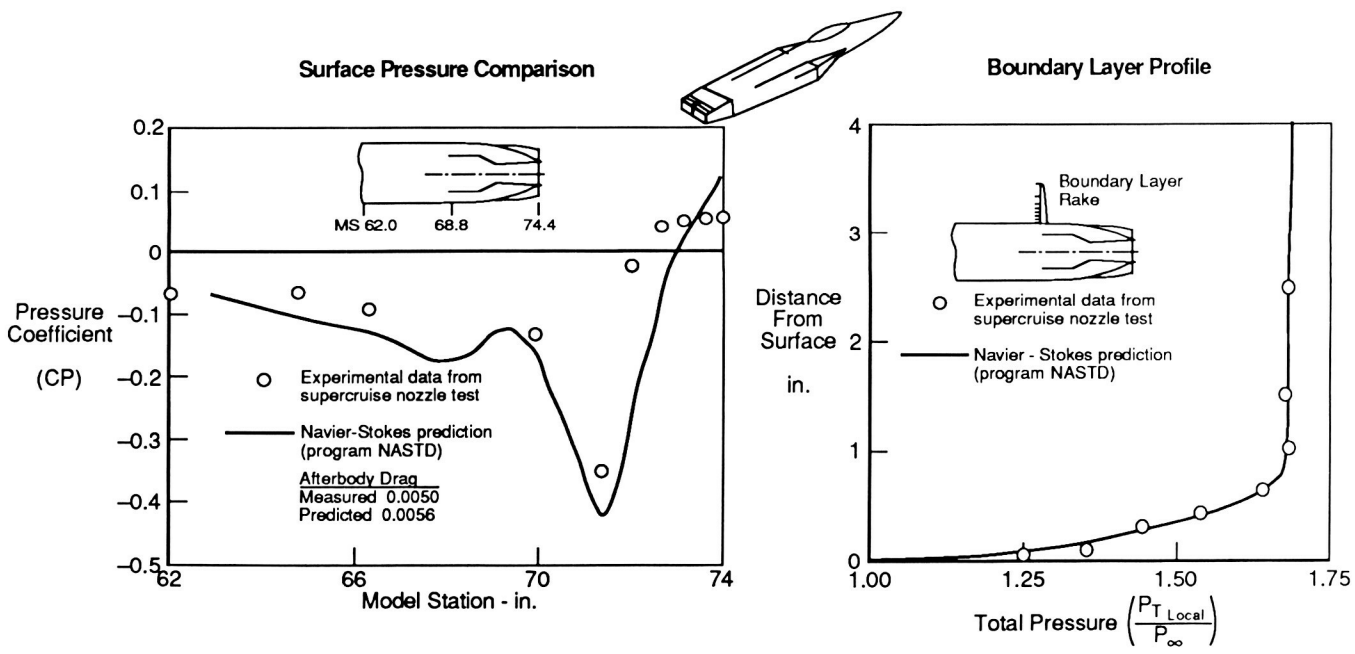

Figure 23. Aftbody NASTD Calculation - Tandem 2-D C-D Nozzle, Mach 0.9

Combined External/Internal Nozzle Flow - The FANSI program has been modified to analyze 2D nozzle flow for a range of nozzle configurations including Single Expansion Ramp Nozzle (SERN) designs and ejector nozzles. As with other applications, this effort is based on using multiple, non-overlapping computational zones.

The boundary conditions in the internal and external flowfields can be set independently. Inflow data can be uniform or arbitrarily specified. Sample results for transonic analysis of a hypersonic nozzle design are presented in Figure 24.

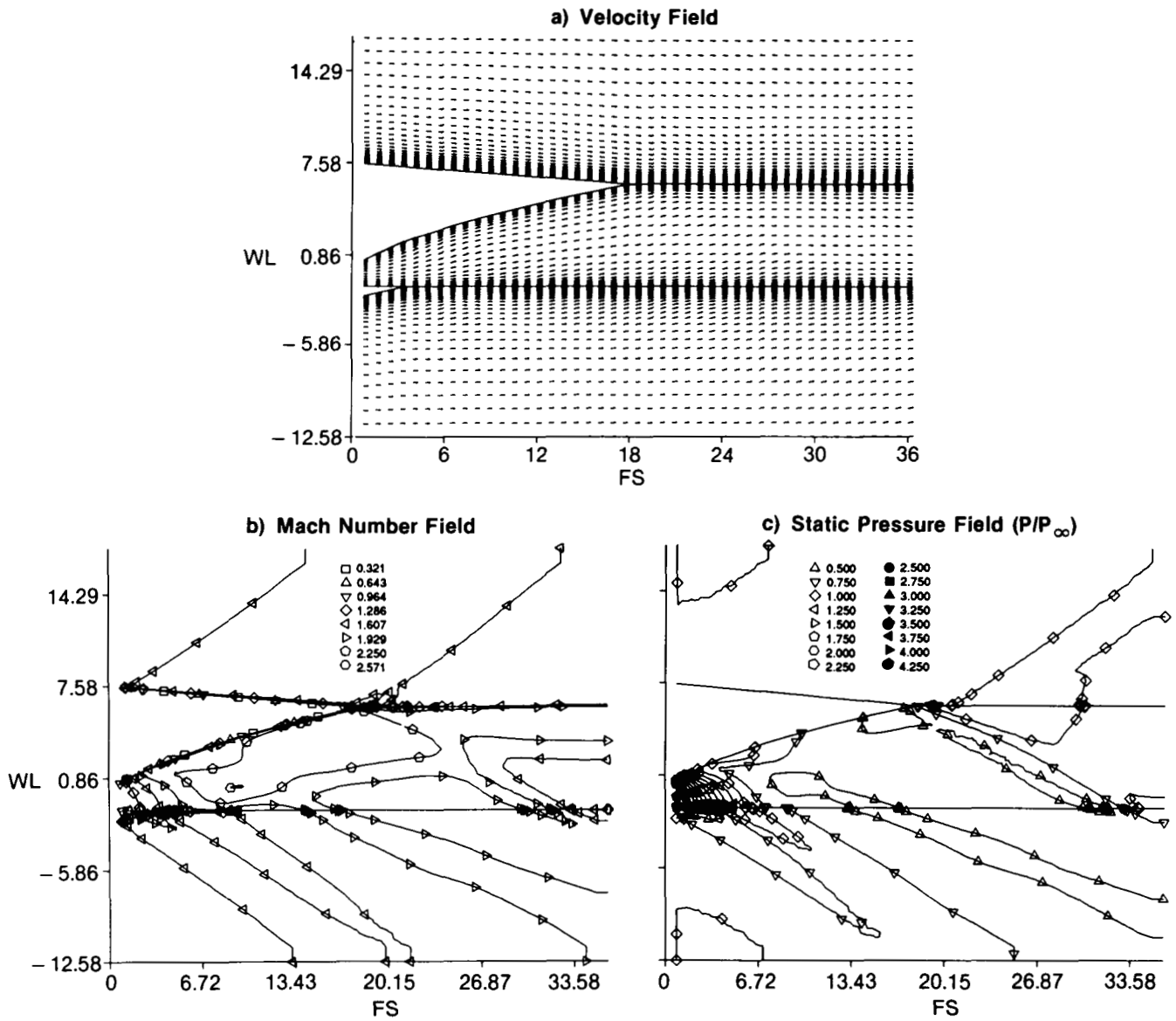

Figure 24. SERN Flowfield Analysis, Program FANSI
$M_\infty = 1.5$ $P_{t_j}/P_\infty = 8.07$ $T_{t_\infty} = 727°R$ $T_{t_j} = 560°R$

ORIGINAL PAGE IS
OF POOR QUALITY

Recent emphasis has been on the analysis of ejector nozzles. Sample FANSI results for a nozzle with one secondary stream are presented in Figure 25.

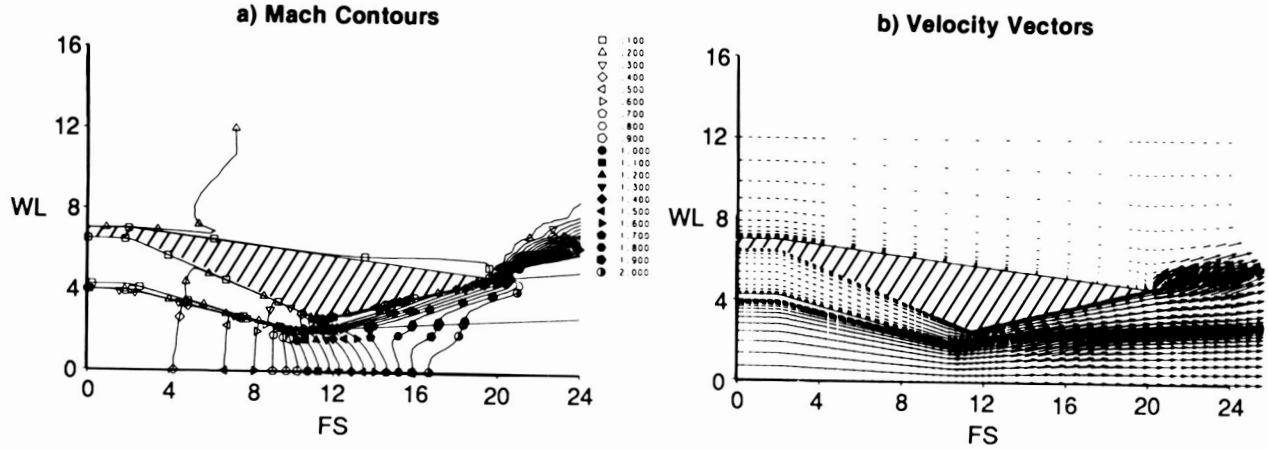

Figure 25. Ejector Nozzle Flowfield, Program FANSI
$M_\infty = 0.2$

SUMMARY

Computational Fluid Dynamics procedures are becoming familiar tools in the design of aircraft propulsion components and integrated systems. To an increasing degree, CFD methods are entering the design process in several ways:

- Evaluating and screening alternate concepts.
- Refining design concepts.
- Improving our understanding of complex flowfields.
- Selecting wind tunnel parametric variations.
- Designing wind tunnel instrumentation.
- Interpreting test data.

Current CFD methods can be used very effectively, but the engineering labor and computer costs of CFD application are often very high. More efficient algorithms always will be desired. Improvements are needed in developing trusted algorithms which do not require tuning to specific problems. Current solution costs, which have improved greatly over the years, are still often seen by project engineers as excessive.

At MCAIR, the problem in CFD applications generally is in the mesh generation tools, rather than the flow solvers. Mesh generation methods often are based on limited geometry input schemes which have been developed for specific classes of configurations. The trend is toward man-in-the-loop, interactive grid generation. This offers maximum geometric capability and is an approach which is being actively pursued at MCAIR. However, this approach carries an operational cost: it usually takes a skilled CFD engineer at the workstation providing the interactive guidance.

ORIGINAL PAGE IS
OF POOR QUALITY

A complete CFD system will, in our opinion, require interactive grid generation capability for new, complex problems. However, one goal is to provide non-interactive mesh generation methods for as many classes of problems as possible. All examples presented in this paper used non-interactive mesh generation.

Perhaps the most striking advances recently have been in graphical display tools (hardware and software) for CFD results. These tools have gone a long way toward convincing engineering managers that CFD is an indispensable tool.

The current challenge at MCAIR is to integrate CFD into the engineering environment. To accomplish this, we need to:

- Streamline the handling of data.
- Develop a base of validated CFD experience.
- Modify "research" grid and flowfield codes into "engineering" codes which do not require a CFD expert for most applications.
- Provide the support tools to allow the project engineer to accomplish his goals quickly.
- Educate our personnel in the potential and the limitations of CFD analysis.

The last item is perhaps the most significant. In the past, extravagant claims have been made for CFD analysis ("electronic wind tunnel"). The challenge now is to bring this technology into the enginneering workplace on a routine basis. This will be accomplished by making realistic claims and then delivering the promised data on time.

CFD has become an accepted tool in many areas of aerospace engineering. It has the potential to change drastically the way we do business. But we have only scratched the surface in exploiting the current technology.

The major growth in engineering applications will result from the CFD community recognizing the needs of project engineers and managers. Project personnel need tools which can be applied quickly, with confidence, to realistic flight vehicle geometries. Validation data should be available to establish confidence in the quality of results by comparison with wind tunnel or flight data. Guidelines are required to set all input parameters which are not defined by the physical problem to be analyzed. The codes must be usable without iterative adjustment of input data to obtain the needed results. The high potential of CFD will be realized when this technology is used effectively by project engineers, in conjunction with an array of other tools, to design a vehicle which will accomplish a specific mission.

ACKNOWLEDGMENT

This paper presents the work of several engineers at MCAIR in addition to the author. Particular acknowledgment must be made of the contributions of Robert H. Bush, U.Y. (Peter) Chun, John A. Ladd, Wade W. McLain, James A. Rhodes, Richard K. Scharnhorst, and Patrick G. Vogel in developing the capabilities discussed here.

Some of the solutions presented above were obtained in cooperative investigations with USAF Wright Aeronautical Laboratories (Figures 4 and 21) with NASA Langley Research Center (Figure 2), and with NASA Lewis Research Center (Figurew 8, 9, and 11).

REFERENCES

1. Bush, R.H., "External Compression Inlet Predictions Using an Implicit, Upwind, Multiple Zone Approach," AIAA Paper 85-1521-CP, presented at AIAA 7th Computational Fluid Dynamics Conference, Cincinnati, 15-17 July 1985.

2. Bush, R.H., P.G. Vogel, W.P. Norby, and B.A. Haeffele, "Two Dimensional Numerical Analysis for Inlets at Subsonic through Hypersonic Speeds," AIAA Paper 87-1751, presented at AIAA/SAE/ASME 23rd Joint Propulsion Conference, 29 June - 2 July 1987, San Diego.

3. Cosner, R.R., "Fast Navier-Stokes Solution of Transonic Flowfield about Axisymmetric Afterbodies," AIAA Paper 80-0193, presented at AIAA 18th Aerospace Sciences Meeting, Pasadena, 14-16 January 1980.

4. Cosner, R.R., "Relaxation Solution for Viscous Transonic Flow about Fighter-Type Forebodies and Afterbodies," AIAA Paper 82-0252, presented at AIAA 20th Aerospace Sciences Meeting, Orlando, 11-14 January 1982.

5. Mace, J.L., and R.R. Cosner, "Analysis of Viscous Transonic Flow Over Aircraft Forebodies and Afterbodies," AIAA Paper 83-1366, presented at AIAA/SAE/ASME 19th Joint Propulsion Conference, Seattle, 27-29 June 1983.

6. Yaros, S.F., and R.R. Cosner, "Evaluation of a Velocity-Split Solution of the Navier-Stokes Equations for Fighter Forebodies," AIAA Paper 84-2160, presented at AIAA 2nd Applied Aerodynamics Conference, Seattle, 21-23 August 1984.

7. Buning, P.G., and Steger, J.L., "Graphics and Flow Visualization in Computational Fluid Dynamics," AIAA Paper 85-1507, proceedings of AIAA 7th Computational Fluid Dynamics Conference, Cincinnati, 15-17 July 1985.

8. Zulauf, J.M., "Real-Time Imaging in a CFD Environment," Computer Graphics World, Vol. 10, No. 8, pg. 40 (August 1987).

9. Cawthon, J.A., E.L. Crosthwait, and P.P. Truax, "Supersonic Inlet Design and Airframe-Inlet Integration Program (Project Tailor-Mate)," AFFDL-TR-71-124 (May 1973).

10. Bare, E.A., Reubush, D.E., Haddad, R., Hathaway, R.W., and Compton, M., "Investigation of a Delta-Wing Fighter Model Flow Field at Transonic Speeds," AIAA Paper 87-1749, presented at AIAA/SAE/ASME/ASEE 23rd Joint Propulsion Conference, San Diego, 29 June - 2 July 1987.

11. Norby, W.P., B.A. Haeffele, and R.R. Burley, "Isolated Testing of Highly Maneuverable Inlet Concepts," NASA CR 179544, December 1986.

12. Lee, C.C., and W.A. Price, "Subsonic Diffusers for Highly Survivable Aircraft," AFWAL-TR-86-3025 (Final Report for the Period September 1982 - April 1986), May 1986.

13. Cosner, R.R., "Integrated Flowfield Analysis Methodology for Fighter Inlets," AIAA Paper 85-3071, presented at AIAA/AHS/ASEE Aircraft Design, Systems and Operations Meeting, 14-16 October 1985, Colorado Springs. Also presented as AIAA Paper 86-1463, presented at AIAA/SAE/ASME/ASEE 22nd Joint Propulsion Conference, 16-18 June 1986, Huntsville.

14. Hiley, P.E., and D.L. Bowers, "Advanced Nozzle Integration for Supersonic Strike Fighter Application," AIAA Paper 81-1441, presented at AIAA/SAE/ASME 17th Joint Propulsion Conference, Colorado Springs, 27-29 July 1981.

N89-20944

AERODYNAMIC ANALYSIS OF THREE ADVANCED CONFIGURATIONS USING THE TRANAIR FULL-POTENTIAL CODE

M. D. Madson, R. L. Carmichael, and J. P. Mendoza
NASA Ames Research Center, Moffett Field, California
Moffett Field, California

ABSTRACT

Computational results are presented for three advanced configurations: the F-16A with wing tip missiles and under-wing fuel tanks, the Oblique Wing Research Aircraft (OWRA), and an Advanced Turboprop research model. These results were generated by the latest version of the TranAir full-potential code, which solves for transonic flow over complex configurations. TranAir embeds a surface-paneled geometry definition in a uniform rectangular flow-field grid, thus avoiding the use of surface-conforming grids, and decoupling the grid generation process from the definition of the configuration. The new version of the code locally refines the uniform grid near the surface of the geometry, based on local panel size and/or user input. This method distributes the flow-field grid points much more efficiently than the previous version of the code, which solved for a grid that was uniform everywhere in the flow field. TranAir results are presented for the three configurations and are compared with wind tunnel data.

INTRODUCTION

The ability of linear potential panel method codes to compute flows about very general configurations has allowed them to be applied to a wide variety of configurations (Refs. 1-8). These codes give reliable results for configurations in which local flows do not deviate greatly from the freestream flow. For flows in the transonic regime, where both subsonic and supersonic flow exists, linear potential methods become inappropriate due to the violation of the small perturbation assumption. Nonlinear flow codes are required in order to predict transonic flows about aircraft, but are generally limited to relatively simple configurations due to "the difficulty in generating 'suitable grids' " (Ref. 9). Recent work (Refs. 10,11) has shown that improved grid generation techniques allow for increasingly complicated geometries to be analyzed. Unfortunately, simplifications to the actual geometry are generally required, as well as a good deal of time in generating the grid.

TranAir, a transonic full-potential code, utilizes the surface paneling technology of PANAIR (Refs. 12-15) in the definition of the computational model. The paneled definition of the configuration is then embedded in a relatively coarse rectangular array of flow-field grid points. The modeling generality afforded by the use of surface panels, and the decoupling of the flow-field grid definition from the definition of the geometry, allows TranAir to routinely solve transonic flow problems about very complex configurations.

The previous version of TranAir utilized a uniform grid which remained constant throughout the solution process. This uniform grid approach generally causes the grid to be much finer than necessary to predict the linear Prandtl-Glauert flow which prevails away from the geometry and not fine enough to adequately predict the rapidly changing flow properties near the surface of the geometry. The grid refinement capability allows the definition of a much coarser initial grid, so that the grid away from the boundary is not unnecessarily fine. The code then refines the initial uniform grid near the surface of the geometry where a finer grid is necessary in order to resolve the rapidly changing flow field. The refinements are based on local panel size and/or user input. The user may control the levels of refinement over regions of the geometry, thus controlling the distribution, and to some extent the number, of grid points generated for a given problem. The grid refinement capability generates a much more efficient grid upon which to obtain a solution. For

ORIGINAL PAGE IS
OF POOR QUALITY

test cases analyzed by both the original uniform grid version and the new refined grid version of TranAir, the total number of grid points defined for the problem by the new version of the code was consistently 50% less than was defined by the previous version of TranAir, while at the same time yielding more accurate solutions.

DESCRIPTION OF THE METHOD

The TranAir program may be broken into three distinct sections: the input processor, the solver, and the output processor. A very brief description of each of these sections is presented here. A detailed description of the inner workings of the code, including the mathematics behind the solution process, is reserved for future publication.

Input Processor

The input processor reads the input file describing the configuration and flow conditions, checks the geometry for proper abutments and defines appropriate boundary unknowns and their locations. Most of the code for the input processor was taken directly from the pilotcode version of PANAIR. This helped in quickly producing reliable input processor code, as well as assuring compatability between PANAIR and TranAir input files.

Solver

The solver first defines an initial uniform grid about the input geometry based on values input by the user, who defines the minimum and maximum values of the grid in each direction, as well as the number of grid points in each direction. After setting up the initial grid, the solver successively refines the grid based on the size of the surface panels contained within each grid box. These refinements are limited to the neighborhood of the aircraft surface, and the user may control the minimum and maximum levels of the refinements. In addition, the user may specify a region (volume) of interest about portions of the geometry where additional control over the refinement is desired. Within this region, the user specifies minimum and maximum levels of refinement, which are independent of the refinements specified over the geometry outside of the region. In the near future, a solution–adaptive refinement capability will be introduced to allow grid refinement to be based on the current state of the solution to the system of equations.

Having produced a refined computational grid, the solver constructs finite element operators on that grid. A trilinear basis function for the potential is associated with each finite element. Discretized operators are obtained using the Bateman variational principle (Ref. 16) in a manner which is fully conservative and second–order accurate. This discretization yields a set of nonlinear algebraic equations which simulate the original full–potential partial differential equation. Operators in supersonic regions are altered using a first–order artificial dissipation for shock capturing.

The set of nonlinear algebraic equations is solved by an iterative process. An orthogonal direction algorithm called GMRES (Generalized Minimum RESidual) (Refs. 17,18) is used to drive the solution process in conjunction with multiple preconditioners. The preconditioners consist of a fast Poisson solver, which is particularly effective for regions where the flow remains subcritical, and an incomplete factorization of the sparse matrix produced by linearizing the set of nonlinear algebraic equations. The sparse matrix is defined by selecting a subset of the entire system of equations and by closing the set through the imposition of a Dirichlet boundary condition. This 'reduced set' of points consists of all finite element nodes which make up a refinement of a box on the global Cartesian grid plus all nodes which make up a finite element where the flow is supersonic. A nested dissection ordering based on the physical location of finite elements in the computational grid is used to order the sparse matrix system. The incompete factorization is performed by using a drop tolerance when factoring the sparse matrix. If any element is smaller than either of its diagonals by the value of the specified drop tolerance, it is set to zero. The preconditioners seem to work

ORIGINAL PAGE IS
OF POOR QUALITY

more effectively in combination than would a single preconditioner by itself.

A significant advantage of the formulation is that the flow-field grid need only extend to a point where the flow is linear, rather than to a point where the flow is unperturbed. For cases in which there exist regions of supersonic flow, the flow-field grid must be large enough to include the supersonic regions. The equation solved about the perimeter of the grid changes from the nonlinear full-potential equation to the linear Prandtl-Glauert equation. The ends of the computational grid can be relatively close to the configuration because the unknowns defined on the global Cartesian grid consist of sources for the velocity potential. These sources exist on a grid which is theoretically infinite in extent, but the sources go to zero rapidly as a function of distance from boundary surfaces. In fact, the sources are generally weak in the entire computational domain except near shocks, surface boundaries and wakes. The potential induced by specified sources is computed efficiently by a convolution integral of the sources with a discrete exterior Green's function.

Output Processor

Once the solution process is completed, either by executing the maximum number of iterations specified by the user, or by reducing the value of the residual below a user specified minimum, the value of the potential at each grid point has been obtained. From these values, information about the flow both in the field and on the aircraft surface may be obtained. Velocities in the flow field and on the surface may be computed, from which the user may obtain forces and moments for the configuration, and pressure coefficients, streamlines, and Mach contours both in the field and on the surface of the geometry. One of the output options creates a file with all requested information about the flow at each point on the surface. A translator program may be written which loads the information in the output file into a database management system such as RIM (Relational Information Manager, Ref. 19), which in turn may be used to generate information for input to various 2-D and 3-D graphics programs and displays. Other files may be generated by TranAir, which can be read by PLOT3D (Ref. 20) a 3-D dynamic display graphics program which runs on a graphics workstation.

DESCRIPTIONS OF THE MODELS

Three configurations were modeled for which transonic results were desired. These models demonstrate the ability of TranAir to analyze complex geometries in the transonic flow regime. Descriptions of each of these configurations are presented below.

F-16A w/Wing Tip Missiles and Under-Wing Fuel Tanks

The TranAir model of the F-16A includes all the components of the actual geometry. The model also includes the geometry for an AIM-9 wing tip missile and launcher, and for a 370-gallon under-wing fuel tank and pylon. The complete F-16A definition is shown in Figure 1. Previous publications have presented TranAir results for the basic F-16A with no external stores (ref. 21), and with the addition of the 370-gallon underwing fuel tanks (ref. 22). The addition of the missile/launcher geometry to the definition of the F-16A shows the flexibility of TranAir in being able to quickly add complex pieces of geometry to an existing configuration and successfully analyze the new model.

The paneled definitions of the tip missile and launcher, and the fuel tank and pylon, were created on a Calma CAD/CAM machine based on blueprint drawings. The definition of the launcher and missile is true to the actual geometry with the exception of the small gap that exists between the missile and the launcher. For simplicity, this region was faired over. The fins on the missile were modeled as flat plates, which is very close to the shape of the actual fins. Wakes were defined from the trailing edge of the launcher, the base of the missile, and the trailing edges of all the fins. Wakes from the trailing edge of each of the forward fins were defined such that they ended at the leading edge of the corresponding aft fin. This was done to conserve the circulation generated by the forward set of fins. The launcher wake was connected to the outboard wing wake by a wake 'filler' network.

ORIGINAL PAGE IS
OF POOR QUALITY

ORIGINAL PAGE IS
OF POOR QUALITY

The fuel tank and pylon were also modeled true to the actual geometry, with the exception of the fins on the aft portion of the fuel tank. The top fin was omitted in order to simplify the wake modeling process. Since there was no sideslip angle in the computations, this simplification was considered to be reasonable. The side fins were modeled as flat plates, which is very close in shape to the actual fins. The wake from the pylon passes through the horizontal tail, so the wake had to be broken into two wakes. One passes over the tail, and one passes under the tail. The paneling on the horizontal tail networks had to be modified slightly so that there were network abutments where the wakes intersect the upper and lower tail surfaces.

The wind tunnel model of the F-16A had a flowthrough nacelle. The TranAir model of the nacelle inlet is a network of porous panels, on which the boundary conditions are (1) the velocity on the upstream side of the panels is the normal component of the freestream velocity, and (2) the perturbation potential on the downstream side of the panels is zero. The nacelle exhaust is closed off by a network of panels in the same manner as the inlet. The boundary conditions used on this network are (1) the total potential is constant on the downstream side of the network, and (2) the perturbation potential is zero on the upstream side. The constant total potential on the downstream side combined with wake networks emanating from the afterbody perimeter cause the flow to separate smoothly from the afterbody, rather than turning through a right angle as would occur if the base panels were modeled with solid-surface boundary conditions (Fig. 18 from Ref. 12).

TranAir allows one-half of the geometry to be input for cases which have one plane of symmetry, such as the F-16A model. The right half of the F-16A definition is comprised of 6388 surface panels and 754 wake panels. The right half of the initial uniform grid for this case contained $33 \times 11 \times 17$ points in the x, y, and z directions, respectively. Regions (volumes) of interest were specified around the wing, the fuel tank, and the tip missile assembly. Within these three regions, a minimum of three levels of refinement were specified, with a maximum of four levels in the tank and missile regions, and five levels in the wing region. The final refined grid from which a solution was generated contained approximately 71,000 grid points, which is less than half of the total number of grid points used by the original version of TranAir to obtain previous F-16 results. A spanwise two-dimensional cut of the refined grid is shown in Figure 2. This figure shows the refinement of the grid around the wing, as well as the fuel tank and missile assemblies. The refinement around the leading edge of the wing was one to two levels finer than the station seen in Figure 2, which is nearer to the trailing edge.

Advanced Turboprop Research Aircraft

The Advanced Turboprop configuration is designed to cruise at $M_\infty = 0.8$ and $C_L = 0.5$. The wind tunnel model is a combination pressure and force model having an active propeller which is driven by a compressed air turbine housed in the nacelle. Since the propeller slipstream induces upwash on the wing inboard of the nacelle and downwash on the wing outboard of the nacelle, the wing definition included twist designed to compensate for these effects. As a result of the wing twist, the power-off (propeller removed) wing pressures outboard of the nacelle achieve a fairly high suction peak. Wind tunnel data was generated for both power-on and power-off cases in order to study the power effects for the model.

The TranAir model does not include the definition of the propeller, or any of the related slipstream effects. The paneled definition of the right hand side of the advanced turboprop model, as well as the symmetric left hand side, is shown in Figure 3. The paneling was created on a Calma CAD/CAM machine based on geometry information provided by McDonnell Douglas. The paneled definition of one-half of the symmetric configuration consists of 1019 surface panels and 96 wake panels.

The absence of any tail surfaces in the definition of the TranAir model is consistent with the design of the wind tunnel model. The TranAir model differs from the wind tunnel model in only one respect, at the nacelle exhaust nozzle. The vertical plane of the exhaust nozzle on the wind tunnel model faces slightly inboard. The TranAir model defined the exit plane to be parallel to the $y - z$ plane. The definition of wakes for this configuration was fairly standard, with wakes emanating from the wing trailing edge, and from the nacelle exhaust nozzle and the fuselage base.

ORIGINAL PAGE IS
OF POOR QUALITY

The initial global grid box for this case, which was defined only for the right hand side of this symmetric configuration, contained 33 $\times$ 11 $\times$ 17 points in the x, y, and z directions, respectively. A region of interest was defined around the leading edge of the wing, and the rest of the wing. The leading edge region specified a minimum of four, and a maximum of five, levels of refinement. The aft region specified a minimum of three, and a maximum of five, levels of refinement. A region around the nacelle specified a mimimum of three, and a maximum of four, levels of refinement. A spanwise two-dimensional cut showing the refined grid across the fuselage, wing and nacelle is shown in Figure 4.

Oblique Wing Research Aircraft

NASA has studied the feasibility of using oblique wing airplanes for flight at transonic and low supersonic speeds for many years. Airplanes embodying this concept should prove useful for missions that require variable geometry configurations. In order to resolve some of the remaining uncertainties associated with the oblique wing concept, a proposal to convert the NASA Digital Fly-By-Wire Airplane to the Oblique Wing Research Aircraft was made. As part of the overall research program associated with this airplane, a detailed comparison of wind tunnel with theoretical results is being made. The original numerical calculations were generated by PANAIR, a linear potential flow code. The same paneled definition of the Oblique Wing configuration was analyzed by TranAir in an attempt to more accurately predict the characteristics of the oblique wing in transonic flow, particularly when the wing is swept.

The configuration studied here was tested in 1986 in the Ames 11- by 11-foot Transonic Wind Tunnel. The wing has subsequently undergone considerable redesign, particularly with respect to planform area. The wing was designed to have an area of 250 sq.ft. on the full scale airplane, with a span of 50 ft. The wind tunnel model is an 0.087 scale model of the wing attached to a model of the F-8 fuselage.

The paneled definition of the Oblique Wing model included the wing at a 30° sweep angle, the fuselage, empennage, and ventrals. The ventrals and the horizontal and vertical tails were modeled as thin (flat plate) surfaces. The wing definition was generated on a Calma CAD/CAM machine. The same numerical definition was used to generate both the TranAir model and wind tunnel model of the wing. The paneled configuration, shown in Figure 5, consists of 1134 surface panels and 175 wake panels. Most of the surface panels (750 out of 1134) are used in the definition of the wing, with the paneling on the fuselage and empennage being relatively coarse. Both sides of the configuration were defined due to the absence of a plane of symmetry for the configuration. Wake networks were attached to the trailing edges of all lifting surfaces, including the vertical tail. Since the configuration is asymmetric, the vertical tail may generate significant side force, even at zero sideslip, and thus the vertical tail wake could not be omitted from the definition. The wing wakes pass through the vertical tail, so the tail had to be defined by two networks which abut along the line defined by the wing wakes.

The initial global grid box for this case contained 33 $\times$ 17 $\times$ 11 points in the x, y, and z directions, respectively. This box enclosed both sides of the geometry, rather than just one-half of the geometry, due to the asymmetry of the configuration. A region of interest was defined around the wing, with a minimum of four, and a maximum six, levels of refinement. Regions were also defined at the wing tips, and at the horizontal and vertical tails. These regions specified lesser degrees of refinement than was specified for the wing. The final refined grid from which a solution was generated contained approximately 46,000 grid points. A streamwise two-dimensional cut showing the refined grid along the centerline of the geometry is shown in Figure 6. As can be seen, the grid is relatively coarse over most of the fuselage, and much finer in the vicinity of the wing.

RESULTS

Wind tunnel results were available for all three of the configurations presented. The F-16A and Advanced Turboprop wind tunnel models generated pressure data, as well as force and moment data. The Oblique

ORIGINAL PAGE IS
OF POOR QUALITY

Wing wind tunnel model was a force model only. The TranAir results presented here were obtained on a Cray X-MP/48, using 32 million words of a 128 million word solid-state storage device (SSD). Comparisons of TranAir results with wind tunnel data are presented below.

F-16A w/Wing Tip Missiles and Under-Wing Fuel Tanks

As was mentioned previously, TranAir results for the F-16A using the original version of the code have been published (Refs. 21,22). The main conclusion from these results was that, due to machine memory limitations, the uniform grid scheme did not allow the grid to be fine enough to resolve the flow near leading edges and tips of lifting surfaces, even though as many as 200,000 grid points were used. For the F-16A configuration shown in Figure 1, the final refined grid generated by the new version of TranAir consisted of only 71,000 points. The TranAir predicted C_p's for the F-16A with wing tip missiles and fuel tanks are shown in Figure 7 for $M_\infty = 0.6$ and $\alpha = 4°$.

The previously published wing pressure results showed reasonable agreement with wind tunnel data (Ref. 23) with two exceptions. Leading edge suction peaks were not captured because the grid was very coarse relative to the geometry. Also, pressures at the wing tip were in poor agreement with wind tunnel data. The poor agreement was due to both the relative coarseness of the grid at the tip, and the fact that no wind tunnel data existed for the F-16A without wing tip missiles and launchers.

The effect of adding the tip missile and launcher geometry to the definition of the F-16A, as well as the improved resolution of the flow due to the grid refinement capability, is evident in Figure 8. This figure shows wing tip C_p predictions from both versions of TranAir, as well as from wind tunnel data. The results from the original version of TranAir did not include the wing tip missiles and launchers in the definition of the geometry. The poor leading edge results, however, were caused by poor resolution of the grid in the region, rather than the absence of the missile geometry. Results from the new version of TranAir show much better agreement with wind tunnel data. This improvement in the predicted pressures can be attributed to both the addition of the missile/launcher geometry to the TranAir model and the grid refinement capability which more accurately resolves the flow in the region.

Advanced Turboprop Research Aircraft

Figure 9 shows the TranAir and wind tunnel C_p predictions for $M_\infty = 0.6$ and $\alpha = 2°$ at two wing stations. These results show TranAir predictions which are in reasonable agreement with wind tunnel data. The tap station shown in Figure 9a is inboard of the nacelle. The absence of a pressure peak near the leading edge reflects the negative twist inboard of the nacelle designed to offset the propeller upwash. Due to the spacing of the wing paneling on the computational model, TranAir results were not available at exactly the same tap station as the wind tunnel data. The closest available data on the TranAir model was 3% inboard from the wind tunnel station, which could explain the slight difference in C_p predictions between TranAir and wind tunnel data. The tap station in Figure 9b is outboard of the nacelle. The high suction peak reflected in the wind tunnel data is a result of the upward wing twist outboard of the nacelle designed to offset propeller downwash. TranAir results for the outboard tap station do not predict the magnitude of the suction peak. This is most likely due to the refined grid still being too coarse near the leading edge. Another possible explanation is the relative coarseness of the wing paneling. Both possibilities will be explored in future research. The TranAir C_p prediction over the entire configuration for $M_\infty = 0.6$ and $\alpha = 2°$ is shown in Figure 10.

Oblique Wing Research Aircraft

Results for the Oblique Wing geometry were obtained for $M_\infty = 0.8$ and $\alpha = 5°$, at a 30° wing sweep angle. Figure 11 shows the TranAir prediction of C_p for the entire configuration. Since no wind tunnel pressure data are available, this figure must be used to judge whether or not the predicted pressures seem reasonable.

ORIGINAL PAGE IS
OF POOR QUALITY

Figure 12 shows plots of C_L and C_m vs. α, in which TranAir data are compared with wind tunnel data and PANAIR predictions. Although PANAIR results showed reasonable agreement with wind tunnel results, the effects of applying a linear potential code to a transonic flow problem are evident. These plots show that TranAir predictions compare much better with wind tunnel data than do the PANAIR predictions. The lift curve from the TranAir data is in good agreement with the wind tunnel curve, although the slopes differ slightly. The TranAir data was obtained with a relatively coarse flow-field grid (45,000 points), with the majority of points existing near the wing surface. By refining the grid more around the fuselage and the empennage, as well as the wing, a more accurate lift prediction should be possible.

The pitching moments predicted by TranAir were parallel to the wind tunnel data, and were closer to the wind tunnel data than the PANAIR prediction. The extrapolated value of the zero-lift pitching moment for TranAir differs by a significant amount. Several possible factors may contribute to this offset. The fuselage definition used for the PANAIR and TranAir models was not identical to the one used for the wind tunnel model. The nose region on the wind tunnel model of the F-8 fuselage has been modified several times over many years of testing, while the existing computational model retains the original definition of the nose. These modifications to the nose, besides affecting the aerodynamics of the fuselage, have made it difficult to maintain a reliable reference point on the fuselage. The location on the fuselage of the computational definition of the wing was approximated, and its distance from the horizontal tail could differ by a significant amount from that of the wind tunnel model. This possible discrepancy will be clarified and the proper adjustments to the computational model will be made. Another possible cause of pitching moment discrepancy is the modeling of the horizontal tail surfaces as flat plates. Future work will include the modeling of the tail surfaces with the same thickness as for the wind tunnel model.

It is encouraging that TranAir predictions for the transonic Mach no. are in better agreement with wind tunnel data than the linear potential predictions from the PANAIR code. Since, in the transonic flow regime, the flow violates the small perturbation assumption upon which linear potential flow is based, the PANAIR predictions should not be as accurate as those obtained by a nonlinear full-potential flow code such as TranAir.

FUTURE PLANS

Several enhancements are to be incorporated into the existing TranAir code. Some of these enhancements are in the implementation process, while others are scheduled to be completed by the end of the first quarter of 1989.

Most of the current effort is directed toward the implementation of a solution adaptive grid refinement capability. The current refinement method, which is based on local panel size and user input, requires a good deal of insight by the user as to where more grid points might be necessary in order to more accurately predict the flow in critical areas. Also, the refinement is limited to the neighborhood of the surface of the geometry. The solution adaptive refinement technique will evaluate the solution everywhere on the grid, and make further refinements in regions where the solution is less accurate. Refinements will also be allowed to extend into the flow field in order to accurately capture shocks.

The current code requires the freestream Mach no. to be less than 1.0. The flow field is allowed to have regions of supersonic flow, but the freestream value of the Mach no. must be subsonic. Near term effort will be directed toward implementing a supersonic freestream capability.

TranAir currently employs a trilinear basis function for the potential. This causes the velocity within a grid box to be approximately constant. Work is being done to implement a second-order basis function, which would then allow the velocity to vary across a grid box. This should combine with the grid refinement capability to improve the accuracy of the predictions.

Some effort will go into studying the feasibility of adding a 'viscous' term to the full-potential equation. This would enable the code to 'capture' wakes from sharp leading edges and trailing edges of lifting surfaces.

For the current version of TranAir, the user must define wakes in the same manner as required by linear potential flow codes. A wake-capturing capability would remove the burden of manual wake definition from the user, as well as more accurately defining the shape and location of the vortex sheets from the lifting surfaces.

SUMMARY

The TranAir full-potential code solves transonic flow problems about very general and complex configurations. A surface-paneled geometry definition is embedded in a uniform rectangular flow-field grid. This uniform grid is then refined in the neighborhood of the geometry based on the local surface panel size and/or user input. Finite element operators are constructed on the refined grid. Discretized operators are obtained in a conservative, second-order accurate fashion. A set of nonlinear algebraic equations which simulate the full-potential partial differential equation are generated, and are solved by an iterative process. Operators in supersonic regions are altered using a first-order artificial dissipation for shock capturing. TranAir results are shown for three different configurations: the F-16A with wing tip missiles and under-wing fuel tanks, the Oblique Wing Research Aircraft, and the Advanced Turboprop research model. These results demonstrate the ability of the code to routinely analyze complex configurations in the transonic flow regime. Future work will include the addition of a solution adaptive grid refinement capability, a higher-order basis function for the potential, a supersonic freestream capability, and the addition of a viscous term to the full-potential equation in order to capture wakes from sharp leading edges and trailing edges of lifting surfaces.

ACKNOWLEDGEMENTS

The TranAir code is being developed under NASA contract NAS2-12513 by the Boeing Military Airplane Company. The authors wish to thank F. T. Johnson, J. E. Bussoletti, S. S. Samant, D. P. Young, and R. G. Melvin for their dedicated work in the development of the TranAir code.

REFERENCES

[1] Madson, M. D., and Erickson, L. L., "Application of PAN AIR to an Advanced Supersonic Fighter/Attack Aircraft", AIAA Paper 85-4093, 1985.

[2] Snyder, L. D., and Erickson, L. L.,"PAN AIR Prediction of NASA Ames 12-Foot Pressure Wind Tunnel Interference on a Fighter Configuration", AIAA Paper 84-0219, 1984.

[3] Ghaffari, F., "PAN AIR Application to the F-106B", NASA Contractor Report 178165, 1986.

[4] Miller, S. G., and Youngblood, D. B., "Applications of USSAERO-B and the PAN AIR Production Code to the CDAF Model: A Canard/Wing Configuration", AIAA Paper 83-1829, 1983.

[5] van den Broek, G. J., "The Use of a Panel Method in the Prediction of External Store Separation", AIAA Journal of Aircraft Vol. 21, No. 5, May, 1984.

[6] Smith, B. E., and Ross, J. C., "Application of a Panel Method to Wake Vortex/Wing Interaction and Comparison with Experiment", AIAA Paper 84-2182, 1984.

[7] Fornasier, L., and Heiss, S., "Application of HISSS Panel Code to a Fighter-Type Aircraft Configuration at Subsonic and Supersonic Speeds", AIAA Paper 87-2619, 1987.

[8] Ross, J. C., "Applicability of a Panel Method, Which Includes Non Linear Effects, to a Forward-Swept-Wing Aircraft", AIAA Paper 84-2402, 1984.

ORIGINAL PAGE IS
OF POOR QUALITY

[9] Holst, T. L., Slooff, J. W.,Yoshihara, H., and Ballhaus, W. F., Jr., "Applied Computational Transonic Aerodynamics", AGARD AG-266, 1982.

[10] Karman, S. L., Steinbrenner, J. P., and Kisielewski, K. M., "Analysis of the F-16 Flow Field by a Block Grid Euler Approach", AGARD Paper 18, 58th Meeting of the Fluid Dynamics Panel Symposium on Applications of Computational Fluid Dynamics in Aeronautics, 1986.

[11] Flores, J., Reznick, S. G., Holst, T. L., and Gundy, K., "Transonic Navier-Stokes Solutions for a Fighter-Like Configuration", AIAA Paper 87-0032, 1987.

[12] Carmichael, R. L., and Erickson, L. L., "PAN AIR - A Higher Order Panel Method for Predicting Subsonic or Supersonic Linear Potential Flows About Arbitrary Configurations", AIAA Paper 81-1255, 1981.

[13] Derbyshire, T., and Sidwell, K. W., "PAN AIR Summary Document (Version 1.0)", NASA CR-3250, 1982.

[14] Magnus, A. E., and Epton, M. A., "PAN AIR - A Computer Program for Predicting Subsonic or Supersonic Linear Potential Flows about Arbitrary Configurations using a Higher Order Panel Method (Version 1.0), Vol. I, Theory Document", NASA CR-3251, 1981.

[15] Sidwell, K. W., Baruah, P. K., and Bussoletti, J. E., "PAN AIR - A Computer Program for Predicting Subsonic or Supersonic Linear Potential Flows about Arbitrary Configurations using a Higher Order Panel Method (Version 1.0), Vol. II, User's Manual", NASA CR-3252, 1981.

[16] Bateman, H., "Irrotational Motion of a Compressible Inviscid Fluid", Proceedings of the National Academy of Sciences, Vol. 16, 1930, pp. 816-825.

[17] Wigton, L. B., Yu, N. J., and Young, D. P., "GMRES Acceleration of Computational Fluid Dynamics Codes", AIAA Paper 85-1494, 1985.

[18] Saad, Y. and Schultz, M. H., "GMRES: A Generalized Minimal RESidual Algorithm for Solving Non-symmetric Linear Systems", Research Rep. YALEU/DCS/RR-254, Aug. 1983.

[19] Fishwick, P. A., and Blackburn, C. L., "Managing Engineering Data Bases: The Relational Approach", Computers in Mechanical Engineering (Underlined), Vol. 1, No. 3, Jan. 1983, pp. 8-16.

[20] Buning, P. G., and Steger, J. L., "Graphics and Flow Visualization in Computational Fluid Dynamics", AIAA Paper 85-1507. 1985.

[21] Erickson, L. L., Madson, M. D., and Woo, A. C., "Application of the TranAir Full-Potential Code to Complete Configurations", ICAS Paper ICAS-86-1.3.5, 1986.

[22] Madson, M. D., "Transonic Analysis of the F-16A with Under-Wing Fuel Tanks: An Application of the TranAir Full-Potential Code", AIAA Paper 87-1198, 1987.

[23] Hammond, D. G., "Wind Tunnel Data Report, 1/9-Scale F-16 Pressure Loads Test, AEDC 16'T Test TF-397 (Phase I and II), Vol. II of VI", General Dynamics Report No. 16PR135, 1976.

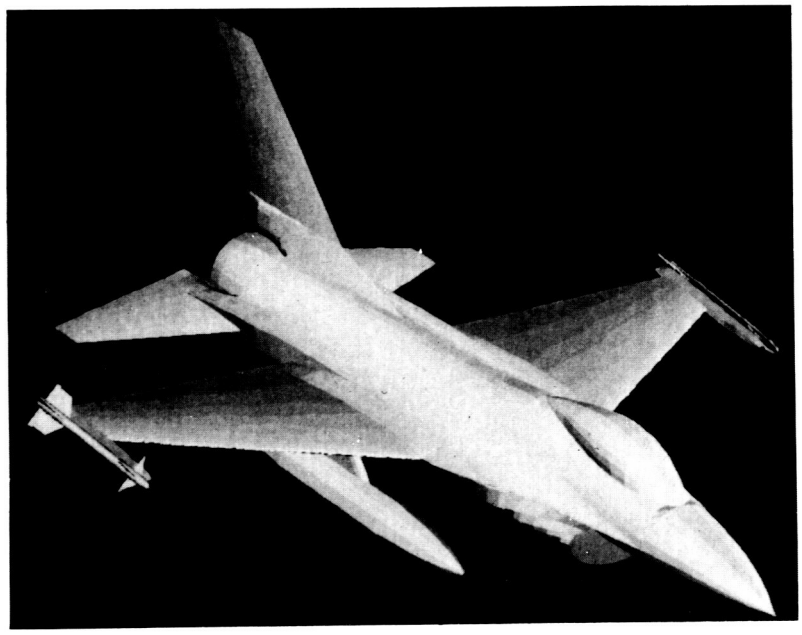

Figure 1. Surface panel definition of F-16A configured with wing tip missiles and under-wing fuel tanks.

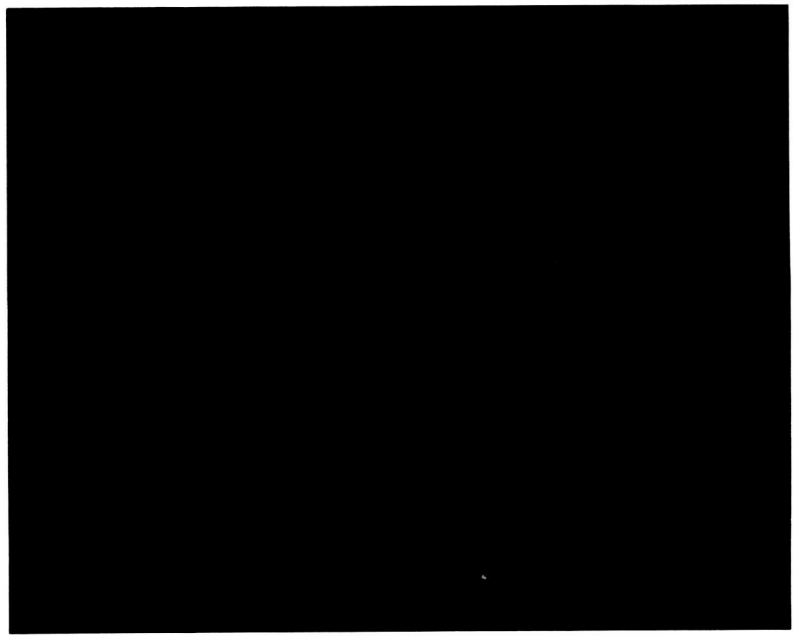

Figure 2. Spanwise two-dimensional cut of refined grid for F-16A configuration near wing trailing edge.

ORIGINAL PAGE
BLACK AND WHITE PHOTOGRAPH

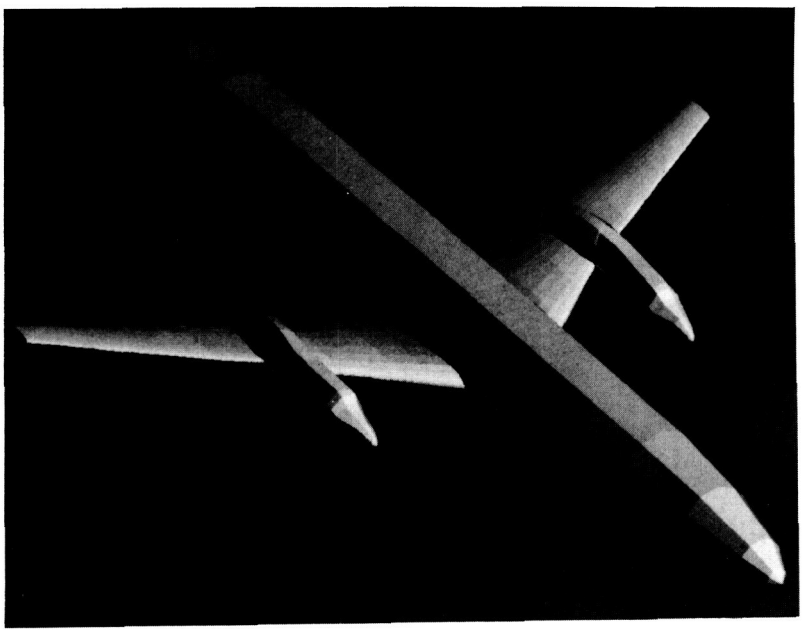

Figure 3. Surface panel definition of the Advanced Turboprop research model (ATP).

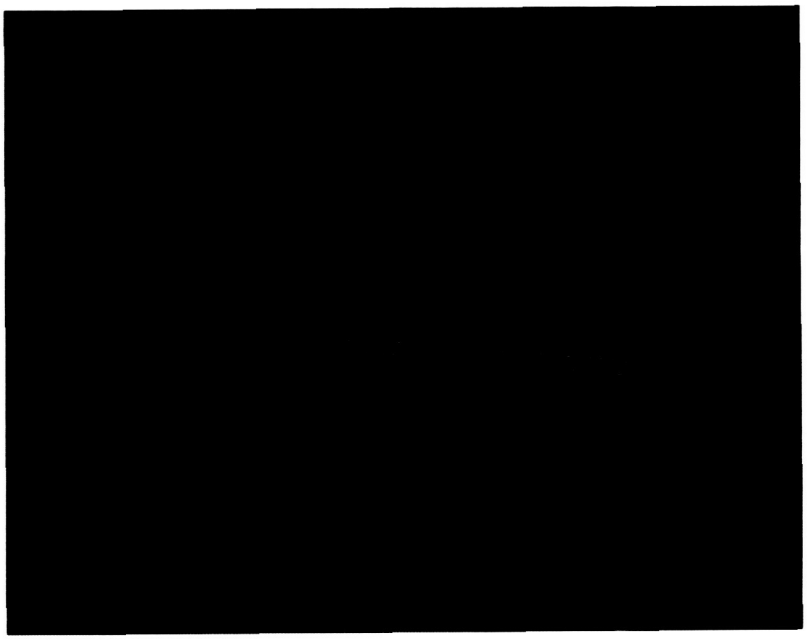

Figure 4. Spanwise two-dimensional cut of refined grid for the ATP through the wing/nacelle intersection.

ORIGINAL PAGE
BLACK AND WHITE PHOTOGRAPH

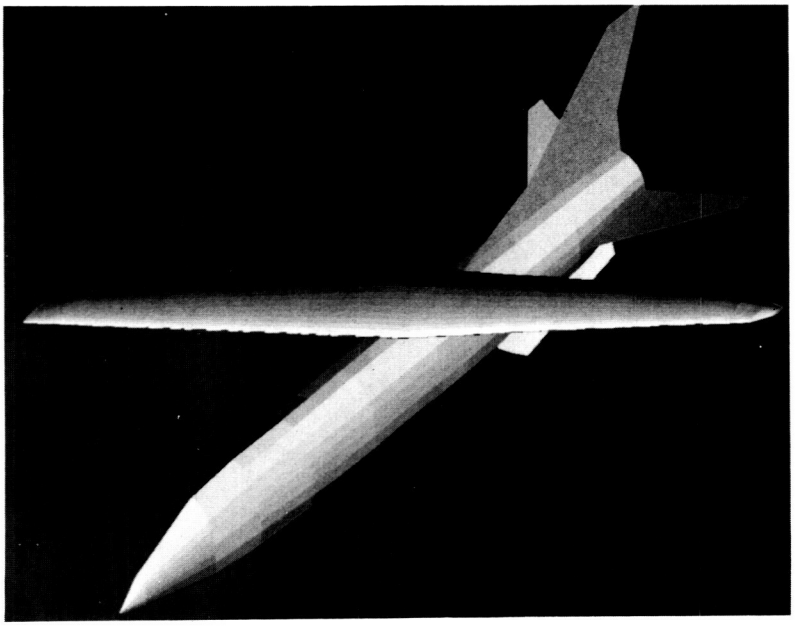

Figure 5. Surface panel definition of the Oblique Wing Research Aircraft (OWRA), wing sweep = 30°.

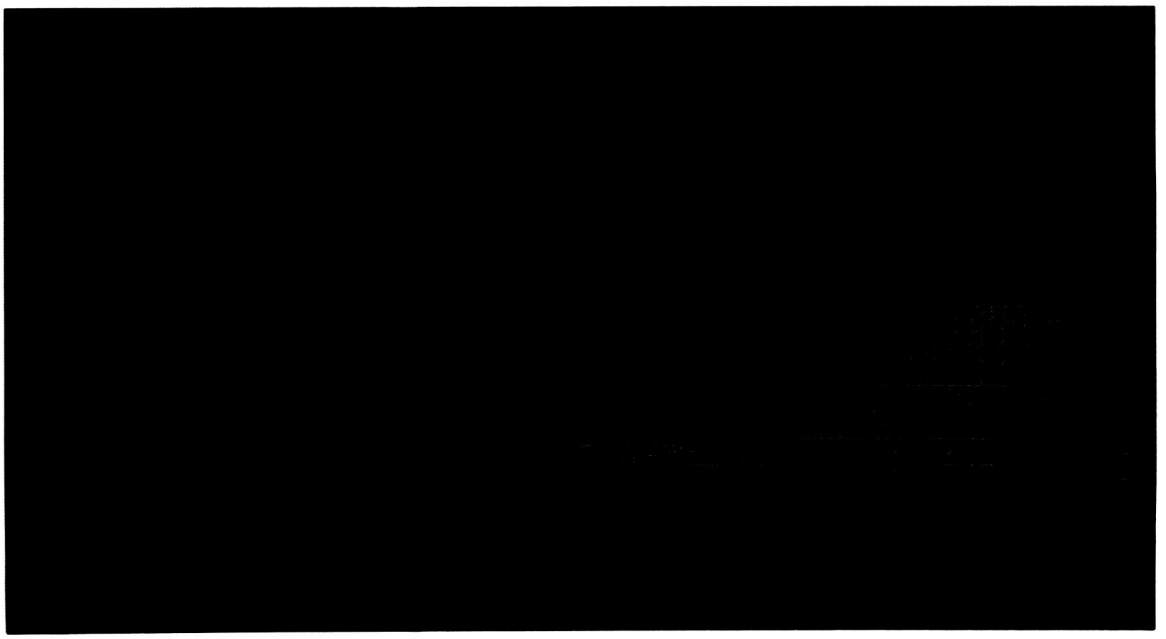

Figure 6. Streamwise two-dimensional cut of refined grid for the OWRA at the centerline of the configuration.

ORIGINAL PAGE
BLACK AND WHITE PHOTOGRAPH

ORIGINAL PAGE
COLOR PHOTOGRAPH

Figure 7. TranAir C_p results for the F-16A, $M_\infty = 0.6$, $\alpha = 4°$.

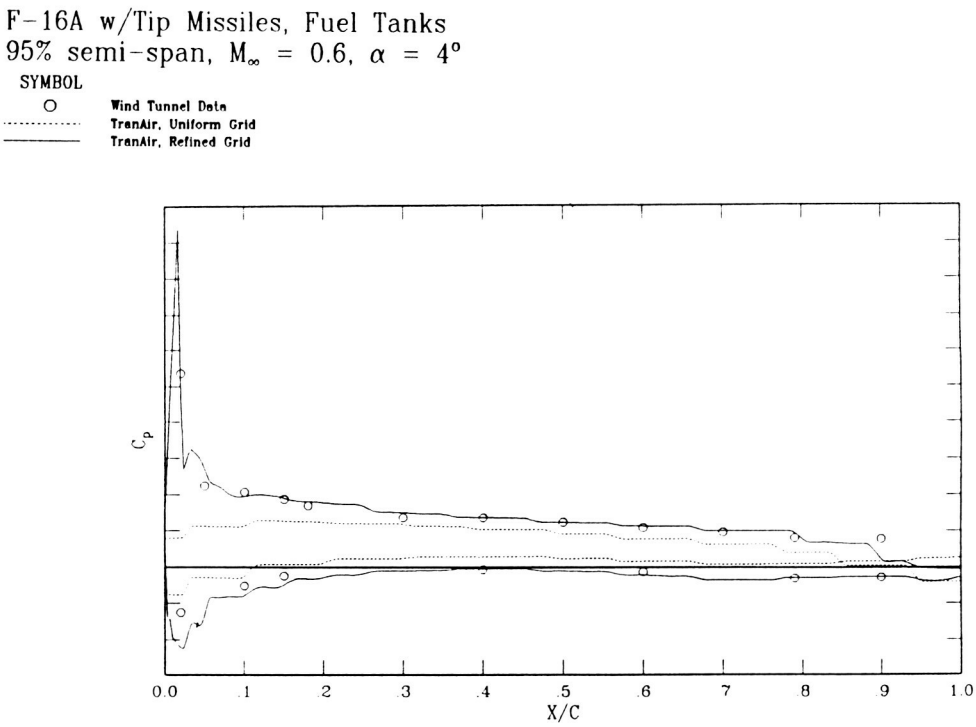

Figure 8. TranAir C_p results for the F-16A compared with wind tunnel data at 95% semi-span station, $M_\infty = 0.6$, $\alpha = 4°$.

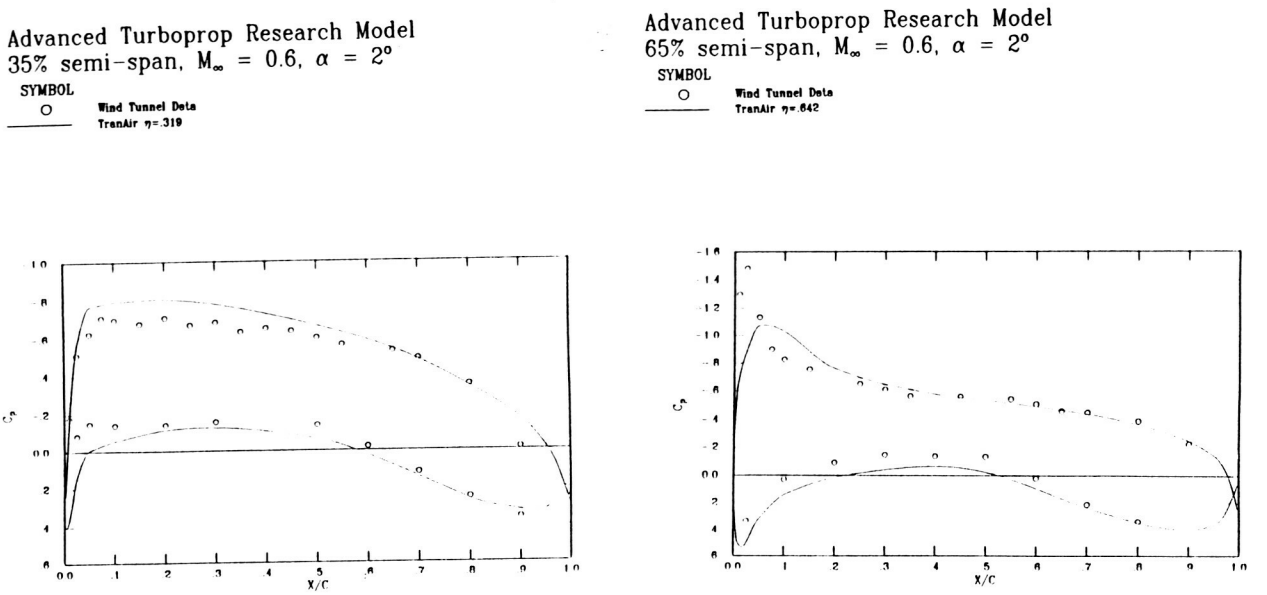

Figure 9. TranAir C_p results for the ATP compared with wind tunnel data, $M_\infty = 0.6$, $\alpha = 2°$.
a 35% semi-span station.
b. 65% semi-span station.

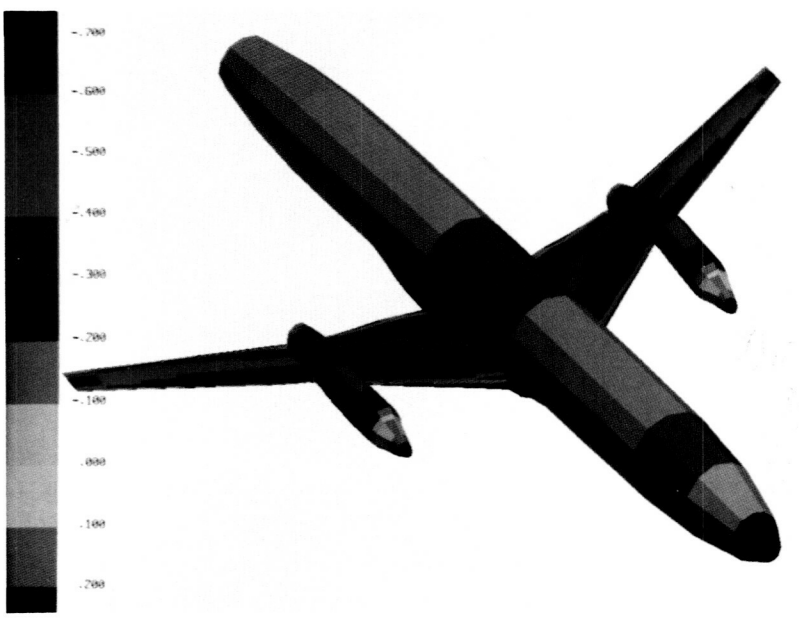

Figure 10. TranAir C_p results for the ATP, $M_\infty = 0.6$, $\alpha = 2°$.

ORIGINAL PAGE
COLOR PHOTOGRAPH

ORIGINAL PAGE
COLOR PHOTOGRAPH

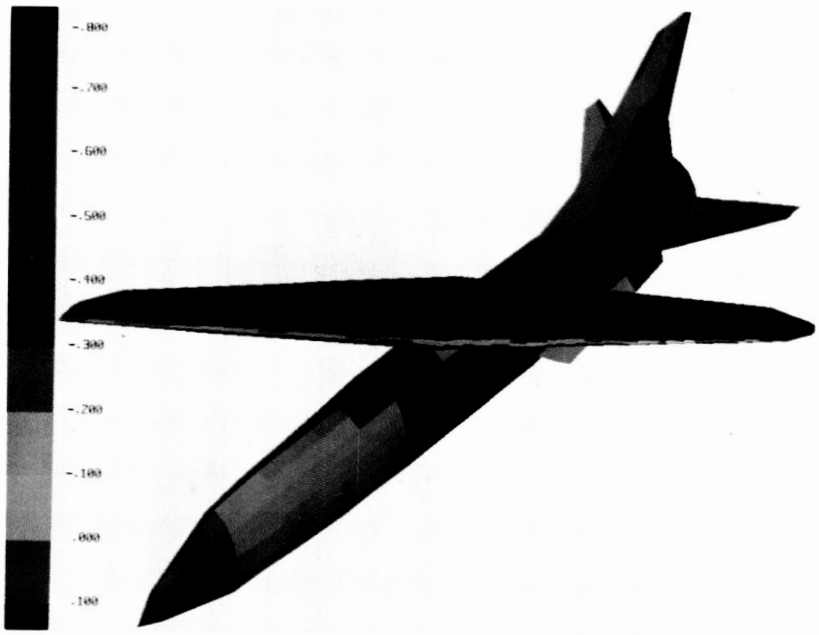

Figure 11. TranAir C_p results for the OWRA, $M_\infty = 0.8$, $\alpha = 5°$.

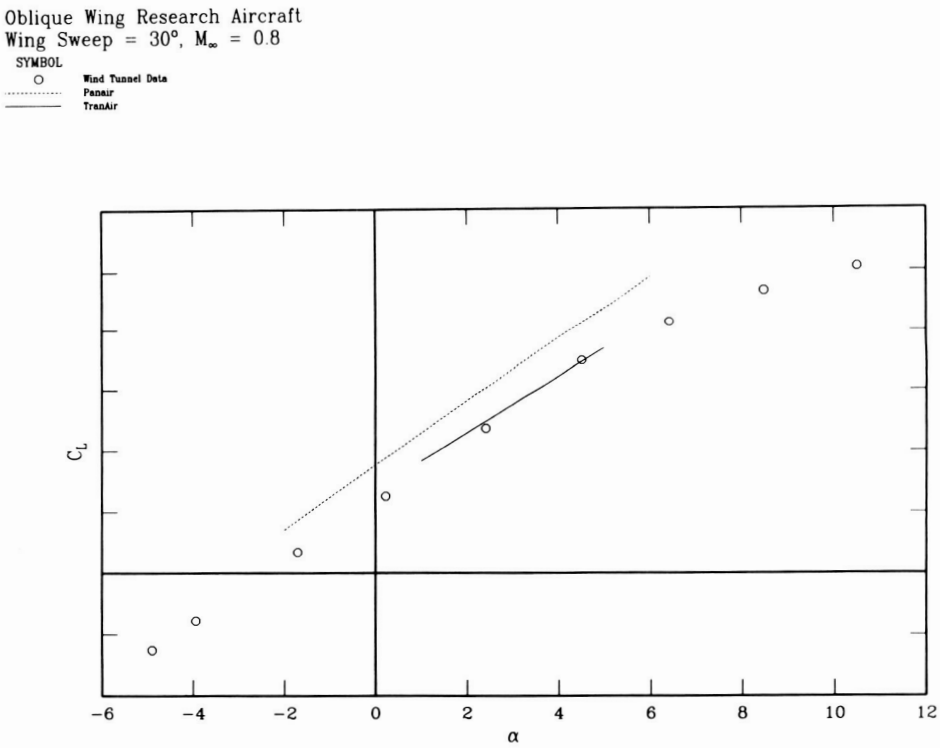

Figure 12. TranAir lift and pitching moment results for the OWRA compared with wind tunnel data, $M_\infty = 0.8$, $\alpha = 5°$.
a. Lift coefficient vs. angle-of-attack.

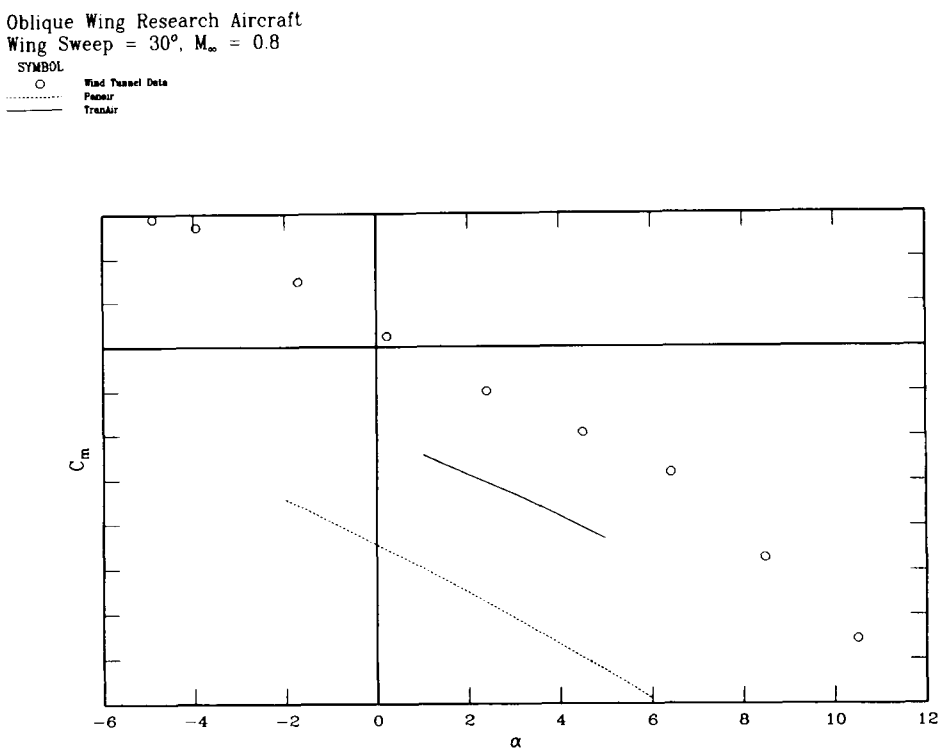

Figure 12. TranAir lift and pitching moment results for the OWRA compared with wind tunnel data, $M_\infty = 0.8$, $\alpha = 5°$.

b. Pitching moment vs. angle-of-attack.

ORIGINAL PAGE IS
OF POOR QUALITY

N89-20945

METHOD TO PREDICT EXTERNAL STORE CARRIAGE LOADS AT TRANSONIC SPEEDS*

Bruce S. Rosen
Grumman Aircraft Systems Division
Bethpage, New York

SUMMARY

A computational method developed to provide an inviscid transonic analysis for isolated and underwing, pylon-mounted stores is described. Wing, fuselage, pylon, and store body and fin components are modelled simultaneously by computing solutions on a five-level embedded grid arrangement. Flow field accuracy in the vicinity of the store is enhanced by the use of cylindrical grids which conform to the actual store body shape. A completely automated grid generation procedure facilitates applications. A finite difference scheme developed specifically for modified transonic small disturbance flow equations enhances the method's numerical stability and accuracy. Treatment of lower aspect ratio, more highly swept and tapered wings is therefore possible. A limited supersonic freestream capability is also provided. For the test cases considered, computed surface pressures and load distributions reveal strong store/airframe interactions. Predicted results are supported by correlations with experimental data. It is concluded that predictions would be improved by simple 2-D or axisymmetric modelling of viscous effects and flow separation.

INTRODUCTION

Prediction of external store carriage characteristics at transonic speeds requires computations for rather complex geometries. Wing, fuselage, pylon, and store body and fin components each need to be modelled. While methods to obtain full potential, Euler, and Navier Stokes solutions for simpler geometries are maturing at a rapid pace, transonic small disturbance (TSD) formulations are still a practical alternative for treatment of these more complex configurations.

The NASA/Grumman Transonic Wing-Body Code (refs. 1,2,3) represents the state of the art for reliable TSD analysis of complex aircraft. An attempt to extend similar wing/fuselage methodology to treat wing/fuselage/pylon/store geometries (refs. 4,5) attributed poor isolated body normal force correlations to the TSD formulation. Since approaches emphasizing the use of more sophisticated flow equations (refs. 6,7,8) are difficult to implement and require further development for practical three-dimensional applications, a more accurate TSD formulation was developed for treatment of store body shapes (ref. 9). This approach was then employed for more accurate treatment of finned stores and store carriage configurations.

---

*This work was supported by NASA Contract NAS1-18105.

The Transonic Store Carriage Loads Prediction (TSCLP) Code which was developed combines refined TSD approaches (refs. 1,2,3,9) for treatment of isolated and underwing, pylon-mounted stores. TSCLP Code prediction accuracy for isolated stores with multiple fore and aft fins was documented in reference 10. For the single pylon-mounted store test case considered, good correlation was also shown in reference 10 between computed and experimental store body surface pressures and load distributions. In this paper, after presenting an overview of the computational method, TSCLP Code prediction capability for store carriage configurations is evaluated in more detail.

SYMBOLS

b	wing span
C_p	pressure coefficient
c_y	store body cross-section side force coefficient
c_z	store body cross-section normal force coefficient
L	fuselage or store body length
M_∞	freestream Mach number
RMAX	store body maximum radius
T,U,V	coefficients of governing flow equation
x,r,θ	cylindrical coordinates
x,y,z	Cartesian coordinates
α	angle of attack
γ	specific heat ratio
η	wing spanwise coordinate, $2y/b$
ϕ	perturbation potential

COMPUTATIONAL METHOD

Treatment of wing/fuselage/pylon geometry is similar to that found in the basic wing-body code (refs. 1,2). Modelling capability for isolated and underwing, pylon-mounted stores is limited to axisymmetric store bodies with multiple fore and aft fins. Store flow field accuracy is enhanced by the use of cylindrical grids which conform to the actual store body shape. Store fins are then treated using a small disturbance, planar representation analogous to that used for wings and pylons. No provision is made in the computations for modelling of viscous effects and/or flow separation.

A completely automated grid generation procedure facilitates applications. Required inputs consist of configuration geometry, freestream flow conditions, and number of solution iteration cycles. Geometry input verification for a Douglas wing/pylon/store test configuration is shown in figure 1. Grid set up for this geometry is shown in figure 2.

Modified TSD flow equations are employed. These permit calculation of flow nonlinearities, including shocks, and at the same time provide the flexibility required for treatment of complex geometries. In Cartesian grids the flow equation is given by

$$T\,\phi_{xx} + U\,\phi_{xy} + V\,\phi_{yy} + \phi_{zz} = 0$$

where subscripts denote partial differentiation, and

$$T = 1 - M_\infty^2 - (\gamma+1)\,M_\infty^2\,\phi_x - ((\gamma+1)/2)\,M_\infty^2\,\phi_x^2$$

$$U = -2\,M_\infty^2\,\phi_y$$

$$V = 1 - (\gamma+1)\,M_\infty^2\,\phi_x$$

In cylindrical grids the flow equation is similarly given by

$$T\,\phi_{xx} + U\,\phi_{xr} + V\,\phi_{rr} + 1/r\,\phi_r + 1/r^2\,\phi_{\theta\theta} = 0$$

where T and V are as above, and

$$U = -2\,M_\infty^2\,(\alpha \sin\theta + \phi_r)$$

The equations are referred to as modified because additional terms are retained relative to the classical TSD flow equation. The $\phi_x^2\,\phi_{xx}$ term is retained to provide a better approximation to the transition between subsonic and supersonic flow. The $\phi_y\phi_{xy}$, $\phi_x\phi_{yy}$ and $\phi_r\phi_{xr}$, $\phi_x\phi_{rr}$ terms are retained to more accurately resolve shock waves which are swept in the x-y (wing) and x-r (fin) planes, respectively.

Finite difference approximations are substituted into the flow equations to arrive at a tridiagonal, successive line over-relaxation scheme. An upwind, rotated difference scheme (ref. 11) provides the proper domain of dependence at supersonic points. A variation of this scheme developed specifically for modified TSD flow equations (ref. 3) determines the rotation from the coefficients T,U,V rather than from local flow angularities. This greatly enhances the method's numerical stability and accuracy. Treatment of lower aspect ratio, more highly swept and tapered wings is therefore possible.

A supersonic freestream capability is also provided. For this, outermost grid boundaries are located a finite distance from the configuration where appropriate inflow, outflow, and radiation-type boundary conditions (ref. 12) are applied. The supersonic freestream capability works well for wing/fuselage combinations, but only limited success was achieved for treatment of stores.

As shown in figure 2, a five-level embedded grid arrangement is employed. Wing and fuselage components are modelled in Cartesian grids, store body and fin components are modelled in cylindrical grids, and the pylon is modelled in both. The grid generation procedure is currently set up to treat wing/store gaps as small as one store diameter, excluding fins, or one-half store radius, including fins, whichever is larger. Communication between embedded grids is accomplished by interpolation of central first derivatives and, where required, upwind second derivatives of the potential in a direction normal to the computational grid boundaries.

As in the basic wing-body code (refs. 1,2), the global coarse grid and wing fine grid systems are used to model the wing and fuselage. A wing/store interaction (WSI) grid is embedded within the global coarse grid in the vicinity of the store. This medium density grid functions as a means of communication between the other Cartesian grids and the cylindrical grids. There are appropriate gaps or holes in the Cartesian grids where the store geometry is not readily modelled. The flow field in this region is computed using a cylindrical C-grid embedded within the WSI grid. A second, finer, cylindrical C-grid is embedded within the first to further improve solution accuracy.

Along with the use of cylindrical C-grids, the more accurate TSD formulation for store body shapes employs exact body surface boundary conditions and isentropic pressure coefficients. Estimates of incremental store body loads due to viscous crossflow effects (ref. 13) are included along with computed inviscid results. These simple estimates are based solely on the store's combined pitch/yaw angle relative to the freestream flow and, as such, are strictly valid for isolated bodies only.

COMPARISONS AND CORRELATIONS

The first case considered is the Douglas wing/pylon/store test configuration introduced in the previous section. Results computed at $M_\infty = 0.75$ and $\alpha = 4°$ for isolated wing and store components are compared in figures 3-5 to those computed for the wing/pylon/store configuration. Overall, the results show the presence of strong store/airframe interactions.

In figure 3, computed wing chordwise surface pressures are compared to experimental data (ref. 14) obtained at a span station somewhere in the vicinity of the pylon. Even for the wing-alone configuration, correlation on the wing upper surface is poor. Airfoil section studies using the more sophisticated 2-D GRUMFOIL method (ref. 15) gave similar predictions, suggesting that test anomalies, rather than flow simulation inaccuracies, are to blame. Nevertheless, the predicted and measured effect of the pylon and store on wing upper surface pressures is a slightly more pronounced leading-edge expansion.

Correlation with data in figure 3 is better on the wing lower surface. The compression in front of and expansion around the pylon leading edge propagates onto the wing lower surface, with measured pressure levels midway between those computed at the inboard and outboard wing/pylon junction. The flow then accelerates along the length of the pylon. It expands even more as it attempts to fill in behind the rather blunt pylon trailing edge, where it then undergoes the usual trailing-edge compression. The large expansion and strong shock predicted at the pylon trailing edge occur in the data to a lesser degree, possibly due to viscous effects and/or flow separation which have not been modelled.

Computed wing spanload distributions are also shown in figure 3. The combined effect of the wing and store is a marked decrease in wing loading which is greatest at the wing/pylon junction itself. The load carried on the pylon appears as a discontinuity in the wing spanload.

Isolated and pylon-mounted store longitudinal pressure distribution predictions are compared in figure 4. The large compressions and expansions associated with the pylon leading and trailing edges can be seen along the store top centerline. Here, the leading-edge expansion terminates in a shock, after which pressure levels are closer to those on the adjacent wing surface. Aft of the pylon, the flow continues to accelerate slightly, until it is overcome by the compression at the wing trailing edge. These effects occur to a lesser degree along the inboard and outboard sides of the store, and even less so along the bottom centerline.

The predicted effects of the airframe on store axial load distributions are shown in figure 5. Most noticeable is a downward load in the area of the wing and pylon leading edge, an upward load due to the expansion in the immediate wing/pylon/store vicinity, and downward loads near the wing and pylon trailing edges. There are also small excursions in side force.

The second case considered is the same Nielsen wing/fuselage/pylon/store test configuration studied in reference 10. Here, results computed at $M_\infty = 0.925$ and $\alpha = 5°$ for the isolated wing/fuselage and store components are compared in figures 6-8 to those computed for the wing/fuselage/pylon and wing/fuselage/pylon/store configurations. As for the Douglas test configuration, the results show the presence of strong store/airframe interactions.

The predicted effects of pylon and store on wing chordwise pressure distributions at the pylon span station are shown in figure 6. The compressions and expansions at the pylon leading and trailing edges propagate onto the wing lower surface. A slight acceleration otherwise occurs along the length of the wing/pylon junction. These effects are more pronounced when the store is present. The compression at the store nose for this case propagates onto the the wing lower surface, accompanied by a slight increase in the size of the wing leading-edge expansion. The effects of the pylon and store on the wing spanload distribution are also shown in the figure. The pylon without a store has a much smaller effect on the wing spanload than does the pylon/store combination.

Computed fuselage bottom centerline pressure distributions are compared to experimental data (ref. 16) in figure 7. For the wing/fuselage configuration, the wing lower surface pressure field propagates only slightly onto the fuselage bottom centerline. With the pylon present, this effect is enhanced. With both pylon and store present, the effect is highly pronounced. These results correlate well with the data.

In reference 10, computed store pressure and axial load distributions for this configuration (as well as for the isolated store) were compared with experimental data (ref. 16). The pylon-mounted store axial load distributions are shown here again, in figure 8. Good correlation is shown for both normal and side force load distributions. The anomaly in predicted side force in the vicinity of the pylon trailing edge is attributed to a small misalignment of predicted inboard and outboard pylon trailing-edge shock locations. Unfortunately, one of the difficulties encountered in predicting store loads at transonic speeds is that relatively large loads result from rather small differences in surface pressures. Modelling of viscous effects and/or flow separation might correct this computational deficiency.

The Nielsen wing/fuselage/pylon/store configuration was tested at supersonic, as well as subsonic, freestream Mach numbers. Although limited success was achieved for supersonic treatment of stores, calculations for this configuration were possible, most likely because the underwing store is in a region of reduced, lower Mach number flow. Results computed at $M_\infty = 1.1$ and $\alpha = 5°$ are shown in figures 9-11.

In figure 9, which shows results for the wing and fuselage, an unexplained variation in wing upper surface pressures at about 70% chord is predicted. Good correlation is shown for the fuselage bottom centerline pressure distribution. Store surface pressures appear in figure 10. Strong shocks which are predicted towards the aft end of the store do not occur in the data, again possibly due to viscous effects and/or flow separation. These discrepancies also compromise the store axial load distribution correlations, which appear in figure 11. Overall, correlation with data is fair, but not as good as for the subsonic case.

CONCLUDING REMARKS

Correlations indicate that the Transonic Store Carriage Loads Prediction Code provides reliable prediction of store carriage aerodynamics, but that even simple 2-D or axisymmetric modelling of viscous effects and flow separation would improve store carriage loads prediction accuracy. A limited supersonic freestream capability was also demonstrated. Even with the limitations of the transonic small disturbance, embedded grid formulation, the method provides a fundamental understanding of store/airframe interactions not available by other means.

REFERENCES

1. Boppe, C.W., "Transonic Flow Field Analysis for Wing-Fuselage Configurations," NASA CR 3243, May 1980.

2. Boppe, C.W., "Aerodynamic Analysis for Aircraft with Nacelles, Pylons, and Winglets," NASA CR 4066, Apr. 1987.

3. Rosen, B.S., "Computational Transonic Analysis of Canted Winglets," Journal of Aircraft, Vol. 21, No. 11, pp. 873-878, Nov. 1984.

4. Thompson, D.S., "A Mesh Embedding Approach for Prediction of Transonic Wing/Body/Store Flow Fields," paper presented at the Numerical Boundary Condition Procedures Symposium, Moffet Field, CA, 19-20 Oct. 1981.

5. Thompson, D.S., "TAS - A Transonic Aircraft/Store Flow Field Prediction Code," NASA CR 3721, Dec. 1983.

6. Dougherty, F.C., Benek, J.A. and Steger, J.L., "On Applications of Chimera Grid Schemes to Store Separation," NASA TM 88193, Oct. 1985.

7. Lijewski, L.E., "Transonic Flow Solutions on a Blunt, Finned Body of Revolution Using the Euler Equations," AIAA Paper 86-1082, May 1986.

8. Cottrell, C.J. and Lijewski, L.E., "A Study of Finned, Multi-Body Aerodynamic Interference at Transonic Mach Numbers," AIAA Paper 87-2480, Aug. 1987.

9. Rosen, B.S., "Body Flow Field Simulation and Force/Moment Prediction at Transonic Speeds," AIAA Paper 85-0423, Jan. 1985.

10. Rosen, B.S., "External Store Carriage Loads Prediction at Transonic Speeds," AIAA Paper 88-0003, Jan. 1988.

11. Jameson, A., "Iterative Solution of Transonic Flows over Airfoils and Wings, Including Flows at Mach 1," Communications on Pure and Applied Mathematics, Vol. 27, pp. 283-309, 1974.

12. Roache, P.J., "Computational Fluid Dynamics," Hermosa Publishers, Albuquerque, N.M., 1972.

13. Allen, J.H., "Estimation of the Forces and Moments Acting on Inclined Bodies of Revolution of High Fineness Ratio," NACA RM A9I26, 1949.

14. Muse, T.C. and Bratt, R.W., "Summary of High Speed Wind-Tunnel Tests of a Douglas Aircraft Store Shape and a 2000-Pound G.P.-AN-M66 Bomb," Douglas Aircraft Company, Inc. Report E.S. 21150, Jun. 1948.

15. Melnik, R.E., Chow, R.R., Mead, H.R. and Jameson, A., "An Improved Viscid/Inviscid Interaction Procedure for Transonic Flow over Airfoils," NASA CR 3805, Oct. 1985.

16. Stahara, S.S. and Crisalli, A.J., "Data Report for a Test Program to Study Transonic Flow Fields about Wing-Body/Pylon/Store Combinations," AFOSR TR-79-1070, May 1978.

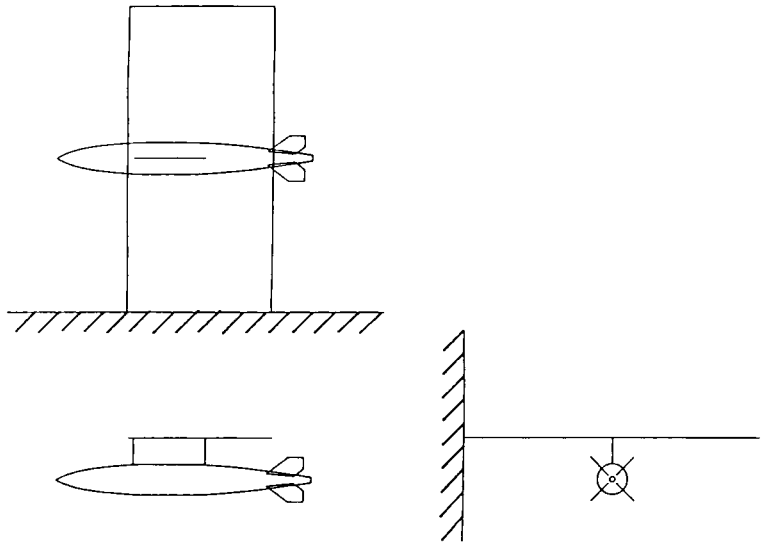

Figure 1. Input geometry verification for Douglas wing/pylon/store.

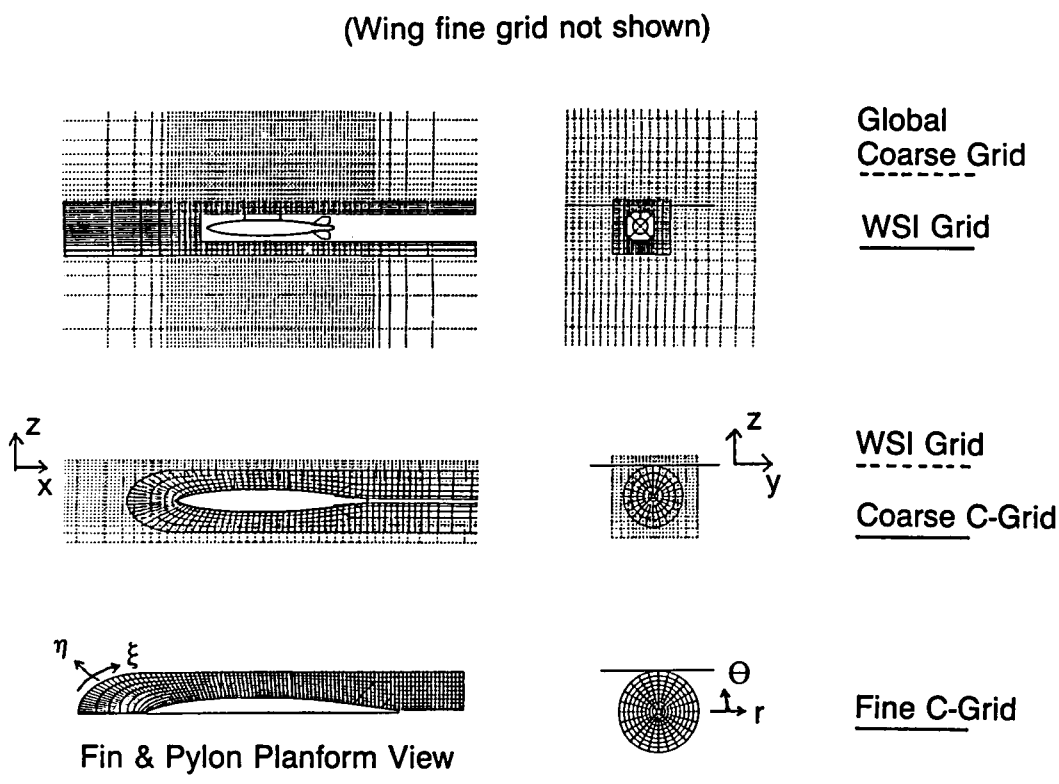

Figure 2. Grid arrangement for Douglas wing/pylon/store.

ORIGINAL PAGE IS
OF POOR QUALITY

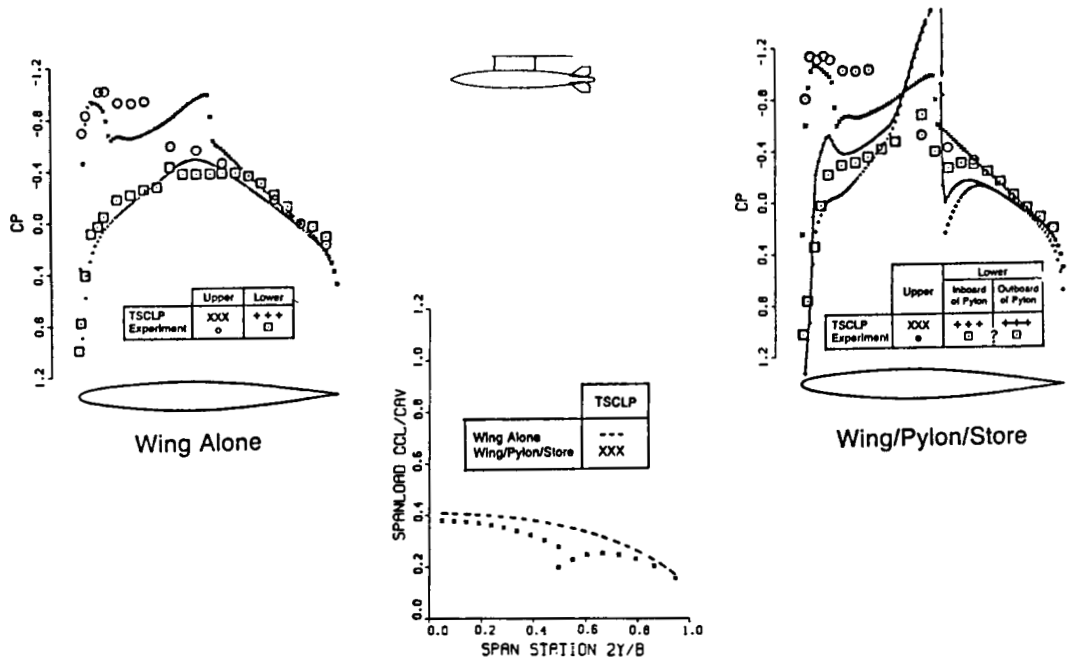

Figure 3. Douglas wing/pylon/store: wing pressure/spanload comparisons at $M_\infty = 0.75$ and $\alpha = 4°$.

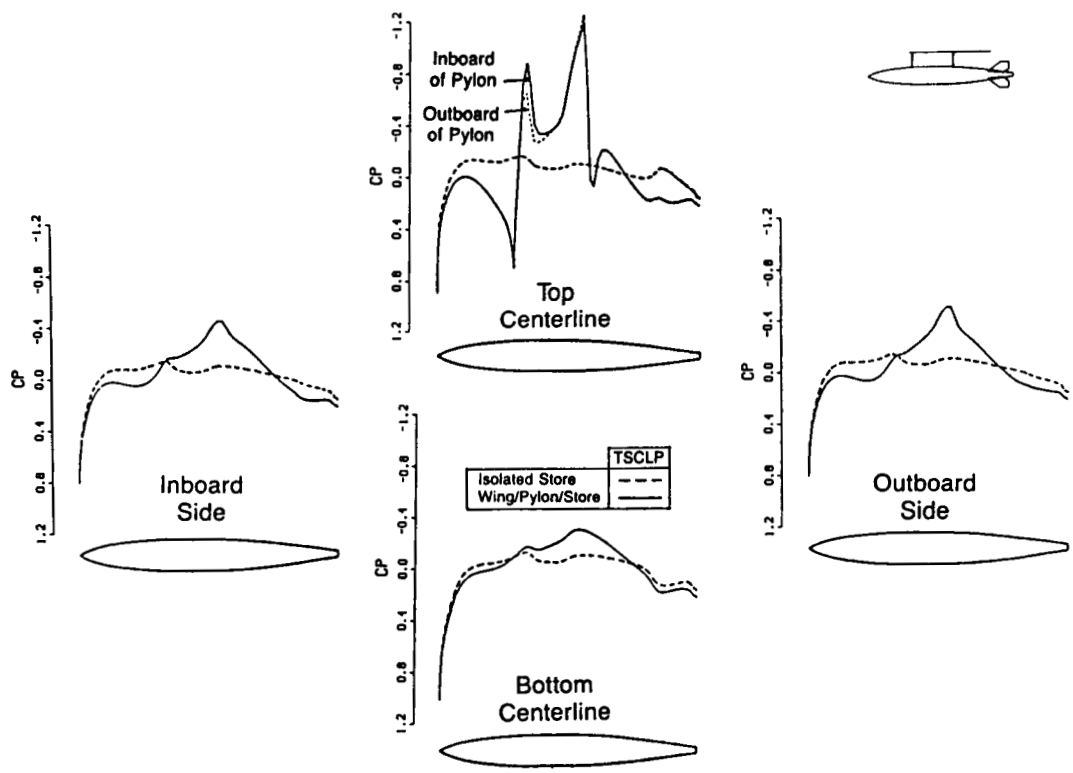

Figure 4. Douglas wing/pylon/store: store body pressure comparisons at $M_\infty = 0.75$ and $\alpha = 4°$.

ORIGINAL PAGE IS
OF POOR QUALITY

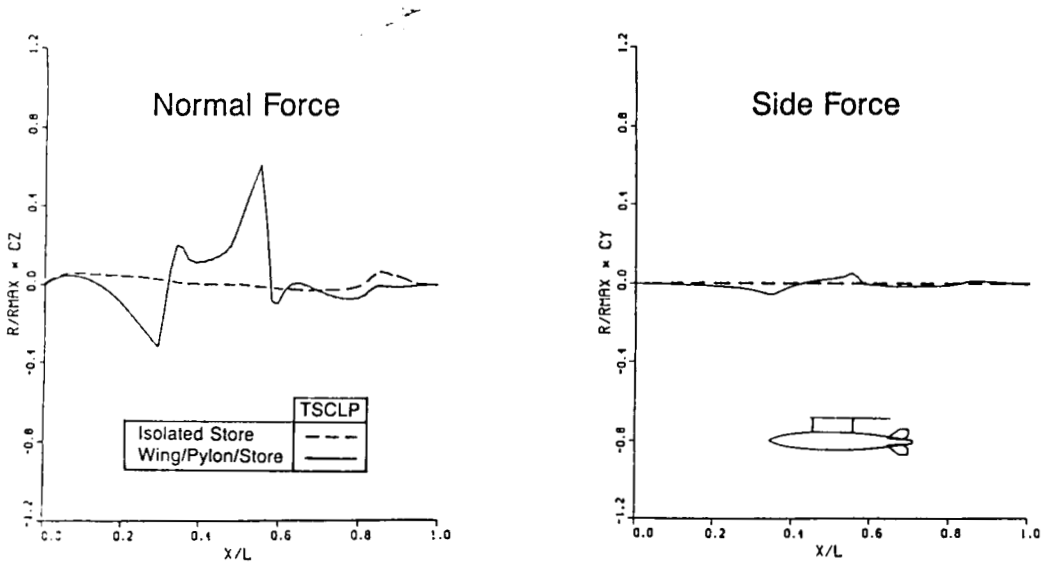

Figure 5. Douglas wing/pylon/store: store body load distribution comparisons at $M_\infty = 0.75$ and $\alpha = 4°$.

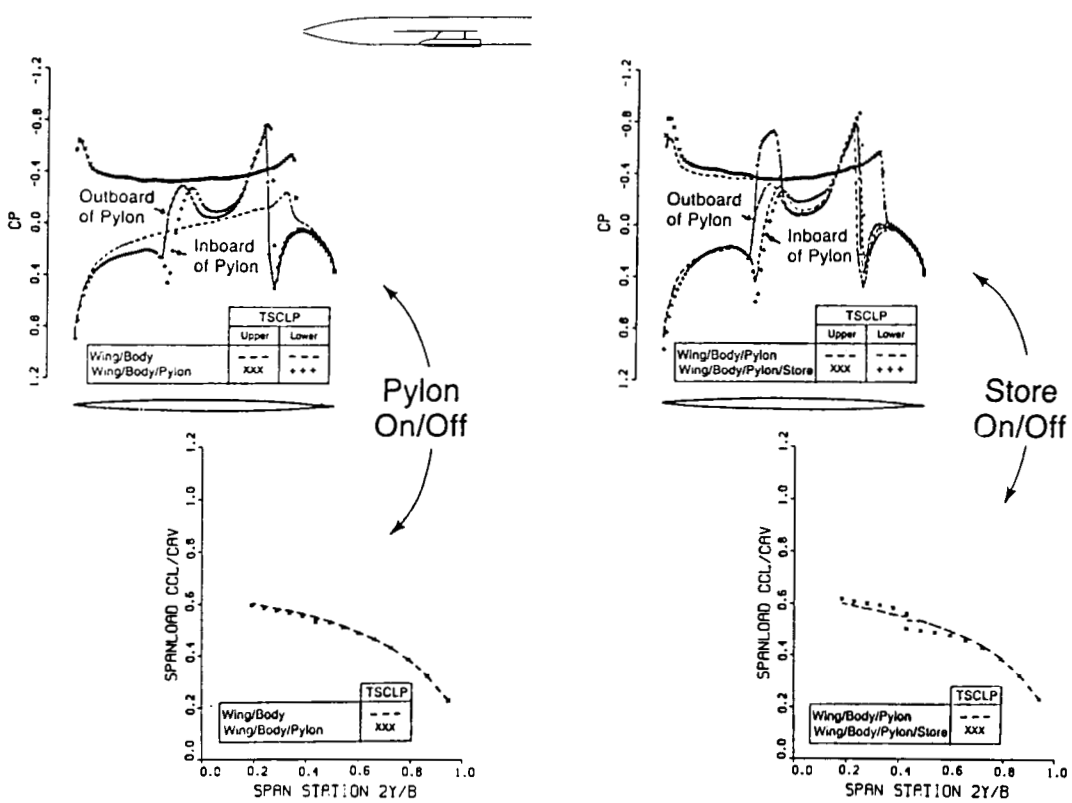

Figure 6. Nielsen wing/fuselage/pylon/store: wing pressure/spanload comparisons at $M_\infty = 0.925$ and $\alpha = 5°$.

ORIGINAL PAGE IS
OF POOR QUALITY

ORIGINAL PAGE IS
OF POOR QUALITY

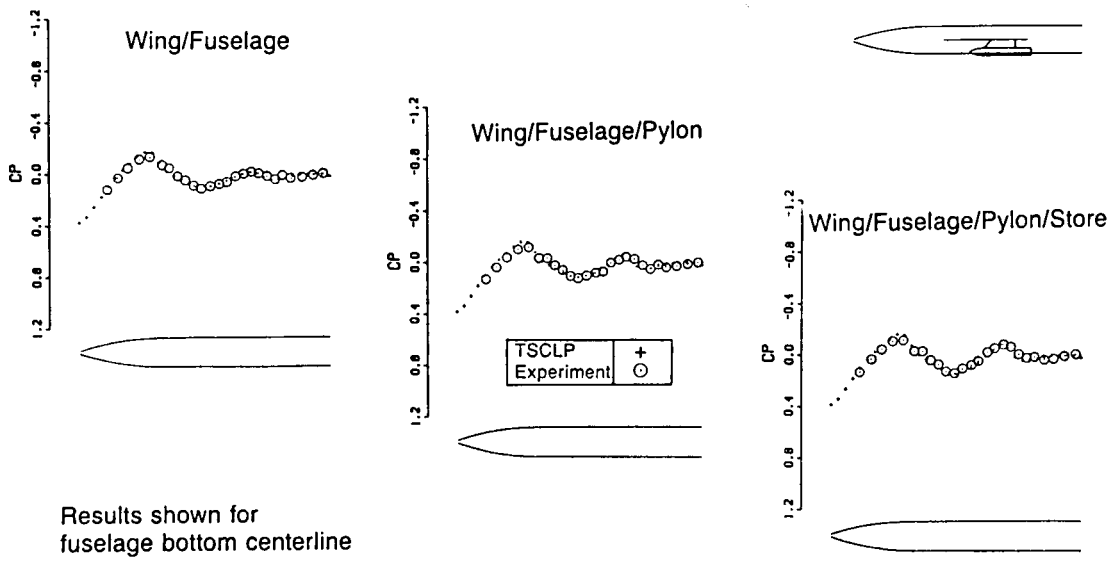

Figure 7. Nielsen wing/fuselage/pylon/store: fuselage pressure comparisons at $M_\infty = 0.925$ and $\alpha = 5°$.

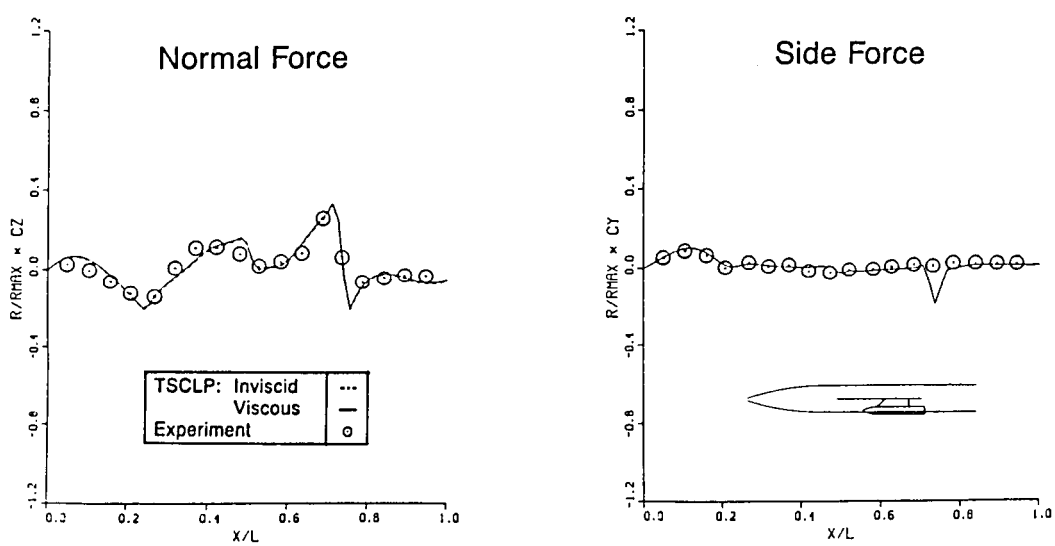

Figure 8. Nielsen wing/fuselage/pylon/store: store load distribution comparisons at $M_\infty = 0.925$ and $\alpha = 5°$.

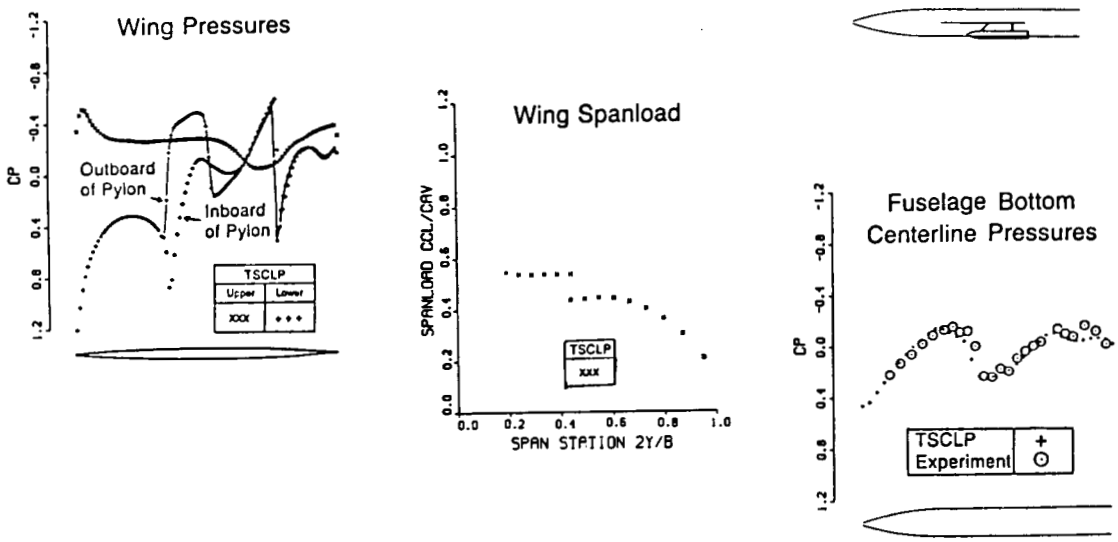

Figure 9. Nielsen wing/fuselage/pylon/store: wing/fuselage pressure/spanload comparisons at $M_\infty = 1.1$ and $\alpha = 5°$.

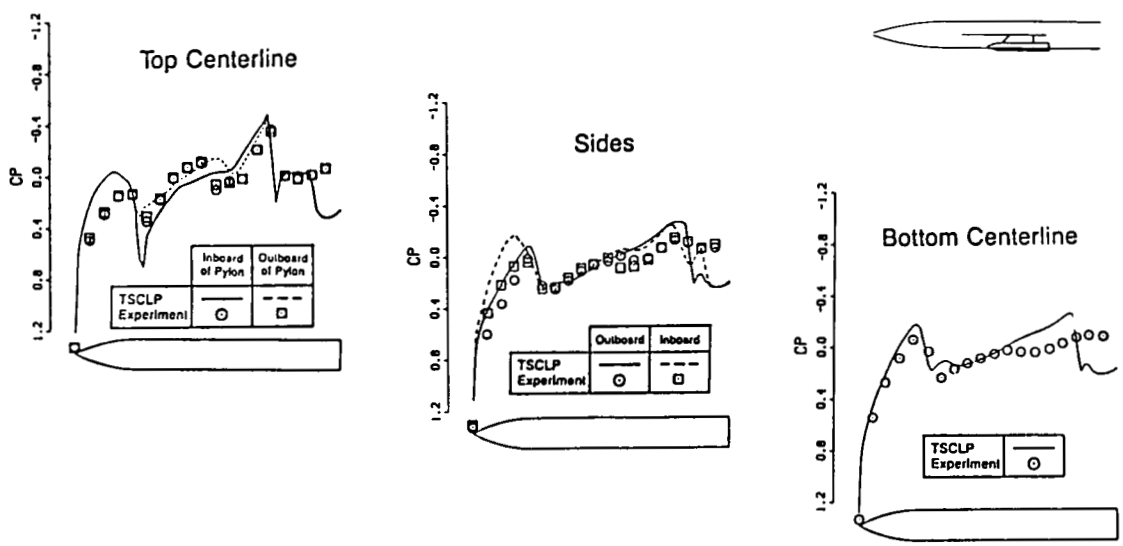

Figure 10. Nielsen wing/fuselage/pylon/store: store pressure comparisons at $M_\infty = 1.1$ and $\alpha = 5°$.

ORIGINAL PAGE IS
OF POOR QUALITY

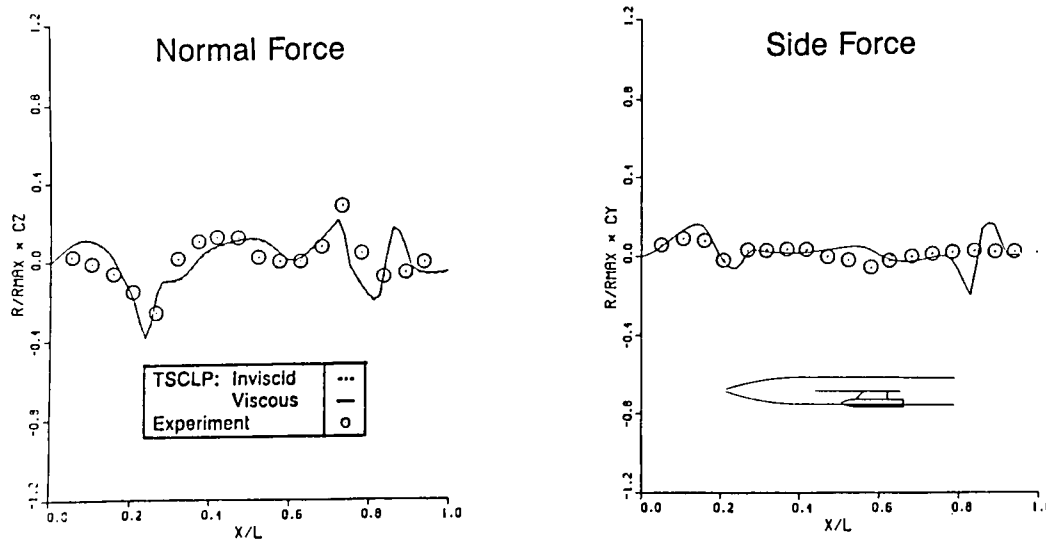

Figure 11. Nielsen wing/fuselage/pylon/store: store load distribution comparisons at $M_\infty = 1.1$ and $\alpha = 5°$.

N89-20946

STEADY AND UNSTEADY TRANSONIC SMALL DISTURBANCE ANALYSIS OF REALISTIC AIRCRAFT CONFIGURATIONS

John T. Batina
David A. Seidel
Robert M. Bennett
Herbert J. Cunningham
Samuel R. Bland
NASA Langley Research Center
Hampton, Virginia

Summary

A transonic unsteady aerodynamic and aeroelasticity code called CAP-TSD has been developed for application to realistic aircraft configurations. The name CAP-TSD is an acronym for Computational Aeroelasticity Program - Transonic Small Disturbance. The code permits the calculation of steady and unsteady flows about complete aircraft configurations for aeroelastic analysis in the flutter critical transonic speed range. The CAP-TSD code uses a time-accurate approximate factorization (AF) algorithm for solution of the unsteady transonic small-disturbance potential equation. The paper gives an overview of the CAP-TSD code development effort and reports on recent algorithm modifications. The algorithm modifications include: an Engquist-Osher (E-O) type-dependent switch to treat regions of supersonic flow, extension of the E-O switch for second-order spatial accuracy, nonisentropic effects to treat strong-shock cases, nonreflecting far field boundary conditions for unsteady applications, and several modifications to accelerate convergence to steady-state. Calculations are presented for several configurations including the General Dynamics one-ninth scale F-16C aircraft model to evaluate the algorithm modifications. The modifications have significantly improved the stability of the AF algorithm and hence the reliability of the CAP-TSD code in general. Calculations are also presented from a flutter analysis of a 45° sweptback wing which agree well with the experimental data. The paper presents descriptions of the CAP-TSD code and algorithm details along with results and comparisons which demonstrate the stability, accuracy, efficiency, and utility of CAP-TSD.

Introduction

Presently, considerable research is being conducted to develop finite-difference computer codes for calculating transonic unsteady aerodynamics for aeroelastic applications.[1] These computer codes are being developed to provide accurate methods of calculating unsteady airloads for the prediction of aeroelastic phenomena such as flutter and divergence. For example, the CAP-TSD[2] unsteady transonic small-disturbance (TSD) code was recently developed for transonic aeroelastic analyses of complete aircraft configurations. The name CAP-TSD is an acronym for Computational Aeroelasticity Program - Transonic Small Disturbance. The new code permits the calculation of unsteady flows about complete aircraft for aeroelastic analysis in the flutter critical transonic speed range. The code can treat configurations with arbitrary combinations of lifting surfaces and bodies including canard, wing, tail, control surfaces, tip launchers, pylons, fuselage, stores, and nacelles. Steady and unsteady pressure comparisons were presented in Refs. 2 and 3 for numerous cases which

demonstrated the geometrical applicability of CAP-TSD. These calculated results were generally in good agreement with available experimental pressure data which validated CAP-TSD for multiple component applications with mutual aerodynamic interference effects. Preliminary aeroelastic applications of CAP-TSD were presented in Ref. 4 for a simple well-defined wing case. The case was selected as a first step toward performing aeroelastic analyses for complete aircraft configurations. The calculated flutter boundaries compared well with the experimental data for subsonic, transonic, and supersonic freestream Mach numbers, which gives confidence in CAP-TSD for aeroelastic prediction.

The CAP-TSD code uses a time-accurate approximate factorization (AF) algorithm recently developed by Batina[5] for solution of the unsteady TSD equation. The AF algorithm involves a Newton linearization procedure coupled with an internal iteration technique. In Ref. 5, the algorithm was shown to be efficient for application to steady or unsteady transonic flow problems. It can provide accurate solutions in only several hundred time steps, yielding a significant computational cost savings when compared to alternative methods. For reasons of practicality and affordability, an efficient algorithm and a fast computer code are requirements for realistic aircraft applications.

Recently, several algorithm modifications have been made which have improved the stability of the AF algorithm and the accuracy of the results.[6,7] These algorithm modifications include: (1) an Engquist-Osher (E-O) type-dependent switch to more accurately and efficiently treat regions of supersonic flow, (2) extension of the E-O switch for second-order-accurate spatial differencing in supersonic regions to improve the accuracy of the results, (3) nonisentropic effects to more accurately treat cases with strong shocks, (4) nonreflecting far field boundary conditions for more accurate unsteady applications, and (5) several modifications which accelerate convergence to steady-state. The work has been a major research activity over the past two years within the Unsteady Aerodynamics Branch at NASA Langley Research Center. The purpose of the paper is to give an overview of the CAP-TSD code development effort and report on the recent algorithm changes and code improvements. The paper documents these developments and presents results which demonstrate the capability.

Symbols

b_o	reference length, $c_r/2$
c	airfoil chord
c_{l_α}	unsteady lift-curve slope
c_r	wing reference chord
C_p	pressure coefficient
k	reduced frequency, $\omega c_r/2U$
M	freestream Mach number
NSUP	number of supersonic points
$q_i(t)$	generalized displacement for mode i
R	residual
t	time, nondimensionalized by freestream speed and wing reference chord
U	freestream speed
α	instantaneous angle of attack
α_o, α_1	mean angle of attack and amplitude of pitch oscillation, respectively

γ	ratio of specific heats
Δt	nondimensional time step
$\bar{\eta}$	fractional semispan
μ	ratio of wing mass to mass of air in the truncated cone that encloses the wing
ρ	freestream flow density
ϕ	disturbance velocity potential
ω	angular frequency
ω_α	natural frequency of the first torsion mode

Subscripts

t	tail
w	wing

Transonic Small-Disturbance Equation

The flow is assumed to be governed by the general frequency modified TSD potential equation which may be written as

$$M^2 (\phi_t + 2\phi_x)_t = [(1 - M^2)\phi_x + F\phi_x^2 + G\phi_y^2]_x + (\phi_y + H\phi_x\phi_y)_y + (\phi_z)_z \qquad (1)$$

Several choices are available for the coefficients F, G, and H depending upon the assumptions used in deriving the TSD equation. For transonic applications, the coefficients are herein defined as

$$F = -\frac{1}{2}(\gamma + 1) M^2, \; G = \frac{1}{2}(\gamma - 3) M^2, \; H = -(\gamma - 1) M^2 \qquad (2)$$

The linear potential equation is recovered by simply setting F, G, and H equal to zero.

Approximate Factorization Algorithm

A time-accurate approximate factorization algorithm was developed[5] to solve the unsteady TSD equation. In this section, the AF algorithm is briefly described.

General Description

The AF algorithm consists of a Newton linearization procedure coupled with an internal iteration technique. For unsteady flow calculations, the solution procedure involves two steps. First, a time linearization step (described below) is performed to determine an estimate of the potential field. Second, internal iterations are performed to provide time-accurate modeling of the flow field. Specifically, the TSD equation is written in general form as

$$R(\phi^{n+1}) = 0 \tag{3}$$

where ϕ^{n+1} represents the unknown potential field at time level (n+1). The solution to Eq. (3) is then given by the Newton linearization of Eq. (3) about ϕ^*

$$R(\phi^*) + \left(\frac{\partial R}{\partial \phi}\right)_{\phi=\phi^*} \Delta\phi = 0 \tag{4}$$

In Eq. (4), ϕ^* is the currently available value of ϕ^{n+1} and $\Delta\phi = \phi^{n+1} - \phi^*$. During convergence of the iteration procedure, $\Delta\phi$ will approach zero so that the solution will be given by $\phi^{n+1} = \phi^*$. In general, only one or two iterations are required to achieve acceptable convergence. For steady flow calculations, iterations are not used since time accuracy is not necessary when marching to steady state.

Mathematical Formulation

The AF algorithm is formulated by first approximating the time-derivative terms by second-order-accurate finite-difference formulae. The TSD equation is rewritten by substituting $\phi = \phi^* + \Delta\phi$ and neglecting squares of derivatives of $\Delta\phi$ (which is equivalent to applying Eq. (4) term by term). The resulting equation is then rearranged and the left-hand side is approximately factored into a triple product of operators yielding

$$L_\xi L_\eta L_\zeta \Delta\phi = -\sigma R(\phi^*, \phi^n, \phi^{n-1}, \phi^{n-2}) \tag{5}$$

where the operators L_ξ, L_η, L_ζ and residual R were derived and presented in Ref. 5. In Eq. (5) σ is a relaxation parameter which is normally set equal to 1.0. To accelerate convergence to steady-state, the residual R may be over-relaxed using $\sigma > 1$. Equation (5) is solved using three sweeps through the grid by sequentially applying the operators L_ξ, L_η, L_ζ as

$$\xi\text{ - sweep: } L_\xi \bar{\Delta\phi} = -\sigma R \tag{6a}$$

$$\eta\text{ - sweep: } L_\eta \bar{\bar{\Delta\phi}} = \bar{\Delta\phi} \tag{6b}$$

$$\zeta\text{ - sweep: } L_\zeta \Delta\phi = \bar{\bar{\Delta\phi}} \tag{6c}$$

Further details of the algorithm development and solution procedure may be found in Ref. 5.

Flow-Tangency Boundary Conditions

The flow tangency boundary conditions are imposed along the mean plane of the respective lifting surfaces and the wakes are assumed to be planar extensions from the trailing edges to the downstream boundary of the finite-difference grid. The numerical implementation of these conditions[2] allows for coplanar as well as non-coplanar combinations of horizontal (canard, wing, horizontal tail, launchers) and vertical (pylons, vertical tail) surfaces. Bodies such as the fuselage, stores, and nacelles are treated using simplified boundary conditions on a prismatic surface rather than on the true surface.[2] The method is consistent with the small-disturbance approximation and treats bodies with sufficient accuracy to obtain the correct global effect on the flow field without the use of special grids or complicated coordinate transformations. This type of modeling is similar to that of Boppe and Stern,[8] where good agreement was shown in comparison with experimental data for configurations with a fuselage and flow-through nacelles.

Time-Linearization Step

An initial estimate of the potentials at time level (n+1) is required to start the iteration process. This estimate is provided by performing a time-linearization calculation. The equations governing the time-linearization step are derived in a similar fashion as the equations for iteration. The only difference is that the equations are formulated by linearizing about time level (n) rather than the iterate level (*).

Algorithm Improvements

Engquist-Osher Type-Dependent Switch

Algorithms based on the TSD equation typically use central differencing in regions of subsonic flow and upwind differencing in regions of supersonic flow. This, of course, allows for the correct numerical description of the physical domain of dependence. The original CAP-TSD code of Ref. 2 used the Murman[9] type-dependent switch to change the spatial differencing. The Murman switch, however, admits nonphysical expansion shocks as a part of the solution and has been shown to be less stable than monotone methods.[10,11] For example, unsteady results for a NACA 64A006 airfoil were presented in Ref. 11 which demonstrated an order of magnitude increase in time step using a monotone algorithm. Therefore, an Engquist-Osher (E-O) monotone switch, similar to that of Ref. 10, has been incorporated within the AF algorithm of the CAP-TSD code.[6] The E-O switch is based on sonic reference conditions and does not admit expansion shocks as part of the solution. Use of the E-O switch also generally increases computational efficiency because of the larger time steps which may be taken.

Second-Order-Accurate Spatial Differencing

Most TSD algorithms are only first-order-accurate spatially in regions of supersonic flow. This is due to the first-order upwind differencing that is typically used to treat these regions. Use of second-order upwind differencing has been shown to improve the accuracy of the solution while

retaining the numerical stability of the first-order method.[12] Consequently, the E-O type dependent switch of the AF algorithm has been extended for second-order spatial accuracy in supersonic regions of the flow.[6] Comparisons of results obtained using first-order and second-order differencing, to be presented, demonstrate the improved accuracy of the second-order method.

Entropy and Vorticity Effects

A serious limitation of the potential flow codes, in general, is the inability to accurately treat cases with strong shock waves. For these cases, the isentropic potential formulation typically overpredicts the shock strength and locates the shock too far aft in comparison with experiment. In fact, it is fairly well known that potential theory predicts non-unique steady-state solutions[13,14] for narrow ranges of Mach number and angle of attack. Simple modifications to potential theory, however, have been shown to eliminate the nonuniqueness problem and consequently provide solutions which more accurately simulate those computed using the Euler equations.[15-18] These modifications include the effects of shock generated entropy and they require only minor changes to existing computer codes.

Rotational effects may also become important when strong shock waves are present in the flow. For example, vorticity is generated by shock waves due to the variation of entropy along the shock. Potential theory, of course, does not account for these effects because of the irrotationality assumption necessary for the existence of a velocity potential. For these cases the Euler equations are generally required to accurately model the flow. Recently, however, simple modifications to potential theory have been developed to model rotational effects.[19,20] These modifications involve a velocity decomposition originally suggested by Clebsch.[21] In this model, the velocity vector is decomposed into a potential part and a rotational part. For most applications of interest to the aeroelastician, the rotational part occurs only in the region downstream of shocks. Therefore, the potential part can be obtained throughout most of the flow field using an existing potential flow code. The rotational part can then either be incorporated as a source term in the governing equation or as a modification to the fluxes, by making simple changes to the solution procedure. These changes consequently include the effects of shock generated vorticity as well as entropy and require relatively straightforward modifications to existing potential codes.

Entropy and vorticity modifications to TSD theory have been implemented within the AF algorithm of the CAP-TSD code as described in Ref. 7. These modifications include: (1) an alternative streamwise flux in the TSD equation which was derived by an asymptotic expansion of the Euler equations,[22] (2) a modified velocity vector which is the sum of potential and rotational parts which in turn modifies the streamwise flux, and (3) the calculation and convection of entropy throughout the flow field. The modified code includes the effects of entropy and vorticity while retaining the relative simplicity and cost efficiency of the TSD formulation. Results obtained including these effects, to be presented, clearly demonstrate the improved accuracy of the AF algorithm.

Nonreflecting Far Field Boundary Conditions

For unsteady applications, the far field boundary conditions can have a significant influence on the accuracy of the solution. Steady-state boundary conditions are inadequate for unsteady

calculations, since disturbances reaching the boundaries are reflected back into the computational domain. These reflected disturbances can propagate into the near field and thus produce inaccurate results. One solution to this problem is to locate the grid boundaries far away to minimize the effect of the boundary conditions. This is generally not an acceptable remedy because of the higher computational cost which results from an increased number of grid points required to discretize a larger computational domain. The more appropriate solution is the use of nonreflecting far field boundary conditions which absorb most of the waves that are incident on the boundaries and consequently allow the use of smaller computational grids.[23] Nonreflecting boundary conditions similar to those of Whitlow[23] have been incorporated within the CAP-TSD code.[6] These boundary conditions are consistent with the AF solution procedure and are described in more detail in Ref. 6. Results obtained with and without the nonreflecting boundary conditions are presented which demonstrate their effectiveness.

Steady-State Convergence Acceleration

Finally, several algorithm changes have been made to accelerate convergence to steady-state.[6] Besides the E-O switch, these changes include: (1) deletion of the time-dependent terms from the residual of the AF algorithm, (2) deletion of all of the time-derivatives of the TSD equation, and (3) over-relaxation of the residual. The effects of these modifications on the steady-state convergence are demonstrated in the results presented herein.

Aeroelastic Solution

In this section the aeroelastic computational procedures are described including the equations of motion and the time-marching solution.

Equations of Motion

The aeroelastic equations of motion are based on a right-hand orthogonal coordinate system with the x-direction defined as positive downstream and the z-direction positive upward.[4] The presentation herein is limited to the case of an isolated wing with motion in the z-direction from an undisturbed position in the z = 0 plane. The equations of motion may be written as

$$M\ddot{q} + C\dot{q} + Kq = Q \tag{7}$$

where q is a vector of generalized displacements, M is the generalized mass matrix, C is the damping matrix, and K is the stiffness matrix. In Eq. (7) Q is the vector of generalized aerodynamic forces defined by

$$Q_i = \frac{\rho U^2}{2} c_r^2 \int_s h_i \frac{\Delta p}{\rho U^2/2} \frac{dS}{c_r^2} \tag{8}$$

where Δp is the lifting pressure which is weighted by the mode h_i. The equations of motion (Eq. (7) are solved by time-integration by first rewriting Eq. (7) as

$$\ddot{q} = -M^{-1}Kq - M^{-1}C\dot{q} + M^{-1}Q \qquad (9)$$

Time-Marching Solution

The aeroelastic solution procedure for integrating Eq. (9) is similar to that described by Edwards, et al.[24] Reference 24 describes for a two-dimensional, two-degree-of-freedom system an aeroelastic solution in terms of a state equation formulation. By a parallel formulation, a linear state equation is developed from Eq. (9) which is solved numerically using the modified state-transition matrix integrator of Ref. 24. This integrator was shown to be superior to six alternative structural integration algorithms.[25]

For aeroelastic analysis, two steps are generally required in performing the calculations. In the first step, the steady-state flow field is calculated to account for wing thickness, camber, and mean angle of attack thus providing the starting flow field for the aeroelastic analysis. The second step is to prescribe an initial disturbance to begin the structural integration. Disturbance velocities in one or more modes, rather than displacements, have been found to be distinctly superior in avoiding nonphysical, strictly numerical transients and their possible associated instabilities. In determining a flutter point, the freestream Mach number M and the associated freestream speed U are usually held fixed. A judiciously chosen value of the dynamic pressure $\rho U^2/2$ is used to compute the free decay transients. These resulting transients of the generalized coordinates are analyzed for their content of damped or growing sine-waves, with the rates of growth or decay indicating whether the dynamic pressure is above or below the flutter value. This analysis then indicates whether to increase or decrease the value of dynamic pressure in subsequent runs to determine a neutrally stable result.

CAP-TSD Code

The AF algorithm is the basis of the CAP-TSD code for transonic unsteady aerodynamic and aeroelastic analysis of realistic aircraft configurations. The present capability has the option of half-span modeling for symmetric cases or full-span modeling to allow the treatment of antisymmetric mode shapes, fuselage yaw, or unsymmetric configurations such as an oblique wing or unsymmetric wing stores. In the present coding of the AF algorithm, the time derivatives are implemented for variable time stepping to allow for step-size cycling to accelerate convergence to steady state. Also, since the L_ξ, L_η, and L_ζ operators only contain derivatives in their respective coordinate directions, all three sweeps of the solution procedure have been fully vectorized.

Results and Discussion

Results are presented for several configurations to demonstrate and evaluate the modifications to the AF algorithm of the CAP-TSD code. Calculations are also presented from a flutter analysis of a

45° sweptback wing to assess the aeroelastic capability of the code.

Flat Plate Airfoil Results

Unsteady results were obtained for a flat plate airfoil at M = 0.85 to test the nonreflecting far field boundary conditions.[6] The flat plate airfoil was selected to allow direct comparison of results with the exact kernel function method of Bland.[26] The boundary conditions were tested by computing the lift coefficient due to the airfoil pitching about the quarter chord. Such unsteady forces are typically determined by calculating several cycles of forced harmonic oscillation with the last cycle providing the estimate of the forces. Alternatively, the forces may be obtained indirectly from the response due to a smoothly varying exponentially shaped pulse.[27] In this procedure, the airfoil is given a small prescribed pulse in a given mode of motion (in this case pitching) and the aerodynamic transients calculated. The harmonic response is obtained by a transfer-function analysis using fast Fourier transforms. Use of the pulse transfer-function technique gives considerable detail in the frequency domain with a significant reduction in cost over the alternative method of calculating multiple oscillatory responses. For the flat plate airfoil, pulse transient calculations were performed using 1024 time steps with $\Delta t = 0.2454$. The amplitude of the pulse was 0.5°. The grid extended 25 chordlengths above and below the airfoil, and 20 chordlengths upstream and downstream of the airfoil. Parallel results were obtained using reflecting (steady-state) and nonreflecting far field boundary conditions as shown in Fig. 1. The results are plotted as real and imaginary components of the unsteady lift-curve slope c_{l_α} as a function of reduced frequency k. Computations using the reflecting boundary conditions, shown in Fig. 1(a) produce oscillations in both the real and imaginary parts for $0 < k < 0.2$. The oscillations are produced by reflected disturbances which propagate back into the near field and contaminate the solution. When the calculation was repeated using the nonreflecting boundary conditions, shown in Fig. 1(b), the oscillations no longer occur since the boundary conditions absorb most of the disturbances that are incident on the grid boundaries. Furthermore, these results are in excellent agreement with calculations from the kernel function method of Ref. 26.

F-5 Wing Results

Calculations were next performed for the F-5 wing[28] to assess the algorithm modifications[6] to CAP-TSD. The F-5 wing has an aspect ratio of 3.16, a leading edge sweep angle of 31.9°, and a taper ratio of 0.28. The airfoil section of the wing is a modified NACA 65A004.8 airfoil which has a drooped nose and is symmetric aft of 40% chord. The F-5 calculations were performed using a constant step size for a total of 500 steps. The freestream Mach number was selected as 0.9 and the wing was at 0° angle of attack. The results were obtained to study the steady-state convergence characteristics of the modified AF algorithm. The results are presented in the form of convergence histories and the number of supersonic (NSUP) points versus the iteration number.

In the original AF algorithm of Ref. 5, the Murman type-dependent switch was used. Results obtained using the unmodified code are presented in Fig. 2. The steady-state convergence is shown in Fig. 2(a); the number of supersonic points (NSUP) normalized by the final value are shown in Fig. 2(b). For aeroelastic analysis where airloads are required rather than pressures, the solution is considered to be converged to engineering accuracy when a three to four order-of-magnitude reduction in the solution error is obtained. The "error" in the convergence history, as defined

herein, is the ratio of the maximum $|\Delta\phi|$ after n iterations to the maximum $|\Delta\phi|$ in the initial solution (first iteration). Two sets of results are plotted corresponding to two values of step size, $\Delta t = 0.1$ and 0.5. For $\Delta t = 0.1$, the rate of convergence is slow and the number of supersonic points oscillates about the final value. Increasing the step size to $\Delta t = 0.5$ improves the rate of convergence and the oscillations in NSUP are significantly damped. The results for $\Delta t = 0.5$ also indicate that the number of supersonic points is initially more than four and one-half times the final value and that "spikes" begin to appear in the convergence history after 150 steps. These spikes, which represent a numerical instability, are due to a large transient caused by the impulsive start from a uniform stream using a large step size. If the calculations were started with a smaller step size, and then the step size increased to the larger value, the numerical instability can be avoided. Also, as shown in Refs. 2 and 5, the step size may be cycled through very large values such as $\Delta t = 5.0$ to achieve faster convergence to steady-state.

The F-5 calculations with $\Delta t = 0.5$ were then repeated with the E-O switch replacing the Murman switch. These results are labeled "unsteady algorithm" in Fig. 3. The curves are almost identical to the $\Delta t = 0.5$ curves of Fig. 2 except that the spikes in the convergence history are absent. The E-O switch is more robust than the Murman switch and thus the calculation remains stable. Furthermore, the rate of convergence to steady-state could be increased by deleting the time derivatives in the residual, over-relaxing the residual, or deleting all of the time derivatives in the TSD equation.[6] By deleting all of the time derivatives, the algorithm solves the steady TSD equation and is therefore referred to as the "steady algorithm." Results obtained using this algorithm are compared with the unsteady algorithm results in Fig. 3. The convergence history computed using the steady algorithm is monotonically decreasing and very smooth in comparison with the unsteady algorithm convergence history. The steady algorithm solution converges faster and does not produce the large initial overprediction of NSUP that is characteristic of the unsteady algorithm. The number of supersonic points converges rapidly to within 2% of its final value in only approximately 25 steps. Over-relaxing the residual of the steady algorithm also further accelerates the convergence to steady-state (not shown).

ONERA M6 Wing Results

To test the accuracy of the modified CAP-TSD algorithm,[6] calculations were performed for the ONERA M6 wing.[29] The M6 wing has an aspect ratio of 3.8, a leading edge sweep angle of 30°, and a taper ratio of 0.562. The airfoil section of the wing is the ONERA "D" airfoil which is a 10% maximum thickness-to-chord ratio conventional section. The freestream Mach number was selected as $M = 0.84$ and the wing was at 3.06° angle of attack. These conditions were chosen for comparison with the tabulated experimental pressure data of Ref. 29. This rather well-known case is a very challenging one, especially for a TSD code, because of the complex double shock wave which occurs on the upper surface of the wing.

Steady-state calculations were performed for the M6 wing by using the AF algorithm with the E-O switch. The results were obtained by cycling the step size through values as large as $\Delta t = 2.0$ for a total of 500 steps. This relatively large step size corresponds to two root chords of travel per time step. A comparison of the resulting CAP-TSD pressures with the experimental pressure data is given in Fig. 4 for $\bar{\eta} = 0.44$. The data indicate that there is a relatively weak highly swept supersonic-to-supersonic shock wave which forms forward near the leading edge. The primary

supersonic-to-subsonic shock which occurs in the midchord region of the wing, coalesces with the first shock in the spanwise direction. Outboard toward the tip, the two shocks merge to form a single supersonic-to-subsonic shock wave. The CAP-TSD results obtained using first-order-accurate differencing in supersonic regions are in fairly good agreement with the data in predicting the overall pressure levels, although differences occur in the regions of the shocks. In general, the leading-edge suction peak is well predicted but the supersonic-to-supersonic shock is smeared. When the calculation was repeated using the second-order-accurate spatial differencing, a significant improvement was obtained in the accuracy of the results. The comparisons in Fig. 4 show that the supersonic-to-supersonic shock is much more sharply captured by the second-order method and consequently the calculated pressures are now in very good agreement with the experimental data. Calculations were also performed for the M6 wing using the original algorithm with the Murman switch. These calculations were unsuccessful because of a numerical instability which was produced by the highly expanded flow about the leading edge of the wing.

An unsteady calculation was also performed for the M6 wing at M = 0.84, to investigate the robustness of the modified algorithm for time-dependent applications. In this demonstration calculation, the wing was forced to oscillate in pitch about a line perpendicular to the root at the root midchord. The amplitude of the motion was 2° peak-to-peak about the mean angle of attack of α_o = 3.06°. The reduced frequency was selected as k = 0.1 and only 300 steps per cycle of motion were used. This corresponds to a step size of Δt = 0.1047. Three cycles of motion were computed to obtain a periodic solution. Unsteady pressure distributions, obtained using first-order and second-order accurate supersonic differencing, are shown in Fig. 5 at the maximum pitch angle (α = 4.06°) for $\bar{\eta}$ = 0.44. Similar to the steady-state results, these pressure comparisons illustrate that the supersonic-to-supersonic shock is more sharply captured by the second-order method. Further instantaneous pressure distributions at two points during the third cycle of motion are shown in Fig. 6 for five span stations along the wing. Pressures at the wing maximum angle of attack (α = 4.06°) and pressures at the wing minimum angle of attack (α = 2.06°) are both presented in the figure. As the wing pitches up, the shocks move aft and the supersonic-to-subsonic shock grows in strength. As the wing pitches down, the shocks move forward and the supersonic-to-supersonic shock is more sharply defined. For this case, both of the shocks oscillate over approximately 10% of the chord during a cycle of motion. Also, the supersonic-to-supersonic shock at $\bar{\eta}$ = 0.80 periodically appears and disappears during a cycle of motion. The results illustrate the large shock motions that the modified AF algorithm is capable of computing. The improved algorithm captures the shocks sharply and is sufficiently robust to compute this complex unsteady flow using only 300 steps per cycle of motion.

To test the entropy and vorticity modifications to TSD theory,[7] further calculations were performed for the M6 wing. Results were obtained at the freestream Mach number of M = 0.92 with the wing at 0° mean angle of attack. These conditions correspond to an AGARD test case for assessment of inviscid flow field methods[30] and were selected for comparison with the tabulated Euler results of Rizzi contained therein. Calculations were performed using: (a) unmodified TSD theory and (b) TSD with entropy and vorticity effects. Steady pressure distributions along three span stations ($\bar{\eta}$ = 0.08, 0.47, and 0.82) of the wing are presented in Fig. 7 from both solutions. For this steady-state case, the flow is symmetric about the wing with shocks on the upper and lower surfaces. As shown in Fig. 7(a), the results from the unmodified TSD theory compare well with the Euler results in predicting the leading-edge suction peak and the overall pressure levels. However, the shock is located too far aft and is too strong outboard near the tip (at $\bar{\eta}$ = 0.82, for example), in comparison with the Euler calculation. When the entropy and vorticity modifications are included in

the calculation, the shock is displaced forward from the previous solution, as shown in Fig. 7(b). Here the shock location and shock strength are in very good agreement with the Euler results at all three span stations on the wing. Consequently, the steady pressure distributions from the modified TSD theory now compare very well with the Euler pressures.

General Dynamics F-16C Aircraft Model Results

Results were also obtained for the General Dynamics F-16C aircraft model[31] to investigate application of the modified algorithm to a realistic aircraft configuration.[6] Shown in Fig. 8 are the F-16C components that are modeled using CAP-TSD. The F-16C is modeled using four lifting surfaces and two bodies. The lifting surfaces include: (1) the wing with leading and trailing edge control surfaces, (2) the launcher, (3) a highly swept strake, aft strake, and shelf surface, and (4) the horizontal tail. The bodies include: (1) the tip missile, and (2) the fuselage. In these calculations, the freestream Mach number was $M = 0.9$ and the F-16C aircraft was at 2.38° angle of attack. Also, the leading-edge control surface of the wing was deflected upwards 2° for comparison with the experimental steady pressure data of Ref. 32. Furthermore, the calculations were performed on a grid which conforms to the leading and trailing edges of the lifting surfaces and contains 324,000 points. Since the grid is Cartesian, it was relatively easy to generate, even for such a complex configuration as the F-16C aircraft. Also, the calculations required only about 0.88 CPU seconds per time step and thirteen million words of memory on the CDC VPS-32 computer at NASA Langley Research Center.

Steady-state calculations were performed for the F-16C aircraft using the AF algorithm with the E-O and Murman switches. The E-O results were obtained using both the first-order and second-order accurate supersonic differencing. Steady pressure comparisons are given in Fig. 9 for three span stations of the wing and one span station of the tail. Both sets of E-O results are presented for comparison with the experimental data. The results obtained using the Murman switch were originally published in Ref. 2. These results are identical to plotting accuracy with the first-order E-O results, and therefore are not shown. The steady pressure comparisons indicate that there is a moderately strong shock wave on the upper surface of the wing and the CAP-TSD pressures agree well with the experimental pressures. For the tail, the flow is predominantly subcritical and the calculated results again agree well with the data. Comparison of pressures computed using first-order and second-order accurate supersonic differencing shows very small differences. The largest difference, for example, occurs on the wing at $\bar{\eta}_W = 0.79$ where the second-order calculation predicts a slightly stronger shock.

Unsteady results were also obtained for the F-16C aircraft to investigate the robustness of the modified algorithm for realistic-aircraft time-dependent applications. For simplicity, the calculation was performed for a rigid pitching motion where the entire aircraft was forced to oscillate about the model moment reference axis at a reduced frequency of $k = 0.1$. The oscillation amplitude was chosen as $\alpha_1 = 1.5°$ which is three times the value used to obtain similar results presented in Ref. 2. Three cycles of motion were computed using 300 steps per cycle of motion corresponding to $\Delta t = 0.1047$. Calculations were performed using both the Murman and E-O switches. The solution using the original algorithm with the Murman switch, however, was numerically unstable for this case as shown in Fig. 10. Instantaneous pressure distributions at time steps 94 and 95 are plotted in the figure, computed using the Murman (Fig. 10(a)) and E-O (Fig. 10(b)) switches. The numerical instability begins in the region of the launcher/tip-missile where

the grid spacing is smallest. Figure 10(a) shows the instability in the form of an oscillation in the wing upper surface pressure distribution at $\bar{\eta}_W = 0.94$ from approximately 30% to 60% chord. The program subsequently failed during step 96 which is 21 steps after the maximum pitch angle in the first cycle of motion. The calculation involving the modified algorithm (E-O switch with the first-order accurate supersonic differencing) is stable, however, as shown in Fig. 10(b). Here the pressure distributions for steps 94 and 95 are very similar and the calculation proceeds with no difficulty. In fact, the modified AF algorithm with the E-O switch is numerically stable for this case with either the first-order or second-order supersonic differencing.

Unsteady pressure distributions along the wing and tail during the third cycle of motion are shown in Fig. 11, computed using the E-O switch with the second-order accurate supersonic differencing. Two sets of calculated pressures are presented corresponding to the aircraft at the maximum ($\alpha = 3.88°$) and minimum ($\alpha = 0.88°$) pitch angles. Comparison of the results indicates that large changes in pressure occur along the upper and lower surfaces of the wing as the aircraft oscillates in pitch. For example, the shock on the wing upper surface oscillates over more than 10% of the chord during a cycle of motion. Also, the shock is approximately twice as strong at the maximum pitch angle as it is at the minimum pitch angle. For the tail, the changes in the pressure distributions due to aircraft pitching are relatively very small in comparison with the changes in wing pressures, as further shown in Fig. 11. The tail is located considerably aft of the pitch axis and thus its motion is plunge dominated which results in much smaller airloads for the low value of k considered.

Wing Flutter Results

To assess the CAP-TSD code for flutter applications, a simple well-defined wing case was selected as a first step toward performing aeroelastic analyses for complete aircraft configurations.[4] The wing being analyzed is a semispan wind-tunnel-wall-mounted model that has a quarter-chord sweep angle of 45°, a panel aspect ratio of 1.65, and a taper ratio of 0.66.[33] The wing is a proposed AGARD standard aeroelastic configuration which was tested in the Transonic Dynamics Tunnel (TDT) at NASA Langley Research Center.[34] A planview of the wing is shown in Fig. 12. The wing has a NACA 65A004 airfoil section and was constructed of laminated mahogany. In order to obtain flutter for a wide range of Mach number and density conditions in the TDT, holes were drilled through the wing to reduce its stiffness. To maintain the aerodynamic shape of the wing, the holes were filled with a rigid foam plastic. A photograph of the model mounted in the TDT is shown in Fig. 13. The wing is being modeled structurally using the first four natural vibration modes which are illustrated in Figs. 14 and 15. Figure 14 shows oblique projections of the natural modes while Fig. 15 shows the corresponding deflection contours. These modes which are numbered 1 through 4 represent first bending, first torsion, second bending, and second torsion, respectively, as determined by a finite element analysis. The modes have natural frequencies which range from 9.6 Hz for the first bending mode to 91.54 Hz for the second torsion mode.

Flutter calculations were performed for the 45° sweptback wing using CAP-TSD to assess the code for aeroelastic applications. Two sets of results are presented corresponding to: (1) using the linear potential equation ($F = G = H = 0$) and modeling the wing aerodynamically as a flat plate (zero thickness) and (2) using the complete (nonlinear) TSD equation and including wing thickness. The first set of results allows for direct comparison with parallel linear theory calculations performed using the FAST subsonic kernel function program.[35] The second set of results more accurately

models the wing geometry as well as the flow physics. All of the results are compared with the experimental flutter data of Ref. 34 which spans the range, $0.338 \leq M \leq 1.141$.

Comparisons of flutter characteristics from the linear calculations with the experimental data are given in Fig. 16. Plots of flutter speed index (defined as $U/(b_o\, \omega_\alpha \sqrt{\mu})$) and nondimensional flutter frequency (defined as ω/ω_α) as functions of freestream Mach number, are shown in Figs. 16(a) and 16(b), respectively. The experimental flutter data defines a typical transonic flutter "dip" with the bottom near M = 1.0 for this case. (Note that these results are shown with an expanded scale.) The bottom of the dip in flutter speed index (Fig. 16(a)) was defined by the approach to the M = 1.072 flutter point during the wind tunnel operation. Results from the CAP-TSD (linear) code are presented at twelve values of M covering the entire Mach number range over which the flutter data was measured. Results from the FAST program are presented for the limited range $0.338 \leq M \leq 0.96$ since the method is restricted to subsonic freestreams. Overall, the linear CAP-TSD results compare well with the experimental data for subsonic as well as supersonic Mach numbers. Note that the subsonic FAST results are also in good agreement with the data. Such a result is not unexpected for this very thin wing of moderate sweep and taper at zero angle of attack. It does indicate that the wing properties are well-defined for benchmark purposes.

In the subsonic Mach number range, the CAP-TSD and FAST calculations predict a slightly unconservative flutter speed, except at M = 0.338, by as much as 2% (Fig. 16(a)), and a higher flutter frequency (Fig. 16(b)) in comparison with the experimental data. In general though, the linear CAP-TSD results agree well with the FAST results in both flutter speed and frequency. The good agreement in this three-way correlation between experiment, linear theory, and CFD flutter results gives confidence in the CAP-TSD code for flutter prediction.

Comparisons of flutter characteristics from the linear and nonlinear CAP-TSD calculations with the experimental data are given in Fig. 17. Figure 17(a) shows flutter speed index versus Mach number and Fig. 17(b) shows nondimensional flutter frequency versus Mach number. Three flutter points are plotted from the nonlinear CAP-TSD calculations corresponding to M = 0.678, 0.901, and 0.96. Comparisons between the two sets of CAP-TSD results show differences due to wing thickness and nonlinear effects. With increasing Mach number these differences become larger. For example, at M = 0.678, 0.901, and 0.96, the flutter speed index decreased by 1%, 5%, and 19%, respectively, as shown in Fig. 17(a). Similar decreases also occur in the flutter frequency (Fig. 17(b)). The decrease in flutter speed at M = 0.901 is largely due to including wing thickness since there are no supersonic points in the flow at this condition. The decrease in flutter speed at M = 0.96 is attributed to both wing thickness and nonlinear effects since an embedded supersonic region of moderate size was detected in the wing tip region. The nonlinear CAP-TSD results at both M = 0.901 and 0.96 are slightly conservative in comparison with the experimental flutter speed index values. Nonetheless, the nonlinear CAP-TSD flutter results compare favorably with the experimental data, which is the first step toward validating the code for general transonic aeroelastic applications.

Concluding Remarks

A transonic unsteady aerodynamic and aeroelasticity code called CAP-TSD has been developed for application to realistic aircraft configurations. The name CAP-TSD is an acronym for Computational Aeroelasticity Program - Transonic Small Disturbance. The code permits the calculation of steady and unsteady flows about complete aircraft configurations for aeroelastic analysis in the flutter

critical transonic speed range. The CAP-TSD code uses a time-accurate approximate factorization (AF) algorithm for solution of the unsteady transonic small-disturbance equation. An overview of the code development effort was given and recent algorithm modifications were described. The algorithm modifications include: an Engquist-Osher (E-O) type-dependent switch to treat regions of supersonic flow, extension of the E-O switch for second-order spatial accuracy, nonisentropic effects to treat strong-shock cases, nonreflecting far field boundary conditions for unsteady applications, and several modifications to accelerate convergence to steady-state. Calculations were presented for several configurations including the General Dynamics one-ninth scale F-16C aircraft model to evaluate the algorithm modifications. The modifications have significantly improved the stability of the AF algorithm and the reliability of the CAP-TSD code in general.

Results were also presented from a flutter analysis of a 45° sweptback wing. The flutter boundaries from CAP-TSD (linear) were in agreement with parallel subsonic linear theory results and compared well with the experimental flutter data for subsonic and supersonic freestream Mach numbers. The preliminary nonlinear CAP-TSD flutter results also compared favorably with the experimental data which is the first step toward validating the code for general transonic aeroelastic applications.

References

[1]Edwards, J. W.; and Thomas, J. L.: "Computational Methods for Unsteady Transonic Flows," AIAA Paper No. 87-0107, Presented at the AIAA 25th Aerospace Sciences Meeting, Reno, Nevada, January 12-15, 1987.

[2]Batina, J. T.; Seidel, D. A.; Bland, S. R.; and Bennett, R. M.: "Unsteady Transonic Flow Calculations for Realistic Aircraft Configurations," AIAA Paper No. 87-0850, Presented at the AIAA/ASME/ASCE/AHS 28th Structures, Structural Dynamics, and Materials Conference, Monterey, California, April 6-8, 1987. Also available as NASA TM 89120, March 1987.

[3]Bennett, R. M.; Bland, S. R.; Batina, J. T.; Gibbons, M. D; and Mabey, D. G.: "Calculation of Steady and Unsteady Pressures on Wings at Supersonic Speeds with a Transonic Small-Disturbance Code," AIAA Paper No. 87-0851, Presented at the AIAA/ASME/ASCE/AHS 28th Structures, Structural Dynamics, and Materials Conference, Monterey, California, April 6-8, 1987.

[4]Cunningham, H. J.; Batina, J. T.; and Bennett, R. M.: "Modern Wing Flutter Analysis by Computational Fluid Dynamics Methods," ASME Paper No. 87-WA/Aero-9, Presented at the ASME Winter Annual Meeting, Boston, Massachusetts, December 13-18, 1987.

[5]Batina, J. T.: "An Efficient Algorithm for Solution of the Unsteady Transonic Small-Disturbance Equation," AIAA Paper No. 87-0109, Presented at the AIAA 25th Aerospace Sciences Meeting, Reno, Nevada, January 12-15, 1987. Also available as NASA TM 89014, December 1986.

[6]Batina, J. T.: "Unsteady Transonic Algorithm Improvements for Realistic Aircraft Applications," AIAA Paper No. 88-0105, Presented at the AIAA 26th Aerospace Sciences Meeting, Reno, Nevada, January 11-14, 1987.

[7]Batina, J. T.: "Unsteady Transonic Small-Disturbance Theory Including Entropy and Vorticity

Effects," AIAA Paper No. 88-2278, Presented at the AIAA/ASME/ASCE/AHS/ASC 29th Structures, Structural Dynamics, and Materials Conference, Williamsburg, Virginia, April 18-20, 1988.

[8]Boppe, C. W.; and Stern, M. A.: "Simulated Transonic Flows for Aircraft with Nacelles, Pylons, and Winglets," AIAA Paper No. 80-0130, Presented at the AIAA 18th Aerospace Sciences Meeting, Pasadena, California, January 14-16, 1980.

[9]Murman, E. M.: "Analysis of Embedded Shock Waves Calculated by Relaxation Methods," Proceedings of AIAA Computational Fluid Dynamics Conference, July 1973, pp. 27-40.

[10]Engquist, B. E.; and Osher, S. J.: "Stable and Entropy Satisfying Approximations for Transonic Flow Calculations," Mathematics of Computation, Vol. 34, No. 149, January 1980, pp. 45-75.

[11]Goorjian, P. M.; Meagher, M. E.; and Van Buskirk, R.: "Monotone Implicit Algorithms for the Small-Disturbance and Full Potential Equations Applied to Transonic Flows," AIAA Paper No. 83-0371, Presented at the AIAA 21st Aerospace Sciences Meeting, Reno, Nevada, January 10-13, 1983.

[12]Goorjian, P. M.; and Van Buskirk, R. D.: "Second-Order-Accurate Spatial Differencing for the Transonic Small-Disturbance Equation," Journal of Aircraft, Vol. 23, November 1985, pp. 1693-1699.

[13]Steinhoff, J.; and Jameson, A.: "Multiple Solutions of the Transonic Potential Flow Equation," AIAA Paper No. 81-1019, Presented at the AIAA 5th Computational Fluid Dynamics Conference, Palo Alto, California, June 1981.

[14]Williams, M. H.; Bland, S. R.; and Edwards, J. W.: "Flow Instabilities in Transonic Small Disturbance Theory," AIAA Journal, Vol. 23, October 1985, pp. 1491-1496.

[15]Klopfer, G. H.; and Nixon D.: "Nonisentropic Potential Formulation for Transonic Flows," AIAA Journal, Vol. 22, June 1984, pp. 770-776.

[16]Hafez, M.; and Lovell, D.: "Entropy and Vorticity Corrections for Transonic Flows," AIAA Paper No. 83-1926, July 1983.

[17]Fuglsang, D. F.; and Williams, M. H.: "Non-Isentropic Unsteady Transonic Small Disturbance Theory," AIAA Paper No. 85-0600, Presented at the AIAA/ASME/ASCE/AHS 26th Structures, Structural Dynamics, and Materials Conference, Orlando, Florida, April 15-17, 1985.

[18]Gibbons, M. D.; Whitlow, W., Jr.; and Williams, M. H.: "Nonisentropic Unsteady Three Dimensional Small Disturbance Potential Theory," AIAA Paper No. 86-0863, Presented at the AIAA/ASME/ASCE/AHS 27th Structures, Structural Dynamics, and Materials Conference, San Antonio, Texas, May 19-21, 1986.

[19]Grossman, B.: "The Computation of Inviscid Rotational Gasdynamic Flows Using an Alternate Velocity Decomposition," AIAA Paper No. 83-1900, 1983.

[20]Dang, T. Q.; and Chen, L. T.: "An Euler Correction Method for Two- and Three-Dimensional Transonic Flows," AIAA Paper No. 87-0522, January 1987.

[21]Clebsch, A.: "Uber die Integration der hydrodynamischen Gleichungen," J. Reine Angew. Math., Vol. 57, 1859, pp. 1-10.

[22]Fuglsang, D. F.: "Non-Isentropic Unsteady Transonic Small-Disturbance Theory," M.S. Thesis, Purdue University, West Lafayette, Indiana, May 1985.

[23]Whitlow, W., Jr.: "Characteristic Boundary Conditions for Three-Dimensional Transonic Unsteady Aerodynamics," NASA TM 86292, October 1984.

[24]Edwards, J. W.; Bennett, R. M.; Whitlow, W., Jr.; and Seidel, D. A.: "Time-Marching Transonic Flutter Solutions Including Angle-of-Attack Effects, Journal of Aircraft, vol. 20, no. 11, November 1983, pp. 899-906.

[25]Edwards, J. W.; Bennett, R. M.; Whitlow, W., Jr.; and Seidel, D. A.: "Time-Marching Transonic Flutter Solutions Including Angle-of-Attack Effects," AIAA Paper No. 82-3685, Presented at the AIAA/ASME/ASCE/AHS 23rd Structures, Structural Dynamics, and Materials Conference, New Orleans, Louisiana, May 10-12, 1982.

[26]Bland, S. R.: "Development of Low-Frequency Kernel-Function Aerodynamics for Comparison with Time-Dependent Finite-Difference Methods," NASA TM 83283, May 1982.

[27]Mohr, R. W.; Batina, J. T.; and Yang, T. Y.: "Mach Number Effects on Transonic Aeroelastic Forces and Flutter Characteristics," AIAA Paper No. 88-2304, Presented at the AIAA/ASME/ASCE/AHS/ASC 29th Structures, Structural Dynamics, and Materials Conference, Williamsburg, Virginia, April 18-20, 1988.

[28]Tijdeman, H.; Van Nunen, J. W. G.; Kraan, A. N.; Persoon, A. J.; Poestkoke, R.; Roos, R.; Schippers, P.; and Siebert, C. M.: "Transonic Wind Tunnel Tests on an Oscillating Wing with External Stores," AFFDL-TR-78-194, December 1978.

[29]Schmitt, V.; and Charpin, F.: "Pressure Distributions on the ONERA M6 Wing at Transonic Mach Numbers," Appendix B1 in AGARD-AR-138, "Experimental Data Base for Computer Program Assessment," May 1979.

[30]Yoshihara, H.: "Test Cases for Inviscid Flow Field Methods," AGARD-AR-211, May 1985.

[31]Fox, M. C.; and Feldman, C. S.: "Model and Test Information Report, 1/9-Scale F-16C and F-16D Force and Loads Model," General Dynamics Report 16PR2179, January 1982.

[32]Feldman, C. S.: "Wind Tunnel Data Report, 1/9-Scale F-16C Pressure Loads Test," General Dynamics Report 16PR2252, July 1982.

[33]Yates, E. C., Jr.: "AGARD Standard Aeroelastic Configurations for Dynamic Response. Candidate Configuration 1. - Wing 445.6," NASA TM 100492, August 1987.

[34]Yates, E. C., Jr.; Land, N. S.; and Foughner, J. T., Jr.: "Measured and Calculated Subsonic and Transonic Flutter Characteristics of a 45° Sweptback Wing Planform in Air and in Freon-12 in the Langley Transonic Dynamics Tunnel," NASA TN D-1616, March 1963.

[35]Desmarais, R. N.; and Bennett, R. M.: "User's Guide for a Modular Flutter Analysis Software System (FAST Version 1.0)," NASA TM 78720, May 1978.

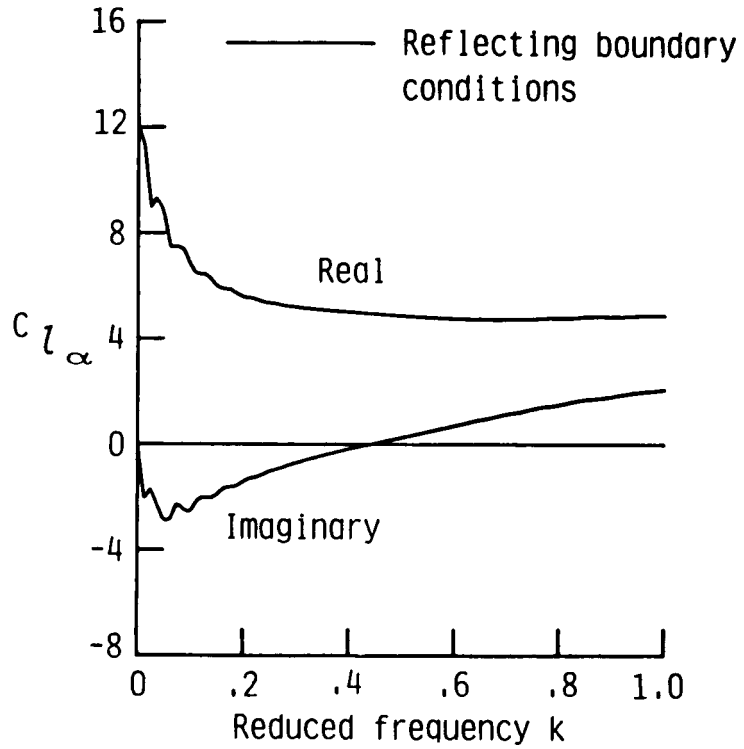

(a) reflecting boundary conditions.

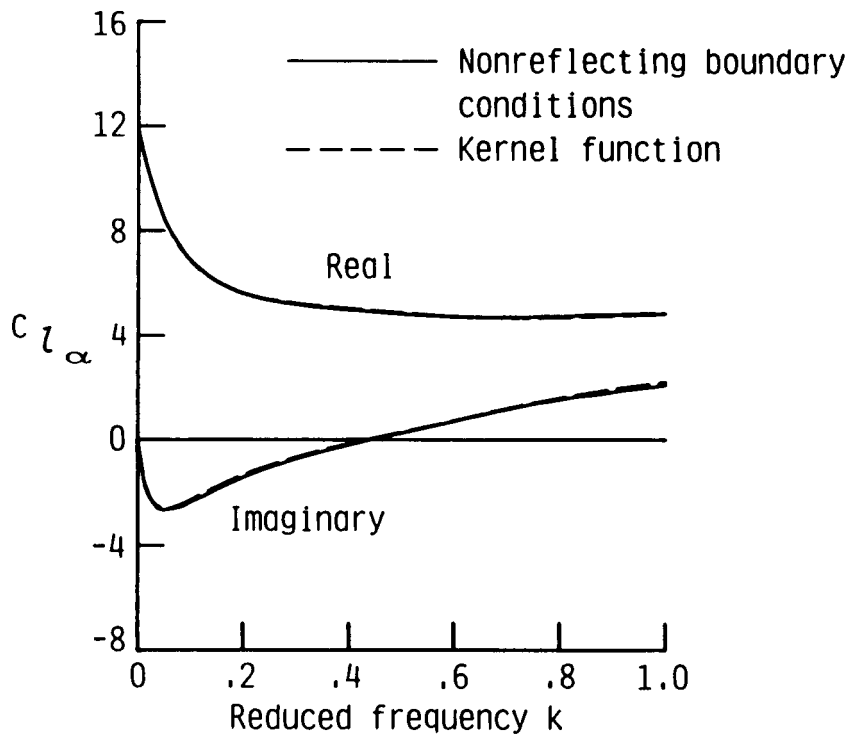

(b) nonreflecting boundary conditions.

Fig. 1 Comparisons of unsteady lift-curve slope for a flat plate airfoil at M = 0.85.

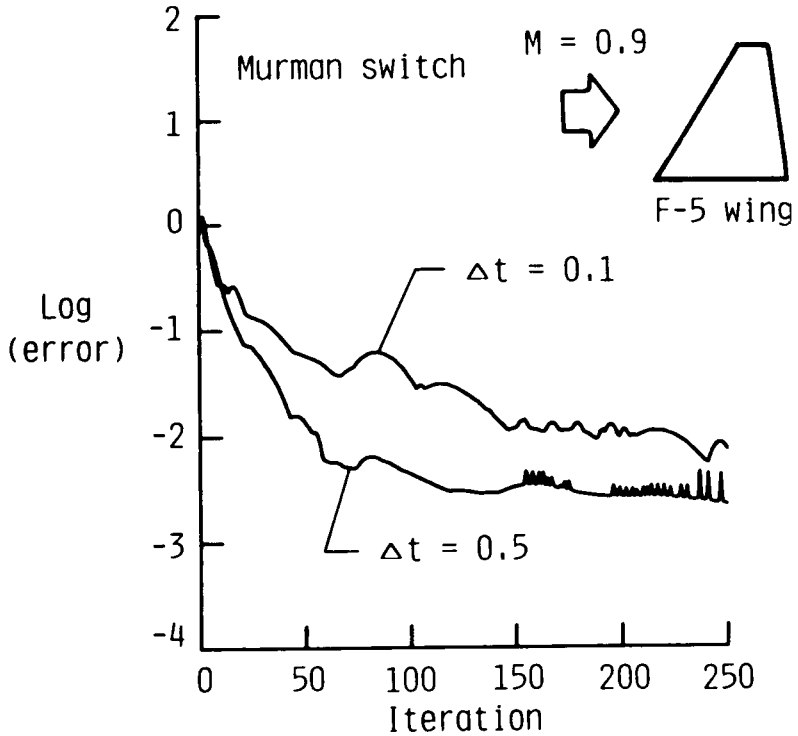

(a) steady-state convergence.

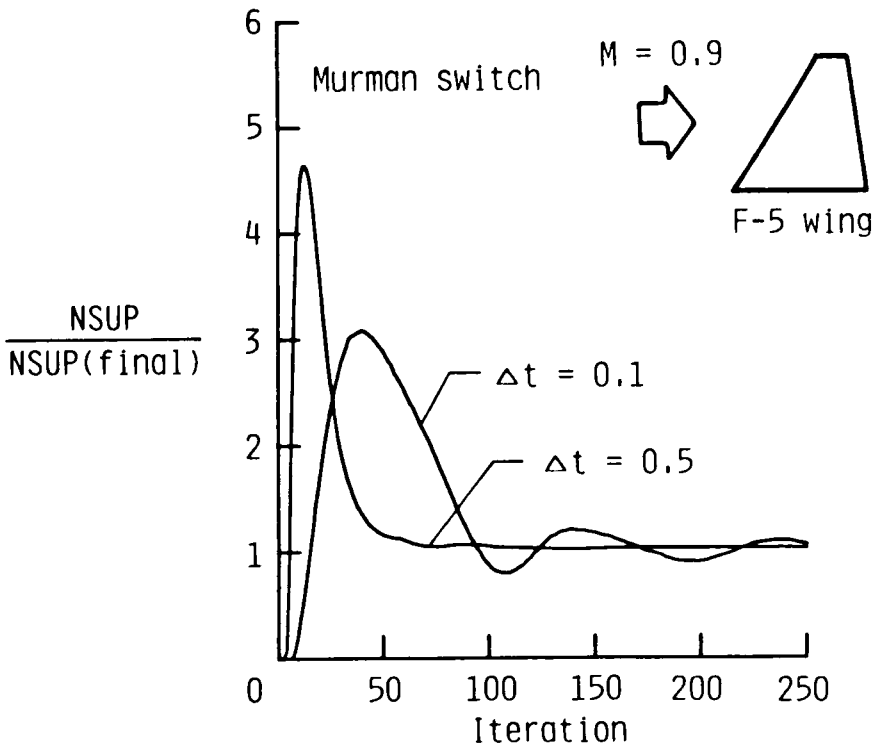

(b) number of supersonic points.

Fig. 2 Effects of step size on the solution computed using the Murman switch for the F-5 wing at M = 0.9 and $\alpha_o = 0°$.

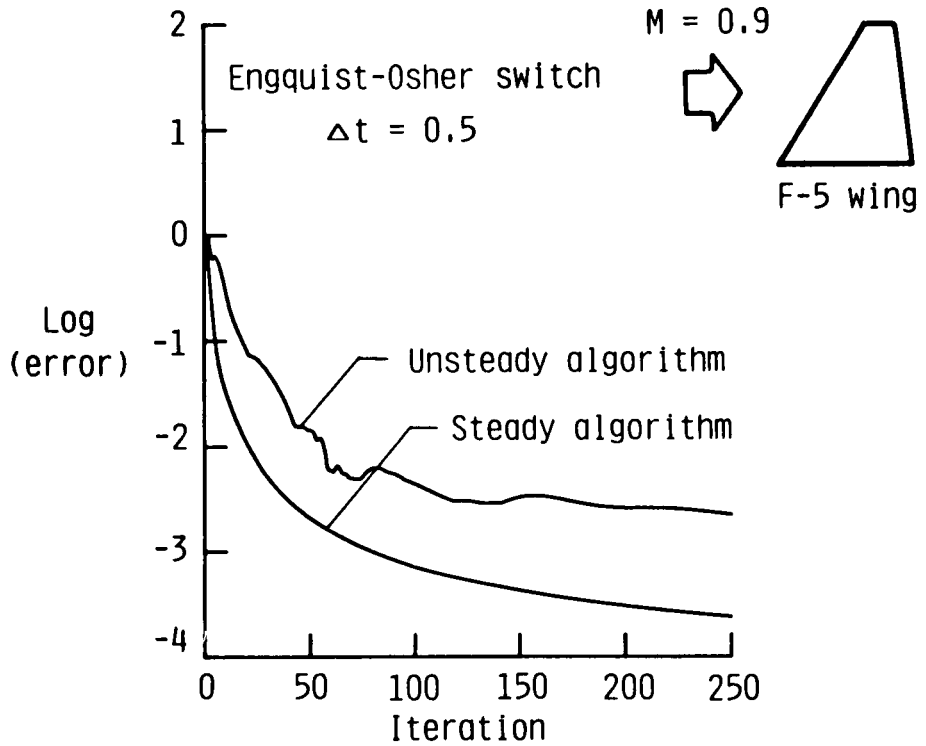

(a) steady-state convergence.

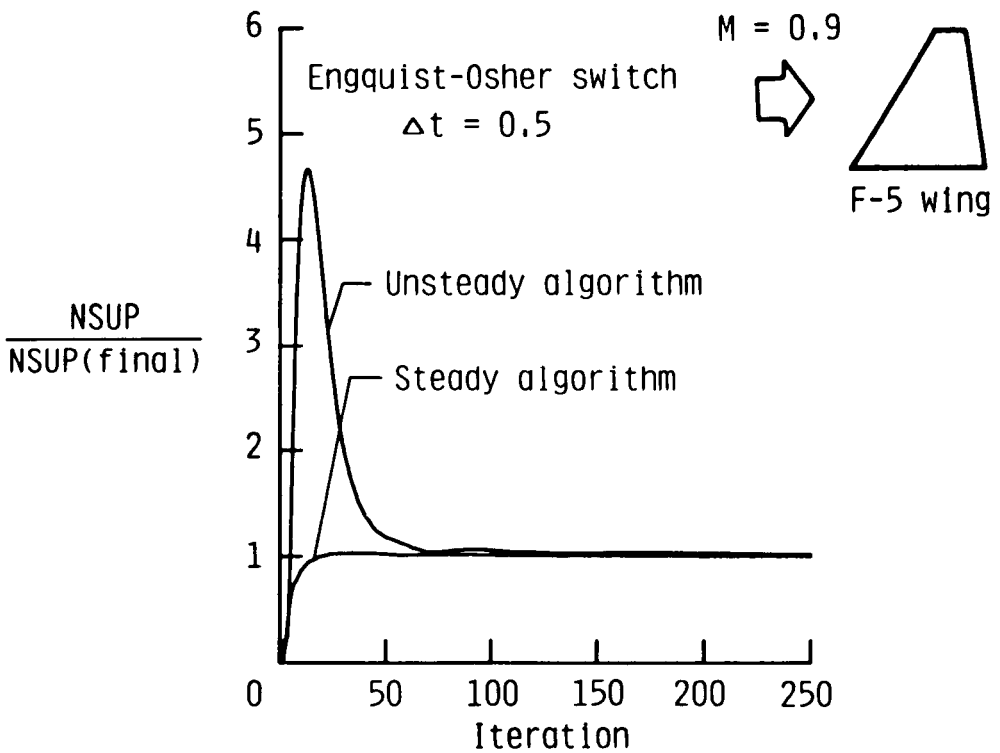

(b) number of supersonic points.

Fig. 3 Effects of deleting all TSD time derivatives on the solution computed using the Engquist-Osher switch for the F-5 wing at M = 0.9 and $\alpha_0 = 0°$.

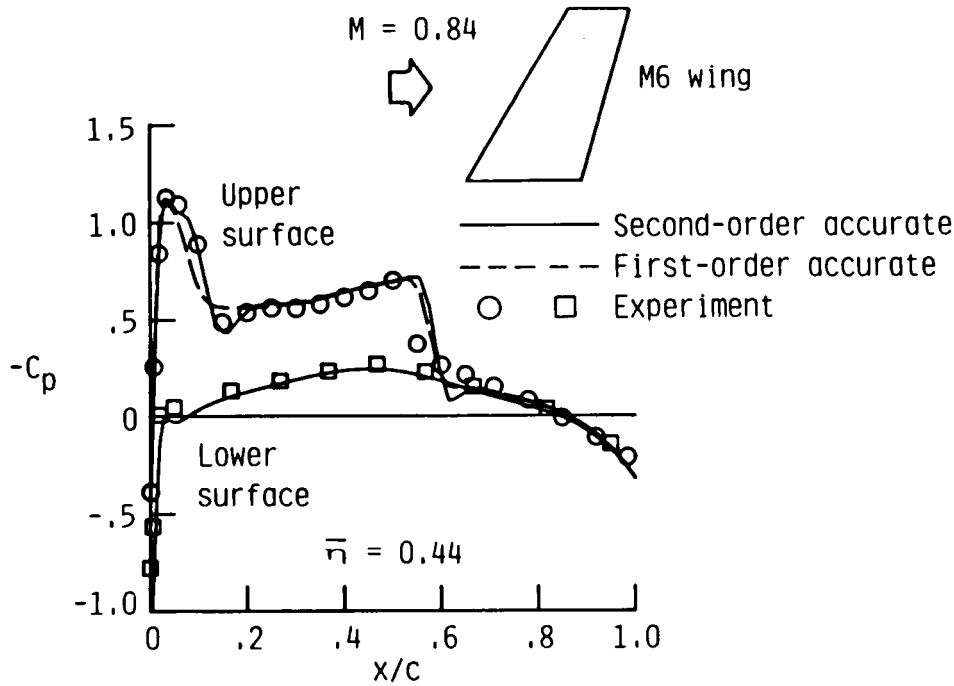

Fig. 4 Effects of first-order and second-order accurate supersonic differencing on the steady pressure distributions of the ONERA M6 wing at M = 0.84 and α_o = 3.06°.

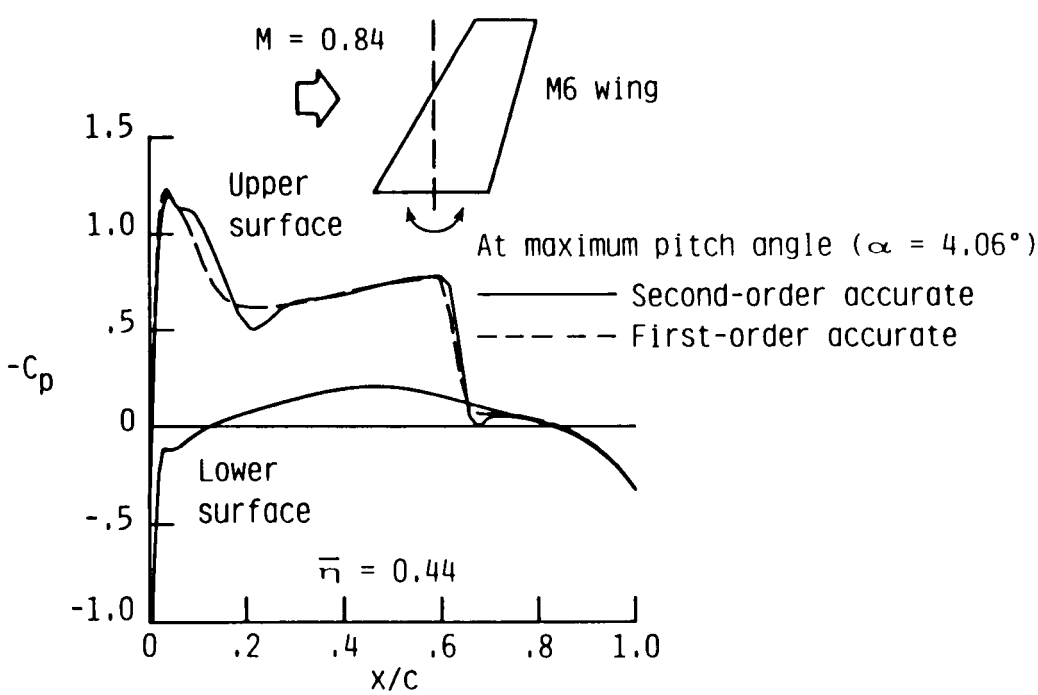

Fig. 5 Effects of first-order and second-order accurate supersonic differencing on the unsteady pressure distributions of the ONERA M6 wing during the third cycle of rigid pitching at M = 0.84, α_o = 3.06°, α_1 = 1.0°, and k = 0.1.

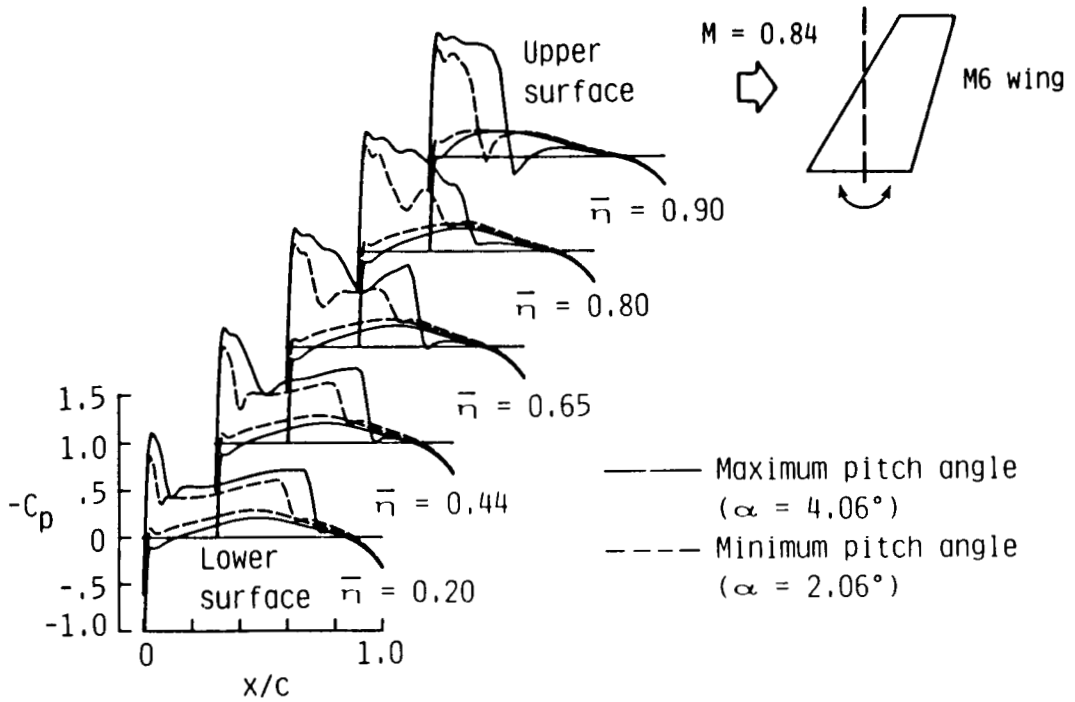

Fig. 6 Instantaneous pressure distributions on the ONERA M6 wing during the third cycle of rigid pitching at M = 0.84, α_o = 3.06°, α_1 = 1.0°, and k = 0.1.

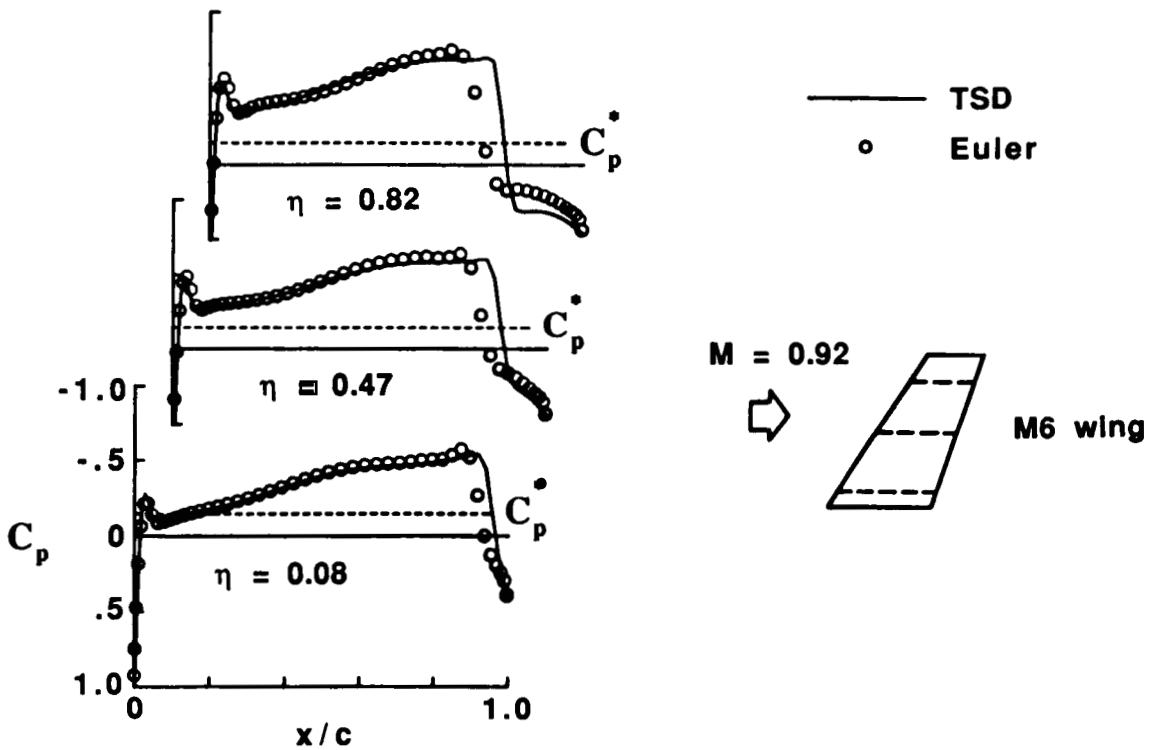

(a) TSD.

Fig. 7 Comparison of steady pressure distributions for the ONERA M6 wing at M = 0.92 and α_o = 0°.

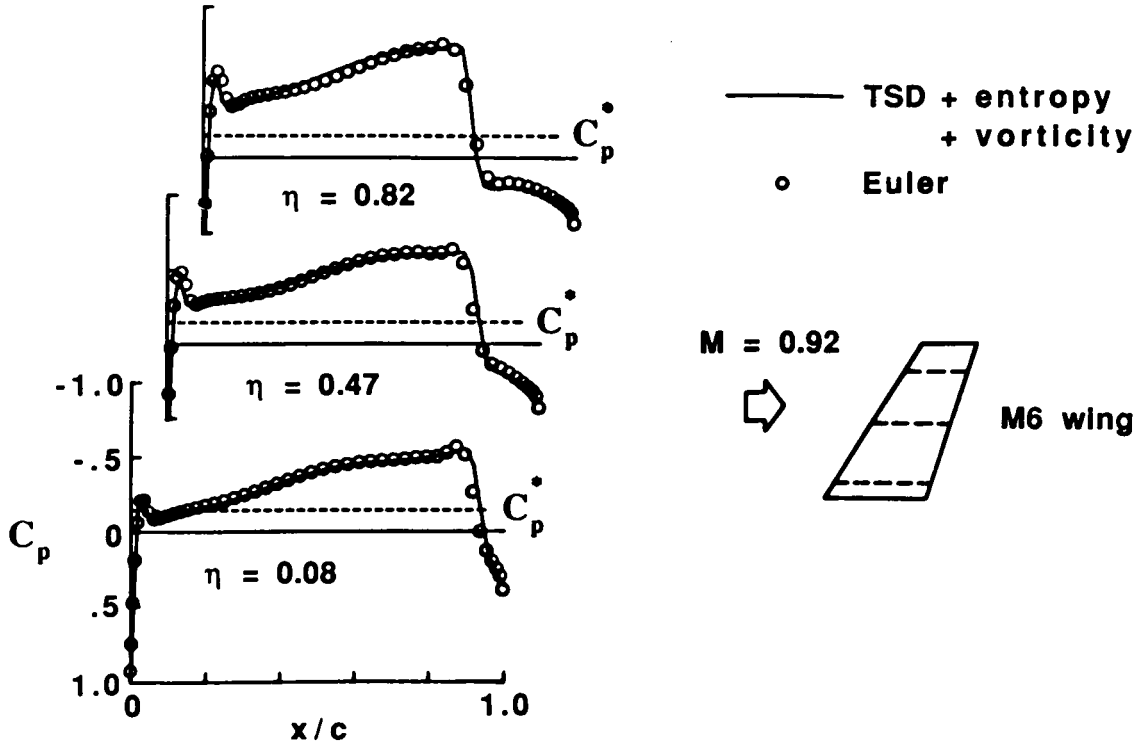

(b) TSD + entropy + vorticity.

Fig. 7 Concluded.

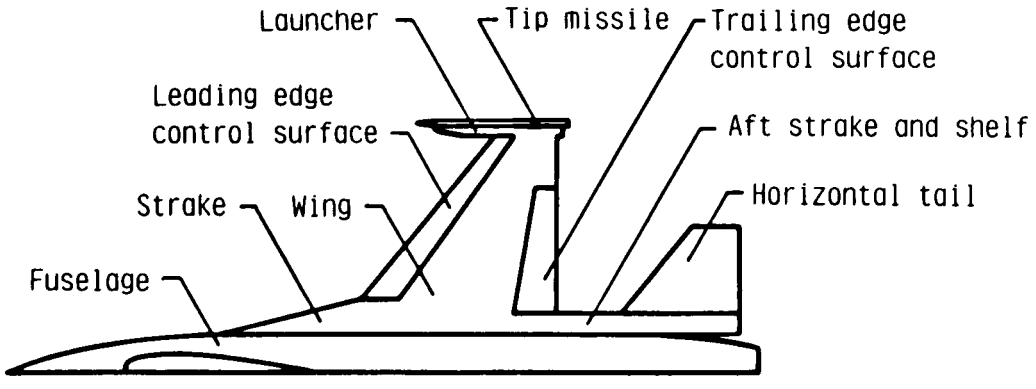

Fig. 8 CAP-TSD modeling of the General Dynamics one-ninth scale F-16C aircraft model.

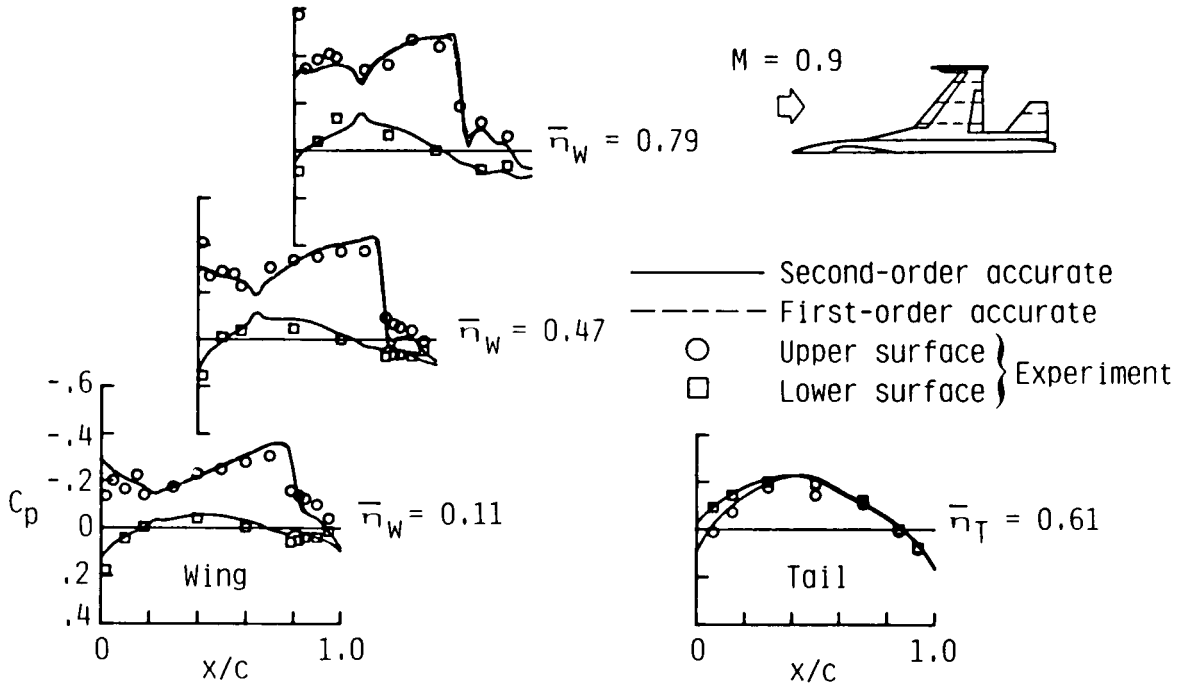

Fig. 9 Comparisons between CAP-TSD steady pressure distributions computed using first-order and second-order accurate supersonic differencing with the experimental pressure data for the wing and tail of the F-16C aircraft model at M = 0.9 and α_o = 2.38°.

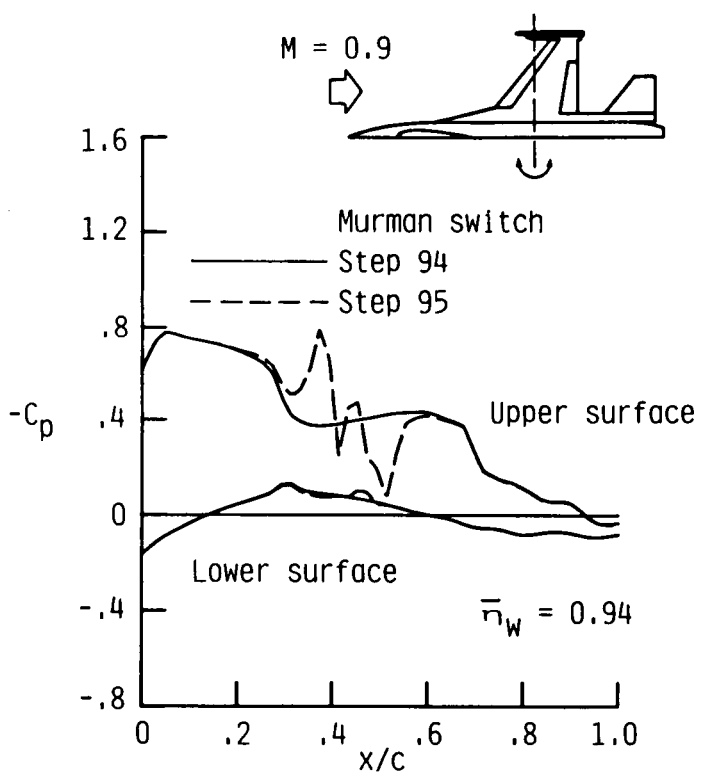

(a) numerical instability with Murman switch.

Fig. 10 Effect of type-dependent switch on numerical stability for rigid pitching of the F-16C aircraft model at M = 0.9, α_o = 2.38°, α_1 = 1.5°, and k = 0.1.

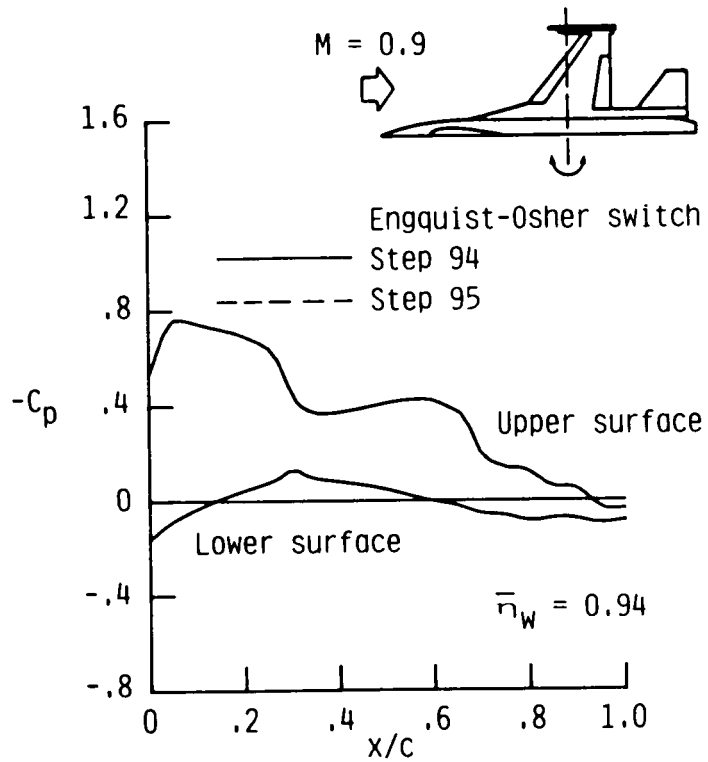

(b) improved numerical stability with Engquist-Osher switch.

Fig. 10 **Concluded.**

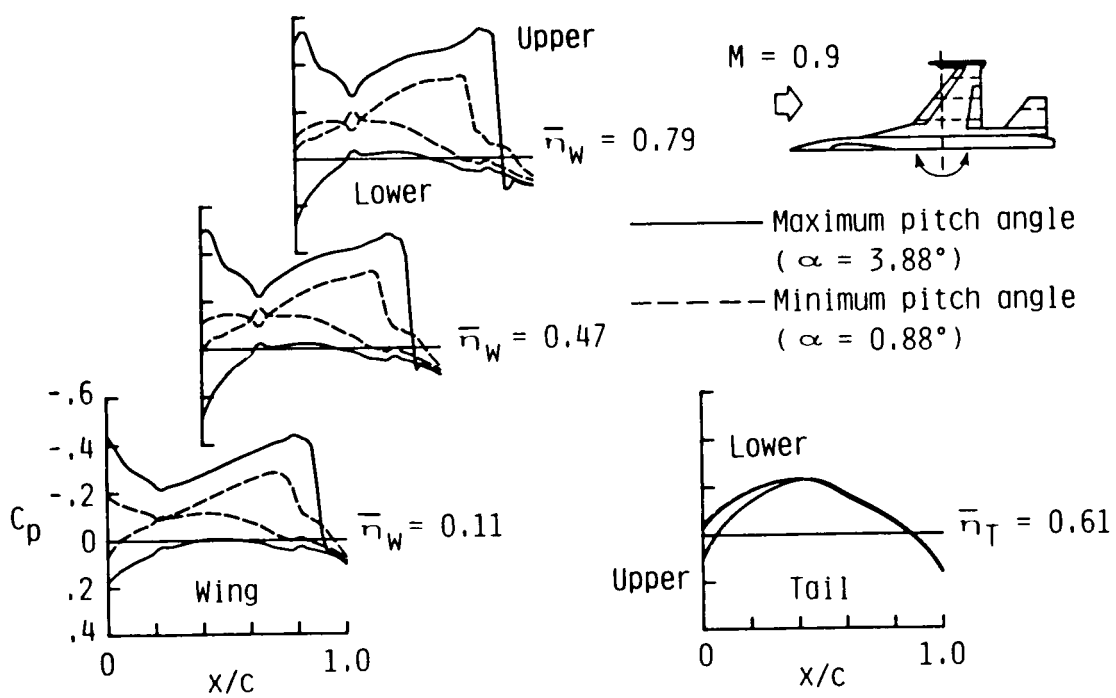

Fig. 11 Instantaneous pressure distributions on the wing and tail of the F-16C aircraft model during the third cycle of rigid pitching at M = 0.9, α_0 = 2.38°, α_1 = 1.5°, and k = 0.1.

ORIGINAL PAGE IS
OF POOR QUALITY

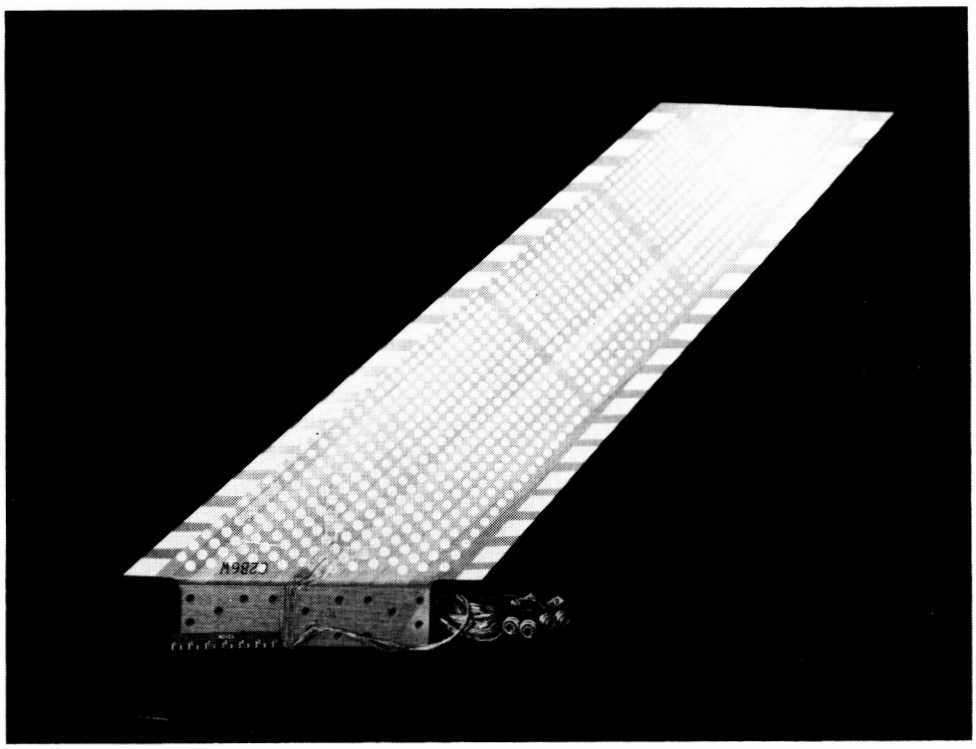

Fig. 12 Planview of 45° sweptback wing.

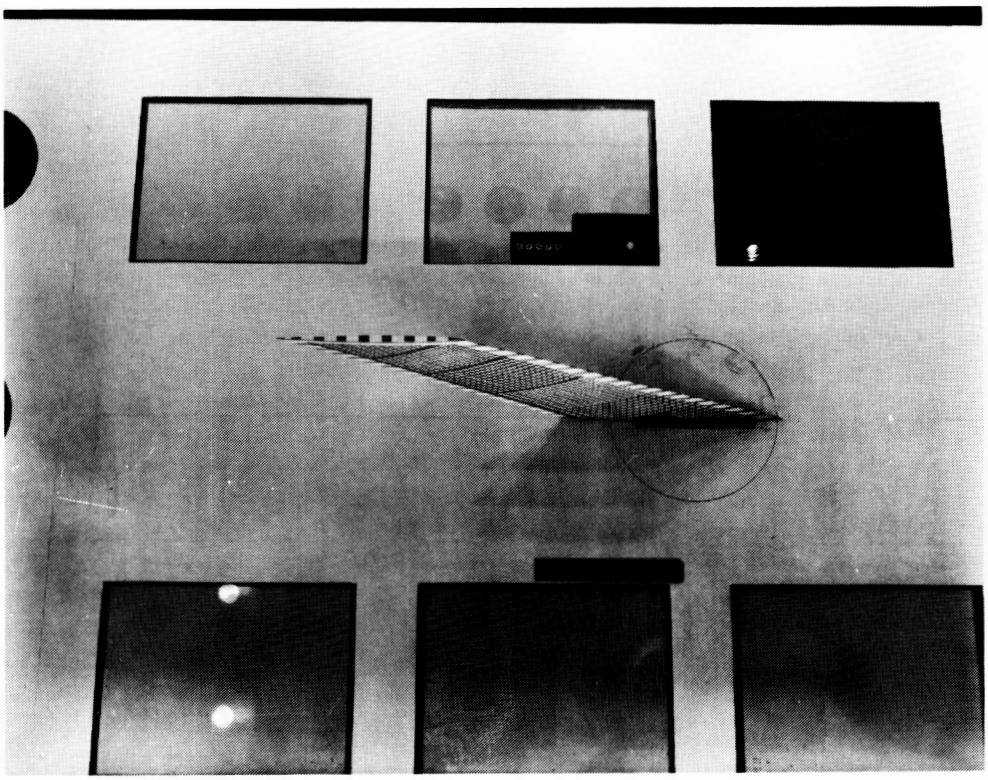

Fig. 13 45° sweptback wing in the NASA Langley Transonic Dynamics Tunnel.

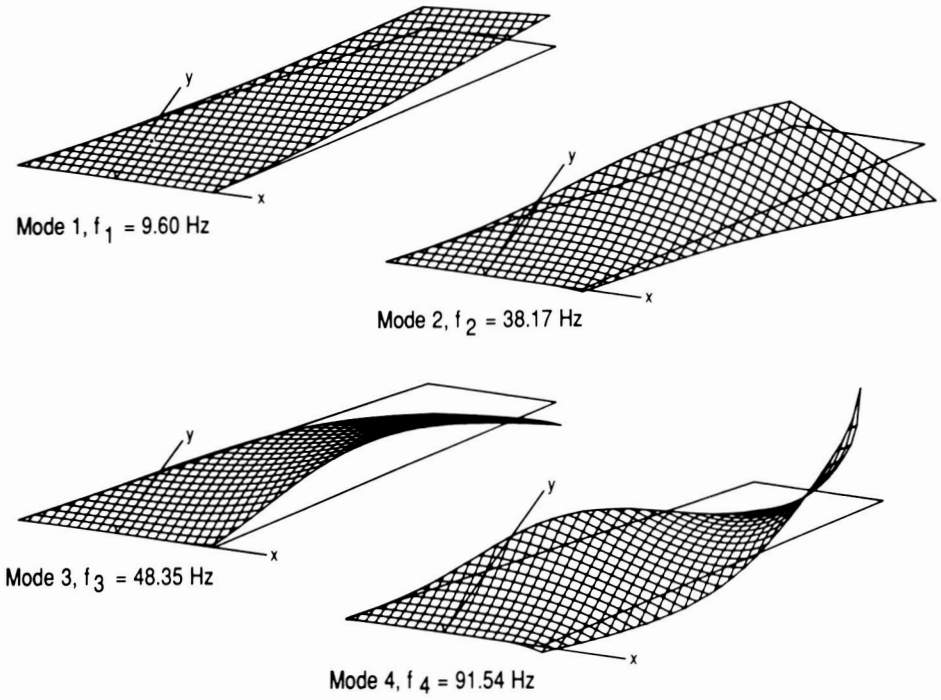

Fig. 14 Oblique projections of natural vibration modes of 45° sweptback wing.

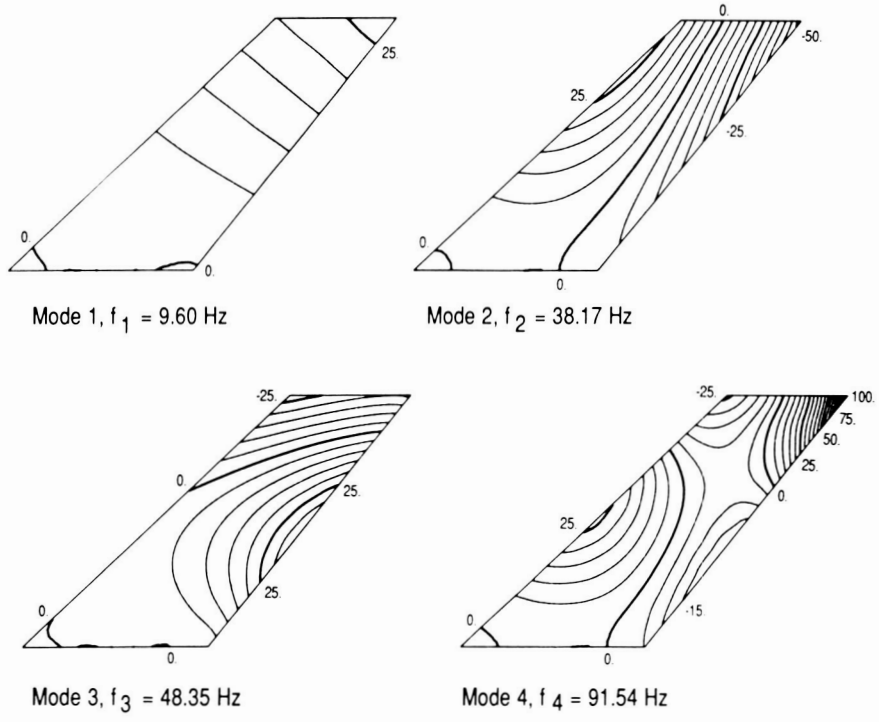

Fig. 15 Deflection contours of natural vibration modes of 45° sweptback wing.

ORIGINAL PAGE IS
OF POOR QUALITY

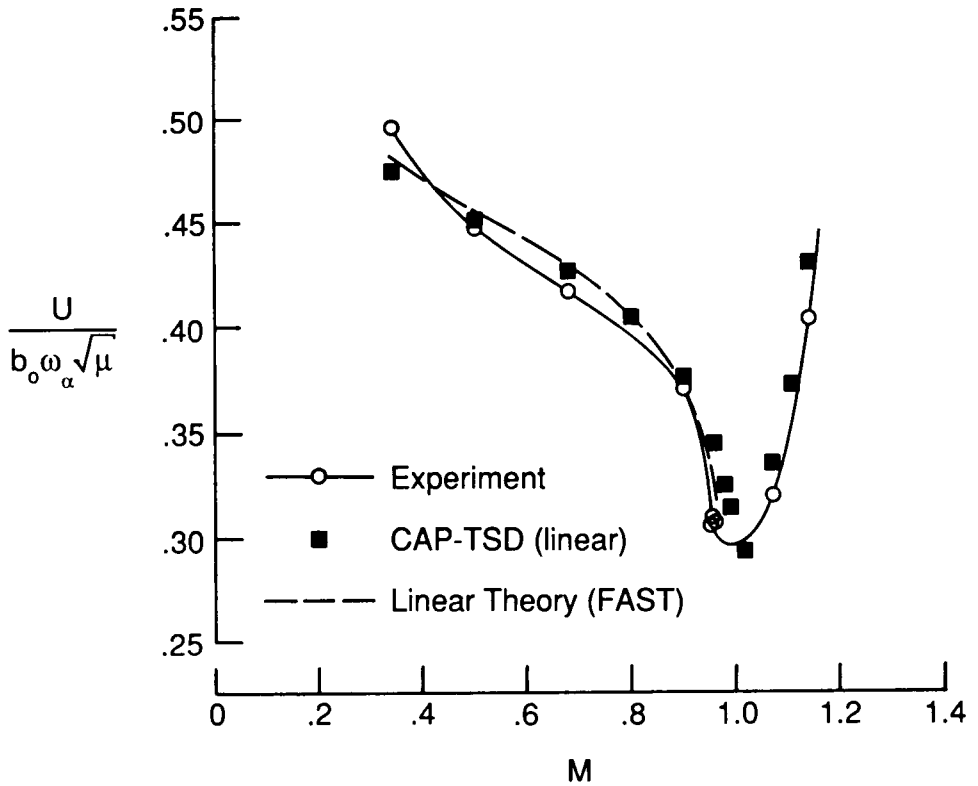

(a) flutter speed index versus Mach number.

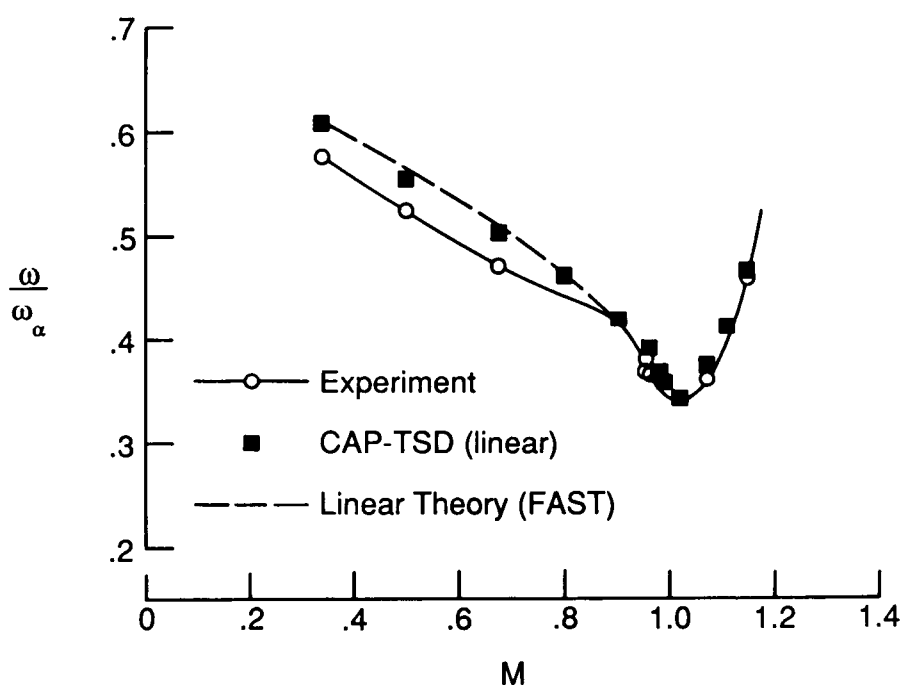

(b) nondimensional flutter frequency versus Mach number.

Fig. 16 Comparisons of linear flutter calculations with experimental data for the 45° sweptback wing.

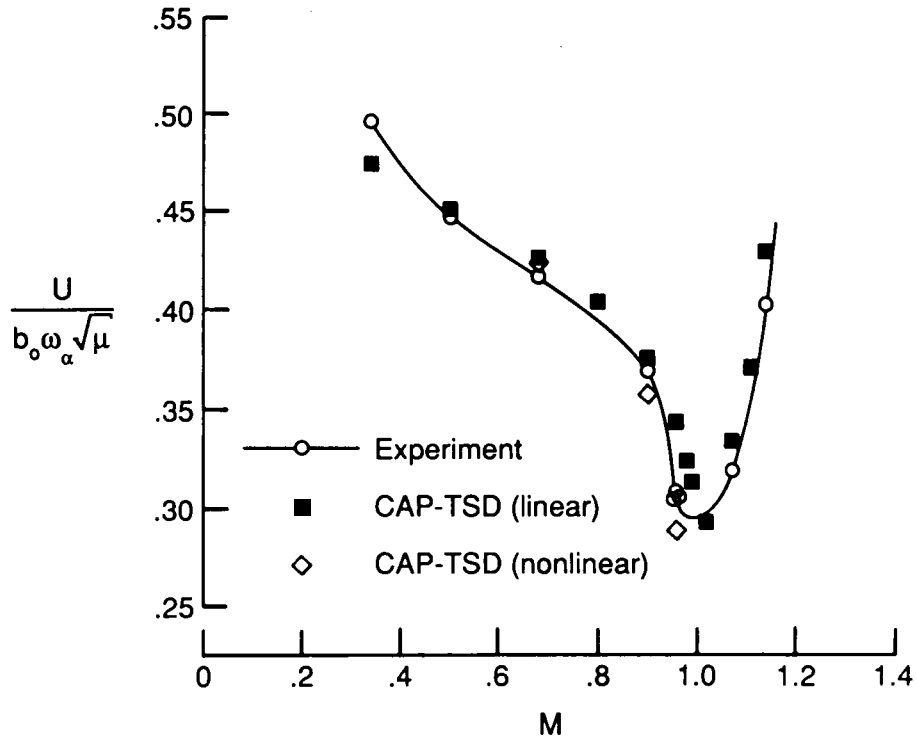

(a) flutter speed index versus Mach number.

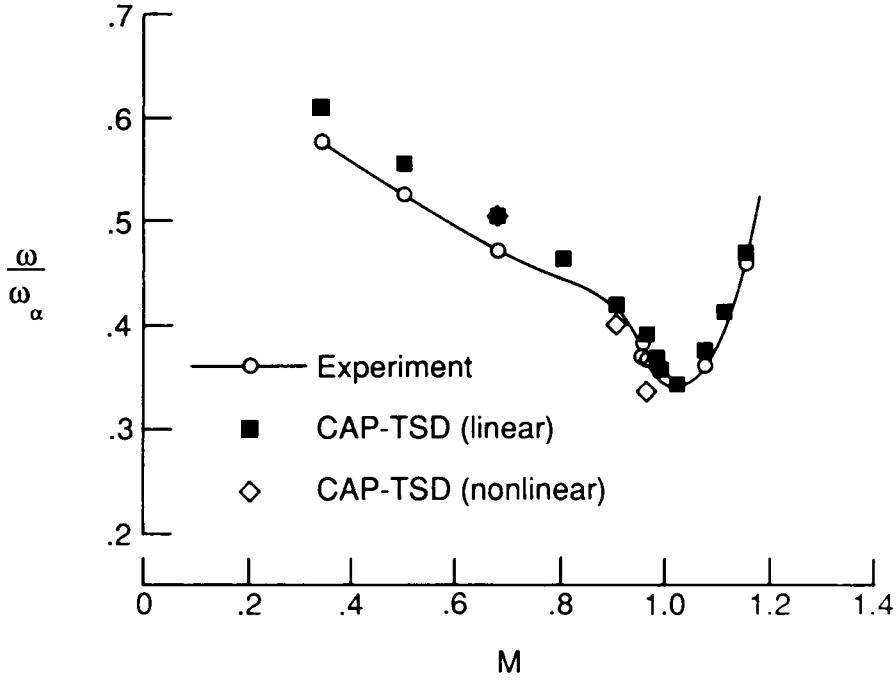

(b) nondimensional flutter frequency versus Mach number.

Fig. 17 Comparisons of linear and nonlinear CAP-TSD flutter predictions with experimental data for the 45° sweptback wing.

N89-20947

INVERSE WING DESIGN IN TRANSONIC FLOW INCLUDING VISCOUS INTERACTION*

Leland A. Carlson, Robert R. Ratcliff, and Thomas A. Gally
Texas A&M University
College Station, Texas

and

Richard L. Campbell
NASA Langley Research Center
Hampton, Virginia

SUMMARY

Several inverse methods have been compared and initial results indicate that differences in results are primarily due to coordinate systems and fuselage representations and not to design procedures. Further, results from a direct-inverse method that includes three-dimensional wing boundary-layer effects, wake curvature, and wake displacement are presented. These results show that boundary-layer displacements must be included in the design process for accurate results.

INTRODUCTION

Over the past several years, a variety of transonic wing design methods and computer codes (refs. 1-5) have been developed. In general, these methods solve the full potential flow equation and utilize the inverse approach in that pressure distributions are specified over all or part of the wing surface. Several include some of the effects of viscous interaction via strip boundary-layer calculations (ref. 1) or two-dimensional computations that include a correction for three-dimensional viscous effects (ref. 3). However, none of these methods includes a true three-dimensional boundary-layer calculation or the effects due to wake curvature, etc., which might have important effects on computed wing designs. In addition, they differ in the number and spacing of grid points, the design approach, the treatment of fuselage effects, and the control of trailing-edge thickness. Obviously whether or not these formulation differences significantly affect design results is of interest.

Currently, the design version of TAWFIVE (refs. 6-7), termed TAW5D (ref. 4), is being extended to include three-dimensional boundary-layer and wake viscous interaction effects and is being used to study various leading-edge relofting/trailing-edge control design procedures. As part of this study, it was believed that it would be interesting to investigate the consequences of differences in both numerical and physical formulations on the design process and resultant wing designs. Thus, this paper will present initial results of two ongoing studies. The first part will compare several inverse

*This work was supported by NASA Grant NSG 1-619.

design methods and their results, while the second portion will discuss the influence of viscous interaction on transonic wing design.

INVERSE METHOD COMPARISON STUDIES

The RAE Wing Body 'A' configuration (ref. 8) at a freestream Mach number of 0.8 and angle of attack of 2 degrees was selected as the test case for the comparison studies. The wing for this configuration has an aspect ratio of 5.5, a leading-edge sweep of 36.7 degrees, and a taper ratio of 0.375, is untwisted, and is composed of RAE 101 symmetrical airfoil sections. Three different inverse design methods were selected for the comparison, the direct-inverse curvilinear coordinate system TAW5D code (ref. 4), the stretched Cartesian grid direct-inverse ZEBRA method (ref. 2-3), and the inverse predictor-corrector FLO30DC approach (ref. 5); and their characteristics and features are listed on Table I.

In order to avoid the complexities associated with various viscous interaction schemes, it was decided to limit this comparison study to inviscid flow; and, since it was believed that one of the primary usages of design codes would be to modify only portions of wings, it was decided to design only between 30 and 70 percent span. The target pressure distribution for the design zone was obtained from an inviscid analysis by the TAW5D code (essentially TAWFIVE, ref. 7), which indicated that the flowfield at the selected conditions was slightly supercritical and that the wing lift coefficient was 0.210. In addition, the starting airfoil shapes were the correct 9% thick sections from root to 30% span, linearly thinning down to a 6% thick symmetrical section at 50% span and back to 9% at 70% span, followed by the correct sections on the outboard portions of the wing.

For the design studies, TAW5D was operated in the span lofting mode in which pressures were only specified at 30, 50, and 70% span. Under this procedure, airfoils were only inversely designed at these stations; and after each design update, in between sections were obtained by linear spanwise lofting. In all cases, the flow at these in between stations was computed in the direct-analysis mode. On the other hand, in the ZEBRA method, pressures were specified at each spanwise station from 30 thru 70%; and in the predictor-corrector, FLO30DC the pressure was specified and an airfoil section designed only at the 50% span location, with linear span lofting to 30% and 70% respectively. In all cases, leading-edge relofting options were selected in order to force the designs to have the proper trailing-edge thicknesses.

PROBLEMS

In setting up the test cases, several interesting problems were encountered. First, analysis computations of the RAE 'A' wing/body configuration by the ZEBRA and TAW5D codes yielded slightly different pressure distributions; and, in order to minimize these differences, the angle of attack used in ZEBRA was decreased to 1.8 degrees so as to match

the wing CL predicted by TAW5D. The corresponding pressure distributions are shown on figure 1; and since both methods solve the same equation, the variations must be due to differences in grid, fuselage, and boundary condition treatments. Near the root, ZEBRA predicts a greater fuselage effect in that the flow is more accelerated on the upper surface; while outboard, the leading-edge grid clustering inherent in TAW5D results in better resolution of the leading-edge region and minimum pressure peak. Near the trailing edge, where the ZEBRA coordinate system is actually finer, there are also some variations in the predicted pressures. However, between 30 and 70% span the two methods are in reasonable agreement, and meaningful design studies for this region should be possible.

The second problem was that FLO30DC could only handle for this case an infinite cylinder fuselage; and, thus, TAW5D and ZEBRA were "modified" to have as an option an infinite fuselage as well as a finite one. Figure 2 compares at the 50% span station on the RAE configuration the pressure distributions calculated by TAW5D associated with these two fuselages, and it can be seen that the effect is only a slight shift in the pressure coefficient level. This trend was true at all span stations, and overall wing and section lift coefficients were essentially identical. Nevertheless, as a result of these differences, two sets of target pressures for the design region were generated, one for the finite wing/body configuration and one for the infinite cylinder fuselage; and these were used as input into the appropriate versions of the codes.

RESULTS AND COMPARISONS

Figures 3-5 show results obtained at the design stations using the TAW5D method. In this case, each section was designed from 10% chord to the trailing edge and leading-edge relofting was utilized to force trailing-edge closure. However, the actual ordinate of the trailing edge was not specified. As can be seen, the starting profiles were a linear variation from the correct section at 30% and 70% span down to a thin symmetrical section at mid-span. While the 30 and 70% stations started with the correct shapes, they were design stations and could and did change during the computation. However, as shown on the figures, all three sections converged to the target shapes; and results for the finite fuselage and infinite fuselage cases were indistinguishable.

Results were also obtained with the ZEBRA code for both the infinite and finite body cases and by the FLO30DC code for the infinite cylinder fuselage using the appropriate pressure inputs. Figures 6-8 compare the designed sectional shapes obtained by the three codes for the infinite fuselage. It should be noted that the ZEBRA results were well converged having maximum ordinate changes of less than 1E-6 of chord when computations were terminated. Also, it can be seen that the FLO30DC and TAW5D results (denoted as CAMPBELL and TAWFIVE on the figures) are virtually identical, even though the methods used entirely different design procedures.

At the 30% span station, the lower surface profile predicted by ZEBRA is in agreement with the other methods, but on the upper surface it is considerably different. Examination of the pressure profiles on figure 1 indicate that at 30% TAW5D and ZEBRA analysis results agree on the lower surface but disagree on the upper. Consequently, when the TAW5D pressures are used as design input to ZEBRA, it is not surprising that a slightly different airfoil section resulted. At 50%, figure 7, where analysis results are in better agreement, particularly on the upper surface, the three methods predict virtually identical upper surfaces although the ZEBRA lower surface profile is slightly thicker; and at 70% span the ZEBRA prediction is again slightly thicker. (Similar differences between TAW5D and ZEBRA were obtained for the finite fuselage case.) Since TAW5D and ZEBRA use similar design procedures and TAW5D and FLO30DC have similar grids and body representations, it can be concluded that the differences in profile shapes portrayed in figures 6-8 are primarily due to coordinate system and fuselage representations.

In order to see infinite versus finite fuselage effects, the infinite cylinder fuselage wing pressures were used as input into both the infinite cylinder and wing/body versions of TAW5D; and a typical result is shown on figure 9. Here the infinite cylinder result is the "correct" profile; and as can be seen, the finite fuselage result is thinner and significantly different near the trailing edge. In fact, at the 30 and 70% stations, the upper and lower surfaces criss-crossed before coming together to satisfy trailing-edge closure. It is believed that this result demonstrates an important effect often encountered in inverse design, i.e., when a pressure distribution that is somehow incompatible with either physical reality or the computational model (in this case the fuselage representation) is used as input, the effect is almost always observed as either unrealistic profiles near the trailing edge or in the inability of the design process to satisfy the design input pressures near the trailing edge or both. In many cases, the "problem" can be solved by slight adjustments in the specified pressure distribution.

Now even though figures 6-8 show that the methods predicted different profiles, the significance of these differences can only be determined by an analysis of the designed wings and a comparison of the analysis results with the desired targets. Since TAW5D had previously been shown to be self consistent (ref. 4) and since the wing designed by TAW5D, fig. 3-5, had the correct airfoil sections, no analysis results for the TAW5D design are presented. However, figures 10-14 compare the target pressure distributions with analysis results by both TAW5D and ZEBRA for the wing designed by ZEBRA, which had different profile sections in the design region. First, it should be noted that in the design region, figures 11-13, the ZEBRA analysis agrees with the target pressure values for the inverse design zone, which extends from 0.1 chord to the trailing edge. This agreement indicates that the ZEBRA method did indeed satisfy the desired pressure boundary conditions. Second, due to inherent grid clustering near the leading edge, the TAW5D analysis of the ZEBRA design probably gives better resolution in the leading-edge region; and, finally, if it is assumed that the TAW5D analysis is the "most accurate" of the methods due to its fuselage and

boundary condition representations, then it is apparent from figures 10-14 that the ZEBRA design closely matches the target pressure distributions and lift coefficients. Overall, the TAW5D analysis of the ZEBRA design predicted a wing lift coefficient of 0.203 compared to the target value of 0.210; and similar results were obtained for both the finite and infinite fuselage cases. In many respects these good results are somewhat surprising considering the airfoil section differences on figures 6-8. In any event, the results shown on figures 10-14 are probably indicative of the level of agreement to be expected when using design methods differing in coordinate systems and fuselage treatment.

To conclude this section, it is believed that the results presented demonstrate the following:

(1) Inverse methods using similar coordinate systems and flow solvers will yield the same wing designs, and

(2) Inverse methods having different coordinate systems and fuselage representations but similar design procedures will yield different section profiles, but the pressure distributions and lift coefficients will be in reasonable agreement.

VISCOUS INTERACTION STUDIES

The configuration selected for these studies was the Lockheed Wing A wing-body (ref. 4 and 7) at a freestream Mach number of 0.8, an angle of attack of 2 degrees, and a mean chord Reynolds number of 24 million. The wing for this combination is composed of supercritical aft-cambered sections and has a quarter chord sweep of 25 deg., a linear twist distribution ranging from 2.28 deg. at the wing body junction to -2.04 deg. at the wing tip, an aspect ratio of eight, and a taper ratio of 0.4. Target pressure distributions were generated by an analysis using TAW5D with full boundary-layer and wake viscous interaction effects. As before, wing design was only between 30 and 70% span, target pressures were specified at 30,50 and 70%, and the span lofting technique described above was utilized. However, in order to properly include viscous interaction, after each boundary layer and wake update, displacement thicknesses were added to the airfoil ordinates at each analysis station to provide the correct displacement surface. Likewise, since at the design stations the displacement surface is the surface computed, the displacement thicknesses were subtracted to yield the ordinates of the actual airfoil at those locations. In addition, leading-edge relofting was utilized in order to obtain proper trailing-edge behavior. However, contrary to the situation for inviscid cases, convergence problems were observed when only the trailing-edge thicknesses were specified. Consequently, the actual trailing-edge ordinates desired at the design stations were specified.

STARTING PROFILE EFFECTS

Obviously, the initial airfoil section profiles should not affect the final designed sections; and, consequently, two cases were studied having significantly different starting profiles. The results for the first case

are shown on figures 15-17, and as can be seen the initial sections linearly varied from the correct aft-cambered profile at 20% span to a conventional non-aft cambered section at mid-span back to the correct aft-cambered section at 80% span. Here, the inverse design procedure started at 0.1 chord; and the initial leading edge at each design station was thinner than the target shape. As shown on the figures, the target sections and designed sections are in excellent agreement, particularly considering the extensive curve fits and interpolations involved in the design and viscous interaction procedures.

For the second test, the initial sections consisted of the correct profiles inboard from the root to 20% and outboard from 80% to the wing tip. However, as shown on figures 18-20, from 30% span through 70% span the initial sections were NACA 0012 airfoils; and linear lofting was used between 20 and 30% and 70 and 80%. In this case the inverse design procedure started at 0.04 chord, and the initial leading edge at each design station was thicker than the target section. As can be seen, the final designed sections are in excellent agreement with the target shapes, particularly in the leading-edge and cove regions.

It should be noted that in both of these cases, the section and wing lift coefficients and the section pressure distributions were essentially identical to the target values. Based upon these results, it is believed that the present viscous inverse design procedure can yield correct target profiles independent of initial airfoil section shapes.

BOUNDARY-LAYER AND WAKE EFFECTS

Studies conducted under the present program have indicated that design including full viscous interaction effects is more computationally intensive and that convergence is slower. Consequently, it was decided to compare the full viscous interaction design results with those obtained including viscous boundary-layer interaction but excluding wake effects and with those obtained assuming inviscid flow. For each case, the input pressure distributions were identical and corresponded to those predicted by a full viscous analysis of the Lockheed Wing A wing/body since those should be the closest to reality. The starting section profiles were those shown on figures 15-17, and the design region was from 30 to 70% span. As before, span relofting and leading-edge relofting were both used in all three cases.

The final section profiles resulting from these computations are shown on figures 21-23, and at all design stations the sections obtained by ignoring wake effects are very close but slightly thicker than those corresponding to the full viscous case. Further, while the inviscid case profile is very close to the others at 50% span, they are significantly different from those including viscous effects at 30 and 70% span. The results at 50% are not surprising since at that station the boundary layer is relatively thin over much of the surface and the design is strongly influenced by the viscous pressure boundary conditions at 30 and 70% span. However, the cove region is not well predicted; and, as can be seen on figure 22, the upper surface inviscid profile here is thinner than the full

viscous result, rather than thicker as would normally be expected. In this case, specification of the trailing-edge ordinate and use of relofting has forced a change in the leading-edge shape such that the final inviscid case airfoil upper surface is slightly thinner than expected.

At the 30 and 70% stations, it is believed that the shapes predicted by the inviscid computation are due to the fact that these design locations sense the viscous pressures specified at 50% but are strongly influenced by the inviscid pressures computed inboard and outboard respectively. In other words, as shown in the analysis case in reference 6, three-dimensional viscous effects also appear to be very important in the design case. Based upon these results, it appears that the effect of wake curvature and displacement on the airfoil section designs is relatively small. However, if the flowfield is assumed to be inviscid and only a portion of the wing is designed, the use of realistic pressure distributions as input to design stations may lead to unusual or even erroneous profiles, particularly at the boundaries of the design region.

ANALYSIS AND COMPARISON OF DESIGNS

As in the code comparison studies, the effect of including or excluding viscous effects can only be determined by comparing analysis results for the designed wings. Consequently, each of the wings portrayed on figures 21-23 was analyzed using TAW5D including boundary-layer interaction and wake displacement and curvature effects. Full viscous interaction effects were included because it was believed that such a representation would be the most realistic representation of the actual flow to be expected about the designed wing/body combination. The results of these analyses are shown in Table II and on figures 24-28. On these figures, the viscous pressures are very close to the target pressures; and comparison of the pressure distributions and sectional lift coefficients indicates that from a practical standpoint the differences between full viscous design and design including wing boundary layer but excluding wake effects is negligible.

However, analysis of the inviscidly designed wing indicates that in the design region, figures 25-27, the sections determined by inviscid design have lower than expected lifts and pressure distributions significantly different than the targets. (At this point, it should be noted that the "inviscid" curves on figures 24-28 are from a full viscous analysis of the inviscidly designed wing and are not the result of an inviscid analysis.) In addition, three-dimensional effects lead to lift losses and more forward shock locations on the sections inboard and outboard of the design region, even though these sections have the correct airfoil shapes. As can be seen, the effect is particularly significant on the outboard region. It should be noted that this decrease in lift due to designing inviscidly instead of including viscous effects is consistent with results previously obtained for airfoils (ref. 9).

It is believed that these initial results demonstrate the following:

(1) Section profiles for wings in transonic flow can be designed using the direct-inverse technique including the interaction effects of the three-dimensional wing boundary-layer and wake curvature and displacement. The resulting profiles are independent of the starting shapes.

(2) For the conditions considered, wake effects have very little effect on the designed airfoil shapes or on the wing pressure distributions.

(3) For the conditions considered, at least the wing boundary-layer displacement effect must be included in the design process. Otherwise, the designed wing will have less lift and different pressure distributions than desired.

CONCLUDING REMARKS

In summary, several inverse methods have been compared and initial results indicate that differences in results are primarily due to coordinate systems and fuselage representations and not to design procedures. Also, results from an inverse method that includes three dimensional wing boundary-layer effects, wake curvature, and wake displacement have been presented. These results show that boundary-layer displacements must be included in the design process for accurate results.

REFERENCES

1. Henne, P. A.: Inverse Transonic Wing Design Method. Journal of Aircraft, vol. 18, no. 2, February 1981, pp. 121-127.

2. Weed, R. A., Carlson, L. A., and Anderson, W. K.: A Direct-Inverse Three Dimensional Transonic Wing Design Method for Vector Computers. AIAA Paper No. 84-2156, August 1984.

3. Carlson, L. A. and Weed, R. A.: Direct-Inverse Transonic Wing Analysis-Design Method with Viscous Interaction. Journal of Aircraft, vol. 23, no. 9, September 1986, pp. 711-718.

4. Gally, T. A. and Carlson, L. A.: Inviscid Transonic Wing Design Using Inverse Methods in Curvilinear Coordinates. AIAA Paper No. 87-2551, August 1987.

5. Campbell, R. L. and Smith, L. A.: A Hybrid Algorithm for Transonic Airfoil and Wing Design. AIAA Paper No. 87-2552, August 1987.

6. Streett, C. L.: Viscous-Inviscid Interaction for Transonic Wing-Body Configurations Including Wake Effects. AIAA Journal, vol. 20, no. 7, July 1982, pp. 915-923.

7. Melson, N.D. and Streett, C. L.: TAWFIVE: A Users' Guide. NASA Technical Memorandum 84619, September 1983.

8. Treadgold, D. A., Jones, A. F., and Wilson, K. H.: Pressure Distribution Measured in the RAE 8'x6' Transonic Wind Tunnel on RAE Wing 'A' in Combination with an Axisymmetric Body at Mach Numbers of 0.4, 0.8, and 0.9. Experimental Data Base for Computer Program Assessment, Appendix B1, AGARD-AR-138, May 1979, pp. B4-1 -B4-25.

9. Carlson, L. A.: Inverse Transonic Airfoil Design Including Viscous Interaction. NASA CP-2001, Vol. 4, November 1976, pp. 1387-1395.

TABLE I. -- CHARACTERISTICS OF INVERSE METHODS

Method	TAW5D	ZEBRA	FLO30DC
Coordinate System	Body Fitted	Stretched Cartesian	Body Fitted
Boundary Conditions	On Surface	At Z = 0	On Surface
Fuselage	General Shape	Axisymmetric Body Approx. by Source/Sinks	Infinite Cylinder
Design Method	Direct-Inverse	Direct-Inverse	Predictor-Corrector
Grid	160x24x32	90x30x30	160x24x32
Points on Airfoil Section	105 with LE Clustering	100 almost equally spaced	105 with LE Clustering
Number of Span Stations	21	21	21

TABLE II. -- RESULTS OF ANALYSIS OF DESIGNED WINGS

	Target	Full Viscous Design	No Wake Design	Inviscid Design
cl at 50%	.514	.509	.506	.427
Wing CL	.483	.478	.477	.419

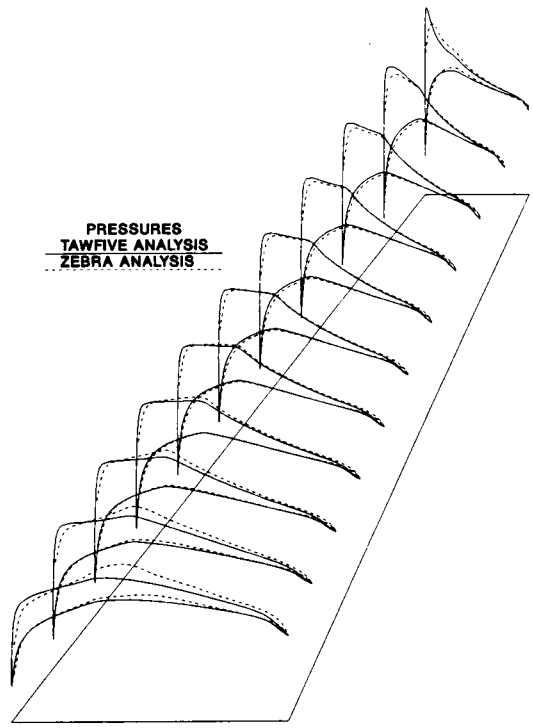

Figure 1. Comparison of analysis results for RAE wing body 'A' at Mach No. = 0.8, AOA = 2 degrees.

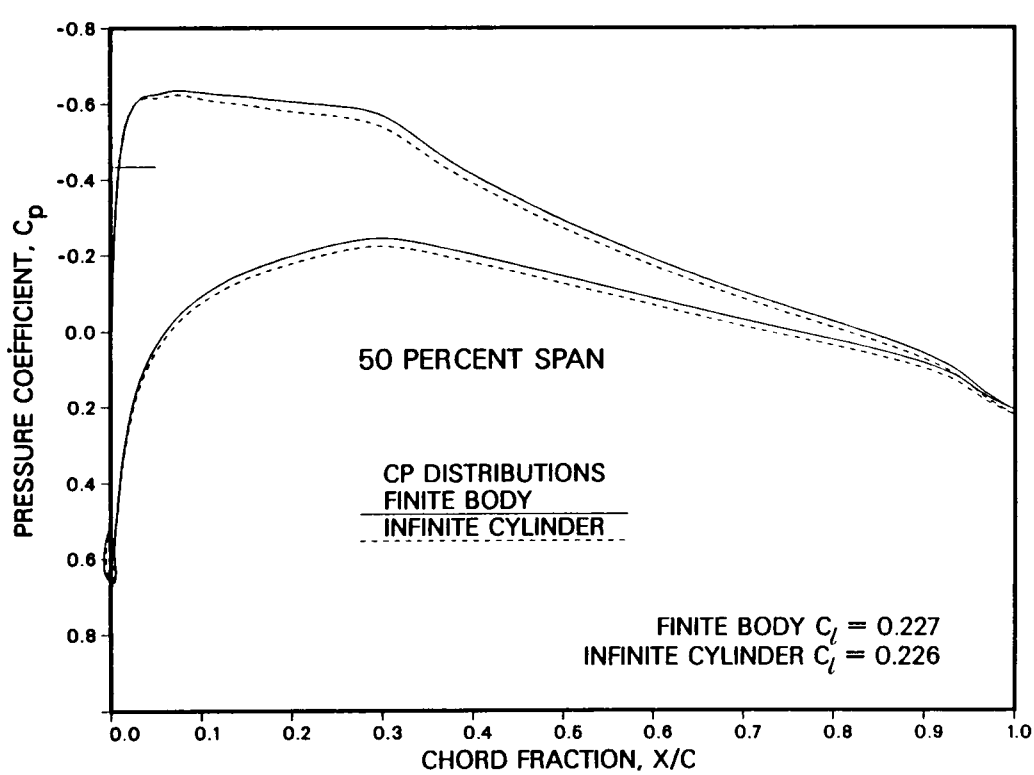

Figure 2. Comparison of finite fuselage midspan pressures with infinite cylinder fuselage results for RAE wing body 'A'.

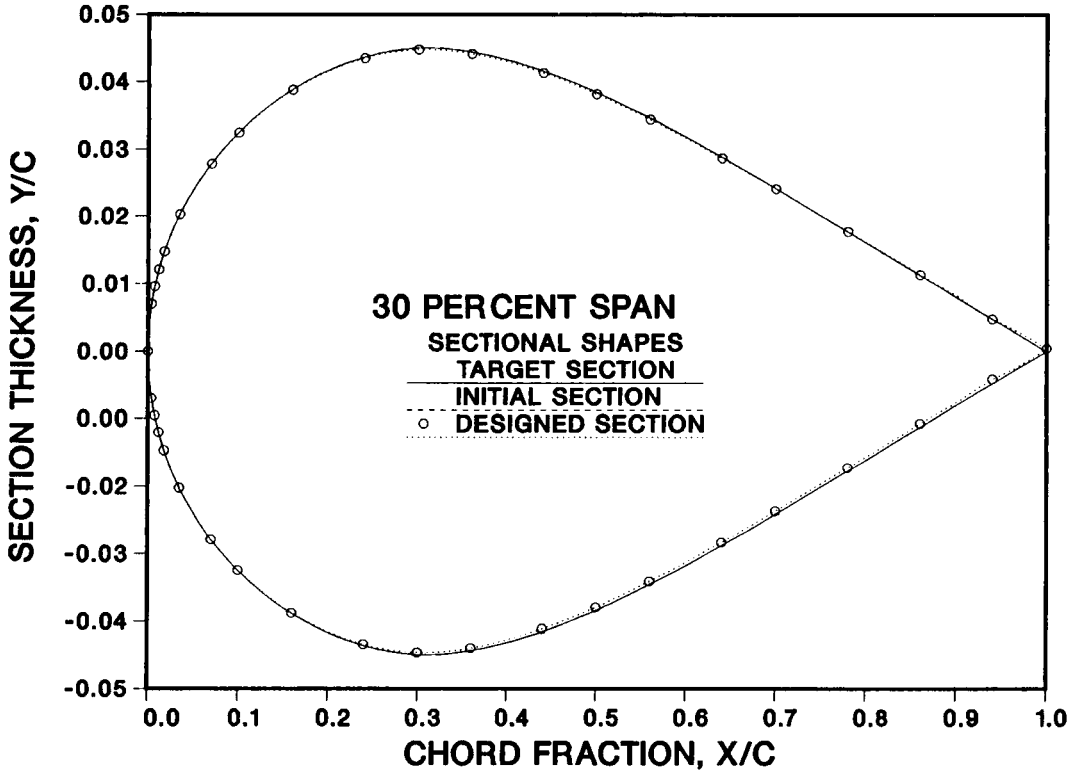

Figure 3. Comparison of section designed by TAW5D at 30 percent span for RAE wing body 'A' with initial and target sections.

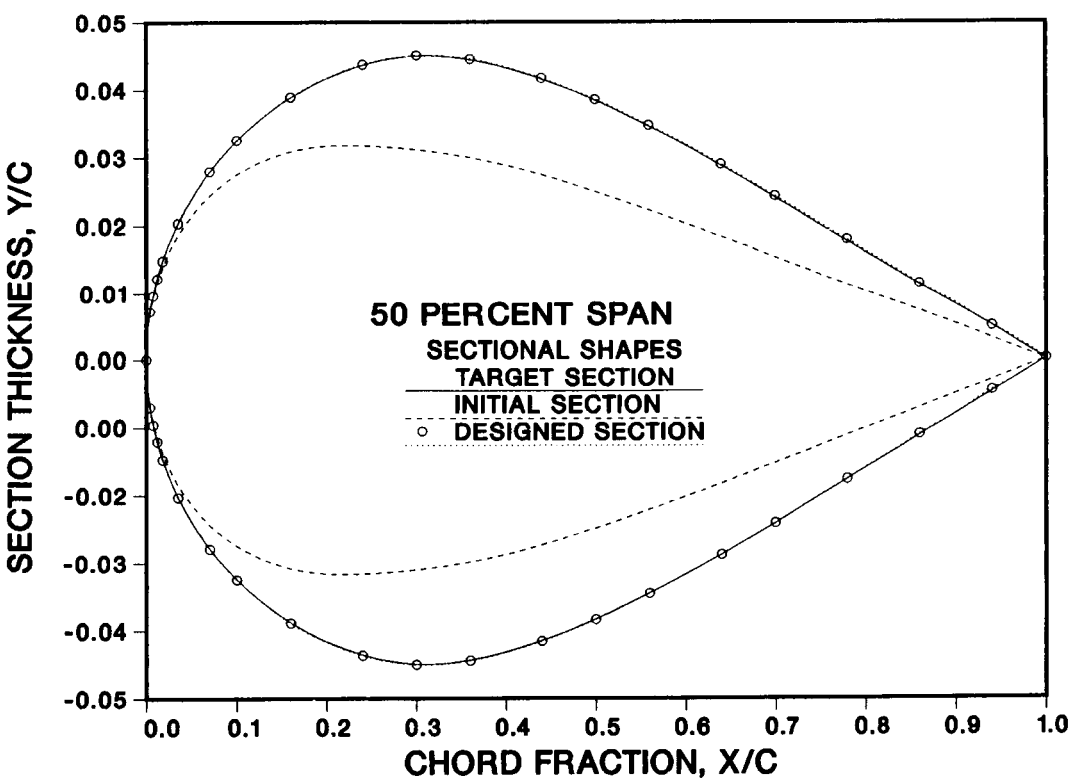

Figure 4. Comparison of section designed by TAW5D at 50 percent span for RAE wing body 'A' with initial and target sections.

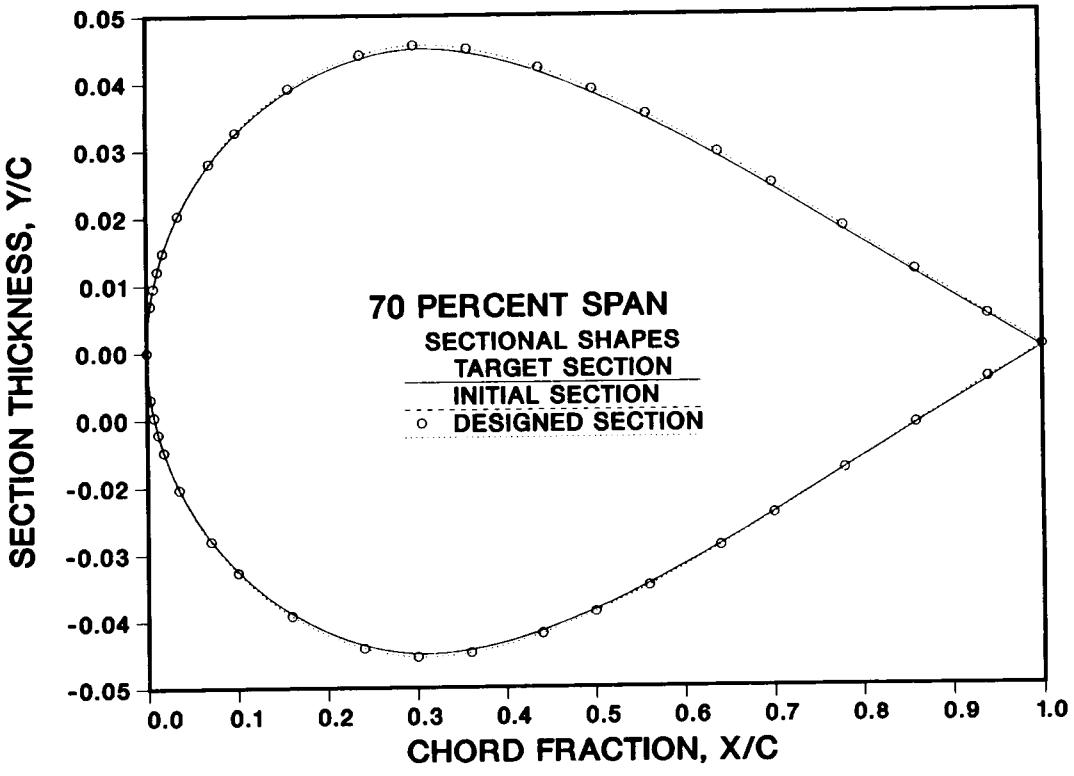

Figure 5. Comparison of section designed by TAW5D at 70 percent span for RAE wing body 'A' with initial and target sections.

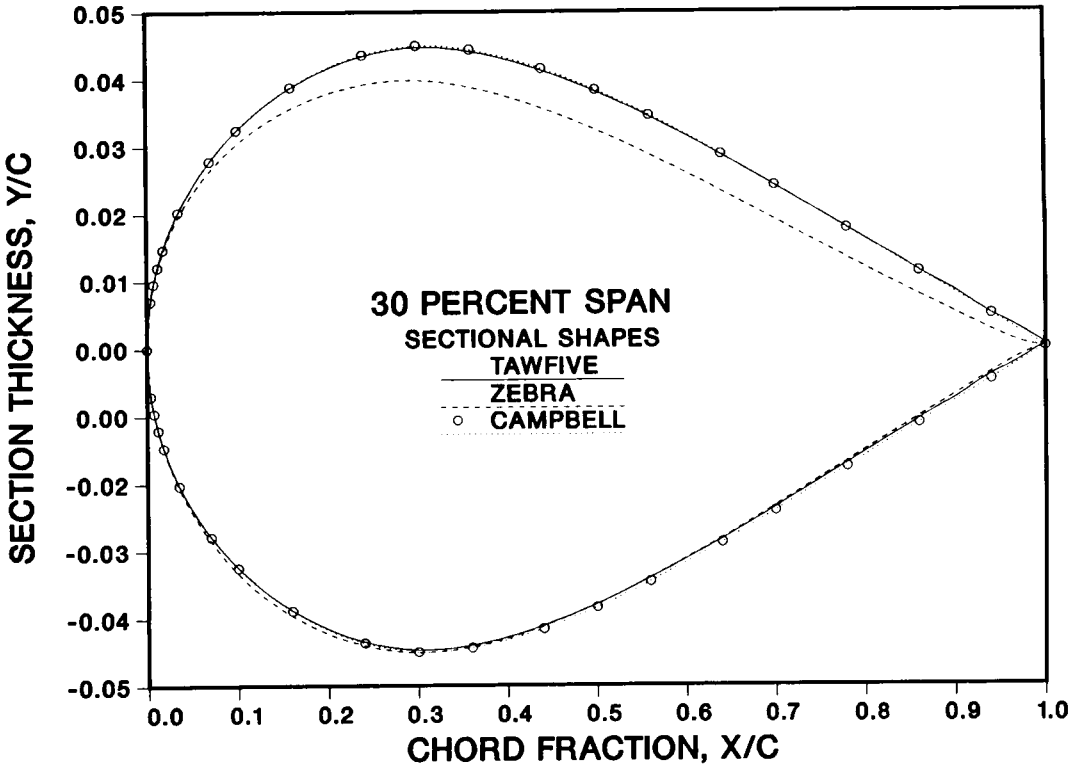

Figure 6. Comparison of sections designed by different methods at 30 percent span for RAE wing 'A' with infinite fuselage.

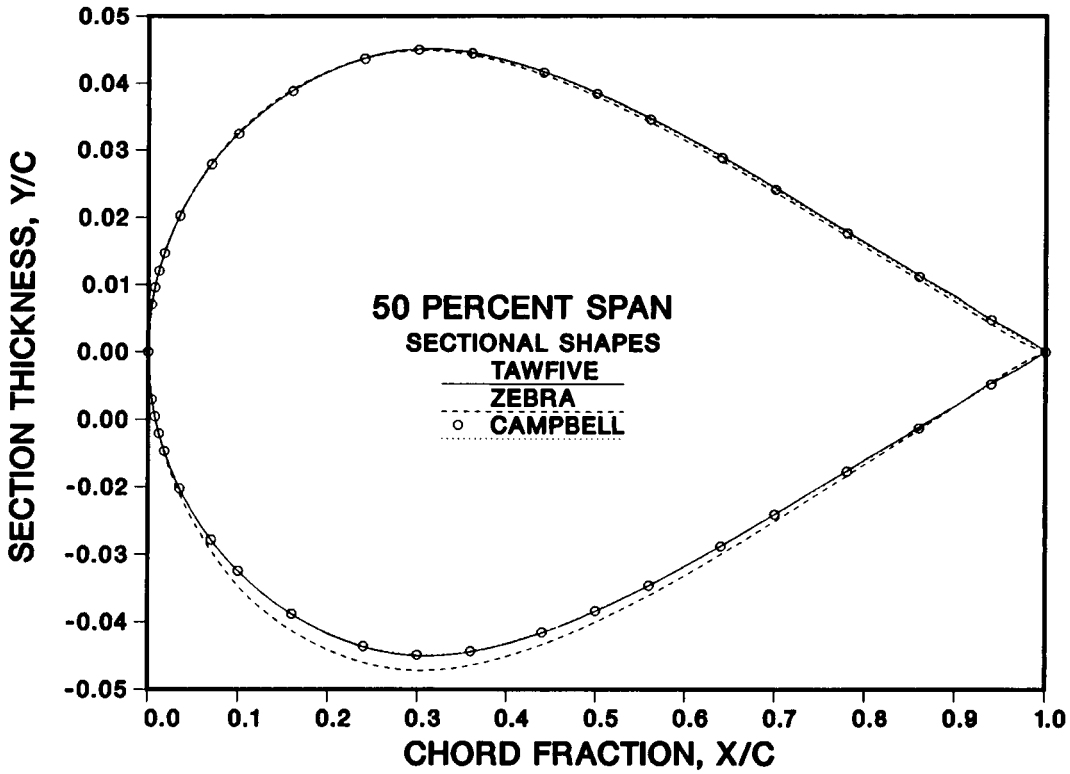

Figure 7. Comparison of sections designed by different methods at 50 percent span for RAE wing 'A' with infinite fuselage.

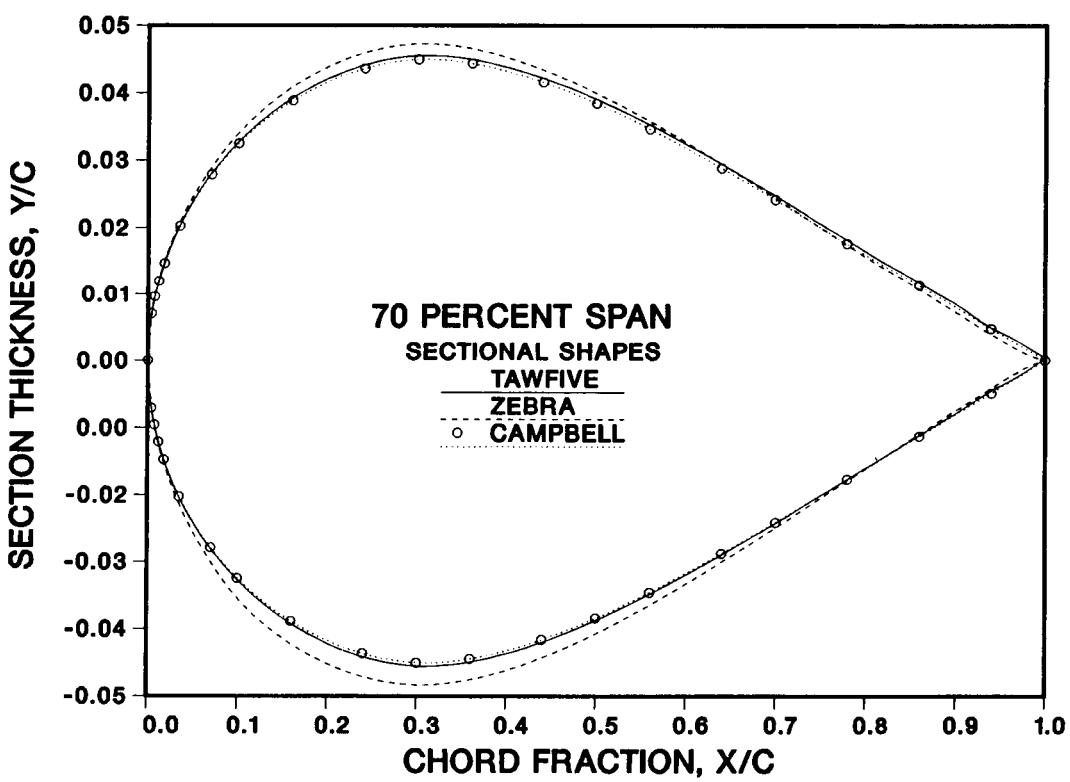

Figure 8. Comparison of sections designed by different methods at 70 percent span for RAE wing 'A' with infinite fuselage.

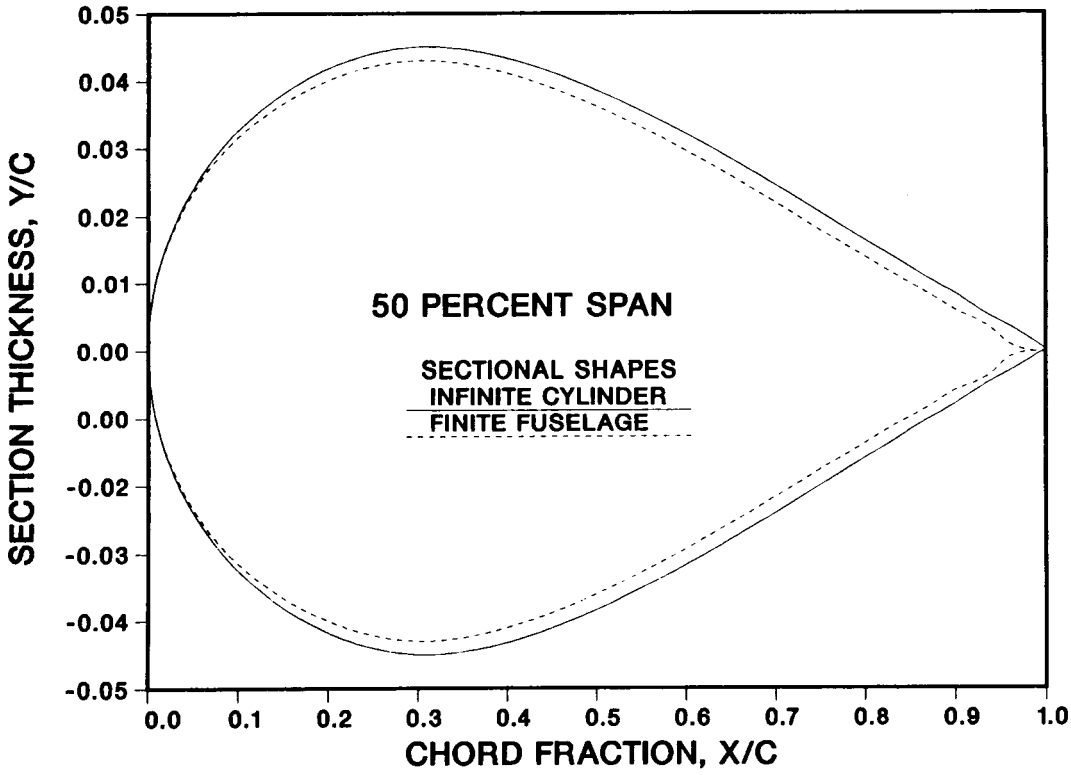

Figure 9. Comparison of sections designed by finite and infinite fuselage versions of TAW5D using infinite fuselage wing pressures as input in both cases (RAE wing 'A').

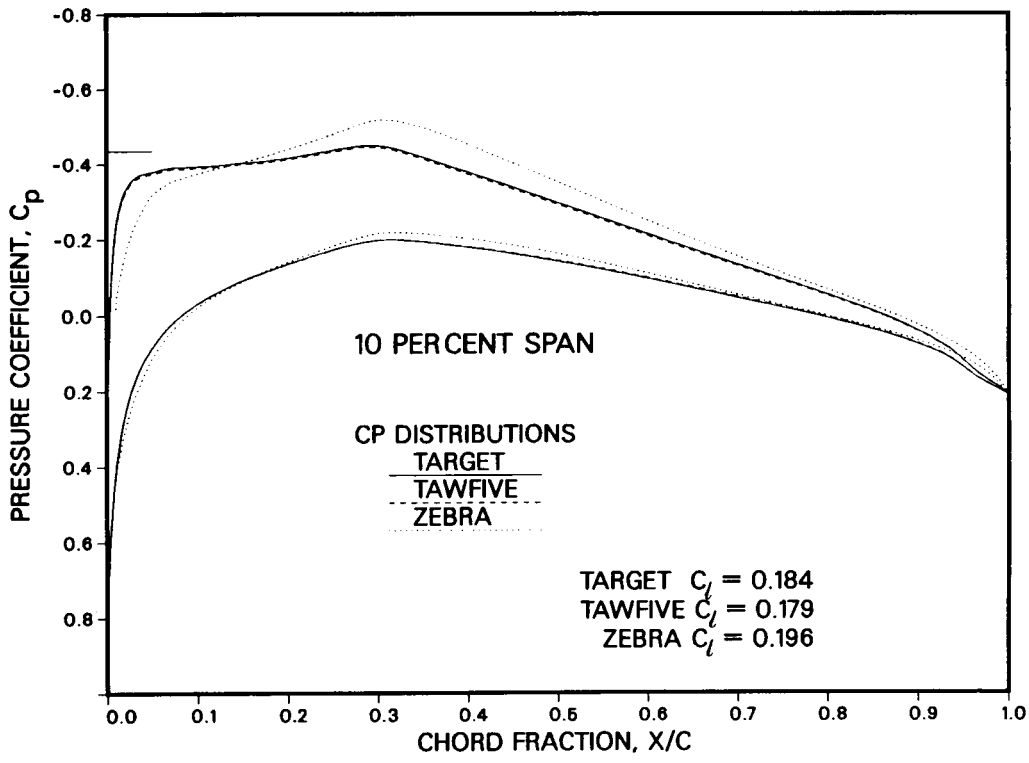

Figure 10. Comparison at 10 percent span of target values with pressures obtained by analyses of the wing designed by ZEBRA (RAE wing body 'A', Mach = 0.8, AOA = 2 degrees).

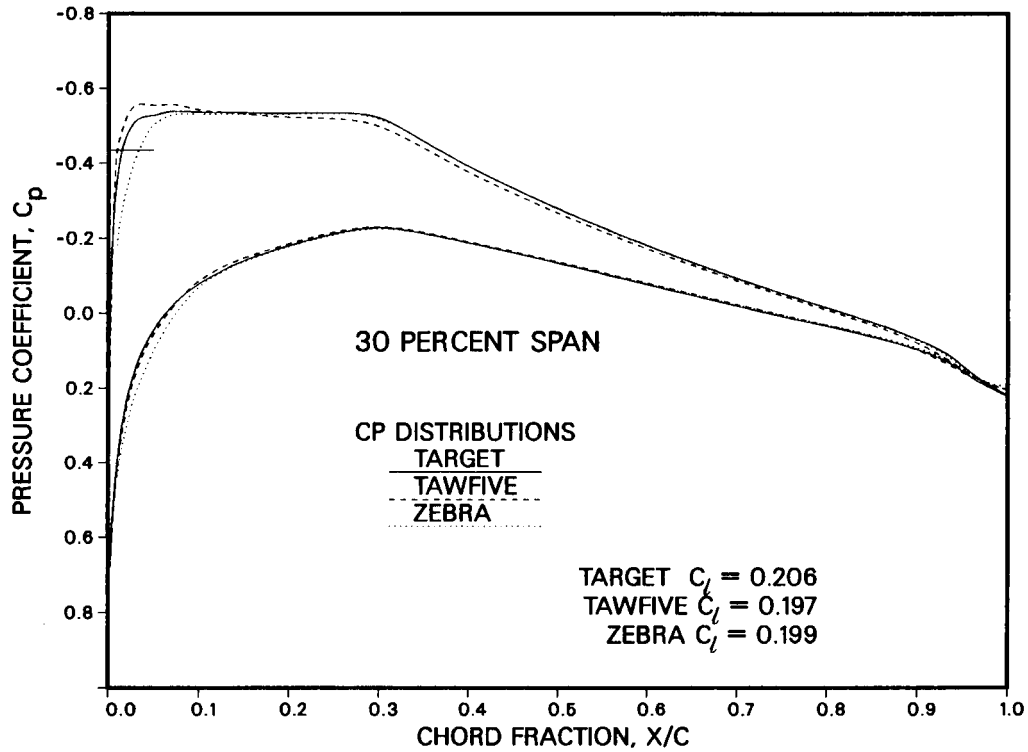

Figure 11. Comparison at 30 percent span of target values with pressures obtained by analyses of the wing designed by ZEBRA (RAE wing body 'A', Mach = 0.8, AOA = 2 degrees).

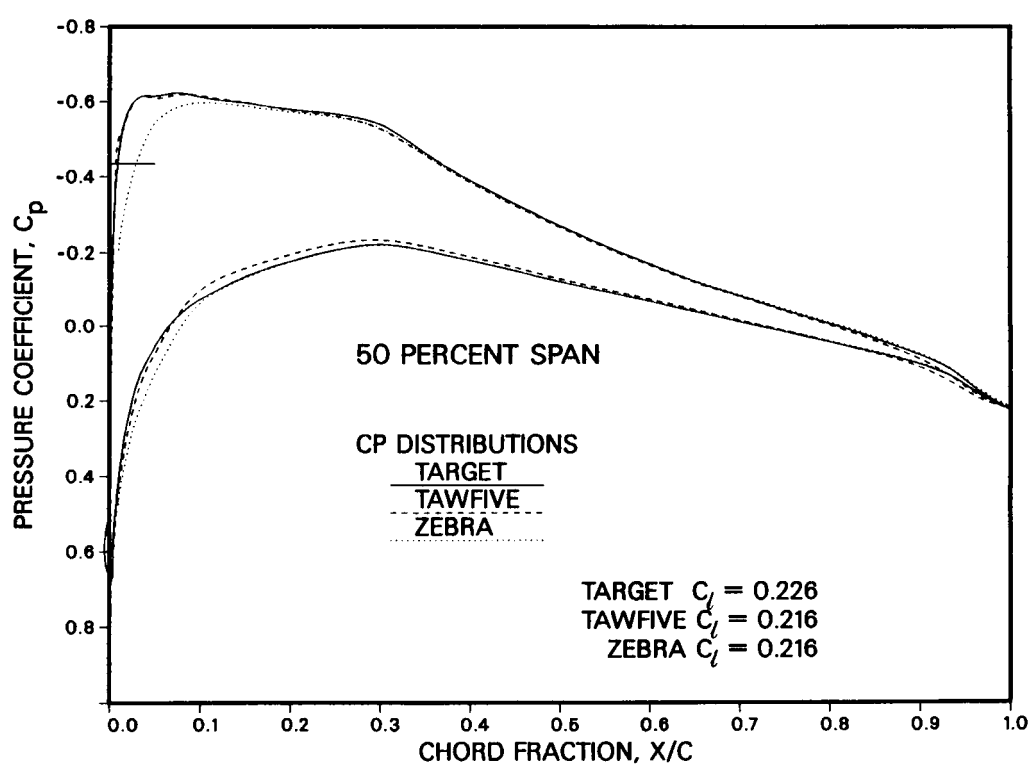

Figure 12. Comparison at 50 percent span of target values with pressures obtained by analyses of the wing designed by ZEBRA (RAE wing body 'A', Mach = 0.8, AOA = 2 degrees).

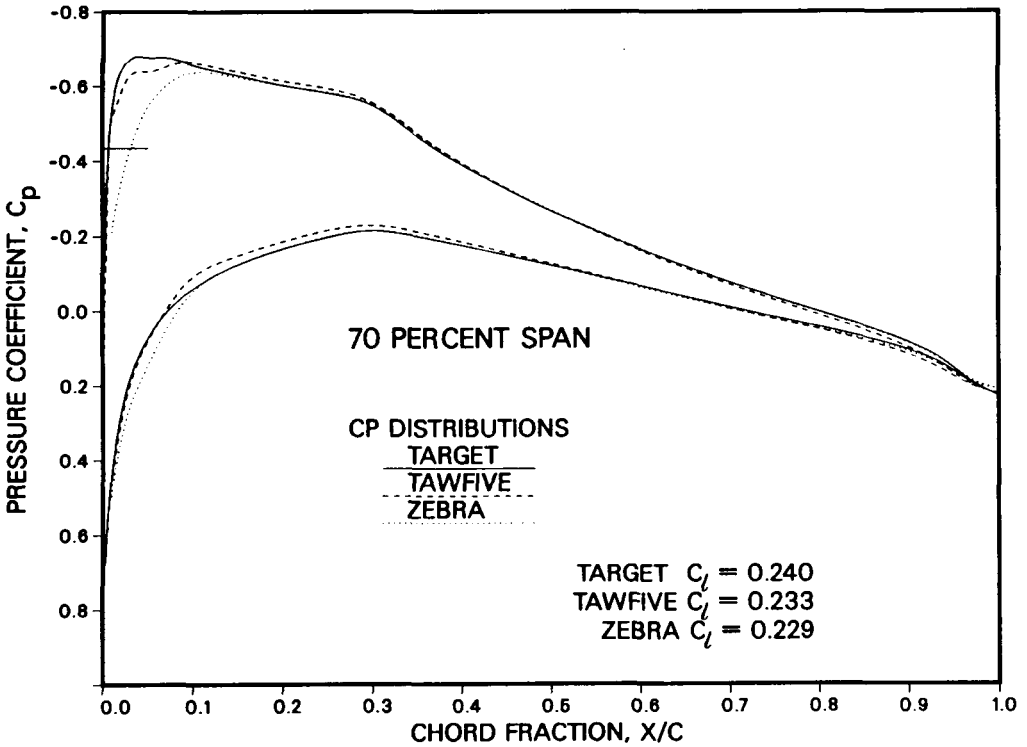

Figure 13. Comparison at 70 percent span of target values with pressures obtained by analyses of the wing designed by ZEBRA (RAE wing body 'A', Mach = 0.8, AOA = 2 degrees).

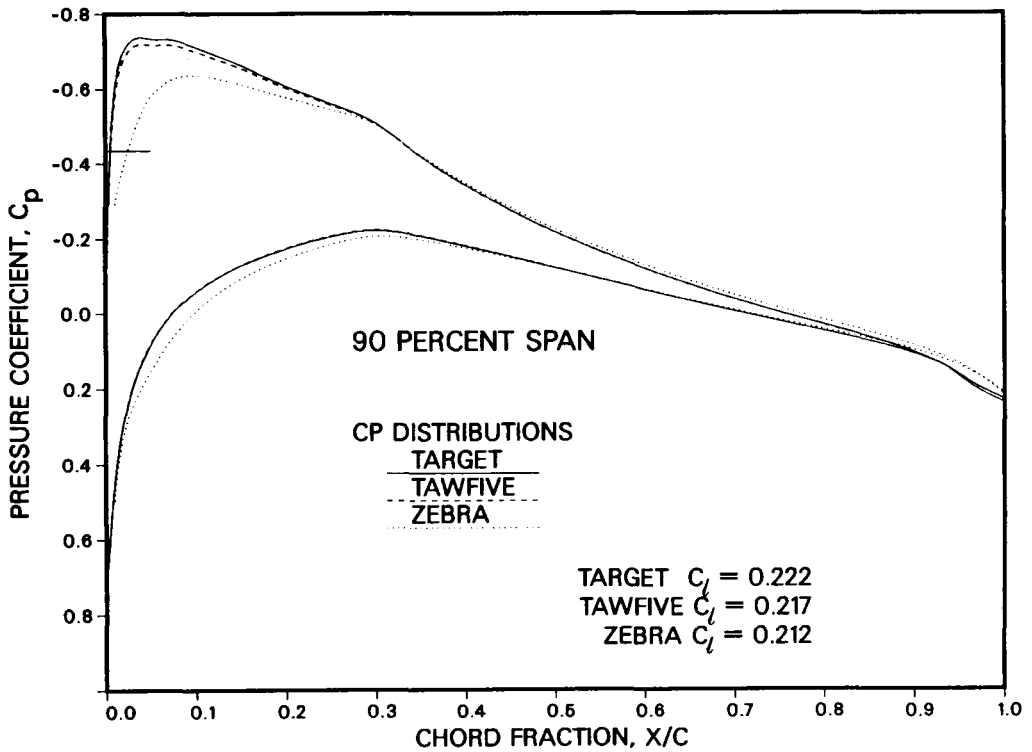

Figure 14. Comparison at 90 percent span of target values with pressures obtained by analyses of the wing designed by ZEBRA (RAE wing body 'A', Mach = 0.8, AOA = 2 degrees).

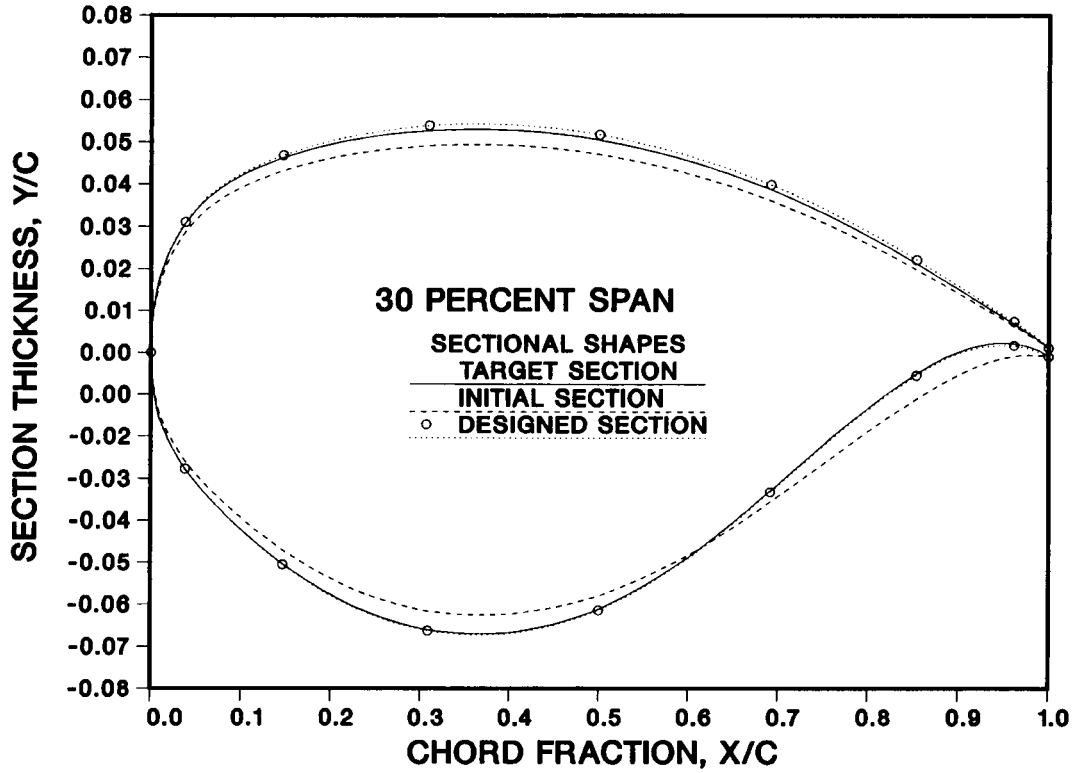

Figure 15. Comparison of section designed by TAW5D at 30 percent span for Lockheed Wing A wing body with target and first type of initial section.

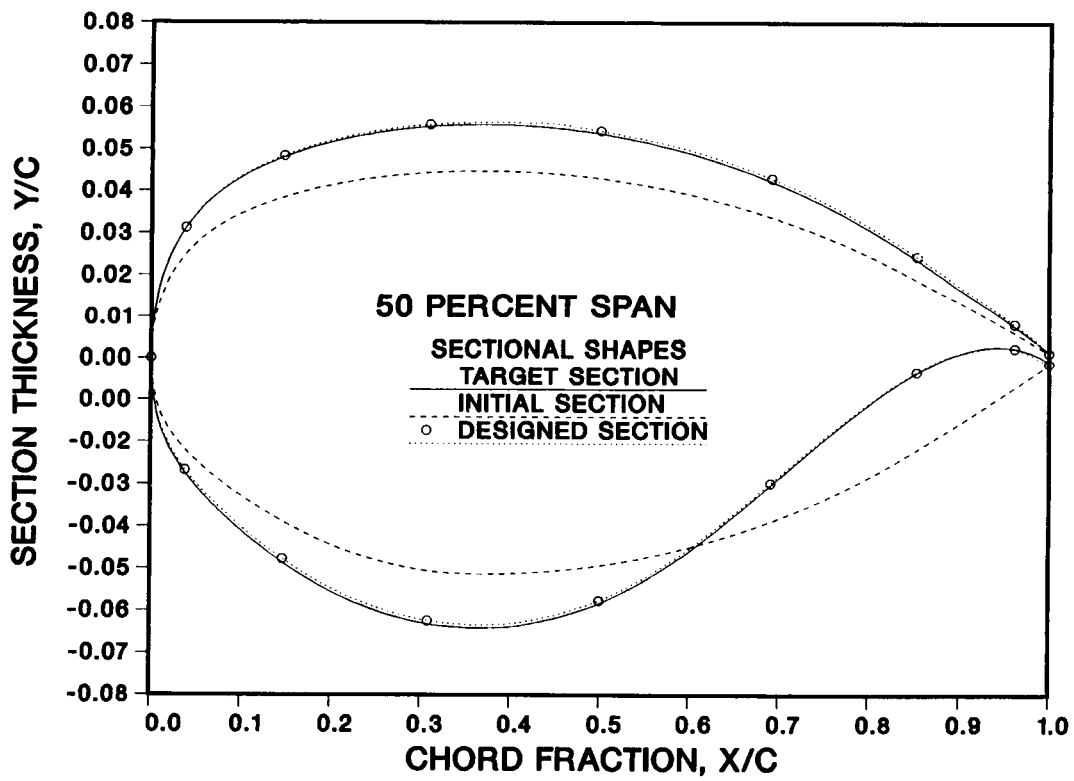

Figure 16. Comparison of section designed by TAW5D at 50 percent span for Lockheed Wing A wing body with target and first type of initial section.

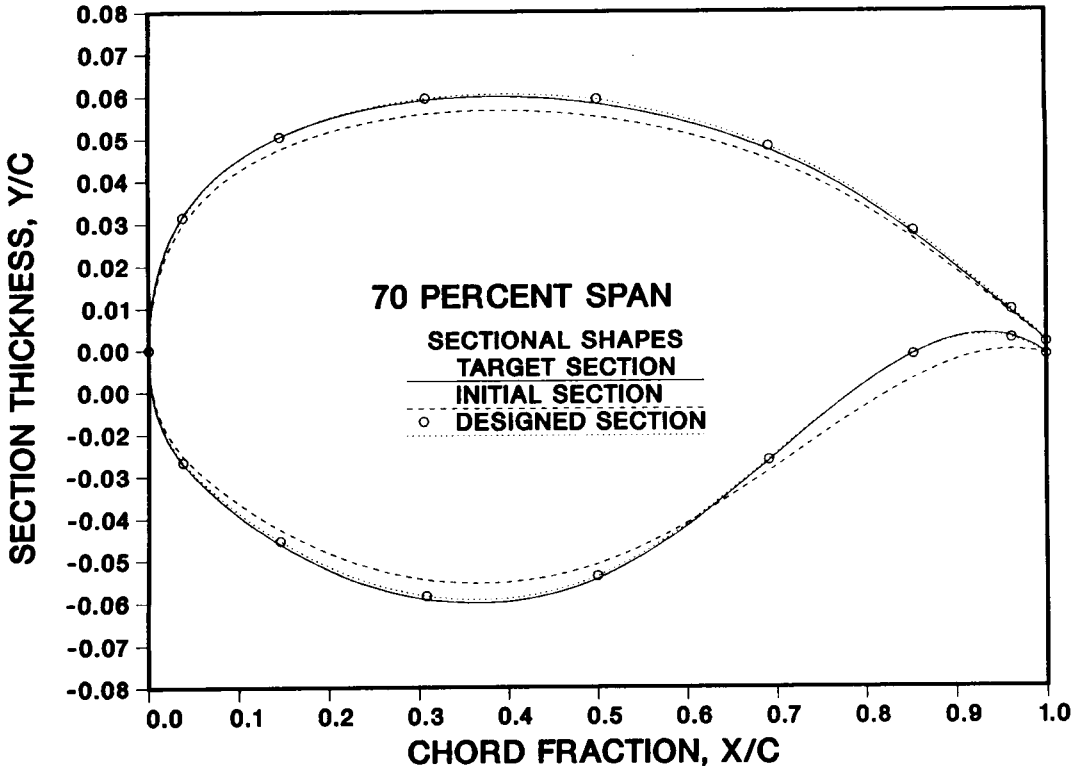

Figure 17. Comparison of section designed by TAW5D at 70 percent span for Lockheed Wing A wing body with target and first type of initial section.

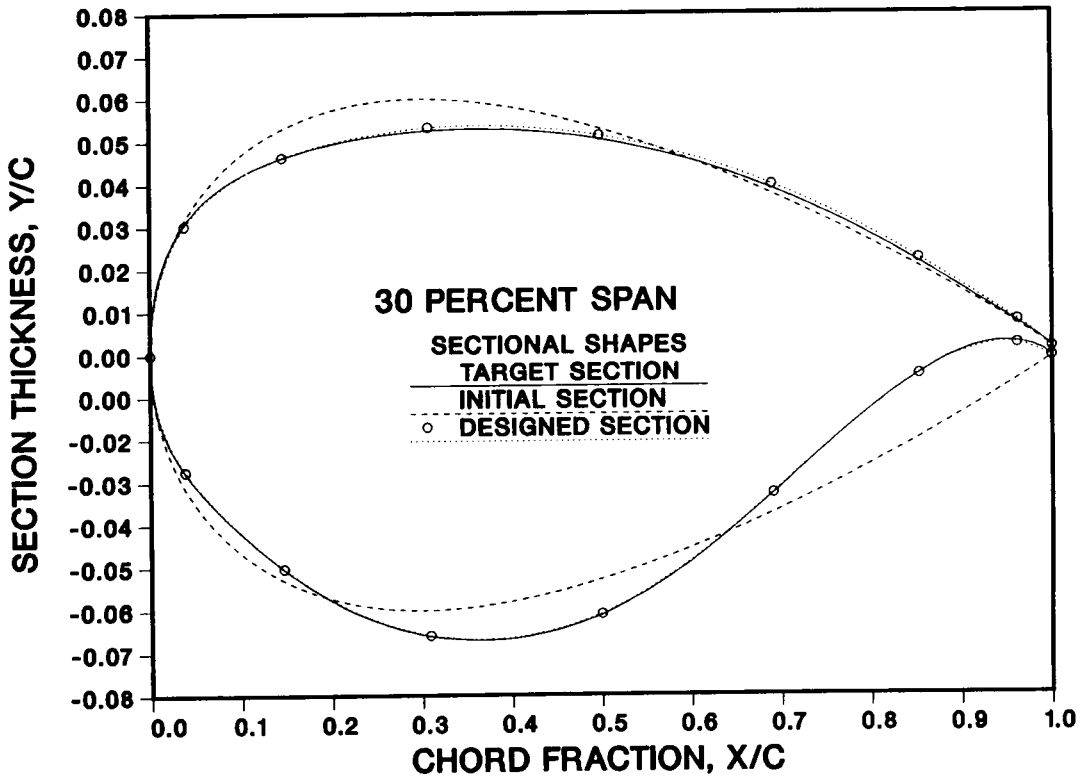

Figure 18. Comparison of section designed by TAW5D at 30 percent span for Lockheed Wing A wing body with target and second type of initial section.

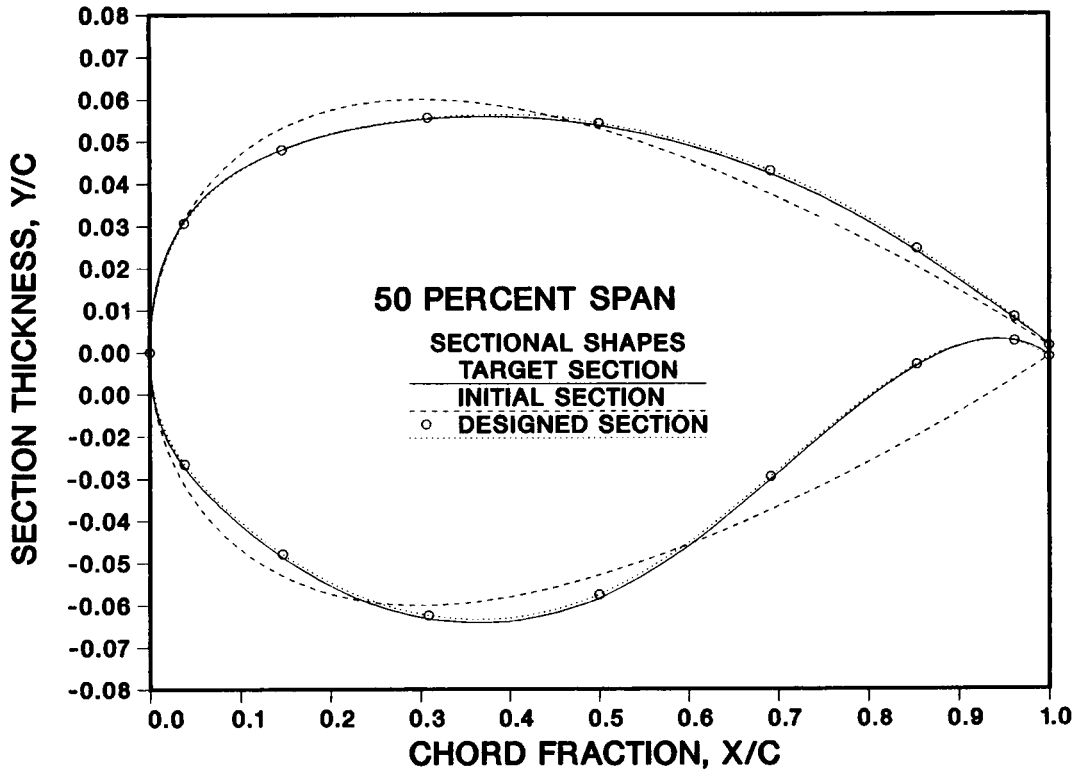

Figure 19. Comparison of section designed by TAW5D at 50 percent span for Lockheed Wing A wing body with target and second type of initial section.

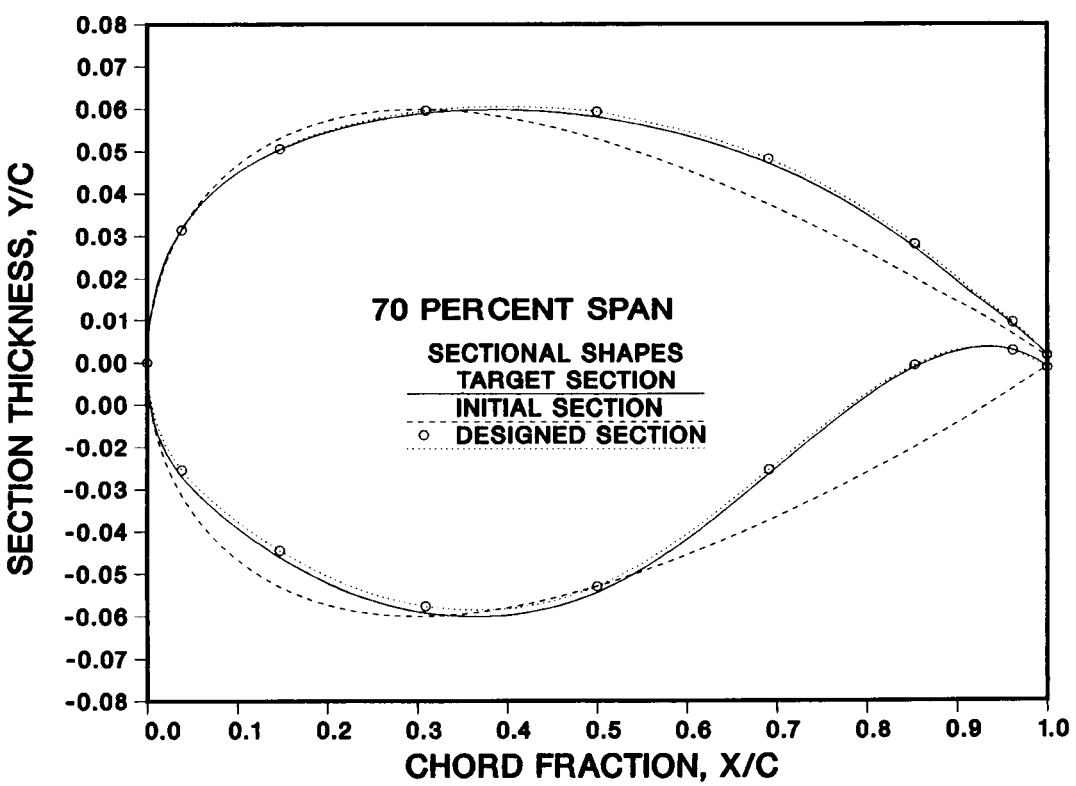

Figure 20. Comparison of section designed by TAW5D at 70 percent span for Lockheed Wing A wing body with target and second type of initial section.

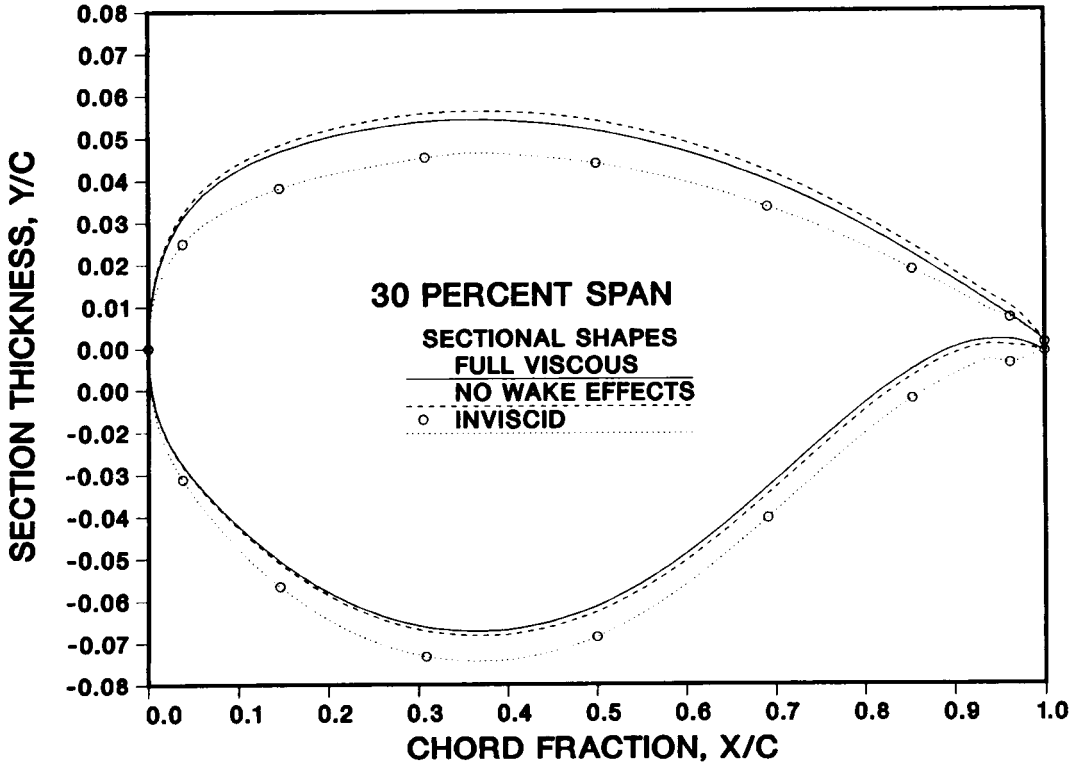

Figure 21. Comparison of sections designed at 30 percent span using different viscous interaction assumptions for Lockheed Wing 'A' wing body.

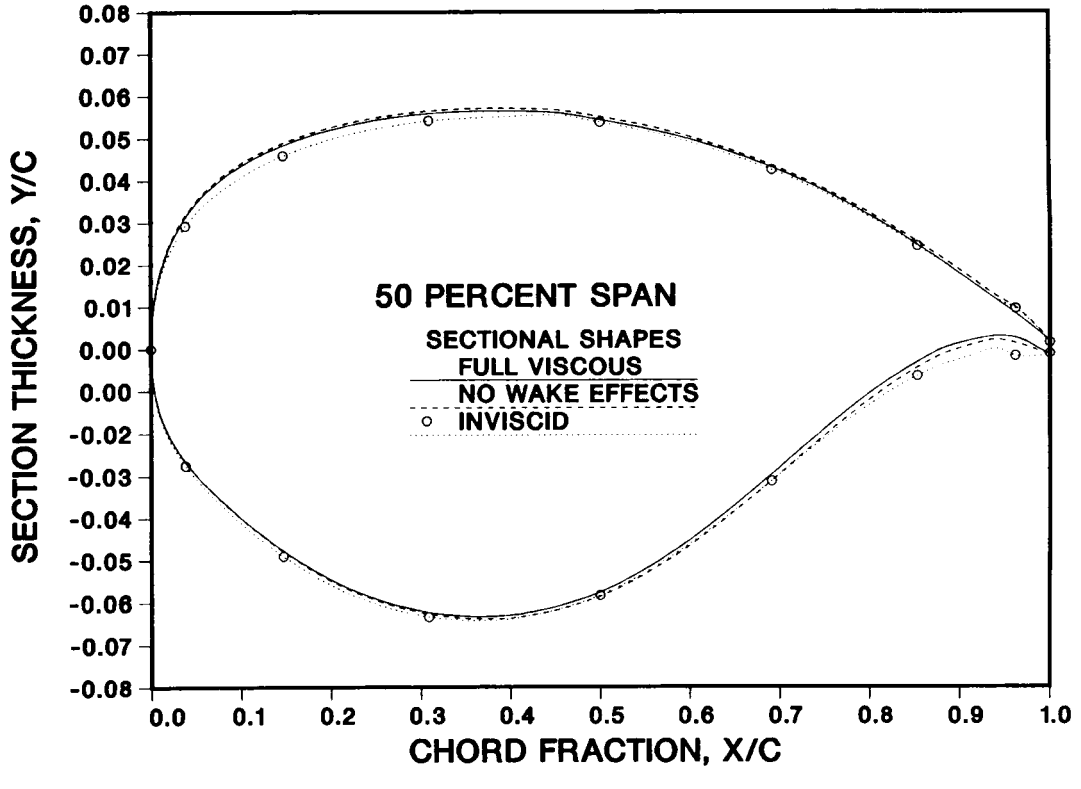

Figure 22. Comparison of sections designed at 50 percent span using different viscous interaction assumptions for Lockheed Wing 'A' wing body.

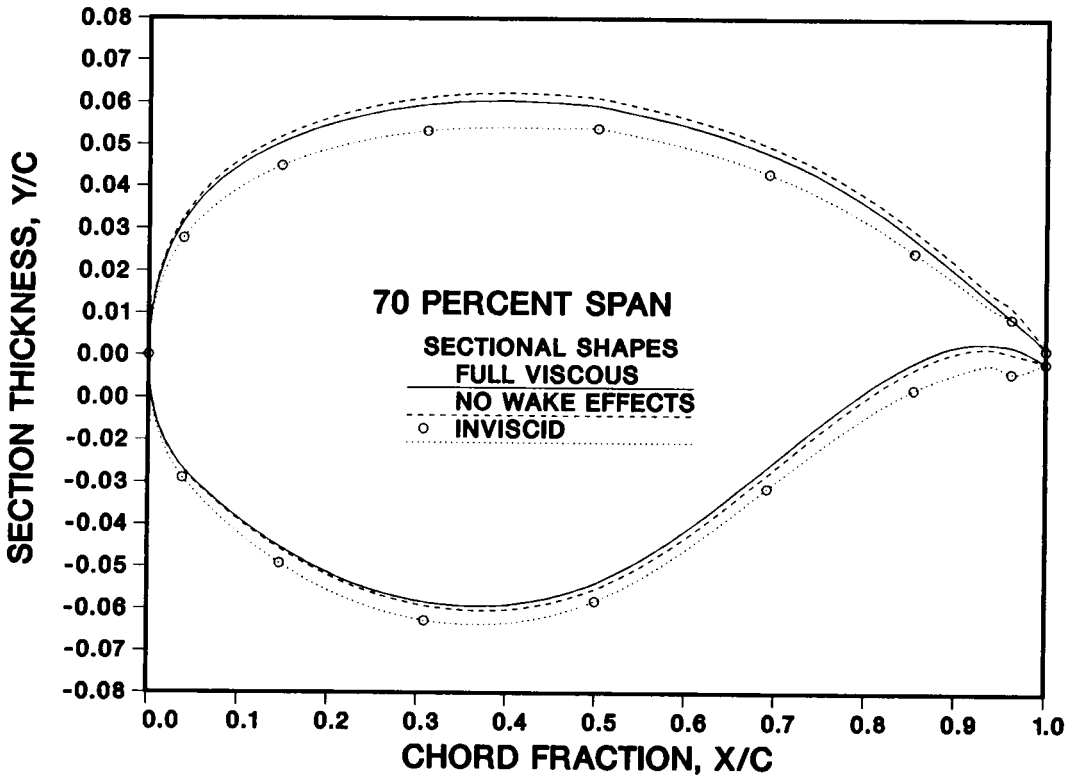

Figure 23. Comparison of sections designed at 70 percent span using different viscous interaction assumptions for Lockheed Wing 'A' wing body.

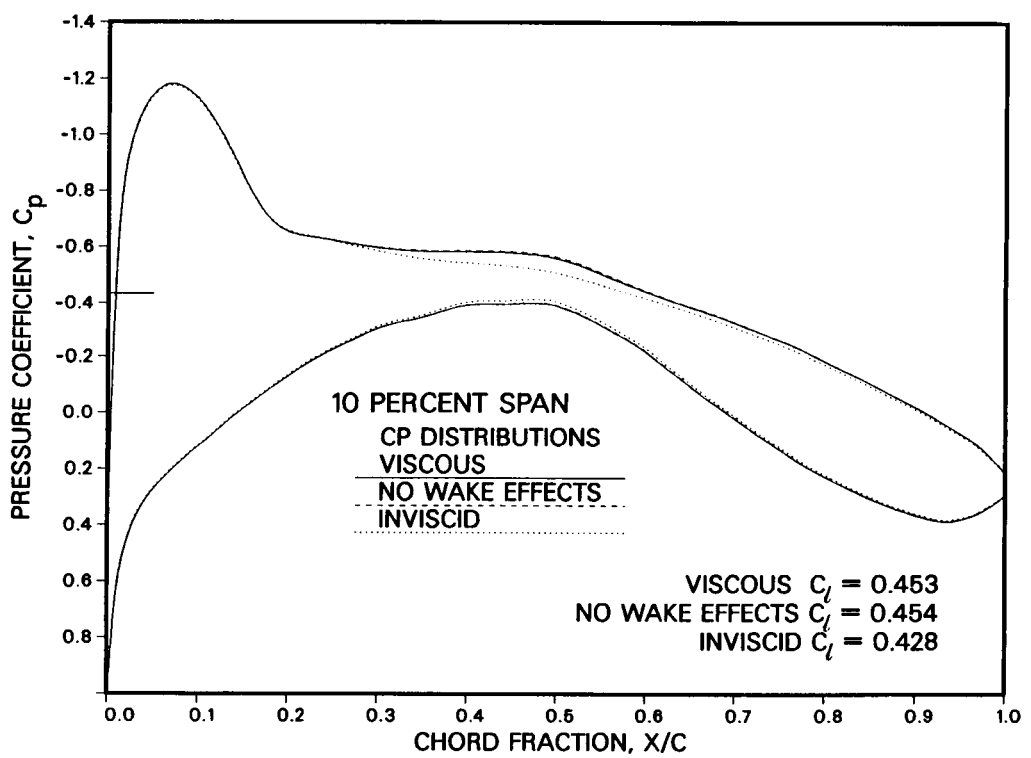

Figure 24. Comparison of pressures at 10 percent span obtained by viscous analyses of the wings designed using different viscous interaction assumptions (Lockheed Wing 'A', Mach = 0.8, AOA = 2 degrees, Reynolds No. = 24 million).

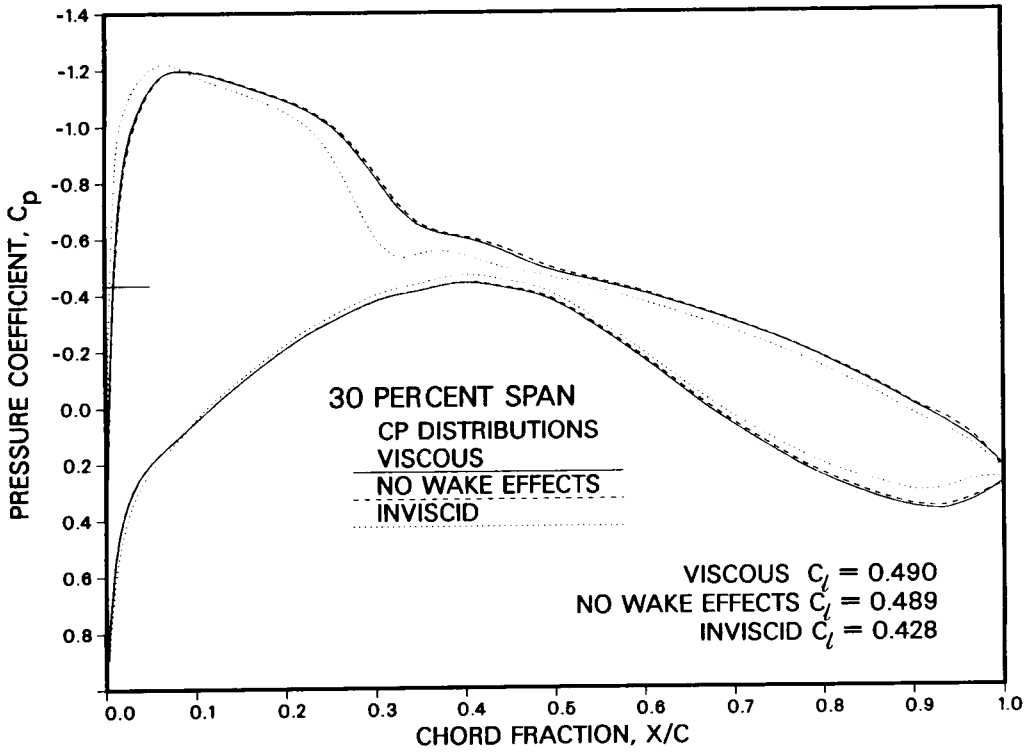

Figure 25. Comparison of pressures at 30 percent span obtained by viscous analyses of the wings designed using different viscous interaction assumptions (Lockheed Wing 'A', Mach = 0.8, AOA = 2 degrees, Reynolds No. = 24 million).

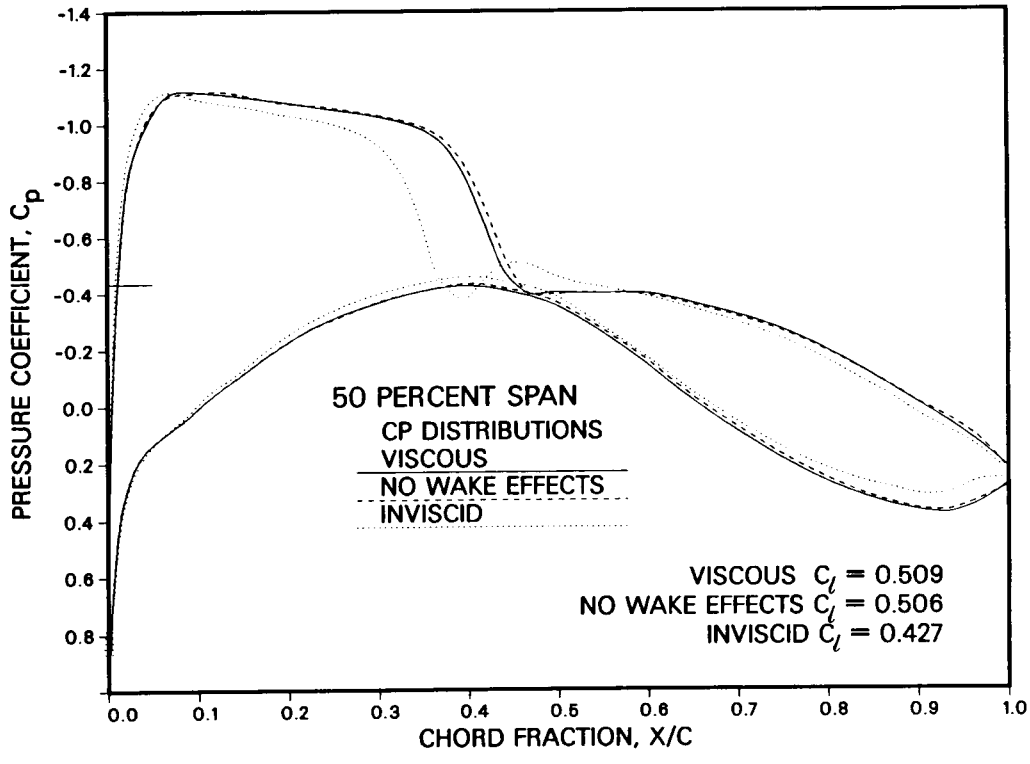

Figure 26. Comparison of pressures at 50 percent span obtained by viscous analyses of the wings designed using different viscous interaction assumptions (Lockheed Wing 'A', Mach = 0.8, AOA = 2 degrees, Reynolds No. = 24 million).

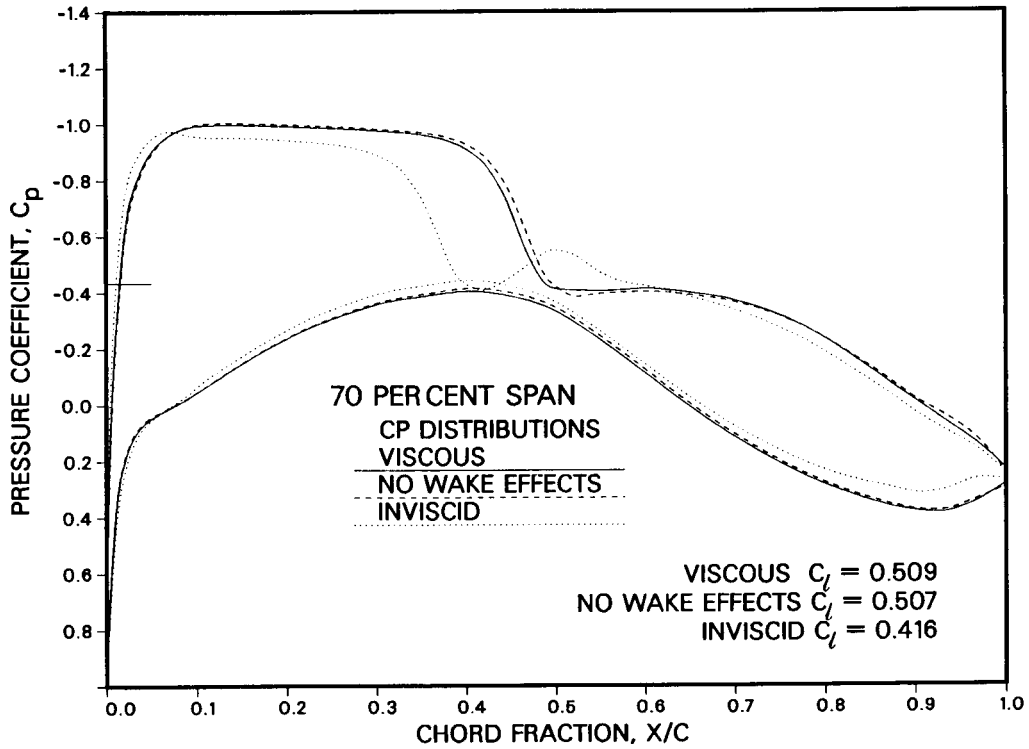

Figure 27. Comparison of pressures at 70 percent span obtained by viscous analyses of the wings designed using different viscous interaction assumptions (Lockheed Wing 'A', Mach = 0.8, AOA = 2 degrees, Reynolds No. = 24 million).

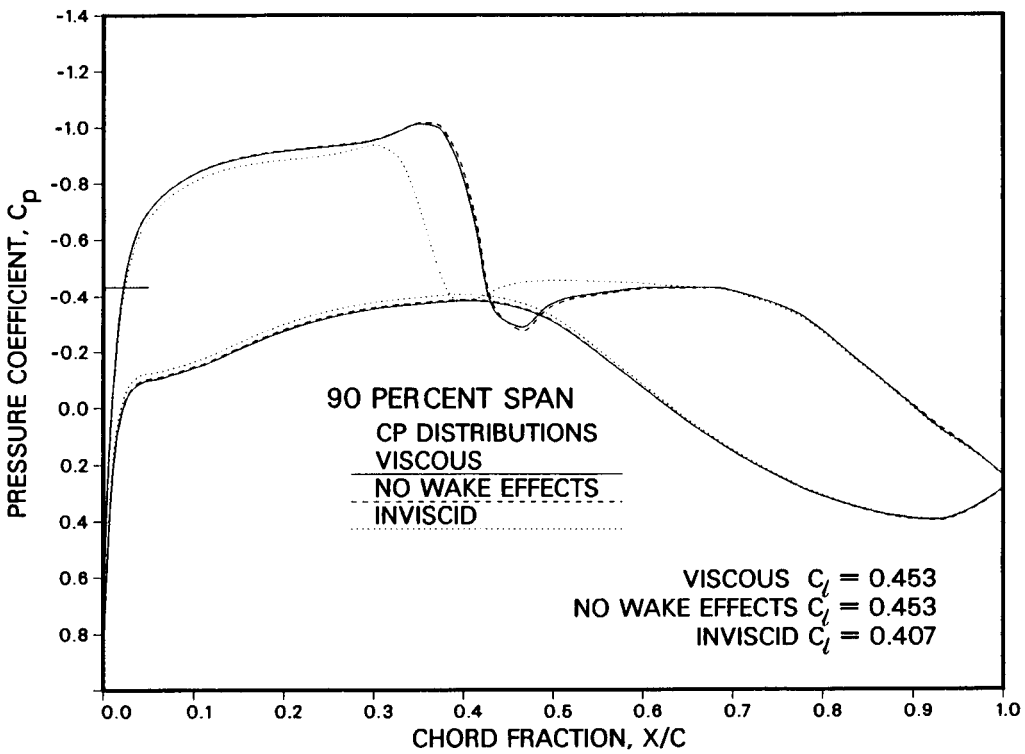

Figure 28. Comparison of pressures at 90 percent span obtained by viscous analyses of the wings designed using different viscous interaction assumptions (Lockheed Wing 'A', Mach = 0.8, AOA = 2 degrees, Reynolds No. = 24 million).

N89-20948

EULER/NAVIER-STOKES CALCULATIONS OF TRANSONIC FLOW PAST FIXED- AND ROTARY-WING AIRCRAFT CONFIGURATIONS†

J. E. Deese and R. K. Agarwal
McDonnell Douglas Research Laboratories
St. Louis, MO

INTRODUCTION

Computational fluid dynamics has an increasingly important role in the design and analysis of aircraft as computer hardware becomes faster and algorithms become more efficient. Progress is being made in two directions: more complex and realistic configurations are being treated and algorithms based on higher approximations to the complete Navier-Stokes equations are being developed. The obvious goal is the solution of complete aircraft flowfields with the full Navier-Stokes equations.

The literature indicates that linear panel methods can model detailed, realistic aircraft geometries in flow regimes where this approximation is valid. Solutions for nonlinear potential equations for flowfields about nearly complete aircraft configurations have also been available for some time. Recently, Euler methods have progressed to the point of computing flowfield solutions for complete aircraft.

As algorithms incorporating higher approximations to the Navier-Stokes equations are developed, computer resource requirements increase rapidly. Generation of suitable grids becomes more difficult and the number of grid points required to resolve flow features of interest increases. Coupling greater grid density with the greater execution time per point needed to solve more complex equations creates requirements for large memory and long run-time. As a result, early work with the Euler and Navier-Stokes equations dealt with one- and two-dimensional flows or three-dimensional flow about simple geometries. Recently, the development of large vector computers has enabled researchers to attempt more complex geometries with Euler and Navier-Stokes algorithms.

This paper describes the results of calculations for transonic flow about a typical transport and fighter wing-body configuration using thin-layer Navier-Stokes equations, and about helicopter rotor blades using both Euler/Navier-Stokes equations. The two codes employed in the calculations have been developed at McDonnell Douglas Research Laboratories and are designated as MDTSL30 (thin-layer Navier-Stokes fixed wing-body code) and MDROTH (Euler/Navier-Stokes rotary-wing code). Both codes have been fully vectorized for optimum performance on a Cray supercomputer. The codes have also been microtasked on a four-processor Cray X-MP/48 for reducing the wall-clock time by judicious use of various Cray software techniques.

†This research was conducted under the McDonnell Douglas Independent Research and Development program.

PRECEDING PAGE BLANK NOT FILMED

The calculations presented in this paper have been performed on a Cray X-MP/48 Cray X-MP/14, Cray 2, or Convex C-2. Some of the results are presented in color-graphics form produced at a Silicon Graphics IRIS 2400T work station.

COMPUTATION OF WING/BODY FLOWFIELDS

Transonic flowfields about wing/body configurations are calculated by use of both the Euler and the Navier-Stokes equations. A code designated MDTSL30 has been developed at McDonnell Douglas Research Laboratories to compute flowfields by solving the Euler, thin-layer, or slender-layer approximations to the Navier-Stokes equations.

The thin-layer approximation retains viscous terms in one direction. For high-Reynolds-number turbulent flow, the dominant viscous effects are the result of diffusion normal to a body surface. The thin-layer approximation is then suitable for geometries where the body can be mapped onto a single plane in the computational space, retaining viscous terms normal to this plane. A typical example is an isolated wing or fuselage.

The slender-layer approximation retains viscous terms in two directions, neglecting only streamwise terms. This approximation is useful for calculating viscous flows in regions where two aerodynamic surfaces interact, such as the wing-body junction or the wing-tip region. Viscous effects on both the fuselage and wing surfaces can be modeled with the slender-layer approximation.

The MDTSL30 code computes the turbulent flowfield by solving the three-dimensional, Reynolds-averaged, thin-layer, or slender-layer approximation to the Navier-Stokes equations on body-conforming, curvilinear grids. These equations are solved by employing Jameson's finite-volume explicit Runge-Kutta time-stepping scheme. Turbulent effects are modeled by employing the Baldwin-Lomax algebraic eddy viscosity model.

The details of the methodology and the test calculations performed to verify the code are described by Deese and Agarwal,[1] Agarwal, Deese, and Underwood,[2] and Agarwal and Deese.[3] Microtasking was achieved by employing various Cray software tools as described by Booth and Misegades.[4]

Calculations have been performed for three different configurations: (1) the ONERA-M6 wing, (2) a typical transport wing-body configuration, and (3) a typical fighter wing-body configuration.

<u>ONERA-M6 Wing</u>: $M_\infty=0.84$, $\alpha=3.0°$, $Re_c=11.7\times10^6$

This standard test case was run on a mesh that had 192 cells wrapped around the wing, 32 cells normal to the wing surface and 36 cells in the spanwise direction. There were 136 cells on the wing surface in the wrap-around direction and 24 on the wing surface in the spanwise direction. The value of $y^+ = \frac{y\sqrt{\tau_w \rho}}{\mu}$ at the center of the first cell was approximately four with about ten cells in the boundary-layer. The grid was constructed by stacking 2-D sectional grids along the wing-span. The 2-D sectional grids were generated using the MDRL algebraic grid generation code.

Figure 1 compares pressure distributions on the wing at five span stations as predicted using the Euler and thin-layer models. Agreement with experimental data[5] is good in the leading edge and trailing edge region. Shock smearing is greater than desirable, but can be attributed to the size of the cells in the mid-chord region. Cell width is typically 2-3% of the chord in this area with shocks being smeared over three or four cells. More grid points in the wraparound direction or a better distribution with less clustering in the leading- and trailing-edge regions would produce sharper shocks.

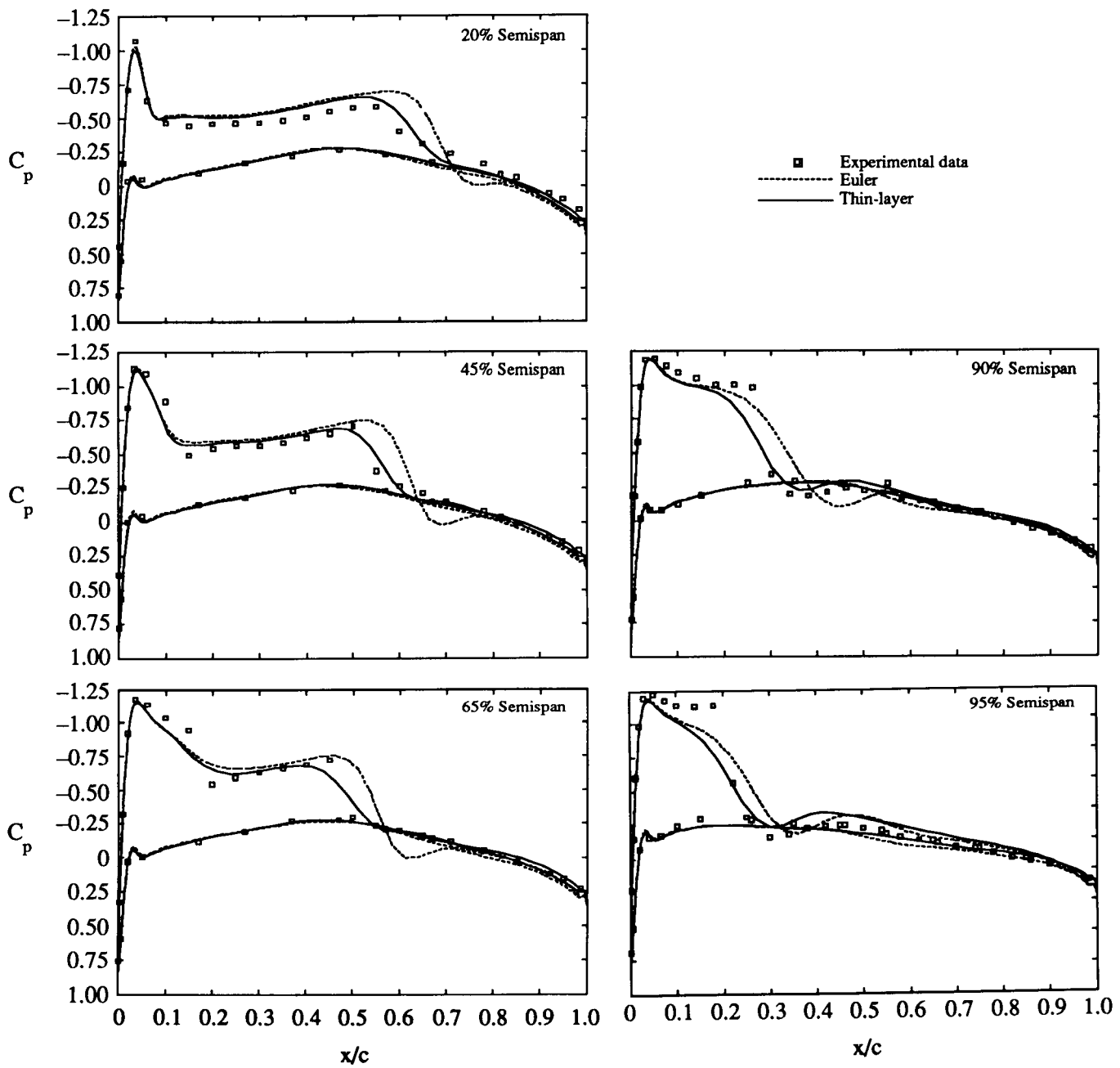

Figure 1. Pressure distributions on an ONERA-M6 wing at various spanwise stations; $M_\infty = 0.84$, $\alpha = 3.0°$, $Re_c = 11.7 \times 10^6$, $192 \times 32 \times 36$ mesh.

The thin-layer model produces a more accurate prediction of the wing pressure distribution than the Euler model. Shock strength is too large and shock position is too far downstream when the Euler model is used. The thin-layer model, which includes the effects of the boundary layer, captures shock location and strength more accurately.

This case was also run on a smaller 140×48×32 grid on a four processor X-MP/48 to demonstrate the microtasking capability. The grid was limited by the eight megaword capacity of the machine. Table I gives a summary of the results. Total runtime using the microtasked version of the code was one hour on each of the four available processors for a total CPU time of four hours. The residuals dropped approximately four orders of magnitude in 2500 iterations at a Courant-Friedrichs-Levy (CFL) number of 0.9. The actual speedup in wall-clock time of 3.73 achieved by microtasking is very close to the theoretical maximum of 3.77 as determined by Amdahl's Law.

Table I. Performance evaluation of transonic viscous wing code MDTSL 30 on Cray X-MP/48.

- Test Case: ONERA M6 Wing
  $M_\infty = 0.84$, $\alpha = 3.0°$, $Re_c = 11.7 \times 10^6$
- Mesh used: 140 (chordwise)×48 (wing-normal)×32 (spanwise)
- Main Memory Required: 7.5 million words
- Processing rate on one processor: 2.3×10^{-5} CPU seconds/ mesh point iteration
- 98% of total CPU time spent in four key subroutines - EULER, FILTER, TSL1, EMUTURB
- Theorectical speedup on 4-processors (Amdahl's Law):
  $$SP = \frac{\text{CPU time}}{\text{wall clock time}} = \frac{1}{\frac{(0.98)}{4} + (1 - 0.98)} = 3.77$$
- Actual speedup achieved after microtasking = 3.73
- Processing rate on 4-processors: 6.3×10^{-6} wall clock seconds/mesh point/iteration
- Total CPU time of microtasked code is 5% less than original code
- Number of iterations N = 2500
- Root-mean-square residual at N = 1 is 0.106×10^4
- Root-mean-square residual at N = 2500 is 0.4830
- Reduction/cycle = 0.997
- Total Cpu time = 14400.00 s

Transport Wing-Body: $M_\infty=0.76$, $\alpha=2°$, $Re_c=6.4\times10^6$

The grid lines on the surface of a typical transport wing-body configuration are shown in Figure 2. A 160(chordwise)×34(wing-normal)×42(spanwise) mesh for this configuration was generated with the 3-D grid-generation code of Chen et al.[6] There are 96 cells on the wing in the chordwise direction and 34 in the spanwise direction. The value of y^+ at the center of the first cell along the wing surface ranges from 1.5 to 3 while the value of y^+ at the center of the first cell along the fuselage surface varies from 1.0 to 2.5.

ORIGINAL PAGE
COLOR PHOTOGRAPH

Figure 2. Typical transport configuration with surface grid lines.

Figure 3 shows the pressure distribution at five spanwise locations on the wing computed with the Euler and thin-layer Navier-Stokes codes and their comparison with experimental data. Thin-layer terms over the wing and the fuselage have been included in the calculations. As in the case of the ONERA-M6, the effect of including the thin-layer terms is to weaken shocks on the wing upper surface, move them forward, and improve the comparison with experimental data.

A comparison of the slender-layer pressure distributions with thin-layer calculations and experimental data are shown in Figure 4. As expected there is little difference between the pressure distributions over the wing. The major effect of including slender-layer terms should be near the wing-fuselage junction. No experimental data was available for comparison in this region.

Figure 5 shows pressure contours on the upper surface of the transport wing-body as displayed on an IRIS color graphics workstation. The location of the shock on the upper surface can be clearly identified.

<u>Transport Wing-Body</u>: $M_\infty=0.76$, $\alpha=4.2°$, $Re_c=6.4\times10^6$

Thin-layer calculations were performed for the transport wing-body at an angle-of-attack of 4.2°. Navier-Stokes terms were included over the wing but not the fuselage to reduce run time, so a 160×34×32 cell grid was used with clustering only near the wing surface. The value of y^+ at the center of the first cell ranges from 1.5 to 3.0.

At this angle of attack, a significant region of separated flow appeared on the upper surface of the wing. Figure 6 shows the streamwise velocity just above the wing surface. The separated flow region runs from about 30% of the local chord to the trailing edge starting at about 40% of the span and continuing to near the 80% span station.

Computed pressure distributions are compared with experimental data for five spanwise locations in Fig. 7. Near the fuselage and near the wing-tip the predictions compare well with experimental data. In the separated flow region the code

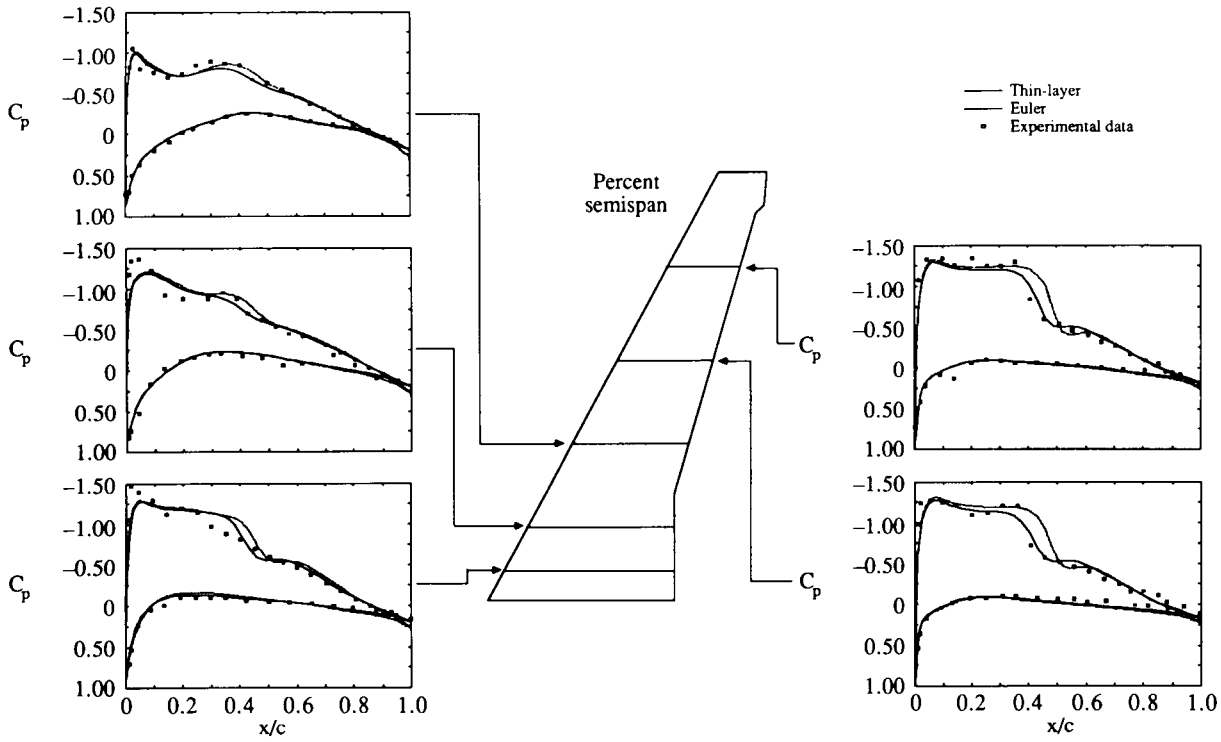

Figure 3. Comparison of Euler and thin-layer Navier-Stokes pressure distributions with experimental data for a typical transport wing-body at $M_\infty = 0.76$, $Re_c = 6.4 \times 10^6$, $\alpha = 2.0°$, $160 \times 34 \times 42$ mesh.

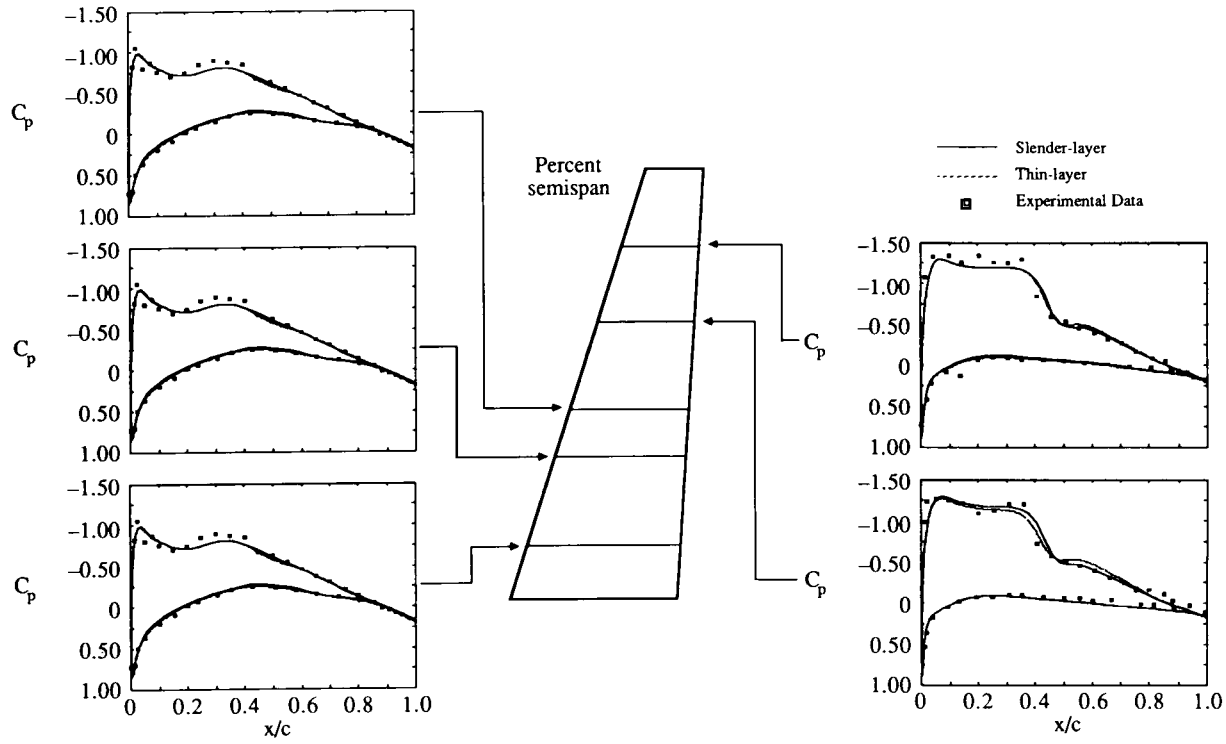

Figure 4. Comparison of slender-layer and thin-layer Navier-Stokes pressure distributions with experimental data for a typical transport wing-body at $M_\infty = 0.76$, $Re_c = 6.4 \times 10^6$, $\alpha = 2.0°$, $160 \times 34 \times 42$ mesh.

ORIGINAL PAGE
COLOR PHOTOGRAPH

ORIGINAL PAGE
COLOR PHOTOGRAPH

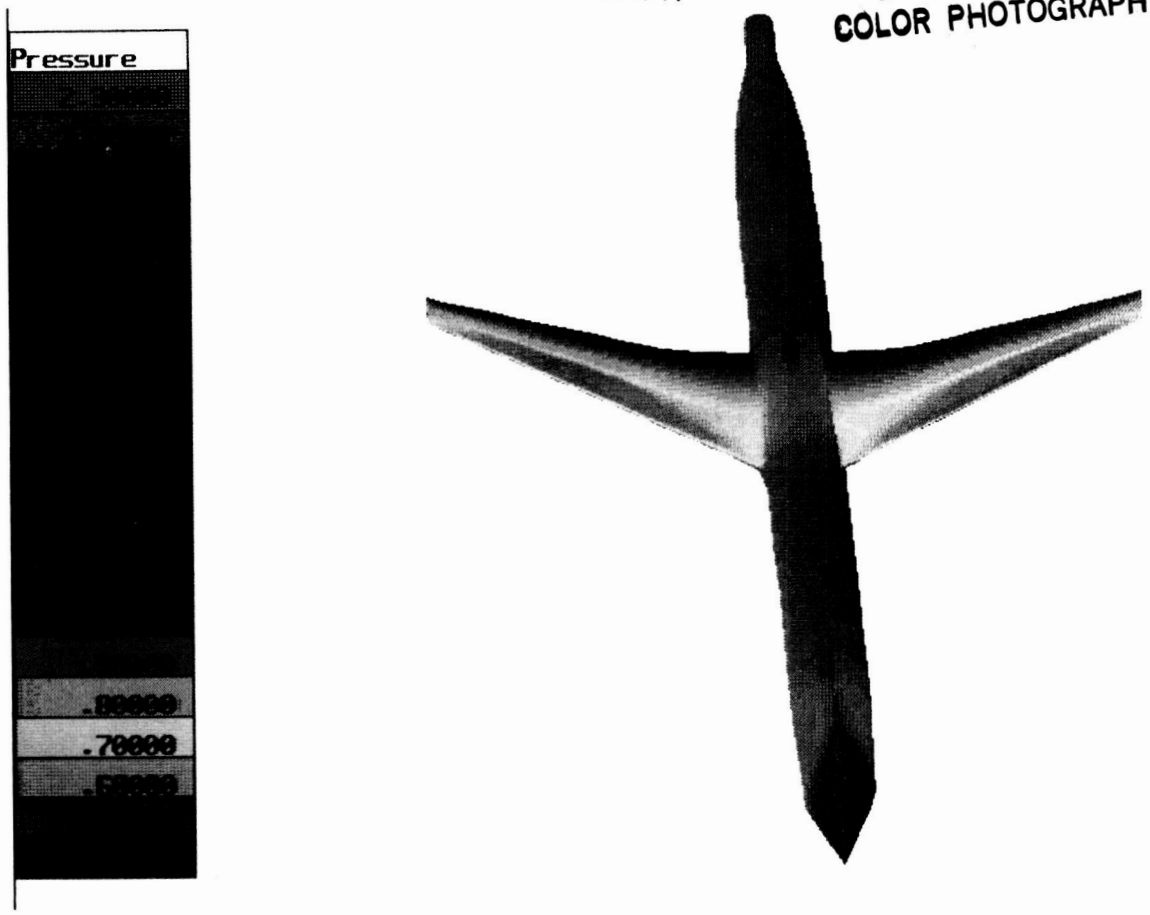

Figure 5. Pressure distribution, P/P_∞, on the upper surface of a typical transport wing-body, $M_\infty = 0.76$, $Re_c = 6.4 \times 10^6$, $\alpha = 2.0°$.

predicts the shock to be too far downstream and stronger than was found experimentally. This result is consistent with experience using the Baldwin-Lomax turbulence models for transonic airfoil calculations under separated flow conditions.

A color contour map of the wing-body upper surface pressure is shown in Fig. 8. Again the shock location is clearly defined.

<u>Fighter Wing-Body</u>: M_∞=0.90, α=4.8°, Re_c=5.4×10^6

The grid lines on the surface of a typical fighter wing-body configuration are shown in Fig. 9. The mesh was generated using the 3-D grid-generation code of Chen et al.[6] The grid has 144 cells in the chordwise direction, 34 cells normal to the wing, and 32 cells in the spanwise direction. Only the thin-layer terms near the wing have been included for this configuration so there is no grid clustering near the fuselage to accommodate viscous effects. There are 96 cells on the wing surface in the chordwise direction and 24 in the spanwise direction. The value of y^+ at the center of first cell along the wing surface ranges from 1.0 to 3.0.

Figure 10 shows the pressure distribution at five spanwise locations on the wing computed with the Euler and thin-layer Navier-Stokes codes and their comparison with experimental data. Again the viscous effects tend to weaken the wing upper surface

ORIGINAL PAGE
COLOR PHOTOGRAPH

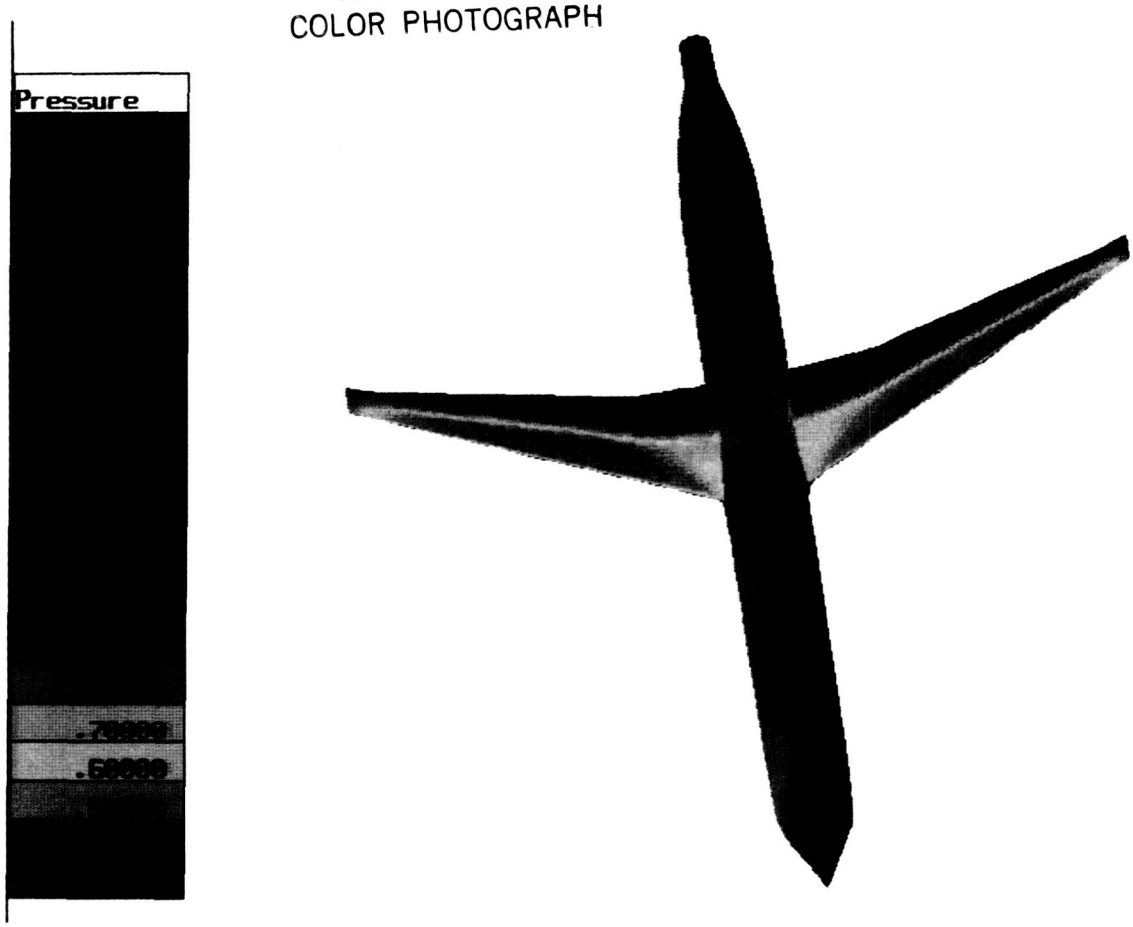

Figure 6. Velocity contours, $u/\sqrt{P_\infty/\rho_\infty}$, on the upper surface of a typical transport wing-body at $M_\infty = 0.76$, $Re_c = 6.4 \times 10^6$, and $\alpha = 4.2°$.

shocks and move them forward, although the effect is less pronounced for this configuration than for the transport wing-body discussed earlier.

Pressure contours on the upper surface of the fighter wing-body are displayed in Fig. 11.

COMPUTATION OF HELICOPTER ROTOR FLOWFIELDS IN HOVER AND FORWARD FLIGHT

An Euler/Navier-Stokes code, designated MDROTH, has been developed at McDonnell Douglas Research Laboratories for calculating the transonic flowfield of a multibladed helicopter rotor in hover and forward flight.

The code solves the three-dimensional Euler or Navier-Stokes equations in a rotating coordinate system on body-conforming curvilinear grids around the blades. The equations are recast in absolute-flow variables so that the absolute flow in the far field is uniform, but the relative flow is non-uniform. Equations are solved for the absolute-flow variables by employing Jameson's finite-volume explicit Runge-Kutta time-stepping scheme. Rotor wake effects are modeled in the form of a correction applied to the geometric angle-of-attack along the blades. This correction is

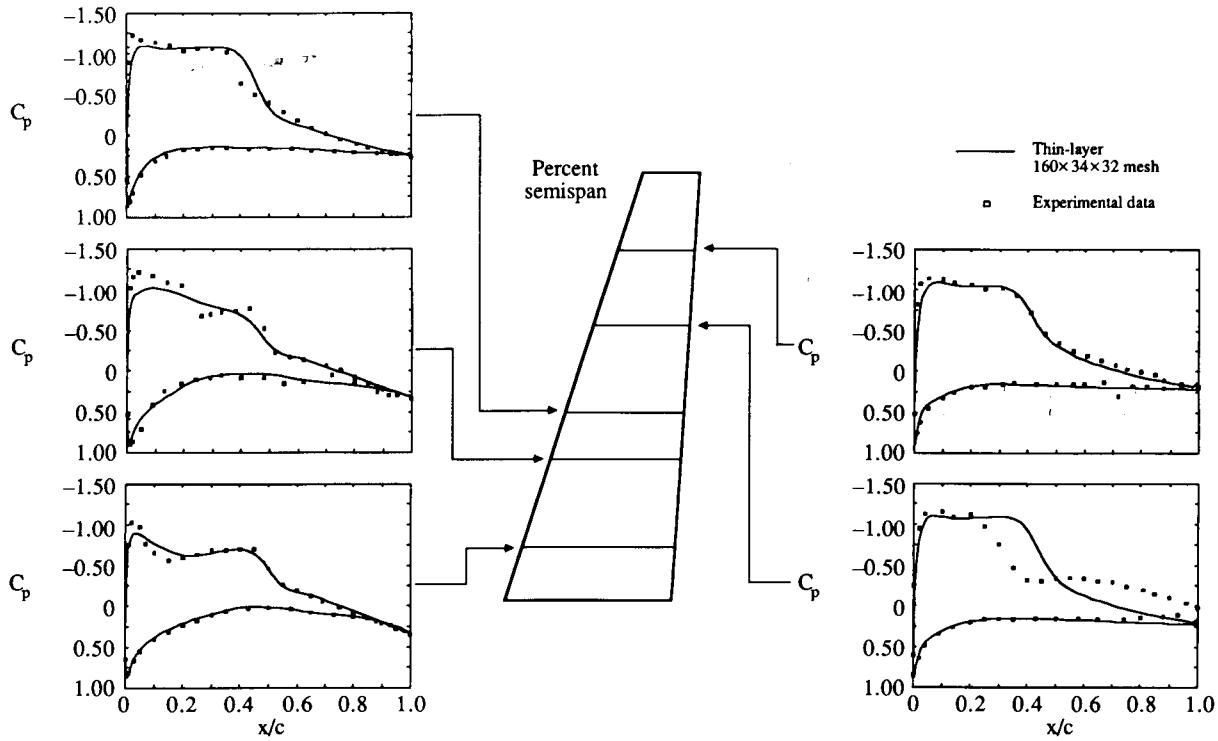

Figure 7. Comparison of thin-layer Navier-Stokes pressure distributions with experimental data for a typical transport wing-body at $M_\infty = 0.76$, $Re_c = 6.4 \times 10^6$, $\alpha = 4.2°$.

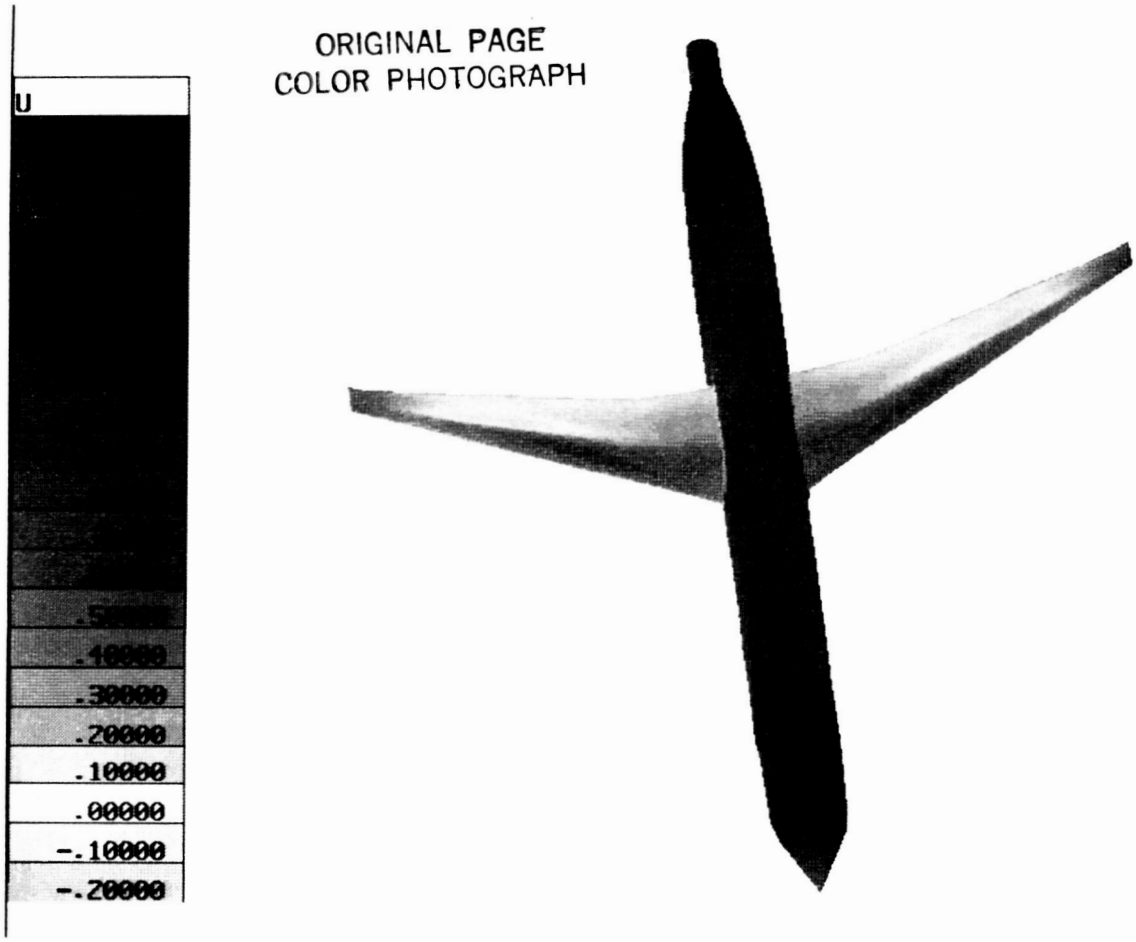

Figure 8. Pressure contours, P/P_∞, on the upper surface of a typical transport at $M_\infty = 0.76$, $Re_c = 6.4 \times 10^6$, and $\alpha = 4.2°$.

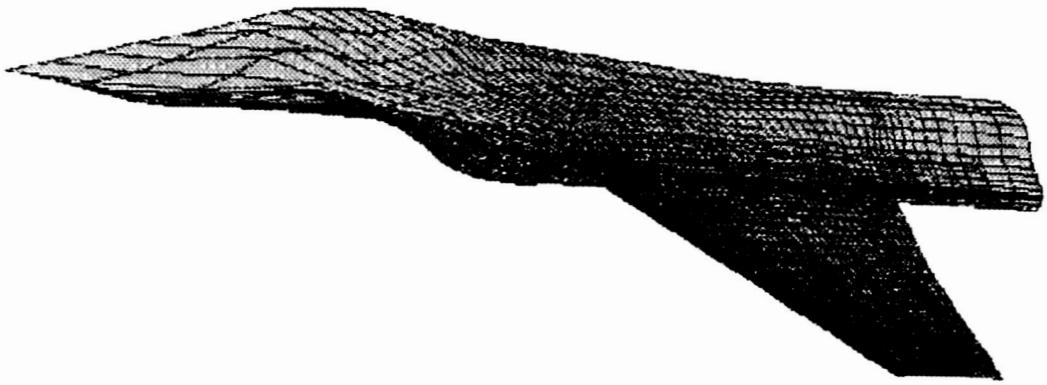

Figure 9. Typical fighter configuration with surface grid lines.

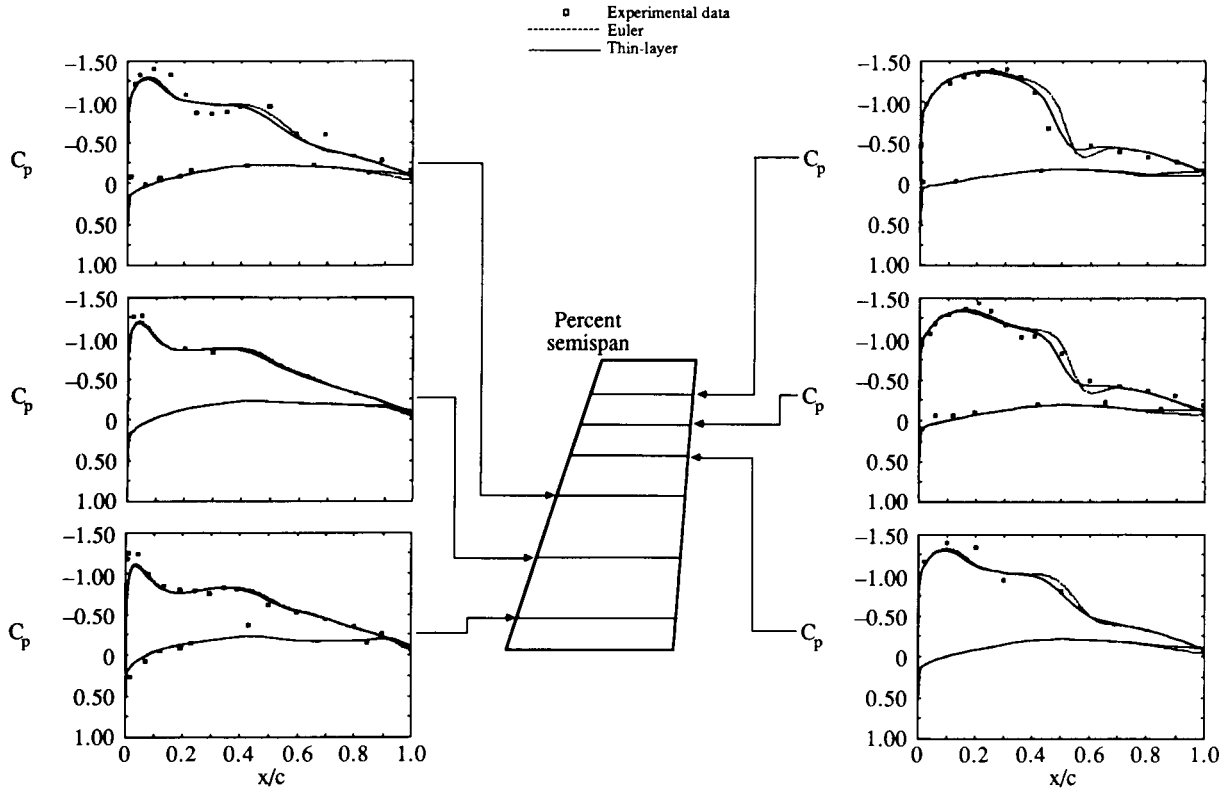

Figure 10. Comparison of Euler and thin-layer Navier-Stokes pressure distributions with experimental data for a typical fighter aircraft wing-body at $M_\infty = 0.90$, $Re_c = 5.4 \times 10^6$, $\alpha = 4.8°$, $144 \times 34 \times 32$ mesh.

ORIGINAL PAGE IS
OF POOR QUALITY

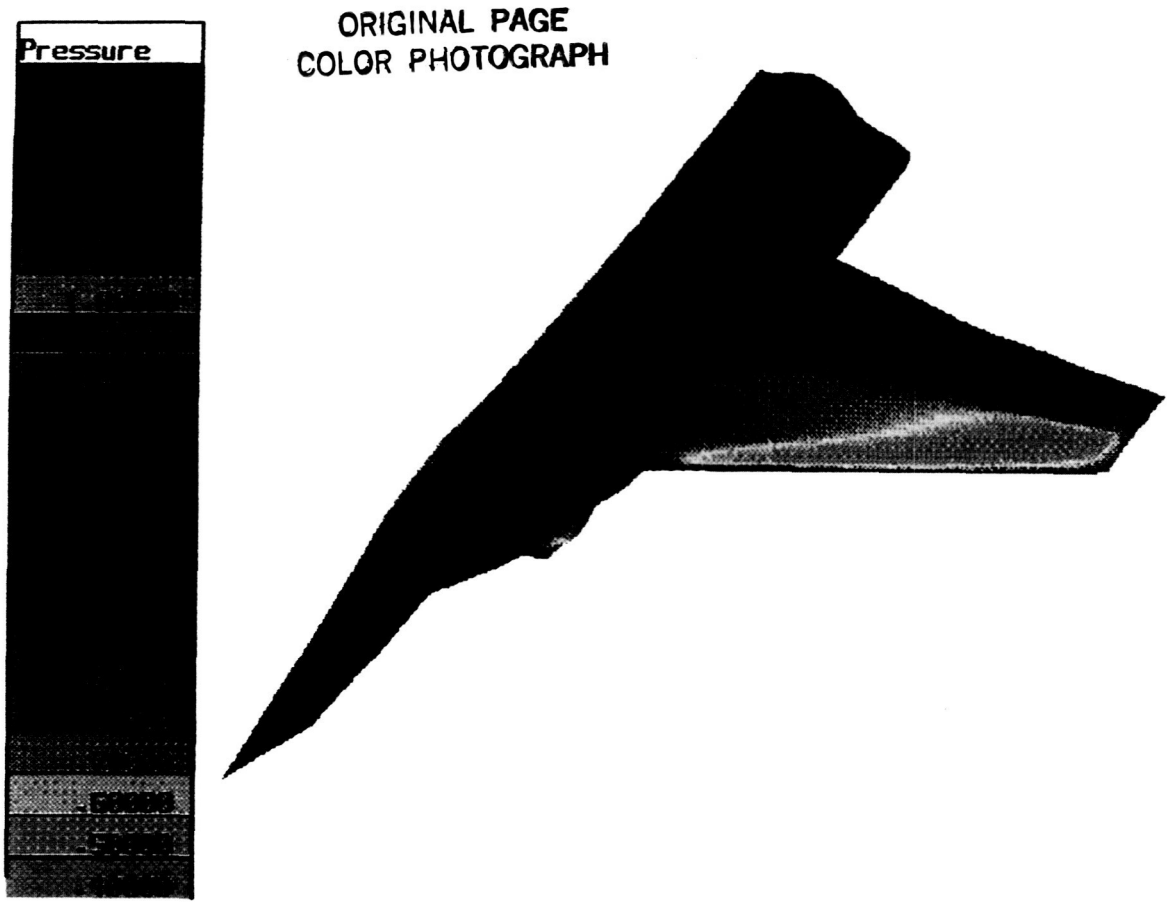

Figure 11. Pressure contours, P/P_∞, on the upper surface of a typical fighter configuration; $M_\infty = 0.9$, $Re_c = 5.4 \times 10^6$, $\alpha = 4.8°$.

obtained by computing the local induced downwash with a free-wake analysis program. The details of the methodology are described by Agarwal and Deese.[7-9]

A set of test calculations was performed by Agarwal and Deese[7-9] to verify the code for a model rotor in hover and forward flight at various collective pitch angles. The model rotor has two, untwisted, untapered blades of aspect ratio equal to six and a NACA 0012 airfoil section. Experiments on this rotor have been performed by Caradonna and Tung[10] at NASA Ames Research Center for a range of blade tip Mach numbers, M_t, and collective pitch angles, θ_c.

Like MDTSL30, the MDROTH code has been fully vectorized for optimum performance on a single-processor Cray X-MP and microtasked on a four-processor Cray X-MP/48 to reduce the wall-clock time by judicious use of Cray software techniques (Booth and Misegades[4]). The actual speedup in wall-clock time achieved by microtasking (3.73) is very close to the theoretical speedup possible (3.77), as was the case for MDTSL30.

Figure 12 shows the main features of the flowfield of a two-bladed rotor in hover, with the imbedded finite-difference grid and the coordinate system. The flowfield is characterized by transonic shocks, complex vortical wakes, and blade-vortex interactions.

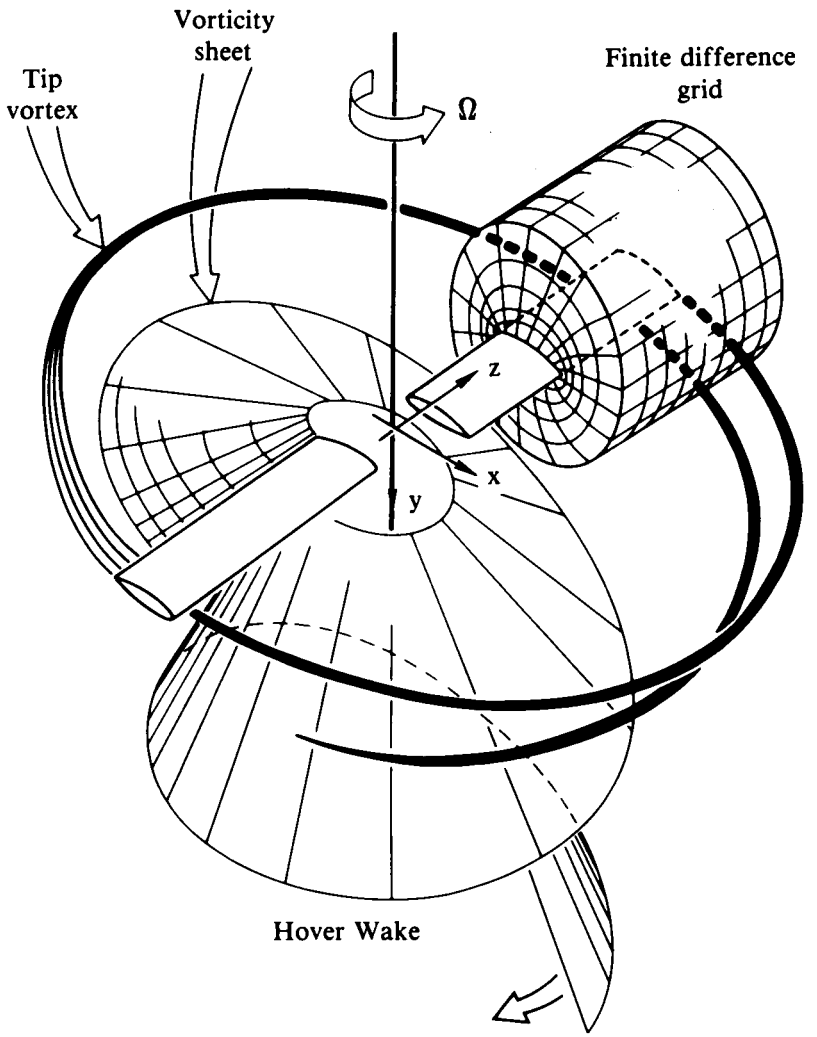

Figure 12. Schematic of a helicopter rotor flowfield in hover.

Hover Flowfield Calculations - Euler Solutions

Computations have been performed for the flowfield of a model helicopter rotor in hover. The rotor has two blades of aspect ratio equal to six which are untwisted, untapered and have the NACA 0012 airfoil section. Experiments on this rotor have been performed by Caradonna and Tung[10] for a range of blade tip Mach numbers and collective pitch angles, θ_c. Euler calculations are presented for a hovering rotor at a tip Mach number of $M_t = 0.44$ with a collective pitch angle of $\theta_c = 8.0°$ and at $M_t = 0.88$ with $\theta_c = 8.0°$.

Rotor-wake effects are modeled in the form of a correction applied to the geometric angle of attack of the blades. The free-wake analysis program HOVER of the McDonnell Douglas Helicopter Company was used to calculate the induced downwash velocity v_i at each span station. For both the cases presented here, the induced angle of attack α_i can be taken as approximately 3.8° over 95% of the span so that the effective angle of attack becomes $\alpha_e = \theta_c - \alpha_i = 4.2°$.

These computations were performed on a 98(chordwise)×33(blade-normal) ×21(spanwise) mesh. A typical computation requires two million words of main memory, and $2.1 \cdot 10^{-5}$ seconds of CPU time per mesh point for each iteration. A converged solution required approximately six minutes of CPU time on a single processor of Cray X-MP/48 using the fully vectorized version of MDROTH.

Comparisons of computed pressure distributions with experimental data (Caradonna and Tung[10]) are shown in Fig. 13 for a hovering rotor at a tip Mach number of $M_t = 0.44$ and collective pitch angle $\theta_c = 8°$, and in Fig. 14 for $M_t = 0.88$ and collective pitch angle $\theta_c = 8°$. Both cases indicate good agreement; further improvement can be achieved by refining the wake model.

Hover Flowfield Calculations - Navier-Stokes Solutions

Navier-Stokes calculations for the model helicopter rotor in hover have been performed at $M_t = 0.44$, $\theta_c = 8.0°$ and $M_t = 0.61$ and $\theta_c = 8.0°$. A 97×33×33 mesh with grid clustering near the blade surface was used to resolve the viscous layer. The effective angle of attack is 4.2° for both cases.

Figure 15 shows pressure distributions for the $M_t = 0.44$ case, while $M_t = 0.61$ results are presented in Fig. 16. Including the viscous effects had little effect on the surface pressure for those two cases. No other data are available for comparison.

Forward Flight Flowfield Calculations - Euler Solutions

Forward flight calculations have been performed for the model NACA 0012 rotor, the OLS rotor, the MDHC 500E rotor, and the AH-64 Apache rotor. All forward flight computations have been performed on a 97×33×33 mesh. A typical calculation for the full rotor cycle from ψ=0° to ψ=360° requires 12 to 16 hours of CPU time on a Cray X-MP/14; approximately 80 iterations are required for one degree movement in the azimuth direction. The code is run in time-accurate mode starting with ψ=0 and freestream conditions.

Figures 17 and 18 show a comparison of the computed pressure distributions on the model helicopter rotor in forward flight with experimental data[10] for a location near the blade tip, and

(a) tip Mach number $M_t = 0.7$, advance ratio μ=0.3, and collective rotor pitch angle θ_c=0°,

(d) tip Mach number M_t=0.8, advance ratio μ=0.2, and collective rotor pitch angle θ_c=0°, respectively.

In both cases, the computed results show good agreement with the experimental data.

Computations were performed for the OLS rotor blade at $M_t = 0.63$, $\mu = 0.30$ and a collective pitch angle $\theta_c = 0$. Results from the NASA Ames Research Center code CAMRAD were used to determine the effective angles-of-attack along the OLS rotor blade at various azimuth angles. Pressure distributions computed with the Euler code are compared with inflight data at the 95% span station as shown in Fig. 19. The calculations show good agreement with the experimental data.

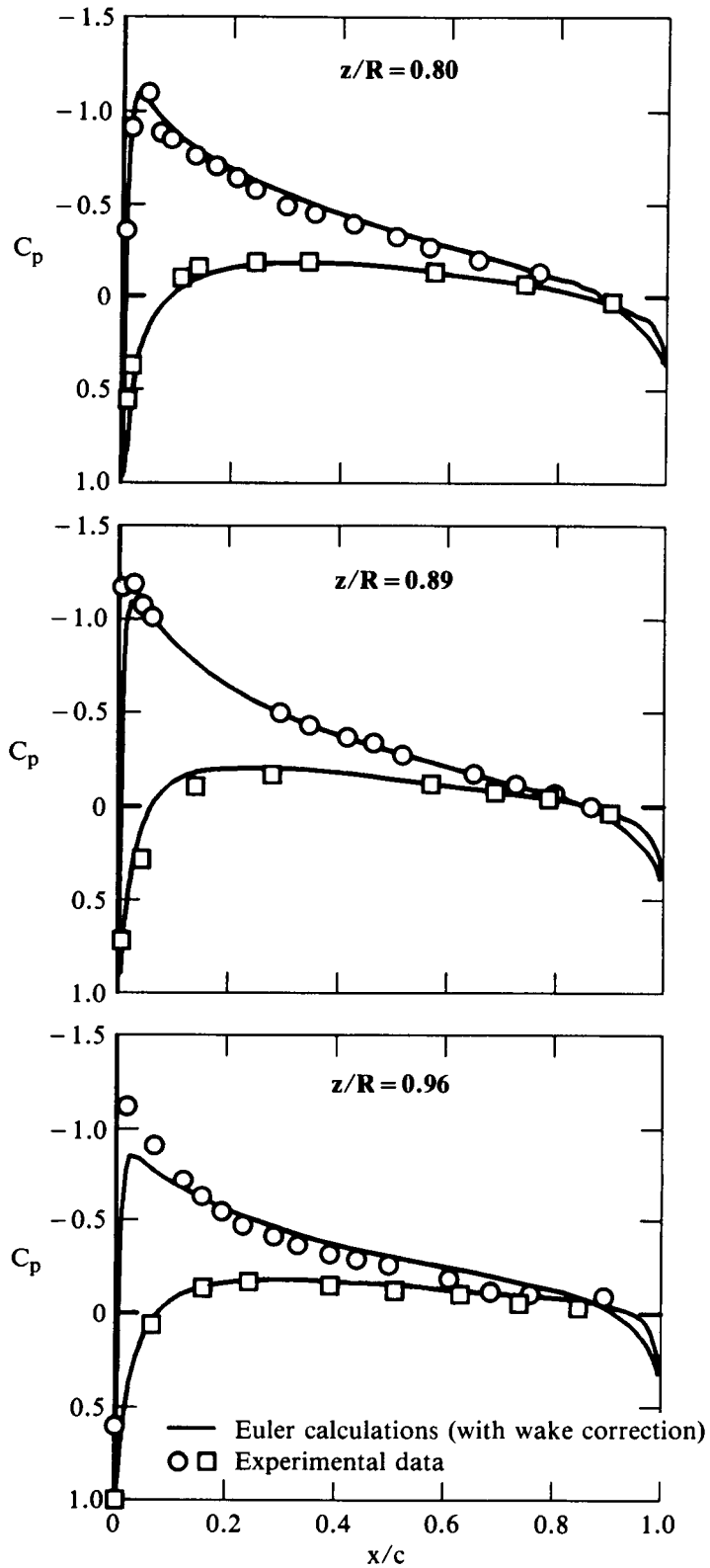

Figure 13. Surface pressure distributions on a lifting rotor in hover; $M_t = 0.4$, $\theta_c = 8°$, AR = 6, untwisted, untapered, NACA 0012 blade, 97 × 33 × 21 mesh.

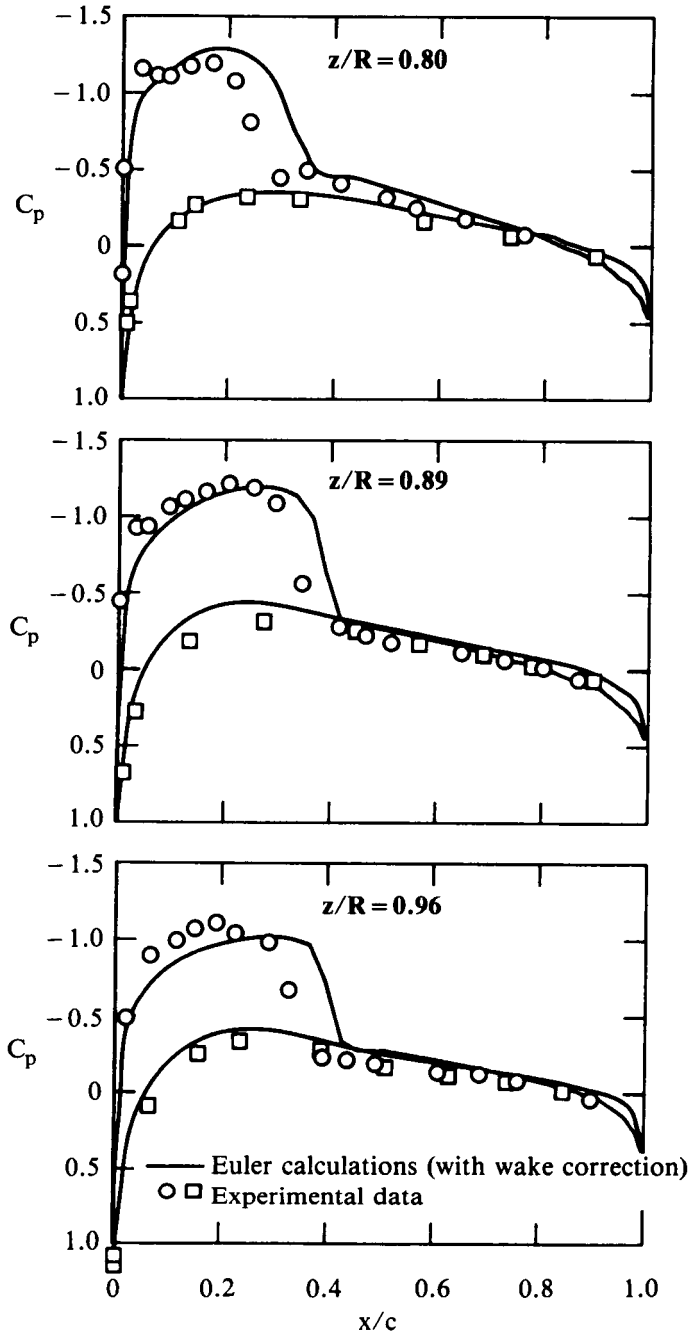

Figure 14. Surface pressure distributions on a lifting rotor in hover; $M_t = 0.88$, $\theta_c = 8°$, AR = 6.0, untwisted, untapered, NACA 0012 blade, 97 × 33 × 21 mesh.

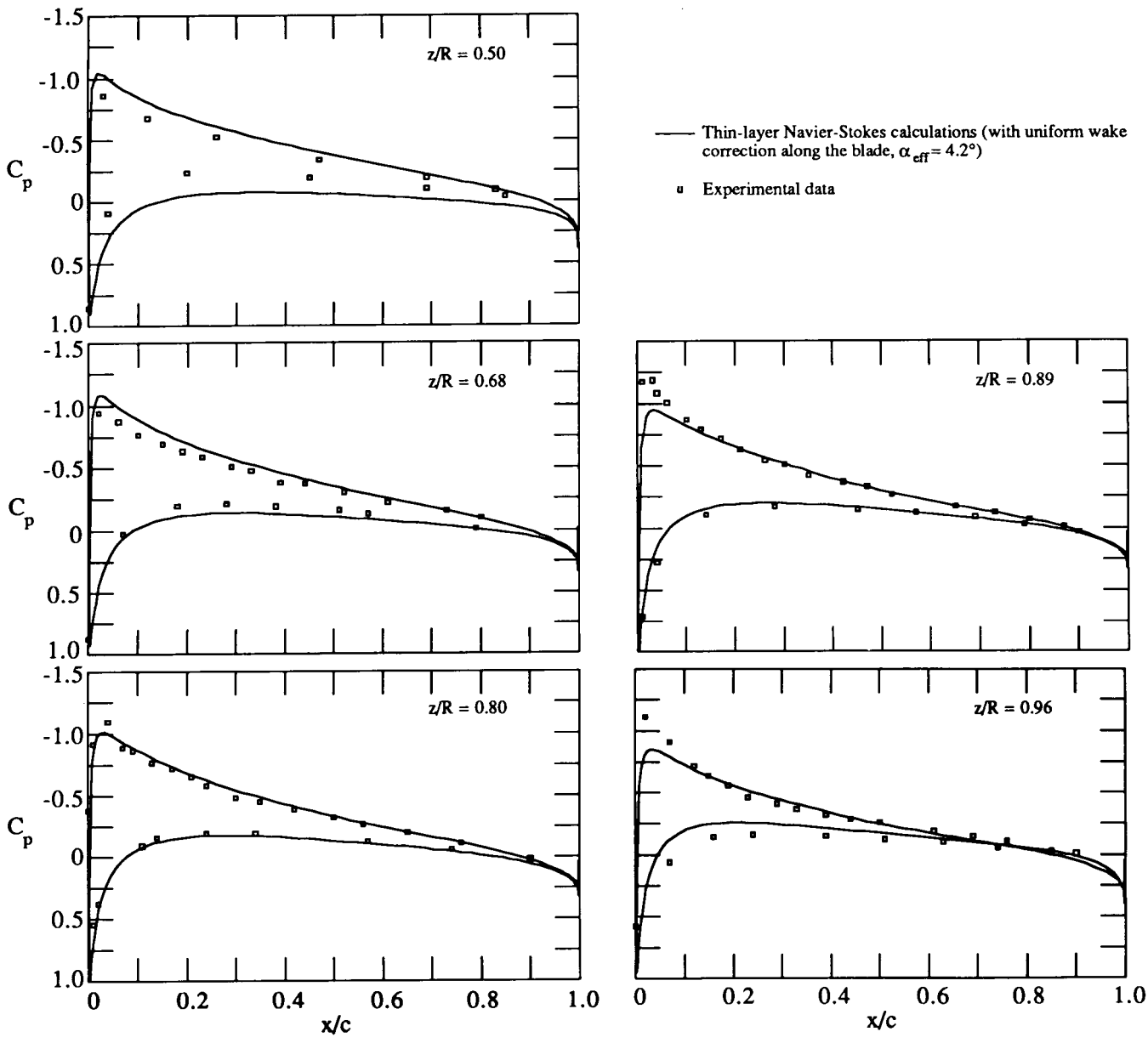

Figure 15. Surface pressure distribution on a lifting rotor in hover; $M_t = 0.44$, $Re_c = 2 \times 10^6$, $\theta_c = 8°$, AR = 6.0, untwisted, untapered, NACA-0012 blade, $97 \times 33 \times 33$ mesh.

Figure 20 shows the pressure distribution, using the Euler code, computed on the 500-E rotor blade for a location near the blade tip. The calculation was performed for M_t = 0.58, μ = 0.312, and θ_c = 0° using effective angles-of-attack given by CAMRAD. Mach number contours on the blade upper surface at various rotor angles are shown in Fig. 21. No experimental data are available for this case.

The final forward flight results to be presented are for a helicopter rotor. Calculations were performed at a tip Mach number, M_t = 0.65 and μ = 0.33. Effective angles-of-attack were determined using CAMRAD. Pressure distributions at the 95% span station are shown in Fig. 22. Mach contours on the blade upper surface are

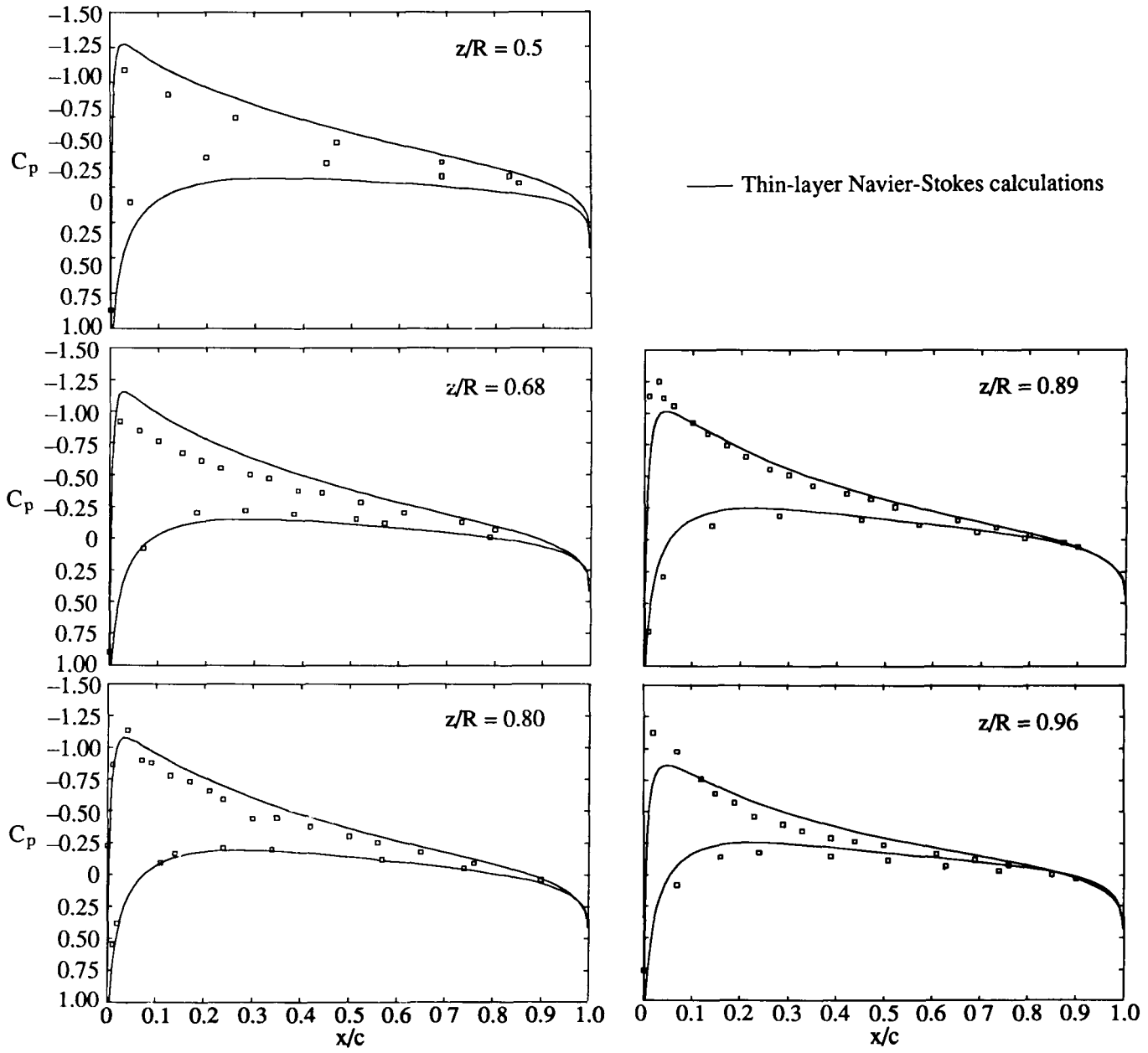

Figure 16. Surface pressure distributions on a lifting rotor in hover; $M_t = 0.612$, $Re_c = 2.67 \times 10^6$, $\theta = 8°$, AR = 6, untwisted, untapered, NACA-0012 blade, $97 \times 33 \times 33$ mesh.

displayed at various azimuth angles in Fig. 23. An expanded view of the Mach contours near the tip at ψ = 90° is shown in Fig. 24. A significant region of supersonic flow is apparent on the upper surface. Experimental data are not available for comparison.

CONCLUDING REMARKS

An extensive program to develop advanced CFD codes based on the Euler and Navier-Stokes equations is being conducted at the McDonnell Douglas Research Laboratories for applications to helicopters, transport and fighter aircraft, and

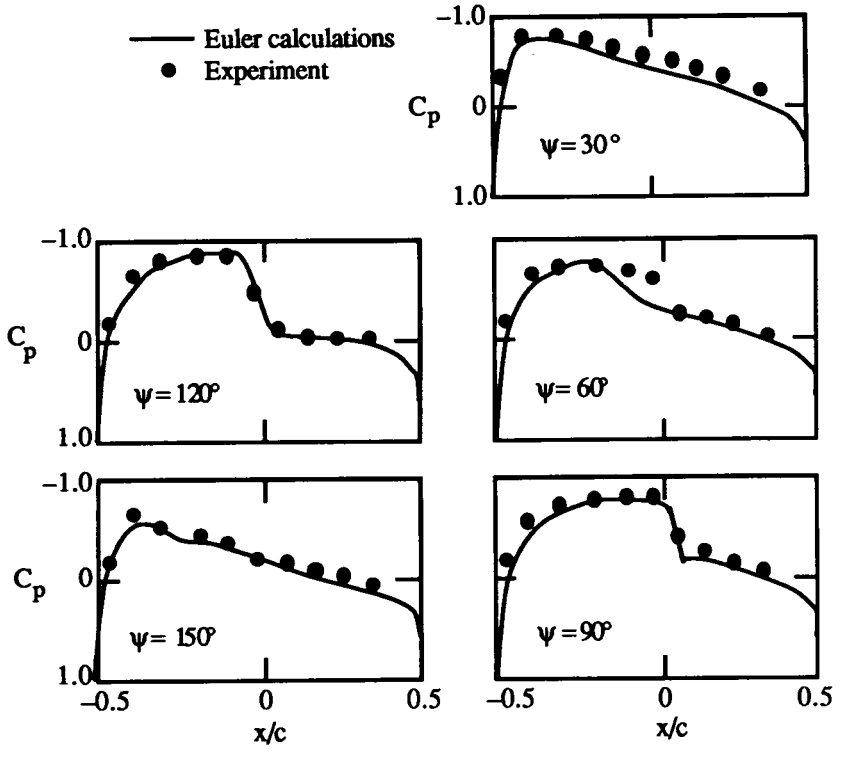

Figure 17. Pressure distribution on a model rotor-blade of NACA 0012 airfoil section and AR = 6 in forward flight; tip Mach number $M_t = 0.7$, advance ratio $\mu = 0.3$, collective pitch $\theta_c = 0$, $96 \times 32 \times 32$ mesh.

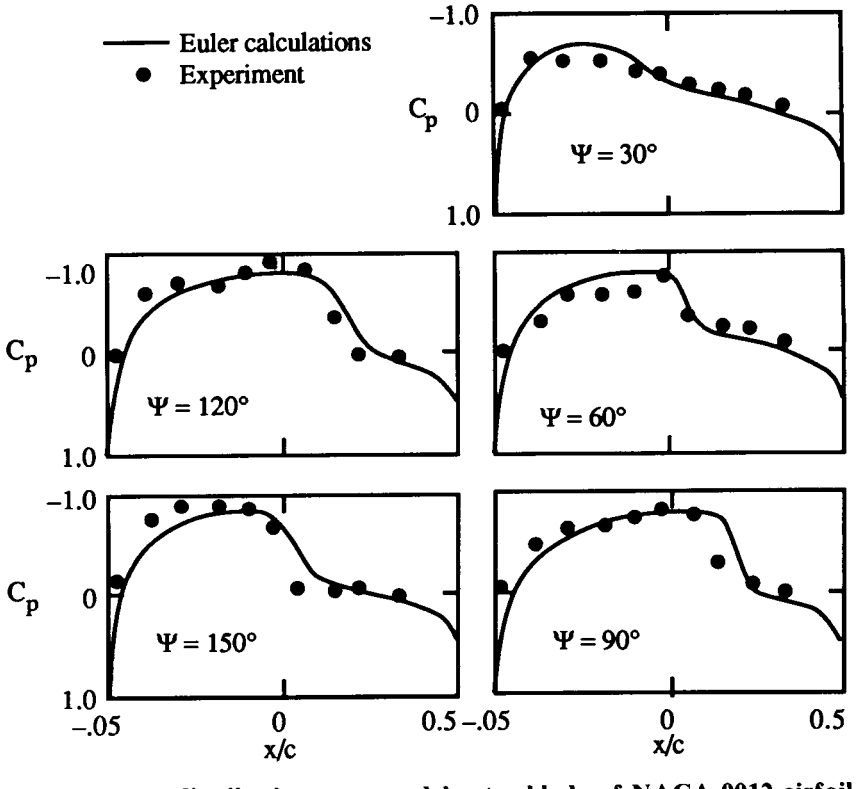

Figure 18. Pressure distribution on a model rotor-blade of NACA 0012 airfoil section and aspect ratio 6 in forward flight; tip Mach number $M_t = 0.8$, advance ratio $\mu = 0.2$, $96 \times 32 \times 32$ mesh.

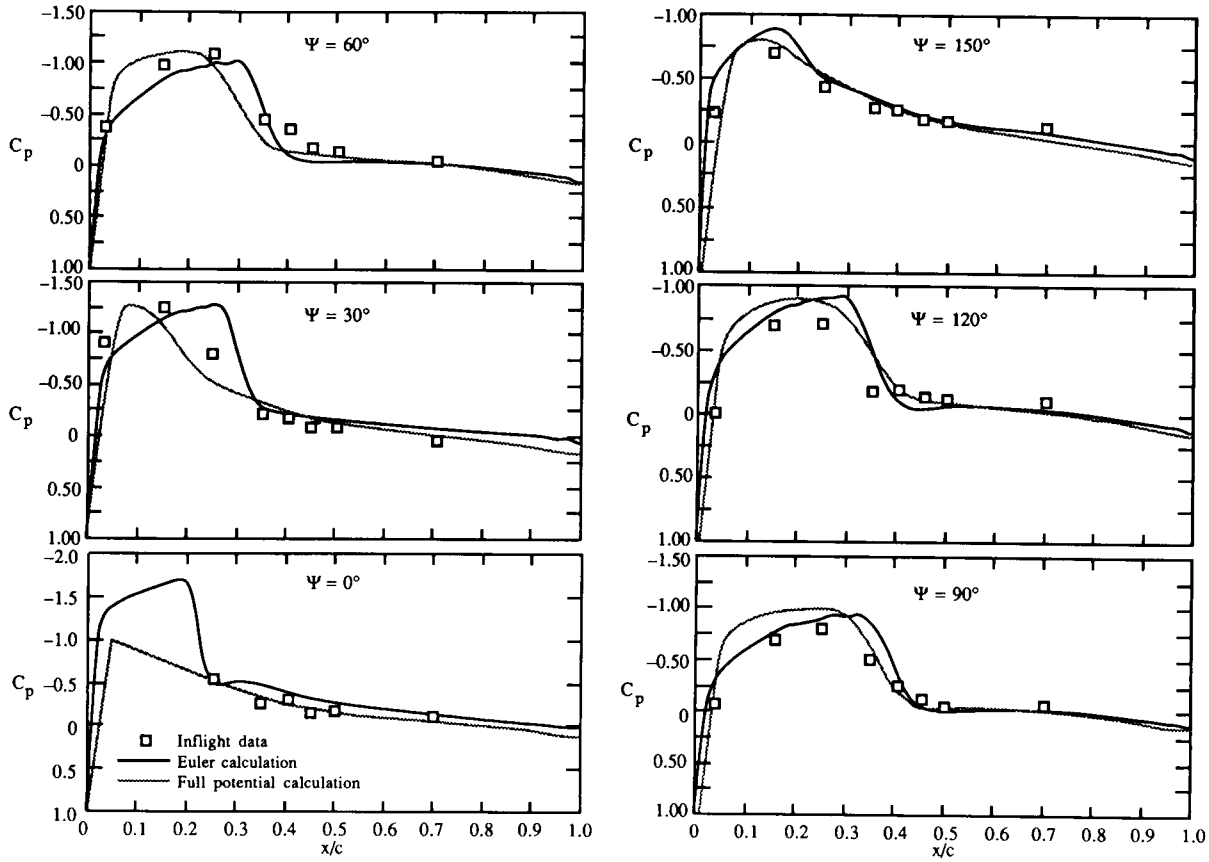

Figure 19. Pressure distribution on the upper surface of the OLS rotor-blade in forward flight at 95% span location; tip Mach number $M_t = 0.63$, advance ratio $\mu = 0.30$, collective pitch $\theta_c = 0$, $96 \times 32 \times 32$ mesh.

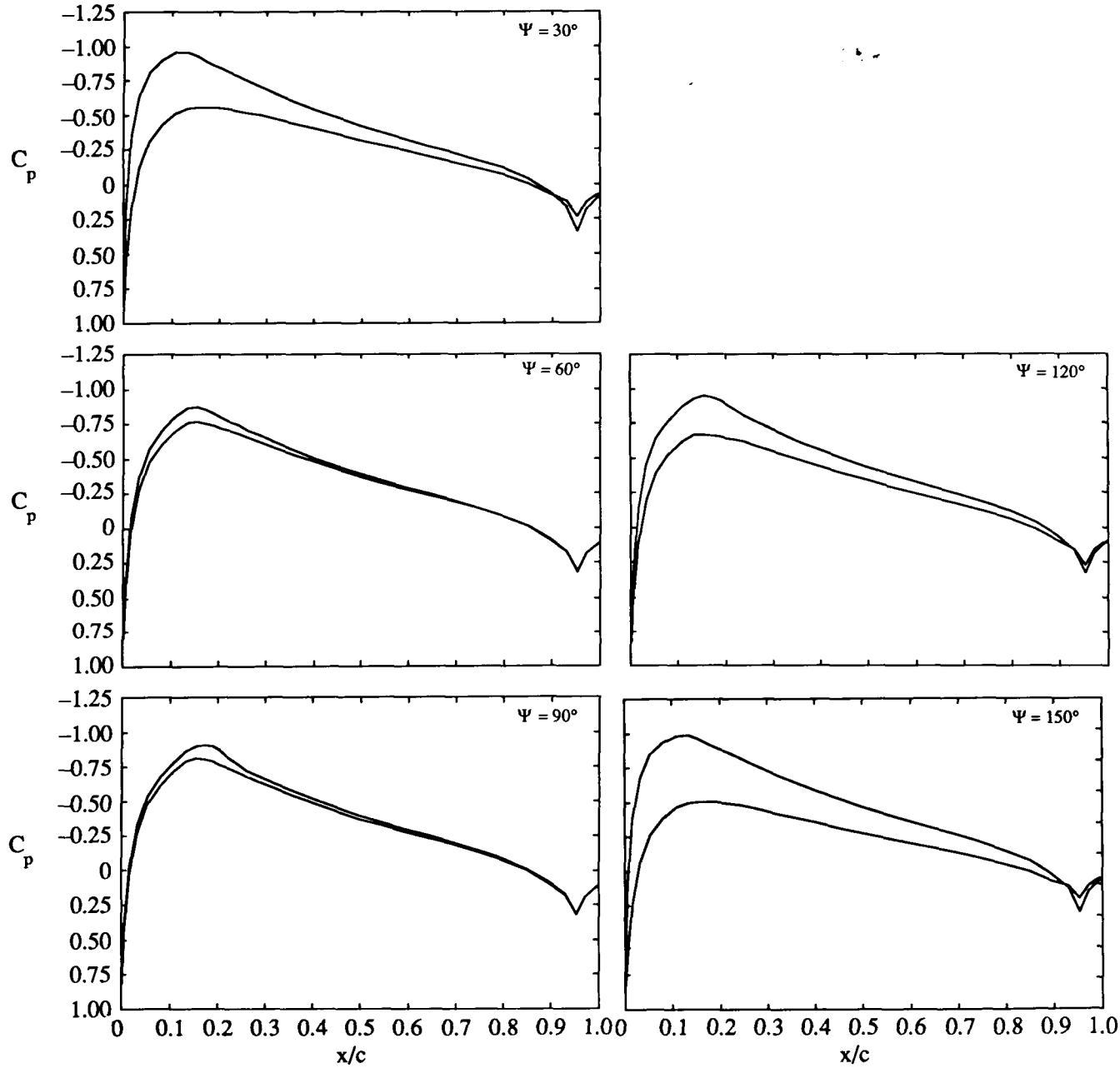

Figure 20. Computed pressure distributions on the upper and lower surface of the MDHC 500E rotor-blade in forward flight at 95% span location; $M_t = 0.58$, $\mu = 0.312$, $96 \times 32 \times 32$ cell mesh.

missiles and hypersonic vehicles. Representative calculations about a transport wing-body, a fighter wing-body, and a helicopter rotor clearly demonstrate that the state-of-the-art in CFD has progressed to the point that turbulent-flow calculations about complete fixed- and rotary-wing aircraft configurations may be achieved in the near future.

Efficient use of large computers, including multiple-processor facilities, is receiving special attention.

ORIGINAL PAGE
COLOR PHOTOGRAPH

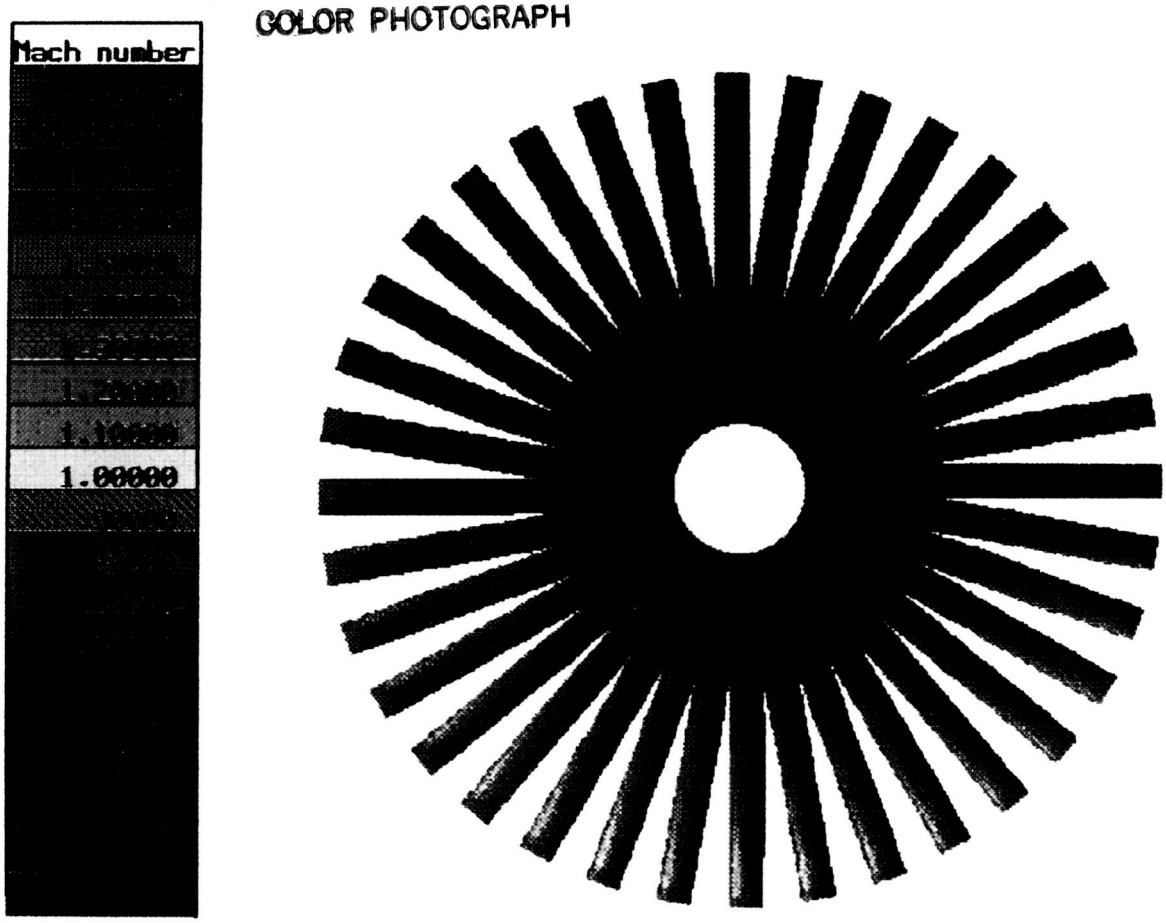

Figure 21. Mach number contours on the upper surface of the 500E rotor-blade; $M_t = 0.58$, $\mu = 0.312$.

ACKNOWLEDGMENTS

The authors would like to thank M. Uram of the McDonnell Douglas Aerospace Information Services Company for programming assistance and K. P. Misegades of Cray Research for microtasking the code for the Cray X-MP/48. The authors would also like to thank D. Pritchard and D. S. JanakiRam of McDonnell Douglas Helicopter Company and N. L. Sankar of Georgia Institute of Technology for many useful discussions and assistance in various aspects of the rotor flowfield calculations. Some calculations were performed on the Cray Research X-MP/48, others were performed on the Numerical Aerodynamic Simulator. The authors gratefully acknowledge this assistance.

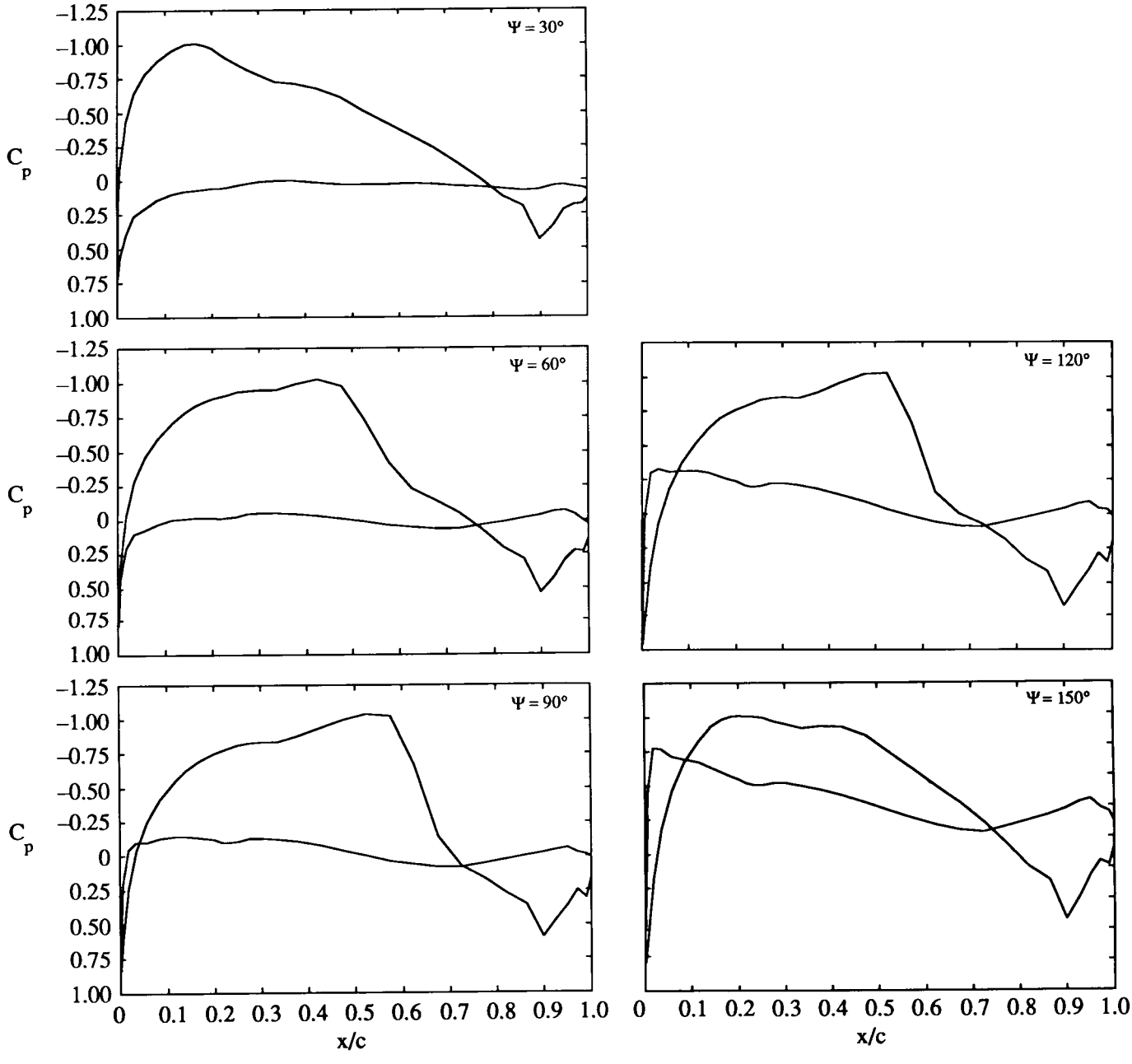

Figure 22. Computed pressure distributions on the upper and lower surface of a helicopter rotor-blade in forward flight at 95% span location; $M_t = 0.65$, $\mu = 0.33$, $96 \times 32 \times 32$ cell mesh.

ORIGINAL PAGE
COLOR PHOTOGRAPH

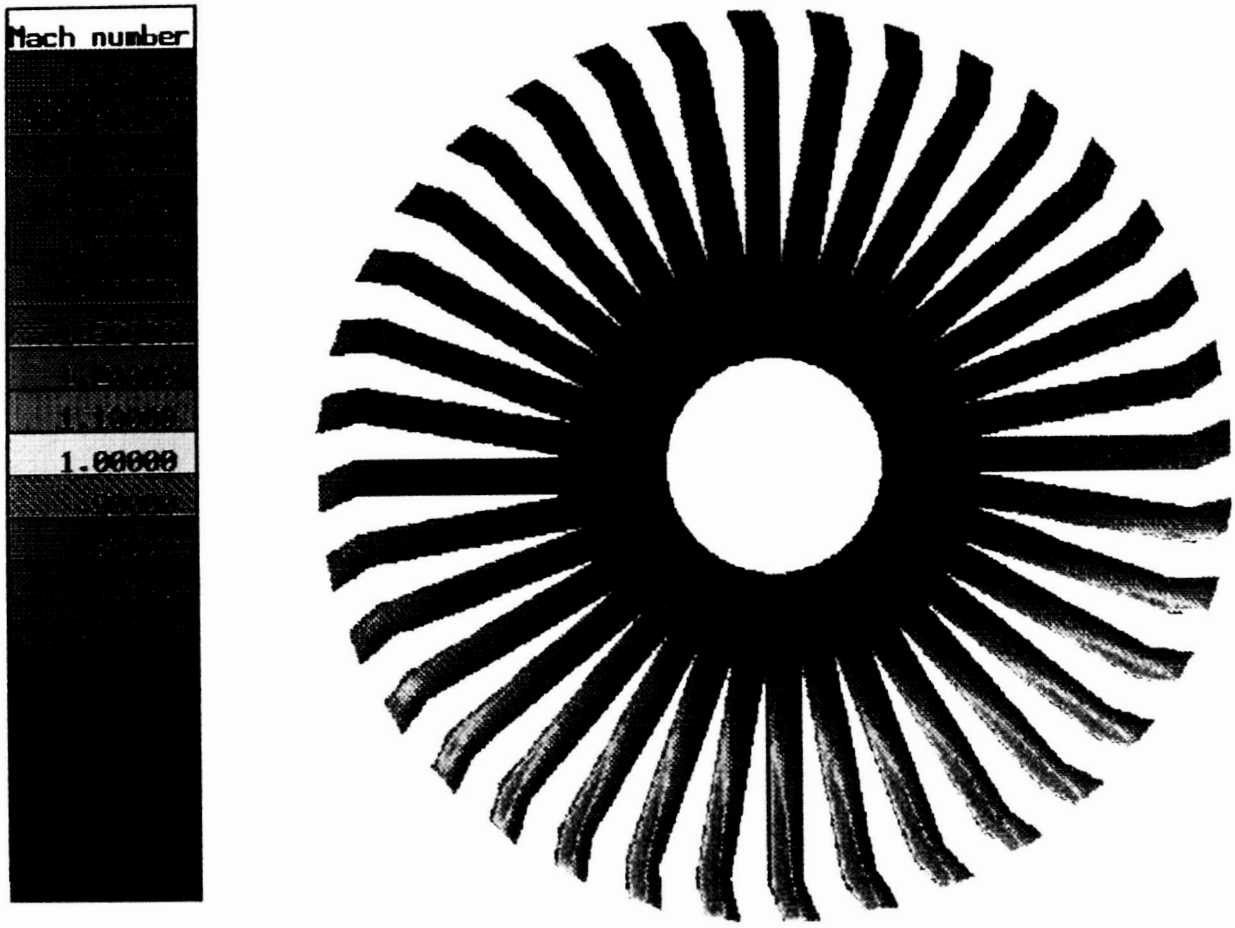

Figure 23. Mach number contours on the upper surface of a helicopter rotor-blade; $M_t = 0.65$ and $\mu = 0.33$.

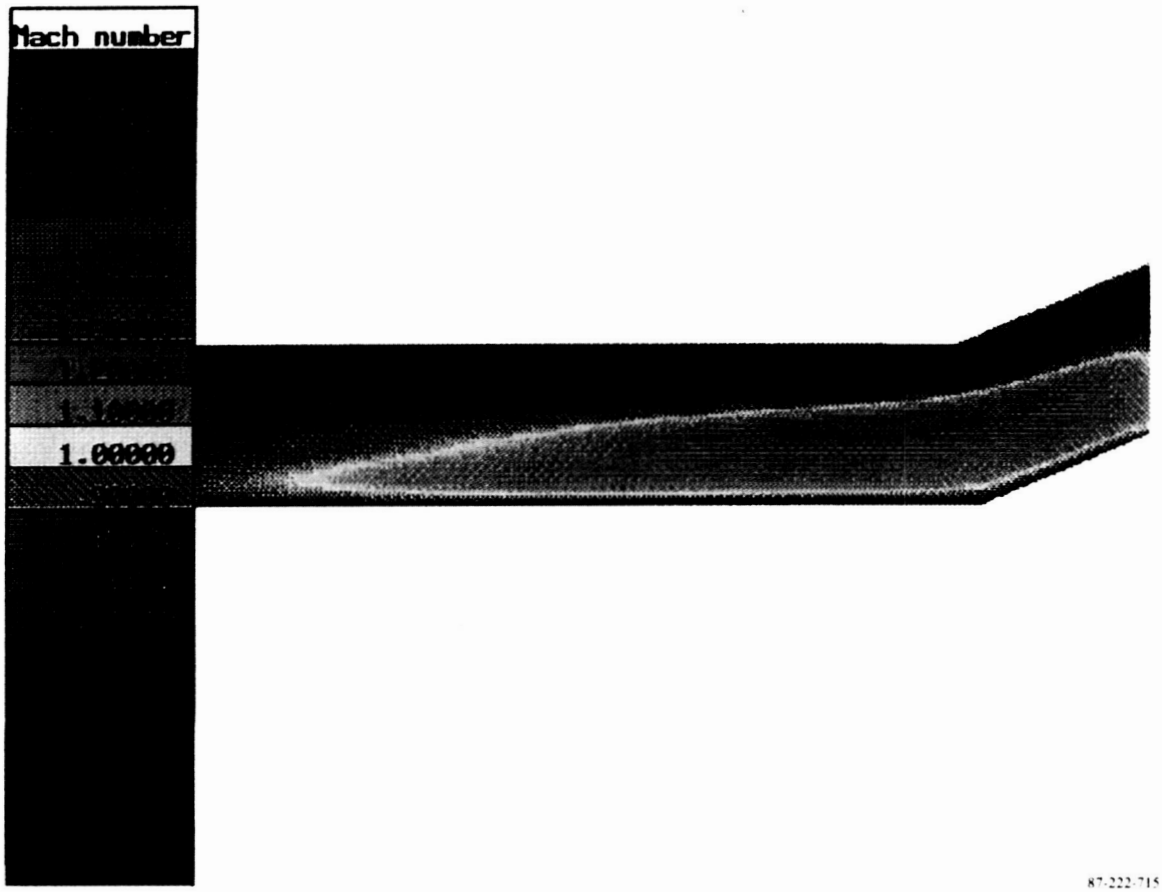

Figure 24. Mach number contours on the upper surface of a helicopter rotor-blade; $M_t = 0.65$, $\mu = 0.33$, and $\Psi = 90°$.

ORIGINAL PAGE
COLOR PHOTOGRAPH

REFERENCES

1. Deese J.E. and Agarwal R.K. (1987), Navier-Stokes Calculations of Transonic Viscous Flow About Wing-Body Configurations, AIAA paper 87-1200, AIAA 19th Fluid Dynamics, Plasma Dynamics, and Laser Conference, Honolulu, Hawaii, June 1987.

2. Agarwal R.K. and Deese J.E., and Underwood R.R. (1985), Computation of Transonic Viscous Wing-Body Flowfields Using Unsteady Parabolized Navier-Stokes Equations, AIAA paper 85-1595, AIAA 17th Fluid Dynamics, Plasma Dynamics, and Laser Conference, Cincinnati, Ohio, June 1985.

3. Agarwal R.K. and Deese J.E. (1984), Computation of Viscous Airfoil, Inlet, and Wing Flowfields, AIAA paper 84-1551, AIAA 16th Fluid Dynamics, Plasma Dynamics, and Laser Conference, Snowmass, Colorado, June 1984.

4. Booth M. and Misegades K. (1986), Microtasking: A New Way to Harness Multiprocessors, Cray Channels, vol. 8, pp. 27-29.

5. Schmitt V. and Charpin F. (1973), Pressure Distributions on the ONERA-M6 Wing at Transonic Mach Numbers, AGARD-AR-138, chapter B-1.

6. Chen L.T., Vassberg J.C., and Peavey C.C. (1984), A Transonic Wing-Body Flowfield Calculation with Improved Grid Topology and Shock-Point Operators, AIAA paper 84-2157, AIAA 16th Fluid Dynamics, Plasma Dynamics, and Laser Conference, Snowmass, Colorado, June 1984.

7. Agarwal R.K. and Deese J.E. (1987), Euler Calculations for Flowfield of a Helicopter Rotor in Hover, J. Aircraft, vol. 24, pp. 231-238.

8. Agarwal R.K. and Deese J.E. (1987), An Euler Solver for Calculating the Flowfield of a Helicopter Rotor in Hover and Forward Flight, AIAA paper 87-1427, AIAA 19th Fluid Dynamics, Plasma Dynamics, and Laser Conference, Honolulu, Hawaii, 8-10 June, 1987.

9. Agarwal, R. K. and Deese, J. E. (1988), Navier-Stokes Calculations of the Flowfield of a Helicopter Rotor in Hover, AIAA paper 88-0106, AIAA 26th Aerospace Sciences Meeting, Reno, Nevada, January 1988.

10. Caradonna F.X. and Tung C. (1981), Experimental and Analytical Studies of a Model Helicopter Rotor in Hover, Vertica, vol. 5, pp. 149-161.

N89-20949

NAVIER-STOKES AND VISCOUS-INVISCID INTERACTION

Joseph L. Steger and William R. Van Dalsem
NASA Ames Research Center, Moffett Field, Califorinia

INTRODUCTION

A symposium of this type generally attempts to collect two types of papers: papers that present new work and those that try to summarize and act as pathfinders. The latter class of paper is generally written by harried researchers who no longer have time to verify that their ideas seldom work as initially conceived. The reader can readily surmise that this paper belongs to the latter category.

The first part of this paper will simply discuss some considerations toward developing numerical procedures for simulating viscous compressible flows. Both Navier-Stokes and boundary-layer field methods are considered. For the most part, this discussion draws on our own experiences using finite difference procedures and does not pretend to cover the literature. The remaining parts of this paper will deal with two topics with which the authors are involved: 1) a simple formulation for the three-dimensional boundary-layer equations in arbitrary generalized coordinates, and 2) discussion of a technique which we have referred to as the fortified Navier-Stokes (FNS) approach. Both topics are directed towards a long-term effort to build a general purpose compressible flow solver that can optionally take advantage of approximate solution methods both to improve accuracy and efficiency. The three-dimensional boundary-layer procedure in generalized coordinates fulfills a need that we feel has not been adequately satisfied, that is, a simple boundary-layer procedure that can share grids, turbulence models, and even variables with a Navier-Stokes procedure (specifically, a boundary-layer code that does not require special assumptions such as coordinate orthogonality in any one direction). The fortified Navier-Stokes scheme is a procedure that allows approximate techniques or any known information to be incorporated into the Navier-Stokes scheme in a rather benign way. If the approximations break down, the method can still proceed as a less efficient conventional Navier-Stokes solver.

Throughout this paper the question of turbulence modeling will be avoided. Although it is generally acknowledged that current turbulence models are inadequate for complex flow field simulation, our own intuition is that other problems must be dealt with first. Too often, poor results have been blamed on turbulence models when error in specifying boundary conditions and poor grid resolution are the real culprits. Certainly the problem of turbulence modeling cannot be properly assessed until these errors are eliminated and we can routinely deal with complex three-dimensional flows.

PRECEDING PAGE BLANK NOT FILMED

BACKGROUND

Numerical algorithms for viscous flow simulation are designed with several goals in mind. The simulation must be accurate, efficient, and simple and robust so as to minimize the amount of engineering manhours time needed to obtain a solution. Because we do not have sufficient computer resources (and perhaps sufficiently well conditioned algorithms) compromises have to be made. Viscous flow simulation is often carried out using either a coupled boundary-layer inviscid-flow model or the Reynolds-averaged Navier-Stokes equations. For supersonic flow and channel flows, parabolized Navier-Stokes equations which can be marched in attached flow regions have been used as well.

Viscous-inviscid interaction schemes for airfoil analysis have been one and even two orders of magnitude faster than Navier-Stokes schemes, but they have proved to be difficult to generalize to complex three-dimensional separated flow situations and require considerable amount of engineering time to set up. Moreover, the limitations of the boundary-layer equations are not fully understood. For this reason, Navier-Stokes schemes are generally used to simulate complex flows even though they require considerably more computer work per point and usually lead to stiffer sets of equations to solve. Consequently, in viscous flow simulation using the Navier-Stokes equations the computational fluid dynamicist may spend the majority of his or her time trying to make the numerical algorithm more efficient. In viscous flow simulation using matched boundary-layer and inviscid flow equations the main task is to make the codes general enough to reproduce complex flow yet simple enough to economize on the engineering resource. Thus one approach entails making a general scheme more efficient, the other entails making an efficient scheme more general.

Navier-Stokes

The Navier-Stokes equations are considered to be adequate for most aerodynamic applications and can be used for regions with massive flow separation. Navier-Stokes algorithms that are capable of treating complex geometries use finite difference methods or related finite volume and finite element methods. Because a limited number of grid points are available, regions of massive separation are generally computed in high Reynolds number flow as rotational inviscid flow even though the viscous terms may be retained throughout. Compared to other methods of simulating strongly interacting flows, Navier-Stokes simulation is straightforward and does not require as extensive engineering 'set-up' time as viscous-inviscid interaction methods. However, Navier-Stokes schemes tend to be computer time and storage intensive. As a result, considerable effort is being expended to improve the computational efficiency of Navier-Stokes codes. This effort has, in fact, been successful to the point that algorithm improvements have been keeping pace with improvements in computer hardware. Overall computational efficiency has been improved in a number of ways including use of space varying time steps relaxation variables, use of a sequence of mesh refinements to establish approximate solutions, inclusion of various ways to reduce inversion work, improved numerical dissipation terms, more accurate difference approximations, and more implicit treatment of terms. References 1 to 21 provide one or two pointers to some of the commonly used Navier-Stokes code and descriptions of some the algorithmic changes alluded to above.

Two examples of complex three-dimensional flow simulations carried out with a Navier-Stokes scheme are shown in figures 1 to 4. Figures 1 to 3 show results for jet in a cross flow

which were extracted from reference 22, while figure 4 shows preliminary results ('oil-flow') for supersonic flow over the integrated Space Shuttle vehicle (unpublished work of Buning, Chiu, Obayashi, Rizk, and Steger of a NASA Ames Research Center Space Shuttle flow simulation group). Both results were carried out on one processor of a CRAY 2 computer, used about a quarter of a million grid points, and took from 4 to 8 hours of computer time. Although the jet in cross flow represents a simple configuration, the flow field is complex and more grid resolution (or better numerics) is needed to better resolve the flow features which are unsteady. The simulation of the integrated shuttle vehicle uses a chimera composite grid approach (ref. 23), but binding linkages, plume effects, external fuel feed lines etc. have not yet been modeled.

Viscous-Inviscid Interaction

Solution algorithms using viscous-inviscid interaction schemes are perhaps equally divided between those which use integral boundary-layer methods and those that use either finite difference or finite element methods — field boundary-layer methods. Integral boundary-layer methods are quite fast and with use of good correlation functions, they can give good accuracy. However, they require modeling of the flow physics, in addition to the turbulence model. As a result it is difficult to decide whether errors are due to turbulence modeling or the integral method modeling. The integral methods also require extensive correlation with experimental data. For these reasons we have preferred field methods over integral methods. (It has also been our experience that once the the boundary-layer and inviscid flow equations are coupled, the computer time savings accrued by using an integral boundary-layer scheme over a field scheme is minimal.)

Compared to Navier-Stokes schemes, viscous-inviscid interaction methods require significantly less computer time to simulate viscous flow with up to small regions of separation. For high Reynolds number flow, accuracy can be equal to Navier-Stokes simulation, however, depending on the problem, engineering 'set-up' time can be higher. For strong viscous interaction, current boundary-layer based schemes tend to break down, although we believe that if the boundary-layer equations can be properly interacted with the inviscid rotational flow equations, for many problems they can give high Reynolds number flow results comparable to the Navier-Stokes equations.

Viscous flow simulation using boundary-layer procedures requires special adaptations and thus has an intensive user workload. For example, if separation is encountered, the boundary-layer algorithm must be converted from the direct to the inverse mode to avoid singular behavior at the separation point. A scheme to update the inverse mode quantity, generally τ_w or δ^*, must then be provided so that the pressure predicted by the boundary-layer and inviscid schemes are consistent. In conventional viscous - inviscid interaction, the influence of the viscous layer is imposed by displacement thickness or transpiration velocity. An advantage of using either transpiration or an effective body displacement is that the inviscid flow can be computed using a grid that is relatively coarse compared to what is needed for the viscous grid. Moreover, the inviscid grid need not necessarily be body conforming in the way that a high Reynolds number Navier-Stokes grid must be. However, matching to a highly rotational inviscid outer flow is not straightforward; and, in many cases, it is necessary to account for the viscous flow curvature and the pressure gradients of the shear layers.

As an example of the inviscid-viscous interaction approach, the results of computing flow about the RAE 2822 airfoil at $M_\infty = 0.73$ and $C_l = 0.803$ are shown. Figures 5 - 7 show

comparisons of the C_p, C_f, and δ^* distributions found experimentally (ref. 24), those computed by the interaction method (ref. 25), and those computed by Mehta (ref. 26) using a Navier-Stokes code. Mehta performed his computations at $\alpha = 2.79°$ (and computed a $C_l = 0.793$); the present computations were performed at $\alpha = 2.81°$ to match the measured $C_l = 0.803$. The present results are in good agreement with both the Navier-Stokes and experimental results. These simulations were obtained on 223x31 inviscid and 223x50 viscous grids using a quite fast transonic full potential code (ref. 27) and equally fast boundary-layer finite difference code (ref. 28). The calculations were carried out in 1984 and for the cases presented, the required Cray-XMP CPU time was 7 to 15 sec, and on the average, 0.0006 sec/grid point were required to obtain a converged solution. In contrast, our most efficient thin-layer Navier-Stokes code at that time (ref. 7) required about 0.03 to 0.06 sec/grid point to obtain a converged solution.

Zonal Equation Methods

The traditional choice in viscous flow simulation is between either a viscous-inviscid interaction approach using simplified equations or a Navier-Stokes scheme used throughout the field. In practise, however, various kinds of zonal methods are often used. A zonal equation method generally entails regional use of simplified methods with a Navier-Stokes scheme so as to speed up iterative convergence, reduce computational work, or even improve the numerical accuracy of the Navier-Stokes simulations. Simple zonal ideas are almost always used in high Reynolds number flow Navier-Stokes simulations. For example, for high Reynolds number flow, the Navier-Stokes equations revert to Euler equations in any region in which sufficient grid resolution is not provided, so an obvious zonal scheme is to neglect viscous terms in these regions. Special treatment at wall boundaries using 'wall functions' (ref. 29) have also been employed.

In a zonal approach the simplified equations must be able to readily share variables and mesh points with the global scheme. Otherwise, sometimes awkward conversions of variables or messy interpolations between equation sets are required.

One kind of zonal approach is to simply embed Navier-Stokes equations in complex (usually separated or highly vortical) regions of the flow and use simplified equations elsewhere. This requires some care in establishing zones, and the zonal interfacing can be tedious. Alternately a zonal approach can use a global Navier-Stokes and Euler formulation throughout, but use simplified equations embedded into the global scheme to reduce computational work or improve accuracy. The subtle difference between this zonal approach and the former (which is perhaps chiefly observed in the coding) is that, if the approximation behind the simplified equation is no longer valid, simulation can still proceed with the more general scheme. The fortified Navier-Stokes scheme (to be highlighted in a latter Section) and related embedding schemes which use vorticity, potential, and other like forms of the equations (refs. 30-32) are pronounced examples of the latter kind of zonal scheme. An advantage of a general zonal approach is that it is possible to directly compare the effects of using the simplified equation set to the general equation set and thus learn the limitations of the approximation. As experience is gained, it is then likely that the simplified equation sets will be able to assume more of the computational work.

GENERALIZED BOUNDARY-LAYER EQUATIONS

The boundary-layer equations are restricted to high Reynolds number flow and require the use of a body conforming coordinate system. In developing the usual boundary-layer equations, both the independent variables and the dependent velocity variables are transformed to the new body conforming coordinates. For body surfaces with little curvature, the boundary-layer equations cast in terms of the new dependent variables essentially simplify back to a flat plate or Cartesian-like form of the equations along a developed surface. If the body has appreciable curvature, however, the equations require additional terms and can be difficult to solve numerically. They are particularly more complex if a nonorthogonal coordinate system is used, yet for many applications it is difficult to generate an orthogonal coordinate system along the body surface.

The thin-layer Navier-Stokes equations use body conforming coordinates and only viscous terms in the normal-like direction are retained. With the pressure specified in the viscous layer, the momentum equations of the thin-layer Navier-Stokes equations are readily solved for the original Cartesian velocity components provided only the independent variables are transformed to body coordinates. This is because with pressure specified, the thin-layer momentum equations are essentially equivalent to an uncoupled set of scalar convection-diffusion equations. Moreover, the boundary-layer approximation of specifying the pressure in the viscous layer is equivalent to solving a linear combination of the thin-layer momentum equations – the combination needed to transform the Cartesian velocity components u, v, and w into an equivalent normal-like velocity (see ref. 33). Consequently, although three thin-layer momentum equations in transformed independent variables are readily solved for u, v, and w, for pressure prescribed in the viscous layer only two linear combinations of the u, v, and w velocity components should be retained – the combination that is equivalent to the velocities along the body surface coordinates. Thus equivalent boundary-layer equations can be formulated from the thin-layer equations for pressure specified in the viscous layer; and, because only the independent variables are transformed, complex coordinate source terms can be avoided. Moreover, this alternate form of the boundary-layer equations does not require that any of the coordinates be orthogonal, and software (grids, boundary condition routines, etc.) developed for many Navier-Stokes schemes can be readily utilized.

Governing Equations

A form of the boundary-layer equations for general curvilinear coordinates $\xi = \xi(x, y, z)$, $\eta = \eta(x, y, z)$, and $\zeta = \zeta(x, y, z)$ is given by reference 33 (with η chosen away from the surface):

η Momentum

$$\begin{aligned}\nabla\eta \cdot (\nabla\xi p_\xi + \nabla\eta p_\eta + \nabla\zeta p_\zeta) = &\rho U(u\partial_\xi\bar{\eta}_x + v\partial_\xi\bar{\eta}_y + w\partial_\xi\bar{\eta}_z) \\ &+ \rho V(u\partial_\eta\bar{\eta}_x + v\partial_\eta\bar{\eta}_y + w\partial_\eta\bar{\eta}_z) \\ &+ \rho W(u\partial_\zeta\bar{\eta}_x + v\partial_\zeta\bar{\eta}_y + w\partial_\zeta\bar{\eta}_z)\end{aligned} \tag{1a}$$

or for very dominant $\nabla\eta \cdot \nabla\eta$

$$p_\eta = 0 \tag{1b}$$

ξ and ζ Momentum

Predict values of $\vec{q} = (u, v, w)^t$ from

$$\rho u_t + \rho U u_\xi + \rho V u_\eta + \rho W u_\zeta + (\xi_x p_\xi + \eta_x p_\eta + \zeta_x p_\zeta) = J\partial_\eta[J^{-1}(\mu m_1 u_\eta + (\mu/3) m_2 \eta_x)] \quad (2a)$$

$$\rho v_t + \rho U v_\xi + \rho V v_\eta + \rho W v_\zeta + (\xi_y p_\xi + \eta_y p_\eta + \zeta_y p_\zeta) = J\partial_\eta[J^{-1}(\mu m_1 v_\eta + (\mu/3) m_2 \eta_y)] \quad (2b)$$

$$\rho w_t + \rho U w_\xi + \rho V w_\eta + \rho W w_\zeta + (\xi_z p_\xi + \eta_z p_\eta + \zeta_z p_\zeta) = J\partial_\eta[J^{-1}(\mu m_1 w_\eta + (\mu/3) m_2 \eta_z)] \quad (2c)$$

and retain the two linear combinations

$$U = \nabla\xi \cdot \vec{q}$$

$$W = \nabla\zeta \cdot \vec{q}$$

Energy

$$\rho H_t + \rho u H_\xi + \rho v H_\eta + \rho w H_\zeta - p_t = J\partial_\eta[J^{-1}(\mu m_1 m_3 + (\mu/3) m_2(\eta_x u + \eta_y v + \eta_z w))] \quad (3)$$

where

$$m_1 = \eta_x^2 + \eta_y^2 + \eta_z^2$$

$$m_2 = \eta_x u_\eta + \eta_y v_\eta + \eta_z w_\eta$$

$$m_3 = [(u^2 + v^2 + w^2)_\eta]/2 + Pr^{-1}(\gamma - 1)^{-1}(a^2)_\eta$$

Constitutive

$$\frac{\rho}{\rho_\infty} = \frac{pT_\infty}{p_\infty T} \quad (4a)$$

where

$$\frac{T}{T_\infty} = \frac{(\gamma - 1)}{a_\infty^2}[H - \frac{(u^2 + v^2 + w^2)}{2}] \quad (4b)$$

Continuity

$$(J^{-1}\rho)_\tau + (J^{-1}\rho U)_\xi + (J^{-1}\rho V)_\eta + (J^{-1}\rho W)_\zeta = 0 \quad (5)$$

Throughout ρ, p, and T denote fluid density, pressure, and temperature, u, v, w are Cartesian velocity components referenced to an inertia system, H is the stagnation enthalpy, a is the sound speed, and μ is the viscosity coefficient. The transform Jacobian is given by $J = |\frac{\partial(\xi,\eta,\zeta)}{\partial(x,y,z)}|$, and

the overbar on η_x, η_y, and η_z denotes scaling, $\overline{\eta}_x = \eta_x/\sqrt{\eta_x^2+\eta_y^2+\eta_z^2}$ etc. The operator $\vec{\nabla}$ denotes the vector gradient so that $\vec{\nabla}\eta \cdot \vec{q} = \eta_x u + \eta_y v + \eta_z w = V$, and V is the vertical contravariant velocity.

The six equations (η momentum (1); two linear combinations of (2a), (2b), and (2c) to form U and W; energy (3); state (4a); and continuity (5)) can be used to determine the six variables p, U, W, H, ρ, V. The Cartesian velocity components are then obtained from

$$\begin{pmatrix} u \\ v \\ w \end{pmatrix} = \begin{bmatrix} x_\xi & x_\eta & x_\zeta \\ y_\xi & y_\eta & y_\zeta \\ z_\xi & z_\eta & z_\zeta \end{bmatrix} \begin{pmatrix} U \\ V \\ W \end{pmatrix} \tag{6}$$

Numerical Scheme

This formulation has been applied to steady state problems using the time-like boundary-layer scheme reported by Van Dalsem and Steger in reference 34. For a prescribed edge pressure, the equations are solved iteratively from an assumed initial state in the following way with $p_\eta = 0$. Using central spatial differencing in η and upwind differencing in ξ and ζ, equations (2) to (3) are used to update u, v, w, and H. As pressure was already obtained using one linear combination of the momentum equations, only two linear combinations of the momentum equations can be used to determine the velocities. Thus, U and W are formed from u, v, and w. The equation of state, (4a), is used to update ρ, with T defined from equation (4b). The third linear combination of u, v, w is obtained by solving continuity for V using already updated U, W, and ρ. The continuity equation has central space differencing in ξ and ζ, and trapezoidal differencing in η so that V is obtained by marching outwards from the body surface. The final updated form of the Cartesian velocity components is then obtained from updated U, V, W using equation (6). This process is then repeated until convergence.

The boundary-layer equations are solved with either specified initial data profiles or the stagnation region can be captured with the upwind differencing as part of the iteration process. At the outer edge in η, variables can be specified if known, or, for specified edge pressure, the edge variables can be computed as part of the boundary-layer method. In this case the $\rho V \partial_\eta$ terms in momentum and energy are backward differenced away from the edge if $V > 0$, or dropped if $V < 0$. Likewise the viscous terms must be dropped at just the outer edge point. Periodic, symmetry, or outflow conditions are used at all other ξ and ζ boundaries at which initial data are not specified.

Numerical Results

Boundary-layer calculations to verify this formulation have been carried out on a 6 : 1 prolate spheroid at 10° and 30° angle of attack and at two different Reynolds numbers, 7.7×10^6 and 43×10^6 based on diameter. The geometry and a top view of the computed limiting streamlines for the 30° angle of attack case are shown in figure 8. Streamwise separation was avoided by confining the boundary-layer calculation from $x/L = 0.02$ to $x/L = 0.8$ where x is the axial distance and L is the body length. The initial profiles in ξ, edge conditions, turbulent eddy viscosity values, and even the grid itself were taken from the Navier-Stokes calculations described in reference 35. Throughout, the simplified η momentum equation, $p_\eta = 0$, was used.

As reported in references 33 and 35, good agreement between the boundary-layer method, the Navier-Stokes calculation and even experiment is obtained for attached flow regions. For latter reference, a boundary-layer computed profile at $x/L = 0.65$ and $\phi = 120°$ ($\phi = 0°$ is the windward plane of symmetry) is shown in figure 9 along with the computed thin-layer Navier-Stokes result.

Calculations were also carried out for the 10° case in which the boundary-layer code was run from $x/L = 0.8$ to $x/L = 1.1$ – the latter x/L location is back on the supporting sting which was modeled in the Navier-Stokes simulation. In this region streamwise separation occurs. As shown by the separated profile at $x/L = 0.96$and $\phi = 120°$, figure 10, the boundary-layer equations solved in the direct mode break down very rapidly unless the outer 'edge' is taken very close to the wall. To prevent breakdown the constant height edge had to be taken so sufficiently close that for this profile the flow is not just rotational but still fully viscous. Breakdown of the boundary-layer equations in direct mode (i.e. pressure specified) is not surprising. Of interest, though, is that the boundary-layer equations do give good results in the direct mode provided that good outer edge values (not irrotational values) are given sufficiently close to the wall.

FORTIFIED NAVIER-STOKES

In a typical high-Reynolds number Navier-Stokes simulation the fine-grid resolution is generally provided in a thin zone near the body surface, and the outer flow is effectively resolved as rotational inviscid flow (unless the turbulent coefficients are quite large, in which case extensive modeling is required). Because of the fine-grid resolution required near the body, a given algorithm often operates much less efficiently on the Navier-Stokes equations than it does on the Euler equations, even though the work per step may be similar and the viscous terms may enhance stability. However, on this same refined viscous grid, the boundary-layer equations can be efficiently and accurately solved. As a result one can speculate that by using a boundary-layer algorithm near the wall, it may be possible to significantly improve the productivity of the Navier-Stokes algorithm. A convenient way of imposing the boundary-layer equations in this way is by a general method which we have termed fortified Navier-Stokes (FNS).

Fortified Approach

As an alternative to the traditional "zonal" concept of solving the various flow zones on separate grids and patching the zones together, the Navier-Stokes equations can be applied throughout and the solution of simplified or subset equations can be embedded into the more general or global algorithm by means of a forcing function (fig. 11). In this way, the approximate solution scheme is used to enhance or "fortify" the more general scheme so as to improve the overall accuracy or efficiency. For example, the thin-layer Navier-Stokes equations can be represented in a form

$$\partial_\tau(\hat{Q}) + \partial_\xi(\hat{F}) + \partial_\eta(\hat{G}) + \partial_\zeta(\hat{H}) = Re^{-1}\partial_\eta \hat{S}$$

where $\hat{Q}$ is the solution vector, $\hat{F}$, $\hat{G}$, and $\hat{H}$ are flux terms, and $\hat{S}$ is the viscous stress term in η. These equations can be fortified through the addition of a dissipative forcing term as (refs. 36-38)

$$\partial_\tau(\hat{Q}) + \partial_\xi(\hat{F}) + \partial_\eta(\hat{G}) + \partial_\zeta(\hat{H}) = Re^{-1}\partial_\eta \hat{S} + \overline{C}(\hat{Q}_{bl} - \hat{Q}) \tag{7}$$

where $\hat{Q}_{bl}$ denotes $\hat{Q}$ formed from the boundary-layer solution. The positive definite operator $\overline{C}$ is chosen such that $-\overline{C}\hat{Q}$ is a damping term and is easily invertable, for example

$$\overline{C} = \chi I \tag{8a}$$

with I the identity, or

$$\overline{C} = -\chi(\partial_{\xi\xi} + \partial_{\eta\eta} + \partial_{\zeta\zeta}) \tag{8b}$$

The parameter χ is picked as a large positive coefficient that blends to zero outside of the forced region of the viscous layer. Inside the viscous layer $\hat{Q}_{bl}$ approaches $\hat{Q}$ so no error is generated by the addition of the term $\overline{C}(\hat{Q}_{bl} - \hat{Q})$. For a frozen $\hat{Q}_{bl}$, such an implicitly imposed forcing term can be used to favorably alter the stability properties of numerical solution algorithms. (Analysis of this approach has been presented in references **37** and **38**.) Outside of the forced region of the viscous layer χ is zero and only the thin-layer Navier-Stokes equations are solved.

By adding subset equation forcing terms to the Navier-Stokes equations, the Navier-Stokes and subset equations interact strongly over entire regions rather than just at interface boundaries. Moreover, the subset equations can be applied selectively to only those regions where they are clearly valid. In principle, if during an iterative solution process the approximation method become suspect in a certain region, the forcing can be turned off, and the region can be resolved with only the global Navier-Stokes scheme. Because of this flexibility, the generality of the Navier-Stokes equations is retained with the FNS approach, while some of the efficiency of the subset algorithms is recovered.

Numerical Implementation

The fortified terms have been implemented in an implicit approximately factored algorithm for the three-dimensional thin-layer Navier-Stokes equations written in general coordinates. The basic two-factor solution algorithm (refs. **14, 15**) uses central spatial differencing in the η and ζ directions and upwinding in the ξ direction. The forcing term with $\overline{C} = \chi I$ has been added to the basic algorithm as (refs. 37,38)

$$\begin{aligned}
&\left[I(1+h\chi) + h\delta_\xi^b(\hat{A}^+)^n + h\delta_\zeta \hat{C}^n - hRe^{-1}\bar{\delta}_\zeta J^{-1}\hat{M}^n J - D_i|_\zeta\right] \\
&\times [I(1+h\chi)]^{-1} \times \left[I(1+h\chi) + h\delta_\xi^f(\hat{A}^-)^n + h\delta_\eta \hat{B}^n - D_i|_\eta\right] \Delta\hat{\mathbf{Q}}^n = \\
&- \Delta t\{\delta_\xi^b[(\hat{\mathbf{F}}^+)^n - \hat{\mathbf{F}}_\infty^+] + \delta_\xi^f[(\hat{\mathbf{F}}^-)^n - \hat{\mathbf{F}}_\infty^-] + \delta_\eta(\hat{\mathbf{G}}^n - \hat{\mathbf{G}}_\infty) + \delta_\zeta(\hat{\mathbf{H}}^n - \hat{\mathbf{H}}_\infty) \\
&- Re^{-1}\bar{\delta}_\zeta(\hat{\mathbf{S}}^n - \hat{\mathbf{S}}_\infty)\} - (D_e|_\eta + D_e|_\zeta)(\hat{\mathbf{Q}}^n - \hat{\mathbf{Q}}_\infty) + h\chi(\hat{\mathbf{Q}}_f - \hat{\mathbf{Q}}^n)
\end{aligned} \tag{9}$$

Here $h = \Delta t$ (first order in time), or $h = \frac{\Delta t}{2}$, (second order in time) and a free stream base solution is subtracted out to improved accuracy in the far field. The operators δ_ξ^b and δ_ξ^f are backward and forward three-point difference operators. The flux $\hat{\mathbf{F}}$ has been eigensplit and the matrices $\hat{A}, \hat{B}, \hat{C}$, and $\hat{M}$ result from local linearization of the fluxes about the previous time level. Because central-space-difference operators are used in η and ζ, implicit D_i and explicit

D_e numerical dissipation terms are included in equation (9). With this implementation, χ can become very large without concern for large factorization errors, and χ contributes to the diagonal dominance of both left-hand factors.

Results

The FNS method has been tested on a simple geometry which roughly models an infinitely swept wing - a 7.75% thick sine-wave bump-on-a-wall with a 35° leading edge sweep. The flow was computed with a thin-layer Navier-Stokes algorithm (refs. 14,15) and with the FNS scheme using the Van Dalsem and Steger boundary-layer field method (ref. 34). The flow was first computed using the standard Navier-Stokes algorithm alone on both a fine mesh (29 points in the flow direction, 50 points normal to the wall, 5 points in the span direction) and a coarse mesh which has only 20 points in the critical normal direction. The same minimum normal spacing at the wall was used in both the coarse- and fine-mesh computations. This flow was also computed with the FNS approach using the coarse Navier-Stokes mesh (20 points in the normal direction) and, near the wall, a superimposed fine boundary-layer mesh (50 points in the normal direction). In all the FNS computations presented here, χ was proportional to the vorticity; hence, it is automatically large within the boundary-layer and rapidly drops to zero near the edge of the boundary-layer. The drag history in figure 12 shows that the coarse-grid standard Navier-Stokes computation does not predict the drag accurately, and that the FNS method obtains essentially the same drag level in 50 iterations that the fine-grid standard Navier-Stokes computation reached in 400 iterations. The computed near-surface particle traces are shown in figures 13a-c. Both the FNS method and the fine-grid standard Navier-Stokes computations predict a constant chord-line separation line, whereas the coarse-grid standard Navier-Stokes computation does not quite capture this qualitative feature.

The swept infinite wing geometry described above was modified to yield a three-dimensional flow by reducing the aspect ratio of the wing to one. Also, to resolve spanwise changes, the grid dimension in this direction was increased from 5 to 15. The resulting particle traces (figs. 14a-d) show the same trends as described for the infinite span example. Also shown in figure 14d is the result obtained when the viscous terms and no-slip boundary conditions are removed from the global numerical algorithm (thus making it an Euler formulation). In this case, the entire influence of viscosity must be carried by the boundary-layer algorithm, which is not a difficulty for this case. The drag history versus CRAY-XMP CPU time for these computations is presented in figure 15. As before, the coarse-grid standard Navier-Stokes computation is not accurate, and the fine-grid standard Navier-Stokes computation is expensive, whereas the FNS (and Euler) computations yield the same drag level as does the fine-grid standard Navier-Stokes computation, but for one-twentieth of the cost.

CONCLUDING REMARKS

Because efficient viscous-inviscid interaction methods have been difficult to extend to complex three-dimensional flow simulations, Navier-Stokes procedures are more frequently being utilized even though they require considerably more work per grid point. It would seem a mistake, however, not to make use of the more efficient approximate methods in those regions in which they are clearly valid. Ideally we should like a general purpose compressible flow solver that can optionally take advantage of approximate solution methods both to improve accuracy and efficiency. Some potentially useful steps toward this goal have been described in this paper – a generalized three-dimensional boundary-layer formulation and the fortified Navier-Stokes procedure. Further work remains in merging these steps and more.

REFERENCES

1. MacCormack, R. W.: Current Status of Numerical Solutions of the Navier-Stokes Equations. AIAA Paper No. 85-0032, Jan., 1985.

2. Shang, J. S.: An Assessment of Numerical Solutions of the Compressible Navier-Stokes Equations. AIAA J. of Aircraft, Vol. 2, No. 5, May 1985, pp 353-370.

3. Holst, T.L.: Numerical Solution of the Navier-Stokes Equations About Three-Dimensional Configurations — A Survey. Presented at the NASA Conference on Supercomputing in Aerospace, Moffett Field, CA, March 10-12, 1987.

4. Briley, W. R. and McDonald, H.: Solution of the Multidimensional Compressible Navier-Stokes Equations by a Generalized Implicit Method. J. Comp Physics, Vol. 24, No. 4, August, 1977.

5. Warming, R. F. and Beam, R. M.: On the Construction and Application of Implicit Factored Schemes for Conservation Laws. Symposium on Computational Fluid Dynamics, New York, April 1977, SIAM-AMS Proceedings, Vol. 11, 1977.

6. Pulliam, T. H. and Steger, J. L.: On Implicit Finite Difference Simulations of Three-Dimensional Flows. AIAA J., Vol. 18, Feb. 1979.

7. Pulliam, T. H. and Steger, J. L.: Recent Inprovements in Efficiency, Accuracy, and Convergence of an Implicit Approximate Factorization Algorithm. AIAA Paper 85-0360 Jan. 1985

8. MacCormack, R. W.: A Numerical Method for Solving the Equations of Compressible Viscous Flow. AIAA 81-0110, Jan. 1981.

9. Shang, J. S. and Scherr, S. J.: Navier-Stokes Solution of the Flow Field Around a Complete Aircraft. AIAA Paper No. 85-1509, July, 1985.

10. Thomas, J. L. and Walters, R. W.: Upwind Relaxation Algorithms for the Navier-Stokes Equations. AIAA Paper No. 85-1501 CP, July 1985.

11. Thomas, J. L., Taylor, S. L. and Anderson, W. K.: Navier-Stokes Computations of Vortical Flows Over Low Aspect Ratio Wings. AIAA-87-0207, Reno, Nevada, January 1987.

12. Holst, T. L., Kaynak, U., Gundy, K. L., Thomas, S. D., Flores, J., and Chaderjian, N.: Numerical Solution of Transonic Wing Flows Using an Euler/Navier-Stokes Zonal Approach. AIAA Paper No. 85-1640, July, 1985.

13. Flores, J., Holst, T. L., Kaynak, U., Gundy, K. and Thomas, S. D.: Transonic Navier-Stokes Wing Solution Using a Zonal Approach. Part 1. Solution Methodology and Code

Validation. AGARD 58th Fluid Dynamics Panel Symposium, Aix-en-Provence, France, April, 1986.

14. Ying, S. X., Steger, J. L., Schiff, L. B., and Baganoff, D.: Numerical Simulation of Unsteady, Viscous, High Angle of Attack Flows Using a Partially Flux-Split Algorithm. AIAA Paper No. 86-2179, Aug. 1986.

15. Steger, J. L., Ying, S. X., and Schiff, L.B.: A Partially Flux-Split Algorithm for Numerical Simulation of Compressible Inviscid and Viscous Flow. *Proceedings of the Workshop on Computational Fluid Dynamics*, Institute of Nonlinear Sciences, University of California, Davis, California, 1986.

16. Rai, M. M.: Navier-Stokes Simulations of Rotor-Stator Interaction Using Patched and Overlaid Grids. AIAA Paper No. 85-1519, July, 1985.

17. Chima, R. V.: Development of an Explicit Multi-Grid Algorithm for Quasi-Three-Dimensional Viscous Flows in Turbo Machinery. NASA TM 87128, Jan. 1986.

18. Kumar, A.: Numerical Simulation of Scramjet Inlet Flow Fields. NASA TP-2517, May 1986.

19. Chakravarthy, S. R.: Relaxation Methods for Unfactored Schemes. AIAA Paper 84-0165, Jan. 1984.

20. Shankar, V. and Chakravarthy, S.: Development and Application of Unified Algorithms for Problems in Computational Science. NASA Conference Publication 2454, Supercomputing in Aerospace, March 1987.

21. Fujii, K. and Schiff, L. B.: Numerical Simulation Over a Strake-Delta Wing. AIAA-87-1229, Honolulu, Hawaii, June 1987.

22. Van Dalsem. W. R., Panaras, A. G., and Steger, J. L.: Numerical Investigation of a Jet in Ground Effect with a Crossflow. Proceedings of the 1987 SAE International Powered Lift Conference and Exposition, Santa Clara, CA, Dec. 7-10, 1987.

23. Benek, J. A., Buning, P.G., and Steger, J.L.: A 3-D Chimera Grid Embedding Technique. AIAA Paper No. 1523, AIAA 7th Computational Fluid Dynamics Conference. Cincinnati, Ohio, July 15-17, 1985.

24. Cook, P. H., McDonald, M. A., and Firmin, M. C. P.: Aerofoil RAE 2822-Pressure Distributions and Boundary-Layer and Wake Measurements. AGARD AR 138, Paper A6, 1979.

25. Van Dalsem, W. R., and Steger, J. L.: Finite-Difference Simulation of Transonic Separated Flow Using a Full Potential-Boundary Layer Interaction Approach. AIAA Paper 83-1689, Presented at the 16th Fluid and Plasma Dynamics Conference, Danvers, Massachusetts, July 12-14, 1983.

26. Mehta, U.: Reynolds Averaged Navier-Stokes Computations of Transonic Flows Around Airfoils. Presented at the Second Symposium on Aerodynamic Flows, Long Beach, California, January 17-20, 1983.

27. Dougherty, F. C., Holst, T. L., Gundy, K. L., and Thomas, S. D.: TAIR - A Transonic Airfoil Analysis Computer Code. NASA TM-81296, 1981.

28. Van Dalsem, W. R.: Simulation of Separated Transonic Airfoil Flow by Finite-Difference Viscous-Inviscid Interaction. Ph.D. Thesis, Stanford University, June 1984.

29. Rubesin, M. W. and Viegas, J. R.: A Critical Examination of the Use of Wall Functions as Boundary Conditions in Aerodynamic Calculations. Third Symposium on Numerical and Physical Aspects of Aerodynamic Flows, California State University, Long Beach, Calif., Jan. 1985.

30. Hafez, M. M., Habashi, W. G., Przybytkowski, S. M. and Peeters, M. F.: Compressible Viscous Internal Flow Calculations by a Finite Element Method. AIAA Paper No. 87-0644, Jan. 1987.

31. Davis, R. L., Carter, J. E., and Hafez, M. M.: Three-Dimensional Viscous Flow Solutions with a Vorticity-Stream Function Formulation. AIAA Paper No. 87-0601, Jan. 1987.

32. Rao, K. V., Pletcher, R. H., Steger, J. L., and Van Dalsem, W. R.: A Three-Dimensional Dual-Potential Procedure with Applications to Wind Tunnel Inlets and Interacting Boundary-Layers. Iowa State University, Report ISU-ERI-87296, June 1987.

33. Steger, J. L. , Van Dalsem, W. R., Panaras, A. G., and Rao, K. V., A Formulation for the Boundary-Layer Equations in General Coordinates. NASA TM 100079, 1988.

34. Van Dalsem, W. R. and Steger, J. L. Efficient Simulation of Separated Three-Dimensional Viscous Flows Using the Boundary-Layer Equations, AIAA J. Vol. 25, no. 3, pp. 395-400, 1987.

35. Panaras, A. G. and Steger, J. L. : A Thin-Layer Navier-Stokes Solution of the Flow about a Prolate Spheroid, AGARDOGRAPH, Report of WG 10, Yoshihara, H. ed., 1988.

36. Steger, J. L., and Van Dalsem, W. R.: Developments in the Simulation of Separated Flows Using Finite-Difference Methods. *Proceedings of the Third Symposium on Numerical and Physical Aspects of Aerodynamic Flows*, California State University, Long Beach, California, 1985.

37. Van Dalsem, W. R., and Steger, J. L.: Using the Boundary-Layer Equations in Three-Dimensional Viscous Flow Simulation. *Proceedings of the 58th Meeting of the AGARD Fluid Dynamics Panel Symposium on Applications of Computational Fluid Dynamics in Aeronautics*, Aix-en-Provence, France, 1986.

38. Van Dalsem, W. R. and Steger, J. L.: The Fortified Navier-Stokes Approach. Proceedings of the Workshop on Computational Fluid Dynamics held by the Institute of Nonlinear Sciences at the University of California, Davis, June 17-18, 1986.

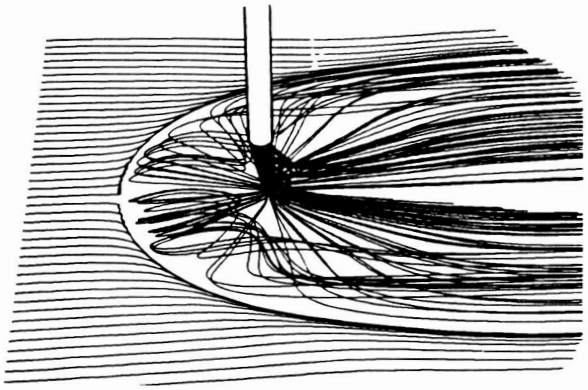

a. (laminar)

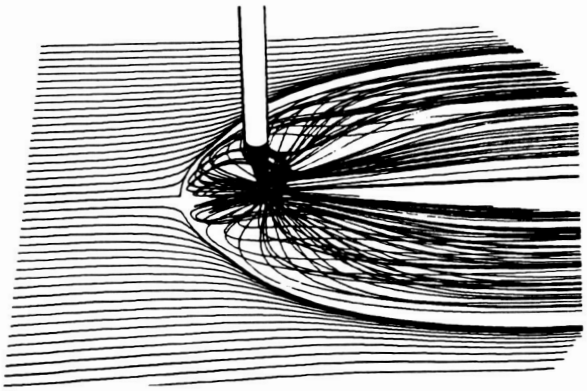

b. (turbulent)

Figure 1. Jet in ground effect issuing into a crossflow with $\frac{V_\infty}{V_{jet}} = 0.223$ and a nozzle height located 3 jet diameters above the wall.

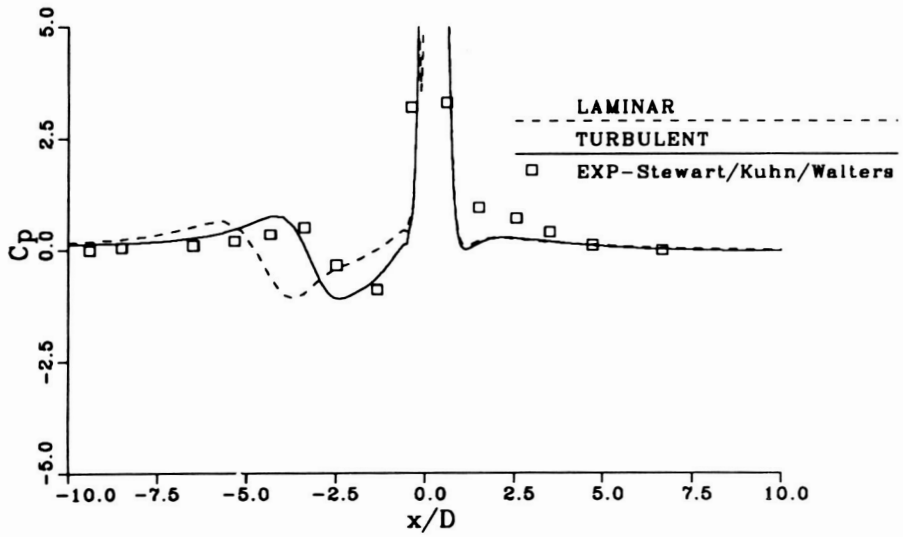

Figure 2. Centerline C_p distributions for the jet in ground effect with $\frac{V_\infty}{V_{jet}} = 0.223$ and a nozzle height located 3 jet diameters above the wall.

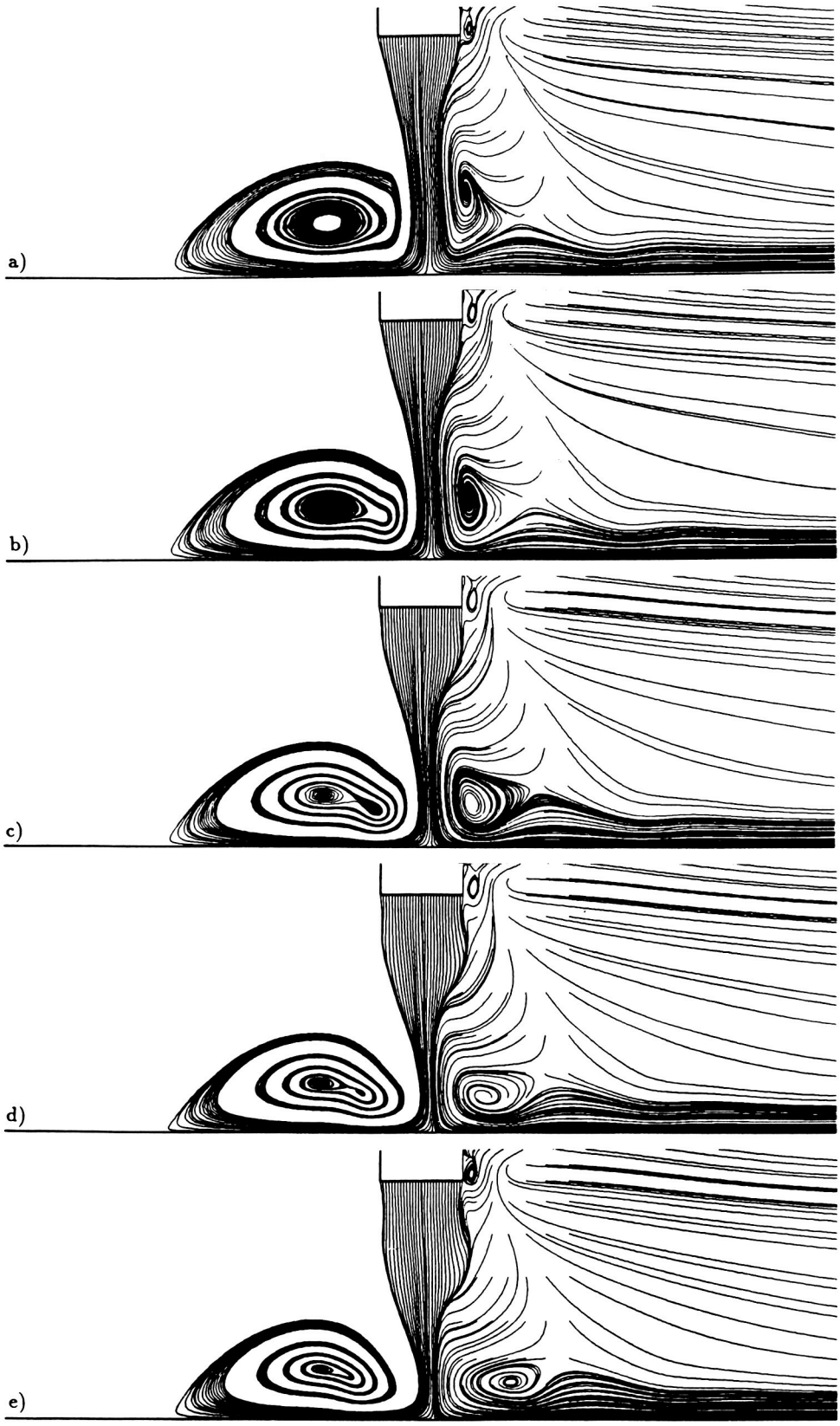

Figure 3. Time history of particle traces indicating the interaction of the ground vortex and the ring vortex.

ORIGINAL PAGE IS
OF POOR QUALITY

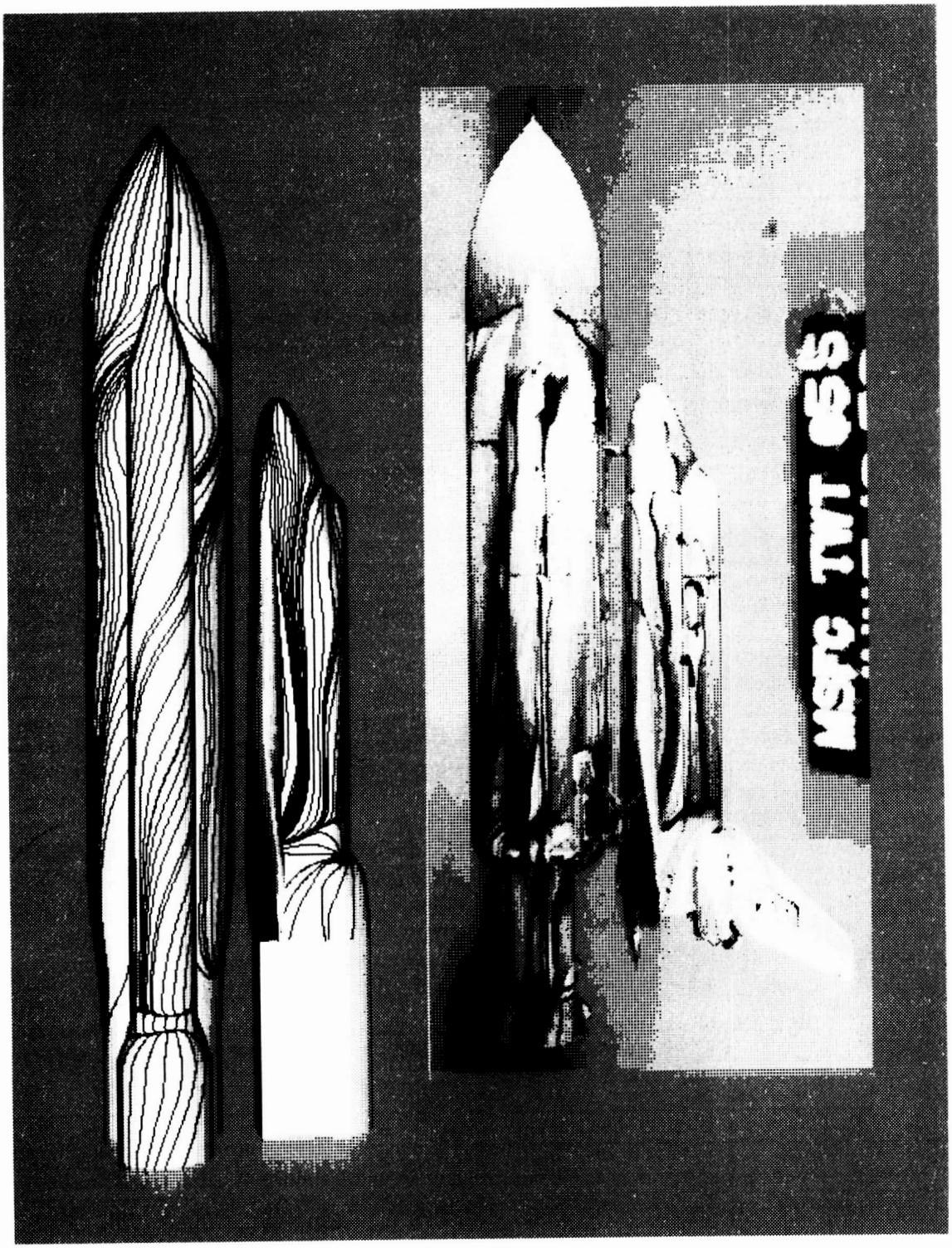

Figure 4. Simulated oil flow (limiting streamlines) compared to experiment for the integrated space shuttle at $M_\infty = 2.0, \alpha = -4°$.

ORIGINAL PAGE
BLACK AND WHITE PHOTOGRAPH

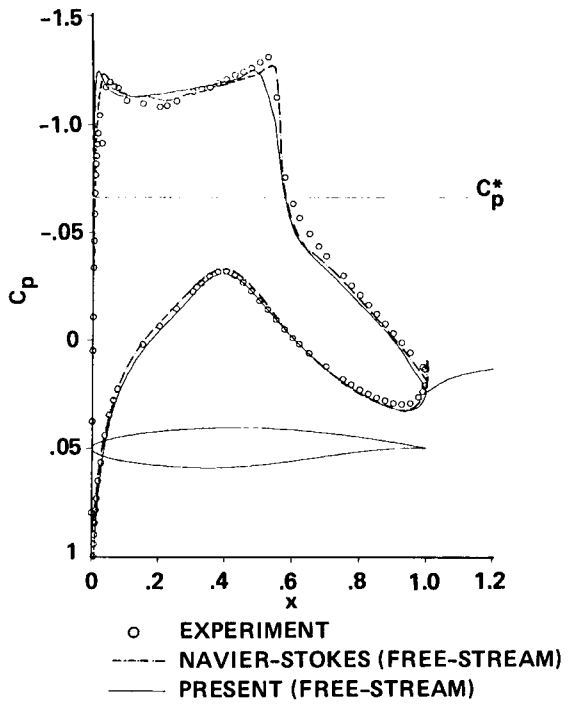

Figure 5. Computed and experimental pressure distributions for RAE 2822 airfoil at $M_\infty = 0.73, Re_\infty = 6.50 \times 10^6, C_l = 0.803$.

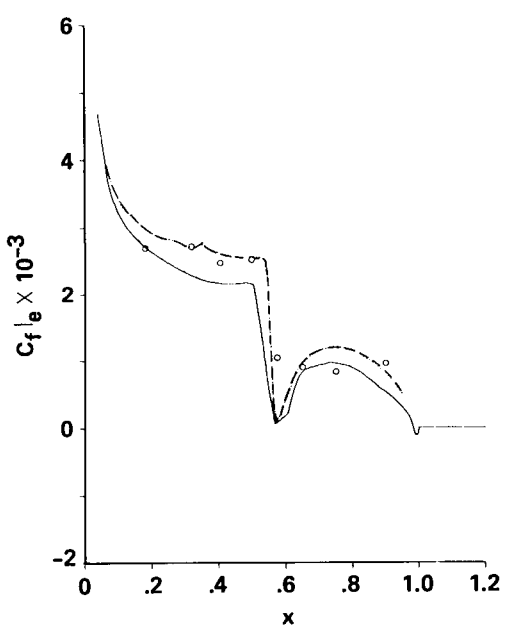

Figure 6. Computed and experimental $C_f|_e$ distributions for RAE 2822 airfoil at $M_\infty = 0.73, Re_\infty = 6.50 \times 10^6, C_l = 0.803$.

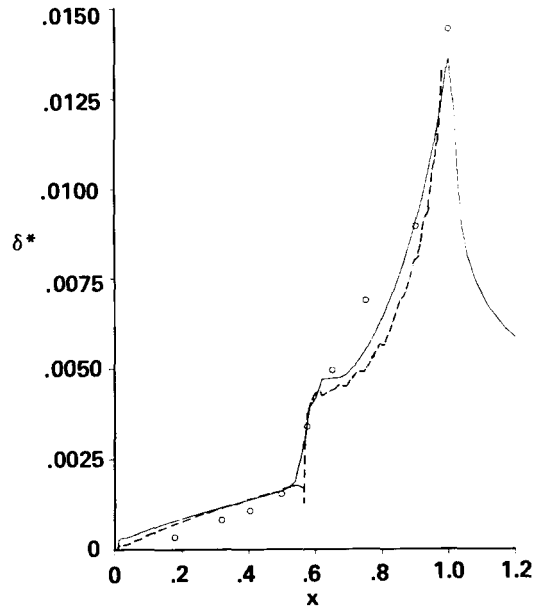

Figure 7. Computed and experimental δ^* distributions for RAE 2822 airfoil at $M_\infty = 0.73, Re_\infty = 6.50 \times 10^6, C_l = 0.803$.

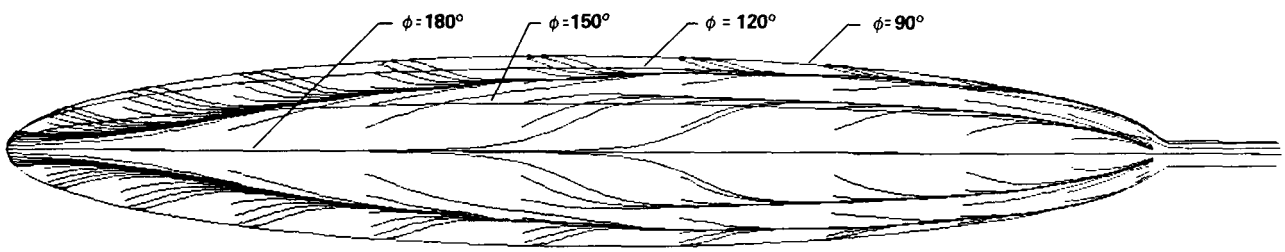

Figure 8. Top view of 6 : 1 prolate spheroid showing thin-layer Navier-Stokes and boundary-layer ($0.02 \leq x/L \leq 0.80$) computed limiting streamlines for $M_\infty = 0.25$, $\alpha = 30°$, and $Re = 43 \times 10^6$.

ORIGINAL PAGE IS
OF POOR QUALITY

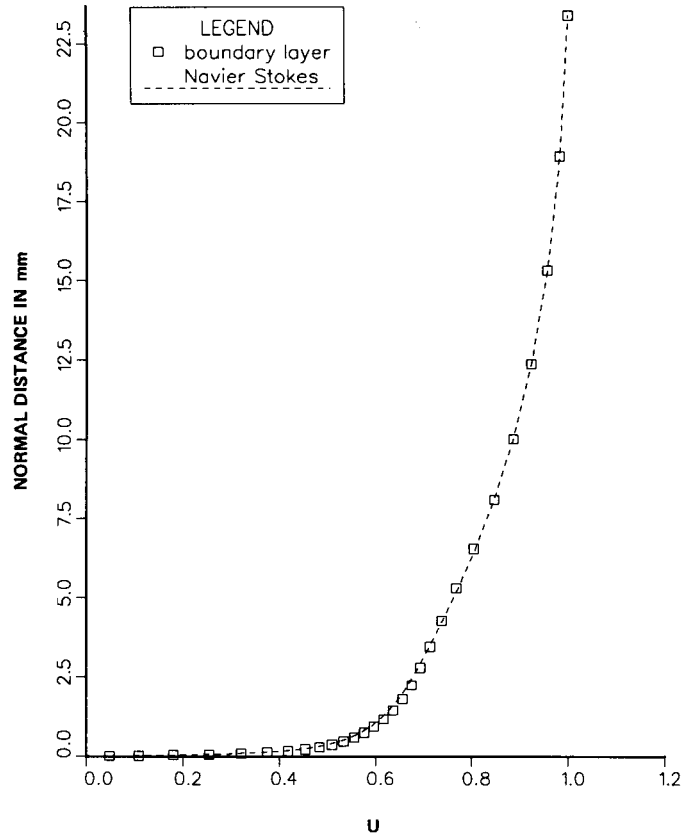

Figure 9. A typical computed attached profile (contravariant U versus normal height) at $x/L = 0.65$ and $\phi = 120°$ on the prolate spheroid at 10° angle of attack using boundary-layer and thin-layer Navier-Stokes equations.

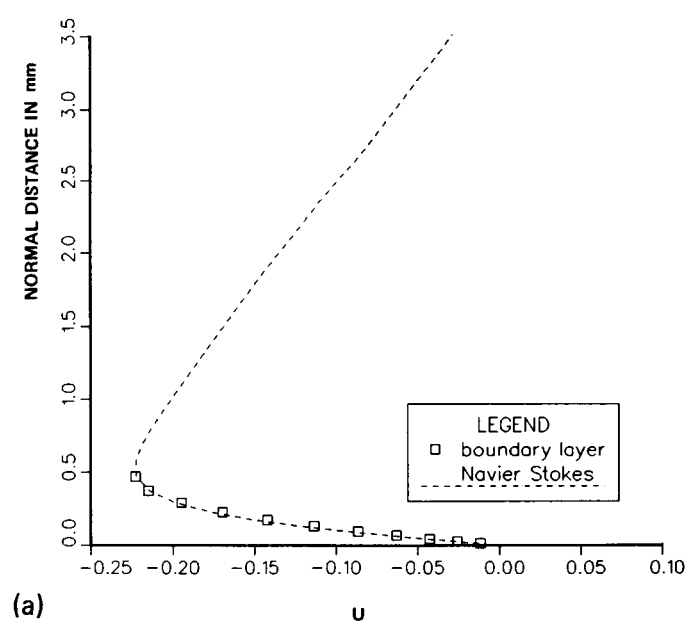

Figure 10. A separated profile at $x/L = 0.96$ and $\phi = 120°$ on the prolate spheroid at 10° angle of attack showing breakdown of the direct mode boundary-layer computation as the outer edge is moved away from the wall.

ORIGINAL PAGE IS
OF POOR QUALITY

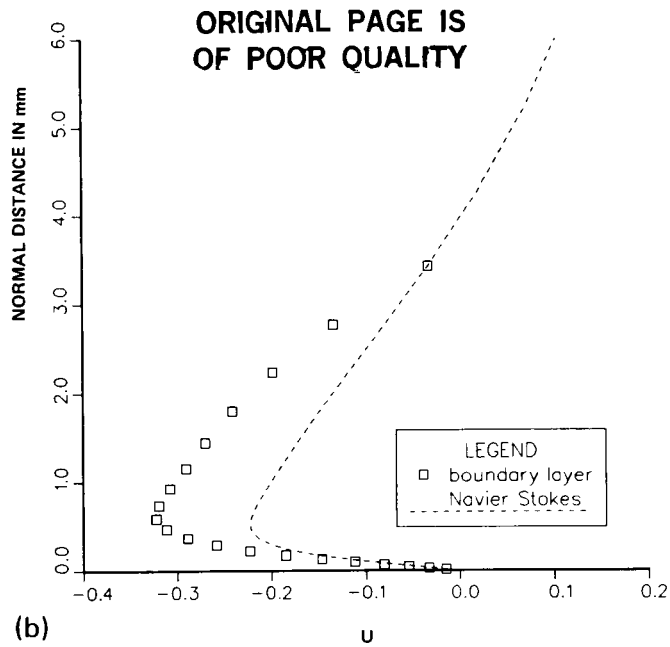

(b)

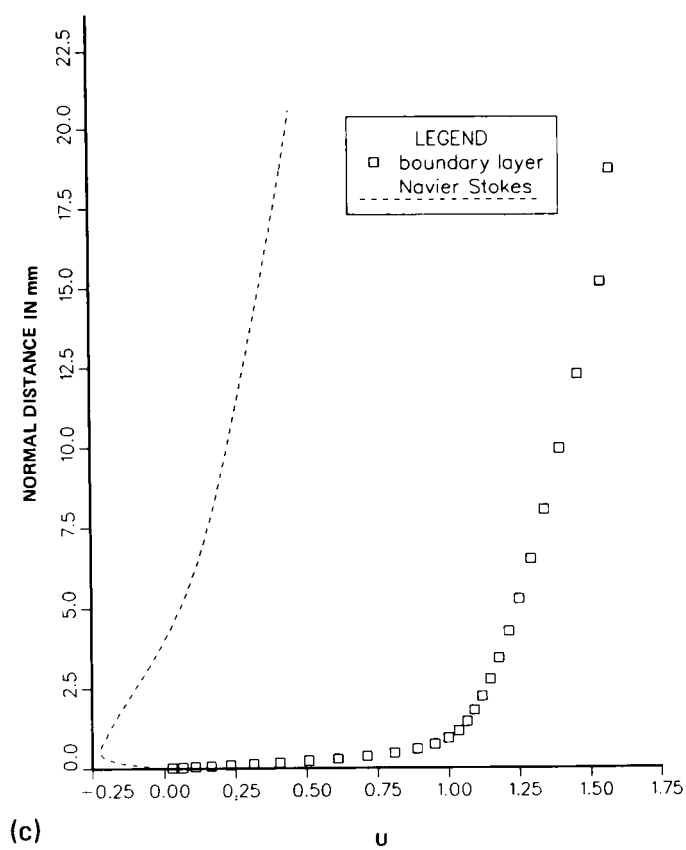

(c)

Figure 10. Concluded.

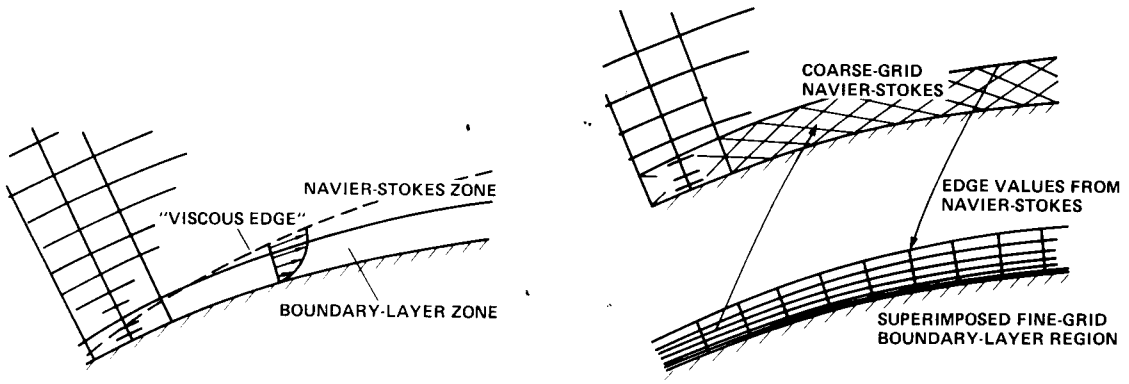

Figure 11. Boundary-layer forced Navier-Stokes schemes.

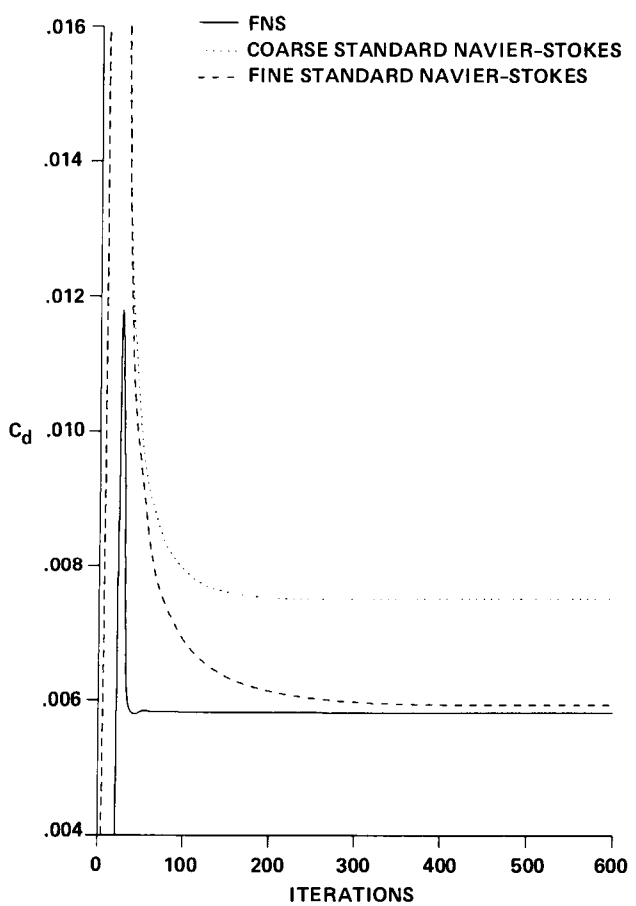

Figure 12. Drag coefficient history versus iterations for the turbulent flow over a 7.75% sine wave bump with a 35° leading-edge sweep, $Re = 5 \times 10^5$, and $M_\infty = 0.5$.

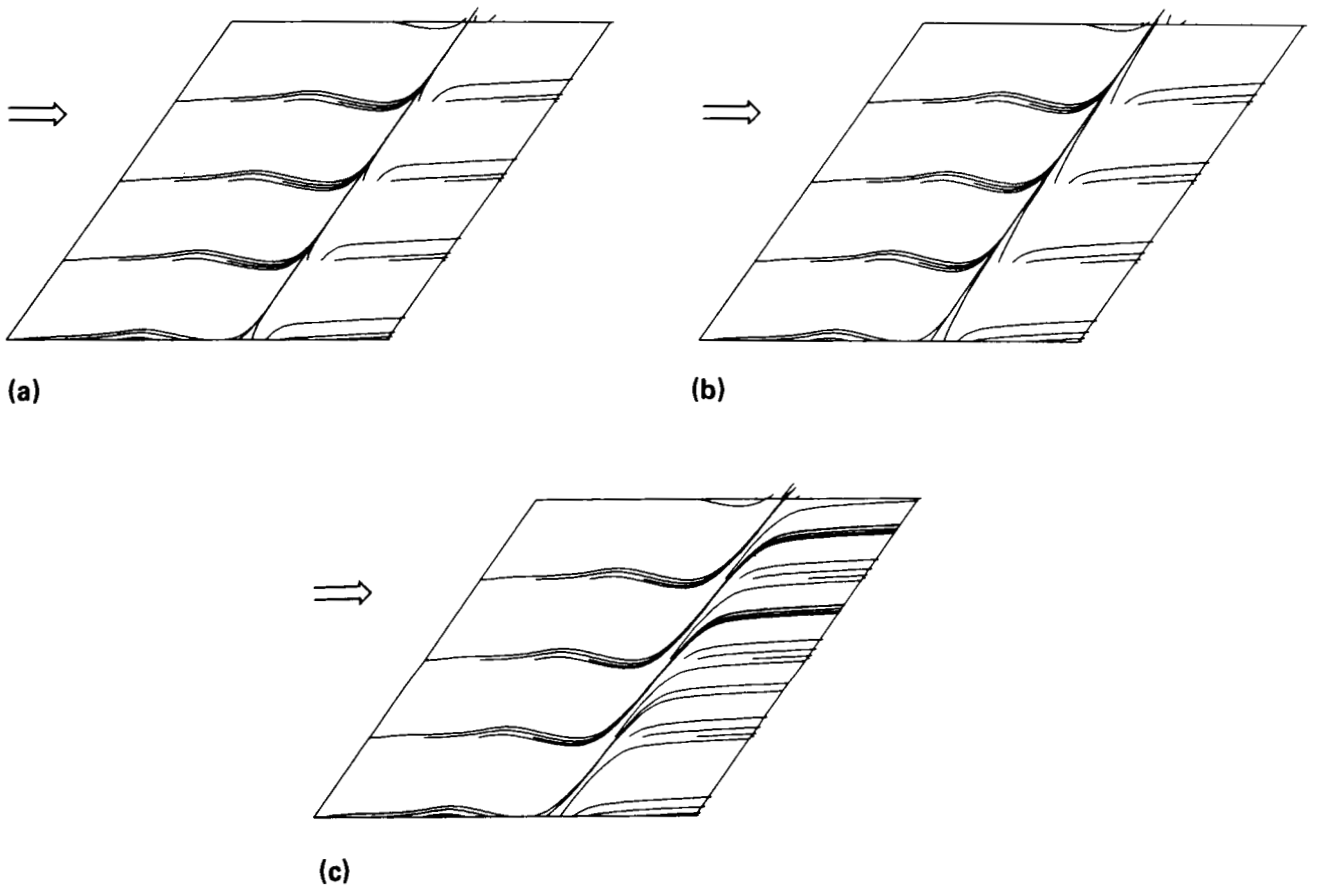

Figure 13. Computed near-surface particle traces for the bump flow: a) Fortified Navier-Stokes; b) standard Navier-Stokes (fine mesh); c) standard Navier-Stokes (coarse mesh).

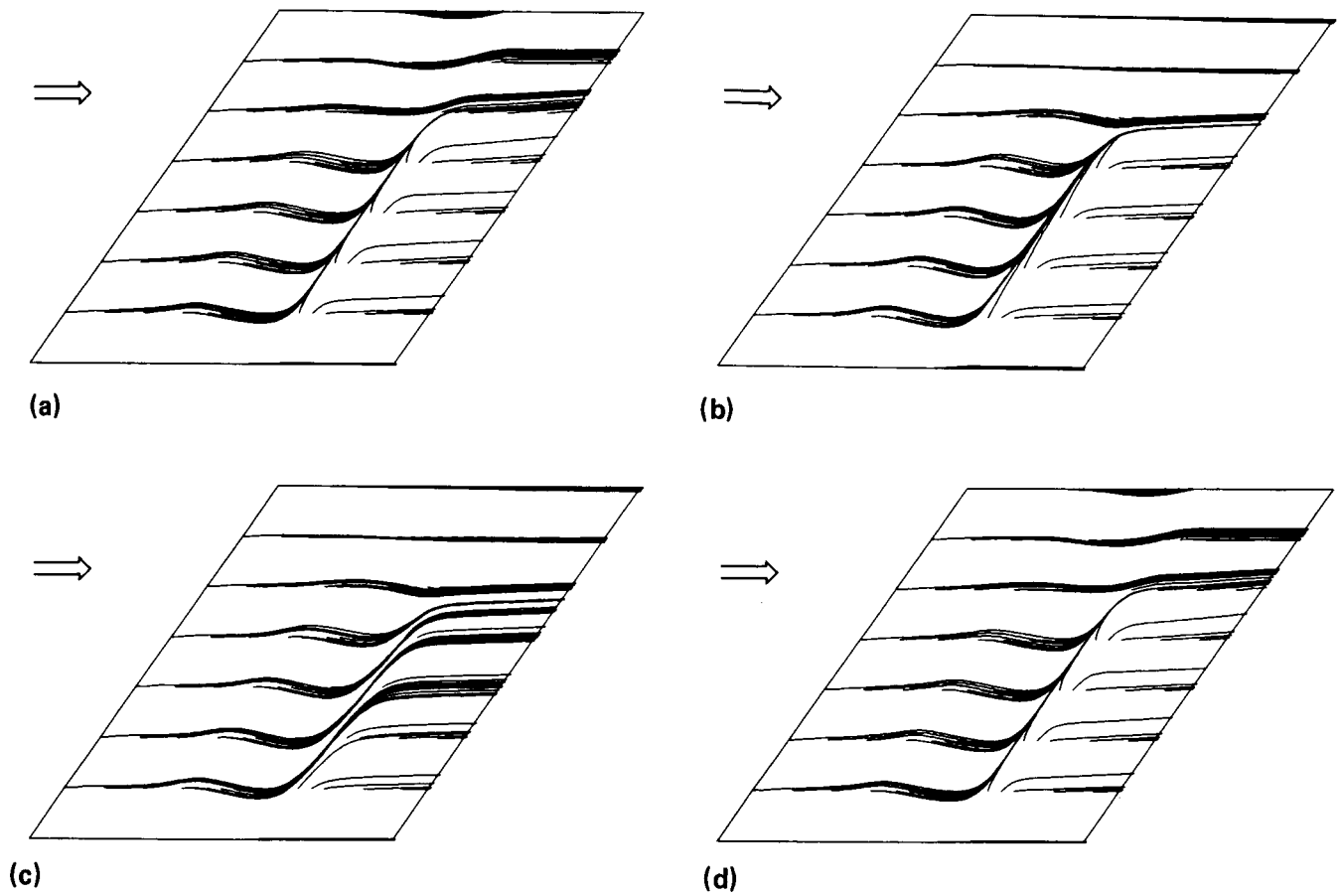

Figure 14. Computed near-surface particle traces for the turbulent flow over a 7.75% sine wave bump with a 35° leading-edge sweep, $Re = 5 \times 10^5$, $M_\infty = 0.5$, and AR=1: a) Fortified Navier-Stokes; b) standard Navier-Stokes (fine mesh); c) standard Navier-Stokes (coarse mesh); d) Fortified Euler.

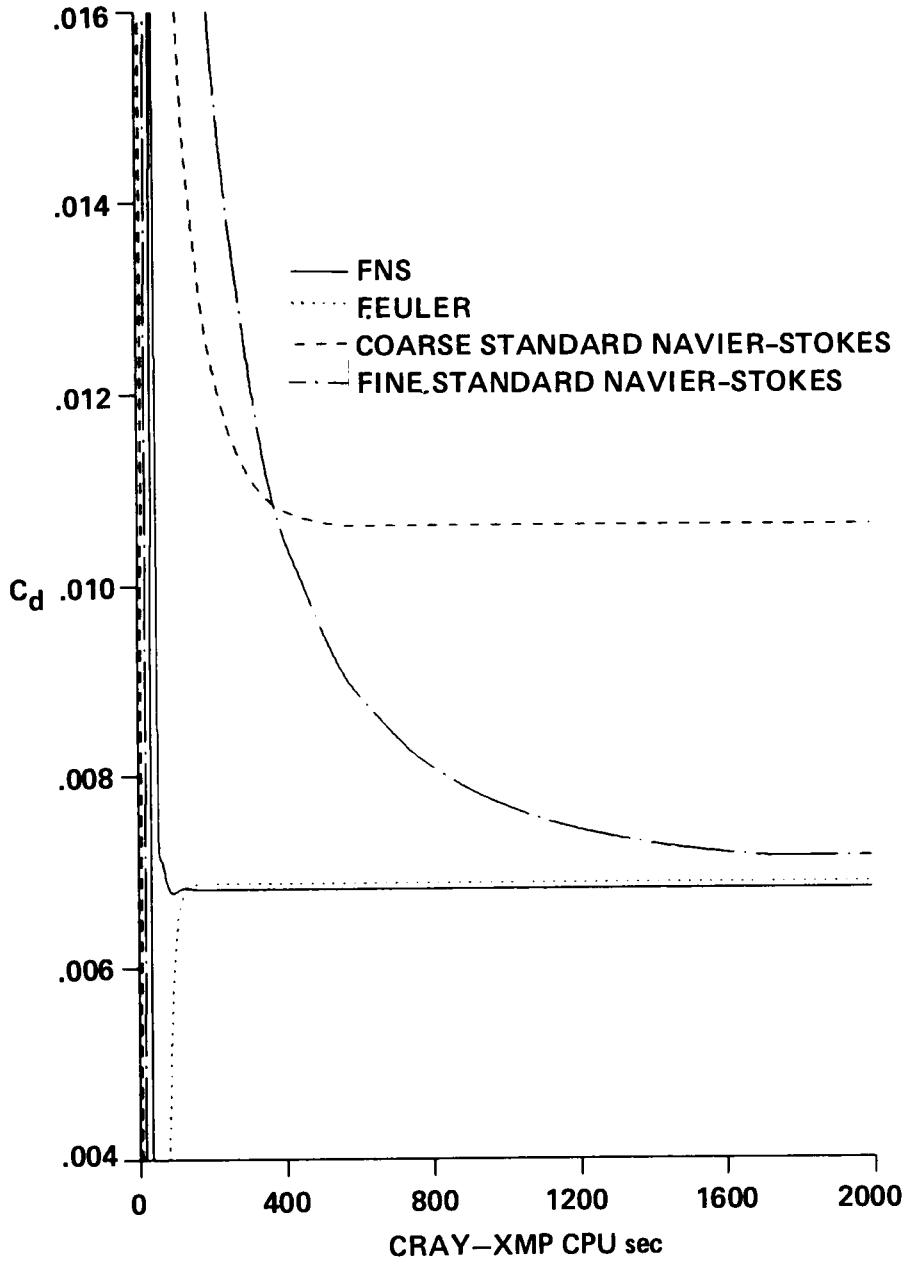

Figure 15. Drag coefficient history versus CRAY-XMP processor time for flow of figure 14.

N89-20950

3-D EULER AND NAVIER-STOKES CALCULATIONS FOR AIRCRAFT COMPONENTS

Veer N. Vatsa
NASA Langley Research Center, Hampton, Virginia

Bruce W. Wedan
Vigyan Research Associates, Hampton, Virginia

Eli Turkel
ICASE, Hampton, Virginia

Abstract

An explicit multistage Runge-Kutta type of time-stepping scheme is used for solving transonic flow past a transport type wing/fuselage configuration. Solutions for both Euler and Navier-Stokes equations are obtained for quantitative assessment of boundary-layer interaction effects. The viscous solutions are obtained on both a medium resolution grid of approximately 270,000 points and a fine grid of 460,000 points to assess the effects of grid density on the solution. Computed pressure distributions are compared with the experimental data.

Introduction

The availability of present generation supercomputers has made it feasible to compute transonic flow over realistic aircraft components, which is evident from the multitudes of papers that have appeared in the literature on this subject in the last 3-4 years. Euler solutions for essentially complete aircraft configurations [1-2] are now available. In addition, Navier-Stokes solutions for aircraft components, such as wings, fuselage-shaped bodies and simple configurations [3-8] have also become available recently. Another problem that has received special attention recently is that of flow over a simple aircraft component, such as a wing, mounted inside a wind tunnel [9-12]. Navier-Stokes solutions for such problems, including simulation of tunnel walls and sting support, are very useful for estimating wind tunnel wall-interference effects.

In the present paper, a multistage Runge-Kutta type of time-stepping scheme developed by Jameson and coworkers [13-14] for Euler equations, and extended to three-dimensional Navier-Stokes equations by Vatsa [5], is applied to the computation of a transport -type wing/fuselage configuration under transonic flow conditions. The accuracy of this numerical scheme has been tested extensively for high Reynolds number viscous flow over simple components such as prolate spheroids and wings in free-air and inside wind tunnels [5,8,12]. In this paper, the numerical scheme of Ref. 5 is extended to solve the flow over a wing/fuselage configuration.

Governing equations and numerical algorithm

The basic equations describing the general three-dimensional flow are the compressible Navier-Stokes equations. These are written in a body-fitted curvilinear coordinate system (ξ , η , ζ), where ξ, η, and ζ represent the streamwise, normal and spanwise directions

respectively. Since the dominant viscous effects for high Reynolds number flow are confined to a thin viscous layer near the body surface, a thin-layer assumption is employed here by retaining only the viscous diffusion terms along the η-direction, which is normal to the surface. These equations can be written in the conservation law form as :

$$\frac{\partial(J^{-1}U)}{\partial t} + \frac{\partial F}{\partial \xi} + \frac{\partial G}{\partial \eta} + \frac{\partial H}{\partial \zeta} = \frac{\partial G_v}{\partial \eta} \tag{1}$$

where $U = [\ \rho, \rho u, \rho v, \rho w, \rho E\ ]^T$

represents the dependent variables; F, G and H represent the convective fluxes and G_v represents the viscous fluxes. The full form of these terms is readily available in the literature (e.g. see Refs. 3,7,12).

The concepts of eddy viscosity and eddy conductivity are employed to account for the effect of turbulence. The Baldwin-Lomax turbulence model, which is an algebraic model, is used for the present turbulent flow calculations.

A finite-volume algorithm based on Jameson's Runge-Kutta time-stepping scheme is used for obtaining steady-state solutions to the governing equations. The spatial derivatives are replaced with central differences and the solution is advanced in time using a 4-stage Runge-Kutta scheme. Local time-stepping, enthalpy damping and implicit residual averaging techniques are used for accelerating the convergence to steady state.

Artificial dissipation

A blend of second and fourth order artificial dissipation is added to the central-difference scheme for suppressing odd-even point decoupling and oscillations in the vicinity of shock waves and stagnation points. The dissipation model used here is based on the model devised by Jameson and Baker [14] for 3-D Euler equations. Whereas the dissipation model of Ref. 14 works reasonably well for Euler equations on grids with cell aspect ratios of order one, the situation is less satisfactory when seeking solutions to Navier-Stokes equations. This is due to the fact that extremely fine meshes with large stretchings have to be used for accurate resolution of the thin boundary-layer regions that develop at high Reynolds number. This gives rise to high aspect ratio cells and the dissipation model of Ref. 14 results in excessive levels of artificial dissipation under these conditions.

Martinelli [15] and Swanson and Turkel [16] have looked at different ways of reducing the artificial dissipation in 2-D Navier-Stokes computations. Vatsa, Thomas and Wedan [8], and Vatsa and Wedan [12] have studied the effects of artificial dissipation on the accuracy of 3-D Navier-Stokes solutions for transonic flow over prolate spheroids and wings. Based on these studies [8,12,15,16], it was concluded that an effective way to reduce the artificial dissipation levels is to scale the dissipation in the three coordinate directions by their respective eigenvalues instead of scaling the dissipation by the maximum eigenvalue, as was done in the original work of Ref. 14. In addition, the artificial dissipation is scaled with the local Mach number to reduce it even further in the viscous layer. Based on the earlier investigations [8,12], this modified dissipation model provides improved level of accuracy for the solutions of the Navier-Stokes equations, and hence it will be employed in the present paper.

Boundary conditions

The wing/fuselage surface is treated as a solid, no-slip and no-injection boundary. Numerically, this boundary condition is imposed by setting the three velocity components, u,

v and w to zero at the surface. The normal pressure and temperature gradients at this surface are set to zero. Only one-half of the wing/fuselage configuration (left-half) is simulated and hence a symmetry condition in the spanwise direction is imposed at $\zeta = 0$ for all variables except the cross-flow velocity component, w, which is taken to be antisymmetric. The farfield boundary condition is based on Riemann invariants for one-dimensional flow normal to the boundary, as discussed by Jameson and Baker [14] and Thomas and Salas [17]. Extrapolation on all variables is used at the downstream boundary.

Grid generation

A transfinite interpolation scheme based on Eriksson's [18] methodology is used for generating the three-dimensional grids for the wing/fuselage configuration under consideration here. A C-O grid topology is employed for accurate resolution of the wing leading-edge and wing-tip regions. Grid clustering is used to provide good resolution in regions of large flow gradients. A partial view of the grid is shown in Fig.1. As can be seen from this figure, the grid generation code employed here can be used to generate reasonable grids for wing/fuselage configurations. The main deficiencies in this grid topology are the lack of resolution in the fuselage nose region and significant skewness in the wing-root and wing-tip regions, which may be relieved through the concepts of block-structured grids.

Results and discussion

In this paper, we will concentrate on calculations for a transport-type wing/body configuration, specifically the Pathfinder I [19]. Experimental pressures for this configuration were obtained in the NTF wind tunnel at NASA Langley, Virginia. The test conditions for the case considered here are M_∞=0.801, α=1.998^0 and a Reynolds number of 3 million. Transition of the flow to turbulence was taken to be at 10% of the chord on the wing, and at the fuselage nose for all the calculations presented here. The position of transition corresponds to the experimental placement of transition strips for the wing.

The present computations were made for a mid-mounted wing configuration, while the configuration tested had a low-mounted wing. This was done mainly to obtain solutions within the time constraint required by this symposium, since the surface definition of the mid-mounted wing configuration was readily available from an earlier investigation [20]. It is not known what total effect this may have had on the present solutions, however based on the interacting boundary layer calculations of Ref. 20, the effect on the solution from the wing position should be apparent only in the vicinity of the wing/fuselage juncture. It is planned to repeat the present Navier-Stokes computations in near future for the low-mounted wing configuration to simulate the experimental set up more precisely. It should also be pointed out that the calculations performed here used nominal wing coordinates obtained from spanwise linear interpolation of a limited amount of data describing the wing. As a result the computational model of the wing contained some localized curvature discontinuities which resulted in pressure oscillations in the solution. These oscillations are small, however, and the overall solution was not affected.

The first set of calculations to be presented are for a medium resolution grid of 161 $\times$ 41 $\times$ 41 points in the streamwise, spanwise and normal directions, respectively. The normal spacing of the grid was 4 $\times 10^{-5}$ at the wing and fuselage surface, giving a y^+ value of approximately 5 for the viscous calculations. Of the 40 cells in the spanwise direction, 16 of these were placed on the fuselage. Both viscous and inviscid calculations were performed on this grid. Fig. 2 shows the convergence history for the viscous calculations on this grid in terms of orders of reduction in the average residual and the number of supersonic points non-

dimensionalized by the final value. This is typical for the calculations presented in this paper in that generally 5 orders of reduction were obtained for the average residual in about 2000 iterations.

The computed pressures are compared with the experimental data at 4 span stations in Fig. 3. The first span station ($\eta = 0.131$) is shown only to indicate the effect of the mid-mounted wing as opposed to the low wing. As seen in this figure, the mid-fuselage mounting of the wing provides flow relief on both the upper and lower surfaces, and thus the acceleration of the flow is not as great as for the experiment. This is particularly evident on the upper surface of the wing where, with the low-wing configuration, there is actually contraction of the stream-tube in the juncture region due to the outward bulge of the fuselage above the wing. As is apparent at the next span station, this problem is reduced away from the juncture region.

Comparing the inviscid and viscous solutions in Fig. 3, it can be seen that the overall effect of including the boundary layer is to increase the pressure on the upper surface of the wing, bringing it more in line with the experimental values. In addition, there is a decrease in the computed pressure in the trailing edge region on the lower surface of the wing due to a filling in of the cove. Some oscillations in the pressure are apparent at the inboard stations for the viscous calculations, which are the result of the non-smooth geometry discussed previously. These oscillations are not seen in the inviscid calculations, however, which is attributed to much higher levels of artificial dissipation resulting from the dissipation model employed for the inviscid calculations (see Ref. 14). The major deficiency in these calculations is the lack of resolution of the leading edge acceleration and shock position and strength. In an earlier paper, Vatsa and Wedan [12] have shown that inadequate grid resolution in either the streamwise or spanwise directions will result in similar disagreements, thus the calculations were repeated for this case on a finer grid.

The next set of calculations are for a finer grid consisting of $193 \times 49 \times 49$ points. Again, 16 of the spanwise cells were placed on the fuselage. The net increase in resolution on the wing surface was approximately 70%. The normal spacing off the surface and farfield boundaries were kept nearly the same, thus the additional 8 cells in the normal direction had the effect of reducing the stretching rate of the grid, and thus the magnitude of the added artificial dissipation. The pressure comparisons with experiment are shown in Fig. 4 for an inboard, mid-span, and an outboard span station. At the mid-span section, the finer grid improves the agreement between the calculations and the experiment in that the leading edge pressure peak and shock position and strength are better resolved. There is no significant difference between the two calculations at the inboard station, however. Both calculations miss the acceleration in the leading edge region and the shock. It is possible that the disagreement between the computed and experimental pressures at this station is due to the wing mounting position. Experimentally, the flow in the leading edge region of the wing is supersonic from the wing root/fuselage juncture to the tip, with a well developed shock structure. For the calculations, however, the flow is subsonic at the wing root, thus the shock which forms over the mid and outboard regions of the wing must vanish as the root juncture region is approached. This discrepancy will be resolved in future calculations, where the wing will be properly located on the fuselage for more accurate representation of the experimental geometry. A different situation exists at the outboard station, in that the finer grid calculation overpredicts the leading edge pressure peak and indicates a shock that is further downstream and stronger than the experimental data. This is attributed to a certain amount of experimentally observed washout of the tip due to aerodynamic loads during testing. An attempt will also be made to ascertain the magnitude of this, and include it in future calculations.

Surface streamline plots from the calculations are shown in Fig. 5 for the upper and lower surfaces of the wing. As can be seen in this figure, the flow is well behaved over the entire wing under these conditions, aside from the small streamwise extent of trailing edge separation on the upper surface. A significant amount of spanwise flow can also be observed on the lower surface in the cove region of the wing. Although, no experimental oil flows were

taken for this test, these patterns have been compared with oil flow photographs obtained for a similar configuration in another wind tunnel [21]. The streamline patterns from the calculations have qualitatively the same nature as indicated in those oil flows.

The streamline patterns for the fuselage as obtained from the calculations are also shown in Fig.5 . Again, no experimental verification of this pattern is available for this configuration. The streamline patterns, however, compare favorably with those observed previously by Vatsa and Wedan for calculations of a wing mounted on a side wall in a wind tunnel [12]. The streamline patterns from both calculations show the displacement of the streamlines away from the wing surface both above and below the wing, and a plume-type structure emanating from the wing trailing edge and extending downstream.

Conclusions

Viscous and inviscid flow calculations have been performed for a transport-type wing/body configuration and compared to experimental data at Mach number of 0.801, an angle of attack of 1.998 degrees, and a chord Reynolds number of 3 million. The viscous calculations showed significant improvement over the inviscid calculations, particularly over the upper surface of the wing and in the cove region on the lower surface. The upper surface shock and the flow in the leading edge region were resolved more accurately on the finer grid over the mid and outboard sections of the wing. Significant differences exist between the computed and experimental pressures over the inboard region of the wing. This has been attributed to the mid-wing modeling of the configuration in the computations as opposed to the actual low-wing experimental configuration. These calculations will be repeated in the near future for a low-mounted wing configuration in order to obtain more accurate simulation of the experimental setup. Finally, the streamline patterns on the wing and fuselage compare qualitatively with patterns observed from previous computations and experimental tests of similar configurations.

References

1. Jameson, A., Baker, T.J. and Weatherill, N.P., "Calculation of Inviscid Transonic Flow Over a Complete Aircraft", AIAA Paper 86-0103, Jan. 1986.

2. Sawada, K. and Takanashi, S., "A Numerical Investigation on Wing/Nacelle Interferences of USB Configurations", AIAA Paper 87-0455, Jan. 1987.

3. Fujii, K., and Obayashi, S., "Navier-Stokes Simulations of Transonic Flows over a Wing-Fuselage Combination", AIAA J., Vol. 25, Dec. 1987, pp.1587-1596.

4. Thomas, J.L., Taylor, S.L. and Anderson, W.K., "Navier-Stokes Computations of Vortical Flows Over Low Aspect Ratio Wings", AIAA Paper 87-0207, Jan. 1987.

5. Vatsa, V.N., "Accurate Numerical Solutions for Transonic Viscous Flow Over Finite Wings", Journal of Aircraft, Vol. 24, June 1987, pp.377-385.

6. Holst, T.L., Gundy, K.L., Flores, J. and Chaderjian, N.M., "Numerical Solution of Transonic Wing Flows Using an Euler/Navier-Stokes Zonal Approach", AIAA Paper 85-1640, July 1987.

7. Agarwal, R.K., Underwood, R.R. and Deese, J.E., "Computation of Three-Dimensional Transonic Viscous Flowfields Using Unsteady Parabolized Navier-Stokes Equations", AIAA Paper 85-1595, July 1985.

8. Vatsa, V.N., Thomas, J.L. and Wedan, B.W., "Navier-Stokes Computations of Prolate Spheroids at Angle of Attack", AIAA Paper 87-2627-CP, Aug. 1987.

9. Obayashi, S., Fujii, K. and Gavali, S., "Navier-Stokes Simulation of Wind-Tunnel Flow Using LU-ADI Factorization Algorithm", NASA TM 100042, Feb. 1988.

10. Chaderjian, N.M., "Navier-Stokes Simulation of Transonic Wing Flowfields Using a Zonal Grid Approach", NASA TM 100039, Jan. 1988.

11. Kaynak, U. and Flores, J., "Advances in the Computation of Transonic Separated Flows Over Finite Wings", AIAA Paper 87-1195, June 1987.

12. Vatsa, V.N. and Wedan, B.W., "Navier-Stokes Solutions for Transonic Flow Over a Wing Mounted in a Tunnel", AIAA Paper 88-0102, Jan. 1988.

13. Jameson, A., Schmidt, W. and Turkel, E., "Numerical Solutions of the Euler Equations by Finite Volume Methods Using Runge-Kutta Time-Stepping Schemes," AIAA Paper 81-1259, 1981.

14. Jameson, A. and Baker, T.J., "Solution of the Euler Equations for Complex Configurations", AIAA Paper 83-1929, July 1983.

15. Martinelli, L., "Calculation of Viscous Flows with Multigrid Methods", Ph.D. Dissertation, MAE Department, Princeton University, 1987.

16. Swanson, R.C. and Turkel, E., "Artificial Dissipation and Central Difference Schemes for the Euler and Navier-Stokes Equations", AIAA Paper 87-1107, June 1987.

17. Thomas, J.L. and Salas, M.D., "Far-Field Boundary Conditions for Transonic Lifting Solutions to the Euler Equations", AIAA Paper 85-20, Jan. 1985.

18. Eriksson, L.E., "Transfinite Mesh Generation and Computer Aided Analysis of Mesh Effects", Ph.D. Thesis, Uppsala University, Sweden, March 1984.

19. Young, C.P., Jr., "Pathfinder Model Program for the National Transonic Facility", NASA CP 2183, 1980, pp. 37-52.

20. Melson, N.D., "Three-Dimensional Transonic Viscous Inviscid Interaction Program", NASA TM 89037, 1986, pp. 3.

21. Bartlett, D.W. ,"Wind-Tunnel Investigation of Several High Aspect Ratio Supercritical Wing Configurations on a Wide Body Type Fuselage", NASA TMX 71996, July 1977.

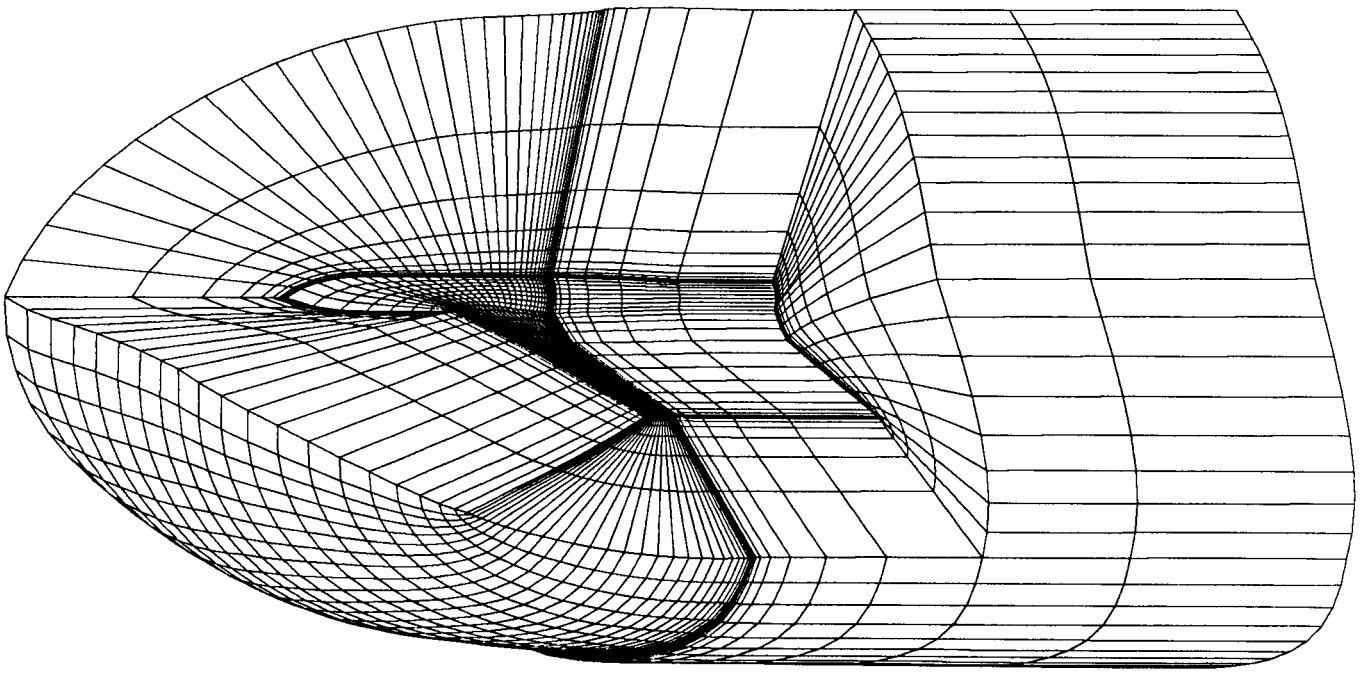

Fig.1 Partial view of Pathfinder wing/fuselage grid

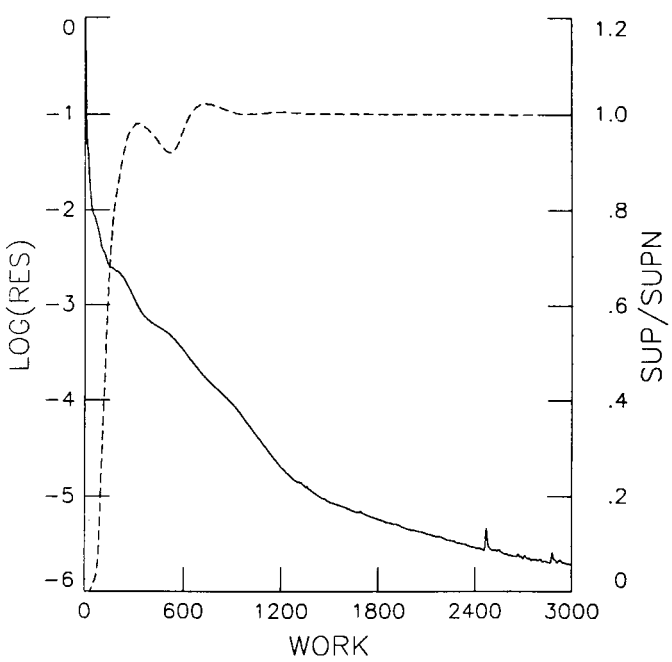

Fig.2 Convergence history for Navier-Stokes calculations on 161x41x41 grid

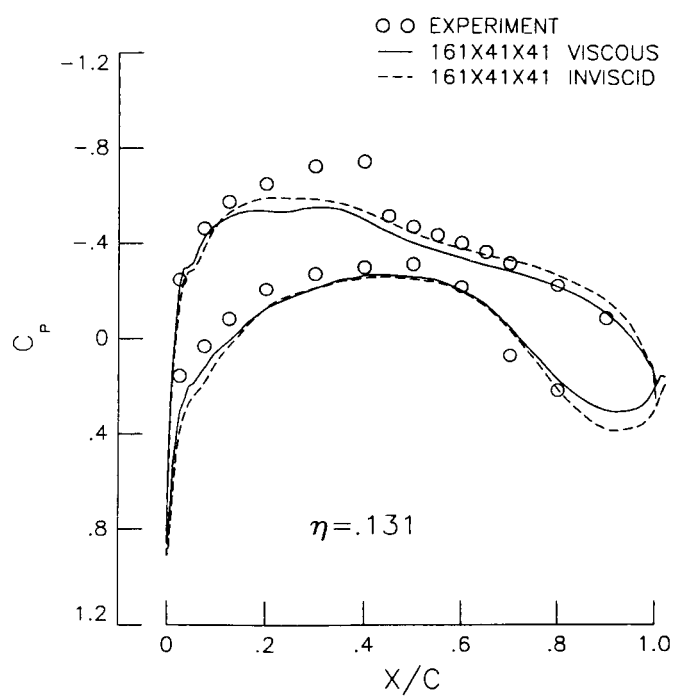

Fig.3 Viscous and inviscid pressure comparisons on 161x41x41 grid with experimental data

(cont.)

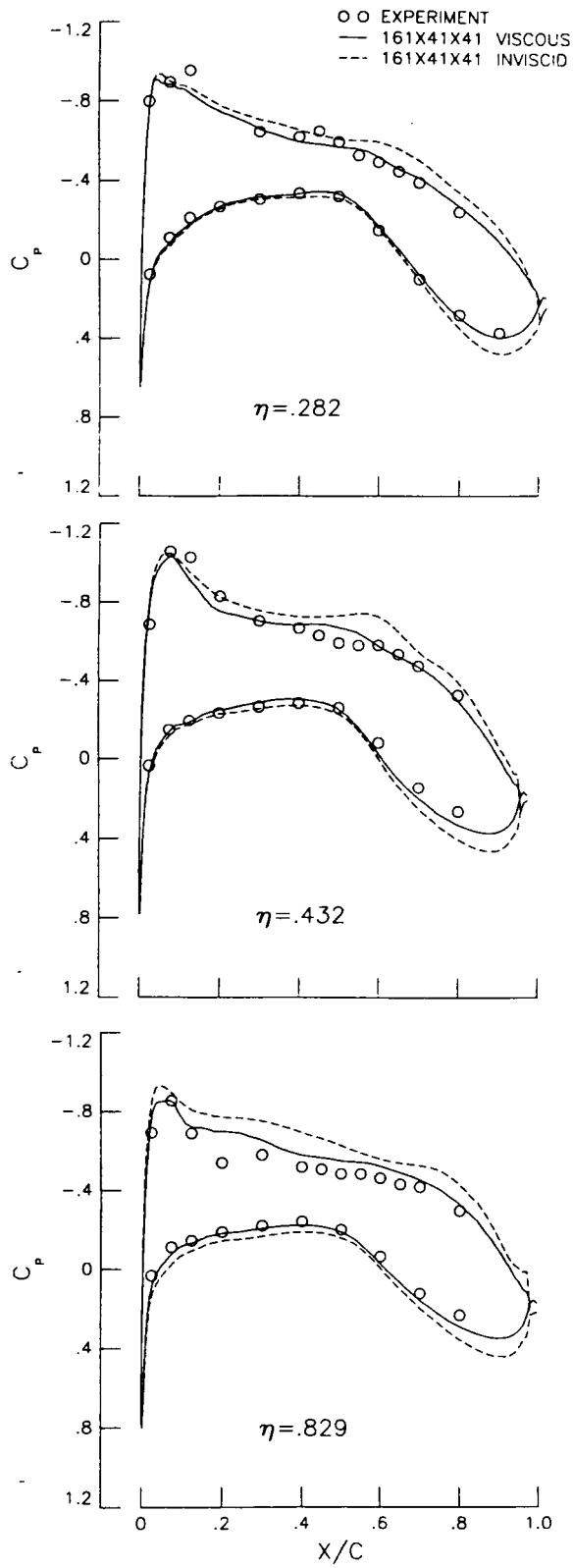

Fig.3 Viscous and inviscid pressure comparisons on 161x41x41 grid with experimental data

(concluded)

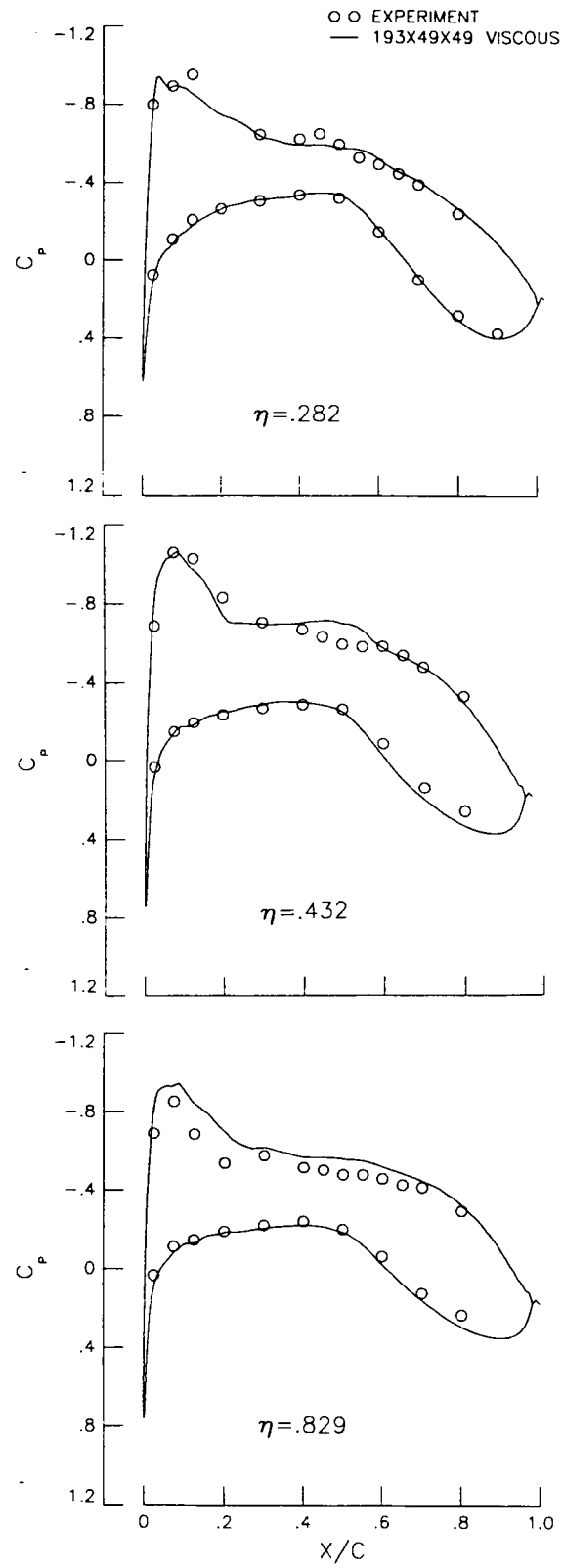

Fig.4 Comparision of viscous pressure distributions on 193x49x49 grid with experimental data

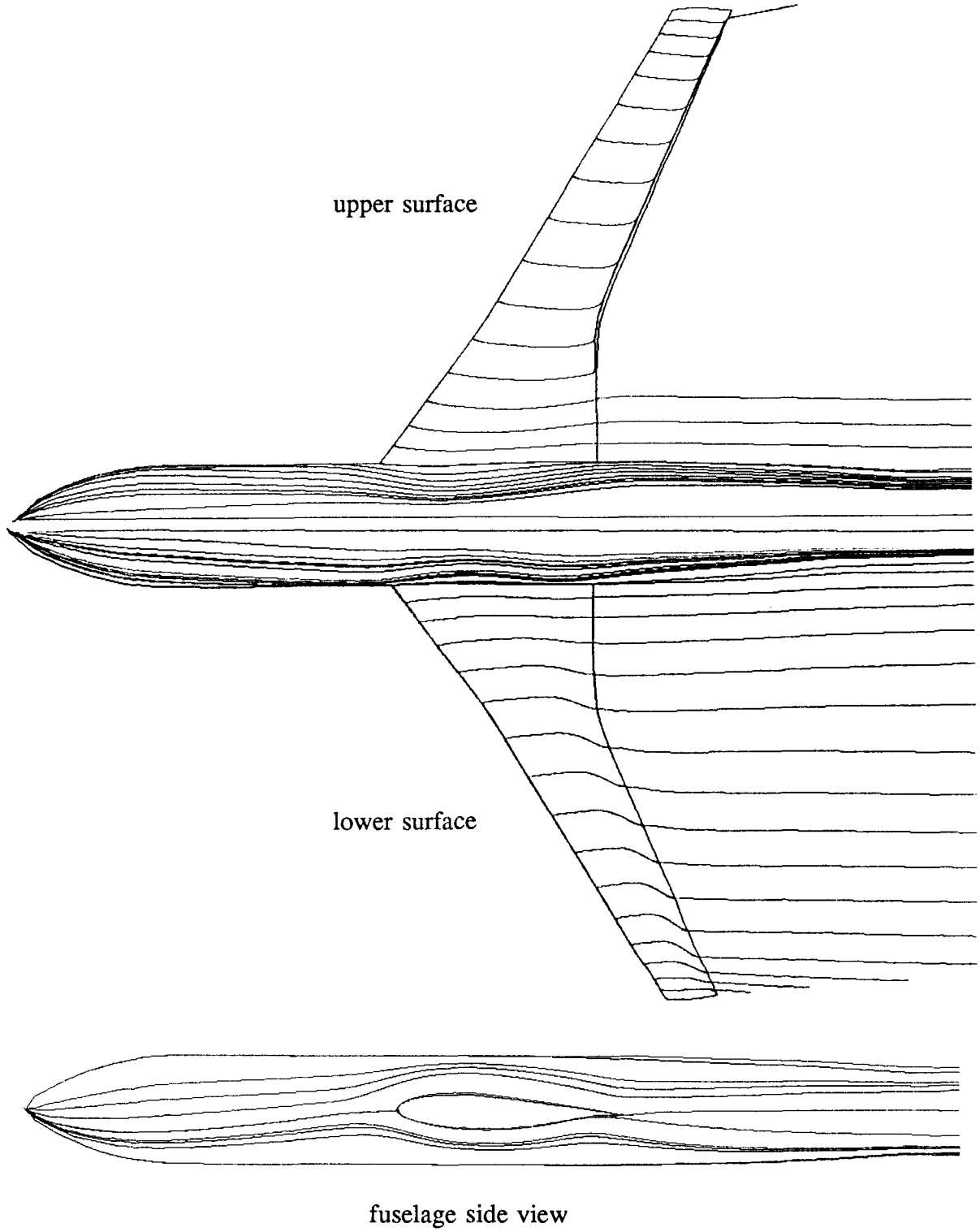

Fig.5 Surface streamline patterns on Pathfinder wing/fuselage configuration

N89-20951

TURBULENCE AND MODELING IN TRANSONIC FLOW

Morris W. Rubesin and John R. Viegas
NASA Ames Research Center
Moffett Field, California

ABSTRACT

A review is made of the performance of a variety of turbulence models in the evaluation of a particular well-documented transonic flow. This is done to supplement a previous attempt to calibrate and verify transonic airfoil codes by including many more turbulence models than used in the earlier work and applying the calculations to an experiment that did not suffer from uncertainties in angle of attack and was free of wind tunnel interference. It is found from this work, as well as in the earlier study, that the Johnson-King turbulence model is superior for transonic flows over simple aerodynamic surfaces, including moderate separation. It is also shown that some field equation models with wall function boundary conditions can be competitive with it.

INTRODUCTION

The accuracy of aerodynamic computations, at realistic Reynolds numbers where boundary-layer turbulence exists, depends on two distinct, yet interrelated elements. These are the numerical and the physical aspects of the solution scheme. Currently, practical aerodynamic problems have to be solved in a manner where the physical aspects of turbulence, present at the Reynolds numbers of interest, are treated with statistical models. Although such turbulence models can be avoided with time- and space-accurate solutions of the dynamics of turbulence, to date such computations have been confined to very simple flow fields at extremely low Reynolds numbers. Their costs are much too high to be considered for design work in the foreseeable future (ref.1), even if sub-grid models can be developed to allow handling the Reynolds numbers of practical interest.

The statistical equations for turbulent flows, corresponding to the basic Navier-Stokes equations for compressible flows, are derived by first expanding the instantaneous values of the dependent variables, such as velocity components, density, and temperature into the sum of mean and fluctuating quantities. The equations are then either averaged in time, over periods much longer than the time scales of the largest turbulence eddies, or are ensemble-averaged. When transonic flows are considered, simpler equations result when the velocity terms are weighted with the local density in the averaging process. Except for existence or absence of the time-dependent terms, the resulting equations have the same form for either

PRECEDING PAGE BLANK NOT FILMED

time- or ensemble-averaging and are called the Reynolds-averaged equations. The dependent variables in these equations are composed of the mean quantities of the velocity and state variables and of moments of their instantaneous quantities. These moments are called Reynolds stresses or heat flux, and it is the evaluation of these quantities that is central to physical turbulence modeling.

In recent years, there has been a considerable expenditure of man-power and computer costs in developing numerical techniques for solving the Reynolds-averaged equations. Today, the flow fields about three-dimensional bodies as complicated as wing-body configurations can be computed in a reasonable time with numerically accurate techniques. The basic algorithms are becoming more efficient and robust, complex meshes are being generated routinely, and codes run sufficiently economically so that mesh-independent solutions can be tested and demonstrated. Color graphics permit detailed and illuminating visualization of the results. Yet despite this enormous rate of progress and maturation of the field of computational fluid dynamics (CFD), the design community still regards the results to be useful only in a qualitative sense and is pressuring the CFD community to calibrate and verify their codes against carefully obtained experimental data so that these codes can be established as accurate design tools.

Because the numerical aspects of a problem can be systematically isolated and improved upon, differences between the output of a good and carefully applied numerical code and experimental data are generally identified as a weakness of the turbulence model. Of course, not all computations are done with the proper care, so that some differences between experimental data and computed results can be numerical as well as physical. That this occurs in published results will be demonstrated by some of the examples shown in the following section.

One attempt to calibrate and verify some existing codes for computing two-dimensional airfoils at transonic speeds was the Viscous Transonic Airfoil Workshop held at the AIAA 25th Aerospace Sciences Meeting at Reno, Nevada, in January 1987, and reported in reference 2. Fifteen different author groups participated, with codes that included 16 Navier-Stokes methods, 2 Euler/boundary-layer methods, and 5 full-potential/boundary-layer methods. The turbulence models variously employed in the Navier-Stokes methods included the classical algebraic eddy viscosity model of Cebeci-Smith (ref. 3), the Baldwin-Lomax algebraic eddy viscosity model (ref. 4), the Johnson-King model (ref. 5), which accounts for turbulence lag with an ordinary differential equation for growth of the maximum shear stress that is then used to scale an algebraic eddy viscosity , and the Coakley q-omega model (ref. 6), the sole representative of the class of two field equation models that define length and velocity scales for an eddy-viscosity evaluation throughout the boundary layer, including the region near the surface. The interactive inviscid-/viscous-layer codes either use the Cebeci-Smith model in the differential equations applying to the boundary layer or an integral model.

The results of this workshop will be summarized in the following section. These results have to be considered to be tentative because they apply to airfoil experiments that experienced wall effects, with an attendant uncertainty in the experimental data, and, also, only a limited number of turbulence models were

ORIGINAL PAGE IS
OF POOR QUALITY

represented in the Navier-Stokes computations. To complement this work, a later section of this paper is devoted to the detailed comparison of computed results, from a single computer code that contains a larger number of turbulence models, with the data of an experiment that is relatively free of wind tunnel wall effects and contains measurements of the turbulence itself. These comparisons, as well as the earlier work with the airfoils, are then used here to develop some conclusions regarding the state of the art of modeling turbulence in two-dimensional transonic flows.

SUMMARY OF VISCOUS TRANSONIC AIRFOIL WORKSHOP

The results of the AIAA Viscous Transonic Airfoil Workshop (ref. 2) are summarized on figure 1, where the coefficient of lift is plotted against the coefficient of drag, expressed in counts, for three different airfoils at various Mach numbers and angles of attack. On this figure, the solid circles represent the experimental data. The open circles represent the inviscid/viscous interaction schemes, without distinction as to whether Euler or full potential equations apply to the inviscid region or whether differential or integral methods are used in the boundary layer. The remaining symbols refer to Navier-Stokes calculations. The open squares represent the Baldwin-Lomax algebraic eddy viscosity model; the squares with ticks represent the Cebeci-Smith model; the diamonds represent the Johnson-King lag model, and finally, the triangle represents Coakley's two-equation model.

Figure 1(a) shows the comparison of calculated CL(CD) with the experimental data on an NACA 0012 airfoil (ref. 7) for three conditions of Mach number and angle of attack, all at a chord Reynolds number of nine million. In the lower left-hand corner, there are shown the data and computed results at $M = 0.7$ and at an angle of attack of 1.49°, which includes wind tunnel interference corrections recommended by the experimenter. All of the computed results yield results that are within 10% of the lift, and only two of the inviscid/viscous interactive methods miss the drag by as much as 20 counts. Thus, for attached flows that are weakly transonic, all the computation methods give reasonable quantitative results.

The datum point and computed values of $C_L(C_D)$, at $M = 0.55$ and a corrected angle of attack of 8.34°, are shown in the upper portion of figure 1(a). Under these conditions, the flow over the top of the airfoil had a supersonic bubble followed by a shock wave at about 0.1 chord, where a slight separation occurred. Again, except for two of the viscous/inviscid interactive schemes, the lift is calculated to be between 1% high and 8% low by the various methods. The closest points to the experimental values in terms of C_L and C_D are the Navier-Stokes solutions using the Baldwin-Lomax and Cebeci-Smith models. It is important to note

that equivalent methods, i.e. those solving, ostensibly, the same conservation and modeling equations, also show significant differences, especially in drag. For example, the two Navier-Stokes codes that utilized the Johnson-King model, the diamonds, show differences of over 50 counts in drag coefficient, although lift only differs by about 1%. Similar differences are seen in the results produced by codes employing the Baldwin-Lomax or Cebeci-Smith models. In this example, it is seen that the numerical differences between codes with supposedly the same turbulence models can be larger than the differences produced by the different turbulence models within a single code. These observations bring into serious question the premise stated earlier that code verification processes will be tests primarily of the physical, rather than the numerical aspects of a code. It appears, in this example, that the numerical aspects of some of the codes may have not been treated with sufficient care to make the solutions of each code numerically "correct", thereby permitting their solutions to be differentiated by their physical modeling.

A point that has to be made here is that there are often some arbitrary decisions made in the application of a particular turbulence model, and that some of the differences shown in the last example could be caused by differences in how those decisions were made rather than related to the numerics. For example, in the Cebeci-Smith model, the displacement thickness is used to define the eddy viscosity in the outer region of the boundary layer. The evaluation of a displacement thickness is unambiguous only if the irrotational flow outside the boundary layer produces a uniform velocity component parallel to the surface. This is not the case in the current example and in most complex flows. In fact, this difficulty in defining the displacement thickness was the underlying reason for the changes that were introduced into the Baldwin-Lomax model. This latter model also can suffer from ambiguities, as its velocity scale in the outer regions of the boundary layer can be multivalued. This results in an imprecise prescription of the eddy viscosity in this region. Another significant choice that can introduce differences in the solutions can be the distance of the first mesh point from the surface. If this point does not lie well within the viscous-dominated region of the boundary layer, errors in the skin friction determined by a particular turbulence model can occur. From the published results, it is not possible to discern what differences such choices may have made in the various solutions shown on the figure.

A third example of flow over a NACA 0012 airfoil is shown in the lower right of figure 1(a). Here the Mach number is 0.799 and the corrected angle of attack is 2.26°. Under these conditions, a shock wave developed on the upper surface at about mid-chord that was sufficiently strong to cause significant boundary-layer separation. Again, ostensibly similar methods yield a spread in the results. In this case, however, the two computations with the Johnson-King model agree rather well and, in terms of both C_L and C_D, are the closest to the experimental result, except for the same interactive method that gave the best results in the previous example (ref. 8). In this case the two-equation model gave poorer results than some of the algebraic eddy viscosity models. Also, as in the previous example, most of the codes gave values of drag much larger than the experimental value.

Figure 1(b) shows $C_L(C_D)$ for the RAE 2822 airfoil for two test conditions in reference 9. The symbols have the same meaning as in figure 1(a). Both sets of experimental conditions were obtained at chord Reynolds numbers of $6.5*10^6$. The data point on the left represents the test results at $M = 0.725$ at a corrected angle of attack equal to 2.92°. A shock wave developed on the upper surface at about $X/C = 0.52$; but its strength was insufficient to separate the boundary layer. Under these conditions, the bulk of the computational results cluster about the experimental datum point within ±10% on either axis. It is surprising that the computation with the Johnson-King model, the diamond, which was generally the more successful model in figure 1(a), yields one of the poorer results in this case. Here too, the differences between supposedly similar methods show differences as large as those identified with different turbulence models, albeit both sets of differences are relatively small.

The point on the right of this figure corresponds to test conditions at higher Mach number and angle of attack, namely, $M = 0.75$ and 3.19°. Under these wind tunnel conditions, the upper surface experiences a shock wave, still at $X/C = 0.52$, but with a strength sufficient to cause boundary-layer separation according to most of the turbulence models. Here the better computed results are due to three viscous/inviscid interactive models, including that of reference 8, and the Johnson-King model in a Navier-Stokes code. The Coakley two-equation model and the eddy viscosity models cluster together at high values of drag.

The third figure of this group, figure 1(c), relates to an experiment (ref. 10) conducted with a supercritical transonic flow airfoil, designated the VA-2, that was developed in West Germany. For this case, the only computed results that exist are from a single code developed by Coakley (ref. 10) which contains the Cebeci-Smith, Johnson-king, and Coakley's q-omega models. In this case, the tests were conducted at a chord Reynolds number of $6*10^6$ and a wind tunnel angle of attack of 1°. The point on the left of the figure represents the datum at $M = 0.73$, where a shock wave developed at $X/C = 0.35$. All the models overpredict the lift, and underpredict the drag. As with most of the cases with the other airfoils, the two-equation model gave results essentially identical with those of the Cebeci-Smith model. The Johnson-King model yielded lift within a few percent of the experimental value, but the drag was 30 counts too low, and no better than the values from the other models.

The point on the right of figure 1(c). corresponds to a Mach number of 0.78, where the shock wave moved to $X/C = 0.645$, rather far back on the airfoil. Again, the lift is predicted well by the Johnson-King model, whereas the other models do much better with regard to drag.

Several conclusions can be drawn from the above discussion of the comparison of calculated $C_L(C_D)$ with the experimental data from three different airfoils in transonic flow. These are as follows:

1. In two-dimensions, some interactive inviscid/viscous methods can be competitive with Navier-Stokes computations containing the better turbulence models.

2. In the Navier-Stokes codes, the algebraic models of Cebeci-Smith and Baldwin-Lomax yield similar results, which are generally equivalent to results from the the more complex Coakley two-equation q-omega model.

3. The Navier-Stokes codes that yield the best results in most of the cases employ the Johnson-King model.

These must be treated as tentative conclusions. Although the data represent the state of the art, they suffer, as do most wind tunnel experiments, from wall interference effects, especially those cases where the airfoils experienced larger regions of separation. A manner of accounting for the wind tunnel effects is to "correct" the geometrical angle of attack to some effective value. In the computations cited above, the effective angles of attack used by the various author groups differed from each other and the reasons for selecting particular values were not stated in reference 2. How much the uncertainty in the angle of attack in each case affects the results shown in reference 2 is not clear. In addition, the assessment in reference 2 suffers from a limited number of turbulence models, and in the case of the two-equation model does not represent the best of that class.

To provide a broader assessment of the state of two-dimensional transonic turbulence modeling, we decided to complement the work described above by computing the flow field of a transonic flow whose data have been shown to be free of wind tunnel interference (ref. 11) and angle of attack uncertainty, and to include additional turbulence models. Since all but one of these models are included in a single Navier-Stokes code, the uncertainties introduced by different codes and solution algorithms are also essentially eliminated. These results are described and discussed in the following section.

TRANSONIC FLOW TURBULENCE MODEL COMPARISONS

Experimental Basis for Comparison

The experiment chosen as the standard for the turbulence model comparisons utilized the transonic flow over a circular arc bump affixed to a hollow circular cylinder aligned with the flow direction (ref. 11). The bump acts aerodynamically in a manner similar to the top surface of an airfoil. The configuration of this wind tunnel model and the flow conditions for which most of the turbulence model comparisons were made are shown on figure 2. The thin-walled cylinder was 15.2 cm in diameter and extended 61 cm upstream of the bump's leading edge. The bump had a chord of 20.32 cm and a thickness of 1.91 cm. At its leading edge, the bump departed from its circular arc shape and blended smoothly into the upstream cylinder. Natural transition occurred on the cylinder, and the resulting turbulent boundary-layer thickness at the leading edge of the bump was about 1 cm. This was sufficiently thick to allow boundary layer measurements, but not so thick as to introduce significant streamwise curvature effects. The measurements included surface pressure, mean velocities, and the Reynolds stresses. These latter data, being profile measurements, allow examination of the reasons for the success or

failures of individual turbulence models. Another decided advantage of using this experiment as a standard is the fact that the wind tunnel model was run in both the NASA Ames Research Center 2 × 2 ft and 6 × 6 ft transonic wind tunnels and that the pressure distributions at the same Mach and Reynolds numbers were essentially the same (ref. 12). This suggests that the data used to test the turbulence models are relatively free of wind tunnel interference. Of course, another advantage of this data set is the lack of ambiguity regarding the angle of attack, as was the case with the airfoils. A shortcoming of using these data, however, is that they were used to develop the Johnson-King model and, therefore, it would be expected that the best performance other models could be made to achieve would be to approach the behavior of this lag model. Therefore, testing a variety of turbulence models with these data can lead to a necessary condition for other turbulence models to satisfy, but is not sufficient for ascertaining the relative performance of turbulence models for flows with separation more massive than occurred within the referenced experiment.

Numerical Procedure

The primary numerical procedure used in computations shown here was originally developed by C. C. Horstman (ref. 13) based on MacCormack's 1981 algorithm (ref. 14). The code has been modified into a series of codes to accommodate the various turbulence models compared in this paper. The MacCormack method used here is basically an explicit second-order, predictor-corrector finite-difference method, modified by an efficient implicit algorithm. In the calculations, the computational domain extended in the flow direction from -140 cm to +90 cm, relative to the onset of the bump. In the radial direction the domain extended from the surface of the model to a radius of 90 cm. The mesh size was 129 × 45, and allowed variable spacing in both the axial and radial directions. In the streamwise direction, the mesh varied from 0.16 cm, near the shock wave, to 12 cm at the downstream boundary. Normal to the surface, an exponentially stretched mesh was used that allowed the first mesh point from the surface to lie well within the sublayer, for those cases where integrations were performed to the surface. When wall functions were used, the near wall mesh centers were generally well into the fully turbulent flow, except at the stations close to and within the separation zone.

The upstream boundary conditions were prescribed by uniform free stream conditions, with the total pressure and temperature held constant and the static properties found from relationships based on the method of characteristics. The downstream conditions set all axial gradients to zero. In all cases, the surface boundary conditions were zero velocity and near adiabatic wall temperature. Uniform free stream conditions were applied at the far-radial boundary, as justified in reference 15.

As discussed in the next section, the Wilcox-Rubesin turbulence model (ref. 16) required a different numerical algorithm, namely MacCormack's 1976 hybrid method, reference 17.

Turbulence Models Considered in Comparative Analysis

In this comparison of turbulence models, the following turbulence models were applied: Cebeci and Smith (ref. 3), Johnson and King (ref. 5), Jones and Launder (ref. 18), Viegas and Rubesin (refs. 19 and 20), Coakley (refs. 6 and 21), and Wilcox and Rubesin (ref. 16). One feature characteristic of all these models is that Reynolds stresses are expressed in terms of an eddy viscosity in a Boussinesq constitutive relationship.

The Cebeci-Smith turbulence model divides the boundary layer into an inner and outer zone, where the eddy viscosity is expressed algebraically in each layer. In the inner layer, the eddy viscosity is expressed with a length scale that is the distance from the surface and and with a velocity scale that is the shear velocity at the wall. In the outer layer these scales are the displacement thickness, computed neglecting density variations, and the boundary-layer edge velocity. The extent of the inner layer is determined by requiring the minimum of the eddy viscosities corresponding to the inner and outer layers be used at each position from the surface. This model has become the standard for use with attached boundary-layer flows. In its current application (ref. 15) the van Driest damping function, used to account for viscous effects in the sublayer and buffer layer, was corrected for non-zero values of the streamwise pressure gradient.

Next in mathematical complexity is the turbulence model of Johnson and King. This model also divides the boundary layer into two zones where the eddy viscosities are expressed algebraically. In the inner layer, however, the velocity scale used in this model depends on the maximum shear stress within the boundary layer, not the wall shear stress (e.g. expressed as shear velocity) as in the Cebeci and Smith model. This maximum shear stress is found from the solution of an ordinary differential equation that represents the rate of the development of the maximum shear stress with distance along the surface. The equation is expressed conveniently in terms of the departure of shear stress and eddy viscosity from their corresponding quantities in equilibrium with the mean motion. Compared to the Cebeci and Smith model, the Johnson and King model contains two additional modeling coefficients, one that scales the rate of development of the maximum shear stress and another that scales the effect of turbulence diffusion within that rate equation. The values of these coefficients were chosen by comparison with the data of reference 18, as well as with those from the bump experiment (ref. 11). The computed results using this model are from reference 5.

The next turbulence model to be discussed is that of Jones and Launder, reference 19. This model is an example of turbulence models that employ two additional partial differential field equations to evaluate the velocity and length scales of the turbulence, thereby allowing for the rate processes in the development in the local state of the scales of turbulence. In this model, the dependent variable in the first equation is the kinetic energy of turbulence, whereas that in the second equation is the rate of dissipation of the turbulence kinetic energy. In establishing the eddy viscosity, the kinetic energy of turbulence acts as the velocity scaling parameter, while the length scale is composed of an algebraic combination of the kinetic energy and the rate of dissipation of kinetic energy. This model also

possesses the feature of special viscous terms in these turbulence field equations that allow integrations to the surface. The model has been extended to account for compressibility, necessary in the computation of transonic flows, by use of mass weighting the turbulence equations and allowing for non-zero mean velocity divergence in the constitutive relationship for the eddy viscosity.

It has been shown that the popular Jones-Launder turbulence model yields poor values of skin friction in the presence of a shock wave in transonic flow, and that the introduction of wall functions, originally designed to save computation costs, surprisingly improved the prediction of skin friction (ref. 20). Accordingly, the compressible-flow, wall-function models of Viegas and Rubesin were applied to the Jones-Launder model for the test case considered here. These wall-function approaches allowed use of fewer mesh points normal to the surface and reduced the stiffness of the turbulence equations; both effects lead to considerable saving in computation costs over that of the Jones-Launder model itself.

These wall-function methods depend on establishing the wall shear from a knowledge of the mean velocity at the center of the first mesh volume off the surface and from the turbulence kinetic energy at the centers of the first two points off the surface. The latter kinetic energy information reflects the local axial pressure gradient along the surface. In addition, these wall-function methods rely on careful integrations of the production and dissipation of the kinetic energy across the first mesh volume in order to have the mean kinetic energy identified with the mesh volume reflect the presence of the sublayer and buffer layers that exist there. In the first of the wall function methods (ref. 20), the "law of the wall" was used with fixed coefficients appropriate strictly for flat plates at constant pressure. In the second wall function method (ref. 21), these coefficients were allowed to vary, reflecting the behavior of the sublayer to strong axial pressure gradients, and in addition, provisions were made for the presence of the lower portion of the wake region of the boundary layer. These modifications are influential only in regions approaching separation, and in the separation zone, and immediately after reattachment. It should be noted that it was the added viscous terms (the so-called "low Reynolds number terms") which allowed integrations to the surface in the Jones Launder model that caused its difficulties and were eliminated through the use of the wall function approaches.

Another turbulence model used in these comparisons was that of Wilcox and Rubesin (ref. 16). This model is similar to that of Jones and Launder in that two turbulence field equations also are employed to yield turbulence scale quantities on which to base the eddy viscosity. In this model, the variable used to develop the length scale is the specific rate of dissipation, i.e. the rate of dissipation divided by the kinetic energy. The turbulence model differs from the Jones-Launder model in another very significant way; it does not require additional viscous terms to permit integrations to the surface, but accomplishes this through the use of damped coefficients in the high Reynolds number terms. A drawback of this turbulence model is that the second equation uses the square of the specific dissipation rate as its dependent variable. This is a quantity that varies with distance from the surface to the fourth power, a variation that is too rapid for the second-order

finite differencing used in the computations to be accurate in the vicinity of the surface. To avoid inaccuracies, very near the surface an analytical expression is used to evaluate the dissipation rate variable. This analytical expression, however, causes instabilities at the match point with the numerical solution of the second modeling equation. In addition, this model has particularly stiff mathematical characteristics when wall functions are not used. These instabilities and stiffness characteristics prevented this model from being incorporated into the same algorithm as was used for all the other turbulence models (ref. 20). Consequently, the results presented here for the model of Wilcox and Rubesin were obtained with the older, less efficient, more complicated, but more robust hybrid code of MacCormack (ref. 17). The results of this model shown here are restricted to the surface pressure distribution, the only recoverable results available to the authors (ref. 15).

To relieve the near-surface numerical difficulties associated with the Wilcox-Rubesin model, Coakley (refs. 6 and 22) developed turbulence models in which the dependent variables of the turbulence field equations were the slower varying square root of the kinetic energy and the first power of the specific dissipation rate. Coakley introduced low Reynolds number and damping terms that reduced or eliminated the types of unusual stiffness associated with the Wilcox-Rubesin and the Jones-Launder turbulence models and allowed efficient computation. In defining the coefficients of these new equations, Coakley transformed those of Jones and Launder into what is called here "Coakley-1" and those of Wilcox and Rubesin into "Coakley-2". Recall that the airfoil computations shown earlier were based on the Coakley-1 turbulence model.

Results of Turbulence Model Comparison

Figures 3(a) and 3(b) show the comparison of computed results based on the variety of turbulence models with the experimental surface-pressure data obtained in reference 11. The figures display the pressure coefficient distribution over the downstream half of the bump followed by one-half chord length of the cylinder. On these figures the experimental data, corresponding to a Mach number of 0.875 and a Reynolds number of $13.1 \times \times 10^6$, are represented by the open circles, whereas the computed results are indicated with solid lines. The same data points are common to all the figures. Figure 3(a) compares the turbulence models of Cebeci-Smith, Johnson and King, and Coakley's two versions of the two equation model. As expected, the Johnson-King model produces excellent results, in both locating the position of the shock wave and representing the pressure levels in the region of separation (see table 1). On the other hand, use of the classic Cebeci-Smith turbulence model yields a shock-wave location that is about 1/10th chord downstream from the experimental value, and much higher pressures in the region of separation. The results based on the use of the Coakley-1 model are quite similar to those of the Cebeci-Smith model. This behavior illustrates why Coakley's higher-order model results in the airfoil calculations shown in figure 1 were so similar to those from the Cebeci-Smith or Baldwin-Lomax algebraic models. The modified model, Coakley-2, shows some improvement in establishing both the location of the shock wave and in

the pressure level in the vicinity of separation. Figure 3(b) shows the same curves for the turbulence models of Jones-Launder, Wilcox-Rubesin, and three-examples of the Viegas-Rubesin wall function methods as applied to the Jones-Launder model. It is observed that the Jones-Launder model yields results quite similar to those of Coakley-2, with a slightly better prediction of the shock location but with essentially the same pressures in the separation zone. The other two-equation model, Wilcox-Rubesin, shows pressure coefficients that are uniformly lower than the others. These latter results are from computations made with the older hybrid code in which upstream boundary conditions were not consistent with requirements along characteristic lines as is made in the more modern codes. If the computed results from the Wilcox-Rubesin model are moved downward, i. e. the C_p are lowered uniformly, they agree essentially with those from Jones-Launder or Coakley-2. These comparisons reveal that the two-equation turbulence models, except for Coakley-1, yield about the same pressure-distribution results regardless of dependent variable used in the second scale equation or of the differences in the details of how the equations are modified to permit integration to the surface.

The remaining figures on figure 3(b) demonstrate the results from computations employing the wall-function techniques of references 20 and 21 with the Jones-Launder turbulence model. These techniques can reduce computation costs by about an order of magnitude (ref. 20). In these cases, the slightly low values of C_p shown ahead of the shock wave are believed to be caused by use of slightly high value of free-stream dynamic pressure. The basis of this observation is that comparisons directly in pressure show better agreement.

The figure on the lower right represents the results from the simpler wall function version, reference 20. Two curves are presented, representing the results corresponding to different sizes of the initial mesh volumes adjacent to the surfaces. These are identified by the value of y^+, the dimensionless wall distance corresponding to the center of the mesh volume and values of the wall shear stress about a chord upstream of the bump's leading edge. Because an exponential version of the logarithmic "law of the wall" is used to define surface shear in this wall-function technique, it is desirable to assure that the y^+ lies well within the fully turbulent flow, that is, to have a value greater than about 30. Accordingly, two values of y^+ were tried, namely $y^+ = 140$ and $y^+ = 60$. It is observed that the computed location of the shock wave is sensitive to the choice of the y^+. The pressure level in the separation zone, however, is not as sensitive to the different y^+. The case with $y^+ = 60$ gives results that are a decided improvement over those from the original Jones-Launder model. For this wall-function scheme, it appears that the size of the first mesh cell adjacent to the surface becomes another modeling decision, or constant, in the process. Partially to remedy this matter, the second wall-function scheme was developed in reference 21. While reducing the sensitivity of the results to the value of y^+, the effect was not entirely eliminated and the y^+ still remains a modeling parameter. The results with $y^+ = 140$ and the improved wall-function technique are shown in the lower-left of the figure. These results are very good in establishing both the location of the shock wave and pressure levels in the region of separation, and are the nearest rival to the Johnson-King model. With $y^+ = 60$, for this wall-function model, values of

pressure coefficient indicated a movement of the predicted location of the shock wave of $x/c = 0.02$ from the $y^+ = 140$ case, and otherwise acted similarly to the $y^+ = 60$ case of wall function 1. The $y^+ = 60$ case with the wall function 2 model also showed some waviness in the pressure coefficient in the separated zone that we believe was caused by the absence of a buffer region in this model.

When the values of skin friction evaluated by the various models are compared, it is found that they differ to a very large extent. Unfortunately, no measurements of skin friction were made in the experiment of reference 11 so that no conclusions regarding the relative merit of the the various turbulence models regarding skin friction can be made. The experiment did contain measurements of the mean points of separation and reattachment obtained by means of the oil film technique. These data and the points that bound the regions in the computations where skin friction is negative (i.e., the separation zone) are indicated in table 1. Again, the superiority of the Johnson-King model is demonstrated as it almost duplicates the experimental data. The wall-function techniques with chosen values of y^+ are next in performance, showing reattachment locations on the cylinder roughly 0.1 of the bump's chord upstream of the measured location. Finally, all of the two-equation models with integration to the surface show separation points approximately 0.3 chord downstream of the measured values and reattachment points about 0.1 chord upstream.

Figure 4 shows the development of the displacement thickness over the rear half of the bump and on the downstream cylinder. Recall that it is the displacement thickness that produces the influence of the viscous region upon the inviscid flow. As in figure 3, the experimental data are shown with open circles and are repeated on each of the graphs to facilitate the comparison of the various models. In figure 4(a), it is seen that the classic Cebeci-Smith model gives results that are quite inferior to the Johnson-King model. The Coakley-1 model, in this case, performs a bit better than does the Cebeci-Smith model, and the improvements in Coakley-2 are quite significant in the region of rising displacement thickness. In figure 4(b), the Jones-Launder model is shown again to yield results essentially the same as those of Coakley-2. The Viegas-Rubesin wall-function-1 approach with $y^+ = 140$ produces similar results. The other wall-function approaches, with their selected values of y^+, yield results for displacement thickness that surprisingly are even better than those of the Johnson-King model.

Another interesting variable with which to compare the performance of the various turbulence models is the the shape factor. It is a quantity that enters the momentum integral equation used in some of the inviscid-viscous interactive schemes, and also can be used to infer the behavior of the momentum thickness, since all of the turbulence models yielded reasonably accurate values of the displacement thickness. Figure 5 shows the development of the shape factor over the latter half of the bump and on the downstream cylinder. One feature evident from all the computed results is a dip in the shape factor at the onset of separation, something that is not evident in the experimental data. The cause of this is unknown. Other than this, it is seen in figure 5(a) that the shape factor given by the Johnson-King model generally behaves the best of the models. The Cebeci-Smith and the Coakley-1

models fail to develop the steep rise in the shape factor evident in the data in the separation region. This is evidence that the momentum integral computed by these models in this region must be much higher than the actual. This behavior is corrected to some extent by the Coakley-2 model and the Jones-Launder model shown in figure 5(b) The wall function models give mixed results. The case of the Viegas-Rubesin wall function 1 with $y^+ = 60$, which gave the better results for the other variables considered previously than did the case with $y^+ = 140$, overshoots the data in the region just aft of the point of separation. This shows that the local momentum thickness computed with $y^+ = 60$ must be yielding low values of the momentum thickness there. The Viegas-Rubesin wall-function-2 computation with $y^+ = 140$ shows similar tendencies but behaves quite well over the downstream cylinder. The irregularities shown in this latter figure are believed to be the result of locally low values of the y^+ in the region of separation. This can allow the center of the first mesh volume off the surface to be either within a fully turbulent and/or fully laminar zone of the boundary layer (one of the features that is permitted by this version of the wall function models). Blending these distinct layers with a buffer layer could possibly have avoided the bumps and valleys of the computation.

To further illustrate the relative behavior of the various turbulence models, the velocities in the axial direction predicted by the computations are compared in figure 6 with the corresponding measured data. All the profiles are at stations within the experimentally determined separation zone over the trailing-edge region of the bump and the cylinder downstream. The velocities are normalized by the free-stream velocity and plotted as functions of the vertical distance from the surface expressed in centimeters. With linear coordinates, a plot such as this only shows the behavior of what is usually termed the outer portion of the boundary layer. The sublayer and buffer layer cannot be seen distinctly without recourse to logarithmic plotting. These profiles are shown at values of $x/c = 0.75$, 0.875, 1.00 (the trailing edge of the bump), and 1.125. Recall that separation and reattachment was indicated at $x/c = 0.67$ and 1.17. At $x/c = 0.75$, roughly 1/10th chord downstream of the mean separation, it is surprising that the Johnson-King model does not show the best agreement with the velocity data in view of its success in predicting the surface pressure and integral thicknesses. A possible explanation of this behavior is given in reference 12 where it is shown that better agreement between the velocity computations and the experimental data can be achieved by shifting the computed results downstream by only about 0.03 chord. Another way of arguing this point is to note that at $x/c = 0.75$ very rapid changes to the flow field are occurring so that small misalignments between the computations and the experimental data in the streamwise direction cause large apparent profile errors. Subject to this observation as a caveat, it is found that the Coakley-2 and Jones-Launder models give the best fits to the velocity data at this station. Since the flows for these latter models have not yet separated at this station, their agreement with the far field velocity data shows how sensitive near-wall turbulence modeling is to the prediction of surface phenomena. Again, there are similarities in the results of the Cebeci-Smith and Coakley-1 models, and in the wall-function models 1 and 2 with $y^+ = 60$ and 140, respectively. Errors in the velocities toward the outer part of the boundary layer are indications of poor representation of the surface pressure at a particular station, and indicate the largest errors for the

Cebeci-Smith and Coakley-1 models. This observation is consistent with the pressure coefficient results shown on figure 3(a) at $x/c = 0.75$.

The remaining velocity profiles are at stations where flow-field changes are less rapid, and are more indicative of the performance of the various turbulence models. Except for the Cebeci-Smith and Coakley-1 models, all the turbulence models give results for the velocity profiles that are very representative of the experimental data. Apparently, far-field velocity data in and near a region of separation are not critically sensitive to turbulence models employed. Of course, in the near-wall region, this is not the case as the skin friction demonstrated by the various models differed considerably in magnitude and even in sign at some stations. Also, the position of separation is sensitive to the near-wall velocity behavior, and also differed considerably with the different turbulence models.

A final comparison of the performance of the various models is shown in figure 7, where profiles of the Reynolds shear stress parallel to the streamwise direction are compared with the corresponding experimental measurements. Recall that a linear plot in distance from the surface shows principally the behavior of the outer part of the boundary layer. The stations shown cover the experimental region of separation and are the same as those used for the mean velocities in figure 6.

The most striking feature of the series of plots on figure 7 is the similarity of the general behavior all the turbulence models. This behavior is rather surprising when consideration is given to fact that the zones of separation predicted by many of the models had little relationship to the experimental zone covered by these figures. For example, the Coakley-1 model barely shows any separation, yet the Reynolds stresses predicted by it are not that grossly different from those of the Johnson-King model. From this it can be inferred that the Reynolds stresses outside the viscous sublayer and buffer region are rather insensitive to the presence or absence of separation. This observation is consistent with the concept in the algebraic eddy viscosity models that the the proper scaling in the outer part of the boundary layer is the displacement thickness and the velocity at the boundary layer edge, which are more similar in the computations based on the various models than are their zones of separation.

In detail, it is observed that none of the models yields values of Reynolds shear stress as large at the measured values at the downstream stations. The Cebeci-Smith and Coakley-1 models perform the poorest in this regard. The more successful models, however, are those whose peaks of shear stress are larger in magnitude and occur closer to the distances from the surface shown by the maxima in the experimental data. Modeling the outer region of the boundary layer seems to be important in this flow, and may explain why models that account for the out of equilibrium conditions there, through a lag equation or field equations, are the more successful.

CONCLUDING REMARKS

It is generally accepted that there is no unique way of modeling turbulence in transonic flow fields. Consequently, a model can only be gauged by its degree of success in computing a particular type of flow field. To do this, it is necessary to eliminate, as much as it is possible to do so, experimental errors in the data used for model assessment. We tried to do this here by dealing with a two-dimensional flow field that was free of uncertainties due to wind tunnel wall effects and to unknown angles of attack, in contrast to the ambiguities that exist in the current crop of airfoil experiments that were used to assess computation codes and turbulence models earlier. Also, past assessments dealt only with a limited number of turbulence models; two algebraic eddy viscosity models, a lag model that determines the growth of the maximum shear stress along a surface that is then used to scale an algebraic eddy viscosity across the boundary layer, and a single version of two-equation modeling where the variables upon which an eddy viscosity is evaluated are found from field equations. In the present paper, five more two-equation eddy viscosity models have been considered, two of which involve the use of wall functions to represent surface boundary conditions and avoid carrying integration to the surface.

The preceding descriptions of the comparative performance of these turbulence models reflect the two main underlying turbulence modeling philosophies. One approach argues that for a specific class of flows it is best to begin with a simple model and adapt it just enough to capture the most essential elements of the new flow. The other approach is to apply a so-called "universal" model. These employ field equations for their basic variables and can be applied without change to any type of flow. In principle, a good version of the latter type of model would yield accurate quantitative results for a disparate variety of flows. In practice, however, it is found that while the models can be applied rather easily computationally to new situations, the results they give in particular cases are often not as accurate as would be desired for aerodynamic design purposes.

The Johnson-King model is representative of the first approach applied to the development of an accurate model for the prediction of transonic flows over simple aerodynamic bodies. A key element in its development was the recognition that it was essential to account for the nonequilibrium between the turbulence and mean flow in the outer portions of the viscous layers. In contrast, the earlier models of Cebeci-Smith and Baldwin-Lomax assume complete equilibrium between the turbulence and the mean motion. Johnson and King introduced nonequilibrium in the streamwise direction by utilizing an equation to evaluate the rate of development of the maximum shear stress in the boundary layer. This maximum shear stress was then used to scale the eddy viscosity in algebraic expressions across the boundary layer. This latter step implies an equilibrium in the direction normal to the surface. The model required the introduction of two additional modeling constants beyond those used in the algebraic eddy viscosity models. As was shown earlier, this Johnson-King model could be adjusted to produce excellent results for the mean velocities and surface pressures over the axisymmetric bump. This is not surprising as these

experimental data were used to define the additional modeling constants used in the model. Significantly, however, it was found that this model gave good comparisons with low-speed data (ref. 23) and also, as was demonstrated earlier, generally produced the best comparisons among the Navier-Stokes methods with the three sets of independent airfoil data. This suggests that the Johnson-King model has the breadth to be applied with confidence in a predictive sense to some new transonic flow provided it has separation zones comparable in size to those in the flow over the transonic bump.

Several examples were shown of the performance of "universal" two-equation eddy viscosity models integrable to the surface (refs. 6, 19, and 22). These models utilized coefficients that were based on flows in pipes or attached boundary layers, and were unmodified to reflect the requirements of transonic flows with shock waves. Although these models allow the turbulence and mean motion to be out of equilibrium in both the streamwise and normal directions, it was found that the Coakley-1 model gave essentially the same overall results as the equilibrium model of Cebeci-Smith. Note that computations of the transonic flow over the bump have not been made with the Baldwin-Lomax model, but, based on past modeling experience (ref. 2) this model is expected to yield results similar to those of the Cebeci-Smith model. Some improvement occurred with the Coakley-2 model, where the modeling coefficients were altered from those of Coakley-1, but the results were no better than given by the earlier Jones-Launder model. It is not clear why the Coakley-2 model, designed to account more accurately for separated flows at supersonic speeds, did not give more accurate results for the transonic flow considered here. Perhaps the level of effort of trying to improve the Coakley-1 model was less than was exerted by Johnson and King; or the act of improving the field equation models is just inherently more difficult than with the simpler models. In either case, the Coakley-2 model still leaves something to be desired in the prediction of transonic flows.

The other models shown were applications of the use of wall functions to the Jones-Launder model. Implicit in the use of wall functions is the assumption that the near-wall region is one where equilibrium between turbulence and mean flow exists. These wall functions were developed principally to save computer effort by reducing the numerical stiffness and the number of mesh points employed. They have not been tailored for any particular flow or two-equation turbulence model and are quite general. The wall functions have been adapted to three two-equation models of turbulence (two k,epsilon models and the Wilcox-Rubesin model) and successfully applied to a variety of complex flows and over a range of Mach numbers. Generally, the wall functions have made the computer codes more robust and, with a judicious choice of the size of the first mesh volume, can obtain enhanced agreement between the numerical results and the experimental measurements. Such improvements had previously been observed in several transonic duct flow calulations (refs. 20 and 21). Their use here, with dimensions of the first mesh volume that resulted in values of $y^+ = 60$ and 140 for Viegas-Rubesin wall functions methods 1 and 2, respectively, also reduced computation costs and improved the comparison of the computations with the experimental results of the transonic bump flow. It should be noted that these wall functions were of the type that perform accurate integrations

of the production and dissipation of the turbulence kinetic energy within the first mesh volume off the surface. This allows accounting for the larger fraction of the viscous-flow region compared to fully turbulent flow region within this mesh volume that occurs at the stations in or near the separated flow.

It can be concluded from this review that algebraic eddy viscosity turbulence models that assume complete equilibrium between the turbulence and the mean motion, when coupled with the Navier-Stokes equations, are inadequate to yield the accuracies in the calculation of transonic flows that are necessary for aerodynamic design. Based on comparisons with airfoil data and over an axisymmetric bump, it has been found that the Johnson-King model remedied this situation in two dimensional flows by merely adding the complexity of an additional ordinary differential equation to account for the non-equilibrium growth of the maximum shear stress in the boundary layer along the surface. Equilibrium of the turbulence and mean flow is still assumed across the boundary layer. Of course, if an airfoil design contains a surface jet, or multiple control surfaces, situations can develop within the boundary layer where more than one maximum in shear stress can occur and ambiguity in the model develops. Also, the extension of the concept of basing algebraic eddy viscosities on a maximum shear stress to three-dimensional flows will require considerable development and loss of simplicity.

Two-equation models that can be integrated to the surface require further careful development before they can be considered to be predictive models. Emphasis in this development should be on the improvement of performance in the near-wall regions under severe adverse streamwise pressure gradients and in regions of separation. The effort to do this is worthwhile because of the particular adaptability of this class of closure models to new situations. Some examples of this are: three-dimensionality, surface jets, and multi-element airfoils and wings. In design computations involving many changes of parameters, the cost savings introduced by wall functions should not be overlooked. Thus, wall functions should be improved to further reduce the sensitivity of the results to differences in the dimensions of the first mesh volume off the surface.

It is also significant that, to date, some of innovations to turbulence modeling that have shown some promise in low-speed, incompressible flows have not been applied yet to transonic flows. One example of this is the algebraic stress model that eliminates the controversial eddy viscosity constitutive relationship (ref. 24). This approach has inherent advantages when isotropies in the Reynolds stresses are expected to depart from those associated with two-dimensional shear flows. Examples of situations where this is likely to happen are three-dimensional flows, regions of intense streamwise curvature, and in the presence of shock waves. Another example of developments in incompressible flow computations is the four-equation approach, where the shear stress, the most important Reynolds stress, is determined through an additional field equation and the different roles played by the large and small eddies of turbulence, which primarily exchange momentum and dissipate turbulence, respectively are introduced through another kinetic energy equation (ref. 25). In addition, it has been shown that modeling which represents each Reynolds stress with a field equation and utilizes a single-scale equation can

be applied at acceptable computer costs to transonic flows (ref. 26), and fine-tuning of this approach to improve its accuracy is warranted not necessarily as a design tool, but as a standard of comparison and guide for the simpler approaches. Finally, in view of the success of some of the interactive inviscid/viscous methods in predicting the airfoil lift and drag coefficients of figure 1, it would be interesting to see these methods applied to the transonic bump flow and to compare the results to those presented here that were based on solutions to the Reynolds-averaged Navier-Stokes equations.

REFERENCES

1. Rubesin, M. W.: Turbulence Modeling. Supercomputing in Aerospace, NASA CP 2454, 1987.

2. Holst, T. L.: Viscous Transonic Airfoil Workshop Compendium of Results. AIAA Paper No. 87-1460, June 1987.

3. Cebeci, T. and Smith, A. M. O.: Analysis of Turbulent Boundary Layers. Academic Press, 1974.

4. Baldwin, B. S. and Lomax, H.: Thin-Layer Approximation and Algebraic Model for Separated Turbulent Flows. AIAA Paper 78-257, Jan. 1978.

5. Johnson, D. A. and King, L. S.: A Mathematically Simple Turbulence Closure Model for Attached and Separated Turbulent Boundary Layers. AIAA Journal, Vol. 23, Nov. 1985, pp. 1684-1692.

6. Coakley, T. J.: Turbulence Modeling Methods for the Compressible Navier-Stokes Equations. AIAA Paper No. 83-1693, July 1983.

7. Harris, C. D.: Two-Dimensional Aerodynamic Characteristics of the NACA 0012 Airfoil in the Langley 8-Foot Transonic Pressure Tunnel. NASA TM 81927, 1981.

8. Drela, M. and Giles, M. B.: Viscous-Inviscid Analysis of Transonic and Low Reynolds Number Airfoils. AIAA Paper No. 87-0424, Jan. 1987.

9. Cook, P. H., McDonald, M. A., and Firmin, M. C. P.: Aerofoil RAE 2822-Pressure Distributions, and Boundary Layer and Wake Measurements. AGARD-AR-138, 1979.

10. Mateer, G. G., Seegmiller, H. L., Coakley, T. J., Hand, L. A., and Szodruch, J.: An Experimental Investigation of a Supercritical Airfoil at Transonic Speeds. AIAA Paper No. 87-1241, June 1987.

11. Bachalo, W. D. and Johnson, D. A.: Transonic, Turbulent Boundary Layer Separation Generated on an Axisymmetric Flow Model. AIAA Journal, Vol. 24, No. 3, March 1986, pp. 437-443.

12. Johnson, D. A.: Transonic Separated Flow Predictions with an Eddy-Viscosity/ Reynolds-Stress Closure Model. AIAA Journal, Vol. 25, No. 2, February 1987, page 252.

13. Johnson, D. A., Horstman, C. C., and Bachalo, W. D.: Comparison Between Experiment and Prediction for a Transonic Turbulent Separated Flow. AIAA Journal, Vol. 20, No. 6, June 1982, pp. 737-744.

14. MacCormack, R. W.: A Numerical Method for Solving the Equations of Compressible Flow. AIAA Journal, Vol. 20, Sept. 1982, pp. 1275-1281.

15. Horstman, C. C. and Johnson, D. A.: Prediction of Transonic Separated Flows. AIAA Journal, Vol. 22, No. 7, July 1984, page 1001.

16. Wilcox, D. C. and Rubesin, M. W.: Progress in Turbulence Modeling for Complex Flow Fields Including the Effects of Compressibility. NASA TP 517, April 1980.

17. MacCormack, R. W.: An Efficient Numerical Method for Solving the Time-Dependent Compressible Navier-Stokes Equations at High Reynolds Number. Computing in Applied Mechanics, AMD Vol. 18, The American Society of Mechanical Engineers, 1976; also NASA TM X-73,129, 1976.

18. Jones, W. P. and Launder, B. E.: The Prediction of Laminarization with a Two-Equation Model of Turbulence. International Developments in Heat Transfer, Vol. 15, 1972, pp. 303-314.

19. Viegas, J. R., and Rubesin, M. W.: Wall-Function Boundary Conditions in the Solution of the Navier-Stokes Equations for Complex Compressible Flows. AIAA Paper No. 83-1694, July 1983.

20. Viegas, J. R., Rubesin, M. W. and Horstman, C. C.: On the Use of Wall Functions as Boundary Conditions for Two-Dimensional Separated Compressible Flows. AIAA Paper No.85-0180, Jan. 1985.

21. Vuong, S. T. and Coakley, T. J.: Modeling of Turbulence for Hypersonic Flows With and Without Separation. AIAA Paper No. 87-0286, Jan. 1987.

22. Simpson, R. L., Chew, Y. T., and Shivaprasad, B. G.: The Structure of a Separating Turbulent Boundary Layer, Part 1: Mean Flow and Reynolds Stresses. Journal of Fluid Mechanics, Vol. 113, April 1983, pp. 23-51.

23. Sindir, M. M. S.: Numerical Study of Turbulent Flows in Backward-Facing Step Geometries: Comparison of Four Models of Turbulence. Ph.D. Dissertation, University of California, Davis, 1982.

24. Wilcox, D. C.: Multiscale Model for Turbulent Flows. AIAA Paper No. 86-0029, Jan. 1986.

25. HaMinh, H., Rubesin, M. W., Vandromme, D., and Viegas, J. R.: On the Use of Second Order Closure Modelling for the Prediction of Turbulent Boundary Layer/Shock Wave Interactions: Physical and Numerical Aspects. International Symposium on Computational Fluid Dynamics, Tokyo, Japan, Sept. 9-12, 1985.

TABLE 1.- LOCATION OF SEPARATION AND REATTACHMENT, x/c

	Separation Point	Reattachment Point
Experiment	0.67	1.17
Cebeci-Smith	0.73	1.04
Johnson-King	0.68	1.17
Coakley 1	0.99	1.00
Coakley 2	0.96	1.04
Jones-Launder	0.94	1.04
Viegas-Rubesin Wall Function 1		
$y^+ = 60.0$	0.68	1.08
$y^+ = 140.0$	0.85	1.06
Viegas-Rubesin Wall Function 2		
$y^+ = 140.0$	0.69	1.11

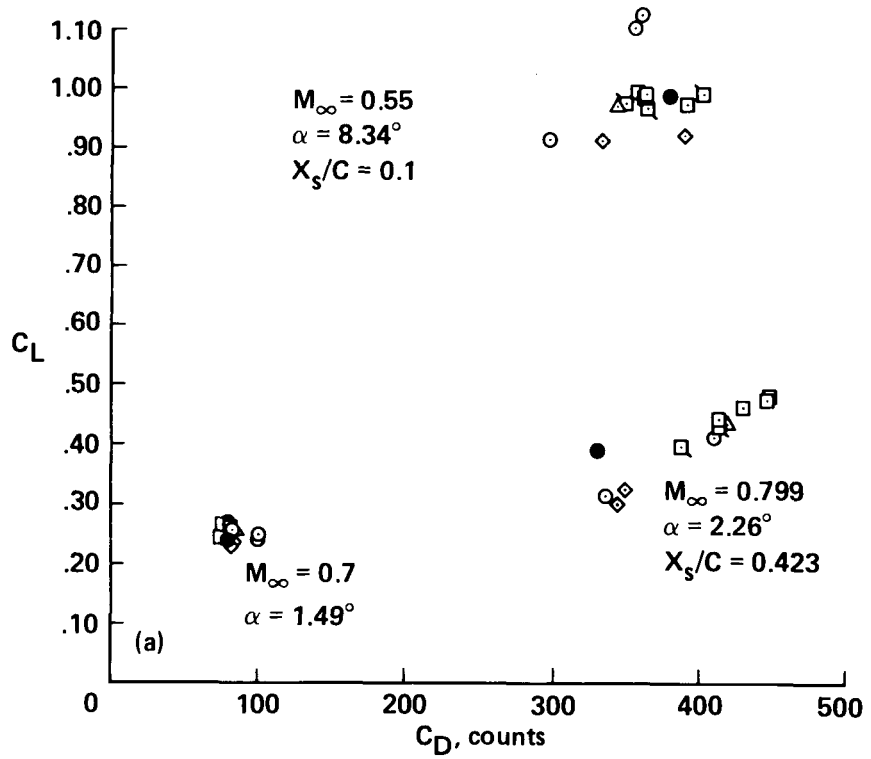

(a) NASA 0012, $Re_c = 9 \times 10^6$.

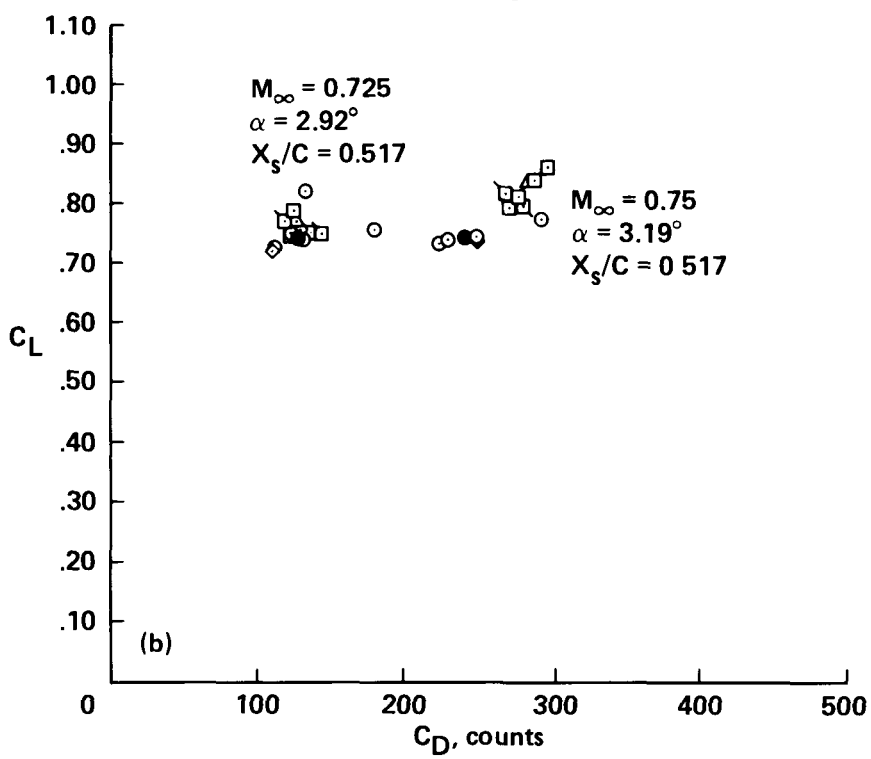

(b) RAE 2822, $Re_c = 6.5 \times 10^6$.

Figure 1.- Comparison of measured and computed force coefficients of transonic airfoils. Symbol legend: experimental data ●; solutions from interactive methods ○; Navier-Stokes solutions with Baldwin-Lomax model □; Cebeci-Smith model ⊡; Johnson-King model ◇; and Coakley-1 model △.

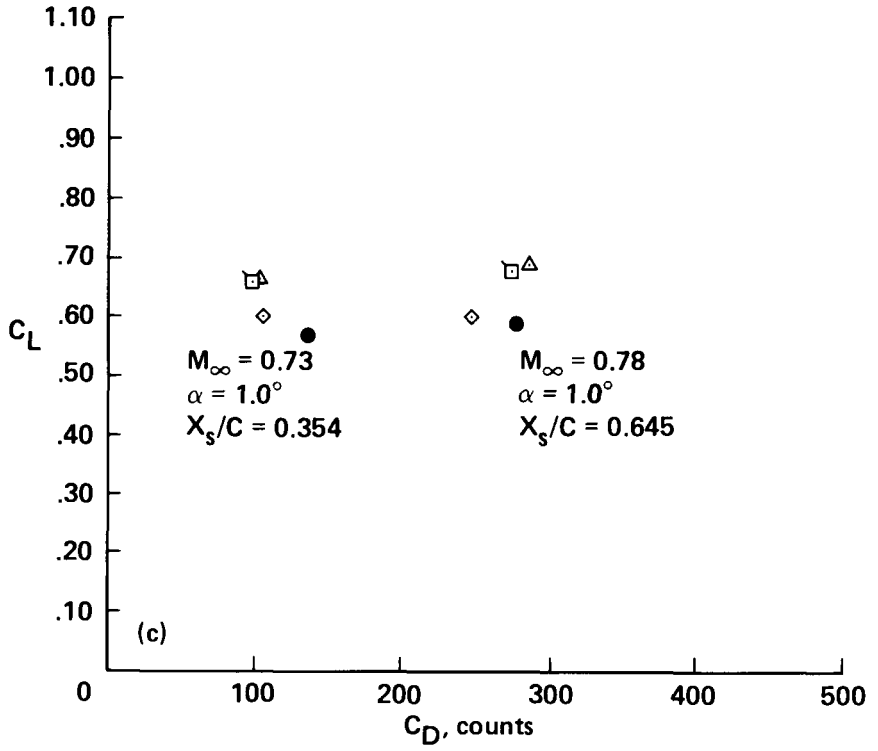

(c) VA-2, $Re_c = 6 \times 10^6$.

Figure 1.- Concluded.

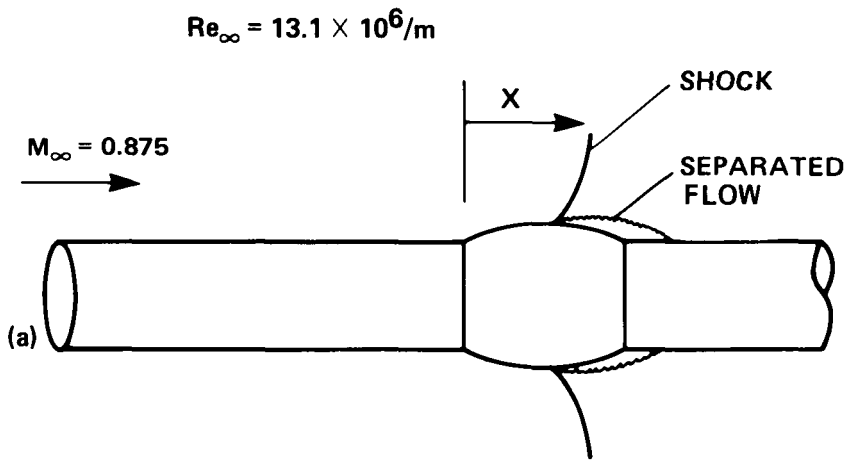

Figure 2.- Schematic diagram of transonic bump model and wind tunnel conditions (ref. 11).

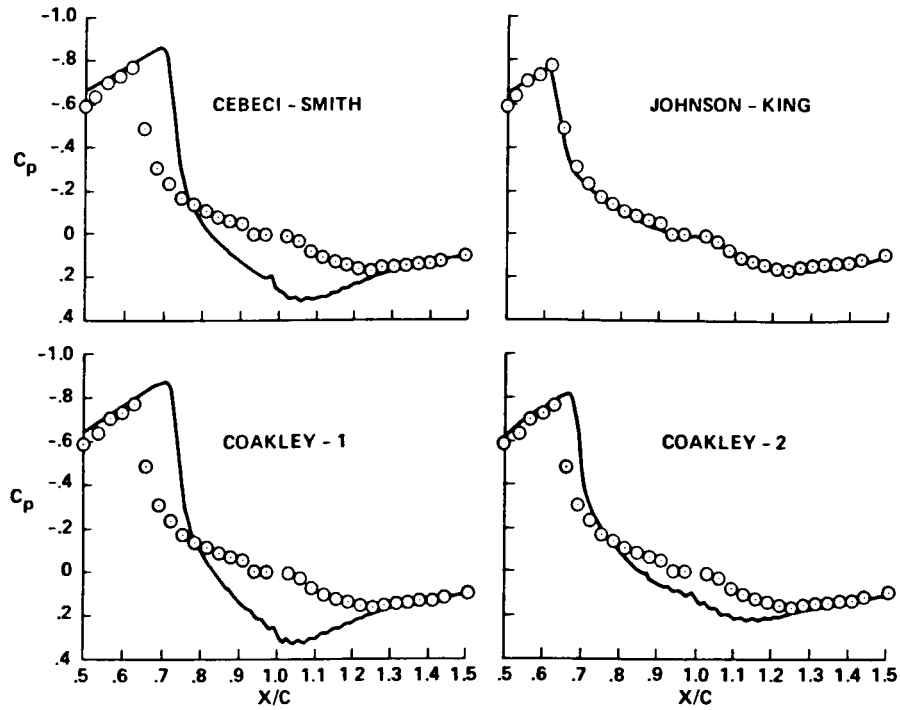

(a) Turbulence models of Cebeci-Smith, Johnson-King, Coakley-1, and Coakley-2.

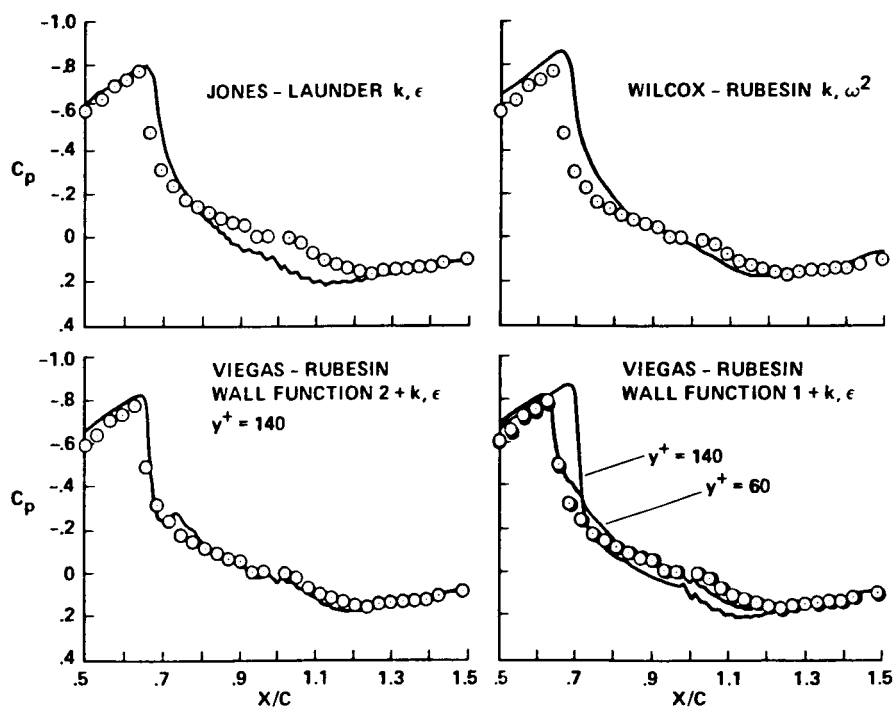

(b) Turbulence models of Jones-Launder, Wilcox-Rubesin, Viegas-Rubesin Wall Functions 1 and 2.

Figure 3.- Pressure distribution over the circular arc bump. The same experimental data, represented by open circles, are repeated in each figure.

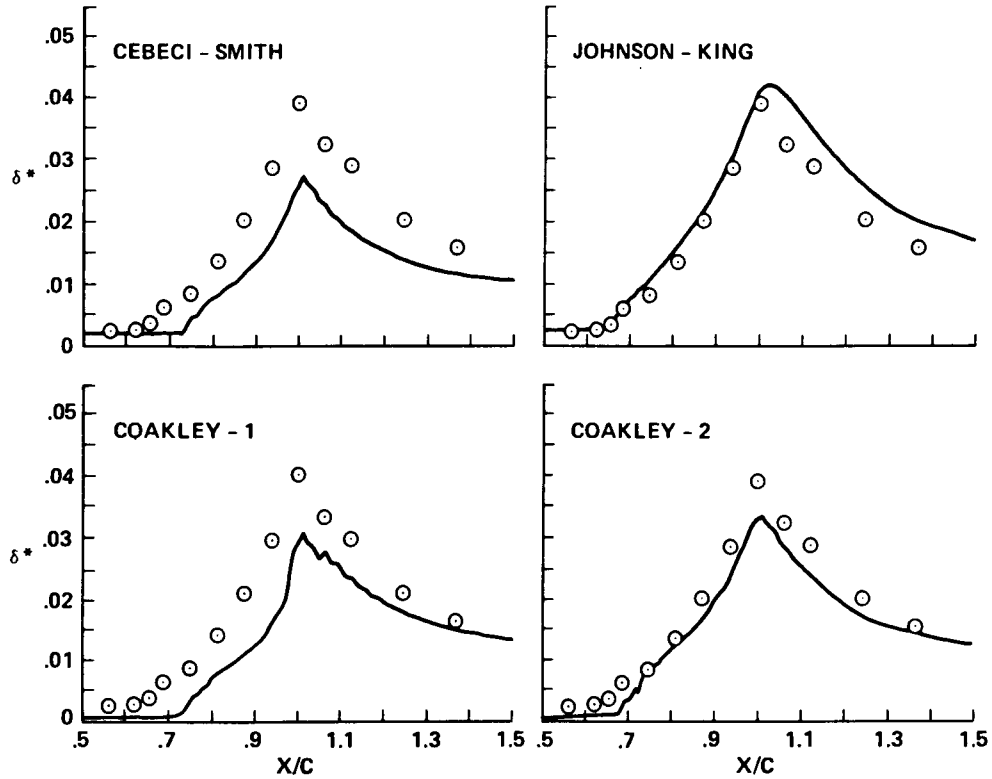

(a) Turbulence models of Cebeci-Smith, Johnson-King, Coakley-1, and Coakley-2.

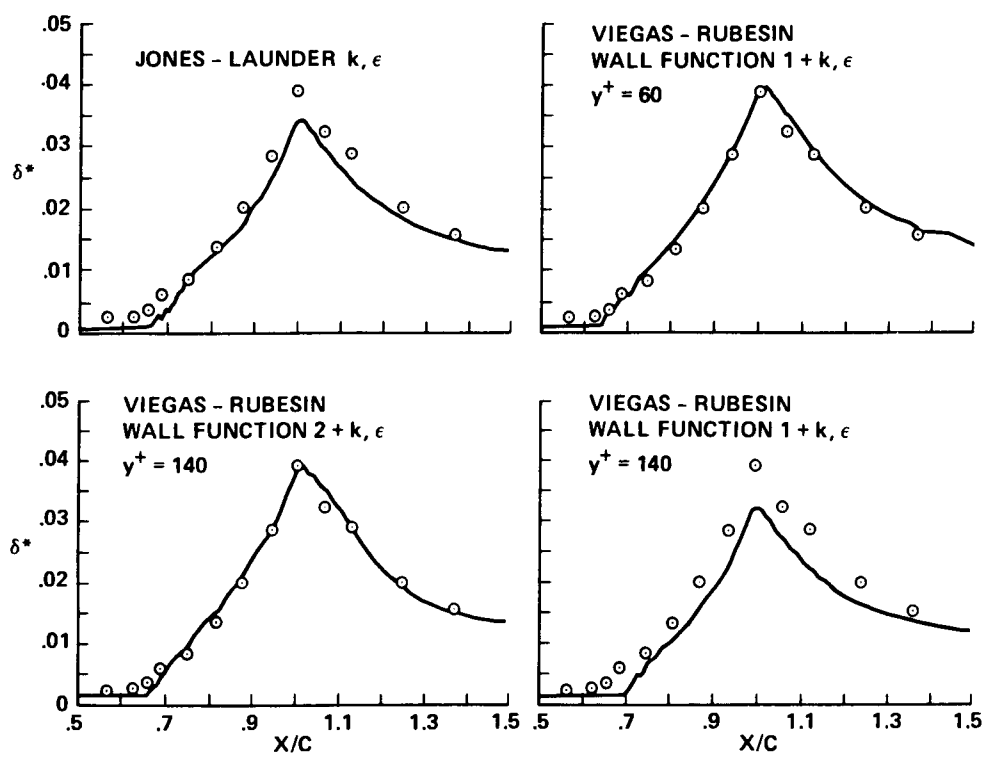

(b) Turbulence models of Jones-Launder, Wilcox-Rubesin, Viegas-Rubesin Wall Functions 1 and 2.

Figure 4.- Displacement thickness over the circular arc bump. The same experimental data, represented by open circles, are repeated in each figure.

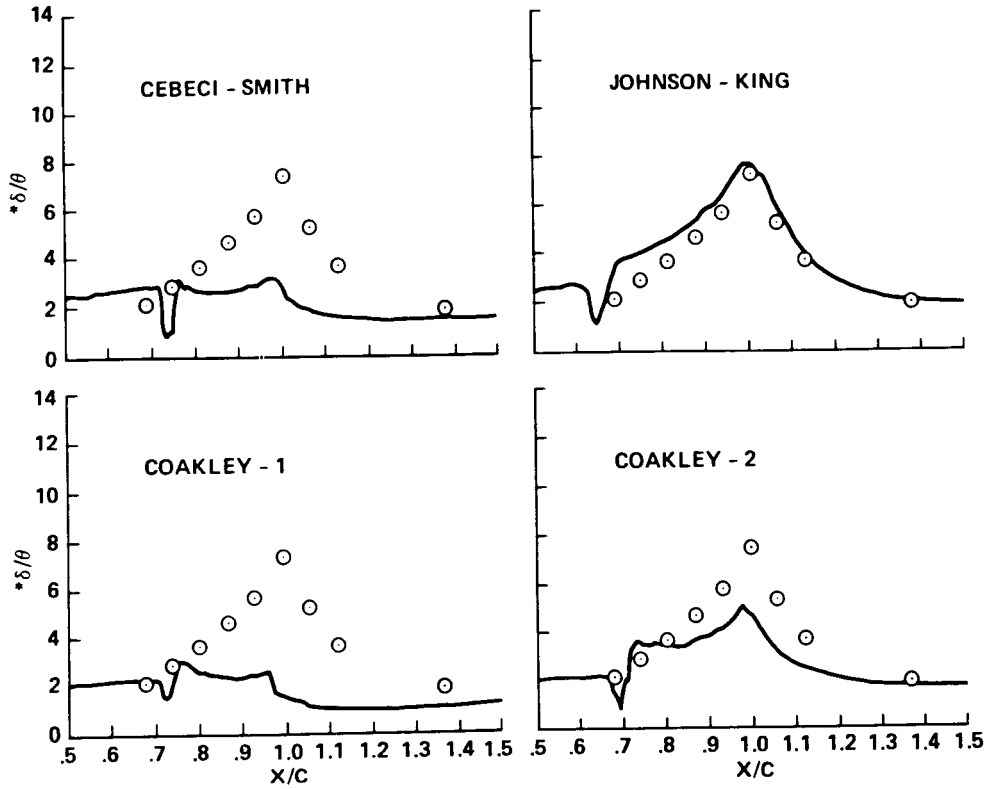

(a) Turbulence models of Cebeci-Smith, Johnson-King, Coakley-1, and Coakley-2.

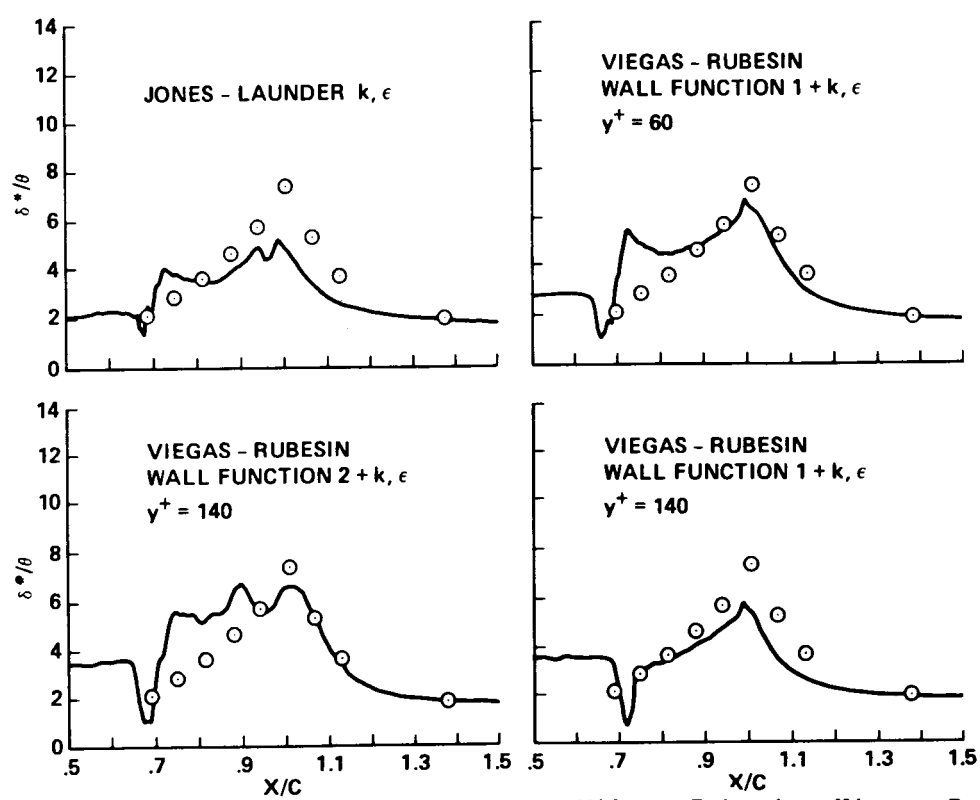

(b) Turbulence models of Jones-Launder, Wilcox-Rubesin, Viegas-Rubesin Wall Functions 1 and 2.

Figure 5.- Shape factor over circular arc bump. The same experimental data, represented by open circles, are repeated in each figure.

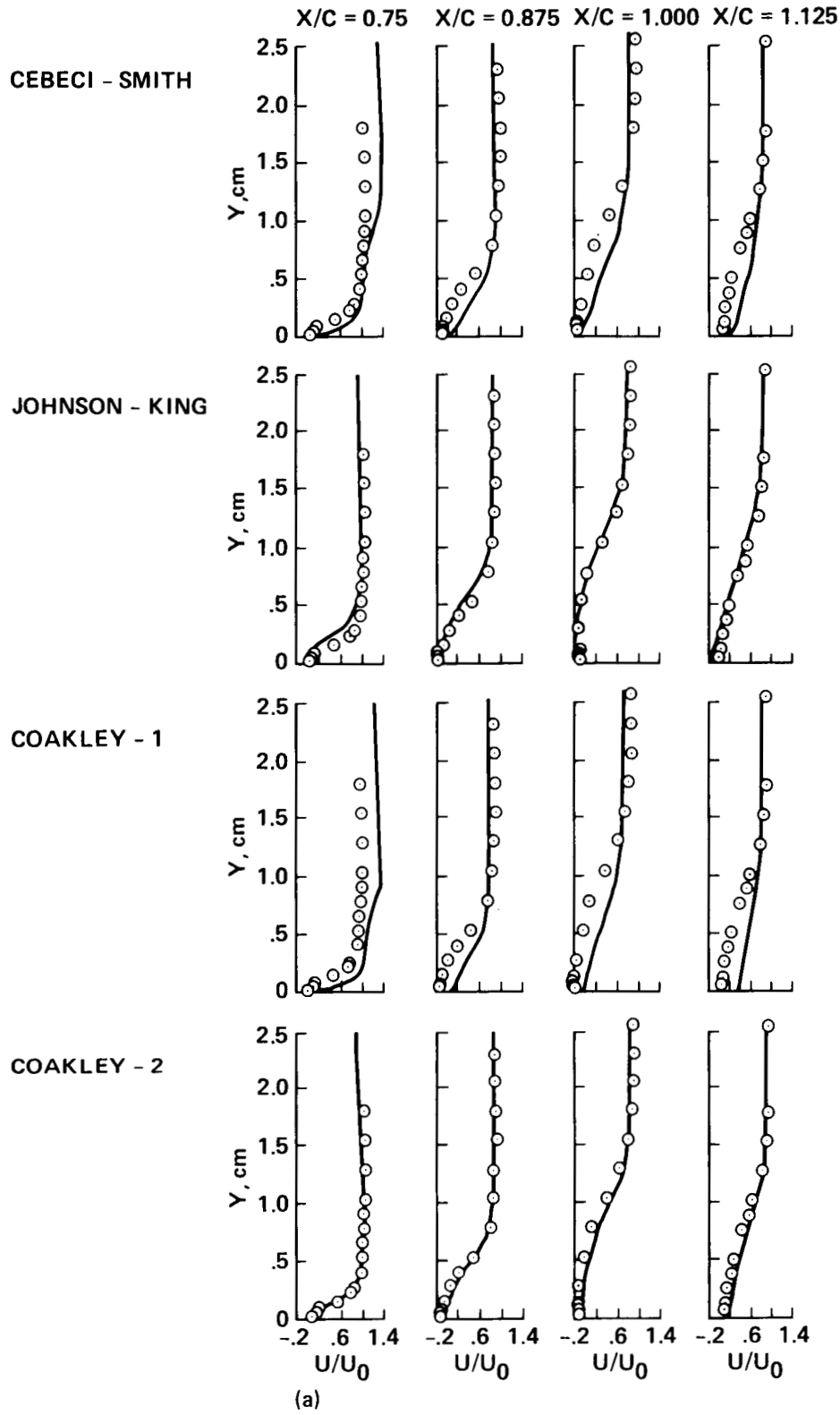

(a) Turbulence models of Cebeci-Smith, Johnson-King, Coakley-1, and Coakley-2.

Figure 6.- Mean velocity profiles over the separation zone on the circular arc bump. The same experimental data, represented by open circles, are repeated in each figure.

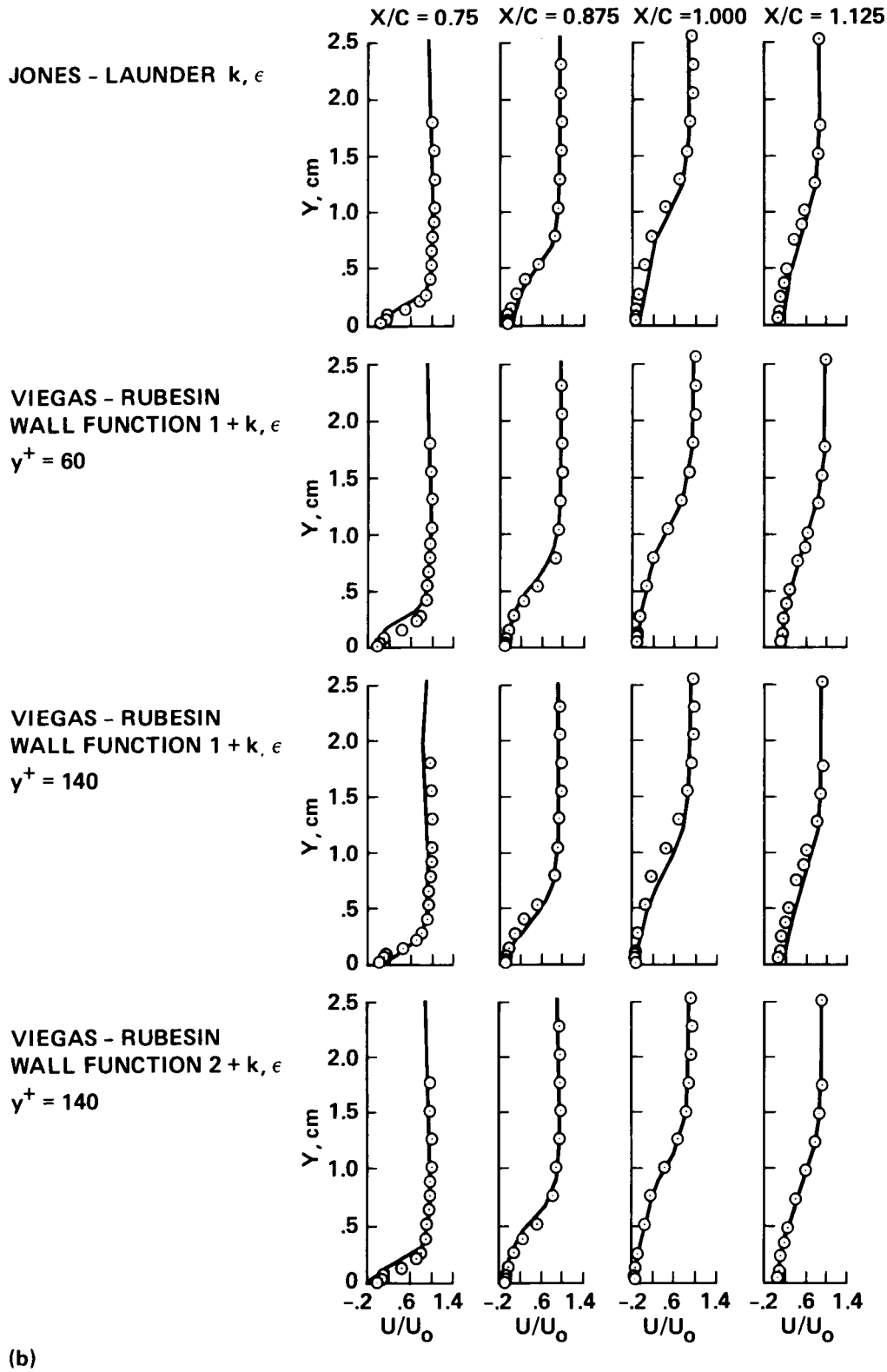

(b) Turbulence models of Jones-Launder, Wilcox-Rubesin, Viegas-Rubesin Wall Functions 1 and 2.

Figure 6.- Concluded.

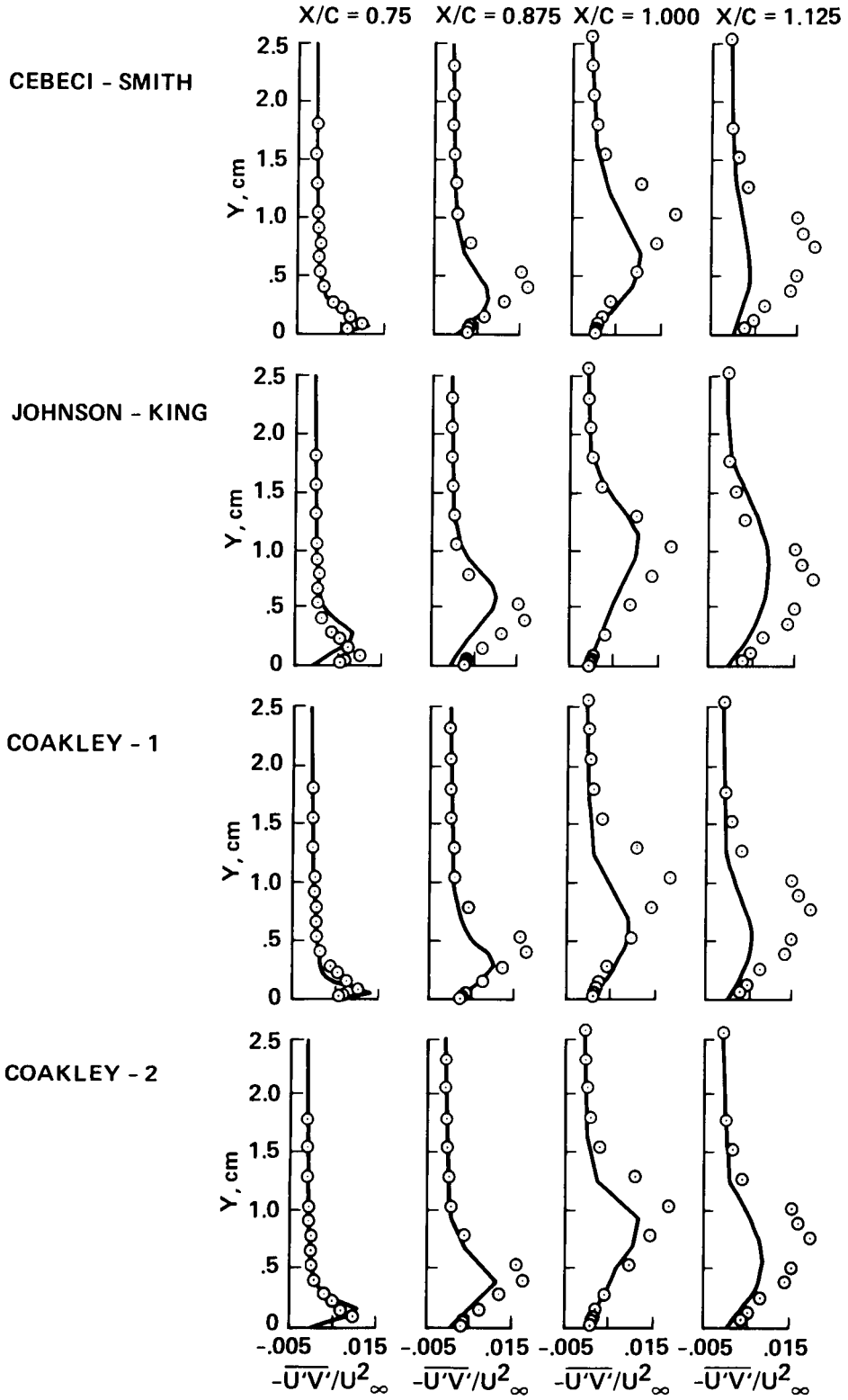

(a)

(a) Turbulence models of Cebeci-Smith, Johnson-King, Coakley-1, and Coakley-2.

Figure 7.- Shear stress profiles in the separation zone on the circular arc bump. The same experimental data, represented by open circles, are repeated in each figure.

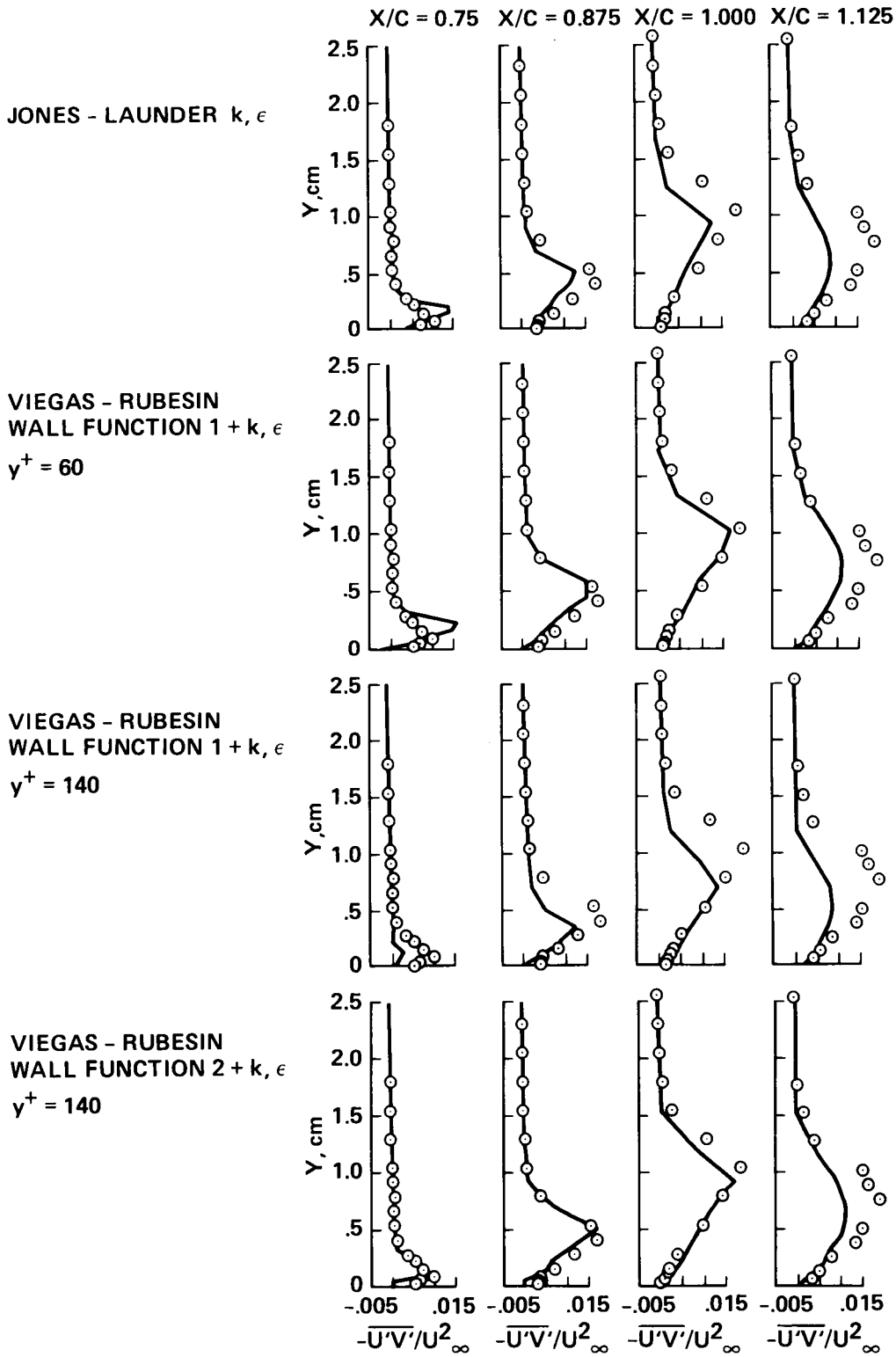

(b)

(b) Turbulence models of Jones-Launder, Wilcox-Rubesin, Viegas-Rubesin Wall Functions 1 and 2.

Figure 7.- Concluded.

N89-20952

TURBULENT EDDY VISCOSITY MODELING IN TRANSONIC SHOCK/BOUNDARY-LAYER INTERACTIONS

G. R. Inger*
Department of Aerospace Engineering
Iowa State University
Ames, Iowa

Abstract

The treatment of turbulence effects on transonic shock/turbulent boundary layer interaction is addressed within the context of a triple deck approach valid for arbitrary practical Reynolds numbers $10^3 \leq Re_{\delta^*} \leq 10^{10}$. The modeling of the eddy viscosity and basic turbulent boundary profile effects in each deck is examined in detail using the Law of the Wall/Law of the Wake concepts as the foundation. Results of parametric studies showing how each of these turbulence model aspects influences typical interactive zone property distributions (wall pressure, displacement thickness and local skin friction) are presented and discussed.

1. INTRODUCTION

Although a number of both asymptotic[1] and nonasymptotic[2] triple deck theories of non-separating transonic shock/turbulent boundary layer interaction have been advanced, none has fully addressed in a unified way all aspects of turbulence-effect modeling in the problem. Indeed, certain such theories have never explicitly addressed the eddy viscosity aspect of the problem at all but have merely used a crude empirical power law profile for the incoming boundary layer as the sole account of the turbulent aspect nature of the flow[3]; others have ignored entirely the important influence of the velocity-defect region[4]. The present paper seeks to remedy these deficiencies in treating turbulent interactions by providing a complete and unified analysis of the turbulence modeling within the context of the eddy viscosity approach combined with Law of the Wall/Law of the Wake concepts. Since it has proved applicable to an extremely wide range of Reynolds numbers[5] and highly adaptable to practical flow field calculation schemes[6,7,8], we adopt for this purpose the non-asymptotic triple deck theory originated by Lighthill[9] for quasi-laminar flow and later refined by Inger for fully turbulent flow[2].

2. RATIONALE OF THE PRESENT TRIPLE DECK APPROACH

Since it is the foundational framework used to address the various turbulence-modeling issues, a brief outline of the triple-deck approach and the advantages of its non-asymptotic version will first be given. We consider small disturbances of an arbitrary incoming turbulent boundary layer due to a weak external shock and examine the detailed perturbation field within the layer. At high Reynolds numbers it has been established[10,11] that the local interaction disturbance field

*Glenn Murphy Distinguished Professor

in the neighborhood of the impinging shock organizes itself into three basic layered-regions or "decks" (Figure 1): 1) an outer region of potential inviscid flow above the boundary layer, which contains the incident shock and interactive wave systems; 2) an intermediate deck of rotational-inviscid disturbance flow occupying the outer 90% or more of the incoming boundary layer thickness; 3) an inner sublayer adjacent to the wall containing both turbulent and laminar shear stress disturbances, which accounts for the interactive skin friction perturbations (and hence any possible incipient separation) plus most of the upstream influence of the interaction. The "forcing function" of the problem here is thus impressed by the outer deck upon the boundary layer; the middle deck couples this to the response of the inner deck but in so doing can itself modify the disturbance field to some extent, while the slow viscous flow in the thin inner deck reacts very strongly to the pressure gradient disturbances imposed by these overlying decks. This general triple deck structure is supported by a large body of experimental and theoretical studies.[11]

Concerning the importance of the inner shear disturbance deck and the accuracy of deliberately using a non-asymptotic treatment of the details within the boundary layer, we note that while asymptotic ($Re_\delta \to \infty$) theory predicts an exponentially-small thickness and displacement effect contribution of the inner deck, this is not apparently true at ordinary Reynolds numbers, where many analytic and experimental studies have firmly established that this deck, although indeed very thin, still contributes significantly to the overlying interaction and its displacement thickness growth.[2] Thus we take the point of view here that the inner deck is in fact significant at the Reynolds numbers of practical interest. Moreover, it contains all of the skin friction and incipient separation effects in the interaction, which alone are sufficient reasons to examine it in detail. It is further pointed out that application of asymptotic theory results (no matter how rigorous in this limit) to ordinary Reynolds numbers is itself an approximation which may be no more accurate (indeed perhaps less so) than a physically well constructed nonasymptotic theory. Direct extrapolated-asymptotic versus non-asymptotic theory comparisons have definitely shown this to be the case for laminar flows (especially as regards the skin friction aspect) and the situation has been shown to be possibly even worse in turbulent flow. For example, the asymptotic first-order theory formally excludes both the streamwise interactive pressure gradient effect on the shear disturbance deck and both the normal pressure gradient and so-called "streamline divergence" effects on the middle deck; however, physical considerations plus experimental observations and recent comparative numerical studies[12] suggest that these effects may in fact be significant at practical Reynolds numbers and should not be neglected. Of course, second-order asymptotic corrections can be devised to redress this difficulty but, as Regab and Neyfeh[13] have shown, run the risk of breaking down even worse when extrapolated to ordinary Reynolds numbers. In the present work, we avoid these problems by using a deliberately nonasymptotic triple-deck model appropriate to realistic Reynolds numbers that includes the inner deck pressure gradient terms plus the middle deck $\partial p/\partial y$ and streamline divergence effects, along with some simplifying approximations that render the resulting theory tractible from an engineering standpoint.

3. TURBULENCE MODELING ACROSS THE INTERACTION ZONE

3.1) The Outer Deck Flow

Excluding any freestream turbulence, there is no explicit turbulence modeling needed in this upper region of potential inviscid motion; the influence of the

turbulent nature of the flow is felt only indirectly through the displacement effect from the underlying decks. The latter is introduced by the physical coupling conditions that both v'/U_{o_e} and p' be continuous with their middle deck counterparts along $y = \delta_o$.

3.2) Turbulence Effects in the Middle Deck

Frozen Turbulence Approximation

Our analysis of this layer rests on the key simplifying assumption that for non-separating interactions the turbulent Reynolds shear stress changes are small and have a negligible back effect on the mean flow properties along the interaction zone; hence this stress can be taken to be "frozen" along each streamline at its appropriate value in the undisturbed incoming boundary layer. This approximation, likewise adopted by a number of earlier investigators with good results, is supported not only by asymptotic analysis but especially by the results of Rose's detailed experimental studies[14] of a non-separating shock turbulent boundary layer interaction which showed that, over the short-ranged interaction length straddling the shock, the pressure gradient and inertial forces outside a thin layer near the wall are at least an order of magnitude larger than the corresponding changes in Reynolds stress. Furthermore, there is a substantial body of related experimental results on turbulent boundary layer response to various kinds of sudden perturbations and rapid pressure gradients which also strongly support this view[2]. These studies unanimously confirm that, at least for non-separating flows, significant local Reynolds shear stress disturbances are essentially confined to a thin sublayer within the Law of the Wall region (see below) where the turbulence rapidly adjusts to the local pressure gradient, while outside this region where the Law of the Wake prevails the turbulent stresses respond very slowly and remain nearly frozen at their initial values far out of the local equilibrium with the wall stress.

Confining attention, then, to the short range local shock interaction zone where the aforementioned "frozen turbulence" approximation is applicable, the disturbance field caused by a weak shock is one of small rotational inviscid perturbation of the incoming non-uniform turbulent boundary layer profile $M_o(y)$ governed by the equations

$$\frac{\partial}{\partial y}\left[\frac{v'(x,y)}{U_o(y)}\right] = \frac{1-M_o^2(y)}{\gamma\, M_o^2(y)} \cdot \frac{\partial(p'/p_o)}{\partial x} \tag{1}$$

$$\frac{\partial u'}{\partial x} = -\frac{\partial p'/\partial x}{\rho_o(y)\; U_o(y)} - \frac{dU_o}{dy} \cdot \frac{v'}{U_o} \tag{2}$$

$$\frac{\partial^2 p'}{\partial y^2} - \frac{2}{M_o}\frac{dM_o}{dy}\frac{\partial p'}{\partial y} + \left[1-M_o^2 - \frac{2\,u'M_o^2}{U_o}\right]\frac{\partial^2 p'}{\partial x^2} = 0 \tag{3}$$

as a result of the combined particle-isentropic continuity, x-momentum and energy conservation statements. It is noted that, consistent with the assumed short range character of the interaction, the streamwise variation of the undisturbed turbulent boundary layer properties that would occur over this range are neglected,

taking $U_o(y)$, $\rho_o(y)$ and $M_o(y)$ to be arbitrary functions of y only with δ_o, δ_o^* and τ_{w_o} as constants. Note that Eq. (3) is a generalization of Lighthills' well-known pressure perturbation equation for non-uniform flows[9] which includes a non-linear correction term for possible transonic effects within the boundary layer including the diffracted impinging shock above the sonic level of the incoming boundary-layer profile. Eqs. (1)-(3) apply to a wide range of incoming boundary-layer profiles and provide an account of lateral pressure gradients across the interaction boundary layer.

Incoming Turbulent Boundary-Layer Profile

The incoming undisturbed turbulent boundary layer is assumed to be two-dimensional in the x-direction and to possess the classical Law of the Wall/Law of the Wake structure. It is modeled by Walz's[15] composite analytical expression for the resulting velocity profile combined with an adiabatic wall reference temperature method correction for compressibility*, allowing arbitrary non-equilibrium values of its shape factor H_{ij}. Thus if we let π be Coles' (incompressible) Wake Function, $\eta \equiv y/\delta_o$ and denote for convenience $R \equiv .41\ Re\delta_o/[(1+\pi)(T_W/T_e)^{1+\omega}]$ with $\omega = .76$ and $\gamma = 1.4$ for a perfect gas, then the compressible form of Walz's composite profile may be written:

$$\frac{U_o}{U_e} = 1 + \frac{1}{.41}\sqrt{\frac{C_{f_o}}{2}\left(\frac{T_w}{T_e}\right)}\left[\left(\frac{R}{1+R}\right)\eta^2(1-\eta) - 2\pi + 2\pi\,\eta^2\cdot(3-2\eta) + \ln\left(\frac{1+R\eta}{1+R}\right) - (.215+.655R\eta)e^{-3R\eta}\right] \tag{4}$$

subject to the following condition linking π to C_{f_o} and $Re\delta_o^*$:

$$2\pi + .215 + \ln(1+R) = .41 \Big/ \sqrt{\frac{C_{f_o}}{2}\left(\frac{T_W}{T_e}\right)} \tag{5}$$

Eqs. (4) and (5) have the following desirable properties: (a) for $\eta \gtrsim .10$, U_o/U_e is dominated by a Law of the Wake behavior which correctly satisfies both the outer limit conditions $U_o/U_e \to 1$ and $dU_o/dy \to 0$ and $\eta = 1$; (b) for very small values, U_o assumes a Law of the Wall-type behavior consisting of a logarithmic term that is exponentially damped out into a linear laminar sublayer profile $U/U_e = R\eta$ as $\eta \to 0$; (c) Eq. (4) may be differentiated w.r.t. η to yield an analytical expression for dU_o/dy also, which proves advantageous in solving the middle and inner deck interaction problems. Typical non-dimensional turbulent boundary layer velocity profiles that result from Eqs. (4) and (5) are illustrated in Fig. 2. It is evident from this plot that as $H_{i1} \to 1$ the outer (wake) part of the profile vanishes leaving essentially a uniform (and inviscid-like) profile except for a very thin sublayer adjacent to the wall.

*Under the transonic Mach number/adiabatic wall conditions considered here, this gives a good engineering approximation to the compresibility effects while much simpler to implement than the more exact Van Driest transformation[16] approach.

The defining integral relations for δ_i^* and θ_i^* yields the following relationship that links the wake parameter to the resulting compressible shape factor $H_i = (\delta_i^*/\theta_i^*)$:

$$\frac{H_i - 1}{H_i} = \frac{2}{.41}\sqrt{\left(\frac{T_W}{T_e}\right)\frac{C_{f_o}}{2}}\left(\frac{1 + 1.59\pi + .75\,\pi^2}{1 + \pi}\right) \tag{6}$$

Equations (4)-(6) provide a very general and accurate model of the profile in terms of three important physical quantities: the shock strength (Me_1), the displacement thickness Reynolds number Re_δ^* and the Wake function π that reflects the prior upstream history of the incoming boundary layer including possible nonequilibrium pressure gradient and surface mass transfer effects. The resulting relationship of the incompressible shape factor H_i, to the Wake Function as a function of Reynolds number for a typical $M_1 = 1.20$ transonic flow is illustrated in Fig. 3. It is seen from this Figure that Hi_1 approaches a limiting value of unity as $Re_\delta \to \infty$ but that this approach is very gradual, especially for wake function values larger than zero (slightly favorable and adverse pressure gradient upstream flow histories).

With these parameters prescribed, the aforementioned equations may be solved simultaneously for the attendant skin friction C_f, the value of R and, if desired, the H_i appropriate to these flow conditions. Using the adiabatic temperature-velocity relationship.

$$T_o(y) = T_{W,AD} + (T_e - T_{W,AD})\frac{U_o^2(y)}{U_{oe}^2} \tag{7}$$

the associated Mach number profile $M_o(y) = U_o(\gamma R T_o)^{-1/2}$ and its derivative that are needed for the middle deck interaction solution may then be determined.

3.3) Turbulent Shear Stress Disturbances Along the Inner Deck

This very thin layer lies well within the Law of the Wall region of the incoming turbulent boundary-layer profile. The original work of Lighthill[9] treated it by further neglecting the turbulent stresses altogether and considering only the laminar sublayer effect; while this greatly simplifies the problem and yields an elegant analytical solution, the results can be significantly in error at high Reynolds numbers and cannot explain (and indeed conflicts with) the ultimate asymptotic behavior pertaining to the $Re_\delta \to \infty$ limit. The present theory remedies this by extending Lighthill's approach to include the entire Law of the Wall region turbulent stress-effects; the resulting general shear-disturbance sublayer theory provides a non-asymptotic treatment which encompasses the complete range of Reynolds numbers. It is important to note in this connection that our consideration of the entire Law of the Wall combined with the use of the effective inviscid wall concept to treat the inner deck displacement effect eliminates the need for the "blending layer" that is otherwise required to match the disturbance field in the laminar sublayer region with the middle inviscid deck; except for higher order derivative aspects of asymptotic matching, our inner solution

effectively includes this blending function since it imposes a boundary condition of vanishing total (laminar plus turbulent) shear disturbance at the outer edge of the deck.

To facilitate a tractable theory, we introduce the following simplifying assumptions: (a) The incoming boundary-layer Law of the Wall region is characterized by a constant total (laminar plus turbulent eddy) shear stress and a Van Driest-Cebeci type of damped eddy viscosity model. This model is known to be a good one for a wide range of upstream non-separating boundary-layer flow histories. (b) For weak incident shock strengths, the sublayer disturbance flow is assumed to be a small perturbation upon the incoming boundary layer; in the resulting linearized disturbance equations, however, all the physically important effects of streamwise pressure gradient, streamwise and vertical acceleration, and both laminar and turbulent disturbances stresses are retained; (c) For adiabatic flows the undisturbed and perturbatiton flow Mach numbers are both quite small within the shear disturbance sublayer; consequently, the density perturbations in the sublayer disturbance flow may be neglected while the corresponding modest compressibility effect on the Law of the Wall portion of the undisturbed profile is quite adequately treated by the Eckert reference temperature method wherein incompressible relations are used based on wall recovery temperature properties (this is equivalent in accuracy to, but easier than, the use of Van Driest's compressible Law of the Wall profile[17]). (d) The turbulent fluctuations and the small interactive disturbances are assumed uncorrelated in both the lower and middle decks. (e) The thinness of the inner deck allows the boundary-layer-type approximation of neglecting its lateral pressure gradient.

The disturbance field is thus governed by the following continuity and momentum equations:

$$\frac{\partial u'}{\partial x} + \frac{\partial v'}{\partial y} = 0 \tag{8}$$

$$U_o \frac{\partial u'}{\partial x} + v' \frac{dU_o}{dy} + (\rho_{w_o}^{-1}) \frac{dp'_w}{dx} = \frac{\partial}{\partial y} \left(\nu_{w_o} \frac{\partial u'}{\partial y} + \epsilon_{T_o} \frac{\partial u'}{\partial y} + \epsilon'_T \frac{dU_o}{dy} \right) \tag{9}$$

where ρ_{w_o} and ν_{w_o} are evaluated at the adiabatic wall recovery temeperature and where it should be noted that the kinematic eddy viscosity perturbation ϵ'_T is being taken into account. The corresponding undisturbed turbulent boundary layer Law of the Wall profile $U_o(y)$ is governed by

$$\tau_o(y) = \text{const.} = \tau_{w_o} = [\mu_{w_o} + \rho_{w_o} \epsilon_{T_0}(y)] \frac{dU_o}{dy} \tag{10}$$

where according to the Van Driest-Cebeci eddy viscosity model with $y+ = \left(y\sqrt{\tau_{w_o}/\rho_{w_o}}\right)/\nu_{w_o}$

$$\epsilon_T = [.41y \ (1-e^{-y+/A})]^2 \frac{\partial u}{\partial y} \tag{11}$$

which yields for non-separating flow disturbances that

$$\varepsilon_{T_o} = [.41y(1-e^{-y+/A})]^2 \frac{dU_o}{dy} \tag{12}$$

$$\varepsilon_T' \approx \left(\frac{\partial u'/\partial y}{dU_o/dy}\right) \varepsilon_{T_o} \tag{13}$$

Here, A is the so-called Van Driest damping "constant;" we use the commonly accepted value A = 26 although it is understood that a larger value may improve the experimental agreement in regions of shock-boundary layer interaction. Substituting (13) into (9) we thus have the disturbance momentum equation

$$U_o \frac{\partial u'}{\partial x} + v' \frac{dU_o}{dy} (\rho_{w_o}^{-1}) \frac{\partial p_w'}{\partial x} = \frac{\partial}{\partial y} [(\nu_{w_o} + 2 \cdot \varepsilon_{T_o}) \frac{\partial u'}{\partial y}] \tag{14}$$

from which we hav een that inclusion of the eddy viscosity perturbation has exactly doubled th urbulent shear stress disturbance term.

We solve these Equations subject to the wall boundary conditions $U_o(0) = u(x,o) = v(x,o) = 0$ plus an initial condition $u(-\infty,y) = 0$ requiring that all interactive disturbances vanish far upstream of the impinging shock. Furthermore, at some distance δ_{SL} sufficiently far from the wall, u' must pass over to the inviscid solution u'_{inv} along the bottom of the middle deck, this later being governed by

$$U_o \frac{\partial u_{inv}}{\partial x} + v'_{inv} \frac{dU_o}{dy} + \left(\rho_{w_o}\right)^{-1} \frac{dp_w}{dx} \simeq 0 \tag{15}$$

with δ_{SL} defined as the height where the total shear disturbance (proportional to $\partial u/\partial y$) of the inner solution vanishes to a desired accuracy.

4. SOLUTION METHODOLOGY AND RESULTS

The solution to the foregoing triple deck problem is achieved for small linearized disturbances ahead of, behind and below the nonlinear shock jump, which gives reasonably accurate predictions for all the properties of engineering interest when $M_1 \gtrsim 1.05$. The resulting equations can be solved by a Fourier transform method to yield all the essential physics of the mixed transonic viscous interaction field for non-separating flows including the upstream influence, the lateral pressure gradient near the shock and the onset of incipient separation (see References for the details of this solution). Numerous detailed comparisons with experiment have shown that it gives a good account of all the important features of the interaction over a wide range of Mach-Reynolds number conditions.

4.1) Fourier Transformation Method

We only briefly outline here the steps involved, since full details can be found elsewhere. Following Fourier Transformation w.r.t.x., the resulting middle deck pressure problem from Eq. 3 is an ordinary differential equation in y that can be solved numerically quite efficiently for the input turbulent boundary layer profile Mo(y) of Section 3.2. In particular, for the upstream interactive pressure rise we find from the appropriate Fourier inversion process using the calculus of residues that

$$p'_w \simeq \text{CONST.} \times \Delta p \; e^{x/\ell u} \tag{16}$$

where ΔP is the overall shock pressure jump while ℓu is the charactertistic upstream distance given by

$$\ell u \simeq \frac{Me_1^2 \cdot I_o}{\sqrt{Me_1^2 - 1}} + \frac{\sqrt{Me_1^2 - 1} \cdot I_1}{Me_1^2} \tag{17a}$$

in terms of the profile-dependent integrals (evaluated by the aforementioned turbulent Law of the Wall/Law of the Wake model)

$$I_o \equiv \int_{Y_{weff}}^{\delta_o} \left\{\left[1 - M_{on}^2(b)\right]/M_{on}^2(b)\right\} db \tag{17b}$$

$$I_1 \equiv \int_o^{\delta_o} M_{on}^2(b) db \tag{17c}$$

The parameter y_{weff} here is the effective inviscid wall shift given by the displacement thickness of the underlying inner deck.

The corresponding Fourier transformation of the inner deck problem of Section 3.3, followed by the introduction of new inner deck variables and a y-scaling defined by Inger[2], yields a set of ordinary differential equation boundary value problems in a "universal" form that can be solved and tabulated once and for all. An example of this is illustrated in Fig. 4, which shows the resulting inner deck streamwise velocity profiles in terms of the eddy viscosity effect as expressed by the authors' Interactive Turbulence Parameter[2]

$$T \equiv (.41)^2 \frac{\rho_{o_w} \tau_{w_o}}{\mu_{ow}^2} \left(\frac{\mu_{ow}^2 \ell u}{\rho_{o_w} \tau_{w_o}}\right)^{2/3} \tag{18}$$

The typical transonic Reynolds number and wake function-dependence of this parameter is illustrated in Figure 5, where it is seen that it grows to large values with increasing Re_δ, as well as increasing with π.

We further obtain the following result for the deck's displacement thickness:

$$y_{weff} = .766\left(\frac{\mu_{w_o}^2 \ell u}{\rho_{o_w} \tau_{w_o}}\right)^{1/3} H(T) \tag{19}$$

where the eddy viscosity effect-function $H(T)$ is given in Figure 6. The simultaneous solution of Eqs. (17)-(19) for ℓu and y_{weff} implements the matching of thinner and middle decks. The resulting values of this inner deck height expressed as a fraction of the incoming undisturbed boundary layer thickness are plotted versus Reynolds number with as a parameter in Figure 7; also shown for comparison are the corresponding sonic height ratio values. It is clearly seen how rapidly y_{weff}/δ_o decreases with increasing Re_δ, reaching exceedingly small values indeed, relative to the much more gradual decrease in y_{sonic}/δ_o. It is also interesting to note here, as one would expect on physical grounds, that while the inner deck thickness is hardly affected by π, the sonic height (which lies within the wake region) is significantly influenced and increases with the value of the Wake function.

Finally, we note the companion result for the upstream skin friction that

$$\tau_w' \simeq -.72\, p_w'(N)\, f_p(X) \left[\frac{\rho_{w_o} \ell_u^2 \tau_{w_o}}{\mu_{wo}^2}\right]^{-1/3} S(T) \tag{20a}$$

where

$$f_p(x) = \left[\frac{2}{3}\,\frac{\ell_u \left(p_w'\right)^{3/2}}{\int_{-\infty}^{x} \left(p_w'\right)^{3/2} dx}\right]^{2/3} \tag{20b}$$

and $S(T)$ is another interactive-turbulence effect function, also plotted in Figure 6.

Figure 6 is a central result of the present general turbulent shear-disturbance inner deck treatment; it gives a unified account of the inner interactive physics over the entire Reynolds number range from quasi-laminar behavior at $T \ll 1$ (lower Reynolds numbers) to the opposite extreme of wall turbulence-dominated behavior at $T \gg 1$ pertaining to asymptotic theory at very large Reynolds numbers where the inner deck thickness and its disturbance field become vanishingly small.

4.2) Predictive Results Showing the Role of the Turbulence Modeling Parameters

A computer program has been constructed to carry out the foregoing solution method; it involves the middle-deck disturbance pressure solution coupled to the inner deck by means of the effective wall shift combined with an upstream influence solution subroutine (the corresponding local total interactive displacement thickness growth and skin friction are also obtained). This provides a very general fundamental description of the boundary layer in terms of three arbitrary parameters: preshock Mach number, boundary-layer displacement thickness Reynolds number, and the wake function π.

Based on the aforementioned program, an extensive parametric study has been carried out to show the sensitivity of predicted interaction zone properties to the various key turbulent flow modeling parameters. For example, in Figures 8, 9 and 10 we show the influence of the Wake Function on the interactive pressure, displacement thickness and local skin friction distributions. These plots bring out clearly that this wake function effect has a very important influence on the interactive physics (for example, the interaction zone width, upstream influence and thickness all significantly increase with π) and hence is an important element in the turbulent flow modeling. It is important to remember that this wake function effect is totally lost in the leading approximation of the asymptotic triple deck approach (which is based on the limiting value $Hi_1 = 1.0$ pertaining to the infinite Reynolds number limit, wherein the wake component completely vanishes). We further note in this regard the significant corresponding effect on the skin friction levels in the interaction zone (Figure 10).

Another interesting aspect of the turbulence modeling is the eddy viscosity perturbation effect in the inner deck: this is illustrated in Figure 11, where we show how the predicted upstream influence distance is altered by including (or neglecting) this effect. At moderately high Reynolds numbers ($Re_\delta \lesssim 10^6$), the effect is seen to be quite large: neglect of the interactive disturbance to ϵ_T can consequently underpredict ℓu by hundreds of percent. On the other hand, at very large Re where the interactive flow is essentially inviscid-dominated and influenced only by the outer wake region of the incoming boundary layer, the eddy viscosity perturbations have an altogether negligable effect. Figure 11 also brings out the fact that the present theory applies to a very wide range of practical Reynolds numbers.

The predicted influence of the transonic Mach number and wake function on the non-dimensional upstream influence distance ratio $\ell u/\delta o$ at a fixed Reynolds number is presented in Figure 12; it is seen that this ratio noticably decreases with increasing M_e while significantly increasing with the value of π.

REFERENCES

1. Melnick, R.E., Turbulent Interactions on Airfoils at Transonic Speeds--Recent Developments," in AGARD CP-291 (Computation of Viscous-Inviscid Interactions), Sept. 1980, pp. 10-1 to 10-34.

2. Inger, G.R., "Upstream Influence and Skin Friction in Non-Separating Shock Turbulent Boundary Layer Interactions," AIAA Paper No. 80-1411, Snowmass, Colorado, July 1980. See also "Nonasymptotic Theory of Unseparated Turbulent Boundary Layer Interaction," in Numerical and Physical Aspects of Aerodynamic Flows (T. Cebeci, Ed.), Springer-Verlag, N.Y. 1983.

3. Bohning, R. and J. Zierep, "Normal Shock-Turbulent Boundary Layer Interaction at a Curved Wall," in AGARD CP-291, Sept. 1980, pp. 17-1 to 17-8.

4. Adamson, T.C., and Feo, A., "Interaction Between a Shock Wave and a Turbulent Layer in Transonic Flow," SIAM Journal Appl. Math 29, July 1975, pp. 121-144.

5. Inger, G. R., "Application of a Shock-Turbulent Boundary-Layer Interaction Theory in Transonic Flowfield Analysis" in Transonic Aerodynamics, Vol. 81 of Progress in Astronautics and Aeronautics, AIAA, 1981.

6. Nandanan, M., Stanewsky, E., and Inger, G.R., "A Computational Procedure for Transonic Airfoil Flow Including a Special Solution for Shock-Boundary Layer Interaction," AIAA Journal, Vol. 19, Dec. 1981, pp. 1540-46.

7. Lekoudis, S.G., G. R. Inger and M. Khan, "Computation of the Viscous Transonic Flow Around Airfoils with Trailing Edge Effects and Boundary Layer Interactions," Journal of Aircraft, Vol. 21, June 1984, pp. 380-88.

8. Nietubicz, C., J. Danberg and G.R. Inger, "A Theoretical and Experimental Investigation of a Transonic Projectile Flow Field," AIAA Journal 22, Jan. 1984, pp. 35-43.

9. Lighthill, M.J., "On Boundary Layers and Upstream Influence; II. Supersonic Flow Without Separation," Proc. Royal Soc. A 217, 1953, pp. 578-587.

10. Stewartson, K., "Multistructured Boundary Layers on Flat Plates and Related Bodies," in Adv. in Applied Mechanics 14, Academic Press, 1974, pp. 146-235.

11. Inger, G.R., "Application of a Shock-Boundary Layer Interaction Theory to Transonic Airfoil Analysis," AGARD CP-291, Colorado Springs, September 1980.

12. Inger, G.R., "The Modular Application of a Shock/Boundary Layer Interaction Solution to Supercritical Viscous Inviscid Flow Field Analysis," in Compuational Methods in Viscous Flows, Vol. 3, Pineridge Press, U.K., 1984, pp. 475-512.

13. Ragab, S.A., and Nayfeh, A.H., "A Second Order Asymptotic Solution for Laminar Separation of Supersonic Flows Past Compression Ramps," AIAA 78-1132, 1978.

14. Rose, W.C., and Childs, M.E., "Reynolds Shear Stress Measurements in a Compressible Boundary Layer within a Shock Wave-Induced Adverse Pressure Gradient," JFM 65, 1, 1974, pp. 177-188.

15. Walz, A., Boundary Layers of Flow and Temperature, M.I.T. Press, 1969, pp. 113-116.

16. Van Driest, E.R., "Turbulent Boundary Layers in Compressible Fluid," Journal of Aeronaut. Sci. 18, March 1951, pp. 145-60.

17. Burggraf, O.R., "The Compressibility Transformation and the Turbulent Boundary Layer Equation," Journal of Aerospace Sci. 29, 1962, pp. 434-39.

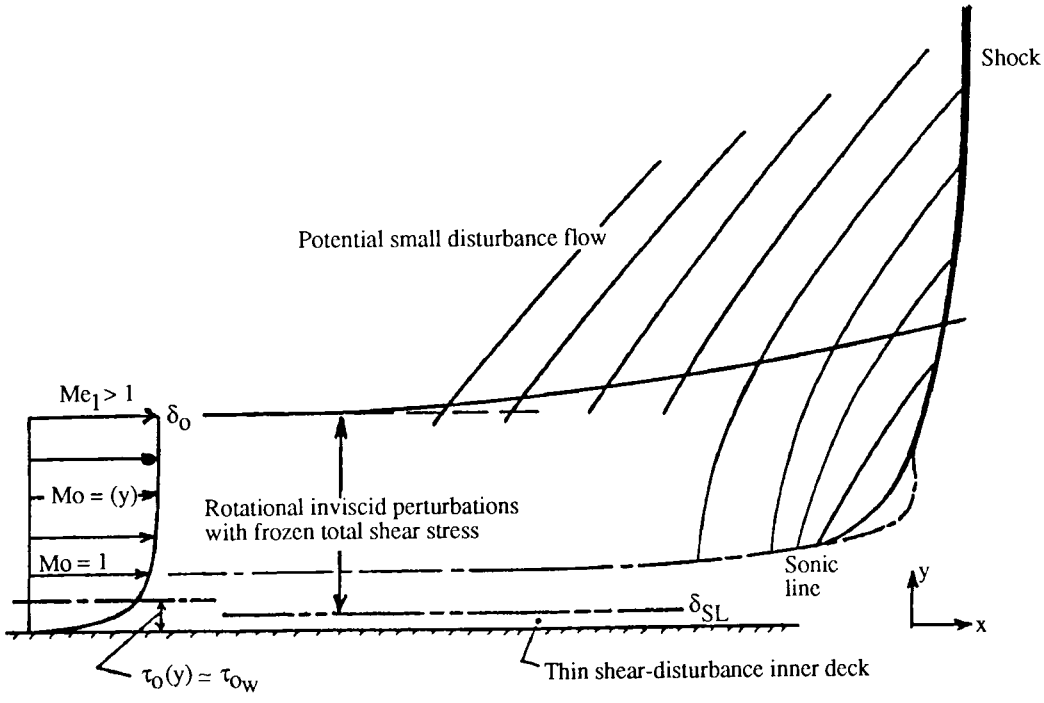

Figure 1. Triple-deck structure of interaction zone.

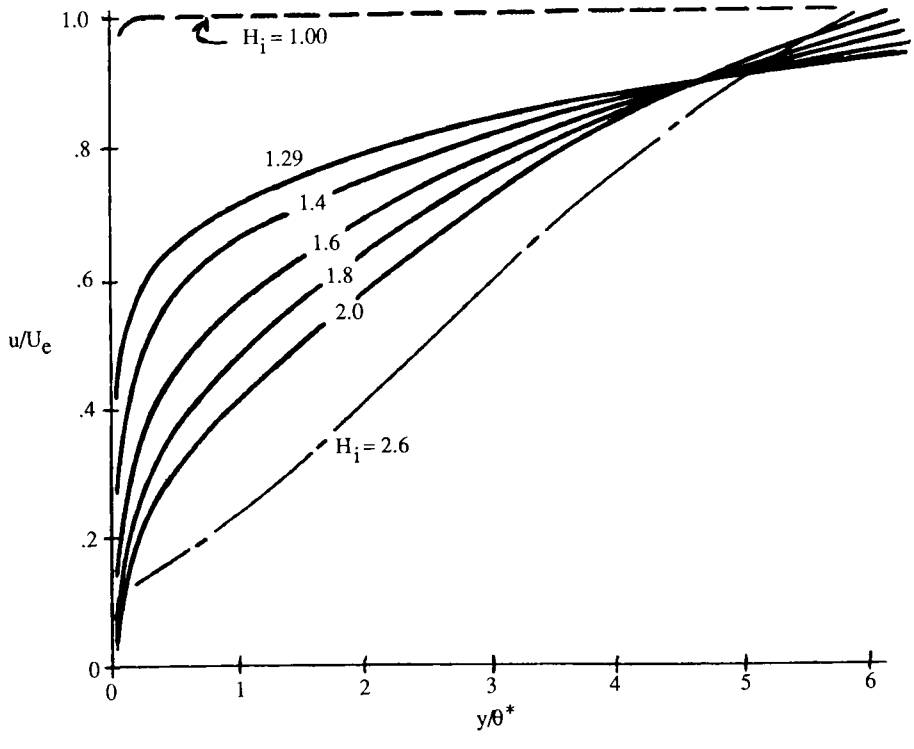

Figure 2. Nondimensional turbulent boundary-layer velocity profiles for various shape factors (after NASA Rept. 772, 1943).

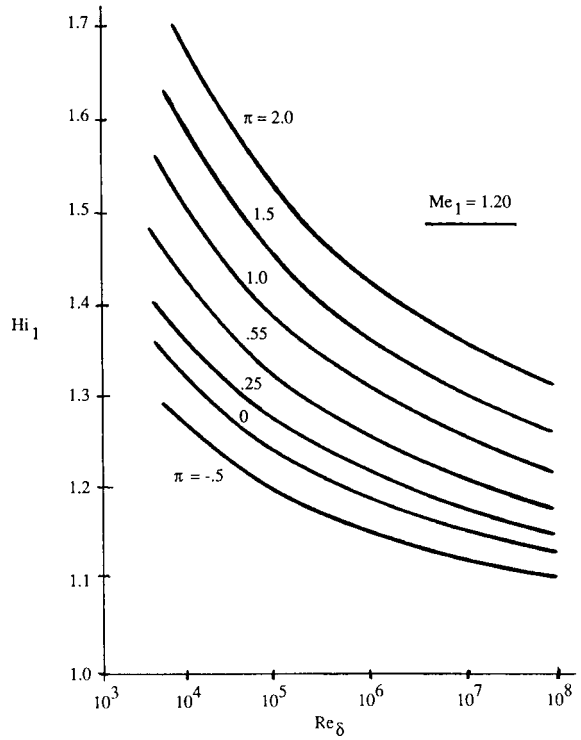

Figure 3. Incompressible shape factor versus Reynolds number with the wake function as parameter.

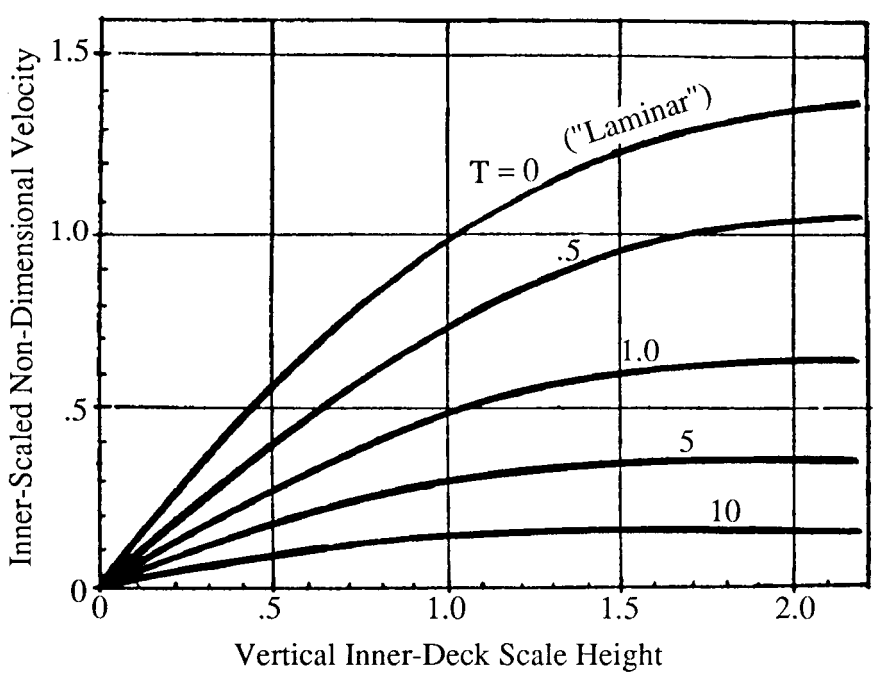

Figure 4. Streamwise disturbance velocity profiles across inner deck for various values of interactive turbulence parameter.

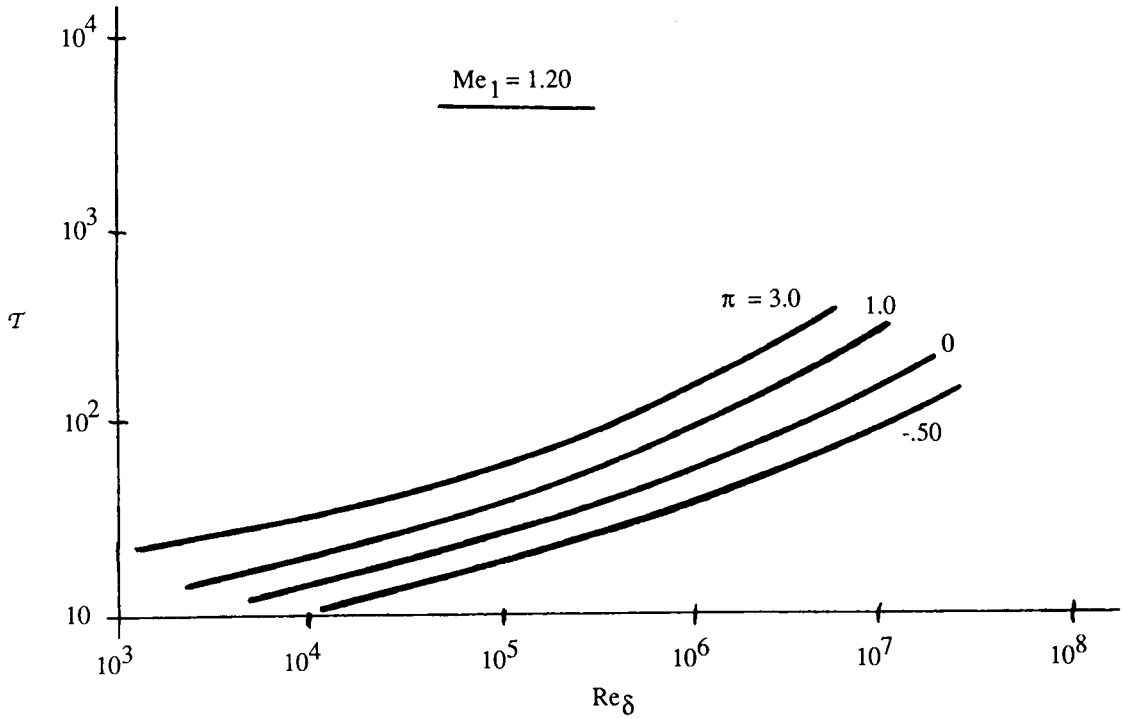

Figure 5. Variation of interactive turbulence parameter with Reynolds number for various wake function values.

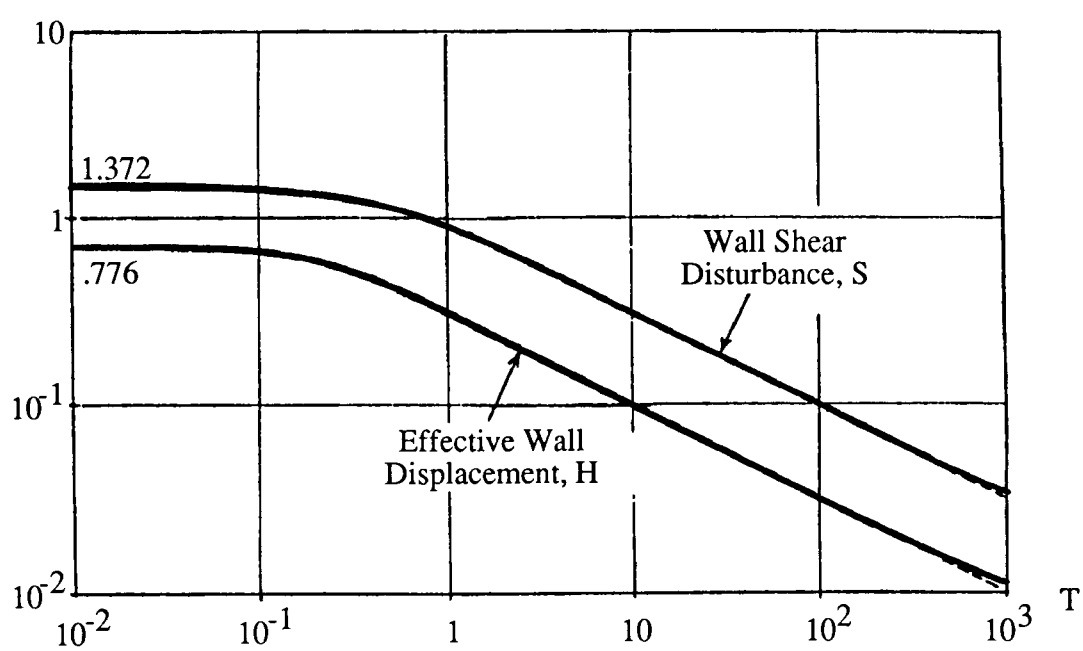

Figure 6. Turbulent interaction parameter effect on interactive displace thickness and skin friction functions.

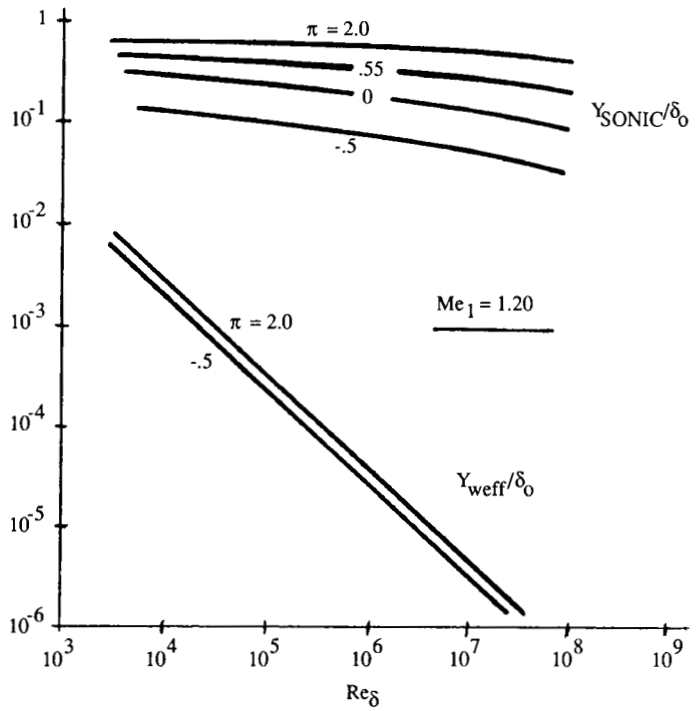

Figure 7. Nondimensionalized inner deck thickness and sonic height variations with Reynolds number with wake function as parameter.

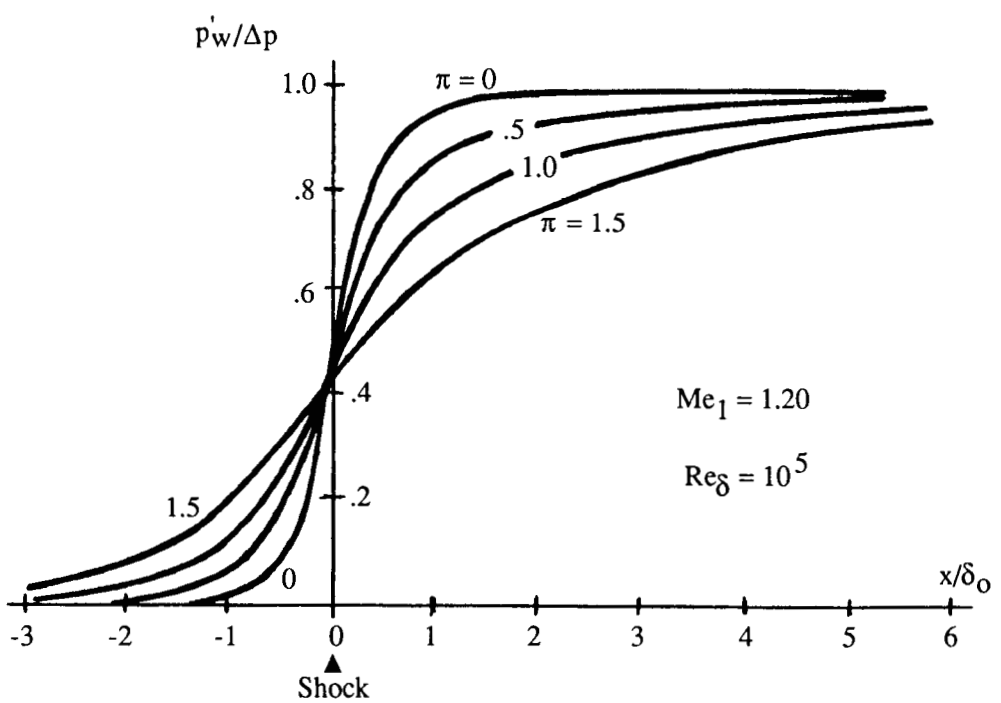

Figure 8. Wake function effect on interaction wall pressure distribution.

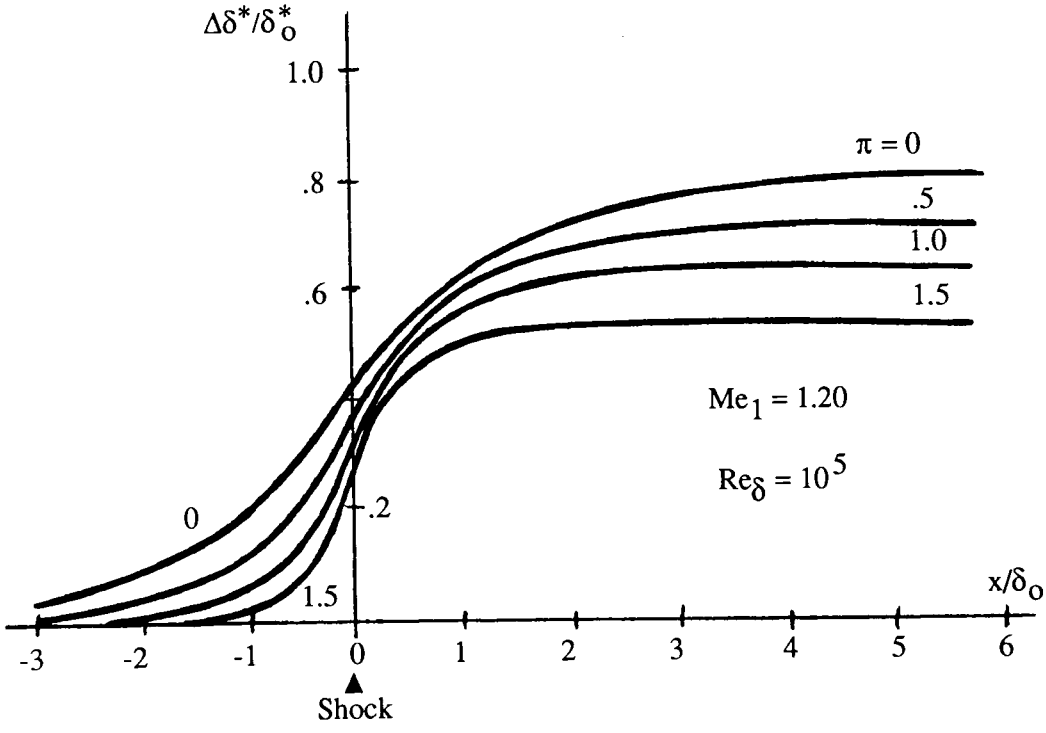

Figure 9. Wake function effect on displacement thickness distribution along interaction zone.

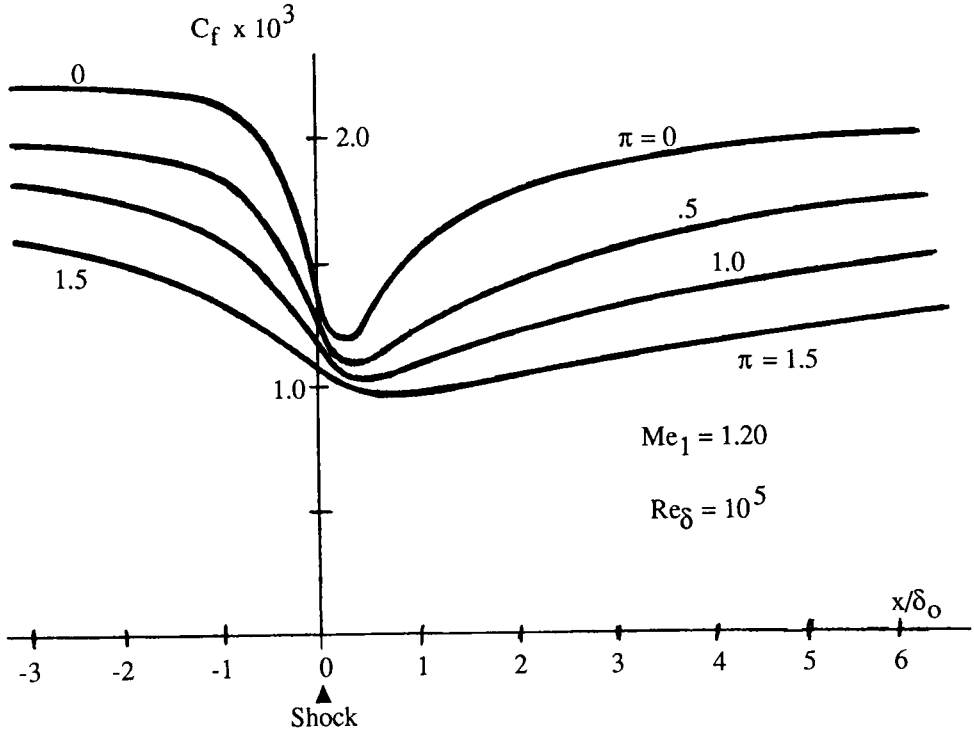

Figure 10. Wake function effect on interaction zone skin friction.

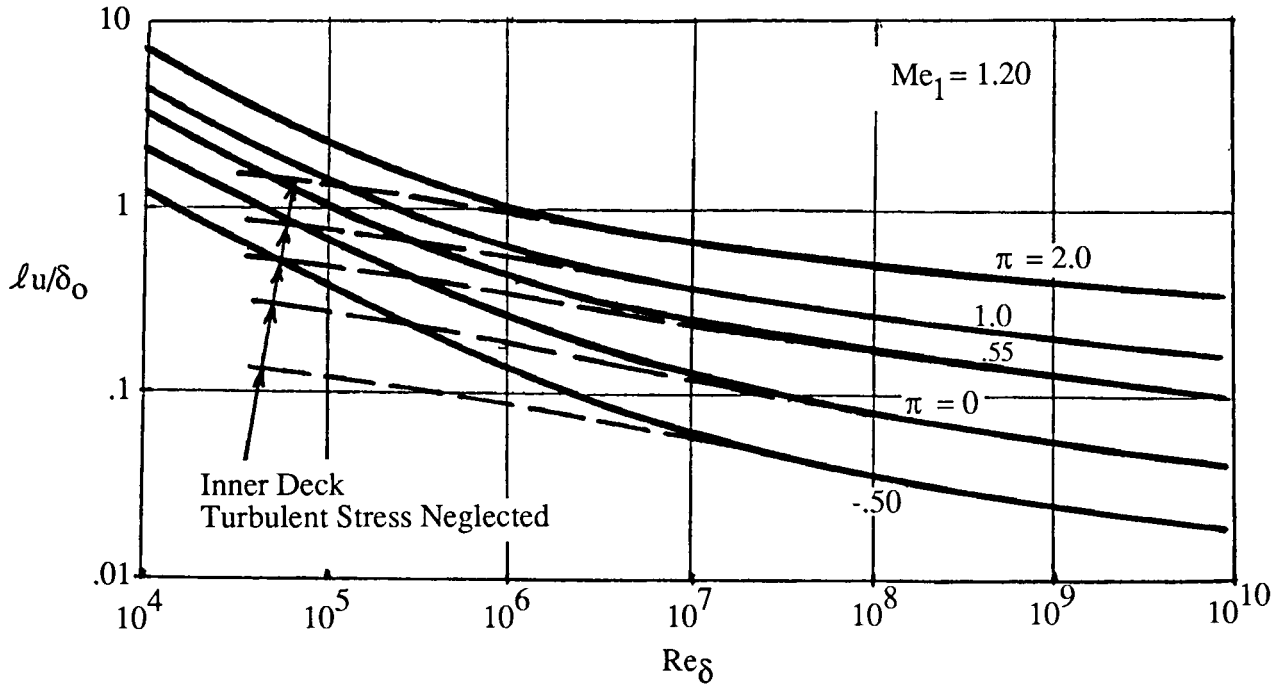

Figure 11. Influence of inner deck eddy viscosity perturbations on upstream influence variation with Reynolds number.

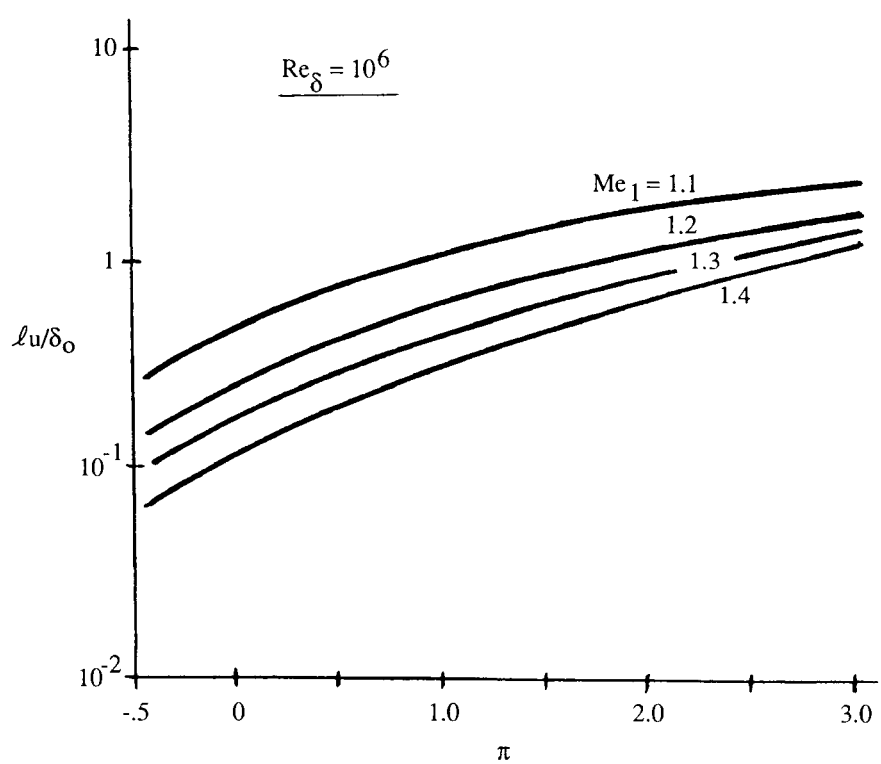

Figure 12. Upstream influence versus wake function with Mach number as parameter.

PRECEDING PAGE BLANK NOT FILMED

N89-20953

STABILITY OF COMPRESSIBLE BOUNDARY LAYERS

Ali H. Nayfeh
Department of Engineering Science and Mechanics
Virginia Polytechnic Institute and State University
Blacksburg, VA

ABSTRACT

The stability of compressible two- and three-dimensional boundary layers is reviewed. The stability of 2D compressible flows differs from that of incompressible flows in two important features: There is more than one mode of instability contributing to the growth of disturbances in supersonic laminar boundary layers and the most unstable first-mode wave is three-dimensional. Whereas viscosity has a destabilizing effect on incompressible flows, it is stabilizing for high supersonic Mach numbers. Whereas cooling stabilizes first-mode waves, it destabilizes second-mode waves. However, second-order waves can be stabilized by suction and favorable pressure gradients. The influence of the nonparallelism on the spatial growth rate of disturbances is evaluated. The growth rate depends on the flow variable as well as the distance from the body. Floquet theory is used to investigate the subharmonic secondary instability.

1. INTRODUCTION

The aim of this paper is to review the state of the art of the stability of compressible boundary layers. The study discusses the influence of Mach number, Reynolds number, cooling, suction, pressure gradients, wave angle, and nonparallelism. Subharmonic secondary instability is also discussed.

The earliest attempt at formulating a compressible stability theory was made by Kuchemann (ref. 1) who neglected viscosity, the mean temperature gradient, and the curvature of the mean velocity profile. Lees and Lin (ref. 2) and Lees (ref. 3) were the first to derive the basic equations for the linear parallel stability analysis of compressible boundary layers. This theory was extended by Dunn and Lin (ref. 4), Reshotko (ref. 5), and Lees and Reshotko (ref. 6). These early theories were asymptotic or approximate in nature and proved to be valid only up to low supersonic Mach numbers. The use of direct computer solutions to exploit the full compressible stability equations was initiated by Brown (ref. 7) and Mack (ref. 8). An extensive treatment of the parallel stability theory for compressible flows is given by Mack (refs. 9-15). As the Mach number increases, the dissipation terms become important and a three-dimensional disturbance cannot be treated by an equivalent two-dimensional method as is usually done for the incompressible case. Mack (refs. 10,15) found that neglecting the dissipation terms can lead to a 10% error in the disturbance amplification rate.

It is an interesting facet of compressible two-dimensional boundary layers that the most unstable first-mode wave need not be parallel to the freestream as the Mach number approaches one. At supersonic speeds the most unstable first-mode wave is oblique or three-dimensional.

The most important feature of the stability of supersonic laminar boundary layers is that there can be more than one mode of instability contributing to the growth of the disturbance. The first mode is similar to the Tollmien-Schlichting instability mode of incompressible flows, while the second and higher unstable modes are unique to compressible flows. Mack (ref. 10) found that there are multiple

PRECEDING PAGE BLANK NOT FILMED

values of wave numbers for a single disturbance phase velocity whenever there is a region of supersonic mean flow relative to the disturbance phase velocity. For incompressible flows, higher modes are associated with higher wave numbers at different phase speeds. In contrast with the first mode, the most unstable second mode is two-dimensional. As the Mach number increases to the hypersonic regime, the second mode displays growth rates that are higher than those of the three-dimensional first mode. However, the maximum growth rate is less than that of the first mode at zero Mach number.

These stability theories treat the mean flows as quasiparallel flows. Some incomplete attempts to account for the nonparallel flow effects by including either the normal velocity or some of the streamwise derivatives of the mean flow were given by Brown (ref. 16), Gunness (ref. 17), and Boehman (ref. 18). Complete nonparallel theories for two-dimensional flows were developed by El-Hady and Nayfeh (ref. 19) and Gaponov (20) and for three-dimensional flows by Nayfeh (21) and El-Hady (22). The growth rate in a parallel flow is independent of the flow variable and the distance from the wall, whereas the growth rate in a nonparallel flow (growing boundary layer) depends on the flow variable and the distance from the wall. This complicates the interpretation of experimental data for comparison with the results of stability theory.

In contrast with the case of incompressible flows, rigorous stability experiments are very difficult at supersonic speeds because (a) the spatial and temporal resolution of instruments at supersonic speeds is less than those at low speeds, (b) with the exception of Kendall, experimenters have less control and knowledge of the disturbances at supersonic speeds, and (c) the interference of traversing probes at high speeds is due to the high aerodynamic loads which necessitate strong and bulky walls. Therefore, most of the information on the stability of high-speed flows is macroscopic rather than microscopic. The term macroscopic refers to measurements of the onset of turbulence and the extent of the transition region, whereas the term microscopic refers to measurements of the evolution in space and time of the fluctuations present in the flow that are sufficient for the identification of the instabilities that lead to transition and the validation of the proposed theoretical models. It should be noted that macroscopic experiments are difficult to relate directly to stability theory, whereas microscopic experiments, which provide information about the unstable disturbances and their growth, can be better related to stability theory, which studies the development of individual components of the disturbances corresponding to a certain frequency or a wavepacket. Thus, microscopic experiments that use controlled disturbances are more desirable for corroboration with theory than experiments that study natural disturbances arising from one source or another in the boundary layer. The natural disturbances represent a set of space and time components, whereas controlled experiments can provide disturbances with a given frequency and a given spanwise wavenumber.

Whereas experimenters developed various credible techniques to introduce controlled artificial disturbances in incompressible boundary layers, the technique of Kendall seems to be the only credible technique at supersonic speeds. Laufer and Vrebalovich (ref. 23) used a high-speed valve and Demetriades used a siren mechanism attached to a flat plate to introduce their artificial disturbances. The valve opened and closed a narrow slit in the surface of the plate to allow periodic air pulses of certain frequency to disturb the boundary layer. Kendall introduced small artificial disturbances by a glow discharge between two electrodes embedded in the surface of the flat plate skewed at a specified angle to the spanwise direction,

thereby introducing disturbances with a specified wave angle. The rest of the available experiments were performed using natural disturbances.

Almost all measurements reported on the experimental stability of boundary layers were made by means of either hot-wire anemometers or hot films following disturbances in these boundary layers. The hot-wire response is a combination of velocity, density, and temperature fluctuations. The hot-wire response when operated at high constant overheat is proportional to the mean square of the mass-flow fluctuations. To describe the disturbance fully, one needs measurements of all fluctuation characteristics such as the rms amplitude, spectra, and propagation speed as functions of both y and x. Almost all reported experiments for compressible flows measured $|\rho u|$ at various x-stations by placing hot wires or hot films at a transverse location where the mean-flow conditions are the same. Laufer and Vrebalovich (ref. 23) reported measurements at different constant y/L positions, while Kendall (refs. 24,25), Demetriades (refs. 26-28), Lebiga et al (ref. 29), and Stetson, Thompson, Donaldson and Siler (refs. 30-33) reported measurements at one constant y/L located in the wideband energy peak.

Laufer and Vrebalovich (ref. 23) carried out measurements of the neutral stability curves, amplification rates, wavelengths, and amplitude distributions at the Mach numbers 1.6 and 2.2. They performed their measurements in the JPL 20" supersonic wind tunnel where the freestream turbulence level was reduced to about 1% by means of damping screens. Laufer and Vrebalovich performed their measurements for natural as well as artificial disturbances. The stability characteristics of natural disturbances in supersonic flows at Mach numbers between 1.6 and 8.5 were examined by Kendall (refs. 24,25) in the JPL 20" supersonic wind tunnel. In some of these experiments, the side walls of the tunnel were turbulent and hence radiated sound. Mack (ref. 12) tried to compare the free oscillations in the parallel stability theory with Kendall's data. The comparison was satisfactory only for the case M_∞ = 4.5. In an attempt to account for the response of the boundary layer to the incoming sound waves, Mack (ref. 12) included a forcing term at the first neutral stability point and found a better agreement with Kendall's data. The same characteristic features of the boundary-layer response to the incoming sound waves were observed by Lebiga et al (ref. 29) in their experiments at M_∞ = 2. Demetriades (refs. 26,27) presented experimental results for hypersonic boundary-layer flows. He studied the streamwise amplitude variation of both natural disturbances and disturbances artificially excited with a siren mechanism attached to a flat plate.

2. PROBLEM FORMULATION

In this paper, we consider the linear quasi-parallel as well as the nonparallel stability of two- and three-dimensional compressible boundary layers. Moreover, we consider the linear secondary instability of two-dimensional primary waves in a two-dimensional compressible boundary layer. The basic equations for the linear stability analysis of parallel-flow compressible boundary layers were first derived by Lees and Lin (ref. 2), Lees (ref. 3), and Dunn and Lin (ref. 4), using the small disturbance theory. For excellent references on the compressible parallel stability theory, we refer the reader to the papers of Mack. For the nonparallel theory of compressible boundary layers, we refer the reader to the papers by El-Hady and Nayfeh (ref. 19) and Nayfeh (ref. 21).

Lengths, velocities, and time are made dimensionless using a suitable reference length L^*, the freestream velocity U^*_∞, and L^*/U^*_∞, respectively. The pressure is made dimensionless using $\rho^*_\infty U^{*2}_\infty$, where ρ^*_∞ is the freestream density. The temperature, density, specific heats, viscosity, and thermal conductivity are made dimensionless

using their corresponding freestream values. The gas is assumed to be perfect. Since the pressure is constant across the boundary layer

$$\rho_m T_m = 1 \text{ and } p_m = \frac{1}{\gamma M_\infty^2} \tag{2.1}$$

where the subscript m refers to mean flow quantities, γ is the ratio of the specific heats of the gas, and M_∞ is the freestream Mach number.

To formulate the problem so that the disturbance equations can be specialized to all these cases, we assume the basic flow to be a time-dependent three-dimensional flow and superpose on it small disturbances to obtain total flow quantities of the form

$$\hat{q}(x,y,z,t) = q_b(x,y,z,t) + q(x,y,z,t) \tag{2.2}$$

Here $q_b(x,y,z,t)$ stands for a basic state quantity and $q(x,y,z,t)$ stands for a small unsteady disturbance. Substituting the total flow quantities $\hat{u}$, $\hat{v}$, $\hat{w}$, $\hat{\rho}$, $\hat{p}$, $\hat{\mu}$, and $\hat{T}$ into the Navier-Stokes equations, subtracting the basic state, and linearizing, we find to first order that the disturbance equations are given by

$$\frac{\partial \rho}{\partial t} + \frac{\partial}{\partial x}(\rho_b u + \rho u_b) + \frac{\partial}{\partial y}(\rho_b v + \rho v_b) + \frac{\partial}{\partial z}(\rho_b w + \rho w_b) = 0 \tag{2.3}$$

$$\begin{aligned}
&\rho_b\left(\frac{\partial u}{\partial t} + u_b \frac{\partial u}{\partial x} + u \frac{\partial u_b}{\partial x} + v_b \frac{\partial u}{\partial y} + v \frac{\partial u_b}{\partial y} + w_b \frac{\partial u}{\partial z} + w \frac{\partial u_b}{\partial z}\right) + \rho\left(\frac{\partial u_b}{\partial t}\right. \\
&\quad \left. + u_b \frac{\partial u_b}{\partial x} + v_b \frac{\partial u_b}{\partial y} + w_b \frac{\partial u_b}{\partial z}\right) = -\frac{\partial p}{\partial x} + \frac{1}{R}\left\{\frac{\partial}{\partial x}\left[\mu_b\left(r \frac{\partial u}{\partial x} + m \frac{\partial v}{\partial y} + m \frac{\partial w}{\partial z}\right)\right.\right. \\
&\quad \left. + \mu\left(r \frac{\partial u_b}{\partial x} + m \frac{\partial v_b}{\partial y} + m \frac{\partial w_b}{\partial z}\right)\right] + \frac{\partial}{\partial y}\left[\mu_b\left(\frac{\partial u}{\partial y} + \frac{\partial v}{\partial x}\right) + \mu\left(\frac{\partial u_b}{\partial y} + \frac{\partial v_b}{\partial x}\right)\right] \\
&\quad \left. + \frac{\partial}{\partial z}\left[\mu_b\left(\frac{\partial w}{\partial x} + \frac{\partial u}{\partial z}\right) + \mu\left(\frac{\partial w_b}{\partial x} + \frac{\partial u_b}{\partial z}\right)\right]\right\}
\end{aligned} \tag{2.4}$$

$$\begin{aligned}
&\rho_b\left(\frac{\partial v}{\partial t} + u_b \frac{\partial v}{\partial x} + u \frac{\partial v_b}{\partial x} + v_b \frac{\partial v}{\partial y} + v \frac{\partial v_b}{\partial y} + w_b \frac{\partial v}{\partial z} + w \frac{\partial v_b}{\partial z}\right) + \rho\left(\frac{\partial v_b}{\partial t} + u_b \frac{\partial v_b}{\partial x}\right. \\
&\quad \left. + v_b \frac{\partial v_b}{\partial y} + w_b \frac{\partial v_b}{\partial z}\right) = -\frac{\partial p}{\partial y} + \frac{1}{R}\left\{\frac{\partial}{\partial x}\left[\mu_b\left(\frac{\partial u}{\partial y} + \frac{\partial v}{\partial x}\right) + \mu\left(\frac{\partial u_b}{\partial y} + \frac{\partial v_b}{\partial x}\right)\right]\right. \\
&\quad + \frac{\partial}{\partial y}\left[\mu_b\left(m \frac{\partial u}{\partial x} + r \frac{\partial v}{\partial y} + m \frac{\partial w}{\partial z}\right) + \mu\left(m \frac{\partial u_b}{\partial x} + r \frac{\partial v_b}{\partial y} + m \frac{\partial w_b}{\partial z}\right)\right] \\
&\quad \left. + \frac{\partial}{\partial z}\left[\mu_b\left(\frac{\partial v}{\partial z} + \frac{\partial w}{\partial y}\right) + \mu\left(\frac{\partial v_b}{\partial z} + \frac{\partial w_b}{\partial y}\right)\right]\right\}
\end{aligned} \tag{2.5}$$

$$\rho_b\left(\frac{\partial w}{\partial t} + u_b \frac{\partial w}{\partial x} + u \frac{\partial w_b}{\partial x} + v_b \frac{\partial w}{\partial y} + v \frac{\partial w_b}{\partial y} + w_b \frac{\partial w}{\partial z} + w \frac{\partial w_b}{\partial z}\right) + \rho\left(\frac{\partial w_b}{\partial t} + u_b \frac{\partial w_b}{\partial x}\right.$$

$$\left. + v_b \frac{\partial w_b}{\partial y} + w_b \frac{\partial w_b}{\partial z}\right) = - \frac{\partial p}{\partial z} + \frac{1}{R} \left\{\frac{\partial}{\partial x} \left[\mu_b\left(\frac{\partial w}{\partial x} + \frac{\partial u}{\partial z}\right) + \mu\left(\frac{\partial w_b}{\partial x} + \frac{\partial u_b}{\partial z}\right)\right]\right.$$

$$+ \frac{\partial}{\partial y} \left[\mu_b\left(\frac{\partial v}{\partial z} + \frac{\partial w}{\partial y}\right) + \mu\left(\frac{\partial v_b}{\partial z} + \frac{\partial w_b}{\partial y}\right)\right] + \frac{\partial}{\partial z} \left[\mu_b\left(m \frac{\partial u}{\partial x} + m \frac{\partial v}{\partial y}\right.\right.$$

$$\left.\left.\left. + r \frac{\partial w}{\partial z}\right)\right] + \frac{\partial}{\partial z} \left[\mu\left(m \frac{\partial u_b}{\partial x} + m \frac{\partial v_b}{\partial y} + r \frac{\partial w_b}{\partial z}\right)\right]\right\} \tag{2.6}$$

$$\rho_b\left[\frac{\partial T}{\partial t} + u \frac{\partial T_b}{\partial x} + u_b \frac{\partial T}{\partial x} + v \frac{\partial T_b}{\partial y} + v_b \frac{\partial T}{\partial y} + w \frac{\partial T_b}{\partial z} + w_b \frac{\partial T}{\partial z}\right]$$

$$+ \rho\left[\frac{\partial T_b}{\partial t} + u_b \frac{\partial T_b}{\partial x} + v_b \frac{\partial T_b}{\partial y} + w_b \frac{\partial T_b}{\partial z}\right] = (\gamma - 1)M_\infty^2\left[\frac{\partial p}{\partial t} + u \frac{\partial p_b}{\partial x} + u_b \frac{\partial p}{\partial x}\right.$$

$$\left. + v_b \frac{\partial p}{\partial y} + w \frac{\partial p_b}{\partial z} + w_b \frac{\partial p}{\partial z} + \frac{1}{R} \Phi\right] + \frac{1}{RPr} \left\{\frac{\partial}{\partial x} \left(\mu_b \frac{\partial T}{\partial x} + \mu \frac{\partial T_b}{\partial x}\right)\right.$$

$$\left. + \frac{\partial}{\partial y} \left(\mu_b \frac{\partial T}{\partial y} + \mu \frac{\partial T_b}{\partial y}\right) + \frac{\partial}{\partial z} \left(\mu_b \frac{\partial T}{\partial z} + \mu \frac{\partial T_b}{\partial z}\right)\right\} \tag{2.7}$$

$$\frac{p}{p_b} = \frac{T}{T_b} + \frac{\rho}{\rho_b} \tag{2.8}$$

where Φ is the perturbation dissipation function defined by

$$\Phi = \mu_b\left\{2r\left(\frac{\partial u_b}{\partial x} \frac{\partial u}{\partial x} + \frac{\partial v_b}{\partial y} \frac{\partial v}{\partial y} + \frac{\partial w_b}{\partial z} \frac{\partial w}{\partial z}\right) + 2m\left[\frac{\partial u_b}{\partial x} \left(\frac{\partial v}{\partial y} + \frac{\partial w}{\partial z}\right)\right.\right.$$

$$\left. + \frac{\partial v_b}{\partial y} \left(\frac{\partial u}{\partial x} + \frac{\partial w}{\partial z}\right) + \frac{\partial w_b}{\partial z} \left(\frac{\partial u}{\partial x} + \frac{\partial v}{\partial y}\right)\right] + 2\left(\frac{\partial u}{\partial y} + \frac{\partial v}{\partial x}\right)\left(\frac{\partial u_b}{\partial y} + \frac{\partial v_b}{\partial x}\right)$$

$$\left. + 2\left(\frac{\partial u}{\partial z} + \frac{\partial w}{\partial x}\right)\left(\frac{\partial u_b}{\partial z} + \frac{\partial w_b}{\partial x}\right) + 2\left(\frac{\partial v}{\partial z} + \frac{\partial w}{\partial y}\right)\left(\frac{\partial v_b}{\partial z} + \frac{\partial w_b}{\partial y}\right)\right\} + \mu\left\{r\left[\left(\frac{\partial u_b}{\partial x}\right)^2\right.\right.$$

$$\left. + \left(\frac{\partial v_b}{\partial y}\right)^2 + \left(\frac{\partial w_b}{\partial z}\right)^2\right] + 2m\left[\frac{\partial u_b}{\partial x} \frac{\partial v_b}{\partial y} + \frac{\partial u_b}{\partial y} \frac{\partial w_b}{\partial z} + \frac{\partial v_b}{\partial y} \frac{\partial w_b}{\partial z}\right]$$

$$\left. + \left(\frac{\partial u_b}{\partial y} + \frac{\partial v_b}{\partial x}\right)^2 + \left(\frac{\partial u_b}{\partial z} + \frac{\partial w_b}{\partial x}\right)^2 + \left(\frac{\partial v_b}{\partial z} + \frac{\partial w_b}{\partial y}\right)^2\right\} \tag{2.9}$$

The constants r and m are given by

$$r = \frac{2}{3} (e + 2) \text{ and } m = \frac{2}{3} (e - 1) \tag{2.10}$$

where e = 0 corresponds to the Stokes hypothesis. The Reynolds number R and Prandtl number Pr are given by

$$R = \frac{U_\infty^* L_\infty^*}{\nu_\infty^*}, \quad Pr = \frac{\mu_\infty^* c_p^*}{\kappa_\infty^*} \tag{2.11a}$$

where ν_∞^*, μ_∞^*, and κ_∞^* are the freestream kinematic viscosity, dynamic viscosity, and thermal conductivity, respectively, and c_p^* is the dimensional specific heat at constant pressure. We assume that the dynamic viscosity is a function of the temperature only so that

$$\mu = T \left. \frac{d\mu_b}{dT} \right|_{T_b} \tag{2.11b}$$

The boundary conditions at the wall are

$$u = v = w = T = 0 \quad \text{at} \quad y = 0 \tag{2.12}$$

The boundary conditions on the velocity fluctuations u and w represent the no-ship conditions and the boundary condition on the velocity fluctuation v represents the no-penetration condition. For a gas flowing over a solid wall, the temperature remains at its mean value unless the frequency is small (i.e., stationary or near stationary disturbances). The boundary conditions as $y \to \infty$ are

$$u(y),\ v(y),\ w(y),\ p(y), \text{ and } T(y) \text{ are bounded as } y \to \infty \tag{2.13}$$

As will be described later, neutral subsonic disturbances decay to zero as $y \to \infty$, whereas neutral supersonic disturbances do not vanish as $y \to \infty$.

3. QUASIPARALLEL PRIMARY INSTABILITY

In this section, we consider the three-dimensional stability of a steady three-dimensional boundary layer. In general, the mean flow in a boundary layer varies with the streamwise coordinate x and spanwise coordinate z. However, at high Reynolds numbers, this variation is small over distances the order of the wavelengths of the disturbances. Consequently, most stability analyses neglect the streamwise and spanwise variations of the mean flow, the so-called parallel-flow assumption. Thus, the basic flow is approximated by

$$u_b = U_m(y),\ v_b = 0,\ w_b = W_m(y),\ T_b = T_m(y),\ p_b = P_m(x) \tag{3.1}$$

Using the parallel-flow assumption reduces equations (2.3)-(2.9) to a system of linear partial differential equations whose coefficients vary only with y. Consequently, the variables t, x, and z can be separated using the so-called normal mode assumption

$$[u,v,p,T,w] = [\zeta_1(y),\ \zeta_3(y),\ \zeta_4(y),\ \zeta_5(y),\ \zeta_7(y)]\ \exp[i(\alpha x + \beta z - \omega t)] \tag{3.2}$$

where α and β are the wave numbers in the streamwise and spanwise directions, respectively, and ω is the frequency. For a temporal stability, α and β are real

but ω is complex. For spatial stability, ω is real but α and β are complex. For the general case, α, β, and ω are complex.

Substituting equations (3.1) and (3.2) into equations (2.3)-(2.9), (2.12), and (2.13) yields the eigenvalue problem

$$D\zeta_3 + i\alpha\zeta_1 - \frac{DT_m}{T_m}\zeta_3 + i(\alpha U_m + \beta W_m - \omega)(\gamma M_\infty^2\zeta_4 - \frac{\zeta_5}{T_m})$$

$$+ i\beta\zeta_7 = 0 \tag{3.3}$$

$$i(\alpha U_m + \beta W_m - \omega)\zeta_1 + \zeta_3 DU_m + i\alpha T_m\zeta_4 - \frac{T_m}{R}\{-\mu_m(r\alpha^2 + \beta^2)\zeta_1$$

$$- \alpha\beta\mu_m(m + 1)\zeta_7 + i(m + 1)\alpha\mu_m D\zeta_3 + \mu_m' D\zeta_1 + i\alpha\mu_m'\zeta_3$$

$$+ \mu_m D^2\zeta_1 + D(\mu_m' DU_m)\zeta_5 + \mu_m' DU_m D\zeta_5\} = 0 \tag{3.4}$$

$$i(\alpha U_m + \beta W_m - \omega)\zeta_3 + T_m D\zeta_4 - \frac{T_m}{R}\{i(m + 1)\alpha\mu_m D\zeta_1$$

$$+ im\alpha\mu_m'\zeta_1 - (\alpha^2 + \beta^2)\mu_m\zeta_3 + r\mu_m' D\zeta_3 + im\beta\mu_m'\zeta_7$$

$$+ i\alpha\mu_m' DU_m\zeta_5 + i\beta\mu_m' DW_m\zeta_5 + r\mu_m D^2\zeta_3 + i(m + 1)\beta\mu_m D\zeta_7\} = 0 \tag{3.5}$$

$$i(\alpha U_m + \beta W_m - \omega)\zeta_7 + \zeta_3 DW_m + i\beta T_m\zeta_4 - \frac{T_m}{R}\{-(m + 1)\alpha\beta\mu_m\zeta_1$$

$$+ i\beta\mu_m'\zeta_3 + i(m + 1)\beta D\zeta_3 - \mu_m(\alpha^2 + r\beta^2)\zeta_7 + \mu_m' D\zeta_7 + \mu_m D^2\zeta_7\} = 0 \tag{3.6}$$

$$i(\alpha U_m + \beta W_m - \omega)\zeta_5 + \zeta_3 DT_m - i(\gamma - 1)T_m M_\infty^2(\alpha U_m + \beta W_m - \omega)\zeta_4$$

$$- \frac{T_m}{R}[2DU_m(D\zeta_1 + i\alpha\zeta_3) + 2DW_m(i\beta\zeta_3 + D\zeta_7) + \mu_m'(DU_m)^2\zeta_5$$

$$+ \mu_m'(DW_m)^2\zeta_5] - \frac{T_m}{RPr}[-\mu_m(\alpha^2 + \beta^2)\zeta_5 + D(\mu_m D\zeta_5) + D(\mu_m' DT_m\zeta_5)] = 0 \tag{3.7}$$

$$\zeta_1 = \zeta_3 = \zeta_5 = \zeta_7 = 0 \quad \text{at} \quad y = 0 \tag{3.8}$$

$$\zeta_n \text{ are bounded as } y \to \infty \tag{3.9}$$

where $D = \partial/\partial y$.

Introducing the Stuart transformation (ref. 34)

$$k\eta_1 = \alpha\zeta_1 + \beta\zeta_7 \tag{3.10}$$

$$k\eta_7 = \alpha\zeta_7 - \beta\zeta_1 \tag{3.11}$$

where $k = \sqrt{\alpha^2 + \beta^2}$ does not reduce the eighth-order system (3.3)-(3.9) into a sixth-order system due to the coupling in the energy equation due to a single dissipation terms, which couples the energy equation to the other equations for 3D waves in 2D or 3D boundary layers. Neglecting this term reduces the eigenvalue problem from an eight-order complex problem to a sixth-order complex problem, thereby resulting in a large saving in computations. The error introduced to this simplification is a function of the Mach number, Reynolds number, and wave angle. For the case of insulated flat plates, Mack found that the maximum error is less than 5% for all Mach numbers at R = 1500. However, most stability calculations being formed are based on the eighth-order rather than the sixth-order system.

Two methods of solution have been employed (refs. 11,35,36). The first reduces the system of equations (3.3)-(3.7) into an eighth-order system of ordinary differential equations, determines an exact solution outside the boundary layer that satisfies the boundary conditions (3.9), uses the resulting linearly independent solutions as initial conditions to integrate the first-order equations to the wall, employs a Gram-Schmidt orthonormalization scheme to keep the solutions linearly independent, and uses an iterative scheme such as Newton-Raphson procedure to determine the desired complex eigenvalue. The second method uses a finite-difference scheme to reduce the governing equations into a system of algebraic equations that is solved using standard techniques to determine the desired eigenvalue.

According to the first approach, the eigenvalue problem (3.3)-(3.9) is converted into a system of first-order equations by letting

$$\zeta_2 = Du = D\zeta_1, \ \zeta_6 = DT = D\zeta_5, \text{ and } \zeta_8 = Dw = D\zeta_7 \tag{3.12}$$

Then, the eigenvalue problem becomes

$$D\zeta = F(y)\zeta \tag{3.13a}$$

$$\zeta_1 = \zeta_3 = \zeta_5 = \zeta_7 = 0 \quad \text{at} \quad y = 0 \tag{3.13b}$$

$$\zeta_n \text{ are bounded as } y \to \infty \tag{3.13c}$$

where $\zeta^T = \{\zeta_1, \zeta_2, \ldots, \zeta_8\}$ and the elements a_{ij} of the matrix F are given in Appendix A. For a given R and a mean flow U_m, W_m, and T_m, the eigenvalue problem (3.13) provides a dispersion relation of the form

$$\omega = \omega(\alpha, \beta) \tag{3.14}$$

In general, ω, α, and β are complex. Thus, equation (3.14) provides two relations among the six real parameters α_r, α_i, β_r, β_i, ω_r, and ω_i. When four of these parameters are specified, equation (3.14) can be solved for the remaining two parameters. For the case of temporal stability, α and β are assumed to be real and fixed, and equation (3.14) provides $\omega = \omega_r + i\omega_i$. Thus, it follows from equation (3.2) that the temporal growth rate is ω_i. For the case of spatial stability, ω is assumed to be real and fixed, and equation (3.14) provides two relations among the remaining four parameters α_r, α_i, β_r, and β_i. The parameters α_r and β_r define a real wavenumber vector $\vec{k}$ whose magnitude k is given by

$$k = (\alpha_r^2 + \beta_r^2)^{\frac{1}{2}} \tag{3.15a}$$

and whose direction (wave angle) ψ is given by

$$\psi = \arctan\,(\beta_r/\alpha_r) \tag{3.15b}$$

Moreover, the parameters α_i and β_i define a growth vector $\vec{\sigma}$ whose magnitude σ is given by

$$\sigma = (\alpha_i^2 + \beta_i^2)^{\frac{1}{2}} \tag{3.15c}$$

and whose direction (growth direction) $\tilde{\psi}$ is given by

$$\tilde{\psi} = \arctan\,(\beta_i/\alpha_i) \tag{3.15d}$$

In general, the growth and wave directions need not coincide and two more relations need to be specified to complete the formulation of the spatial stability problem. Using the method of multiple scales (refs. 37,38), Nayfeh (refs. 21,39) found that the ratio of the group velocity components must be real, thereby providing a third relation. Maximizing the total growth rate can provide the fourth needed relation. These points are discussed further in Section 4. Nayfeh and Padhye (ref. 40) used the complex group velocity vector to relate the problems of temporal and spatial stabilities.

In the case of 2D spatial stability, the two additional relations are given by $\beta = \beta_r + i\beta_i = 0$ and Eq. (3.14) can be used to determine the complex parameter α for any given ω. For the case of 3D spatial stability in boundary layers that depend on x and y only (such as 2D mean flows and flows over an infinite span swept wing), the analysis in Section 4 shows that β = constant and hence Eq. (3.14) can be used to determine the complex parameter α for any given ω and β. In this case, the growth direction is often taken in the x-direction (i.e., β_i is assumed to be zero).

To account for the slow growth of the boundary layer, one can improve the parallel-flow assumption by calculating the local stability of the mean-flow profiles, thereby obtaining values for α and β that vary slowly with x and z. Thus, equation (3.2) is replaced with

$$[u,v,p,T,w] = [\zeta_1(y),\ \zeta_3(y),\ \zeta_4(y),\ \zeta_5(y),\ \zeta_7(y)]\exp(i\theta) \tag{3.16}$$

where

$$\frac{\partial\theta}{\partial x} = \alpha(x,z), \quad \frac{\partial\theta}{\partial z} = \beta(x,z), \quad \frac{\partial\theta}{\partial t} = -\omega \tag{3.17}$$

and the ζ_n are governed by the eigenvalue problem consisting of equations (3.3)-(3.9). This is the so-called quasi-parallel assumption. As discussed earlier, the growth rate vector is given by

$$\vec{\sigma} = \alpha_i \vec{i} + \beta_i \vec{j}$$

It is independent of the transverse direction and the flow variable whose growth is investigated; neither of these statements is valid for the case of growing boundary layers as discussed in Section 4.

3.1 Inviscid Case

In contrast with the case of incompressible boundary layers, compressible boundary layers, even on flat plates, have inviscid instability, which increases with increasing Mach number. The inviscid instability is governed by equations (3.3)-(3.9) with R being set equal to infinity; that is, it is governed by

$$D\zeta_3 + i\alpha\zeta_1 - \frac{DT_m}{T_m}\zeta_3 + i(\alpha U_m + \beta W_m - \omega)(\gamma M_\infty^2\zeta_4 - \frac{\zeta_5}{T_m}) + i\beta\zeta_7 = 0 \tag{3.18}$$

$$i(\alpha U_m + \beta W_m - \omega)\zeta_1 + \zeta_3 DU_m + i\alpha T_m\zeta_4 = 0 \tag{3.19}$$

$$i(\alpha U_m + \beta W_m - \omega)\zeta_3 + T_m D\zeta_4 = 0 \tag{3.20}$$

$$i(\alpha U_m + \beta W_m - \omega)\zeta_7 + \zeta_3 DW_m + i\beta T_m\zeta_4 = 0 \tag{3.21}$$

$$i(\alpha U_m + \beta W_m - \omega)\zeta_5 + \zeta_3 DT_m - i(\gamma - 1)T_m M_\infty^2(\alpha U_m + \beta W_m - \omega)\zeta_4 = 0 \tag{3.22}$$

$$\zeta_3 = \zeta_5 = 0 \quad \text{at} \quad y = 0 \tag{3.23}$$

$$\zeta_n \text{ are bounded as } y \to \infty \tag{3.24}$$

Equations (3.18)-(3.27) can be combined into a second-order equation governing ζ_3 or ζ_4. To accomplish this, we use the transformation (3.10) and (3.11). Thus, we add α times equations (3.19) to β times equation (3.21) and obtain

$$ik(\alpha U_m + \beta W_m - \omega)\eta_1 + \zeta_3 D(\alpha U_m + \beta W_m) + ik^2 T_m\zeta_4 = 0 \tag{3.25}$$

Using equation (3.22) to eliminate ζ_5 from equation (3.18) and using equation (3.10), we obtain

$$ik\eta_1 + D\zeta_3 + iM_\infty^2 (\alpha U_m + \beta W_m - \omega)\zeta_4 = 0 \tag{3.26}$$

Eliminating η_1 from equations (3.25) and (3.26) yields

$$(\alpha U_m + \beta W_m - \omega)D\zeta_3 - \zeta_3 D(\alpha U_m + \beta W_m) = ik^2 T_m(1 - M_r^2)\zeta_4 \tag{3.27}$$

or

$$D\chi = \frac{i(1-M_r^2)M_\infty^2}{M_r^2}\zeta_4 \tag{3.28}$$

where

$$\chi = \frac{\zeta_3}{\alpha U_m + \beta W_m - \omega} \tag{3.29}$$

and

$$M_r = \frac{(\alpha U_m + \beta W_m - \omega)M_\infty}{k\sqrt{T_m}} \tag{3.30}$$

can be interpreted as the local Mach number of the mean flow in the direction of the wavenumber vector $\vec{k} = \alpha\vec{i} + \beta\vec{j}$ relative to the phase velocity ω/k. In general M_r is complex and it is only real for neutral disturbances. In terms of χ and M_r, equation (3.20) can be rewritten as

$$D\zeta_4 = -\frac{ik^2 M_r^2}{M_\infty^2}\chi \tag{3.31}$$

Eliminating ζ_4 from equations (3.28) and (3.31) yields the following second-order equation governing χ:

$$D^2\chi + D\left[\ln\frac{M_r^2}{1-M_r^2}\right]D\chi - k^2(1 - M_r^2)\chi = 0 \tag{3.32}$$

Eliminating χ from equations (3.28) and (3.31) yields

$$D^2\zeta_4 - D(\ln M_r^2)D\zeta_4 - k^2(1 - M_r^2)\zeta_4 = 0 \tag{3.33}$$

In the freestream, $T_m = 1$, $U_m = 1$ and $W_m = 0$ are constants and hence $M_r = M_f$ is a constant and equations (3.32) and (3.33) reduce to

$$D^2\chi - k^2(1 - M_f^2)\chi = 0 \tag{3.34}$$

and

$$D^2\zeta_4 - k^2(1 - M_f^2)\zeta_4 = 0 \tag{3.35}$$

It is clear from equations (3.34) and (3.35) that neutral disturbances decay in the freestream if and only if $M_f^2 < 1$; these disturbances are termed subsonic waves. When $M_f^2 > 1$, neutral disturbances do not vanish in the freestream and they represent

sound waves or Mach waves of the relative flow; they are termed supersonic waves and may be outgoing or incoming waves. When $M_f^2 = 1$, disturbances are termed sonic waves. The above classification is due to Lees and Lin (ref. 2).

For the case of two-dimensional inviscid waves in a two-dimensional boundary layer, Lees and Lin (ref. 2) established a number of conclusions for the case of temporal waves. Their main conclusions are

(i) The necessary and sufficient condition for the existence of a neutral subsonic wave is the presence of a generalized inflection point $y_s > y_0$ in the boundary layer at which

$$D(\rho_m DU_m) = 0 \tag{3.36}$$

where

$$U_m(y_0) = 1 - \frac{1}{M_\infty} \tag{3.37}$$

The phase velocity $c_s = \omega/\alpha_s$ of this neutral wave is $U_m(y_s)$, the mean velocity at the generalized inflection point y_s, which is larger than $1 - \frac{1}{M_\infty}$.

(ii) A sufficient condition for the existence of an unstable subsonic wave is the presence of a generalized inflection point at $y_s > y_0$; its phase velocity $c > 1 - 1/M_\infty$. Compressible boundary-layer flows over insulated flat plates always have inflection points and hence they are unstable to inviscid disturbances.

(iii) There is a neutral subsonic wave having the wavenumber $\alpha = 0$ and the phase velocity $c = c_0$.

(iv) When $M_r^2 < 1$ everywhere in the boundary layer, there is a unique wavenumber α_s corresponding to the phase velocity c_s for the neutral subsonic wave.

Using extensive numerical calculations, Mack (refs. 11,15) established the existence of an infinite sequence of discrete wave numbers α_{sn}, corresponding to an infinite sequence of discrete modes when $M_r^2 > 1$ somewhere in the boundary layer. He referred to the modes that are additional to the mode found by Lees and Lin as higher modes. In contrast with the first mode whose existence depends on the presence of a generalized inflection point, the higher modes exist whenever $M_r^2 > 1$, irrespective of the presence or absence of a generalized inflection point. The lowest Mach number at which the higher modes exist in the boundary layer on an insulated flat plate is 2.2. It turns out that this is also the lowest Mach number at which subsonic higher-mode disturbances exist. The lowest of the subsonic modes is called the second mode and it is the most amplified of the higher modes.

Later, Mack developed a simple theory that provides an approximation to the infinite sequence of wave numbers α_{sn}. He neglected the second term in (3.32) and expressed the solution of the resulting equation that satisfies the boundary condition v(0) as

$$\chi \approx \pm \sin\left[k_{sn} \int_0^y \sqrt{M_r^2 - 1}\, dy\right], \quad y < y_a \tag{3.38}$$

and the solution that decays as $y \to \infty$ as

$$\chi \approx - i \exp\left[- k_{sn} \int_{y_a}^{y} \sqrt{1 - M_r^2}\, dy\right], \; y > y_a \tag{3.39}$$

where y_a is the value of y where $M_r^2 = 1$. He chose the constant in (3.39) to be -i so that the pressure is real and positive for $y > y_a$. He argued that $D\chi$ must go to zero as $y \to y_a$ because the pressure is continuous and finite at $y = y_a$, thereby obtaining the eigenvalues

$$k_{sn} \int_{0}^{y_a} \sqrt{M_r^2 - 1}\, dy = (n - \tfrac{1}{2})\pi, \; n = 1, 2, 3, \ldots \tag{3.40}$$

We note that the second term in equation (3.32) is singular at y_a and hence the expansions (3.38) and (3.39) are invalid at $y = y_a$. To connect these expansions, one needs to consider the neighborhood of $y = y_a$, determine an expansion there, and match it to both (3.38) and (3.39). Alternatively, the Langer transformation can be used to determine a single uniformly valid expansion. Even such a consistent expansion is valid only when M_r does not vanish anywhere, (i.e., there is no critical layer) and hence there is no generalized inflection point; otherwise, one cannot neglect the second terms in (3.32) and (3.33). An expansion valid when M_r vanishes somewhere is determined below using the Olver transformation. Mack (refs. 11,15) called the waves when $M_r = 0$ inflectional neutral waves and those which occur when $M_r \neq 0$ non-inflectional neutral waves. His numerical results for the case of non-inflectional neutral waves (Figs. 1 and 2) are qualitatively in agreement with his simple theory, whereas his calculations for the case of inflectional waves (Figs. 3 and 4) differ from those obtained from his simple theory. According to his theory, $\zeta_4(\delta)$ is positive for all modes, there are no zeros in the interval $y > y_a$, and the number of zeros in $y < y_a$ increases by one for each successive mode.

To determine a single uniformly valid expansion, we eliminate the second term in equation (3.33) using the transformation

$$\zeta_4 = M_r \phi \tag{3.41}$$

and obtain

$$\phi'' - \left[k^2(1 - M_r^2) - \frac{M_r''}{M_r} + \frac{2M_r'^2}{M_r^2}\right]\phi = 0 \tag{3.42}$$

For the case of non-inflectional waves (i.e., $M_r \neq 0$ everywhere), we use the Langer transformation (refs. 37,38) and obtain the approximate solution

$$\phi \approx \frac{\xi^{1/4}}{\sqrt[4]{1-M_r^2}} \left[c_1 Ai(\xi) + c_2 Bi(\xi)\right] \tag{3.43}$$

and hence

$$\zeta_4 \approx \frac{M_r \xi^{1/4}}{\sqrt[4]{1-M_r^2}} \left[c_1 Ai(\xi) + c_2 Bi(\xi)\right] \tag{3.44}$$

where Ai and Bi are the Airy functions of the first and second kind, respectively,

$$\frac{2}{3}\xi^{3/2} = k\int_{y_a}^{y} \sqrt{1 - M_r^2}\, dy \tag{3.45}$$

and $y = y_a$ is the turning point at which $M_r^2(y_a) = 1$. Since

$$Ai(\xi) \sim \frac{\exp[-\frac{2}{3}\xi^{2/3}]}{2\sqrt{\pi}\,\xi^{1/4}} \text{ as } \xi \to \infty \tag{3.46}$$

and

$$Bi(\xi) \sim \frac{\exp[\frac{2}{3}\xi^{3/2}]}{\sqrt{\pi}\,\xi^{1/4}} \text{ as } \xi \to \infty \tag{3.47}$$

the vanishing of the disturbance as $y \to \infty$ demands that $c_2 = 0$. Then, the boundary condition $v(0) = 0$ or $\zeta_3(0) = 0$ demands that

$$Ai' = 0 \quad \text{at} \quad y = 0 \tag{3.48}$$

But

$$Ai(\xi) \sim \frac{1}{\sqrt{\pi}\,(-\xi)^{1/4}} \sin[\frac{2}{3}(-\xi)^{3/2} + \frac{1}{4}\pi] \text{ as } \xi \to -\infty \tag{3.49}$$

Hence

$$\cos[k\int_0^{y_a} \sqrt{M_r^2 - 1}\, dy + \frac{1}{4}\pi] = 0 \tag{3.50}$$

Consequently,

$$k_{sn}\int_0^{y_a} \sqrt{M_r^2 - 1}\, dy = (n - \frac{3}{4})\pi, \quad n = 1, 2, 3, \ldots \tag{3.51}$$

whose righthand side differs from that of Mack by $\frac{1}{4}\pi$. Moreover, the eigenfunction (3.44) with $c_2 = 0$ differs from that of Mack in the presence of the factor $M_r/\sqrt[4]{1 - M_r^2}$ and the phase $\frac{1}{4}\pi$ in the interval $y < y_a$.

For the case of inflectional waves (i.e., $M_r = 0$ at $y = y_c$, $y_c > y_a$), the expansion (3.43) is not valid as $y \to y_c$ and we need an expansion that is valid in the neighborhood of $y = y_c$. Using the Olver transformation (ref. 37), we find that

$$\phi \sim \frac{[\int_{y_c}^{y} \sqrt{1-M_r^2}\, dy]^{\frac{1}{2}}}{\sqrt[4]{1-M_r^2}} \{b_1 I_{3/2}[k\int_{y_c}^{y} \sqrt{1 - M_r^2}\, dy]$$

$$+ b_2 K_{3/2}[k\int_{y_c}^{y} \sqrt{1 - M_r^2}\, dy]\} \tag{3.52}$$

which is valid in the interval $y > y_a$. Since

$$I_{3/2}(\xi) \to \frac{1}{\sqrt{2\pi\xi}} e^{\xi} \text{ and } K_{3/2}(\xi) \to \sqrt{\frac{\pi}{2\xi}}\, e^{-\xi} \text{ as } \xi \to \infty \tag{3.53}$$

the boundary condition that ζ_4 tends to zero as $y \to \infty$ demands that $b_1 = 0$. This expansion needs to be matched with the expansion (3.43) that is valid at the turning point y_a. Expanding (3.43) for large k and for $y > y_a$, expanding (3.52) for large k and for $y < y_c$, means that $b_1 = 0$, we obtain

$$\sqrt{\frac{\pi}{2k}}\, b_2 e^{k\int_y^{y_c}\sqrt{1-M_r^2}dy} = \frac{c_1}{2\sqrt{\pi}} e^{-k\int_{y_a}^{y}\sqrt{1-M_r^2}dy} + \frac{c_2}{\sqrt{\pi}} e^{-k\int_{y_a}^{y}\sqrt{1-M_r^2}dy} \tag{3.54}$$

Hence, $c_2 = 0$ and

$$b_2 = \frac{c_1\sqrt{k}}{\pi\sqrt{2}} \exp\left[-\int_{y_a}^{y_c} \sqrt{1 - M_r^2}\, dy\right] \tag{3.55}$$

Imposing the boundary condition at the wall that $v(0) = 0$ or $\zeta_3(0) = 0$ yields the eigenvalues as in (3.51). Thus, the difference between inflectional and non-inflectional waves is in the shape of the eigenfunction.

Using extensive numerical computations, Mack established a number of conclusions regarding supersonic stability:

(i) In contrast with incompressible stability theory, there is more than one mode of instability and it is one of the additional modes that is the most unstable. Figure 5 shows the variation of the maximum temporal amplification rate of 2D waves with Mach number. It is clear that below $M_\infty = 2.2$, the boundary layer on an insulated flat plate is virtually stable to inviscid 2D waves and that above $M_\infty = 2.2$ the second mode is the most unstable mode. Moreover, the maximum amplification rate increases sharply as M_∞ increases beyond 2.2. Furthermore, above $M_\infty = 5$, the first mode is not even the second most unstable mode.

(ii) In contrast with incompressible stability theory, 3D first modes are more unstable than their corresponding 2D waves. However, 3D second modes are more stable than their corresponding 2D waves. Figure 6 shows the variation of the temporal amplification rate of the first and second modes with frequency for $M_\infty = 4.5$ and several wave angles. It clearly shows that the most unstable first-mode wave has a wave angle that is approximately 60° and an amplification rate that is approximately twice the maximum amplification rate of its corresponding 2D wave.

(iii) Whereas cooling can stabilize first-mode waves in accordance with the prediction of Lees (ref. 3), cooling destablizes second-mode waves. Figure 7 shows the variation of the maximum temporal growth rate of the first mode at $M_\infty = 3.0$, 4.5, and 5.8 and the second mode at $M_\infty = 5.8$ with the ratio of the wall temperature T_w to the recovery temperature T_r. It is clear that 2D and 3D first-mode waves can be completely stabilized by cooling, whereas second-mode waves are destablished by cooling.

3.2 Viscous Stability for Flat Plates

Again, using extensive numerical calculations, Mack (refs. 10,11) investigated the influence of Mach number on the viscous instability of supersonic flows past flat plates. He found that viscosity is stabilizing for both 2D and 3D first-mode waves when $M_\infty \geq 3.0$ and for second-mode waves at all Mach numbers; that is, the maximum amplification rate (over all frequencies, and wave angles in case of 3D waves, at constant Reynolds number) decreases with decreasing Reynolds number. This result was disputed by Wazzan, Taghavi, and Keltner (ref. 41) who did not find a transition from viscous to inviscid instability with increasing Mach number but found that viscous instability persists to $M_\infty = 6.0$. Mack (ref. 42) reconfirmed his calculations for the case of temporal stability and obtained spatial stability results that agree with his earlier conclusions on the influence of viscosity on compressible stability. Moreover, the spatial stability calculations of El-Hady and Nayfeh (ref. 19) and Nayfeh and Harper (ref. 43) agree with those of Mack for at least three significant figures for all the calculations they performed. Moreover, the calculations of Malik qualitatively agree with those of Mack.

Figure 8 shows the neutral stability curves of 2D waves calculated by Mack at $M_\infty = 1.6$, 2.2, 2.6, 3.0, and 3.8. He plotted α vs. R^{-1} to emphasize the higher Reynolds number region. Comparing the neutral curve for $M_\infty = 1.6$ with that of the Blasius flow (i.e., $M_\infty = 0$) shows that, although they have the same general type, compressiblity drastically reduced the viscous instability, resulting in much lower neutral wave numbers. As the Mach number increases beyond 1.6, the viscous instability continues to weaken although the effect of the increase in inviscid instability continues to extend to lower and lower Reynolds numbers. When M_∞ reaches 3.8, the viscous instability disappears and viscosity acts only to damp out the inviscid instability.

As in the case of inviscid instability, the most unstable first-mode waves are 3D waves. Figure 9 shows the variation of the maximum temporal amplification rate of 2D and 3D waves with Reynolds number for $M_\infty = 1.3$, 1.6, 2.2, and 3.0 and Figure 10 shows the variation of the maximum spatial amplification rate of 2D and 3D waves at $\psi = 50^\circ$ with R for $M_\infty = 1.6$ (ref. 19). The most unstable wave angles of 3D waves are shown in Figure 9. At $M_\infty = 1.3$, the instability of 2D and 3D waves is due to viscosity. As M_∞ increases, the viscous instability decreases for both 2D and 3D waves. Whereas increasing the Mach number results in a drastic decrease in the 2D maximum growth rates, it produces only a slight change in those of the 3D waves.

As in the inviscid case, the numerical results of Mack suggest that the 2D second- and higher-mode waves are more unstable than their corresponding 3D waves. Moreover, the maximum growth rate of second-mode waves drops sharply as the wave angle increases from zero.

The lowest Mach number at which Mack was able to calculate 2D second-mode waves is $M_\infty = 3.0$ at which the minimum critical Reynolds number is 13,900. As pointed out in the preceding section, the inviscid instability increases rapidly with increasing Mach number and hence one would expect the minimum critical Reynolds number to decrease rapidly to lower values as the Mach number decreases. In fact, Mack found that the minimum critical Reynolds numbers drops to 235 as the Mach number increases to 4.5. Moreover, at high Mach numbers second-mode waves have much higher growth rates than oblique first-mode waves.

Whereas cooling can stabilize 2D and 3D first-mode waves, second-mode waves cannot be stabilized by cooling. On the contrary second-mode waves are destablized

by cooling. Malik (ref. 43) studied the influence of cooling on oblique first-mode waves at $\psi = 60°$ for $M_\infty = 2$ and 4.5 and second-mode waves for $M_\infty = 4.5$; in these calculations $R = 1500$ and the stagnation temperature is 560°R. Figure 11 shows that the oblique first-mode wave at $M_\infty = 2$ is completely stabilized when $T_w/T_{ad} = 0.7$, whereas that at $M_\infty = 4.5$ is stablized only when $T_w/T_{ad} = 0.48$. On the other hand, Figs. 11 and 12 show that the second-mode wave is destablished by cooling. In fact, the maximum growth rate increases rapidly with cooling. Malik found that the frequency of most amplified first-mode wave decreases with cooling whereas that of the most amplified second-mode wave increases with cooling.

Malik (ref. 43) also investigated the influence of favorable pressure gradients (Fig. 13) and suction (Fig. 14) on the stabilization of second-mode waves. He found that each of them shifts the band of unstable frequencies to higher values and reduces the peak amplification. Consequently, it appears that, whereas cooling cannot be used to stabilize second-mode waves, they can be stablized using either suction or wall shaping to produce a favorable pressure gradient.

Preliminary results of Malik (ref. 43) indicate that real gas effects tend to destabilize hypersonic boundary layers.

4. NONPARALLEL STABILITY

We confine our consideration to mean flows that are slightly nonparallel, that is, the normal velocity component V_m is small compared with the other components U_m and W_m. This in turn implies that all the mean-flow variables must be weak functions of the streamwise and spanwise coodinates. In other words

$$U_m = U_m(x_1,y,z_1) \ , \ V_m = \varepsilon V_m^*(x_1,y,z_1), \ W_m = W_m(x_1,y,z_1) \tag{4.1}$$

$$p_m = p_m(x_1,z_1) \ , \ T_m = T_m(x_1,y,z_1) \tag{4.2}$$

where $V_m^* = O(1)$. We describe the relatively slow variations of the mean-flow quantities in the streamwise and spanwise directions by the slow scales $x_1 = \varepsilon x$ and $z_1 = \varepsilon z$, respectively, where $\varepsilon = 1/R$.

We use the method of multiple scales (refs. 37,38) to determine a uniformly valid asymptotic expansion of the solution of equations (2.3)-(2.9), (2.12) and (2.13) in the form

$$q(x,y,z,t;\varepsilon) = [q_0(x_1,y,z_1,t_1) + \varepsilon q_1(x_1,y,z_1,t_1) + \ldots]\exp(i\theta) \tag{4.3}$$

where $t_1 = \varepsilon t$, a slow time scale, and

$$\frac{\partial\theta}{\partial x} = \alpha(x_1,z_1) \ , \ \frac{\partial\theta}{\partial z} = \beta(x_1,z_1) \ , \ \frac{\partial\theta}{\partial t} = -\omega \tag{4.4}$$

Assuming the phase θ to be twice continuously differentiable, we have

$$\frac{\partial\alpha}{\partial z_1} = \frac{\partial\beta}{\partial x_1} \tag{4.5}$$

In the case of mean flows that are independent of z, such as 2D mean flows and flows over infinite-span swept wings, $\alpha = \alpha(x_1)$ and $\beta = \beta(x_1)$, because the coefficients of equations (2.3)-(2.9) are independent of z_1. Then, it follows from equation (4.5) that β = constant. Substituting equations (4.1)-(4.4) into equations (2.3)-(2.9), (2.12) and (2.13) and equating coefficients of like powers of ε, we obtain problems describing the zeroth- and first-order disturbances.

4.1 Zeroth-Order Problem

$$L_1(u_o,v_o,w_o,p_o,T_o) = - i\rho_m(\omega - \alpha U_m - \beta W_m)(\frac{p_o}{p_m} - \frac{T_o}{T_m}) + i\rho_m(\alpha u_o + \beta w_o)$$

$$+ D(\rho_m v_o) = 0 \tag{4.6}$$

$$L_2(u_o,v_o,w_o,p_o,T_o) = - i\rho_m(\omega - \alpha U_m - \beta W_m)u_o + \rho_m v_o DU_m + i\alpha p_o$$

$$- \frac{1}{R}\{- \mu_m(r\alpha^2 + \beta^2)u_o + D(\mu_m Du_o) + i\alpha\mu_m(1 + m)Dv_o$$

$$+ i\alpha v_o D\mu_m - \alpha\beta\mu_m(1 + m)w_o + D(\frac{d\mu_m}{dT} T_o)DU_m + \frac{d\mu_m}{dT} T_o D^2 U_m\} = 0 \tag{4.7}$$

$$L_3(u_o,v_o.w_o,p_o,T_o) = - i\rho_m(\omega - \alpha U_m - \beta W_m)v_o + Dp_o$$

$$- \frac{1}{R}\{i\mu_m(1 + m)(\alpha Du_o + \beta Dw_o) + im(\alpha u_o + \beta w_o)D\mu_m$$

$$- (\alpha^2 + \beta^2)\mu_m v_o + D(\mu_m rDv_o) + i(\alpha DU_m + \beta DW_m)\frac{d\mu_m}{dT} T_o\} = 0 \tag{4.8}$$

$$L_4(u_o,v_o,w_o,p_o,T_o) = - i\rho_m(\omega - \alpha U_m - \beta W_m)w_o + \rho_m v_o DW_m + i\beta p_o$$

$$- \frac{1}{R}\{- \alpha\beta\mu_m(1 + m)u_o + i\beta\mu_m(1 + m)Dv_o + i\beta v_o D\mu_m$$

$$- \mu_m(\alpha^2 + r\beta^2)w_o + D(\mu_m Dw_o) + D(\frac{d\mu_m}{dT} T_o)DW_m + \frac{d\mu_m}{dT} T_o D^2 W_m\} = 0 \tag{4.9}$$

$$L_5(u_o,v_o.w_o,p_o,T_o) = - i\rho_m(\omega - \alpha U_m - \beta W_m)T_o + \rho_m v_o DT_m + i(\gamma -1)M_\infty^2 p_o$$

$$\cdot (\omega - \alpha U_m - \beta W_m) - \frac{(\gamma-1)M_\infty^2}{R} \{2\mu_m(DU_m Du_o + DW_m Dw_o)$$

$$+ 2i\mu_m(\alpha DU_m + \beta DW_m)v_o + \frac{d\mu_m}{dT} [(DU_m)^2 + (DW_m)^2]T_o\}$$

$$- \frac{1}{RPr}\{2D\mu_m DT_o + \mu_m D^2 T_o - (\alpha^2 + \beta^2)\mu_m T_o + D^2\mu_m T_o\} = 0 \tag{4.10}$$

$$u_o = v_o = w_o = T_o = 0 \quad \text{at} \quad y = 0 \tag{4.11}$$

$$u_o,v_o,w_o,T_o \to 0 \quad \text{as} \quad y \to \infty \tag{4.12}$$

The solution of the zeroth-order problem can be expressed as

$$[u_o,Du_o,v_o,T_o,DT_o,w_o,Dw_o]^T = A(x_1,z_1,t_1)\zeta(x_1,z_1,y) \tag{4.13}$$

where ζ is a column vector having 8 components and is governed by the quasi-parallel eigenvalue problem (3.13). The function $A(x_1,z_1,t_1)$ is arbitrary at this level of approximation; it will be determined by imposing the solvability condition at the next level of approximation.

4.2 First-Order Problem

Using equation (4.13), we write the first-order problem as

$$Dz_{1n} - \sum_{m=1}^{8} a_{nm}z_{1m} = D_n \frac{\partial A}{\partial t_1} + E_n \frac{\partial A}{\partial x_1} + F_n \frac{\partial A}{\partial z_1} + G_n A \tag{4.14}$$

$$z_{11} = z_{13} = z_{17} = 0, \; z_{15} = 0 \quad \text{at} \quad y = 0 \tag{4.15}$$

$$z_{1n} \text{ is bounded as } y \to \infty \tag{4.16}$$

where

$$z_{11} = u_1, \; z_{12} = Du_1, \; z_{13} = v_1, \; z_{14} = p_1 \tag{4.17}$$

$$z_{15} = T_1, \; z_{16} = DT_1, \; z_{17} = w_1, \; z_{18} = Dw_1 \tag{4.18}$$

and the D_n, E_n, F_n, and G_n are known functions of the ζ_n, α, β, and the mean-flow quantities; they are defined in Appendix B. Since the homogeneous problem (4.14)-(4.16) has a nontrivial solution, the inhomogeneous problem has a solution only if

the right-hand side of equation (4.14) is orthogonal to every solution of the adjoint homogeneous problem (ref. 38)

$$D\zeta_n^* + \sum_{m=1}^{8} a_{mn}\zeta_m^* = 0 \tag{4.19}$$

$$\zeta_2^* = \zeta_4^* = \zeta_8^* = 0, \ \zeta_6^* = 0 \quad \text{at} \quad y = 0 \tag{4.20}$$

$$\zeta_n^* \text{ is bounded as } y \to \infty \tag{4.21}$$

The solvability condition takes the form

$$\int_0^\infty \sum_{n=1}^{8} \left[D_n \frac{\partial A}{\partial t_1} + E_n \frac{\partial A}{\partial x_1} + F_n \frac{\partial A}{\partial z_1} + G_n A\right]\zeta_n^* dy = 0 \tag{4.22}$$

Substituting for the D_n, E_n, F_n, and G_n from Appendix B into equation (4.22) yields the following partial-differential equation governing the modulation of A:

$$\frac{\partial A}{\partial t} + \omega_\alpha \frac{\partial A}{\partial x} + \omega_\beta \frac{\partial A}{\partial z} = \varepsilon h_1(\alpha,\beta,x,z)A \tag{4.23}$$

where ω_α and ω_β are the group velocity components in the x and z directions; they, along with h_1, are given in quadratures, as in Appendix C.

Equation (4.23) shows that A is a function of x and z as well as α and β. To determine the equations describing α and β, we differentiate equations (3.13) with respect to x_1 and obtain

$$D\left(\frac{\partial \zeta_n}{\partial x_1}\right) - \sum_{m=1}^{8} a_{nm}\left(\frac{\partial \zeta_m}{\partial x_1}\right) = iE_n \frac{\partial \alpha}{\partial x_1} + iF_n \frac{\partial \beta}{\partial x_1} + \sum_{m=1}^{8} \frac{\partial a_{mn}}{\partial x_1}\bigg|_{\alpha,\beta} \zeta_m \tag{4.24}$$

$$\frac{\partial \zeta_1}{\partial x_1} = \frac{\partial \zeta_3}{\partial x_1} = \frac{\partial \zeta_5}{\partial x_1} = \frac{\partial \zeta_7}{\partial x_1} = 0 \quad \text{at} \quad y = 0 \tag{4.25}$$

$$\frac{\partial \zeta_n}{\partial x_1} \text{ is bounded as } y \to \infty \tag{4.26}$$

Imposing the solvability condition on equations (4.24)-(4.26) yields

$$\omega_\alpha \frac{\partial \alpha}{\partial x_1} + \omega_\beta \frac{\partial \beta}{\partial x_1} = h_2\ (\alpha,\beta,x_1,z_1) \tag{4.27}$$

where h_2 is defined in Appendix C. Similarly, differentiating equations (3.13) with respect to z_1 and imposing the solvability condition for the resulting problem, we obtain

$$\omega_\alpha \frac{\partial \alpha}{\partial z_1} + \omega_\beta \frac{\partial \beta}{\partial z_1} = h_3(\alpha,\beta,x_1,z_1) \tag{4.28}$$

where h_3 is defined in Appendix C. Using equation (4.5), we rewrite equations (4.27) and (4.28) as

$$\omega_\alpha \frac{\partial\alpha}{\partial x} + \omega_\beta \frac{\partial\alpha}{\partial z} = \varepsilon h_2 \tag{4.29}$$

$$\omega_\alpha \frac{\partial\beta}{\partial x} + \omega_\beta \frac{\partial\beta}{\partial z} = \varepsilon h_3 \tag{4.30}$$

Therefore, equations (4.23), (4.29), and (4.30) describe the modulation of A, α, and β with x, z, and t.

For a monochromatic wave, $\partial A/\partial t = 0$ and equation (4.23) reduces to

$$\omega_\alpha \frac{\partial A}{\partial x} + \omega_\beta \frac{\partial A}{\partial z} = \varepsilon h_1 A \tag{4.31}$$

Nayfeh (ref. 21) argued that, in general, $\omega_\beta/\omega_\alpha$ is complex and hence equation (4.31) is elliptic for real x and z. In order that equation (4.31) be hyperbolic representing a propagating wave, $\omega_\beta/\omega_\alpha$ must be real and equations (4.29)-(4.31) reduce to the ordinary differential equations

$$\frac{dA}{ds} = \frac{\varepsilon h_1 A}{\omega_\alpha}, \quad \frac{d\alpha}{ds} = \frac{\varepsilon h_2}{\omega_\alpha}, \quad \frac{d\beta}{ds} = \frac{\varepsilon h_3}{\omega_\alpha} \tag{4.32}$$

along the characteristic

$$\frac{dx}{ds} = 1 \quad \text{and} \quad \frac{dz}{ds} = \frac{\omega_\beta}{\omega_\alpha} \tag{4.33}$$

Thus,

$$A = A_0 \exp\left[\varepsilon\int(h_1/\omega_\alpha)ds\right] = A_0 \exp\left[\varepsilon\int(h_1/\omega_\alpha)dx\right] \tag{4.34}$$

and

$$\alpha = \varepsilon\int h_2 ds, \quad \beta = \varepsilon\int h_3 ds \tag{4.35}$$

where A_0 is a constant. Therefore, to the first approximation,

$$u \approx A_0 \zeta_1(x,y,z)\exp\left[i\int(\alpha + \beta\frac{\omega_\beta}{\omega_\alpha})dx + \varepsilon\int\frac{h_1}{\omega_\alpha}dx - i\omega t\right] \tag{4.36}$$

For the case of parallel flows, the condition $\omega_\beta/\omega_\alpha$ be real reduces to $d\alpha/d\beta$ being real, which was obtained by Nayfeh (ref. 21) and Cebeci and Stewartson (ref. 44) using the saddle-point method.

4.3 Growth Rate

Defining the growth rate in the streamwise direction as

$$\sigma_x = \text{Real}\left[\frac{\partial}{\partial x}(\ln u)\right]$$

we find from equation (4.36) that

$$\sigma_x = -\left(\alpha_i + \beta_i \frac{\omega_\beta}{\omega_\alpha}\right) + \varepsilon \text{ Real } \left(\frac{h_1}{\omega_\alpha}\right) + \frac{\partial}{\partial x}(\ln\zeta_1) \tag{4.37}$$

The first term is the quasiparallel contribution and the last two terms are due to the growth of the boundary layer. Whereas the second term is independent of the transverse direction, the third term strongly depends on the transverse direction. Hence, in contrast with the parallel or quasiparallel case, the local growth rate depends on both the streamwise and transverse directions. Moreover, the transverse variation depends on the flow variable being investigated.

It follows from equation (4.36) that the amplification factor is

$$\frac{\zeta_n(x,y,z)}{\zeta_n(x_o,y,z)} \exp\left[-\int_{x_o}^{x} \left(\alpha_i + \beta_i \frac{\omega_\beta}{\omega_\alpha}\right)dx + \varepsilon \text{Real} \int_{x_o}^{x} \frac{h_1}{\omega_\alpha} dx\right] \tag{4.38}$$

Again, the amplification factor is a function of the transverse location. However, the variation is a simple one. For a detailed discussion of the case of a wave packet, the reader is referred to the article of Nayfeh (ref. 21).

For the case of two-dimensional flows, β is a constant. Then, for the case of monochromatic waves, equation (4.36) reduces to

$$u \approx A_o\zeta_1(x,y)\exp\left[i\left(\int\alpha dx + \beta z - \omega t\right) + \varepsilon\int \frac{h_1}{\omega_\alpha} dx\right] \tag{4.39}$$

Consequently, the growth direction is the streamwise direction and the growth rate

$$\sigma = \text{Real}\left[\frac{\partial}{\partial x}(\ln u)\right]$$

is given by

$$\sigma = -\alpha_i + \varepsilon\text{Real}\left(\frac{h_1}{\omega_\alpha}\right) + \text{Real}\left[\frac{\partial}{\partial x}(\ln\zeta_1)\right] \tag{4.40}$$

Since ζ_1 is a function of y and, in general, distorts with the streamwise distance, one may term stable disturbances unstable and vice versa. Because of the mode-shape distortion, neutral stability points are a function of both the transverse and streamwise positions. The experiments of Laufer and Vrebalovich (ref. 23) clearly show that the growth of the disturbances and the neutral curves obtained depend on the value of y^*/L^* at which the observations were made. Moreover, a different growth rate would be obtained if one replaces u with another variable such as v, p, w, or T. On the other hand, for the case of parallel flows, the last two terms in equation (4.40) vanish and the growth rate is unique and independent of the varible being used or the transverse direction at which the growth rate is determined. Therefore, to compare the analytical results with experimental data in growing boundary layers, one needs to make the calculations in the same manner in which the measurements are taken. Available experimental stability studies almost exclusively use hot-wire or hot-film anemometers following disturbances in the boundary layer. The hot-wire or hot-film response is a combination of velocity,

density, and temperature fluctuations. The hot-wire response when operated at high constant overheat is proportional to the rms of the mass-flow fluctuations. To describe fully the disturbance, one needs measurements of all fluctuation characteristics such as the rms amplitude, spectra, wave angle, and propagation speed as functions of x, y, and z. Except for the experiment of Kendall (ref. 25), no information is available on the disturbance waveangle. Laufer and Vrebalovich reported measurements at different constant y^*/L^*, whereas Kendall, Demetriades, Legiga et al, and Stetson et al reported measurements at one constant y^*/L^* located in the wideband energy peak. However, available calculations do not agree with each other. Some calculations show large nonparallism influence, whereas other calculations show small influence.

5. SUBHARMONIC INSTABILITY

In this case, the basic flow is taken as the sum of the mean steady flow and a two-dimensional quasiparallel T-S wave; that is

$$u_b = U_m(y) + A[\zeta_1(y)e^{i\theta} + cc] \tag{5.1}$$

$$v_b = A[\zeta_3(y)e^{i\theta} + cc] \tag{5.2}$$

$$p_b = p_m + A[\zeta_4(y)e^{i\theta} + cc] \tag{5.3}$$

$$T_b = T_m(y) + A[\zeta_5(y)e^{i\theta} + cc] \tag{5.4}$$

$$w_b = 0 \tag{5.5}$$

$$\frac{\partial\theta}{\partial x} = \alpha_r \quad \text{and} \quad \frac{\partial\theta}{\partial t} = -\omega \tag{5.6}$$

where cc stands for the complex conjugate of the preceding terms, α_r and ω are real, and A and α_r are approximated locally by constant values. Substituting equations (5.1)-(5.6) into equations (2.3)-(2.9), (2.12) and (2.13) yields a system of partial differential equations whose coefficients are independent of z, periodic in x and t, and dependent in a complicated manner on y. Consequently, the z-variation can be separated and using Floquet theory, one can represent the solutions of the problem as

$$u = \exp(\sigma_x x + \sigma_t t)\cos\beta z \; \phi_1(x,y,t) \tag{5.7}$$

$$v = \exp(\sigma_x x + \sigma_t t)\cos\beta z \; \phi_3(x,y,t) \tag{5.8}$$

$$p = \exp(\sigma_x x + \sigma_t t)\cos\beta z \; \phi_4(x,y,z) \tag{5.9}$$

$$T = \exp(\sigma_x x + \sigma_t t)\cos\beta z \; \phi_5(x,y,t) \tag{5.10}$$

$$w = \exp(\sigma_x x + \sigma_t t)\sin\beta z \; \phi_7(x,y,t) \tag{5.11}$$

where σ_x and σ_t are called the characteristic exponents and the ϕ_n are periodic in x and t. For the subharmonic parametric case, the ϕ_n have a period that is twice the period of the primary flow and to the first approximation equations (5.7)-(5.11) become

$$u = \exp(\sigma_x x + \sigma_t t)\cos\beta z\left[\xi_1(y)\exp(\tfrac{1}{2}i\theta) + cc\right] \tag{5.12}$$

$$v = \exp(\sigma_x x + \sigma_t t)\cos\beta z\left[\xi_3(y)\exp(\tfrac{1}{2}i\theta) + cc\right] \tag{5.13}$$

$$p = \exp(\sigma_x x + \sigma_t t)\cos\beta z\left[\xi_4(y)\exp(\tfrac{1}{2}i\theta) + cc\right] \tag{5.14}$$

$$T = \exp(\sigma_x x + \sigma_t t)\cos\beta z\left[\xi_5(y)\exp(\tfrac{1}{2}i\theta) + cc\right] \tag{5.15}$$

$$w = \exp(\sigma_x x + \sigma_t t)\sin\beta z\left[\xi_7(y)\exp(\tfrac{1}{2}i\theta) + cc\right] \tag{5.16}$$

For the case of temporal stability $\sigma_x = 0$ and $\sigma_t \neq 0$, whereas for the case of spatial stability $\sigma_t = 0$ and $\sigma_x \neq 0$.

Substituting equations (5.1)-(5.6) and (5.12)-(5.16) into equations (2.3)-(2.9), (2.12) and (2.13) and equating the coefficients of $\exp(\frac{1}{2}i\theta)$ on both sides leads to the following problem governing the ξ_n and either σ_x or σ_t (ref. 45):

$$\begin{aligned}
&\left[\sigma_t - \tfrac{1}{2}i\omega + (\sigma_x + \tfrac{1}{2}i\alpha_r)U_m\right](\gamma M_\infty^2\xi_4 - \rho_m\xi_5) + (\sigma_x + \tfrac{1}{2}i\alpha_r)\xi_1 \\
&+ \frac{D\rho_m}{\rho_m}\xi_3 + D\xi_3 + \beta\xi_7 + (\sigma_x + \tfrac{1}{2}i\alpha_r)A(\gamma M_\infty^2\zeta_4 - \rho_m\zeta_5)\bar{\xi}_1 \\
&+ (\sigma_x + \tfrac{1}{2}i\alpha_r)A\zeta_1(\gamma M_\infty^2\bar{\xi}_4 - \rho_m\bar{\xi}_5) + \frac{A}{\rho_m}\frac{\partial}{\partial y}\left[\rho_m(\gamma M_\infty^2\zeta_4 - \rho_m\zeta_5)\bar{\xi}_3\right. \\
&\left.+ \rho_m\zeta_3(\gamma M_\infty^2\bar{\xi}_4 - \rho_m\bar{\xi}_5)\right] + A(\gamma M_\infty^2\zeta_4 - \rho_m\zeta_5)\bar{\xi}_7 = 0
\end{aligned} \tag{5.17}$$

$$
\begin{aligned}
&\Big[\sigma_t - \tfrac{1}{2}i\omega + U_m(\sigma_x + \tfrac{1}{2}i\alpha_r) - \frac{r\mu_m}{\rho_m R}(\sigma_x + \tfrac{1}{2}i\alpha_r)^2 + \frac{\mu_m\beta^2}{\rho_m R}\Big]\xi_1 \\
&+ \frac{\mu_m'}{\rho_m R}\xi_2 + \Big[DU_m - \frac{\mu_m'}{\rho_m R}(\sigma_x + \tfrac{1}{2}i\alpha_r)\Big]\xi_3 + \frac{(\sigma_x + \frac{1}{2}i\alpha_r)}{\rho_m}\xi_4 - \frac{D(\mu_m' DU_m)}{\rho_m R}\xi_5 \\
&- \frac{\mu_m' DU_m}{\rho_m R} - \frac{(m+1)\mu_m\beta}{\rho_m R}(\sigma_x + \tfrac{1}{2}i\alpha_r)\xi_7 - \frac{(m+1)\mu_m}{\rho_m R}(\sigma_x + \tfrac{1}{2}i\alpha_r)D\xi_3 \\
&- \frac{\mu_m}{\rho_m R}D\xi_2 + A\Big\{\zeta_1(\sigma_x + \tfrac{1}{2}i\alpha_r) + \Big[\sigma_t + \tfrac{1}{2}i\omega + U_m(\sigma_x \\
&- \tfrac{1}{2}i\alpha_r)\Big](\gamma M_\infty^2\zeta_4 - \rho_m\zeta_5) - \frac{r\mu_m'\zeta_5}{\rho_m R}(\sigma_x^2 + \tfrac{1}{4}\alpha_r^2)\Big\}\bar{\xi}_1 \\
&+ A\Big[\zeta_3 - \frac{D(\mu_m'\zeta_5)}{\rho_m R}\Big]\bar{\xi}_2 + A\Big[D\zeta_1 + DU_m(\gamma M_\infty^2\zeta_4 - \rho_m\zeta_5) \\
&- \frac{D(\mu_m'\zeta_5)}{\rho_m R}(\sigma_x - \tfrac{1}{2}i\alpha_r)\Big]\bar{\xi}_3 + A\Big[i(\alpha_r U_m - \omega)\zeta_1 \\
&+ DU_m\zeta_3\Big](\gamma M_\infty^2\bar{\xi}_4 - \rho_m\bar{\xi}_5) - \frac{A}{\rho_m R}\Big[\mu_m'(ir\alpha_r\zeta_1 + mD\zeta_3)(\sigma_x + \tfrac{1}{2}i\alpha_r) \\
&+ \mu_m(D^2\zeta_1 + i\alpha_r D\zeta_3) + D\mu_m'(D\zeta_1 + i\alpha_r\zeta_3)\Big]\bar{\xi}_5 - \frac{A\mu_m'}{\rho_m R}(D\zeta_1 \\
&+ i\alpha_r\zeta_3)\bar{\xi}_6 - \frac{A\beta\mu_m'}{\rho_m R}\Big[m(\sigma_x + \tfrac{1}{2}i\alpha_r) + (\sigma_x - \tfrac{1}{2}i\alpha_r)\Big]\bar{\xi}_7 = 0
\end{aligned}
\tag{5.18}
$$

$$- \frac{2(\gamma-1)M_\infty^2 DU_m}{R\rho_m} \xi_2 + [DT_m - \frac{2(\gamma-1)M_\infty^2 DU_m}{\rho_m R}(\sigma_x + -\frac{1}{2} i\alpha_r)]\xi_3$$

$$- \frac{(\gamma-1)M_\infty^2}{\rho_m} [\sigma_t - \frac{1}{2} i\omega + U_m (\sigma_x + \frac{1}{2} i\alpha_r)]\xi_4 + \{\sigma_t - \frac{1}{2} i\omega$$

$$+ U_m (\sigma_x + \frac{1}{2} i\alpha_r) - \frac{(\gamma-1)M_\infty^2 \mu_m' (DU_m)}{R\rho_m} - \frac{1}{\rho_m RPr} [\mu_m(\sigma_x + \frac{1}{2} i\alpha_r)^2$$

$$+ \mu_m' D^2 T_m + D\mu_m' DT_m - \beta^2 \mu_m]\}\xi_5 - \frac{D\mu_m + \mu_m' DT_m}{\rho_m RPr} \xi_6 - \frac{\mu_m}{\rho_m RPr} D\xi_6$$

$$+ A\{i\alpha_r \zeta_5 - \frac{(\gamma-1)M_\infty^2}{\rho_m} [i\alpha_r \zeta_4 + \frac{2m\mu_m}{R} (\sigma_x - \frac{1}{2} i\alpha_r) D\zeta_3$$

$$+ \frac{2ir\mu_m \alpha_r}{R} (\sigma_x - \frac{1}{2} i\alpha_r)\zeta_1]\}\bar{\xi}_1 - \frac{2A(\gamma-1)M_\infty^2}{R\rho_m} [D\zeta_1 + i\alpha_r \zeta_3$$

$$+ \mu_m' DU_m \zeta_5]\bar{\xi}_2 + A\{(\gamma M_\infty^2 \zeta_4 - \rho_m \zeta_5)DT_m + D\zeta_5 - \frac{2(\gamma-1)M_\infty^2}{R\rho_m} (\sigma_x - \frac{1}{2} i\alpha_r)[D\zeta_1$$

$$+ i\alpha_r \zeta_3 + \mu_m' \zeta_5 DU_m]\}\bar{\xi}_3 + A\{\gamma[i(\alpha_r U_m - \omega)\zeta_5 + \zeta_3 DT_m]$$

$$- \frac{(\gamma-1)}{\rho_m}(\sigma_x - \frac{1}{2} i\alpha_r)\zeta_1 \bar{\xi}_4 + A\{- \gamma M_\infty^2 [i(\alpha_r U_m - \omega)\zeta_5 + \zeta_3 DT_m]$$

$$+ [\sigma_t + \frac{1}{2} i\omega + U_m(\sigma_x - \frac{1}{2} i\alpha_r)](\gamma M_\infty^2 \zeta_4 - \rho_m \zeta_5) - \frac{2(\gamma-1)M_\infty^2 \mu_m' DU_m}{R\rho_m} (D\zeta_1$$

$$+ i\alpha_r \zeta_3) - \frac{D\mu_m'}{\rho_m RPr} D\zeta_5 - \frac{\mu_m'}{\rho_m RPr} [(\sigma_x^2 + \frac{1}{4} \alpha_r^2)\zeta_5 + i\alpha_r(\sigma_x + \frac{1}{2} i\alpha_r)\zeta_5$$

$$+ D^2 \zeta_5 - \beta^2 \zeta_5]\}\bar{\xi}_5 + A\{\zeta_3 - \frac{1}{\rho_m RPr} [(D(\mu_m' \zeta_5) + \mu_m' D\zeta_5)]\}\bar{\xi}_6$$

$$- A \frac{2m(\gamma-1)M_\infty^2 \beta\mu_m}{\rho_m R} (i\alpha_r \zeta_1 + D\zeta_3)\bar{\xi}_7 - A \frac{2(\gamma-1)M_\infty^2 \mu_m}{\rho_m R} (rD\zeta_3 + im\alpha_r \zeta_1)D\bar{\xi}_3$$

$$- \frac{A(\gamma-1)M_\infty^2}{\rho_m} \zeta_3 D\bar{\xi}_4 - \frac{A\mu_m'}{\rho_m RPr} \zeta_5 D\bar{\xi}_6 \tag{5.21}$$

$$\xi_1 = \xi_3 = \xi_7 = 0 \quad \text{and} \quad \xi_5 = 0 \quad \text{at} \quad y = 0 \tag{5.22}$$

$$\xi_n \to 0 \quad \text{as} \quad y \to \infty \tag{5.23}$$

where

$$\xi_2 = D\xi_1, \; \xi_6 = D\xi_5, \quad \text{and} \quad \xi_8 = D\xi_7 \tag{5.24}$$

As an alternative to the collocation technique used by Herbert for the incompressible case (refs. 46,47), Nayfeh and Harper (ref. 45) followed Nayfeh and Masad (ref. 48) and used a shooting technique to solve the eigenvalue problem consisting of equations (5.17)-(5.23) after casting them into a first-order system of equations. The boundary conditions (5.23) at infinity were replaced with boundary conditions at some finite value y_{max} of y outside the boundary layer. Thus, for $y > y_{max}$, $U_m \to 1$ and $DU_m \to 0$. Since the primary eigenfunctions ζ_m decay exponentially outside the boundary layer, Nayfeh and Harper (ref. 45) followed Nayfeh and Masad (ref. 48) and chose a large enough y_{max} so that the ζ_m are very small. The error involved was monitored by choosing a certain value of y_{max}, and solving the problem, then increasing y_{max}, resolving the problem and noting the effect of increasing y_{max} on the accuracy of the solution.

Since no numerical or experimental results are available for compressible flows, Nayfeh and Harper checked the compressible code against the incompressible results of Herbert (refs. 46,47) obtained using a collocation method and those of Nayfeh and Masad (ref. 48) obtained using a shooting technique, which are in good agreement with the experimental results of Kachanov and Levchenko (ref. 49). The agreement is excellent. Next, Nayfeh and Harper produced results to evaluate the influence of compressibility on the secondary instability of first- and second-mode waves.

Letting R = 1048.8 and choosing an $F = 83\times10^{-6}$, Nayfeh and Harper solved the eigenvalue problem and obtained the 2D T-S waves for $M_\infty = 0.01$, 0.8, and 1.6. These primary waves are stable having the spatial decay rates -0.0216, -0.0166, and -0.0066. Setting the amplitudes of these primary waves at $a = 0.02/\sqrt{2}$, choosing a value for β, and assuming a value for γ_i, they solved the secondary eigenvalue problem and obtained γ_r. Varying γ_i and repeating the calculations, they determined the maximum value of γ_r over all possible values of γ_i. We note that when $M_\infty > 0$ the maximum value of γ_r does not correspond to $\gamma_i = 0$ as in the incompressible case. The results are shown as the dark curves in Figure 15. The growth rates corresponding to $a = 0.01/\sqrt{2}$ are shown as the light curves in Figure 15. Figure 16 shows the growth rates when a = 0, that is, the growth rates of the free propagating waves. The results in Figures 15 and 16 show that the secondary growth rates are much larger than the growth rates of the free waves. In fact, for $M_\infty = 1.6$, the free wave is stable for all values of β, whereas the secondary wave is unstable for a very wide range of values of β. Increasing the amplitude of the primary wave results in an increase in the growth rates of all secondary waves. For a given Mach number, the growth rate has a broad maximum. This maximum shifts to larger values of β as the amplitude of the primary wave increases. And for a given amplitude of the primary wave, the maximum growth rate shifts to lower values of β as the Mach number increases.

As discussed in Section 3, as M_∞ increases beyond 3.0, higher-modes become unstable and dominate the instability at large Mach numbers. Figure 17 shows the variation of the growth rates of secondary waves with spanwise wavenumber when the

primary wave is a first- or second-mode wave. In both cases, $F = 120\times10^{-6}$, $a = 0.01/\sqrt{2}$, and $\gamma_i = 0$. The first-mode primary wave and its corresponding secondary waves are calculated at R = 1150; the primary wave is slightly unstable. The second-mode primary wave and its corresponding secondary waves are calculated at R = 1950; the primary wave is very stable. It follows from Figure 17 that the maxima of the growth rates of the secondary waves are comparable. Figure 18 shows the growth rates of the free waves (secondary waves when a = 0). The free wave corresponding to the second-mode wave is stable for a wide range of β, whereas the free wave corresponding to the first-mode wave is slightly unstable for the same range of β. Comparing Figures 17 and 18, we conclude that a primary first-mode wave having an amplitude of $0.01/\sqrt{2}$ increases the growth rate of the secondary wave by an order of magnitude. Moreover, the presence of a primary second-mode wave strongly destabilizes the secondary wave.

When the primary wave is a first-mode wave it follows from Figure 17 that the maximum growth rate of the secondary wave occurs when $\beta = 0.199$. Figure 19 shows the variation of the secondary growth rate with frequency. The maximum growth rate increases by about 25% and shifts to an $F \approx 112\times10^{-6}$.

6. EFFECT OF IMPERFECTIONS ON STABILITY OF FLOWS OVER PLATES

The boundary layers over natural laminar-flow components in the presence of surface imperfections (e.g., waviness and steps) must accurately be computed so that the effect of these imperfections on the stability and transition can be evaluated. Moreover, the magnitudes of the imperfections under consideration are such that strong viscid-inviscid interaction and small separation bubbles are unavoidable. Definitely, solutions to the full Navier-Stokes equations can accurately predict such flowfields provided that the grid is so fine that important flow structures are not smeared by the truncation errors or artificial dissipation. However, the number of flow cases that needs to be investigated is very large, and this makes solving the full Navier-Stokes equations a very expensive task. A more economical alternative is to solve the interacting boundary-layer equations.

Ragab, Nayfeh and Krishna (ref. 50) investigated the accuracy of the compressible interacting boundary-layer computations and their limitations in predicting flows over surface imperfections. They compared the results of interacting boundary-layer computations with solutions to the full Navier-Stokes equations. Comparisons were made for the mean flow profiles as well as the stability characteristics such as the growth rates and amplification factors of linear stability waves.

The thin-layer compressible Navier-Stokes equations are solved using the well known computer code "ARC2D" which has been developed at NASA Ames (version 1.5 GAMMA, 72/85). The code incorporates different methods of solutions all of which are implicit in time, and it uses second-order central differences in space. Ragab et al (ref. 50) selected the method of solution in which the diagonal form of the equations are used (refs. 51,52). Mixed second- and fourth-order dissipation terms were added explicitly and implicitly, and the obtained pentadiagonal system of equations was solved directly.

Sheared Cartesian grids were used for all the cases presented here. An example is shown in Figure 20 for a smooth backward-facing step. The equation of the step is

$$y = \frac{1}{2}\, h(1 + \operatorname{erf} \bar{x}),\ \bar{x} = Re^{-3/8}\lambda^{5/4}(x - 1) \tag{6.1}$$

where Re is the Reynolds number based on the distance from the leading edge to the step center ($x = 1$) and $\lambda = 0.332057$. The step specified by equation (6.1) is originally given by Smith and Merkin (ref. 53) who analyzed the incompressible flow using triple-deck theory. The numerical values used in Figure 20 are $Re = 10^6$ and $h = -0.003$. We note that the y-coordinates in Figure 20 are magnified by a factor of 20 relative to the x-coordinates. The inflow boundary of the computational domain is at $x \approx -0.06$ (i.e., the plate leading edge $x = 0$ is included in the domain), and the outflow boundary is located at $x = 2.0$. The top boundary is placed at $y \approx 0.4$. More details about the grid will be given in the results section.

Ragab, Nayfeh and Krishna developed a code for solving the compressible interacting boundary-layer equations. The numerical method is an extension of Veldman's method (ref. 54) to compressible flows. The salient feature of the method is the simultaneous solution of the boundary-layer equations and the inviscid flow, which is given by the small disturbance theory of compressible potential flow. A similar treatment is presented by Davis (ref. 55) and Nayfeh, Ragab, and Al-Maaitah (ref. 56).

In this subsection we compare the mean flow predicted by the Navier-Stokes code ARC2D and the interacting boundary-layer code IBL for the flow over a backward-facing step. The step is specified by equation (6.1). The step height is $h = -0.003$, the Mach number is 0.5, and the Reynolds number is 10^6. The wall is assumed to be insulated.

The grid used in the IBL calculations has a uniform streamwise step size of $\Delta x = 0.005$ and a geometrically stretched grid in the η- direction, where η is the Levy-Lees variable. At the wall $\Delta\eta = 0.05$ and the stretching factor is 1.05. Four grids are used with the Navier-Stokes solver. In grid 1 (136x70), a uniform $\Delta x = 0.005$ is used in the range $0.9 \le x \le 1.1$. For $x < 0.9$ and $x > 1.1$, Δx is stretched geometrically at the rate of 1.05 provided that Δx does not exceed 0.03. If Δx exceeds 0.03, a uniform spacing $\Delta x = 0.03$ is used. The step size in the y direction is geometrically stretched between the wall and the top boundary $y \approx 0.4$ with $\Delta y_1 = 1.5\times10^{-4}$. In grid 2 (136x99), the streamwise grid is the same as in grid 1, and the y grid has 99 points between the wall and $y \approx 0.4$ with $\Delta y_1 = 0.3\times10^{-4}$. In grid 3 (166x120), the streamwise grid in the interval $0.9 \le x \le 2.0$ is the same as that in grid 1 and more points are added in $-.06 \le x \le 0.9$ so that the number of streamwise points is 166, and the y grid has 120 points between the wall and $y \approx 0.4$ with $\Delta y_1 = 0.3\times10^{-4}$. In grid 4 (176x153), the streamwise grid is the same as that in grid 1 except $\Delta x = 0.003$, and the y grid has 153 points between the wall and $y \approx 0.8$ with $\Delta y_1 = 0.3\times10^{-4}$.

The friction-coefficient distribution on the step surface is depicted in Figure 21. We observe that there is an appreciable difference between the results predicted by ARC2D using the different grids. The trends in Figure 21 suggest that the agreement can be improved slightly if a finer grid is used with ARC2D. The results obtained using the IBL code are in good agreement with those obtained using ARC2D with the finest grid. Figure 22 compares the pressure-coefficient distribution predicted using the IBL code with that obtained using ARC2D with the finest grid. The agreement is fairly good. Thus, we conclude that the IBL code can be used to calculate accurately the mean flows over steps, humps, and troughs as long as massive separation and vortex shedding do not occur.

The stability calculations demand highly accurate velocity and temperature profiles - their magnitudes as well as their derivatives. Figure 23 compares the

spatial growth rates $-\alpha_i$ calculated at $x = 0.64$ for an $F = 80\times10^{-6}$ using the IBL predicted profiles with those calculated using the ARC2D predicted profiles with the finest grid. The agreement is very good, indicating that the IBL code predicts fairly well the magnitudes as well as the derivatives of the velocity and temperature profiles. Using these growth rates, we calculate the amplification factor N from

$$N = -\int_{R_0}^{R} 2\alpha_i dR$$

where $R = \sqrt{Re_x}$. The variation of the N factor calculated using the growth rates based on the profiles obtained with the IBL code is compared with those calculated using the growth rates based on the profiles obtained with the ARC2D code with the four grids in Figure 24. The latter N factor distribution seems to converge as the grid is refined to a distribution that comes closer and closer to that obtained using the growth rates based on the profiles predicted by the IBL code, providing a further credibility to the IBL procedure.

Figure 25 shows the influence of the Mach number on the N-factor distribution for the most amplified 2D wave for a backward-facing step having an $h = -0.003$ and a slope of $-4.349°$. It is clear that compressibility is stabilizing.

In Figure 26, for $M_\infty = 0.5$, we show the influence of the disturbance frequency on the N-factor distribution for waves propagating past the same backward-facing step. It is clear that the most dangerous frequency F is about 50×10^{-6}.

7. SWEPT WING BOUNDARY LAYERS

All of the numerical examples discussed in the preceding sections are concerned with the 2D and 3D stability of 2D or axisymmetric boundary-layer flows. In this section, we discuss the stability of 3D boundary layers and in particular boundary layers on transonic sweptback wings because of their aeronautical importance. The stability of 3D boundary layers differs from that of 2D boundary layers in that a 3D boundary layer is subject to crossflow instability and in that the growth direction in a 3D boundary layer need not coincide with the wave direction.

From his flight tests on aircraft with sweptback wings, Gray discovered that the boundary layer became turbulent closer to the leading edge than on a corresponding unswept wing. Using evaporation methods for indicating the state of the boundary layer, he discovered the existence of regularly spaced vortices whose axes lie in the streamwise direction. Since on a swept wing the spanwise pressure gradient deflects the boundary layer toward the region of low static pressure, the flow paths of the boundary-layer profiles differ from the potential flow streamlines and a crossflow developes in the direction normal to the streamlines (i.e., the mean flow is three-dimensional). The crossflow profiles have inflection points, making them dynamically unstable and hence leading to the generation of the vortices. This crossflow instability was confirmed in wind tunnels on large swept wings by Gregory, Stuart and Walker (ref. 34).

The feasibility of using suction to maintain laminar flow in the presence of crossflow instability was shown by Pfenninger et al (ref. 57), Bacon et al (ref. 58), Gault, and Pfenninger and Bacon (ref. 59) on a 30-deg sweptback wing. This feasibility culminated in the successful maintenance of full-chord laminar flow on an X-21 wing.

The problem of laminar-flow control on sweptback wings and the discovery of Gray of the crossflow instability stimulated research into the linear stability of three-dimensional flows. In contrast with the problem of 2-D flows, disturbances in a 3-D flow are always three-dimensional. Stuart (ref. 34) derived the general linear equations that describe the 3-D stability of 3-D incompressible boundary layers over bodies, including the effects of boundary-layer growth and body and streamline curvatures. He showed that the temporal parallel stability problem of a 3-D incompressible flow can be reduced to that of a 2-D stability problem. For a given R and ω, his transformation relates the wave numbers α and β in a 3-D flow with the streamwise and spanwise velocity components U_m and W_m to the wavenumber $k = (\alpha^2 + \beta^2)^{\frac{1}{2}}$ in a 2-D flow having the velocity $U = (\alpha U_m + \beta W_m)/k$. He used the inviscid form of these disturbance equations to explain the crossflow instability as an inflectional instability. Brown (refs. 7,16) numerically solved the temporal viscous eigenvalue problems for flows over a rotating disk and a few sweptback wing boundary layers with distributed suction.

Since the uncoupling of the crosswise stability problem from the streamwise stability problem is artificial, a number of attempts have been directed toward determining the stability of the combined streamwise and spanwise stability problems to determine the suction requirements for maintaining laminar flow over sweptback wings. The form of the 3-D disturbance is given by equations (4.3) and (4.4) leading to the dispersion relation $\omega = \omega(\alpha,\beta,x,z)$. We note that, in contrast with the case of parallel flows, α and β are functions of x and z and the phase function θ cannot be written as $\alpha x + \beta z - \omega t$. Instead α, β, and ω are related to θ as in equations (4.4).

To complete the problem formulation, one needs to specify initial conditions in addition to the governing equations and boundary conditions. For the case of a general pressure disturbance at say the curve x = a,

$$p(x = a,\ y,z,t) = P(y,z,t) \tag{7.1}$$

This arbitrary disturbance will generate a continuum of wave components of the form given by equations (4.3) and (4.4) and the observed wave motion consists of their superpositions. For the case of spatial stability in parallel mean flows, the pressure disturbance can be expressesd

$$p(x,y,z,t) = \iint \zeta_4(y;\beta,\omega)\exp\left[i\alpha(\beta,\omega)x + i\beta z - i\omega t\right]d\omega d\beta \tag{7.2}$$

On the other hand, if the initial condiitons are generated by a source (such as a vibrating ribbon) oscillating at the frequency ω (i.e., monochromatic wave) at the curve defined by x = a, then

$$p(x = a,y,z,t) = \tilde{P}(y,z)\exp(-i\omega t) \tag{7.3}$$

Then, for the case of parallel mean flows, the pressure disturbance can be expressed as

$$p(x,y,z,t) = \exp(-i\omega t)\iint\zeta_4(y;\beta)\exp\left[i\alpha(\beta)x + i\beta z\right]d\beta \tag{7.4}$$

To evaluate the integral in equation (7.2), one needs to solve the eigenvalue problem for all possible values of β and ω and then perform the integration, an expensive procedure. Similarly, to evaluate the integral in equation (7.4), one needs to solve the eigenvalue problem for all possible values of β and then perform the integration, again an expensive procedure. However, if the disturbances are sufficiently weak they will not influence transition until they have traveled a large distance from the source. Then, asymptotic methods, namely the saddle-point method, can be effectively used to determine the following approximations to the integrals in equations (7.2)and (7.4):

$$p(x,y,z,t) \propto \frac{\exp[i\alpha(\beta^*,\omega^*)x+i\beta^* z-i\omega^* t]}{x\left[\frac{\partial^2\alpha}{\partial\beta^2}\frac{\partial^2\alpha}{\partial\omega^2}-\left(\frac{\partial^2\alpha}{\partial\beta\partial\omega}\right)^2\right]^{\frac{1}{2}}} \tag{7.5}$$

where

$$\frac{z}{x} = -\frac{\partial\alpha}{\partial\beta} \quad \text{and} \quad \frac{t}{x} = \frac{\partial\alpha}{\partial\omega} \tag{7.6}$$

and

$$p(x,y,z,t) \propto \frac{\exp[i\alpha(\beta^*)x+i\beta^* z-i\omega t]}{\left[x\frac{\partial^2\alpha}{\partial\beta^2}(\beta^*)\right]^{\frac{1}{2}}} \tag{7.7}$$

where

$$\frac{z}{x} = -\frac{d\alpha}{d\beta} \tag{7.8}$$

It is clear from equations (7.6) and (7.8) that for a physical wave, $\partial\alpha/\partial\beta$ and $\partial\alpha/\partial\omega$ must be real for an arbitrary disturbance and $d\alpha/d\beta$ must be real for a monochromatic disturbance.

The preceding discussion shows that by the time the wave motion is important for transition, it has already evolved to either the state given by equation (7.5) in the case of an arbitrary disturbance (corresponding to natural transition) or the state given by equation (7.7) in the case of a monochromatic disturbance. In both cases, the disturbance is dominated by a single wave component having a fixed ω, β, and α. Using the method of multiple scales or the method of averaging to account for a weak growth of the boundary layer in x and z, one finds that by the time the wave motion is important for transition (i.e., for large x), it has evolved again to the state given by equations (4.3) and (4.4); that is, the disturbance is dominated by a wave packet centered at the frequency ω and spanwise wavenumber β. However, in this case, α, β, and A are not constants; equations (4.23), (4.29) and (4.30) describe their modulation with x, z, and t. To solve these modulation equations (Cauchy problem), one needs to specify initial conditions on non-characteristic curves.

If the initial data consist of a wavepacket centered at the frequency ω, then

$$A\ (x = a,z,t) = A_0(z,t),\ \beta(x = a,z) = \beta_0(z) \tag{7.9}$$

and it follows from equations (4.23), (4.29) and (4.30) that the wave propagates along the characteristics

$$\frac{dt}{ds} = 1,\ \frac{dx}{ds} = \omega_\alpha,\ \frac{dz}{ds} = \omega_\beta \tag{7.10}$$

For a physical problem, ω_α and ω_β must be real. Along these characteristics,

$$\frac{dA}{ds} = \varepsilon h_1 A, \qquad \frac{d\alpha}{ds} = \varepsilon h_2, \qquad \frac{d\beta}{ds} = \varepsilon h_3 \tag{7.11}$$

If the initial data consist of a single frequency (i.e., monochromatic wave), then

$$A(x = a,z) = A_0(z), \; \beta(x = a,z) = \beta_0(z) \tag{7.12}$$

It follows from equations (4.29)-(4.31) that the wave propagates along the characteristics defined by equations (4.33), where $\omega_\beta/\omega_\alpha$ is real. The modulation of A, α, and β along these characteristics is governed by equations (4.32). The solution of equations (4.33) is a one-parameter family of curves.

The question arises how one can use the results of the linear stability theory for transition prediction or evaluation of proposed laminar-flow concepts and requirement on swept wings? Motivated by the success of the so-called e^N method in correlating experimental transition data in incompressible 2D flows, many investigators have attempted to extend it to 3D incompressible and compressible flows. Whereas in 2D flows, the direction of growth is known, namely, the mean flow direction, in 3D flows, the direction of growth is not known a priori. In 2D flows, one can either use spatial stability theory and calculate the spatial growth rate directly or use temporal stability theory, calculate the temporal growth rate, and then calculate the spatial growth rate using the group velocity. Integrating the spatial growth rates yields the N factors.

Srokowski and Orszag (ref. 60) developed a computer code called SALLY using the temporal incompressible stability theory. At any location on the wing, the code iterates on α and β (which are taken to be real) to yield the maximum temporal growth rate for a given dimensional frequency ω_r. Then, several frequencies are examined until a global local maximum is obtained. The resulting amplification rate is then converted into a spatial amplification rate using the real part of the group velocity, which is then integrated along a trajectory defined by the direction of the real part of the group velocity. Hefner and Bushnell (ref. 61) calibrated the results of the envelope method using available transition data on swept-back wings. Later, Malik (ref. 36) developed a code called COSAL, which is the compressible version of SALLY. Although the envelope method is easy to implement, it is artificial because one continuously hops from one wave to another. Moreover, the N factors calculated using the envelope method increase monotonically to the end of the instability region, and hence the envelope method may over estimate the amplitude ratios.

For an infinite swept wing, the mean profiles are independent of the spanwise coordinate, and hence it follows from equations (4.4) and (4.5) that β is constant. Mack (ref. 62) performed crossflow stability calculations over the forward region of a 35° sweptback wing using this condition and determined the N factors for a zero frquency and a band of initial wave numbers. He found that the peak value maximized over all wave numbers is 7.8 compared with 11.2, obtained using the SALLY code. In contrast with the results of the envelope method, which increase monotonically in the instability region, the results of Mack achieve a peak because he followed a given wave from a more unstable region to a less unstable region. Using the temporal theory, Lekoudis (ref. 63) and Mack (ref. 64) determined the influence of suction on

the stability of flows over sweptback wings. Lekoudis (ref. 65) ascertained the influence of cooling on the stability of flows over sweptback wings.

If the wing is not infinite, the mean flow will be a function of both spanwise and streamwise coordinates and hence α and β are functions of x and z. In this case, the wave motion will be dominated by a single frequency spatial wavepacket as discussed above. Based on this theory, Nayfeh (ref. 21) proposed a method for determining the most amplified disturbance propagating from some given initial chord location on a wing. We select one specific wave at an initial point and then follow only that one wave along its trajectory. Then, we change the initial conditions and repeat the calculations to determine the most unstable wave.

To demonstrate the method we choose β_r^*, the dimensional form of β_r, to be a constant at some initial chordwise location $x = a$ for all z. At this initial point we still have three unspecified values β_i, α_r, and α_i. Two of these are determined through numerical integration of the disturbance equations and satisfaction of the boundary conditions through a Newton-Raphson iteration. The third is found by requiring that $\omega_\beta/\omega_\alpha$ be real. This fixes the direction of marching. From here we evaluate

$$\frac{d\alpha}{ds} = \varepsilon \frac{h_2}{\omega_\alpha} \tag{7.13}$$

$$\frac{d\beta}{ds} = \varepsilon \frac{h_3}{\omega_\alpha} \tag{7.14}$$

To stay on the initial wave, we increment the characteristic variable s by ds, evaluate dx and dz from equations (4.33), and correct α and β by

$$\alpha = \alpha + \varepsilon \frac{h_2}{\omega_\alpha} ds \tag{7.15}$$

$$\beta = \beta + \varepsilon \frac{h_3}{\omega_\alpha} ds \tag{7.16}$$

We then renondimensionalize with respect to local edge variables at the new x and z. To test that we are on the same wave, we integrate the disturbance equations at the new x and z with the new α and β to see if the boundary conditions are satisfied and $\omega_\beta/\omega_\alpha$ is real. If they are, we evaluate $d\alpha/ds$ and $d\beta/ds$, increment s, correct α and β, and continue marching along the trajectory. If these conditions are not all satisfied, we decrease the step size ds until they are and then proceed as above. Since A_0 is the amplitude of the disturbance initially, it follows from equations (4.32a) that

$$A = A_0 \exp\left(\int_a^s \varepsilon \frac{h_1}{\omega_\alpha} ds \right) \tag{7.17}$$

Hence

$$u = A_0 \zeta_1(x_1, y, z_1) \exp\left\{ \int_a^x \left[i\left(\alpha + \beta \frac{\omega_\beta}{\omega_\alpha}\right) + \varepsilon \frac{h_1}{\omega_\alpha} \right] dx - i\omega t \right\} \tag{7.18}$$

and the n-factor is given by

$$n = - \int_a^x \left[\alpha_i + \frac{\omega_\beta}{\omega_\alpha} \beta_i - \varepsilon\left(\frac{h_1}{\omega_\alpha}\right)_r\right] dx$$

As we march we compute the n-factor from where the disturbance first goes unstable $\left(\frac{dn}{dx} < 0\right)$ to where it becomes stable again $\left(\frac{dn}{dx} < 0\right)$. Once we compute n we change β_r^* to determine which β_r^* is associated with the largest value of n. This tells us the initial spanwise wavenumber of the most dangerous wave for a given frequency from a given chord location. Then we vary the dimensional frequency to determine the most dangerous frequency.

This approach has been implemented by Padhye and Nayfeh (ref. 66) and Reed and Nayfeh (ref. 67) for the X-21 wing with upper surface chordwise pressure coefficient and suction distribution as shown in Figures 1 and 2. A schematic of the wing is presented in Figure 3 showing the coordinate system used. This wing was designed for laminar-flow control and derived from the NACA 65A210 airfoil. The sweeps at the leading and trailing edges are 33.2 and 19.1 degrees, respectively, and the freestream velocity is 774.4 feet per second. Under the assumption of negligible spanwise (along roots) pressure gradient, there are no twist and tip and wing-body effects included in the analysis. Also they made the assumption of constant Prandtl number and specific heat at constant pressure.

Reed and Nayfeh (ref. 67) focused their attention on the aft region of the wing, specifically the 70-percent location on the 14.66-foot chord. They introduced disturbances at this point and followed them along their trajectories as described above to ascertain their stability characteristics. This initial location lies in the rear adverse chordwise pressure gradient region.

For a specific constant dimensional frequency introduced at the 70-percent chord, to find the spanwise wavenumber maximizing the amplification factor, they consider the wavenumber resulting in local maximum temporal growth rate. That is, they took the frequency ω to be complex and the two wave numbers α and β to be real. They specified ω_r and iterated on α, β and ω_i to satisfy the boundary conditions and the condition that $\omega_\beta/\omega_\alpha$ be real. Then they converted to spatial stability and marched along the direction defined by the group velocity, which is kept real as described above. The amplification factor was computed in marching. This process was done for a whole gamut of frequencies until the frequency with maximum amplification factor was identified. Figure 4 shows results of frequency plotted versus spanwise wavenumber causing maximum growth for disturbances introduced at the 70-percent-chord location. The distribution appears to be linear.

As a result of searching, they found that the most unstable disturbance introduced at 70-percent chord is the one with a frequency of about 330 hertz and spanwise wavenumber of 272 per foot. Figure 5 shows disturbance amplification ratios for frequencies in this neighborhood. If the stability was performed using incompressible theory, the most unstable frequency would be about 200 Hz. The addition of compressibility increases the frequency of the most unstable disturbance. Moreover, compressibility significantly reduces the growth rates and amplification factors.

ACKNOWLEDGEMENT

This work was supported by the Office of Naval Research under Grant # N00014-85-K-0011, NR 4325201 and the National Aeronautics and Space Administration under Grant # NAG-1-714.

ORIGINAL PAGE IS
OF POOR QUALITY

APPENDIX A

$$a_{12} = a_{56} = a_{78} = 1$$

$$a_{21} = \alpha^2 + \beta^2 - i\hat{\omega}R/\mu_m T_m$$

$$a_{22} = - D\mu_m/\mu_m$$

$$a_{23} = - i\alpha(m + 1)DT_m/T_m - i\alpha D\mu_m/\mu_m + RDU_m/\mu_m T_m$$

$$a_{24} = i\alpha R/\mu_m + (m + 1)\gamma M_\infty^2 \alpha\hat{\omega}$$

$$a_{25} = - \alpha(m + 1)\hat{\omega}/T_m - D(\mu_m' DU_m)/\mu_m$$

$$a_{26} = - \mu_m' DU_m/\mu_m$$

$$a_{31} = - i\alpha$$

$$a_{33} = DT_m/T_m$$

$$a_{34} = i\gamma M_\infty^2 \hat{\omega}$$

$$a_{35} = - i\hat{\omega}/T_m$$

$$a_{37} = - i\beta$$

$$a_{41} = - i\chi\alpha(rDT_m/T_m + 2D\mu_m/\mu_m)$$

$$a_{42} = - i\chi\alpha$$

$$a_{43} = \chi[- \alpha^2 - \beta^2 + i\hat{\omega}R/\mu_m T_m + rD^2 T_m/T_m + rD\mu_m DT_m/\mu_m T_m]$$

$$a_{44} = - i\chi r\gamma M_\infty^2[\alpha DU_m + \beta DW_m - \hat{\omega}DT_m/T_m - \hat{\omega}D\mu_m/\mu_m]$$

$$a_{45} = i\chi[r(\alpha DU_m + \beta DW_m)/T_m + \mu_m'(\alpha DU_m + \beta DW_m)/\mu_m - r\hat{\omega}D\mu_m/\mu_m T_m]$$

$$a_{46} = - i\chi r\hat{\omega}/T_m$$

$$a_{47} = - i\chi r\beta DT_m/T_m - 2i\chi\beta D\mu_m/\mu_m$$

$$a_{48} = - i\chi\beta$$

$$a_{62} = - 2(\gamma - 1)M_\infty^2 PrDU_m$$

$$a_{63} = - 2i(\gamma - 1)M_\infty^2 Pr(\alpha DU_m + \beta DW_m) + RPr\ DT_m/\mu_m T_m$$

$$a_{64} = i(\gamma - 1)M_\infty^2 Pr R\hat{\omega}/\mu_m$$

$$a_{65} = \alpha^2 + \beta^2 - iRPr\hat{\omega}/\mu_m T_m - (\gamma - 1)M_\infty^2 Pr\mu_m'[(DU_m)^2 + (DW_m)^2]/\mu_m$$

$$- D^2\mu_m/\mu_m$$

$$a_{66} = - 2D\mu_m/\mu_m$$

$$a_{68} = - 2(\gamma - 1)M_\infty^2 PrDW_m$$

$$a_{83} = - i(m + 1)\beta DT_m/T_m - i\beta D\mu_m/\mu_m + RDW_m/\mu_m T_m$$

$$a_{84} = (m + 1)\gamma M_\infty^2 \beta\hat{\omega} + i\beta R/\mu_m$$

$$a_{85} = - (m + 1)\beta\hat{\omega}/T_m - D(\mu_m' DW_m)/\mu_m$$

$$a_{86} = - \mu_m' DW_m/\mu_m$$

$$a_{87} = \alpha^2 + \beta^2 - i\hat{\omega}R/\mu_m T_m$$

$$a_{88} = - D\mu_m/\mu_m$$

where

$$\mu_m' = d\mu_m/dT_m, \quad DF = \partial F/\partial y,$$

and

$$\hat{\omega} = \omega - \alpha U_m - \beta W_m, \quad \chi = [R/\mu_m - ir\gamma M_\infty^2\hat{\omega}]^{-1}$$

APPENDIX B

$$D_n = i \sum_{m=1}^{8} \frac{\partial a_{nm}}{\partial \omega} \zeta_m$$

$$E_n = -i \sum_{m=1}^{8} \frac{\partial a_{nm}}{\partial \alpha} \zeta_m$$

$$F_n = -i \sum_{m=1}^{8} \frac{\partial a_{nm}}{\partial \beta} \zeta_m$$

where small terms $O(R^{-1})$ can be neglected. The a_{nm} are given in Appendix A.

$$G_1 = G_5 = G_7 = 0$$

$$G_2 = \frac{R}{\mu_m} \Big[\frac{U_m}{T_m}\frac{\partial \zeta_1}{\partial x_1} + \frac{\zeta_1}{T_m}\frac{\partial U_m}{\partial x_1} + \frac{V_m}{T_m}\frac{\partial \zeta_1}{\partial y} + \frac{\zeta_7}{T_m}\frac{\partial U_m}{\partial z_1}$$

$$+ \frac{W_m}{T_m}\frac{\partial \zeta_1}{\partial z_1} + \frac{\partial \zeta_4}{\partial x_1} + \Big(\frac{\gamma M_e^2 \zeta_4}{T_m} - \frac{\zeta_5}{T_m^2}\Big)\Big(U_m \frac{\partial U_m}{\partial x_1} + V_m \frac{\partial U_m}{\partial y}$$

$$+ W_m \frac{\partial U_m}{\partial z_1}\Big)\Big] + O(1)$$

$$G_3 = \frac{\zeta_1}{T_m}\frac{\partial T_m}{\partial x_1} - \frac{\partial \zeta_1}{\partial x_1} - U_m \gamma M_e^2 \Big(\frac{\partial \zeta_4}{\partial x_1} - \frac{\zeta_4}{T_m}\frac{\partial T_m}{\partial x_1}\Big) + \frac{U_m}{T_m}\frac{\partial \zeta_5}{\partial x_1}$$

$$- \frac{2U_m \zeta_5}{T_m^2}\frac{\partial T_m}{\partial x_1} - \Big(\frac{\partial U_m}{\partial x_1} + \frac{\partial V_m}{\partial y} + \frac{\partial W_m}{\partial z_1}\Big)\Big(\gamma M_e^2 \zeta_4 - \frac{\zeta_5}{T_m}\Big)$$

$$- V_m\Big(\gamma M_e^2 \frac{\partial \zeta_4}{\partial y} - \frac{\gamma M_e^2 \zeta_4}{T_m}\frac{\partial T_m}{\partial y} - \frac{1}{T_m}\frac{\partial \zeta_5}{\partial y} + \frac{\partial \zeta_5}{T_m^2}\frac{\partial T_m}{\partial y}\Big)$$

$$- \gamma M_e^2 W_m \Big(\frac{\partial \zeta_4}{\partial z_1} - \frac{\zeta_4}{T_m}\frac{\partial T_m}{\partial z_1}\Big) + \frac{\zeta_7}{T_m}\frac{\partial T_m}{\partial z_1} + \frac{W_m}{T_m}\frac{\partial \zeta_5}{\partial z_1}$$

$$- \frac{2W_m \zeta_5}{T_m^2}\frac{\partial T_m}{\partial z_1} - \frac{\partial \zeta_7}{\partial z_1} + U_m \frac{\zeta_5}{T_m} \gamma M_e^2 \Big(\frac{\partial P_m}{\partial x_1} + \frac{\partial P_m}{\partial z_1}\Big)$$

$$- \gamma M_e^2 \left(\zeta_1 \frac{\partial P_m}{\partial x_1} + \zeta_7 \frac{\partial P_m}{\partial z_1}\right) + O(R^{-1})$$

$$G_4 = - \frac{1}{T_m} \left[U_m \frac{\partial \zeta_3}{\partial x_1} + V_m \frac{\partial \zeta_3}{\partial y} + \zeta_3 \frac{\partial V_m}{\partial y} + W_m \frac{\partial \zeta_3}{\partial z}\right] + O(R^{-1})$$

$$G_6 = - \frac{RPr}{\mu_m} \left[- \frac{\zeta_1}{T_m} \frac{\partial T_m}{\partial x_1} - \frac{U_m}{T_m} \frac{\partial \zeta_5}{\partial x_1} - \frac{V_m}{T_m} \frac{\partial \zeta_5}{\partial y} - \frac{\zeta_7}{T_m} \frac{\partial T_m}{\partial z_1}\right.$$

$$- \frac{W_m}{T_m} \frac{\partial \zeta_5}{\partial z_1} - \left(\frac{\gamma M_e^2 \zeta_4}{T_m} - \frac{\zeta_5}{T_m^2}\right)\left(U_m \frac{\partial T_m}{\partial x_1} + V_m \frac{\partial T_m}{\partial y}\right.$$

$$\left. + W_m \frac{\partial T_m}{\partial z_1}\right) + (\gamma - 1) M_e^2 \left(\frac{\partial P_m}{\partial x_1} \zeta_1 + U_m \frac{\partial \zeta_4}{\partial x_1}\right.$$

$$\left.\left. + V_m \frac{\partial \zeta_4}{\partial y} + \frac{\partial P_m}{\partial z_1} \zeta_7 + W_m \frac{\partial \zeta_4}{\partial z_1}\right)\right] + O(1)$$

$$G_8 = \frac{R}{\mu_m} \left[\frac{U_m}{T_m} \frac{\partial \zeta_7}{\partial x_1} + \frac{\zeta_1}{T_m} \frac{\partial W_m}{\partial x_1} + \frac{V_m}{T_m} \frac{\partial \zeta_7}{\partial y} + \frac{W_m}{T_m} \frac{\partial \zeta_7}{\partial z_1}\right.$$

$$+ \frac{\zeta_7}{T_m} \frac{\partial W_m}{\partial z_1} + \frac{\partial \zeta_4}{\partial z_1} + \left(\frac{\gamma M_e^2 \zeta_4}{T_m} - \frac{\zeta_5}{T^2}\right)\left(U_m \frac{\partial W_m}{\partial x_1} + V_m \frac{\partial W_m}{\partial y}\right.$$

$$\left.\left. + W_m \frac{\partial W_m}{\partial z_1}\right)\right] + O(1)$$

APPENDIX C

$$g_1 = i \sum_{m,n=1}^{8} \int_0^\infty \frac{\partial a_{nm}}{\partial \omega} \zeta_m \zeta_n^* dy$$

$$g_2 = - i \sum_{m,n=1}^{8} \frac{\partial a_{nm}}{\partial \alpha} \zeta_m \zeta_n^* dy$$

$$g_3 = - i \sum_{m,n=1}^{8} \int_0^\infty \frac{\partial a_{nm}}{\partial \beta} \zeta_m \zeta_n^* dy$$

$$\omega_\alpha = g_2/g_1, \quad \omega_\beta = g_3/g_1$$

$$h_1 = - g_1^{-1} \sum_{m=1}^{8} \int_0^\infty G_m \zeta_m^* dy$$

$$h_2 = i g_1^{-1} \sum_{m,n=1}^{8} \int_0^\infty \frac{\partial a_{nm}}{\partial x_1} \bigg|_{\alpha,\beta} \zeta_m \zeta_n^* dy$$

$$h_3 = i g_1^{-1} \sum_{m,n=1}^{8} \int_0^\infty \frac{\partial a_{nm}}{\partial z_1} \bigg|_{\alpha,\beta} \zeta_m \zeta_n^* dy$$

The a_{nm} are defined in Appendix A. The G_m are defined in Appendix B.

REFERENCES

1. Küchemann, D.: Störungsbewegungen in einer Gasströmung mit Grenzschicht, ZAMM, Vol. 18, 1938, pp. 207-222.

2. Lees, L. and Lin, C. C.: Investigation of the Stability of the Laminar Boundary Layer in a Compressible Fluid. NACA Technical Note, No. 1115, 1946.

3. Lees, L.: The Stability of the Laminar Boundary Layer in a Compressible Fluid. NACA Technical Report 876 and NACA TN1360, 1947.

4. Dunn, D. W. and Lin, C. C.: On the Stability of the Laminar Boundary Layer in a Compressible Fluid. Journal of Aeronautical Sciences, Vol. 22, 1955, p. 455.

5. Reshotko, E.: Stability of the Compressible Laminar Boundary Layer. California Institute of Technology, Guggenheim Aeronautical Laboratory, GALCIT Memorandum, 1960, p. 52.

6. Lees, L. and Reshotko, E.: Stability of the Compressible Laminar Boundary Layer. Journal of Fluid Mechanics, Vol. 12, 1962, p. 555.

7. Brown, W. B.: A Stability Criterion for Three-Dimensional Laminar Boundary Layers. Boundary Layer and Flow Control, Vol. 2, G. V. Lachmann ed. (Pergamon Press, New York) 1961, p. 913.

8. Mack, L. M: Numerical Calculation of the Stability of the Compressible Laminar Boundary Layer. California Institute of Technology, Jet Propulsion Laboratory, Report 20-122, 1960.

9. Mack, L. M.: Computation of the Stability of the Laminar Compressible Boundary Layer. Methods in Computational Physics, Vol. 4, Academic Press, 1965, p. 247.

10. Mack, L. M.: The Stability of the Compressible Boundary Layer According to a Direct Numerical Solution. AGARDograph, Vol. 97, Part 1, 1965, p. 483.

11. Mack, L. M.: Boundary-Layer Stability Theory. Jet Propulsion Lab. Document 900-277 (Rev. A), Pasadena, CA, 1969.

12. Mack, L. M.: Linear Stability Theory and the Problem of Supersonic Boundary-Layer Transition. AIAA Journal, Vol. 13, 1975, p. 278.

13. Mack, L. M.: Numerical Solution of Compressible Boundary-Layer Stability. Proceedings of Boundary-Layer Transition Group Meeting, W. D. McCauley ed., Air Force Report BSD-TR-67-213, 1967.

14. Mack, L. M.: Review of Linear Compressible Stability Theory. In Stability of Time Dependent and Spatially Varying Flows (D. L. Dwoyer and M. Y. Hussaini, eds.), Springer-Verlag, New York, 1985, pp. 164-187.

15. Mack, L. M: Boundary-Layer Linear Stability Theory. In Special Course on Stability and Transition of Laminar Flow, AGARD Report No. 709, 1984, pp. 3-1 to 3-81.

16. Brown, W. B.: Stability of Compressible Boundary Layers. AIAA Journal, Vol. 5, 1967, p. 1753.

17. Gunness, R. C.: The Stability Equations for High Mach Number Boundary-Layer Flow. Boeing Document D6-20652, Boeing Corporation, Seattle, WA, 1968.

18. Boehman, L. I.: Recalcuation of Brown's Stability Results. Proceedings of the 12th Midwest Mechanical Conference, University of Notre Dame Press, Notre Dame, IN, Vol. 6, 1971, p. 193.

19. El-Hady, N. M. and Nayfeh, A. H.: Nonparallel Stability of Compressible Boundary Layer Flows. AIAA Paper No. 80-0277, 1980.

20. Gaponov, S. A.: The Influence of Flow Non-Parallelism on Disturbance Development in the Supersonic Boundary Layer. Proceedings of the Eighth Canadian Congress of Applied Mechanics, 1981, pp. 673-674.

21. Nayfeh, A. H.: Stability of Three-Dimensional Boundary Layers. AIAA Journal, Vol. 18, 1980, pp. 406-416.

22. El-Hady, N. M.: On the Stability of Three-Dimensional, Compressible Nonparallel Boundary Layers. AIAA Paper No. 1374, 1980.

23. Laufer, J. and Vrebalovich, T.: Stability and Transition of a Supersonic Laminar Boundary Layer on an Insulated Flat Plate. Journal of Fluid Mechanics, Vol. 9, 1960, p. 257.

24. Kendall, J. M.: Wind Tunnel Experiments Relating to Supersonic and Hypersonic Boundary-Layer Transition. AIAA Journal, Vol. 13, 1975, p. 290.

25. Kendall, J. M.: Supersonic Boundary-Layer Stability Experiments. Proceedings of Boundary Layer Transition Study Group Meeting, ed. W. D. McCauley, Air Force Report BSD-TE-67-213, Aerospace Report TR 0158 (S3816-63)-1 II, 1967.

26. Demetriades, A.: An Experiment on the Stability of Hypersonic Laminar Boundary Layers. Journal of Fluid Mechanics, Vol. 7, 1960, p. 385.

27. Demetriades, A.: Hypersonic Viscous Flow Over a Slender Cone, Part III: Laminar Instability and Transition. AIAA Paper No. 74-535, 1974.

28. Demetriades, A.: Laminar Boundary Layer Stability Measurements at Mach 7 Including Wall Temperature Effects. AFOSR-TR-77-1311, 1977.

29. Lebiga, V. A., Maslov, A. A., and Pridanov, V. G.: Experimental Study of Stability of Supersonic Boundary Layers on a Plate with Blunted Leading Edge. (In Russian), Meck. Zhid i Gaza, Vol. 4, 1977, p. 65.

30. Stetson, K. F., Thompson, E. R., Donaldson, J. C., and Siler, L. G.: Laminar Boundary Layer Stability Experiments on a Cone at Mach 8. Part 1. Sharp Cone. AIAA Paper 83-1761, 1983.

31. Stetson, K. F., Thompson, E. R., Donaldson,J. C., and Siler, L. G.: Laminar Boundary Layer Stability Experiments on a Cone at Mach 8. Part 2. Blunt Cone. AIAA Paper 84-0006, 1984.

32. Stetson, K. F., Thompson, E. R., Donaldson, J. C., and Siler, L. G.: Laminar Boundary Layer Stability Experiments on a Cone at Mach 8. Part 3. Sharp Cone at Angle of Attack. AIAA Paper 85-0492, 1985.

33. Stetson, K. F., Thompson, E. R., Donaldson, J. C., and Siler, L. G.: Laminar Boundary Layer Stability Experiments on a Cone at Mach 8. Part 4. On Unit Reynolds Number and Environmental Effects. AIAA Paper 86-1087, 1986.

34. Gregory, N., Stuart, J. T., and Walker, W. S.: On the Stability of Three-Dimensional Boundary Layers with Application to the Flow Due to a Rotating Disk. Proc. Roy. Soc. London, Vol. A28, 1955, pp. 155.

35. Malik, M. R. and Orszag, S. A.: Efficient Computation of the Stability of Three-Dimensional Compressible Boundary Layers. AIAA Paper No. 81-1277, 1981.

36. Malik, M. R.: COSAL - A Black-Box Compressible Stability Analysis Code for Transition Prediction in Three-Dimensional Boundary Layers. NASA CR-165925, 1982.

37. Nayfeh, A. H.: Perturbation Methods, Wiley-Interscience, New York, 1973.

38. Nayfeh, A. H., Introduction to Perturbation Techniques, Wiley-Interscience, New York (1981).

39. Nayfeh, A. H.: Three Dimensional Stability of Growing Boundary Layers. Laminar-Turbulent Transition, R. Eppler and H. Fasel, Eds. (Springer-Verlag, New York) 1980, p. 201.

40. Nayfeh, A. H. and Padhye, A. R.: The Relation Between Temporal and Spatial Stability in Three-Dimensional Flows. AIAA Journal, Vol. 17, 1979, pp. 1084-1090.

41. Wazzan, A. R., Taghavi, H., and Keltner, G.: The Effect of Mach Number on the Spatial Stability of Adiabatic Flat Plate Flow to Oblique Disturbances. Physics of Fluids, Vol. 27, 1984, pp. 331-341.

42. Mack, L. M.: Remarks on Disputed Numerical Results in Compressible Boundary-Layer Stability Theory. Physics of Fluids, Vol. 27, 1984, pp. 342-347.

43. Malik, M. R.: Prediction and Control of Transition in Hypersonic Boundary Layers. AIAA Paper 87-1414, 1987.

44. Cebeci, T. and Stewartson, K.: On Stability and Transition in Three-Dimensional Flows. AIAA Journal, Vol. 18, 1980, pp. 398-405.

45. Nayfeh, A. H. and Harper, R.: Secondary Instability of Compressible Boundary Layers. Accepted for publication, Physics of Fluids, 1989.

46. Herbert, Th.: Subharmonic Three-Dimensional Disturbances in Unstable Plane Sheaer Flows. AIAA Paper No. 83-1759, 1983.

47. Herbert, T.: Analysis of the Subharmonic Route to Transition in Boundary Layers. AIAA Paper No. 84-0009, 1984.

48. Nayfeh, A. H. and Masad, J.: Subharmonic Instability in Boundary Layers. Accepted for publication, Physics of Fluids, 1989.

49. Kachanov, Yu. S. and Levchenko, V. Ya.: The Resonant Interaction of Disturbances at Laminar-Turbulent Transition in a Boundary Layer. Journal of Fluid Mechanics, Vol. 138, 1984, p. 200.

50. Ragab, S. A., Nayfeh, A. H., and Krishna, R.: Influence of Smooth Steps on the Stability of Compressible Boundary Layers. Accepted for publication, Physics of Fluids, 1989.

51. Pulliam, T. H.: Euler and Thin Layer Navier-Stokes Codes: ARC2D, ARC3D. Notes for Compl. Fluid Dyn. User's Workshop, The Univ. of Tn Space Inst., TN, 1984.

52. Pulliam, T. H. and Chaussee, D. S.: A Diagonal Form of Implicit Approximate Factorization Algorithm. Journal of Computational Physics, Vol. 39, 1981, p. 347.

53. Smith, F. T. and Merkin, J. H.: Triple-Deck Solutions for Subsonic Flow Past Humps, Steps, Concave or Convex Corners and Wedged Trailing Edges. Journal of Computational Physics, Vol. 10, 1982, p. 7-25.

54. Veldman, A. E. P.: A Numerical Method for the Calculation of Laminar, Incompressible Boundary Layers with Strong Viscous-Inviscid Interaction. Report NLR TR 79023, National Aerospace Lab., The Netherlands, 1979.

55. Davis, R. T.: A Procedure for Solving the Compressible Interacting Boundary-Layer Equations for Subsonic and Supersonic Flows. AIAA Paper No. 84-1614, 1984.

56. Nayfeh, A. H., Ragab, S. A., and Al-Maaitah, A.: Effect of Bulges on the Stability of Boundary Layers. Physics of Fluids, Vol. 31, No. 4, 1988, pp. 796-806.

57. Pfenninger, W., Gross, L., and Bacon, T. W.: Experiments on a 30° Swept 12 Percent Thick Symmetrical Laminar Suction Wing in the 5-ft. by 7-ft. Michigan Tunnel. Northrop Corporation, Norvair Division Report NAI-57-317 (BLC-93), 1957.

58. Bacon, J. W., Tucker, V. L., and Pfenninger, W.: Experiments on a 30° Sept 12 Percent Thick Symmetrical Laminar Suction Wing in the 5-ft. by 7-ft. University of Michigan Tunnel. Northrop Corporation, Norvair Division Report NOR-59-328 (BLC-119), 1959.

59. Gault, D. E.: An Experimental Investigation of Boundary Layer Control for Drag Reduction of a Swept Wing Section at Low Speed and High Reynolds numbers. NASA TN D-320, 1960.

60. Srokowski, A. J. and Orszag, A. A.: Mass Flow Requirements for LFC Wing Design. AIAA Paper No. 77-1222, 1977.

61. Hefner, J. N. and Bushnell, D. M.: Application of Stability Theory to Laminar Flow Control. AIAA Paper No. 79-1493, 1979.

62. Mack, L. M.: On the Stability of the Boundary Layer on a Transonic Swept Wing. AIAA Paper No. 79-0264, 1979.

63. Lekoudis, S. G.: Stability of Three-Dimensional Compressible Boundary Layers over Wings with Suction. AIAA Paper No. 79-0265, 1979.

64. Mack, L. M.: Compressible Boundary-Layer Stability Calculations for Sweptback Wings with Suction. AIAA Paper No. 81-0196, 1981.

65. Lekoudis, S.G.: Stability of the Boundary Layer on a Swept Wing with Wall Cooling. AIAA Journal, Vol. 18, 1980, pp. 1029-1035.

66. Padhye, A. R. and Nayfeh, A. H.: Nonparallel Stability of Three-Dimensional Flows. AIAA Paper No. 81-1281, 1981.

67. Reed, H. L. and Nayfeh, A. H.: Stability of Compressible Three-Dimensional Boundary-Layer Flows. AIAA Paper No. 82-1009, 1982.

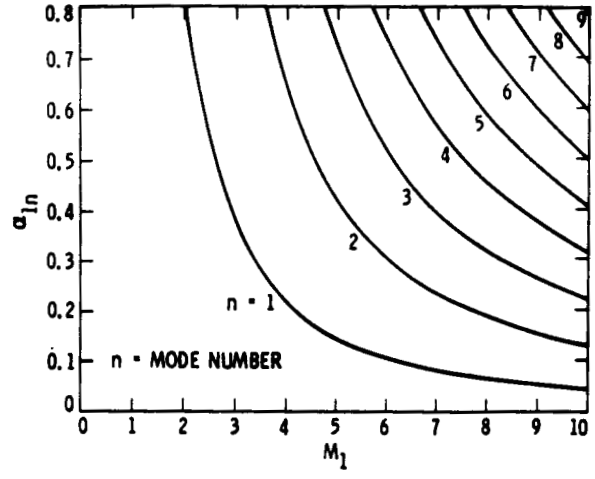

Figure 1. Multiple wave numbers of 2D noninflectional neutral waves (c=1). Insulated wall, wind tunnel temperatures, calculations of Mack (ref. 11).

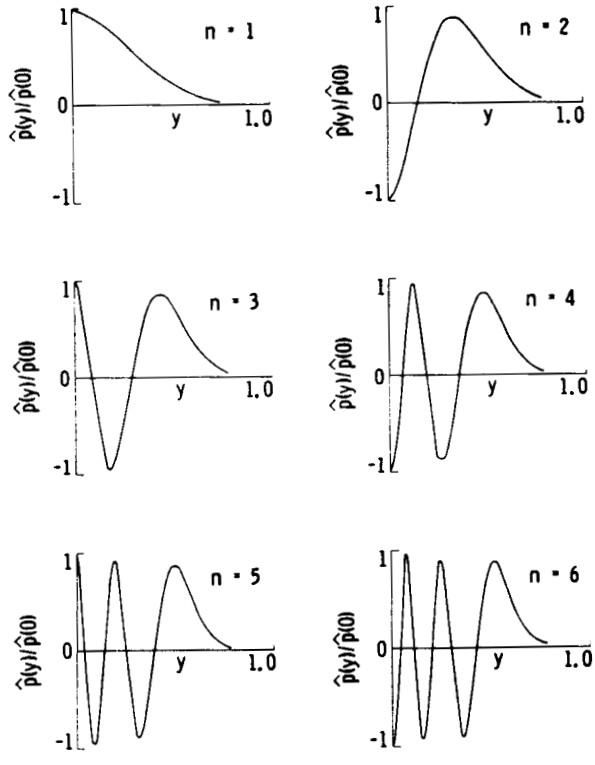

Figure 2. Pressure-fluctuation eigenfunctions of first six modes of 2D noninflectional neutral waves (c=1) at M_∞ = 10. Insulated wall, T^*_∞ = 50°K, calculations of Mack (ref. 11).

ORIGINAL PAGE IS
OF POOR QUALITY

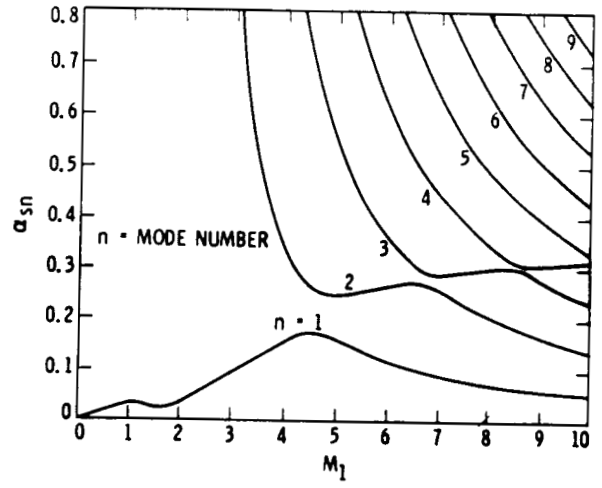

Figure 3. Multiple wave numbers of 2D inflectional neutral waves ($c=c_s$). Insulated wall, wind tunnel temperatures, calculations of Mack (ref. 11).

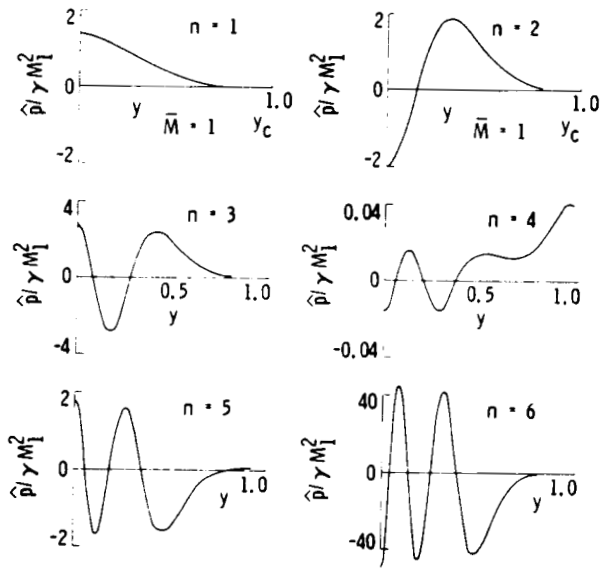

Figure 4. Pressure-fluctuation eigenfunctions of first six modes of 2D inflectional neutral waves ($c=c_s$) at $M_\infty = 10$. Insulated wall, $T_\infty^* =$ 50°K, calculations of Mack (ref. 11).

ORIGINAL PAGE IS
OF POOR QUALITY

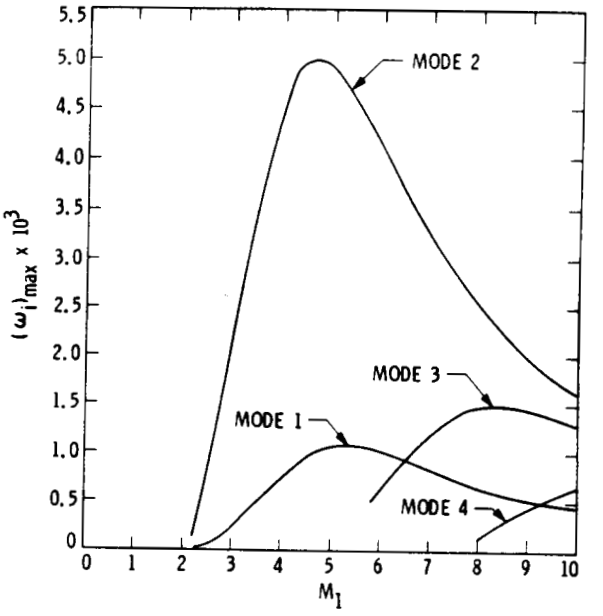

Figure 5. Effect of Mach number on maximum temporal amplification rate of 2D waves for first four modes. Insulated wall, wind tunnel temperatures (ref. 11).

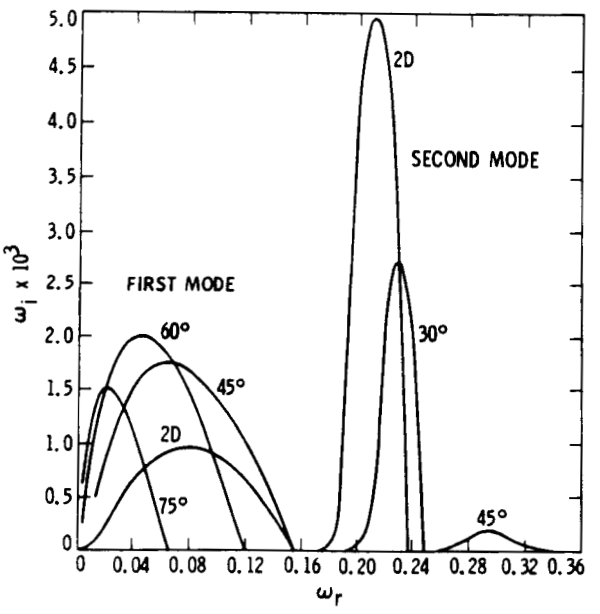

Figure 6. Temporal amplification rate of first and second modes versus frequency for several wave angles at $M_\infty = 4.5$. Insulated wall, $T^*_\infty = 311°K$ (ref. 11).

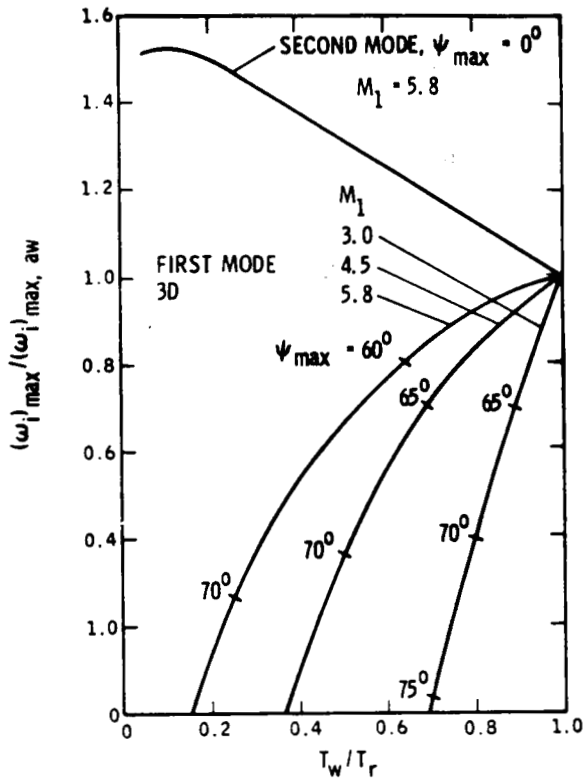

Figure 7. Effect of wall cooling on ratio of maximum temporal amplification rate with respect to both frequency and wave angle of first and second modes at M_∞ = 3.0, 4.5 and 4.8 to insulated-wall maximum amplification rate. Wind tunnel temperatures (ref. 11).

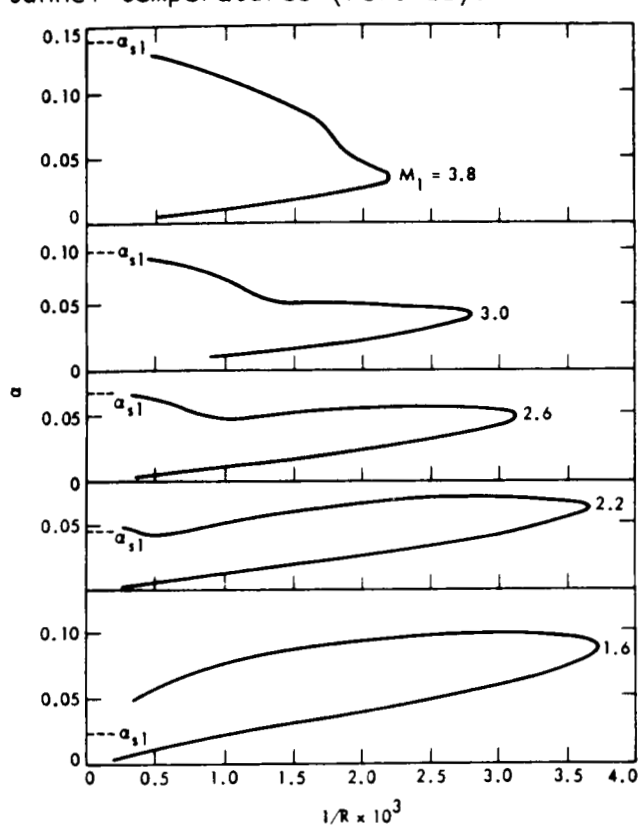

Figure 8. Two-dimensional neutral-stability curves at M_∞ = 1.6, 2.2, 2.6, 3.0, and 3.8; α_{s1} is the first neutral inviscid wavenumber with $c = c_s$ (ref. 11).

ORIGINAL PAGE IS
OF POOR QUALITY

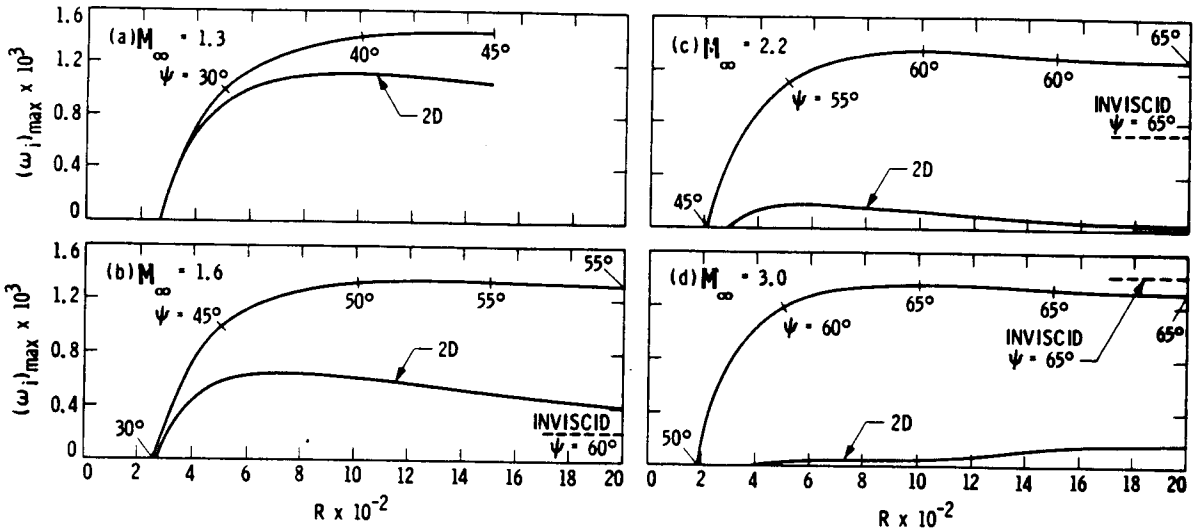

Figure 9. Distribution of maximum temporal amplification rate with Reynolds number at (a) M_∞ = 1.3, (b) M_∞ = 1.6, (c) M_∞ = 2.2 and (d) M_∞ = 3.0 for 2D and 3D waves. Insulated wall, wind tunnel temperatures (ref. 15).

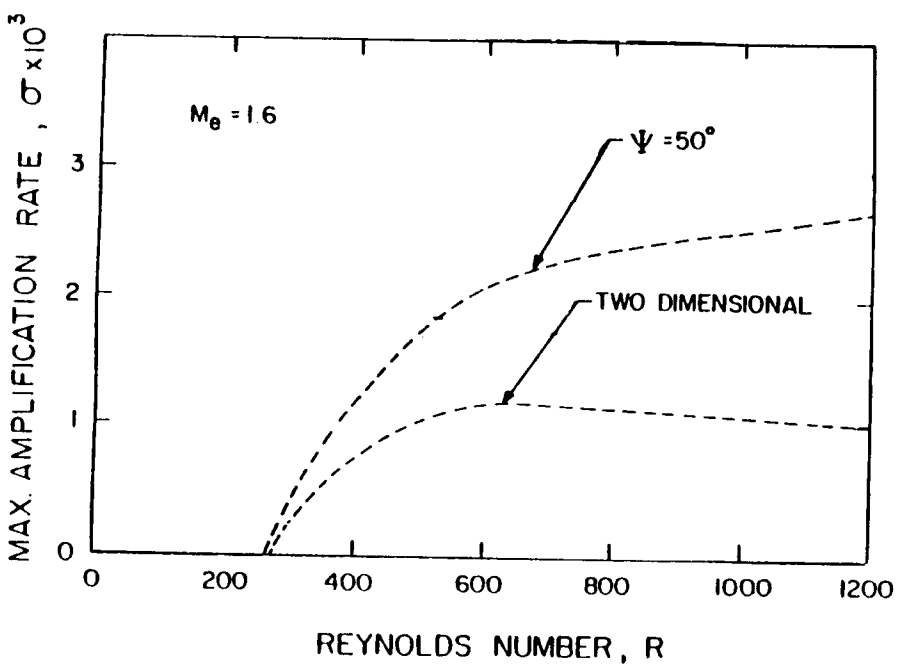

Figure 10. Variation of the maximum spatial amplification rate (with respect to frequency) with streamwise position at M_∞ = 1.6 for an oblique wave at ψ = 50° and a two-dimensional wave (ref. 19)

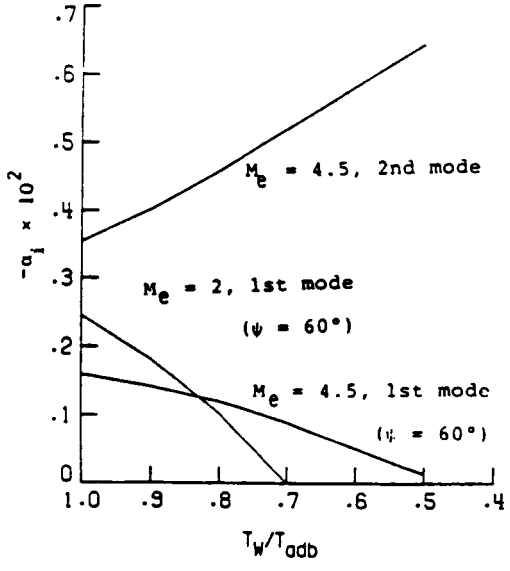

Figure 11. Effect of wall cooling on the most amplified first and second mode disturbances in a flat plate boundary layer at R = 1500 (ref. 43).

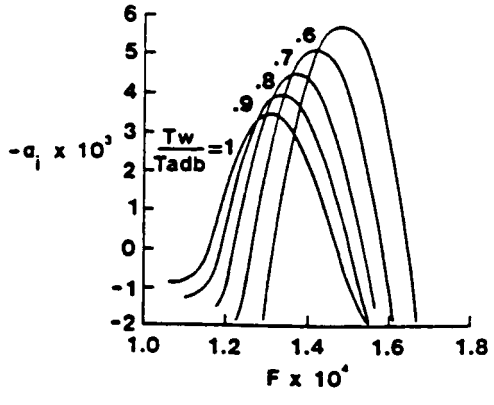

Figure 12. Effect of wall cooling on second mode instability in a boundary layer at M_e = 4.5 and R = 1500 (ref. 43).

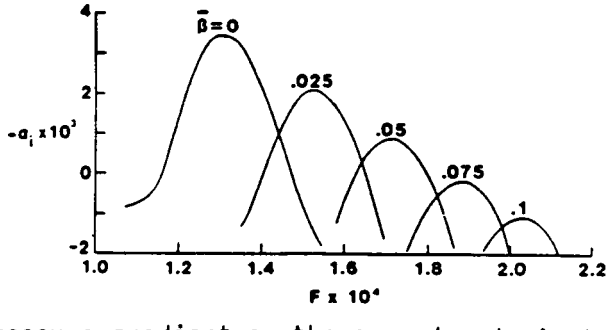

Figure 13. Effect of pressure gradient on the second mode instability in a boundary layer at M_e = 4.5 and R = 1500 (ref. 43).

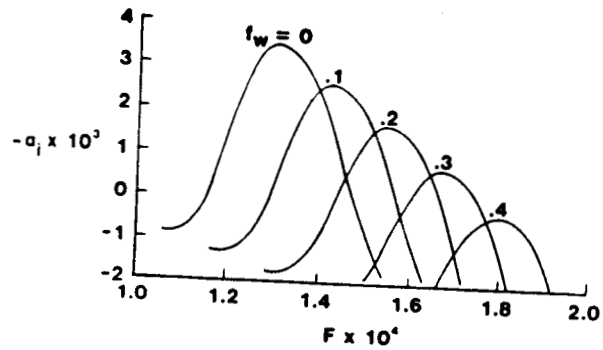

Figure 14. Effect of wall suction on the second mode instability in a boundary layer at M_e = 4.5 and R = 1500 (ref. 43).

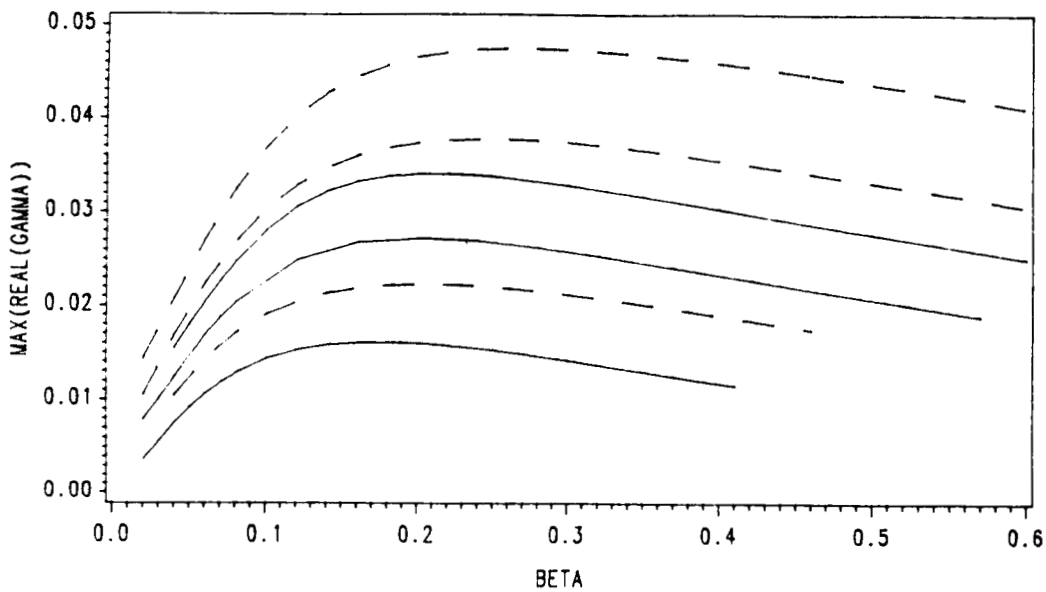

Figure 15. Variation of the maximum growth rate of secondary waves with spanwise wavenumber for three Mach numbers and two amplitudes a of the primary wave at R = 1048.8 and an F = 83×10^{-6} for the primary wave. Dashed curves - a = $0.02/\sqrt{2}$ and solid curves - a = $0.01/\sqrt{2}$. Mach numbers for each set proceeding downward are M_∞ = 0, 0.8, and 1.6.

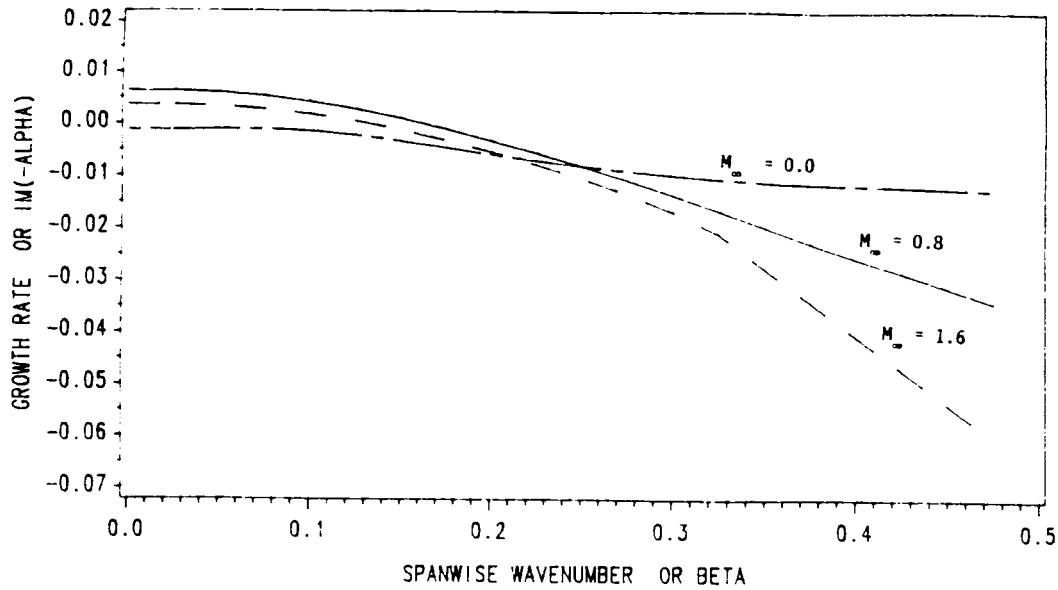

Figure 16. Variation of the growth rate of the free wave with spanwise wavenumber at R = 1048.8 and an F = 42.5×10^{-5} for three Mach numbers.

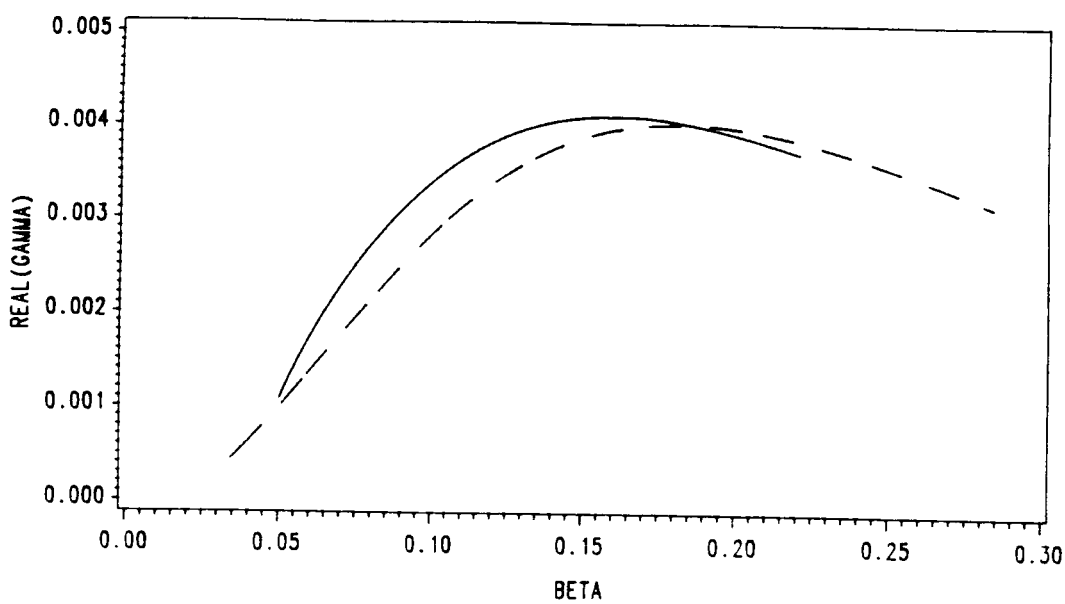

Figure 17. Variation of the growth rate of secondary waves with spanwise wave number for $M_\infty = 4.5$; the amplitude and frequency of the primary wave are $a = 0.01/\sqrt{2}$ and $F = 120 \times 10^{-5}$: (a) first-mode primary wave at R = 1150 and (b) second-mode primary wave at 1950.

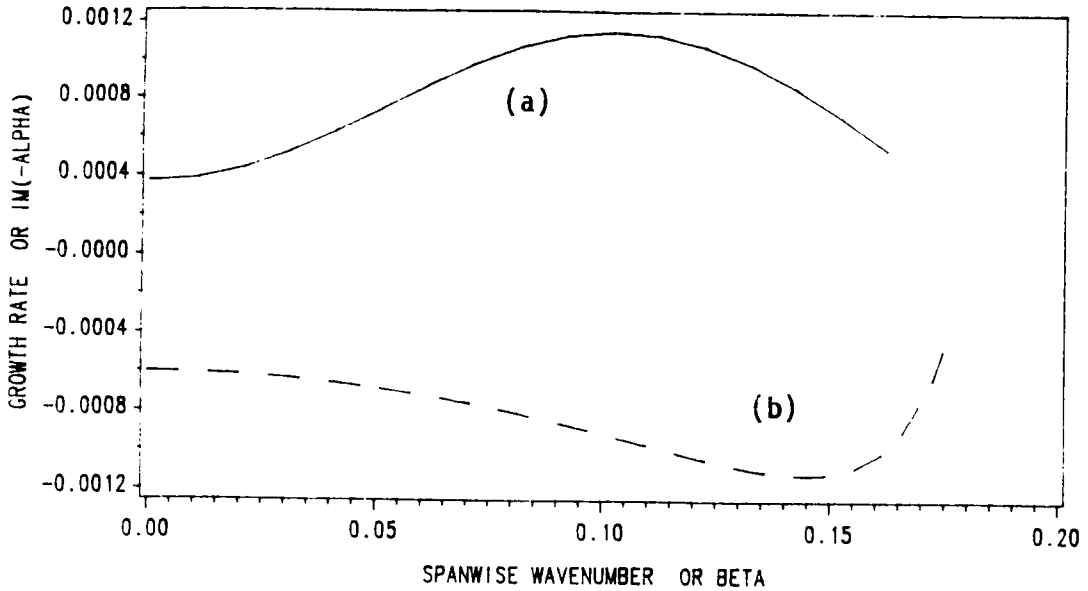

Figure 18. Variation of the growth rate of the free wave with spanwise wavenumber for $M_\infty = 4.5$ and $F = 60\times10^{-5}$: (a) first-mode wave at R = 1150, (b) second-mode wave at R = 1950.

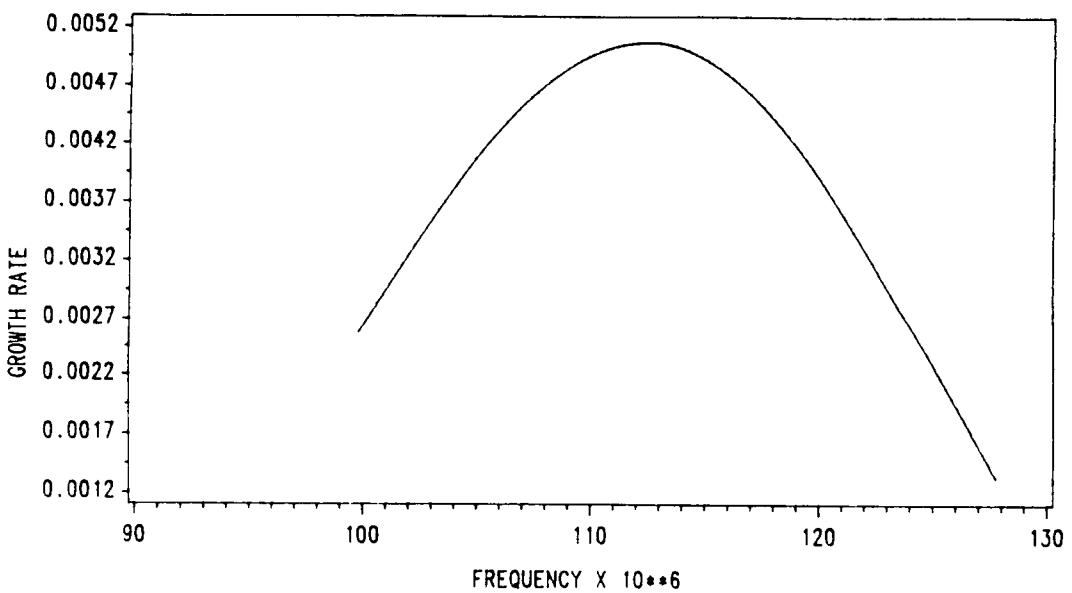

Figure 19. Variation of the secondary growth rate with frequency for $\beta = 0.199$, $M_\infty = 4.5$, and R = 1950; the primary wave is a first-mode wave having an $a^* = 0.01/\sqrt{2}$.

ORIGINAL PAGE IS
OF POOR QUALITY

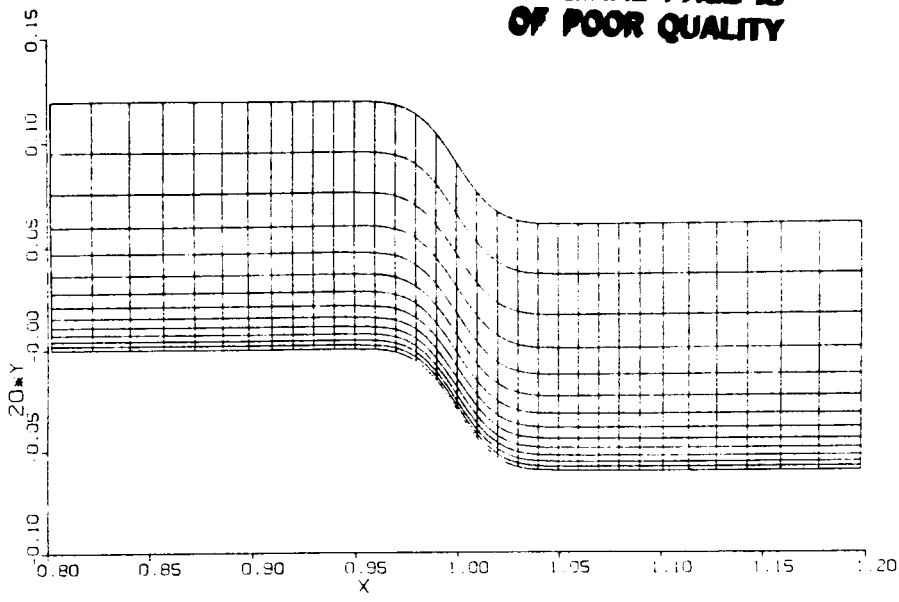

Figure 20. A typical computational grid for a backward-facing step.

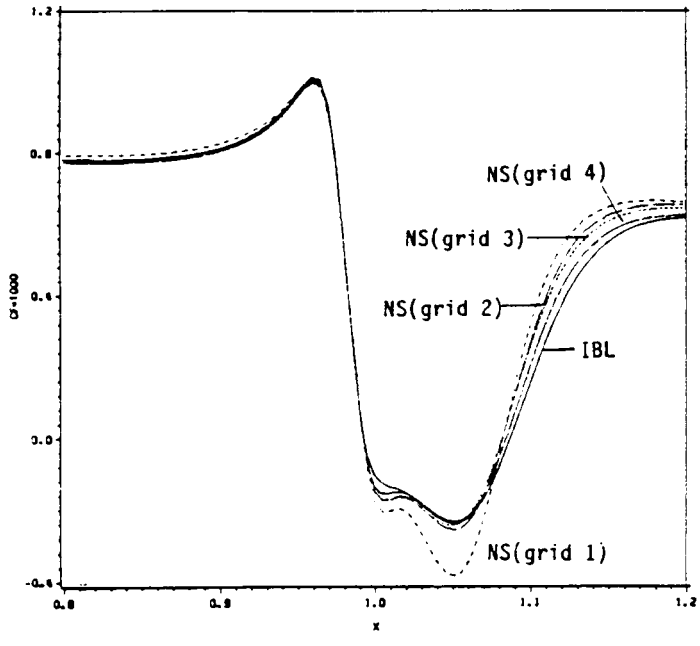

Figure 21. The friction-coefficient distribution calculated over a backward-facing step whose height is -0.003 and center is at Re = 10^5 for an M_∞ = 0.5.

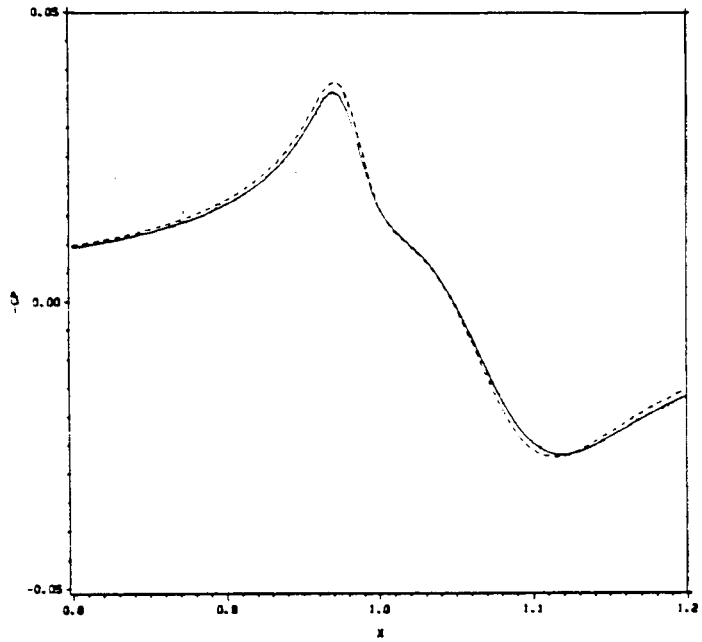

Figure 22. Pressure-coefficient distribution calculated over a backward-facing step whose height is -0.003 and center is at Re = 10^5 for an M_∞ = 0.5: —— IBL, --- Navier-Stokes solver (grid 4).

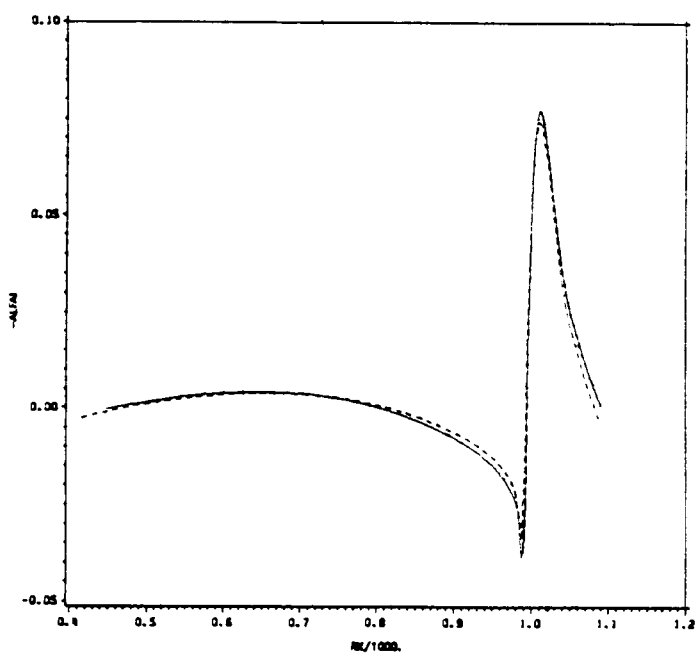

Figure 23. Spatial growth rates of 2D waves having the frequnecy 80×10^{-6} propagating over a backward-facing step whose height is -0.003 and center is at Re = 10^6 for an M_∞ = 0.5: —— IBL, --- Navier-Stokes solver (grid 4).

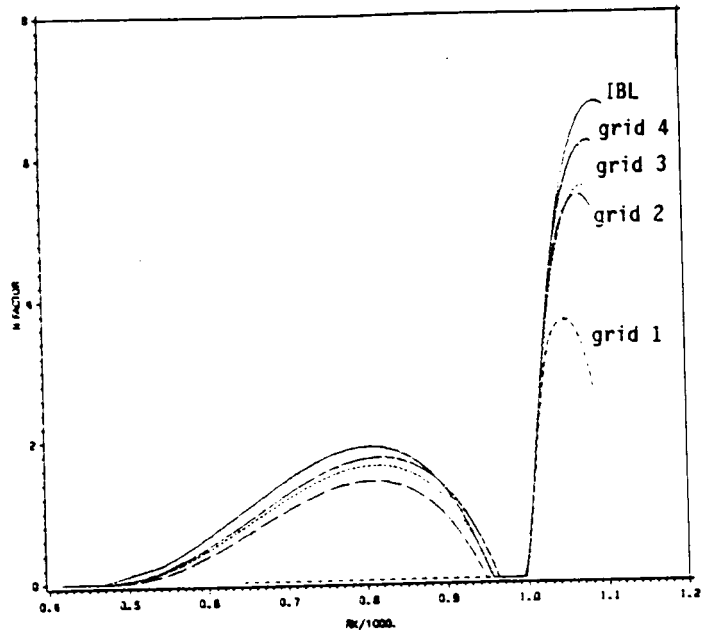

Figure 24. Amplification factor distribution over a backward-facing step whose height is -0.003 and center is at Re = 10^6 for an M_∞ = 0.5 and an F = 80×10^{-6}.

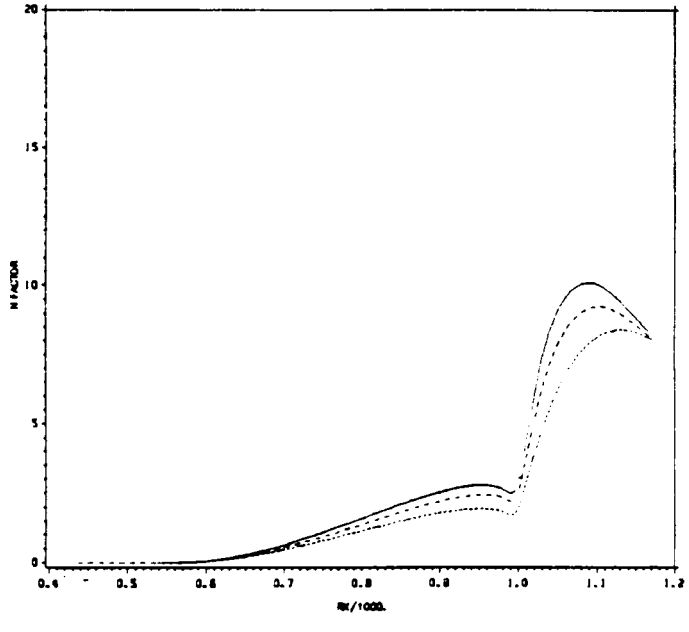

Figure 25. Influence of Mach number on the amplification factor of the most amplified 2D wave propagating over a backward-facing step whose height is -0.003, slope is -4.349°, and center is at Re = 10^5: —— M_∞ = 0.0, --- M_∞ = 0.5, ... M_∞ = 0.8.

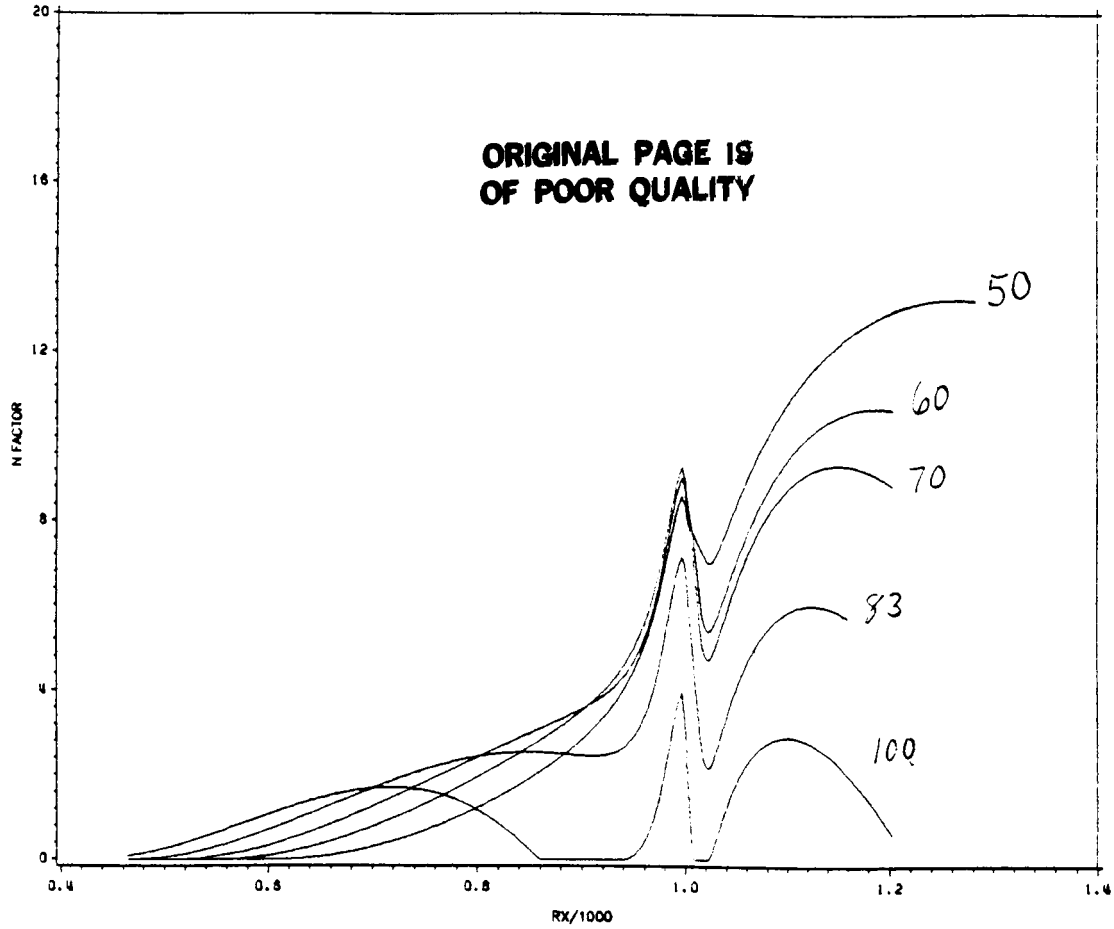

Figure 26. Variation of the N-factor distribution with frequency for waves propagating past a backward-facing step whose height is -0.003, slope is -4.349°, and center is at Re = 10^6; M_∞ = 0.5.

N89-20954

SECONDARY THREE-DIMENSIONAL INSTABILITY IN COMPRESSIBLE BOUNDARY LAYERS

Nabil M. El-Hady
Department of Mechanical Engineering and Mechanics
Old Dominion University
Norfolk, Virginia

SUMMARY

Three-Dimensional linear secondary instability theory is extended for compressible boundary layers on a flat plate in the presence of finite amplitude Tollmien-Schlichting (T-S) wave. The focus is on principal parametric resonance responsible for strong growth of subharmonics in low disturbance environment.

I. INTRODUCTION

Theoretically or experimentally, the compressible stability theory lacks a firm connection with boundary-layer transition. "There is little doubt that transition is preceded by linear instability in many instances, but the way these individual unstable waves act, alone or in combination , to trigger the transition process is not known" [1]. The nonlinear theories and the secondary instability that are much a prominent feature of incompressible stability theory do not exist for compressible boundary layer.

Recently, Erlebacher and Hussaini, [2,3] by using direct simulation of parallel boundary layer, generated numerically a high Mach number vortical structure (peak-valley) similar to that observed and computed for incompressible flows.

Stimulated by this work, we formulated the secondary three-dimensional instability problem for compressible boundary layers. In this paper, we investigate theoretically the effect of finite amplitude two-dimensional (2D) wave on the growth of three-dimensional (3D) perturbations in compressible boundary layers. Hence, this paper covers only a range of Mach numbers up to the transonic, where the critical primary disturbance is 2D. For supersonic boundary layers, the critical primary disturbance is 3D, and it is investigated by the author elsewhere. An analysis similar to that of Herbert [4], Herbert et al. [5] and Nayfeh [6] is followed here but spatial stability is considered for both primary and secondary instabilities.

The primary instability leads to the growth of T-S waves and a streamwise almost periodic modulation of the flow. We study the linear stability of this flow with respect to spanwise periodic 3D disturbance. Floquet theory gives as a solution to the stability equations, all various types of resonance. We

PRECEDING PAGE BLANK NOT FILMED

consider the case of principle parametric resonance responsible for strong growth of subharmonics in low disturbance environment.

II. PRIMARY INSTABILITY AND THE BASIC FLOW

We consider the primary instability of the 2D compressible boundary layer on a flat plate, with respect to 2D quasi-parallel spatially growing T-S disturbances. The critical disturbance is 2D up to the transonic range of Mach numbers [7]. The flow field is governed by the 2D compressible Navier-Stokes equations, the energy equation and the state equation. Dimensionless quantities are introduced by using the reference velocity U_r and the reference length $L = \sqrt{\nu x / U_r}$, so that Reynolds number is given by $R = \sqrt{U_r x/\nu}$, where x measures the distance from the leading edge of the plate, and ν is the fluid kinematic viscosity. The thermodynamic and transport properties of air (treated as perfect gas) are made dimensionless using their corresponding freestream values.

At sufficiently large distance from the leading edge, primary instability of the compressible laminar flow occurs with respect to T-S disturbances. These disturbances take the traveling wave form,

$$(1) \quad (u_p, v_p, p_p, t_p, \mu_p, \rho_p) = A_o \, [\, u(y), v(y), p(y), t(y), \mu(y), \rho(y) \,] \, \exp\, [i(\int \alpha \, dx - \omega t)] + c.c.$$

Where the y-axis is defined normal to the flat plate, u and v are the disturbance velocities, p is the disturbance pressure, t is the disturbance temperature, μ is the disturbance viscosity, and ρ is the disturbance density.

For the spatial stability analysis α is a complex wavenumber given by $\alpha = \alpha_r + i\alpha_i$ and ω is a real disturbance frequency, and c.c. denotes complex conjugate terms. The eigensolutions u,v,p and t are governed by a six-order system of equations that is given in reference 9. The density disturbance is related to the temperature and pressure disturbances through the state equation,

$$(2) \quad \gamma M p = \rho T + \bar{\rho} t$$

while the viscosity disturbance is related to the temperature disturbance by

$$(3) \quad \mu = (d\bar{\mu}/dT)\, t = \hat{\mu}\, t$$

where $\bar{\rho}$ and $\bar{\mu}$ are the mean-flow density and viscosity respectively, γ is the ratio of specific heats and M is the freestream Mach number. The six-order

system is numerically integrated as initial value problem using a combination of shooting [8] and Newton-Raphson iteration technique that employs a Gram-Schmidt orthonormalization procedure. The solution of this eigenvalue problem is calculated by the author elsewhere [7,9].

The linear stability theory of primary instability provides α for a given ω and R. Then the integration of the growth rate $-\alpha_i$ gives the amplification factor ,

$$(4) \qquad \ln (A / A_o) = -2 \int_{R_{op}}^{R} \alpha_i \, dR$$

where A_o is an arbitrary initial amplitude of the primary instability at R_{op} (R where the onset of the primary wave) . The eigensolutions may be normalized such that A measures directly the maximum r.m.s. value of the streamwise disturbance, that is

$$(5) \qquad \max_{0 \leq y < \infty} |u(y)|^2 = 1/2$$

Since the primary instability of boundary -layer flows is induced by viscosity, the growth rates and amplification factors here are typically very small.

Now the basic state under consideration is composed of the sum of the 2D compressible mean flow and a finite amplitude A of the primary T-S wave, that is

$$(6) \qquad (u_b, v_b, p_b, t_b) = (U,0,P,T) + A [u(y), v(y), p(y), t(y)] \exp(i\theta)$$

Where

$$A = A_o \exp(-\int \alpha_i \, dx), \qquad \text{assumed constant, and}$$

$$\theta = \int \alpha_r \, dx - \omega t$$

III. SECONDARY INSTABILITY

We consider the 3D quasi-parallel spatial subharmonic instability of the basic state given by (6). The finite amplitude primary wave acts as a parametric exitation on the secondary instability. Following the analysis of Herbert [4,5] , Nayfeh [6], and El-Hady [10] we apply Floquet theory and express the secondary wave using the normal mode concept,

$$(u_s, v_s, p_s, t_s) = \exp(\int \hat{\gamma}\, dx)[\hat{u}(y), \hat{v}(y), \hat{p}(y), \hat{t}(y)] \exp(\tfrac{1}{2} i\theta) \cos \beta z + c.c.$$

(7)

$$w_s = \exp(\int \hat{\gamma}\, dx)\hat{w}(y) \exp(\tfrac{1}{2} i\theta) \sin \beta z + c.c.$$

where β is a spanwise real wavenumber, and $\hat{\gamma} = \gamma_r + i\gamma_i$ is a characteristic exponent. The spatial growth rate of the secondary wave is given by γ_r, while γ_i can be interpreted as a shift in the streamwise wavenumber. In our calculations, we consider only the case of $\gamma_i = 0$, that is the secondary wave is perfectly synchronized with the basic state.

The secondary wave (7) is superposed on the basic state (6) and the result is substituted into the dimensionless Navier-Stokes equations. The meam flow plus the 2D T-S quantities are substracted, and the resulting equations are linearized in the secondary disturbances. Then one obtains an eigenvalue problem that can be written as

(8) $$T^{-1}(g Z_1 - T^{-1} DT Z_3 + DZ_3 + \beta Z_4) + G(\gamma M^2 Z_6 - T^{-1} Z_7) + A(a_1) = 0$$

(9) $$\{G - \bar{\mu} R^{-1}[(m+2) g^2 - \beta^2]\} Z_1 - R^{-1} D(\bar{\mu} Z_2) + (T^{-1} DU - D\bar{\mu} R^{-1} g) Z_3 - (m+1) \bar{\mu} R^{-1} g (DZ_3 + \beta Z_4) + g Z_6 - R^{-1} D(\hat{\mu} DU) Z_7 - \hat{\mu} R^{-1} DU Z_8 + A(a_2) + A^2(b_2) = 0$$

(10) $$[G - \bar{\mu} R^{-1}(g^2 + \beta^2)] Z_3 - (m+1) \bar{\mu} R^{-1}(g Z_2 + \beta Z_5) - (m+2) R^{-1} D(\bar{\mu} DZ_3) - m R^{-1} D\bar{\mu}(g Z_1 + \beta Z_4) + DZ_6 - \hat{\mu} R^{-1} DU g Z_7 + A(a_3) + A^2(b_3) = 0$$

$$(11) \qquad (m+1)\,\bar{\mu}\,R^{-1}\beta\,(g\,Z_1 + DZ_3) + D\bar{\mu}\,R^{-1}\beta\,Z_3$$

$$[\,G - \bar{\mu}\,R^{-1}g^2 + (m+2)\,\bar{\mu}\,R^{-1}\beta^2\,]\,Z_4 - R^{-1}\,D(\bar{\mu}\,Z_5)$$

$$-\,\beta\,Z_6 + A\,(a_4) + A^2\,(b_4) = 0$$

$$(12) \qquad -2\hat{M}\,\bar{\mu}\,R^{-1}\,DU\,(Z_2 + g\,Z_3) + T^{-1}\,DT\,Z_3 - \hat{M}\,T\,G\,Z_6$$

$$+\{\,G - R^{-1}\,Pr^{-1}\,[\bar{\mu}\,(g^2 - \beta^2) + D(\bar{\mu}\,DT)] - \hat{M}\,R^{-1}\,(DU)^2\,\hat{\mu}\,\}\,Z_7$$

$$-\,R^{-1}\,Pr^{-1}\,(2\,Z_8\,D\bar{\mu} - \bar{\mu}\,DZ_8) + A\,(a_5) + A^2\,(b_5) = 0$$

where

$$Z_1 = \hat{u}\,, \quad Z_2 = D\hat{u}\,, \quad Z_3 = \hat{v}\,, \quad Z_4 = \hat{w}\,,$$

$$Z_5 = D\hat{w}\,, \quad Z_6 = \hat{p}\,, \quad Z_7 = \hat{t}\,, \quad Z_8 = D\hat{t}$$

$$g = (\gamma_r + \tfrac{1}{2}\,i\,\alpha_r)$$

$$G = T^{-1}\,(gU - \tfrac{1}{2}\,i\omega)$$

$$\hat{M} = (\gamma - 1)\,M^2$$

also Pr is Prandtl number, D=d/dy, and m=2(e-1)/3 is the ratio of the coefficients of viscosities, where e=0 corresponds to the Stokes hypothesis.

The boundary conditions are

$$(13) \qquad Z_1 = Z_3 = Z_4 = Z_7 = 0 \qquad \text{at } y = 0$$

$$Z_1\,,\ Z_3\,,\ Z_4\,,\ Z_7 \to 0 \qquad \text{as } y \to \infty$$

Equations (8)-(12) govern the secondary 3D instability of compressible 2D flows. They represent the mass, x-momentum, y-momentum, z-momentum, and energy equations respectively. The coefficients of A and A^2 (a_i, b_i, i=1-5) are given in Appendix A. The coefficients of A in the mass equation and those of A^2 in all other equations are new in this system of equations in contrast to the secondary instability equations for incompressible flows. These coefficients are present mainly due to the density disturbance of both primary and secondary instabilities. In the incompressible limit equations (8)-(12) reduce exactly to that given by El-Hady [10]. When A=0,the system of equations (8)-(13) govern a primary subharmonic 3D wave.

The system of equations (8)-(12) can be written as eight complex equations in the form,

$$
\begin{aligned}
&DZ_1 - Z_2 = 0 \\
&DZ_2 + c_o \, D\bar{Z}_2 + c_1 = 0 \\
&DZ_3 + c_2 \, D\bar{Z}_3 + c_3 = 0 \\
&DZ_4 - Z_5 = 0 \\
&DZ_5 + c_4 \, D\bar{Z}_5 + c_5 = 0 \\
&DZ_6 + c_6 \, D\bar{Z}_6 + c_7 = 0 \\
&DZ_7 - Z_8 = 0 \\
&DZ_8 + c_8 \, D\bar{Z}_8 + c_9 = 0
\end{aligned}
\tag{14}
$$

where the c´s are quadratures in the primary and secondary disturbance quantities, and the overbar indicates a complex conjugate. Equations (14) are numerically integrated as initial value problem from $y = y_e$ (edge of the boundary layer) to the wall. The eigenvalue search used a Newton-Raphson iteration technique to satisfy the last boundary condition at the wall. A well tested code SUPPORT [8] is used which is coupled with an orthonormalization test based on the modified Gram-Schmidt procedure to overcome the stiffness of the integrated system of equations.

The linear stability theory of the secondary instability provides $\hat{\gamma}$ for a given β and R. Then the integration of the growth rate γ_r gives the amplification factor,

$$
\ln (S / S_o) = 2 \int_{R_{os}}^{R} \gamma_r \, dR \tag{15}
$$

where s_0 is an arbitrary initial amplitude of the secondary instability at R_{os} (R where the onset of the secondary wave) . The secondary subharmonic instability is believed to originate from a strong mechanism of combined tilting and stretching of the vortices such as the case of incompressible flows [10], thus the growth rates and amplification factors are expected to be large as they occur on a convective length scale.

IV. RESULTS AND DISCUSSION

For the incompressible limit (M = 0), our compressible secondary instability code gives results that are in full agreement with those obtained by Herbert et al.[5] and by El-Hady [10]. All results reported here are for the nondimensional frequency $F = \omega / R = 60E-6$, that remains fixed as a wave of fixed physical frequency travels downstream.

At M = 0, a primary 2D instability grows between $R_{op} = 554$ and $R_{1p} = 1052$ (first and second neutral points) reaching a maximum amplification factor of A/A0 = 41.68. As Mach number increases, the growth rates of the primary 2D waves decrease as shown in Fig.(1). Also the first and second neutral points, as well as the streamwise location where the maximum growth rate occurs, shift to the left, they occur earlier upstream as Mach number increases. Fig.(2) shows a reduction in the amplification factor of the primary 2D instability as Mach number increases.

Almost in the same region where the primary 2D waves are growing, a broad band of spanwise wavenumbers of primary 3D subharmonic waves are subject to amplification. Fig.(3) shows the growth rate curves of these primary 3D subharmonics (F = 30E-6) for different Mach numbers. These curves possess the same features of the primary 2D waves of having lower growth rates that shift to lower R as Mach number increases. Fig.(4) shows the amplification factors of these primary subharmonics. Both Figs.(3) and (4) suggest that the growth rates and amplification factors of the primary subharmonics are typically so small to bear any resemblance to experimentally observed transition.

However, the growth rates shown in Fig.(5) as function of the spanwise wavenumber $B = 10E+3\ \beta/R$ for secondary 3D subharmonics, are much larger than those for primary 2D waves or primary 3D subharmonics. This strong growth is due to the parametrical exitation by the finite amplitude primary 2D wave. Fig.(5) is calculated at R=850 and a primary 2D amplitude A =.01, for different Mach numbers. For high spanwise wavenumbers ($B \geq .225$), compressibility appears to have a stabilizing effect on the secondary subharmonic instability. In other words, the secondary subharmonic instability is largest at M = 0, and decreases as Mach number increases. But for low spanwise wavenumbers ($B < .225$) the effect of compressibility depends on the value of the spanwise wavenumber.

At fixed F and R, results for different Mach numbers show a destabilizing effect (higher growth rates for the secondary subharmonic) as the primary 2D amplitude A increases. At R=1050, Fig.(6) illustrates the destabilizing effect of increasing A for M =0.8 compared with that for M =0. Fig.(6) reveals that the influence of compressibility on secondary subharmonics is not the only function

of the spanwise wavenumber, but also is a function of the primary 2D amplitude. While at A=.01 compressibility is stabilizing for large values of B and destabilizing for small values of B, it has a destabilizing influence on the secondary subharmonics at A=.002 for all range of spanwise wavenumbers. The figure also shows that at very small amplitudes, considerable growth rates exist in a small band of wavenumbers, that extend to larger values as the amplitude increases.

Fig.(7) shows the effect of Reynolds number R on the growth of the secondary subharmonics at M =0.8. As R increases , an increase in the growth rates exist at fixed F and A.

To evaluate the overall effect of compressibility on the secondary subharmonics, we can combine the influence of increasing the amplitude A of the primary 2D wave and increasing R for various Mach numbers at fixed F. For comparison purposes, the amplification factor of the subharmonic is calculated using equation (15) from R_{OS} (onset of the secondary subharmonic instability) to any R downstream. For different Mach numbers, Fig. (8) shows the variation of the growth rates of the secondary subharmonics with R at a spanwise wavenumber B=.15. The initial primary 2D amplitude used for these calculations is A=.001. Fig.(9) shows the amplification factors decreasing from about 29 at M =0. to 12 at M =0.8.

Figs.(8) and (9) indicate that while the growth rates and amplification factors of the secondary subharmonics are decreased by increasing Mach number,the onset of the secondary instability is almost not affected. This is probably due to the combined effect of the upstream shift of the onset of the primary 2D instability, as well as the growing of the primary amplitude.

V. CONCLUSION

We formulated the secondary three-dimensional instability problem for compressible boundary layers. The effect of finite amplitude two-dimensional T-S wave on the growth of three-dimensional subharmonics is investigated for a range of Mach numbers from 0 to 1.2. Numerical results for F =60E-6 show that the local (at fixed R) effect of compressibility on the secondary subharmonics may be stabilizing or destabilizing depending upon their spanwise wavenumbers, as well as the finite amplitude of the primary 2D wave. However, the overall effect of increasing Mach number is a reduction in the growth rates and amplification factors of the secondary subharmonics, almost with no change in the streamwise location where this instability sets in.

ACKNOWLEDGMENT

This work was supported by NASA Langley Research Center under grant NAG1-729. The author is indebted to P.J. Bobbitt and W.D. Harvey for their interest and support during the course of this work.

REFERENCES

1. Mack, L.M. "Review of Linear Compressible Stability Theory". In Stability of Time Dependent and Spatially Varying Flows. Ed. D.L. Dwoyer and M.Y. Hussaini, Springer Verlag, N.Y., pp. 164-187, 1987.

2. Erlebacher,G. and Hussaini,M.Y. " Incipient Transition Phenomena in Compressible Flows over a Flat Plate." ICASE Report 86-39,1986.

3. Erlebacher, G. and Hussaini, M.Y. "Stability and Transition in Supersonic Boundary Layer". AIAA Paper No. 87-1416, 1987.

4. Herbert, Th." Subharmonic Three-Dimensional Disturbances in Unstable Plane Shear Flows." AIAA Paper No. 83-1759, 1983.

5. Herbert Th., Bertolotti, F.P., and Santos, G.R.," Floquet Analysis of Secondary Instability in Shear Flows." In Stability of Time Dependent & Spatially Varying Flows, Ed. D.L. Dwoyer & M.Y. Hussaini, Spring Verlag, N.Y., pp. 43-57, 1987.

6. Nayfeh, A.H." Nonlinear Stability of Boundary Layers" AIAA Paper 87-0044, 1987.

7. El-Hady N.M. and Nayfeh A.H., " Nonparallel Stability of Compressible Boundary-Layer Flows". AIAA Paper No. 80-0277, 1980 (see also VPI&SU Report No. VPI-E-79.13).

8. Scott, M.R. and Watts, H.A., " Computational Solution of Linear Two-Point Boundary Value Problems Via Orthonormalization". SIAM J. Numer. Anal., Vol. 14, pp. 40-70, 1977.

9. El-Hady, N.M." On the Effect of Boundary-Layer Growth on the Stability of Compressible Flows." NASA-CR 3474, 1981.

10. El-Hady, N.M.," Secondary Subharmonic Instability of Boundary Layers with Pressure Gradients and Suction". Submitted to Phys. Fluids, also NASA-CR 4112, 1988.

11. Orzag, S.A. and Patera, A.T.,"Secondary Instability of Wall Bounded Shear Flows." J. Fluid Mech., Vol. 128, 347, 1983.

APPENDIX A

$$a_1 = f(g\,\bar{Z}_1 + \beta\,\bar{Z}_4) + D(f\,\bar{Z}_3) + g\,u\,\bar{F} + D(v\,\bar{F})$$

$$b_1 = 0$$

$$a_2 = [\,\bar{G} f + T^{-1} g u - m_2 \hat{R} \bar{g} (\bar{g} + i\alpha) t + \hat{R} \beta^2 t\,] \bar{Z}_1$$

$$+ [\,T^{-1} v - R^{-1} D(\hat{\mu} t)\,] \bar{Z}_2 + [\,f DU + T^{-1} Du - R^{-1} \bar{g} D(\hat{\mu} t)\,] \bar{Z}_3$$

$$- \hat{R} t D\bar{Z}_2 - \hat{R} (mg + \bar{g}) t D\bar{Z}_3 + \hat{R} \beta (m_1 \bar{g} + im\alpha) t \bar{Z}_4$$

$$- \hat{R} [m_2 \alpha (i \bar{g} + \alpha) u + (im_1 \alpha + m \bar{g}) Dv + D^2 u\,] \bar{Z}_7$$

$$- \hat{R} (Du + i\alpha v) D(\hat{\mu} \bar{Z}_7) + [\,i(\alpha U - \omega) + v DU\,] F$$

$$b_2 = [(g + i\alpha) \bar{f} u + \bar{g} f \bar{u}\,] Z_1 + (\bar{f} v + f \bar{v}) Z_2 + (\bar{f} Du + f D\bar{u}) Z_3$$

$$+ (\bar{v} Du + v D\bar{u}) F$$

$$a_3 = [\,f \bar{G} + T^{-1} (\bar{g} u + Dv) - \hat{R} (\bar{g}^2 + i \bar{g}\alpha - \beta^2) t\,] \bar{Z}_3$$

$$+ [\,T^{-1} v - m_2 R^{-1} D(\hat{\mu} t)\,] D\bar{Z}_3 - m_2 \hat{R} t D^2 \bar{Z}_3 + i(\alpha U - \omega) v \bar{F}$$

$$+ [\,iT^{-1} \alpha v - m R^{-1} D(\hat{\mu} t) \bar{g}\,] \bar{Z}_1 - \hat{R} (m_1 \bar{g} + i\alpha) t \bar{Z}_2 - m R^{-1} \beta D(\hat{\mu} t) \bar{Z}_4$$

$$- m_1 \hat{R} \beta t \bar{Z}_5 - \{\,\hat{R} [\,(im\alpha + g) Du + (i \bar{g} - \alpha) v + m_2 D^2 v\,]$$

$$- R^{-1} D\hat{\mu} (im \alpha u + m_2 Dv)\} \bar{Z}_7 - \hat{R} (im \alpha u + m_2 Dv\,] \bar{Z}_8$$

$$b_3 = i\alpha (\bar{f} v - f \bar{v}) Z_1 + [(\bar{f} u + f \bar{u}) g + \bar{f} Dv + f D\bar{v}\,] Z_3$$

$$+ (\bar{f} v + f \bar{v}) DZ_3 + [\,2v D\bar{v} + i\alpha (v \bar{u} - \bar{v} u)\,] F$$

$$a_4 = [\, f\,\bar{G} + T^{-1}\bar{g}\,u - \hat{R}\,(\,\bar{g}^2 + i\alpha\, g - m\,\beta\,)\,t\,]\,\bar{Z}_4$$

$$+ [\, T^{-1} v - R^{-1} D(\,\hat{\mu}\, t)\,]\,\bar{Z}_5 - \hat{R}\,[\, t\, D\bar{Z}_5 - \beta\, t\,(\, g + m\,\bar{g}\,)\,\bar{Z}_1$$

$$- m_1\,\beta\, t\, D\bar{Z}_3 - m\,\beta\,(\, i\alpha\, u + Dv\,)\,\bar{Z}_7\,] \;+ R^{-1}\beta\, D(\,\hat{\mu}\, t)\,\bar{Z}_3$$

$$b_4 = (\,\bar{f}\, u + f\,\bar{u}\,)\, g\, Z_4 + (\,\bar{f}\, v + f\,\bar{v}\,)\, Z_5$$

$$a_5 = \{f\,\bar{G} + T^{-1}\bar{g}\,u - 2\hat{M}\,\hat{R}\, DU\,(Du + i\alpha\, v) - Pr^{-1}\,[\hat{R}\, t\,(\,\bar{g}^2 + 2i\alpha\,\bar{g} - \alpha^2 - \beta^2\,)$$

$$+ R^{-1} D(\,\hat{\mu}\, Dt\,)]\}\,\bar{Z}_7 + [\, i\,(\alpha U - \omega)\, t + v\, DT\,]\,\bar{F} - \hat{M}\,\bar{g}\, u\,\bar{Z}_6$$

$$- \hat{M}\, v\, D\bar{Z}_6 + [\, T^{-1} v - Pr^{-1}\,(\, 2\,\hat{R}\, Dt + t\, R\, D\hat{\mu}\,)\,]\,\bar{Z}_8 - \hat{R}\, Pr^{-1}\, t\, D\bar{Z}_8$$

$$+ [\, i\alpha\,(\, T^{-1} t - \hat{M}\, p\,) - 2\,\hat{M}\,\mu\, R^{-1}\bar{g}\,(\, i\alpha\, m_2\, u - m\, Dv\,)\,]\,\bar{Z}_1$$

$$- 2\,\hat{M}\, R^{-1}\,[\,\mu\,(i\alpha\, v + Du) + \hat{\mu}\, t\, DU\,]\,(\,\bar{Z}_2 + \bar{g}\,\bar{Z}_3\,)$$

$$+ (\, T^{-1} Dt + f\, DT - \hat{M}\, Dp\,)\,\bar{Z}_3$$

$$- 2\hat{M}\, R^{-1}\mu\,[\,(\, im\alpha\, u + m_2\, Dv\,)\, D\bar{Z}_3 + m\,\beta\,(\, i\alpha\, u + Dv\,)\,\bar{Z}_4\,]$$

$$b_5 = \{\,(\,\bar{f}\, u + f\,\bar{u}\,)\, g - 2\,\hat{M}\,\hat{R}\,[\,\alpha^2\,\bar{v}\, v + i\alpha\,(\, v\, D\bar{u} - \bar{v}\, Du\,) + m_2\,\alpha^2\,\bar{u}\, u$$

$$+ m\,\alpha^2(\, u\,\bar{v} + \bar{u}\, v\,) + m_2\, Dv\, D\bar{v} + D\bar{u}\, Du\,]$$

$$+ [\, i\alpha\,(\,\bar{u}\, t - u\,\bar{t}\,) + \bar{v}\, Dt + v\, D\bar{t}\,]\, F \;+ (\,\bar{f}\, v + f\,\bar{v}\,)\, Z_8$$

$$+ [\, i\alpha\,(\, t\,\bar{f} - \bar{t}\, f\,) - 2\hat{M}\, R^{-1}\, i\, m_2\alpha\, g\,(\,\bar{t}\, u - t\,\bar{u}\,)\,]\, Z_1$$

$$- 2\,\hat{M}\,\hat{R}\,(\,\bar{t}\, Du + t\, D\bar{u} + i\alpha(\,\bar{t}\, v - t\,\bar{v}\,)\,(\, Z_2 + g\, Z_3\,)$$

$$+ (\,\bar{f}\, Dt + f\, D\bar{t}\,)\, Z_3 - 2\hat{M}\,\hat{R}\, m_2\,(\,\bar{t}\, Dv + t\, D\bar{v}\,)\, DZ_3$$

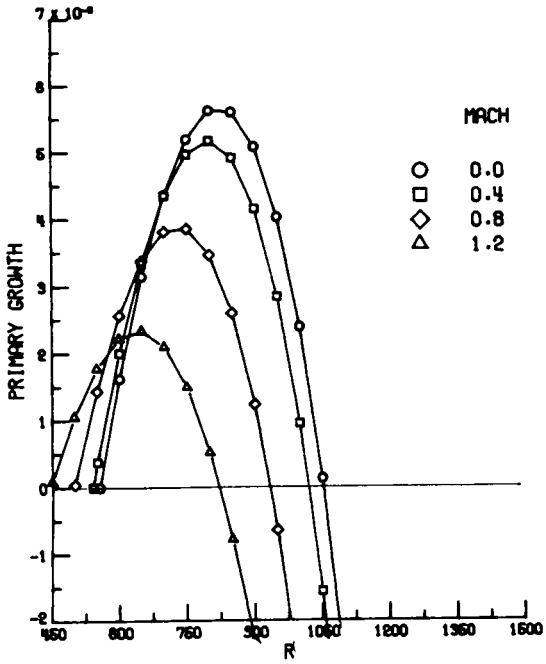

Fig.1 Growth rates of the primary 2D wave (F=60E-6) at different Mach numbers.

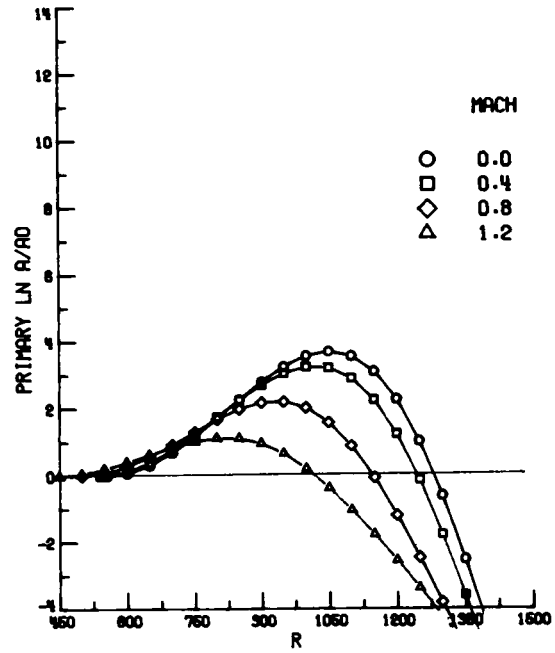

Fig.2 Amplification factors of the primary 2D wave (F=60E-6) at different Mach numbers.

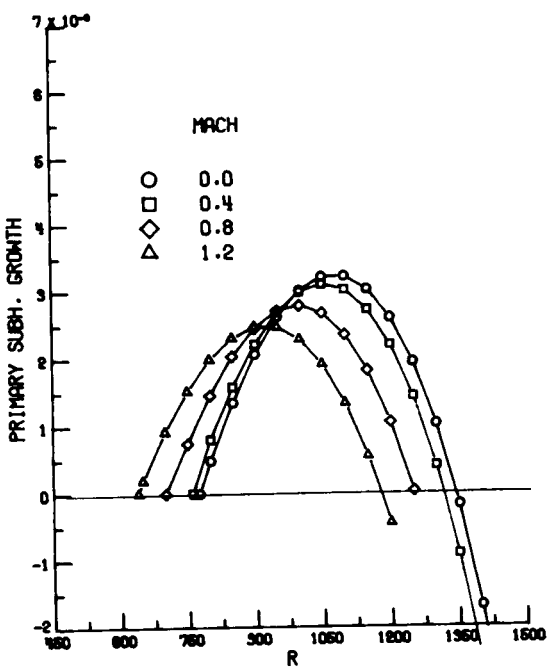

Fig.3 Growth rates of the primary 3D subharmonic wave (F=30E-6 and B=.12) at different Mach numbers.

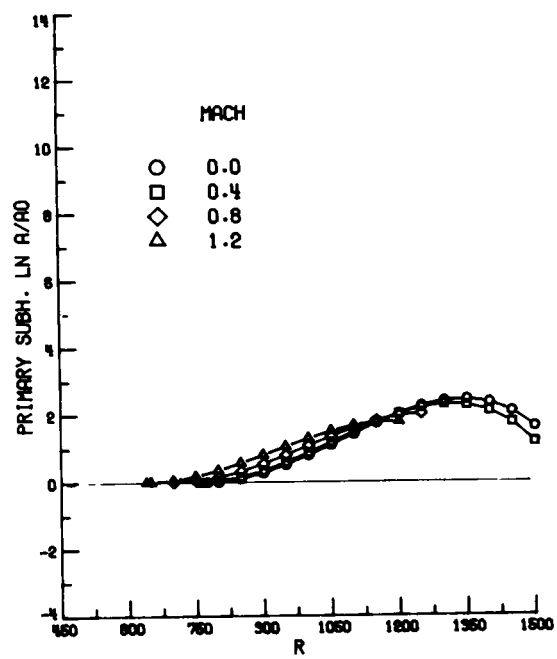

Fig.4 Amplification factors of the primary 3D subharmonic wave (F=30E-6 and B=.12) at different Mach numbers.

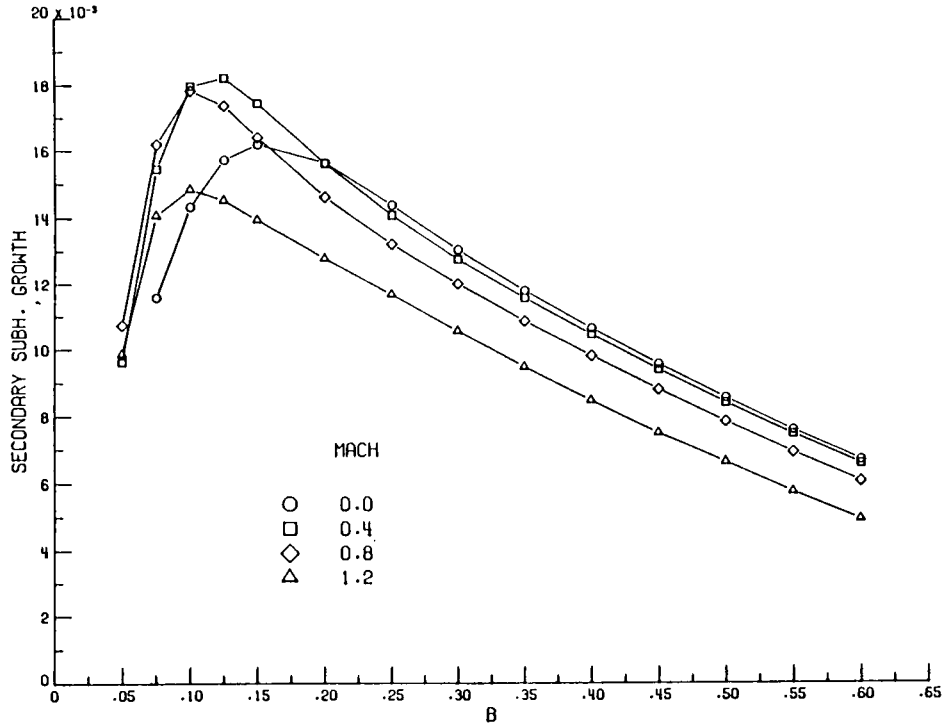

Fig.5 Growth rates of the secondary 3D subharmonic at R=850 and A=.01 as function of the spanwise wavenumber, for different Mach numbers.

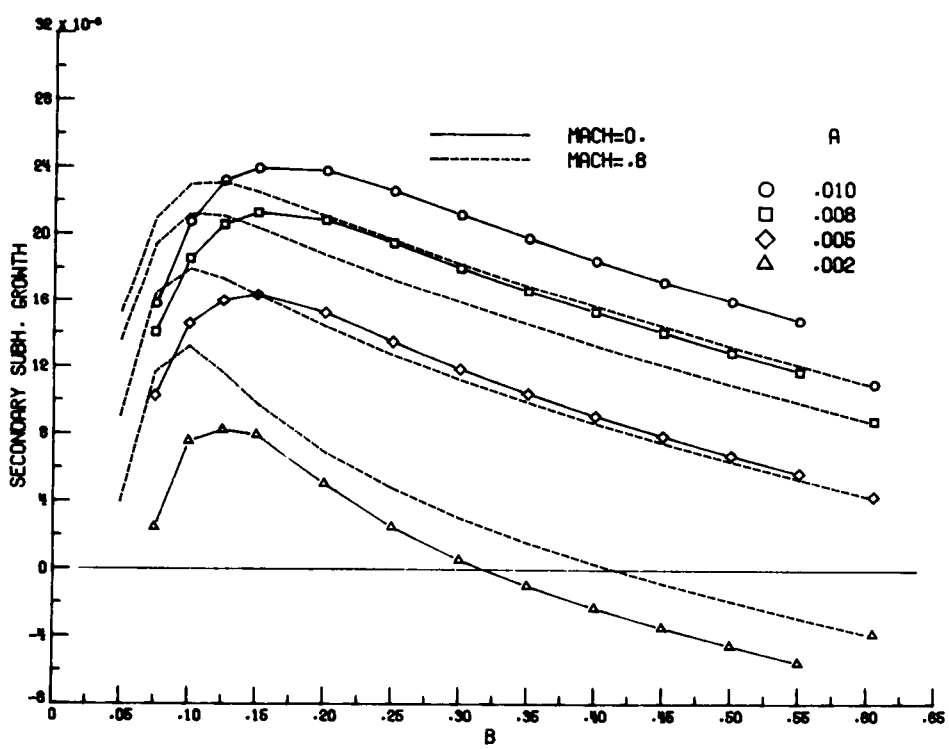

Fig.6 Effect of the primary amplitude A on the growth rates of the secondary 3D subharmonic at R=1050, for Mach numbers 0 and 0.8.

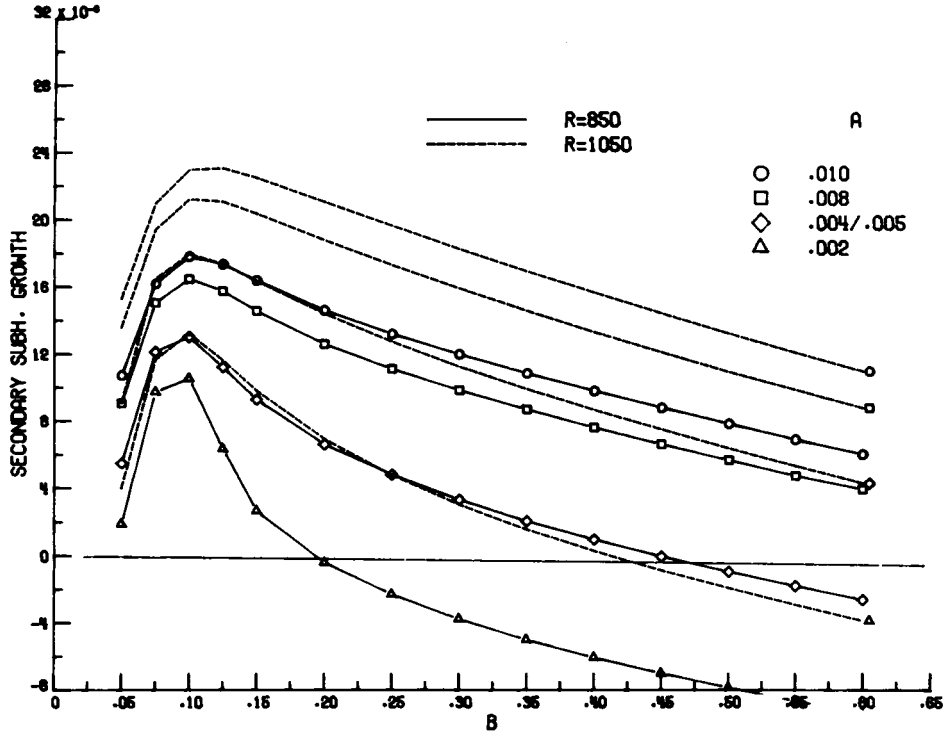

Fig.7 Effect of Reynolds number R on the growth rates of the secondary 3D subharmonics at M =0.8, for different primary amplitude A.

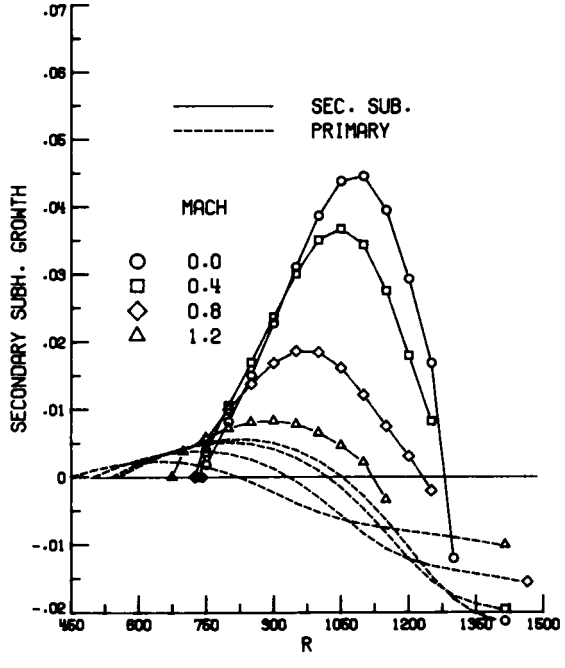

Fig.8 Variation of the growth rates with R of a secondary 3D subharmonic at B=.15 for different Mach numbers.

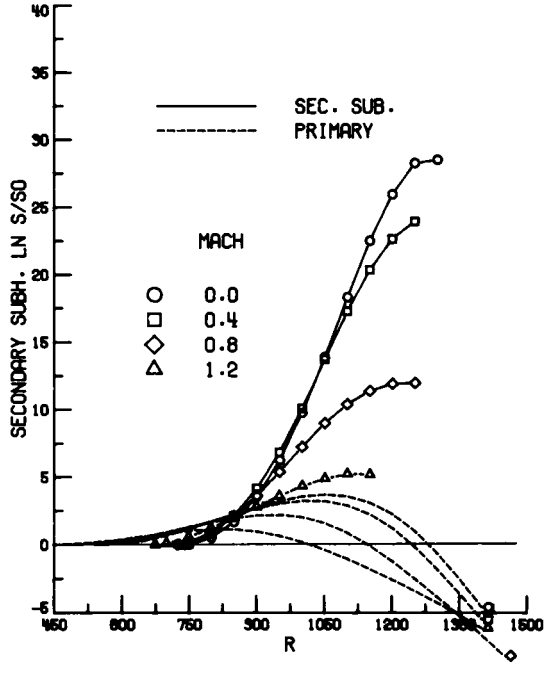

Fig.9 Variation of the amplification factors with R of a secondary 3D subharmonic at B=.15 for different Mach numbers.

N89-20955

TEST TECHNIQUES
A Survey Paper on Cryogenic Tunnels, Adaptive Wall Test Sections, and Magnetic Suspension and Balance Systems

Robert A. Kilgore, David A. Dress and Stephen W.D. Wolf*
Experimental Techniques Branch
NASA Langley Research Center
Hampton, Virginia

Colin P. Britcher
Department of Mechanical Engineering and Mechanics
Old Dominion University
Norfolk, Virginia

SUMMARY

Our ability to get good experimental data in wind tunnels is often compromised by things seemingly beyond our control. Inadequate Reynolds number, wall interference, and support interference are three of the major problems in wind tunnel testing.

Techniques for solving these problems are available. Cryogenic wind tunnels solve the problem of low Reynolds number. Adaptive wall test sections can go a long way toward eliminating wall interference. A magnetic suspension and balance system (MSBS) completely eliminates support interference. We are beginning to realize the potential of these techniques.

This survey paper covers cryogenic tunnels, adaptive wall test sections, and MSBS. We give a brief historical overview and describe the present state of development and application in each area. Finally, we attempt to predict future developments and applications of these test techniques.

INTRODUCTION

There are many reasons why we want good data from our wind tunnels. However, problems with wind tunnels often keep us from getting the quality of data we need. Any list of problems with wind tunnels would include **inadequate Reynolds number, wall interference**, and **support interference**. Fortunately, techniques for solving these major problems are available.

Earlier in this Symposium, Wayne McKinney gave the status of the U.S. National Transonic Facility (NTF) and described the early test results. The NTF is an excellent example of the use of a cryogenic wind tunnel to solve the problem of low Reynolds number. In this survey paper we give information on several other cryogenic tunnels.

We also describe solutions to two other major problems with wind tunnels, wall and support interference. Adaptive wall test sections, first used in the 1930s, go a long way toward getting rid of wall interference. Magnetic suspension of the model, first used in the 1950s, completely eliminates support interference.

The three sections of this paper cover cryogenic tunnels, adaptive wall test sections, and magnetic suspension and balance systems. Each section gives a brief historical overview and describes the present state of development and application. Finally, we predict a bright future for the continued rapid development and application of these test techniques.

---

* NRC Associate

CRYOGENIC WIND TUNNELS

The world's first cryogenic wind tunnel was built at NASA Langley in 1972. Following the development of this small low-speed tunnel, cryogenic tunnels were built at other research centers. This section describes some of these tunnels.

References 1 and 2 are the two parts of a review article on cryogenic tunnels published in *Cryogenics* in 1984. Reference 1 gives the evolution, theory, and advantages of cryogenic tunnels. Reference 2 describes the early use of cryogenic tunnels in the United States at NASA Langley. Reference 2 also briefly describes some of the cryogenic tunnel activities around the world.

Work on the development and use of cryogenic tunnels has continued since 1984. Reference 3 is a recent article in *Cryogenics* which gives an update on cryogenic tunnel activities. The emphasis in reference 3 is on the cryogenic engineering aspects of the cryogenic tunnels. We base this present survey paper on reference 3. However, the emphasis in this survey paper is on the aerodynamic capabilities of the cryogenic tunnels.

We do not attempt to describe every cryogenic tunnel. Rather, we describe selected tunnels to give a general idea of activities around the world. These tunnels also illustrate the wide variety of cryogenic tunnels built since 1972.

England
Royal Aircraft Establishment - Bedford
Cryogenic Test Duct

Law and his colleagues at the Royal Aircraft Establishment (RAE) in Bedford built a simple closed circuit wind tunnel called the Cryogenic Test Duct. The Cryogenic Test Duct is part of the United Kingdom support for the European Transonic Windtunnel (ETW) program.[4]

The photograph in figure 1 shows the general arrangement of the RAE Cryogenic Test Duct. This photograph shows the uninsulated Test Duct. Table 1 gives the basic features of the Cryogenic Test Duct.

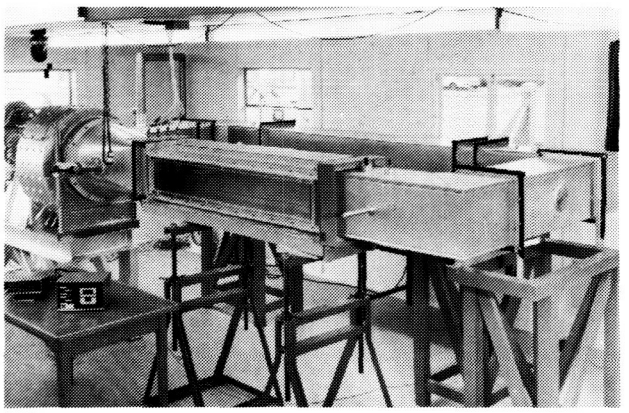

Fig. 1 - Photograph of RAE - Bedford Cryogenic Test Duct.

The 1:1 contraction is a clear sign the Test Duct is not designed for aerodynamic research. However, the Test Duct is ideally suited to provide the required cryogenic gas flow needed to test balances and model components. The Test Duct is simple in both design and construction. A heating and air conditioning shop in Bedford built the Test Duct for RAE.

The Test Duct has a simple calibration device for loading wind tunnel balances mounted in the test section. The test section has transparent side walls which allow direct visual observation during tests. The use of internal insulation permits rapid changes in the operating temperature. Reference 4 gives more details on the design and operation of the RAE Cryogenic Test Duct.

TABLE 1.- Cryogenic Test Duct at RAE-Bedford (England)

Type	closed circuit, centrifugal fan
Material of construction	aluminum
Insulation	external and internal
Cooling	liquid nitrogen
Test gas	nitrogen
Test section size (h,w,l)	0.3 x 0.3 x 1.5 m
Speed range	up to 25 m/s
Contraction ratio	1:1
Stagnation pressure	atmospheric
Stagnation temperature	90 K - ambient
Running time	typically 1 hour
Max. Reynolds number/m	11.4 million
Drive motor	9 kW
Fan speed	up to 2500 rpm
LN_2 tank volume	1.28 m^3

ORIGINAL PAGE IS
OF POOR QUALITY

ORIGINAL PAGE IS
OF POOR QUALITY

University of Southampton
0.1 m Cryogenic Wind Tunnel

Figure 2 shows a photograph of the 0.1 m Cryogenic Wind Tunnel at Southampton.[5] Table 2 gives the basic features for this low-speed tunnel.

Goodyer and his colleagues have used the low-speed tunnel at Southampton for a variety of purposes. These range from searching unsuccessfully for temperature spottiness (thermal turbulence) to successfully developing flow visualization techniques. In 1977, Kell used this tunnel to develop a surface flow visualization technique using liquid propane carrying a pigment.[6] He and Goodyer also found they could use a variety of tuft materials, including wool and cotton, even at 79 K.

Since first running in 1977, several improvements have made this simple cryogenic tunnel a very useful research tunnel.[7] For example, the tunnel now has automatic controls able to hold either Mach number or Reynolds number constant.[8]

Goodyer added three 1 kW electric heaters to the circuit to speed up the warming of the tunnel following cryogenic operation. The heaters also provide close temperature control. The technique is to inject a slight excess of liquid nitrogen over the amount required to balance heat added by the fan. Modulation of the heaters controls temperature to ±0.5 K.

By adding to the heat from the fan, the heaters also make it possible to run at temperatures up to 380 K. The ability to run at high temperatures gives an increased range of test Reynolds numbers. The test gas is usually air when operating at room temperatures or above.

After modifying the tunnel in 1978, Britcher used it with the Southampton 6-component Magnetic Suspension and Balance System (MSBS).[9] We will tell you more about the Southampton MSBS later in this paper.

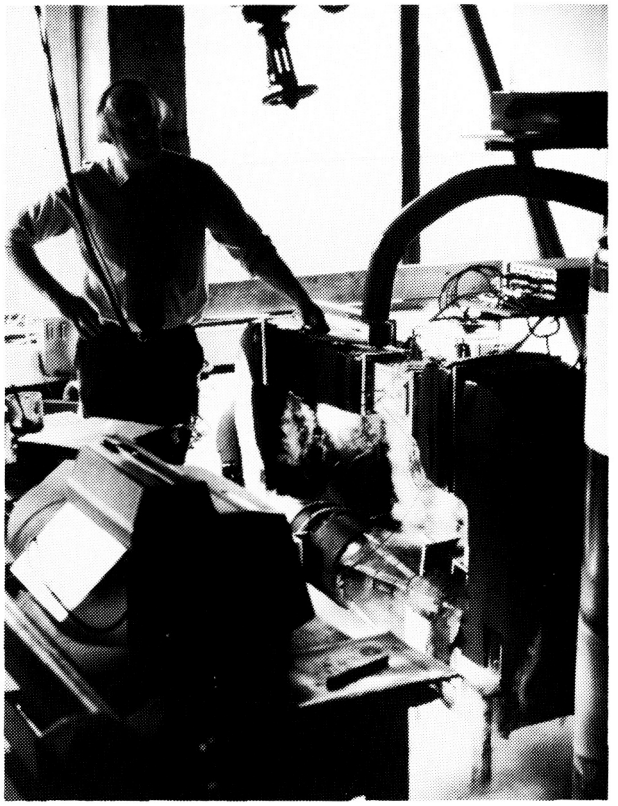

Fig. 2 - 0.1m Cryogenic wind tunnel at Southampton.

TABLE 2.- Cryogenic Low-Speed Tunnel at Southampton (England)

Type	closed circuit, fan
Material of construction	mostly aluminum
Insulation	external
Cooling	liquid nitrogen
Test gas	nitrogen; air (when running hot)
Test section size (h,w,l)	
Regular	0.11 x 0.11 x 0.25 m
MSBS	0.14 x 0.11 x 0.41 m
Speed range	14 - 72 m/s
Mach range	0.04 - 0.40
Contraction ratio	5.4:1
Stagnation pressure	atmospheric
Stagnation temperature	79 - 380 K
Running time	typically 1 hour
Max. Reynolds number/m	50 million
Drive motor	4 kW
Fan speed	up to 7200 rpm
LN_2 tank volume	0.17 m^3

Europe
European Transonic Windtunnel - Köln

Four European countries have joined through AGARD to design and build a large fan-driven transonic cryogenic tunnel. The tunnel is the European Transonic Windtunnel (ETW). The countries funding the ETW are France, the Federal Republic of Germany, the Netherlands, and the United Kingdom. These countries expect the ETW to meet their transonic high Reynolds number testing needs. Table 3 gives the major design features of the ETW.

Each of the four countries is doing research in support of the design and use of the ETW. Sverdrup Corporation has completed the preliminary design of the ETW.

The DFVLR center at Porz-Wahn (near Köln) is the site selected for the ETW. Construction of the ETW will start later this year. Reference 10 gives a complete account of the evolution and status of the ETW project.

Pilot European Transonic Windtunnel (PETW), NAL - Amsterdam

Work on the ETW includes building a 1:8.8 scale pilot tunnel at the National Aerospace Laboratory (NAL) in Amsterdam.[10] The pilot tunnel, known as PETW, has the same operating ranges as proposed for the ETW.

One big difference between the PETW and the ETW is the type of thermal insulation. The PETW is inside an insulated room. The latest design for the ETW calls for internal thermal insulation similar to the insulation used in the U.S. NTF. Table 4 gives the major design features of the PETW.

Researchers at NAL are using the PETW to check the aerodynamic performance of the ETW design. In addition, they are using the PETW to make control studies and gain operational experience.

France
ONERA-CERT - Toulouse
T2 Cryogenic Induction Tunnel

Mignosi and his colleagues at ONERA-CERT modified an injector driven tunnel, T2, for cryogenic operation. They also fitted the T2 with an adaptive wall test section.

The cryogenic modification followed development work in a 1:4 scale model pilot tunnel, T'2. Reference 11 gives a complete description of this work. Figure 3 shows a photograph of the T2. Table 5 gives the main features of the T2.

The T2 and the T'2 are the only cryogenic tunnels driven by induction. The induction drive of the T2 is in the seven turning vanes of the first corner. The hollow vanes receive high pressure dry air which blows through the trailing edges.

TABLE 3.- European Transonic Windtunnel (ETW) at DFVLR Porz-Wahn (W. Germany)

Type	closed circuit, fan
Material of construction	stainless steel
Insulation	internal
Cooling	liquid nitrogen
Test gas	nitrogen
Test section size (h,w,l)	2.0 x 2.4 x 6.9 m
Mach range	0.15 - 1.3
Contraction ratio	12:1
Stagnation pressure	1.25 - 4.5 bars
Stagnation temperature	90 - 313 K
Running time	typically 10 min
Max. Reynolds number/m	228 million
Drive motor	50 MW
Fan speed	up to 1200 rpm
LN_2 tank volume	3000 m^3

TABLE 4.- Pilot European Transonic Windtunnel (PETW) at NAL-Amsterdam (The Netherlands) (1:8.8 version of ETW)

Type	closed circuit, fan
Material of construction	aluminum alloy
Insulation	external, cold box
Cooling	liquid nitrogen
Test gas	nitrogen
Test section size (h,w,l)	0.23 x 0.27 x 0.78 m
Mach range	0.35 - 1.0 continuous 1.20, 1.35 fixed nozzles
Contraction ratio	12:1
Stagnation pressure	1.25 - 4.5 bars
Stagnation temperature	90 - 313 K
Running time	typically 60 min
Max. Reynolds number/m	228 million
Drive motor	1 MW
Fan speed	up to 9000 rpm
LN_2 tank volume	28.5 m^3

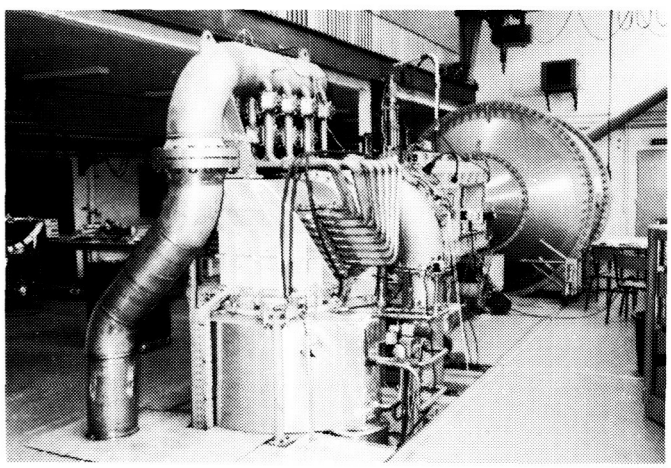

Fig. 3 - T2 cryogenic tunnel, ONERA/CERT.

ORIGINAL PAGE
BLACK AND WHITE PHOTOGRAPH

A digital computer controls the tests in the T2. During a typical airfoil test, they program the computer to cool the stream to 20 K below the intended operating temperature. This under-cooling quickly drives the model to the adiabatic temperature for the intended test conditions. Once the model is at the desired temperature, total pressure and Mach number automatically go to the desired test conditions.

When the test conditions (pressure, temperature, and Mach number) are stable - a matter of only a few seconds - the solid upper and lower test section walls iterate to an interference free condition. Finally, the computer records the model and tunnel wall data. It takes only about 5 minutes from the beginning of a run until they have plotted airfoil data.

TABLE 5.- T2 Cryogenic Tunnel at ONERA/CERT (France)

Type	closed circuit, induction
Material of construction	mild & stainless steels
Insulation	internal
Cooling	liquid nitrogen
Test gas	nitrogen rich air
Test section size (h,w,l)	0.37 x 0.37 x 1.32 m (solid adaptive walls)
Mach range	0.3 - 1
Contraction ratio	20:1
Stagnation pressure	1.6 - 3.5 bars
Stagnation temperature	95 K - ambient
Running time	up to 100 sec +
Max. Reynolds number/m	340 million
LN_2 tank volume	20 m^3

T'3 Cryogenic Fan-Driven Tunnel

There have been additional cryogenic tunnel projects in support of ETW at ONERA-CERT. One of these projects is the T'3 Cryogenic Tunnel, first operated in 1980.[12] The fan-driven T'3 gave valuable information on the design and operation of fan-driven cryogenic tunnels.

The T'3 also has an adaptive-wall test section. The walls of the 10 by 12 cm test section are manually adjusted to the desired streamline shapes. Table 6 gives the main features of the T'3.

TABLE 6.- T'3 Cryogenic Tunnel at ONERA/CERT (France)

Type	closed circuit, fan
Material of construction	stainless steels
Insulation	internal
Cooling	liquid nitrogen
Test gas	nitrogen
Test section size (h,w,l)	0.10 x 0.12 x 0.60 m (solid adaptive walls)
Mach range	0.05 - 0.80
Contraction ratio	13.3:1
Stagnation pressure	1.0 - 4 bars
Stagnation temperature	95 K - ambient
Running time	up to 25 minutes
Max. Reynolds number/m	340 million
Drive motor	125 kW
Fan speed	up to 9800 rpm
LN_2 tank volume	0.58 m^3

Germany
DFVLR
Kryo-Kanal-Köln (KKK) at Köln

Viehweger and his co-workers at the DFVLR Research Center at Porz-Wahn modified a 3 m low-speed tunnel for cryogenic operation.[13] The project started in 1978 with studies of how to modify the tunnel.

The studies included modeling the liquid nitrogen injection process and finding ways of fixing internal insulation to the concrete tunnel. They completed modifications to the tunnel in March of 1985. The first cryogenic operation was in January of 1986.

The Kryo-Kanal-Köln (KKK) is a modern, closed circuit, fan-driven cryogenic tunnel with automatic control of the test conditions. Figure 4 shows an aerial view of the KKK. Table 7 gives the main features of the KKK.

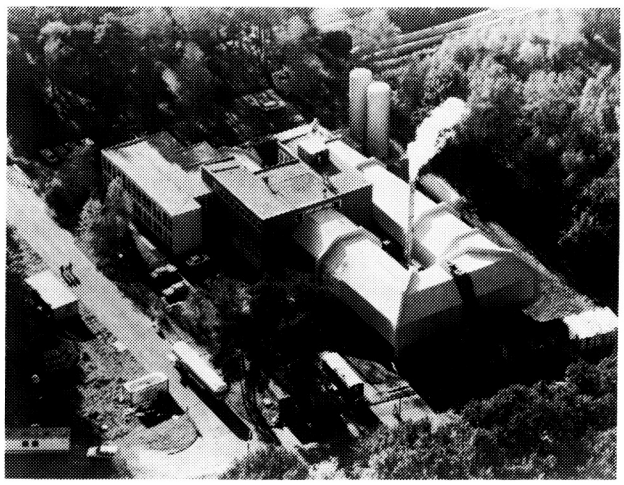

Fig. 4 - Kryo-Kanal-Köln at DFVLR-Köln.

ORIGINAL PAGE
BLACK AND WHITE PHOTOGRAPH

For model changes or modification, there is an access lock and model conditioning room below the test section. Following a run, the model and its support are moved from the test section into the lock.

For major model changes, warm gaseous nitrogen is blown into the closed lock and warms everything to ambient temperature. Fans blow dry air into the lock before the technicians enter to work on the model. The access time is about 4 hours because of the long warm up time for the model support and lifting systems.

For minor changes to the model, the model is moved into the conditioning room. In this relatively small room, warm-up of the model takes only about 30 minutes. A microcomputer controls all model movements in the lock or the conditioning room.

TABLE 7.- Kryo Kanal Köln (KKK) at DFVLR - Köln (W. Germany)

Type	closed circuit, fan
Material of construction	concrete
Insulation	internal
Cooling	liquid nitrogen
Test gas	nitrogen
Test section size (h,w,l)	2.4 x 2.4 x 5.4 m
Mach range	up to 0.38
Contraction ratio	10.3:1
Stagnation pressure	up to 1.12 bars
Stagnation temperature	100 - 300 K
Running time	up to several hours
Max. Reynolds number/m	37 million
Drive motor	1 MW
Fan speed	up to 1000 rpm
LN_2 tank volume	150 m^3

Cryogenic Ludwieg Tube Tunnel at Göttingen

Hefer and his colleagues at DFVLR Göttingen recently brought on line a cryogenic Ludwieg tube tunnel (CLTT). The sketch in Figure 5 shows the layout of the CLTT. Table 8 gives the major design features of the CLTT. Reference 14 describes the design and operation of the CLTT.

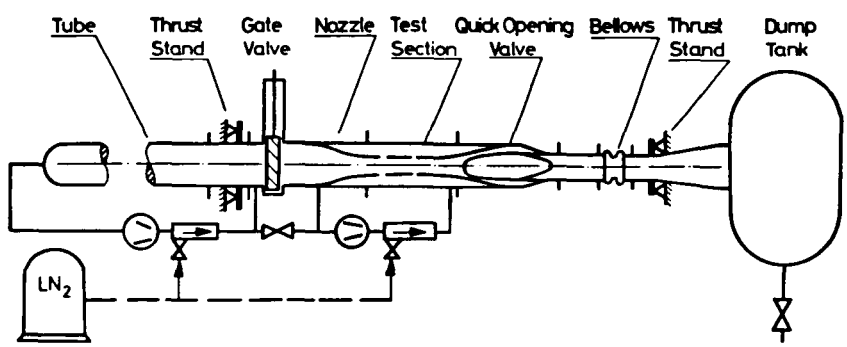

Fig. 5 - Cryogenic Ludwieg Tube Tunnel at DFVLR-Göttingen.

One big advantage seen for the Ludwieg tube tunnel is good flow quality. We expect the researchers at DFVLR Göttingen to use the high Reynolds number capability and good flow quality to develop advanced airfoils.

The present test section of the CLTT has conventional slotted walls. However, Hefer and his colleagues plan to install an adaptive-wall test section as soon as possible.

The proposed adaptive-wall test section will have solid but flexible top and bottom walls. In a slight departure from conventional design, the proposed adaptive-wall test section will have slotted side walls. This arrangement will let them test 3-D models with either adaptive or slotted walls by rotating the plain of symmetry of the models.

TABLE 8.- Cryogenic Ludwieg Tube Tunnel at DFVLR - Göttingen (W. Germany)

Type	Ludwieg tube
Material of construction	stainless steel
Insulation	external
Cooling	liquid nitrogen
Test gas	nitrogen
Test section size (h,w,l)	0.35 x 0.40 x 2.0 m
Mach range	0.25 - 1.0
Charge tube pressure	12.5 bars
Stagnation pressure	up to 10 bars
Stagnation temperature	120 K to ambient
Running time	0.6 to 1.0 sec
Max. Reynolds number/m	400 million
LN_2 tank volume	25 m^3

Japan

There is a lot of cryogenic tunnel activity in Japan. In October of 1987, one of the authors (Kilgore) visited Japan and saw their cryogenic tunnels. He met the people who designed, built, and use the cryogenic tunnels. He also observed two of the tunnels operating.

National Aerospace Laboratory (NAL)
0.1 x 0.1 m Pilot Transonic Cryogenic Tunnel

One company, Ishikawajima-Harima Heavy Industries Company, Limited (IHI) has been the general contractor for the cryogenic tunnels built in Japan. In 1982 IHI designed and built the 0.1 x 0.1 m Pilot Transonic Cryogenic Tunnel for NAL. Figure 6 is a photograph of the NAL cryogenic tunnel. Table 9 gives the main features of the NAL cryogenic tunnel.

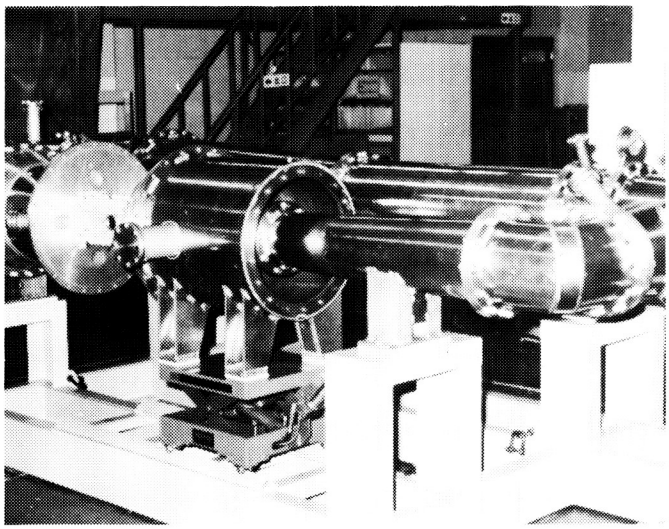

Fig. 6 - Pilot Transonic Cryogenic Tunnel at NAL.

Sawada and his colleagues at NAL use this small tunnel for aerodynamic studies and to gain operational experience. They also use it to support design studies of a larger transonic cryogenic tunnel for Japan. References 15 and 16 give details on the construction and performance of this closed circuit, fan driven tunnel.

Two 6 cm diameter glass windows allow a clear view into the test section. These windows use a vacuum space for thermal insulation rather than the more conventional dry nitrogen purging system.

The 0.1 x 0.1 m tunnel at NAL has a modern digital control and data acquisition system. The researchers at NAL make excellent use of a color video display during all phases of the operation. The computer displays check sheets and prompts to the operator during start up. The computer also displays the tunnel conditions during the run. The interactive design of the control and data acquisition computer makes tunnel operation simple and straightforward.

TABLE 9.- Pilot Transonic Cryogenic Tunnel at NAL (Japan)

Type	closed circuit, fan
Material of construction	A5052 Al-alloy
Insulation	external, purged
Cooling	liquid nitrogen
Test gas	nitrogen
Test section size (h,w,l)	0.1 x 0.1 x 0.3 m
Mach range	up to 1.02
Contraction ratio	18:1
Stagnation pressure	up to 2 bars
Stagnation temperature	90 K - ambient
Running time	more than 2 hours
Max. Reynolds number/m	130 million
Drive motor	55 kW
Fan speed	600 - 5700 rpm
LN_2 tank volume	2.17 m^3

Sawada and his colleagues have made many aerodynamic tests and explored the entire operating envelope of the tunnel. They determined tunnel features such as power factor and transient responses to changes in fan speed and liquid nitrogen flow rate. In all respects, the NAL cryogenic tunnel works satisfactorily and as predicted.

The NAL cryogenic tunnel usually runs 2 days each week. Since first operated in 1984, it has accumulated slightly over 400 hours of running.

Plans for the 0.1 x 0.1 m tunnel include aerodynamic tests on some simple models using a heated three-component strain gage balance.

ORIGINAL PAGE
BLACK AND WHITE PHOTOGRAPH

University of Tsukuba

The Institute of Engineering Mechanics at the University of Tsukuba has two low-speed cryogenic tunnels. One has a 0.1 x 0.1 m test section and the other a 0.5 x 0.5 m test section.

0.1 x 0.1 m Low-Speed Cryogenic Tunnel

The 0.1 x 0.1 m low-speed cryogenic tunnel first ran at cryogenic temperatures in 1980. Adachi and his colleagues have used this tunnel to calibrate sensors and to gain experience with cryogenic tunnels. This tunnel also gave design information for the larger low-speed tunnel at Tsukuba.

Because of the small size of the 0.1 x 0.1 m tunnel, it is no longer used for aerodynamic research. Table 10 gives the design features of this tunnel.

TABLE 10.- 0.1 x 0.1 m Cryogenic Low-Speed Tunnel at Tsukuba (Japan)

Type	closed circuit, fan
Material of construction	stainless steel
Insulation	external
Cooling	liquid nitrogen
Test gas	nitrogen
Test section size (h,w,l)	0.1 x 0.1 x 0.3 m
Speed range	up to 30 m/s
Contraction ratio	3.41:1
Stagnation pressure	up to 2 bars
Stagnation temperature	100 K - ambient
Running time	up to 2 hours
Max. Reynolds number/m	30 million
Drive motor	2.2 kW
Fan speed	1500 - 4300 rpm
LN_2 tank volume	0.175 m^3

0.5 x 0.5 m Cryogenic Tunnel

Figure 7 is a photograph the 0.5 x 0.5 m low-speed tunnel. Table 11 gives the main features of this tunnel.

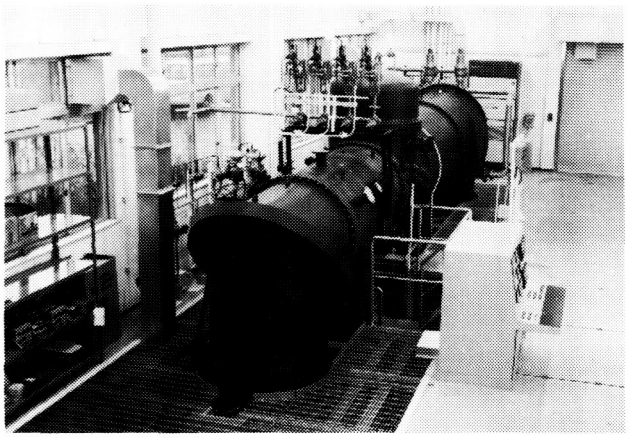

Fig. 7 - 0.5 x 0.5 m Cryogenic Low-Speed Tunnel at Tsukuba.

This tunnel is also a closed circuit, fan-driven tunnel. The maximum operating pressure of this tunnel is quite high at 8.1 bars. A mostly mild steel pressure shell makes this tunnel unique among pressurized continuous-flow cryogenic tunnels. The designers deviated from convention in using mild steel for a cryogenic pressure vessel. They felt safe using mild steel because of the internal insulation system.

Adachi and his colleagues use this tunnel to make a variety of aerodynamic measurements. These include testing various cylinders over a wide range of Reynolds numbers.[17]

TABLE 11.- 0.5 x 0.5 m Cryogenic Low-Speed Tunnel at Tsukuba (Japan)

Type	closed circuit, fan
Material of construction	mostly mild steel
Insulation	internal
Cooling	liquid nitrogen
Test gas	nitrogen
Test section size (h,w,l)	0.5 x 0.5 x 1.2 m
Speed range	7 - 65 m/s
Mach range	up to 0.30
Contraction ratio	6.12:1
Stagnation pressure	1.22 - 8.10 bars
Stagnation temperature	118 K - ambient
Running time	30 min. at max. R
Max. Reynolds number/m	200 million
Drive motor	450 kW
Fan speed	150 - 1500 rpm
LN_2 tank volume	20 m^3

National Defense Academy (NDA)
NDA High Reynolds Number Flow Facility

IHI built a cryogenic tunnel for the Department of Aeronautical Engineering of the Japanese National Defense Academy. IHI delivered this tunnel, the NDA High Reynolds Number Flow Facility, in March of 1985. Yamaguchi and his colleagues use this tunnel for basic fluid mechanics studies at the Academy.

ORIGINAL PAGE
BLACK AND WHITE PHOTOGRAPH

Typical of many small tunnels, the plenum of the NDA tunnel mounts on a trolley to allow access to the test section. The test section has two 30 cm diameter optical windows for flow visualization. Table 12 gives the main features of this tunnel.

Yamaguchi and his colleagues completed the initial tunnel calibration in 1985. The exhaust system now includes a precise automatic control valve and a manual control valve. They plan to add automatic control to the liquid nitrogen injection system. They also plan to add an automatic Mach number controller.

TABLE 12.- High Reynolds Number Flow Facility at NDA (Japan)

Type	closed circuit, centrifugal compressor
Material of construction	18-8 stainless steel
Insulation	external
Cooling	liquid nitrogen
Test gas	nitrogen
Test section size (h,w,l)	0.30 x 0.06 x 1.0 m
Speed range	up to 157 m/s
Mach range	up to 0.80
Contraction ratio	14:1
Stagnation pressure	up to 1.77 bars
Stagnation temperature	108 K - ambient
Running time	up to 40 min.
Max. Reynolds number/m	90 million
Drive motor	75 kW
LN_2 tank volume	5 m^3

United States
University of Illinois at Urbana-Champaign (UIUC)
Cryogenic Heat Transfer Tunnel (CHTT)

Clausing and his co-workers at UIUC have built a low-speed fan-driven cryogenic tunnel. They use their cryogenic tunnel for studies of forced, natural, and combined convective heat transfer. The tunnel provides ideal simulation under conditions requiring very large values of both Reynolds number and Grashof number.

The UIUC tunnel fulfills the need of accurately predicting combined convective losses from large, high temperature bodies such as solar "power tower" receivers. For these receivers, the values of both the Grashof and Reynolds numbers are large. Clausing proposed the Cryogenic Heat Transfer Tunnel (CHTT) as an economical way to get the required large values of Grashof and Reynolds numbers.[18] This tunnel also achieves an appropriate and near constant Prandtl number.

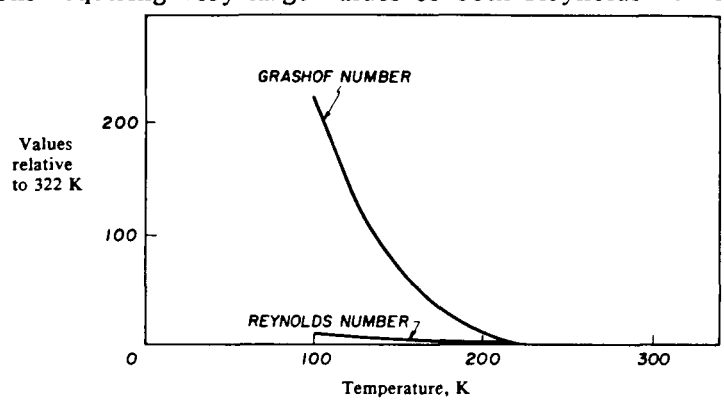

Fig. 8 - Variation of Grashof and Reynolds numbers with temperature.

Figure 8 shows the variations of Grashof number and Reynolds number with temperature. The use of cryogenic temperatures is a good way to get higher Reynolds numbers. It is also an excellent way to get higher Grashof numbers. Furthermore, the cryogenic environment cuts out most of the radiative heat transfer which can cause large errors in natural convection data from conventional facilities. References 19 and 20 discuss both the theory and advantages of the CHTT.

The CHTT is a very successful use of the cryogenic tunnel concept. Table 13 gives the main design features. Reference 21 gives a complete description of this tunnel.

TABLE 13.- Cryogenic Heat Transfer Tunnel at UIUC (USA)

Type	closed circuit, fan
Material of construction	mostly aluminum
Insulation	external, urethane
Cooling	LN_2 heat exchanger with GN_2 injection
Test gas	nitrogen
Test section size (h,w,l)	1.22 x 0.60 x 1.0 m
Speed range	0 - 8 m/s
Contraction ratio	1:1
Stagnation pressure	atmospheric
Stagnation temperature	80 - 300 K
Running time	several minutes
Max. Reynolds number/m	4 million
Drive motor	11.2 kW
Fan speed	0 - 1750 rpm
LN_2 tank volume	1 m^3

NASA Langley
0.3-m Transonic Cryogenic Tunnel

The Low-Speed Cryogenic Tunnel studies ended in the summer of 1972.[22, 23] We then built a small fan-driven transonic cryogenic pressure tunnel. Our desire was to extend our cryogenic tunnel experience to the pressures and speeds needed for a large transonic high Reynolds number cryogenic tunnel.

The design of the Pilot Transonic Cryogenic Tunnel began in December of 1972. It first ran in August of 1973. The first run at cryogenic temperatures was made on October 16, 1973. This was less than 2 years after work started at Langley on cryogenic tunnels.

The Pilot Transonic Cryogenic Tunnel fulfilled its original purpose, that is it proved cryogenic tunnels could work at transonic speeds. In 1976 NASA designated this pilot tunnel a proper NASA facility and renamed it the Langley 0.3-m Transonic Cryogenic Tunnel (0.3-m TCT).

The 0.3-m TCT now sees service in a wide range of experimental programs. These include research in aerodynamics and cryogenic tunnel technology.[24] The basic structure of the tunnel has not changed in its 14 years of operation. However, in 1976 we replaced the original octagonal test section with a slotted wall rectangular test section.

In 1986 we replaced the rectangular test section with a square test section fitted with adaptive walls. We will describe this new test section later in this paper.

We have made changes to the control, instrumentation, and data acquisition subsystems. We have also made changes to the tunnel operating procedures. The tunnel is under completely automatic control. Separate control loops handle liquid nitrogen injection, gaseous nitrogen exhaust, and Mach number. Other digital controllers handle test section side wall boundary-layer removal and streamlining of the flexible top and bottom walls. We are now integrating the separate tunnel control functions under a single supervisory computer.

Table 14 gives the main operating features of the 0.3-m TCT. Reference 24 gives a complete description of the evolution and status of this tunnel.

TABLE 14.- 0.3-m Transonic Cryogenic Tunnel (TCT) at NASA-Langley (USA)

Type	closed circuit, fan
Material of construction	aluminum
Insulation	external, purged
Cooling	liquid nitrogen
Test gas	nitrogen
Test section size (h,w,l)	33 x 33 x 142 cm (solid adaptive walls)
Mach range	0.05 to ≈ 1.3
Contraction ratio	10.7:1
Stagnation pressure	1.1 - 6.2 bars
Stagnation temperature	78 - 340 K
Running time	up to several hours
Max. Reynolds number/m	400 million
Drive motor	2.25 MW
Fan speed	up to 6500 rpm
LN_2 tank volume	212 m^3

U.S. National Transonic Facility (NTF)

The U.S. National Transonic Facility (NTF) is located at NASA Langley. Design of the NTF started in 1975. It came on line late in 1983. The NTF is the largest transonic cryogenic tunnel.[25,26]

McKinney gave the status of the NTF earlier during this Symposium. Therefore, we will not go into any detail about the status of the NTF in this paper. For completeness, we do include the main features of the NTF in Table 15.

TABLE 15.- U.S. National Transonic Facility (NTF) at NASA-Langley (USA)

Type	closed circuit, fan
Material of construction	304 stainless steel, aluminum
Insulation	internal
Cooling	
Cryogenic mode	liquid nitrogen
Air mode	air/water heat exchanger
Test gas	nitrogen or air
Test section size (h,w,l)	2.5 x 2.5 x 7.62 m
Mach range	0.2 - 1.22
Contraction ratio	15:1
Stagnation pressure	1 - 8.9 bars
Stagnation temperature	78 - 340 K
Running time	up to several hours
Max. Reynolds number/m	480 million
Drive motor	94 MW
Fan speed	up to 600 rpm
LN_2 tank volume	946 m^3

Other Cryogenic Tunnels

We have discussed 15 cryogenic tunnels in this survey paper. There are other cryogenic tunnels we did not discuss. There have been some cryogenic tunnel projects started and then abandoned. These include the 1 ft and 4 ft cryogenic blowdown tunnels at the Douglas Company.[27]

There have been some special purpose cryogenic tunnels built, used, and retired after completing their work. In this category is the low-speed cryogenic tunnel built at Langley in 1971-72. In addition, we also built a small cryogenic tunnel at Langley in the early 1980's to study liquid nitrogen injection and evaporation.

Other cryogenic tunnels, such as the Cryogenic Isentropic Light Piston Tunnel at Cranfield,[28] still exist but are no longer used.

Our colleagues in the USSR and China undoubtedly have built cryogenic tunnels. Reference 29 describes a 2.4 x 2.4 m transonic cryogenic tunnel under study by Pan and his colleagues in China. However, we have no contact with these activities and remain mostly ignorant of their work.

Sources of Information

Reference 30 is a recent (September 1987) bibliography on cryogenic tunnels. The 467 papers cited in reference 30 cover most aspects of cryogenic tunnel development and use.

For current information on cryogenic tunnels we have the Cryo Newsletter published by the Experimental Techniques Branch. This informal quarterly newsletter is available from the Editor, Cryo Newsletter, Mail Stop 287, NASA Langley, Hampton, VA 23665-5225.

Final Remarks on Cryogenic Tunnels

Many cryogenic tunnels are in use. Some are large enough to let us test airfoils or aircraft models at full-scale Reynolds numbers.

Progress in building and using cryogenic tunnels has been slower than expected. Sometimes progress is slow because the designers and users of wind tunnels are not experts in cryogenic engineering. However, wind tunnel designers are beginning to learn how to design and install thermal insulation. Model builders are beginning to learn how to build models we can use the first time they are built. We are beginning to include good cryogenic engineering in our designs and operating procedures.

In spite of a few slow starts, some cryogenic tunnels run efficiently and safely on a routine production basis. Data from these tunnels is having a major impact on aerodynamic design. More cryogenic tunnels will come on line in the next year or so. Slightly further in the future the ETW will become operational.

The Japanese will build larger cryogenic tunnels. Sawada at NAL has proposed a 3 x 3 m transonic cryogenic tunnel capable of operating at 10 bars. Our friends at CARDC (China) will probably build their 2.4 x 2.4 intermittent cryogenic tunnel with stagnation pressures to 10 bars.

As with all previous advances in tunnel technology, cryogenic tunnels have been slow to find wide acceptance and application. We are always slow to accept radical changes in how things are done. However, momentum is gathering. The future for cryogenic tunnels is bright. The long awaited goal of testing at full-scale Reynolds number is at hand.

ADAPTIVE WALL TEST SECTIONS

The problem of wall interferences in wind tunnel testing remains despite considerable effort to eradicate it. Over the years, the wind tunnel community has used several well-known techniques to minimize wall interferences. Models are kept small compared with the test section size. Ventilated test sections are used to relieve transonic blockage. Linearized corrections are applied to the model data. Usually, all three techniques are used together in transonic testing. Unfortunately, we find these techniques are inadequate for high levels of accuracy we now demand from wind tunnel testing.

A solution to this dilemma exists. It involves using modern testing techniques which minimize wall interferences at source. (These modern techniques are a re-discovery of one of the first solutions to transonic wall interferences developed in the 1930s.) These techniques adapt the test section boundaries to free air streamline shapes, so the test section walls become invisible to the model. This is the **principle of wall streamlining**. Figure 9 shows the general case for a 3-D model. The test section boundaries follow an arbitrary free air streamtube round the model. (For simplicity we ignore the boundary layer growth on the test section boundaries.) Therefore, the free air flow field is split into a *real part* within the test section and an *imaginary part* round the test section. The imaginary flow field extends to infinity in all directions. The principle is simple but applying the principle is complex. The complexity arises from the need to adjust the test section boundaries for each test condition.

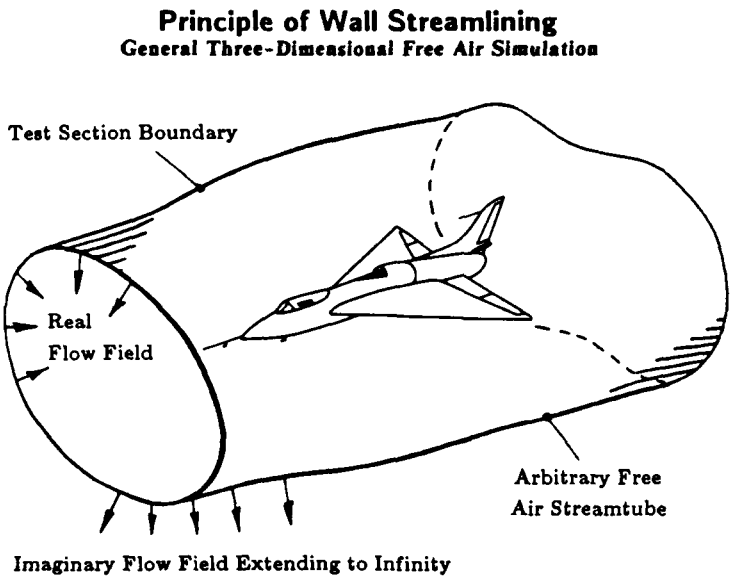

Fig. 9 - Principle of wall streamlining for general 3-D free air simulations.

We define a **streamlining criterion**[31,32] as the condition the adjustable boundaries must satisfy for the walls to be **streamlined/adapted**. (The term *adapted* is equivalent to the term *streamlined*, and we can refer to the *adjustable test section boundaries* as *adaptive walls*.) The streamlining criterion for free air simulations is straightforward. The adaptive walls must not support a local pressure imbalance between the real and imaginary parts of the flow field.

Advantages of Adaptive Walls

Other than the major benefit of minimizing wall interferences for free air simulations, adaptive wall test sections (AWTSs) offer other advantages. With wall interferences minimized, we are free to increase the size of the model for a given test section. Typically, we can double the test Reynolds number, perhaps allowing testing at full scale Reynolds numbers. Larger models are also important for high dynamic pressure tests and provide increased dimensions for more detailing and more volume for instrumentation. We can also expect simpler magnetic suspension of a model using an AWTS because the coils can be closer to the model.

With solid adaptive walls (called flexible walls), the test section boundaries are much smoother than with perforated walls. This smoothness reduces the tunnel drive power required for a given test condition with the model and test section size fixed. In addition, the removal of slots and holes reduces tunnel noise and turbulence levels improving flow quality. For intermittently operating tunnels, the removal of the plenum volume from the tunnel circuit reduces settling times and minimizes flow resonance.

Historical Overview

The modern adaptive wall testing techniques are a re-discovery of one of the first solutions to the problem of transonic wall interference. The National Physical Laboratory (NPL), UK built the first adaptive wall test section in 1938, under the direction of Dr. H. J. Gough.[33] They sought a solution to the problem of transonic blockage. Their research proved streamlining the flexible walls of an AWTS was a viable testing technique for high speed tunnels. They opted for minimum mechanical complexity in their AWTS by using only two flexible walls. Unfortunately, the absence of computers made wall streamlining a slow and labor intensive process. Sir G. I. Taylor developed the first wall adjustment procedure. His procedure was necessarily approximate to cut out the need for any calculations during the streamlining process. Nevertheless, NPL used flexible walled AWTSs into the early 1950s. They generated a large amount of 2- and 3-D transonic data,[34] which we are still uncovering in the literature.

The advent of ventilated test sections in 1946 provided a "simpler" approach to high speed testing, since the adjustments to the test section boundaries are passive. Consequently, ventilated walls superseded adaptive walls which actively control the test section boundaries. The AWTSs of NPL eventually became obsolete and disappeared.

After a 20-year lull, interest in AWTSs was rekindled in the early 1970s. Several researchers independently re-discovered the adaptive wall testing technique in the quest for improved data accuracy at transonic speeds.[32] Some advocated modifications of conventional ventilated test sections (the so-called variable porosity test section), while others opted for the NPL approach using flexible walled test sections.

This renewed interest has led to the establishing of various adaptive wall research groups around the world. Researchers have built many AWTSs of various designs for testing 2- and 3-D models. This development has even led to production type AWTSs.

Fallacies

During the development of any new technology, mistaken beliefs will arise. Adaptive wall technology has not escaped. A selection of mistaken beliefs follows:

The idea of AWTSs first appeared in 1972.
AWTSs will not work in large wind tunnels.
AWTSs will not work at transonic speeds.
AWTSs cannot streamline with sonic flow at the test section boundaries.
The testing technique is too complex to be practical.
The testing technique requires more computer power than conventional test sections.
Knowledge of the flow round the model is a prerequisite for wall streamlining.
Wall streamlining for each data point wastes too much tunnel time.
Operation of an AWTS requires expert knowledge.
2-D testing is trivial and the effects of the walls are not important.

We hope you will agree that these statements are indeed fallacies, after you read this survey.

AWTS Design

As mentioned in the historical overview, the renewed interest in AWTSs encompassed two approaches using ventilated or solid walls. We have observed many interesting designs during the modern era of AWTS development. In 2-D testing, only two walls need to be adaptable and researchers have tested both flexible wall and ventilated wall designs. The complexity of controlling a 3-D boundary has led to a variety of AWTS designs. Moreover, some approximation in the shape of the test section boundaries is inevitable. The magnitude of this approximation has been the subject of much research. The number of adaptive walls necessary in a 3-D AWTS is not simple to answer and must ultimately be a compromise. From practical considerations, the design of a 3-D AWTS must be a compromise between

magnitude of residual interferences (after streamlining), hardware complexity, model accessibility and the existence of a rapid wall adjustment procedure. Table 16 shows the list of current AWTSs in use around the world, highlighting the variety of designs.

The vast research experience reported on 2- and 3-D testing with AWTSs[35] shows flexible walls to have distinct advantages over ventilated walls. These advantages are as follows:

a) Flexible walls can be rapidly streamlined.
b) Flexible walls provide more powerful adaptation control of the test section boundaries.
c) Flexible walls provide simple test section boundaries for adaptation measurements and residual interference assessment.
d) Flexible walls improve flow quality providing reduced interferences and reduced tunnel operating costs.

In 2-D testing, flexible walled test sections have operated with test section height to chord ratios of unity. In addition, we have recorded model normal force coefficients up to 1.54 with the walls streamlined. No ventilated AWTS, past or present, at Calspan, AEDC, or NASA Ames can match these conditions. The demonstrated 2-D capability of flexible walled test sections can be adequate for current production type testing, as shown later.

The old claim that ventilated AWTSs could be simply made from modified conventional ventilated test sections is no longer relevant. From AEDC and NASA Ames research,[36,37] we now know that substantial changes to a conventional ventilated test section are necessary to make it adaptive. Therefore, any update of an existing wind tunnel to adaptive wall status will involve the design of an AWTS insert. Any attempt to modify an existing test section would probably be much more difficult and involve too many compromises.

Researchers have investigated various numbers of adaptive walls in many AWTS designs for transonic 3-D testing. DFVLR used a nominally circular thick rubber tube in their DAM test section[38] with eight circumferential positioning jacks at each streamwise station for boundary control (see Figure 10). Similarly controlled, Technical University of Berlin (TU-Berlin) built an octagonal AWTS[39] with eight flexible walls sealed to one another by spring steel leaves (see Figure 11). AEDC has built the only transonic 3-D variable porosity AWTS[36] which has four adaptive walls and a square cross-section. Here, wall adaptation is by adjustment of the local porosity at each of the four perforated walls (see Figure 12). In addition, researchers have made 3-D tests in 2-D AWTSs at NASA Langley (see Figure 13), University of Southampton,[40] ONERA,[41] and TU-Berlin.[39] These 2-D AWTSs use only two flexible walls and have roughly square cross-sections.

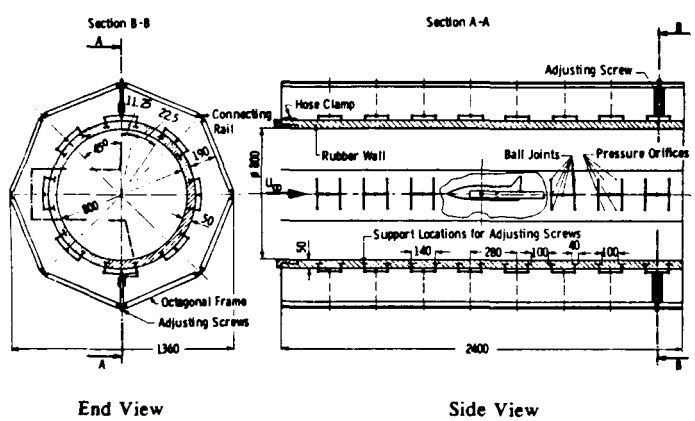

Fig. 10 - DFVLR Göttingen DAM rubber tube AWTS.

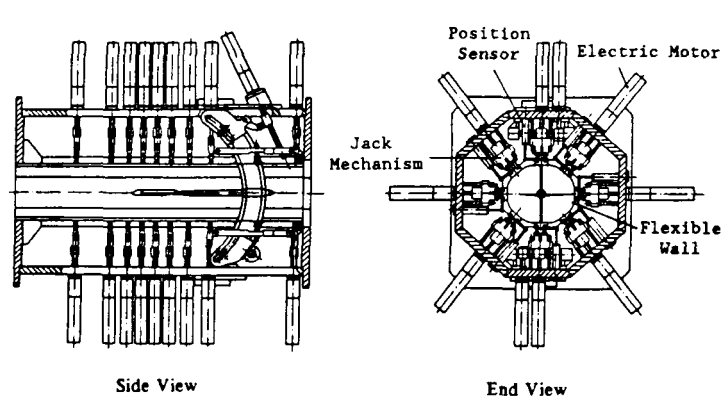

Fig. 11 - TU-Berlin octagonal AWTS with flexible walls.

ORIGINAL PAGE IS OF POOR QUALITY

ORIGINAL PAGE IS
OF POOR QUALITY

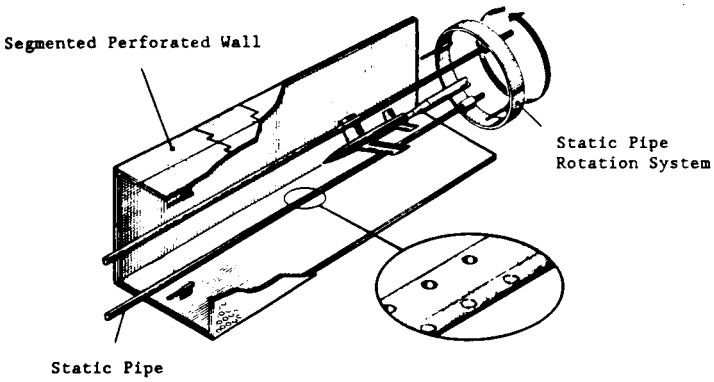

Fig. 12 - AEDC 1T Tunnel AWTS.

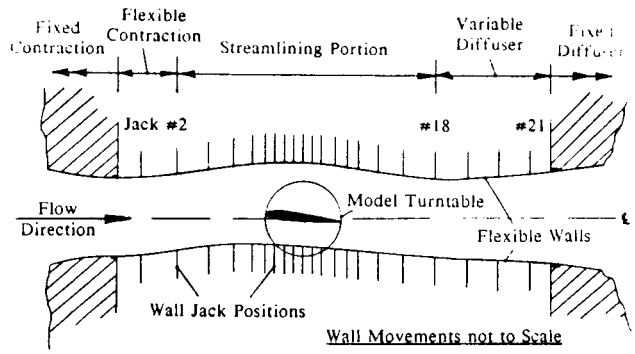

Fig. 13 - NASA Langley 0.3-m TCT flexible walled AWTS.

Experience with 3-D testing in AWTS is not as broad as we would like. Nevertheless, there are strong indications the simpler the AWTS the better the system. Simplicity reduces hardware complexity, gives better model access, and simplifies the assessment of residual interferences. We see no major disadvantages, but we need more research to confirm this. The development of 3-D adaptive wall testing techniques will continue to emphasize the trade-off between boundary adjustments and residual interference corrections. The outcome of this trade-off will effect the AWTS design.

We believe solid flexible walls offer the best approach to use of adaptive wall technologies in 2- and 3-D testing. Of the 14 high speed AWTSs operational worldwide, all but 2 use flexible walls.

Operational Experience with AWTSs

We direct operational experience with AWTS towards the following goals:

Minimization of time attributed to wall streamlining.
Examination of the operating envelope.
Establishment of an operating system for production-type testing.

Since 1975, researchers have made inroads into the time involved in wall streamlining, particularly with flexible walled AWTSs. A major part of this progress has been the development of rapid wall adjustment procedures for flexible walled AWTSs. (The term *rapid* refers to minimization of the number of iterations in the streamlining process.) For 2-D testing, the method of Judd, Goodyer, and Wolf[42,43] (University of Southampton, UK) is now well established for reasons of speed, accuracy, simplicity (we can easily use the method on any mini-computer), and adaptability to general use with flexible walled AWTSs. For 3-D testing, the methods of Wedemeyer/Lamarche[44] (Von Karman Institute, Belgium) and Rebstock[45] (TU-Berlin) show promise in speed and accuracy. Nevertheless, we require more evaluation of these methods before we can regard them as well established.

Other time-saving features of modern AWTSs are computer controlled movement of the adaptive walls and automated acquisition of wall data. However, for the tunnel user to benefit from the full potential of these time-saving features, we require a well defined streamlining criterion. This criterion optimizes the streamlining procedure. We find it necessary to compromise the streamlining criterion, described earlier, to allow for tunnel measurement accuracies. For 2-D testing, AWTSs at ONERA/CERT and TU-Berlin use the condition of insignificant wall adjustments and model flow changes. We prefer the condition of residual wall interferences reduced below acceptable minima used at the University of Southampton[32] and NASA Langley.[46] The acceptable minima are Induced $\alpha < 0.015°$; Induced camber $< 0.07°$; Induced velocity C_P error < 0.007. Unfortunately, we do not yet have a well defined streamlining criterion for 3-D testing. However, we find the net result of these time-saving features is an acceptable time attributed to 2-D wall streamlining, on the order of less than 2 minutes.

The examination of AWTS operating envelopes involves both hardware and software aspects of the AWTS control system. We show the streamlining procedure for any AWTS in Figure 14. The procedure involves an interaction between the tunnel hardware and the software. The hardware provides wall pressure data and wall adjustments as requested by the software. The software for analysis of the wall data contains the wall adjustment procedure and assessment of the wall streamlining quality. We base this quality on the free air streamlining criterion described earlier.

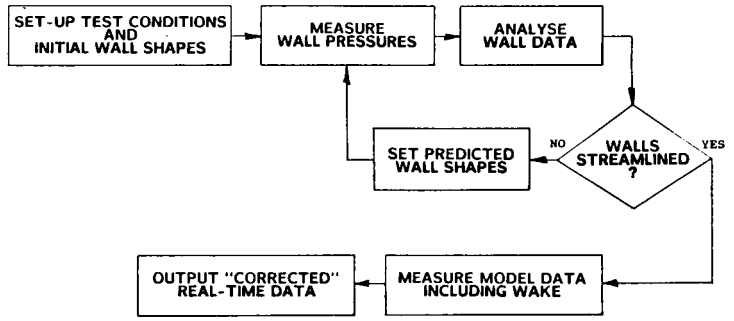

Fig. 14 - Streamlining procedure for each data point.

Good AWTS design should remove wall adjustment problems[32,46] (but we have yet to achieve this idyllic situation in any AWTS). Then only software limitations will restrict the operating envelope. At present, we can experience software limitations because we use linearized theory in the wall adaptation procedures. Since sonic flow on the flexible walls invalidates the procedures, we must restrict the free stream Mach depending on the model size compared with the test section dimensions. However, for 2-D testing, a wall adjustment procedure has been successfully developed based on Judd's method for 2-D testing at up to Mach 0.95.[47] (Software changes involve a more sophisticated representation of the imaginary part of the free air flow field, as discussed later.) Supersonic 2-D testing is also possible using wave theory to predict wall shapes. Software limitations in 3-D testing are not well defined since the software is in its development stage, but testing up to low supersonic is also possible.

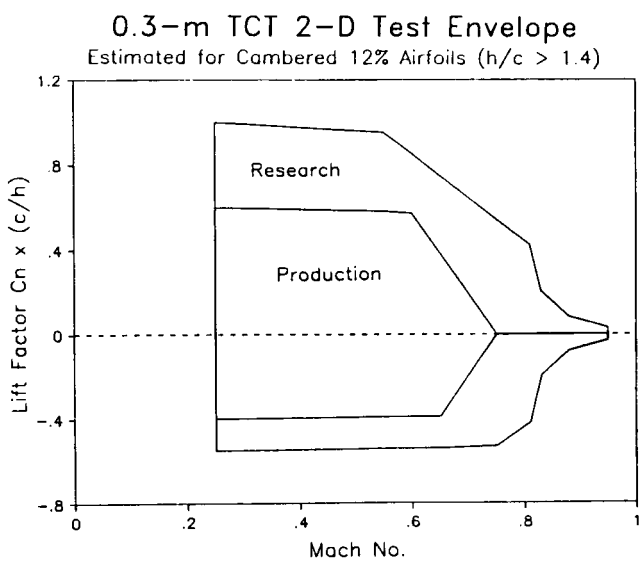

Fig. 15 - A model dependent test envelope for AWTS 2-D testing.

The establishment of an operating system for straightforward production-type testing is a prerequisite for general use of adaptive wall technology. If only experts can use this technology, then only specialist facilities can take advantage of the testing technique. Our research at Langley using the 0.3-m TCT[46] involves the first attempts to develop a production-type operating system. We are attempting to make invisible the complexities of the adaptive wall testing technique to the tunnel operators. Unfortunately, this difficult task is hampered by hardware shortcomings because of our unique application of an AWTS to a continuously operating cryogenic tunnel. Nevertheless, we have established an envelope for 2-D production-type testing (see Figure 15) based on model size and performance. This envelope is restrictive and we plan to expand it by hardware modifications.

Testing Results from AWTSs

There is a wealth of testing experience with AWTSs reported in the literature.[35] Validation testing forms a major part of this experience to determine data quality and limits to the operating envelope. In this section, we highlight the important observations to show the current State of the Art in adaptive wall research. We discuss 2-D and 3-D testing separately. We review data from various tunnels and where possible we include references to allow more detailed study of the results than necessary here. We present this data without prejudice. The data comes exclusively from flexible walled test sections because this design of AWTS is pacing the State of the Art.

ORIGINAL PAGE IS
OF POOR QUALITY

2-D Testing Results from AWTSs

Effects of Wall Streamlining in 2-D Testing

Figure 16 shows the effects of adjusting the flexible walls of a 2-D AWTS on boundary interferences. With the flexible walls straight (simulating a conventional closed tunnel) the airfoil normal force coefficient, C_n, is typical of data with large wall interferences. There are considerable differences between the straight wall and streamlined wall values. This difference in C_n is a demonstration of classical lift interference induced by the test section boundaries, since the streamlined wall data are free of top and bottom wall interferences. Notice at the zero lift angle (near -4.6°) the flexible wall shape has no effect on model C_n. This shows the model blockage is small at zero lift. We took these data at a subsonic Mach number of 0.5. Notice the model experiences stall with the flexible wall streamlined. Meanwhile, with the flexible walls straight, the model C_n shows no stall up to the structural load limit of the model.

These data are for an advanced cambered airfoil tested in the NASA Langley 0.3-m TCT.[46] Notice the high C_n obtained during this test with the flexible walls streamlined. The maximum C_n of 1.54 is the highest ever achieved in any AWTS with the walls streamlined. The test section height to model chord ratio was a low 1.96 for this test.

Flexible Wall Effects on Model Data Through Stall at Transonic Speeds

$M_\infty = 0.7$, $R_c = 12$ million

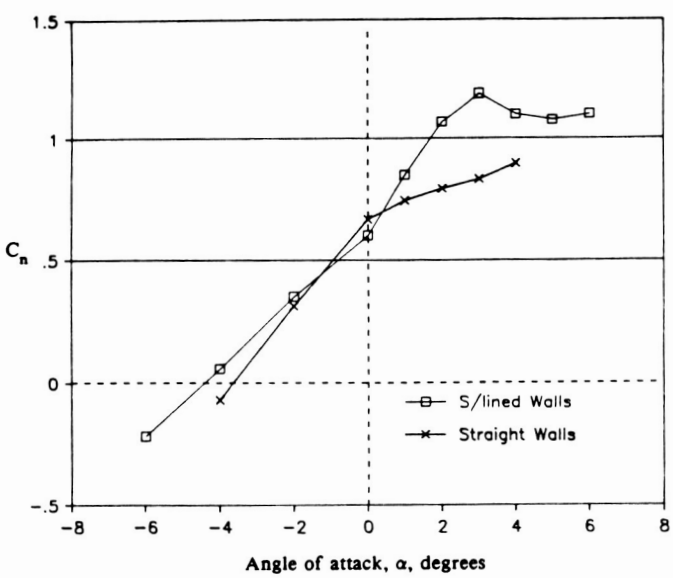

Fig. 17 - Effects of wall streamlining at Mach 0.7.

Flexible Wall Effects on Model Data Through Stall at Subsonic Speeds

$M_\infty = 0.5$, $R_c = 3$ million

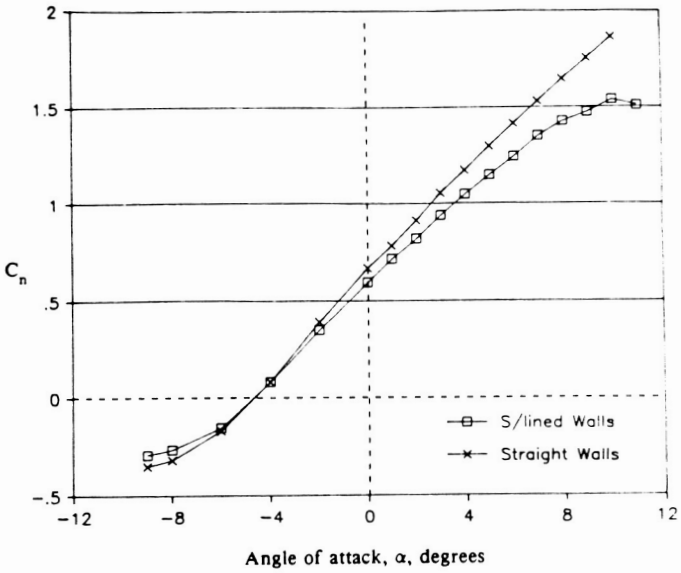

Fig. 16 - Effects of wall streamlining at Mach 0.5.

TSWT Schlieren Pictures

NACA 0012-64 Airfoil : $M_\infty = 0.7$; $\alpha = 4°$

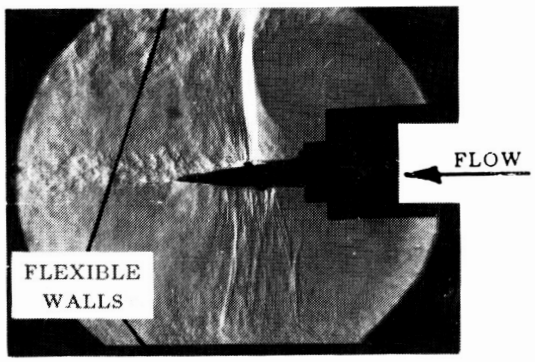

Straight Walls

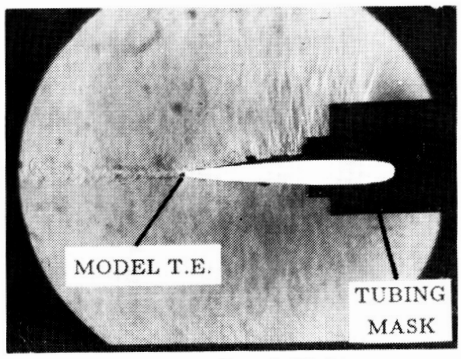

Streamlined Walls

Fig. 18 - Model flow changes with wall adaptation.

At transonic speeds the effects of adjusting the flexible walls are significantly different from the subsonic case. We show this difference in Figure 17. The onset of compressibility is an important factor in this difference. Notice how the lift interference changes sign at an angle of attack of about 0.5°. This is because of the phenomena of test section choking caused by increasing the model blockage. As we increase angle of attack, the model blockage increases due to the growth of shocks on the model surface. If we increase the angle of attack high enough, the flow channel above the model chokes causing significant wall interferences. We show this in Figure 18 with a schlieren picture from the Transonic Self-Streamlining Wind Tunnel (TSWT) at the University of Southampton, UK.[32]

By streamlining the flexible walls we can remove this choking and simulate an interference free flow field around the model. Sometimes, as shown here, the model shock changes position and reduces in strength. This causes a reduction in lift as for the subsonic case. However, the data in Figure 17 show that C_n increases at, for example, an angle of attack of 4°. This sign change is due to the use of different airfoils. (In the schlieren pictures the airfoil is symmetrical; the lift data are from a cambered airfoil.)

We highlight this point to show how unpredictable boundary interferences can be at transonic speeds. This unpredictability is because of the existence of non-linear flow field patches in the test section. Hence, the prediction of accurate corrections to the model data is very difficult using conventional correction techniques at transonic speeds.

Notice the straight and streamlined wall C_n data agree at two lifting angles of attack. While the values of C_n agree for these two cases, detailed pressure distributions do not agree. Interestingly, the zero lift angles do not agree for the two data sets. This shows that the model blockage is not small with the flexible walls set straight. At some higher Mach number the test section (with straight walls) will completely choke making the setting of higher Mach numbers impossible. However, streamlining the flexible walls removes this choking effect and allows us to test at higher Mach numbers.

Assessment of Residual Wall Interferences in 2-D Testing

The claim that 2-D AWTS data are free of wall interferences requires some qualification. We have made many validation tests on well known airfoils to assess the quality of free air simulations in AWTSs. Many published data comparisons show AWTS data matching "interference free" data.[5]

At Langley, we tried an alternative approach. We made an independent assessment of the residual interferences (we make a real time assessment to determine if the walls are streamlined) in the 0.3-m TCT with an AWTS using the NASA Langley Wall Interference Assessment/Correction (WIAC) procedures.[48] Figure 19 shows a plot of model lift coefficient, C_L, versus angle of attack which is an extract from this work. This plot shows how well AWTS data for two different size NACA 0012 airfoils compare to a theoretical prediction of the free air result, before and after correction for residual interferences. The corrections to the AWTS data are small and appear unnecessary for this case at Mach 0.6.

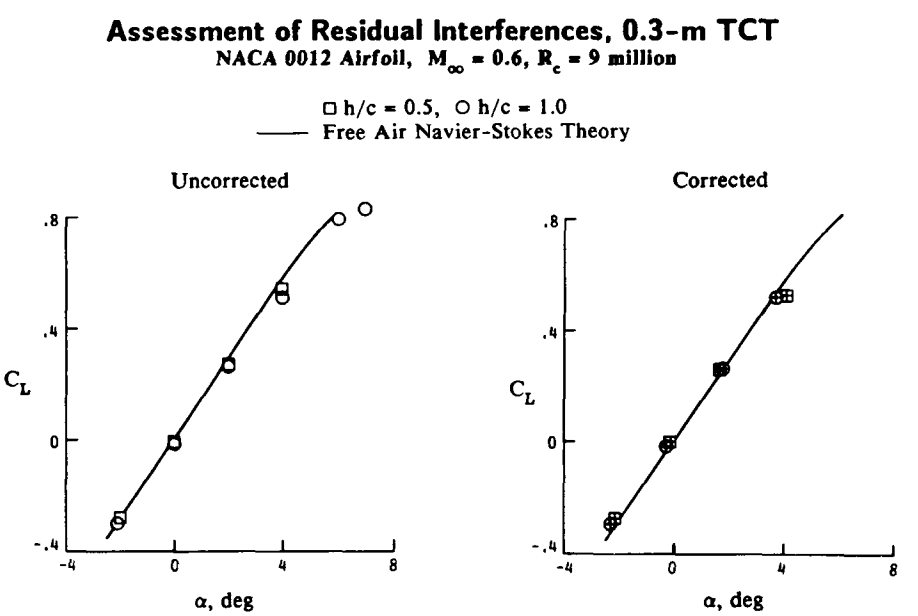

Fig. 19 - Comparison of NACA 0012 airfoil lift for two model chords with and without corrections according to the WIAC procedure.

ORIGINAL PAGE IS
OF POOR QUALITY

Also of significance is the agreement between AWTS data using different size models, one has a chord twice the other. The larger model has a test section height to chord ratio of 1.0. The comparison of model pressure distributions for the different chord airfoils is equally good. These and other[46] observations that the AWTS data are independent of model size further support the claim that the AWTS data are free of wall interferences.

2-D Testing with Sonic Flow at the Test Section Walls

Figure 20 shows wall streamlining for a 2-D airfoil in a fully choked test section is possible. The montage of real and imaginary flow fields comprises a schlieren picture of the test section flow at the airfoil. Shown with this picture are the outlines of the supercritical patches in the imaginary flow field outside the flexible walls. In the test section flow both airfoil shocks reach the flexible walls. The montage shows how well the flow fields match at the flexible wall interfaces to satisfy the free air streamlining criterion. This good match, particularly about the shock locations and sonic points, is an indication of good wall streamlining.

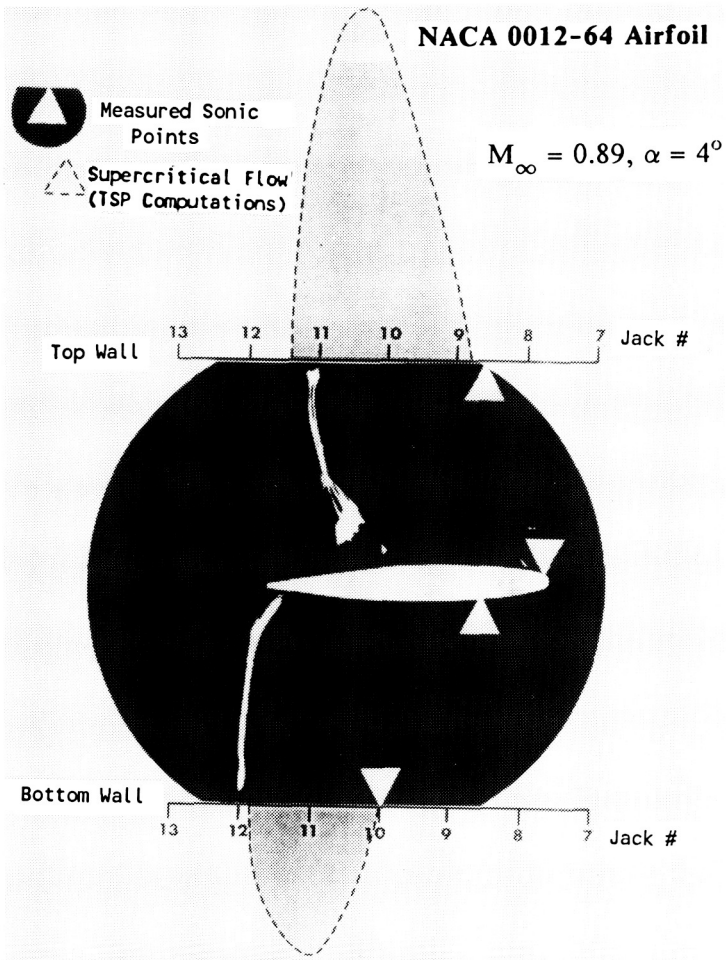

Fig. 20 - Montage of real and imaginary flow fields.

Researchers made this demonstration in TSWT at the University of Southampton during 1986.[47] The test section height to chord ratio for this test is 1.5. They used a modern Transonic Small Perturbation (TSP) code to calculate the imaginary flows. They found an uncomplicated procedure for wall streamlining. The wall adjustment procedure used here is a more sophisticated version of Judd's method, which includes TSP and wall boundary layer calculations.

An important observation from these tests is the non-existence of shock reflections from the flexible wall. For some time skeptics considered the potential of shock reflections as a serious limit to Mach number. We now know this is not the case. Until the oblique bow shock appears ahead of the model near Mach 1.0, there cannot be any reflection problems. Even when an oblique shock appears, there is every indication that any reflections can be at least directed away from the model by a suitable wall curvature.

Effect of Compressibility on Flexible Wall Contours in 2-D Testing

So far, we have only looked at the airfoil data. It is also important to look at the wall contours required for streamlining, because we determine these contours without reference to the model. The wall contours should show expected aerodynamic trends if the wall adjustment procedure is working well.

A very graphic example of aerodynamic trends is the effect of compressibility on the wall contours. The plot in Figure 21 shows TSWT wall contours for two Mach numbers, one subsonic and one transonic.[32] The model, a NACA 0012-64 airfoil, was at a fixed angle of attack of about 4°. The subsonic contours show lift induced upwash ahead of the model and a small model wake shown by the

small movement apart of the walls downstream of the model. The transonic contours show minimal upwash ahead of the model because of loss of lift caused by a shock stall. In the region of the model, the walls move apart an amount equal to the airfoil thickness. Downstream of the model streams a large wake, shown by the large movement apart of the flexible walls. This large wake is due to shock induced flow separations on the model. The exaggerated wall deflection scale helps to amplify the effects of compressibility on the wall contours. We expected these effects. This finding adds to our confidence in the wall adjustment procedure of Judd et al.

These wall contours show the poor performance of the NACA 0012-64 airfoil at high speeds. This poor performance requires more severe flexible wall curvature for streamlining which could limit the test envelope. Better performing cambered airfoils demand less wall curvature at the same test conditions. So, the flexibility requirements of a wall are model dependent. We raise this point because it does complicate the AWTS design process.

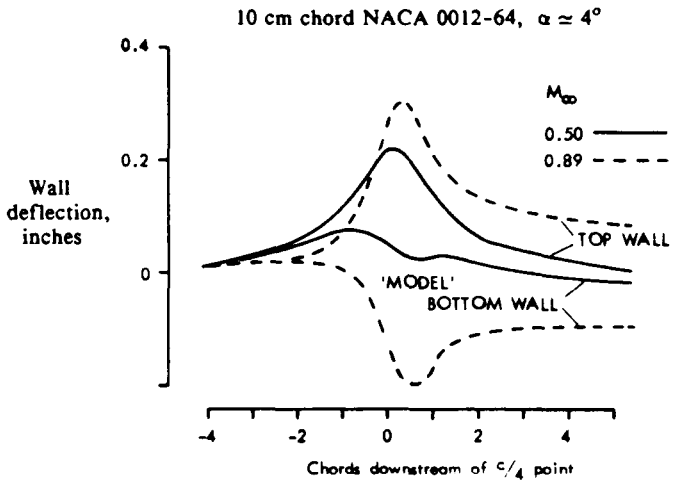

Fig. 21 - TSWT streamline wall contours at two Mach numbers.

Effect of Model Lift on Flexible Wall Contours in 2-D Testing

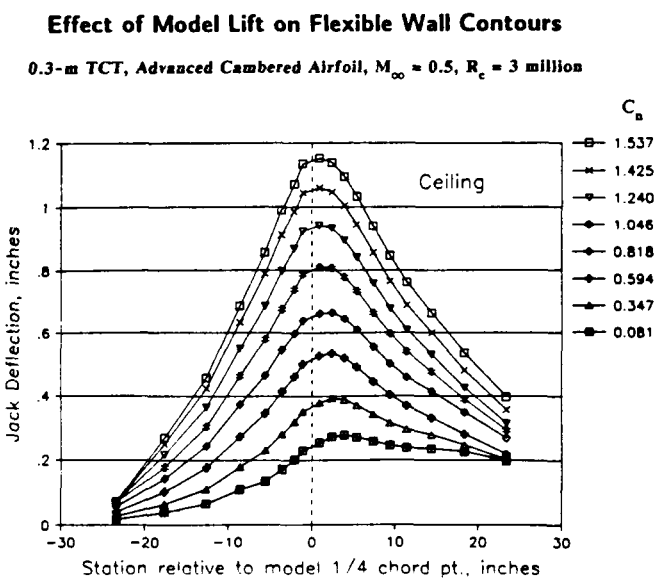

Fig. 22 - Family of streamline wall shapes with increasing model lift.

Figure 22 shows the upwash ahead of a lifting airfoil in the family of top wall (ceiling) contours. In this plot, we increase the model normal force coefficient, C_n, from near zero to 1.537. As C_n increases, so does the wall deflection. This increasing deflection is due to increasing model upwash and an expanding model wake associated with drag rise.

We again emphasize that we determine these contours experimentally without reference to the model. We show here data for a subsonic case to avoid complication of the wall contours associated with the onset of compressibility. Each wall contour fits into the family of shapes as expected.

This family of contours shows the usefulness of using streamlined wall contours for a lower angle of attack as initial contours for a higher angle of attack. The closer the initial wall contours are to the streamline shape, the quicker the streamlining procedure. This is because of reduced physical movement and reduced iterations within the streamlining procedure. In a series of tunnel tests over a range of angle of attack, the change in angle of attack between successive tests is probably up to 2°. This is equivalent to the interval between wall contours shown here. In this case, the choice of the streamlined contours for the last test as the initial contours for the next test is ideal.

Unfortunately, the effects of compressibility and operational requirements complicate this selection of initial contours. At transonic speeds, it is better to select streamline contours for a lower Mach number at the same angle of attack. We achieve operational flexibility by building a library of wall contours and, when necessary, calculating theoretical wall contours for a required set of test conditions.[46] So initial wall shapes are available for any sequence of test conditions.

2-D Testing Observations

There is a significant reduction of wall interferences by using AWTSs. We have found no problems with testing an airfoil through stall (no wall shape induced model hysteresis present). Different size models of the same section give the same results without correction, showing we have removed different levels of wall interferences in each case. Unfortunately, hardware limitations now restrict the test envelope for large airfoils (chords larger than 75 percent of test section height). Therefore, broader comparisons of data from different size models are not possible now.[46] Data repeatability is very good.

We have observed that the model wake in the 0.3-m TCT with an AWTS shows minimal spanwise variation. We speculate that the secondary flows at the airfoil-sidewall junction are small and boundary interferences are minimized. There is every indication the flow in the test section is an excellent simulation of a 2-D free air flow field.

Aerodynamic limits to free stream Mach number will occur if there are shock wave reflections on to the model. Researchers have made 2-D tests close to Mach 1.0[47] and some limited tests at Mach 1.2.[49] We have not yet encountered any fundamental limit to Mach number. However, the usefulness of 2-D testing in the supersonic regime may be only academic, providing experience leading to production supersonic 3-D testing.

The time attributed to wall streamlining should be small and is less than 2 minutes for a good operating system. Researchers have proposed some improvements to the wall adjustment procedure of Judd et al.[47] These improvements are for testing of large models at transonic speeds (when the wall slopes are not small) and for simpler selection of initial wall shapes. We have taken up to 50 data points in an 8-hour work shift. The most time consuming operation in our 0.3-m TCT with an AWTS[46] is the drag rake operation. Our experience shows production type testing is now possible with AWTSs.

3-D Testing Results from AWTSs

Effects of Wall Streamlining in 3-D Testing

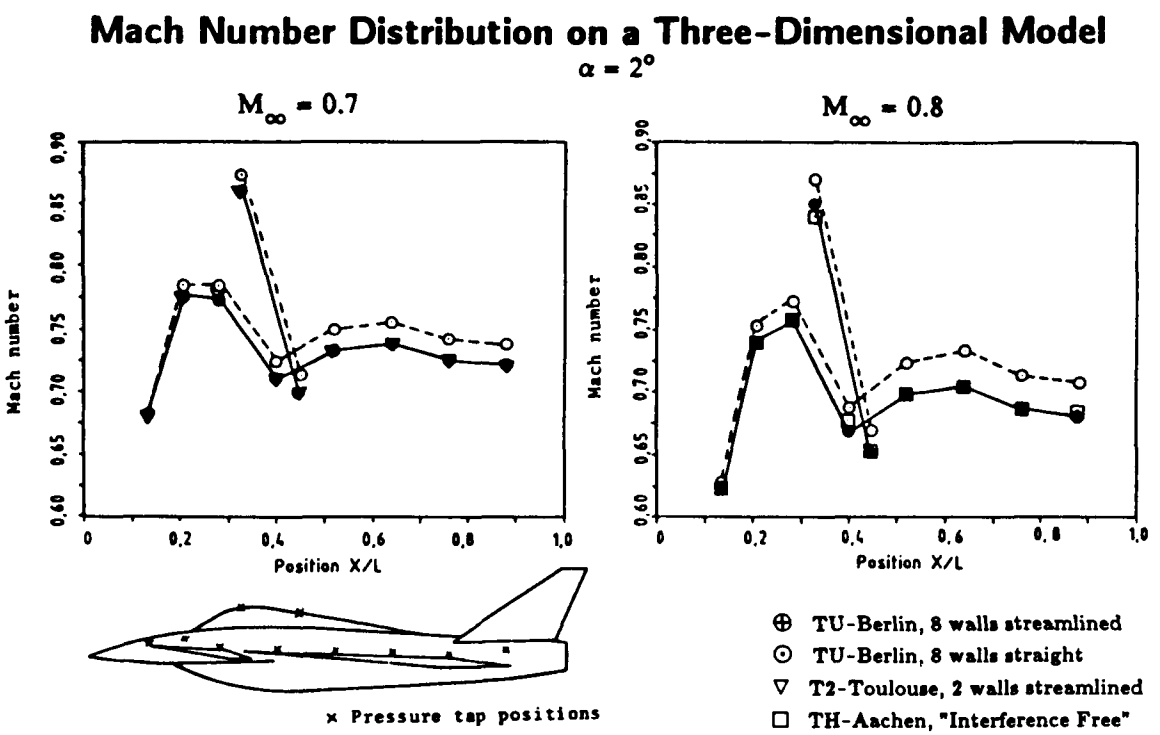

Fig. 23 - Mach number distributions on a 3-D canard model.

Figure 23 shows pressure data measured on a canard model of low aspect ratio (see Figure 24). Researchers have tested this model in several tunnels at free stream Mach numbers of 0.7 and 0.8. Stagnation conditions were ambient. There are two data sets from the TU-Berlin octagonal AWTS.[39] One set is with the eight flexible walls streamlined according to a 3-D wall adjustment procedure of Rebstock.[45] The other set is with the eight walls set straight. The two sets show the levels of interference removed by wall streamlining. Also shown is a data set from the ONERA/CERT T2 tunnel, which has a larger AWTS with two flexible walls.[50] For this data set, researchers streamlined the flexible walls according to a 3-D wall adjustment procedure of Wedemeyer and Lamarche.[44] We show the data from TH-Aachen as "interference free" data, since the model was very small in this tunnel. The comparison between the streamlined wall data and the "interference free" data is excellent. This observation is good for the adaptive wall testing technique but also shows that two flexible walls may be as good as eight.

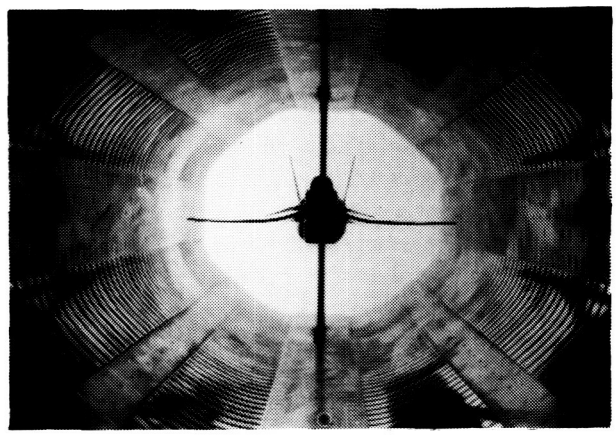

Fig. 24 - Canard model mounted in the TU-Berlin octagonal AWTS.

Figure 25 shows a comparison of lift coefficient, C_L, and drag coefficient, C_D, for the same canard model as before. We compare data sets from the octagonal AWTS and the T2 AWTS with streamlined walls, together with reference data from TH-Aachen.

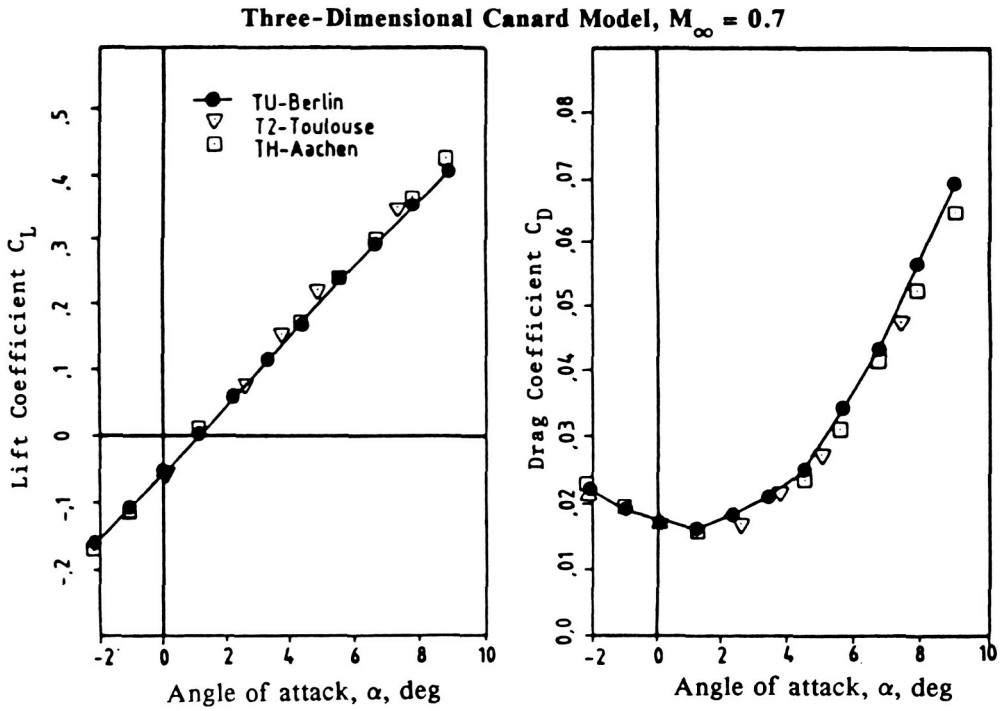

Fig. 25 - Comparison of force data from three tests of the canard model.

The comparison of lift coefficient is reasonable. The T2 data agrees slightly better with the reference data at the higher angles of attack. However, the differences are small and the data from the two AWTS show minimal boundary interferences. This is despite the fact neither AWTS is able to provide perfect control of its test section boundaries in three-dimensions. Model size and type probably have a strong influence on this, since real-time data on 3-D models in an AWTS should require residual corrections. Unfortunately, no publicized AWTS tests have had severe enough test conditions to leave significant residual interferences in the model data, after wall streamlining.

We find a similar comparison to the drag data. Again the T2 data agree slightly better with the reference data at the higher αs. We can explain this weak tendency for the TU-Berlin data to differ at high α as a blockage effect because of the large relative size of the model in the octagonal AWTS (see Figure 24). The nominal blockage of the canard model is 1.3 percent in the octagonal AWTS (the largest reported blockage in a 3-D AWTS test with a non-axisymmetric model) and 0.18 percent in the T2 AWTS.

ORIGINAL PAGE
BLACK AND WHITE PHOTOGRAPH

Flexible Wall Contours for 3-D Tests

The flexible walls of the TU-Berlin octagonal AWTS are usually streamlined after two iterations starting from straight. We depict an example of the required wall shapes in Figure 26 for the top wall only. Notice the large wall deflections necessary downstream of the canard model. These deflections are necessary to accommodate the downwash generated by this high lift configuration.

Interestingly, researchers obtained similar streamlined wall shapes shown in Figure 27 in the ONERA/CERT T2 AWTS with just two flexible walls. They obtained these wall contours during tests of a lifting half model mounted on one sidewall of the AWTS.[41] The free stream Mach number was 0.6. The aerodynamically straight wall contours generate a constant Mach number distribution along the empty test section at Mach 0.6. We use these contours as a reference. They determined the streamlined wall contours by using the 3-D wall adjustment procedure of Wedemeyer and Lamarche.

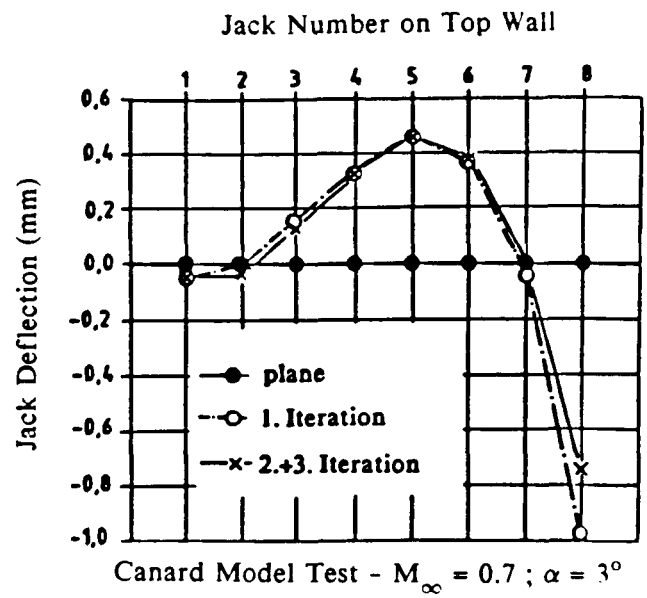

Fig. 26 - Convergence of the top wall contours during a typical 3-D test in the TU-Berlin octagonal AWTS.

For comparison, we also show wall shapes found using a 2-D wall adjustment procedure. There is a fundamental difference between 2-D and 3-D procedures. The 2-D procedure attempts the impossible, that is to remove 3-D wall interferences in a 2-D sense. Meanwhile, the 3-D procedure attempts to modify the 3-D wall interferences so they become correctable. This difference causes the prediction of different wall contours with the same test conditions and model in the tunnel.

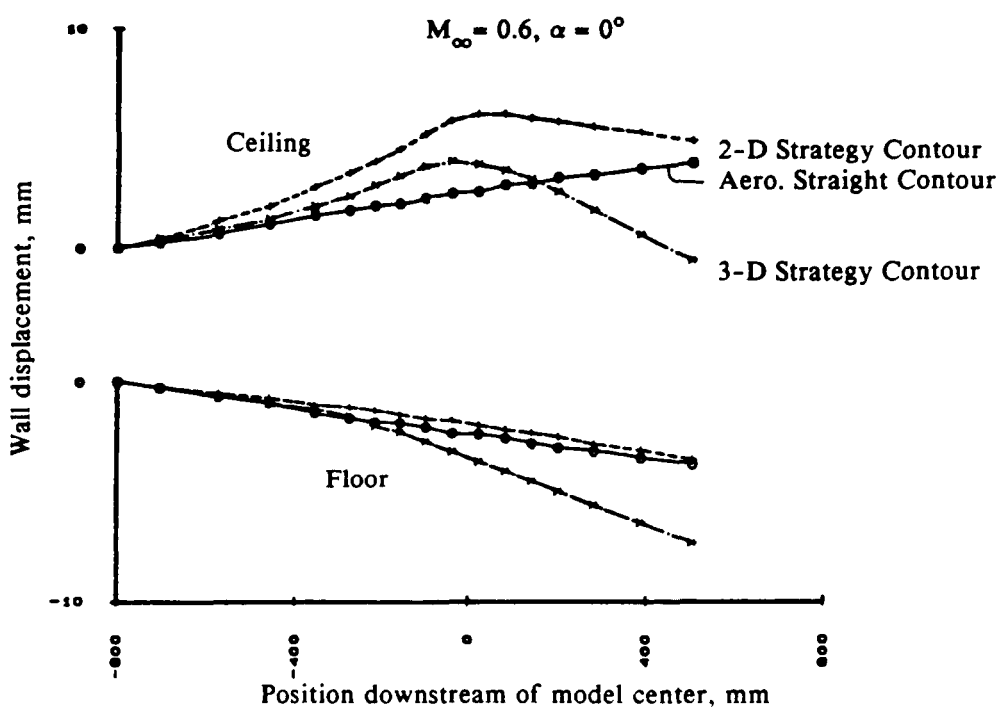

Fig. 27 - Floor and ceiling wall contours from the ONERA/CERT T2 Tunnel during 3-D tests using 2- and 3-D wall adjustment procedures.

From a designer's point of view, the general wall shapes for streamlining in a 3-D test pose some problems. The downstream movements of the flexible walls required for streamlining tend to be large compared with movements encountered in 2-D testing. This movement requirement will make necessary a more complicated fairing arrangement between the downstream end of the test section and the rigid tunnel circuit, if we are not to restrict the test envelope or model size.

Supersonic Tests in a 3-D AWTS

Figure 28 shows pressure distributions on a cone-cylinder at Mach 1.2. DFVLR Göttingen made these tests in their rubber tube DAM AWTS.[38] We show two pressure distributions, one before wall adaptation and one after. This adaptation involved the calculation of adjustments to the rubber tube at one streamwise location to absorb expansion and compression waves.

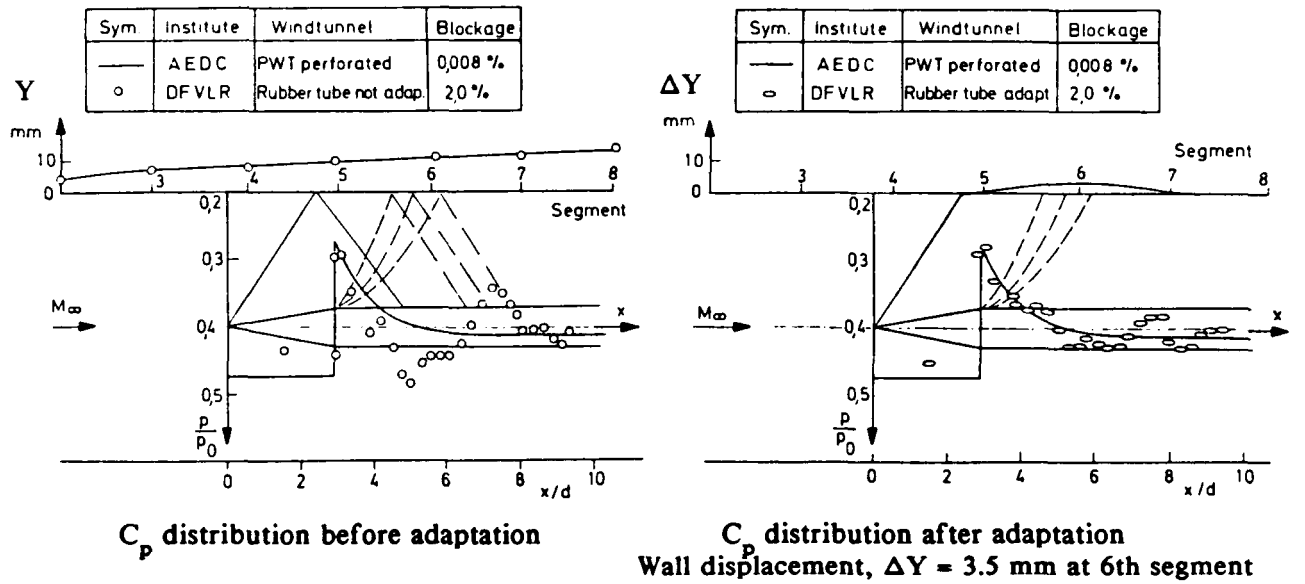

Fig. 28 - 3-D Supersonic Tests in the DFVLR DAM rubber tube AWTS.

Shown with the DFVLR data is reference data from the AEDC PWT tunnel with a very small model. Hence, we can consider this data as "interference free." With the rubber tube straight, there is a reflection of the model bow shock onto the model at x/d = 5.0. We see this interference as a local pressure rise on the model. Wall adaptation significantly reduces this interference.

The researchers at DFVLR did not design this AWTS for supersonic testing. Therefore, finer wall adjustments would only be possible if the wall jacks were closer together. However, a remarkable reduction of wall interference is possible with coarse wall adaptation. There would seem to be no fundamental limit to the use of flexible walls at supersonic speeds.

3-D Testing Observations

Reported validation tests[35] support the claim of minimized wall interferences in 3-D testing using an AWTS. However, the interferences present before any wall adaptation are already small because of the low blockage of 3-D models. This observation highlights the need for improved accuracy in the wall streamlining and makes operation of an AWTS more prone to measurement error. We can improve this situation by using more accurate instrumentation to refine our definition of the test section boundary conditions. Alternatively, we can scale up the complete test section and maintain the same measurement accuracy. In addition, we can increase the model disturbances in the test section by using larger models or testing only at high speeds. However, further research is necessary to determine just how large a 3-D model we can successfully test.

There are limits to the claim of minimized wall interferences in 3-D testing. The most significant limit found in all present AWTSs is flexible wall movement capabilities. This hardware limit severely restricts model lift. In addition, the cross-sectional dimensions of current AWTSs with the test section

height roughly equal to the width unnecessarily restricts the size of non-axisymmetric lifting models. The only way to physically increase model blockage above the conventional 0.5 percent limit is to use low aspect ratio models. (We usually limit the model span to 65 percent of the test section width.) Thus, there is a need for special 3-D AWTSs of perhaps rectangular cross-section designed with a better understanding of the adaptive wall requirements.

The wall adjustment procedures for 3-D testing are still in a development stage. The need for faster and larger capacity mini-computers for real time 3-D computations is now satisfied. However, the total computing power required for 3-D tests in an AWTS is still equivalent to that required for using a conventional test section and computing off-line wall interference corrections. Several important questions about the wall adjustment procedures remain unanswered. How many wall pressure measurements are necessary to adequately define the test section boundaries? Also, where on the model is it best to minimize the wall interferences? We need further research to resolve these questions.

We have not found any aerodynamic limits to the minimization of boundary interferences. Preliminary tests at low supersonic speeds show we can use flexible walled AWTSs to remove oblique shock reflections onto the model. There is every indication routine testing at supersonic speeds is possible, although we have yet to show this.

Alas, the experience with 3-D testing still lags 2-D work. At present, no one uses an AWTS in production type 3-D testing. Researchers have made many 3-D validation tests over the years but have been unable to evaluate the operating envelope for 3-D AWTSs. So, many questions about 3-D testing in AWTSs remain unanswered.

The Future?

The development of AWTSs for 2-D testing has reached an important stage. Routine operation for current production 2-D testing envelopes is possible. We can test large models successfully to obtain significant increases in chord Reynolds number. The use of adaptive wall technologies in routine 2-D testing is a reality and the advantages are available to all.

The experience with 2-D testing has provided an important stepping stone to 3-D testing. Nevertheless, the progress of adaptive wall research in 3-D testing has not been very rapid. The reasons are not clear, but the availability of computers to carry out real-time 3-D flow computations may be a significant factor. Also, considerable 3-D AWTS research effort has gone into developing a wide range of complex AWTS designs, when it now appears the simpler 2-D design may well be adequate. (In hindsight, this effort appears unnecessary but the contribution to overall knowledge is nevertheless important.)

Several research centers are now pursuing the development of AWTSs for 3-D testing. Researchers need to probe the operating limits of the adaptive wall testing technique in 3-D testing. Then we can use the best methods to achieve specific test objectives and to demonstrate all the AWTS advantages. Only after these actions will there be any hope of removing the apparent unwillingness of the wind tunnel community to accept adaptive wall technologies. (This unwillingness is presumably linked to a phobia about the increased test section complexity associated with an AWTS.) Use of adaptive wall testing techniques can significantly raise the quality of wind tunnel data above current levels in several important areas. To achieve perfection, we must make full use of advanced technologies available to us.

TABLE 16. - ADAPTIVE WALL TEST SECTIONS CURRENTLY IN USE

Organization	Tunnel	X–Section (h x w) m	Length m	Approx. Max. Mach No.	Approx. Max R_c millions	Walls	Adaptation Control	Remarks
Arizona University ***	HLAT	0.51 Square	0.914	0.2		2 Arrays of Venetian Blinds 2 Solid	16 Panels of Vanes and a Variable Angle Nozzle	Issue 3
DFVLR ***	HKG	0.75 Square	2.40	>1.2		2 Flexible 2 Solid	? Jacks/Wall	
Genova University **	Low Defl. Cascade	0.2x0.05 Rectangular	1.58	>.9	1	2 Flexible 2 Solid	33 Jacks/Wall	
Genova University **	High Defl. Cascade	0.2x0.05 Rectangular	1.6	>.9	1	2 Flexible 2 Solid	13 Jacks–Ceiling 26 Jacks–Floor	
NASA Ames **	2x2 ft	0.61 Square	1.53	>.85	2	2 Slotted 2 Solid	32 PCCs/Wall	Issue 4
NASA Ames •	HRC–2	0.61x0.41 Rectangular	2.79	>.8	30	2 Flexible 2 Solid	7 Jacks/Wall	
NASA Langley **	0.3–m TCT	0.33 Square	1.417	>1.1	120	2 Flexible 2 Solid	18 Jacks/Wall	Issues 1/2/3/4/5
N P Univ. ** Xian, China	Low Speed	0.256x0.15 Rectangular	1.3	0.12	0.50	2 Flexible 2 Solid	19 Jacks/Wall	Issues 2/5
ONERA/CERT •	T.2	0.37x0.39 Rectangular	1.32	>1.0	30	2 Flexible 2 Solid	16 Jacks/Wall	Issue 2
ONERA •	S5Ch	0.3 Square	?	1.2		1 Multiplate 3 Solid	Transverse Sliding Plates	
RPI **	3x8	0.20x0.07 Rectangular	0.6	0.86		1 Flexible 3 Solid	6 Jacks	
RPI **	3x15	0.39x0.07 Rectangular	?	0.8		2 Flexible 2 Solid	?? Jacks/Wall	
Southampton University •	SSWT	0.152x0.305 Rectangular	0.697	0.1	0.38	2 Flexible 2 Solid	15 Jacks/Wall	40 ° Swept Wing Panel
Southampton University •	TSWT	0.15 Square	1.12	>1.0	2.5	2 Flexible 2 Solid	19 Jacks/Wall	Issue 1/3
Sverdrup *** Technology	AWAT	0.305x0.61 Rectangular	2.438	0.2		3 Multi–Flexible Slats 1 Solid	102 Jacks–Ceiling 51 Jacks/Sidewall	
Tech. Univ. Berlin •	I/II	0.15 Square	0.99	>1.0	2	2 Flexible 2 Solid	13 Jacks/Wall	
Tech. Univ. Berlin ***	III	0.15x0.18 Octagonal	0.83	>1.0		8 Flexible	78 Jacks Total	Issue 6
Umberto Nobile **	FWWT	0.2 Square	1.0	0.6	3.5	2 Flexible 2 Solid	18 Jacks/Wall	

** – 2D Capability
*** – 3D Capability
• – 2D and 3D Capability
PCC – Plenum Chamber Compartments

S.W.D. Wolf
November 1987

Note - The **Remarks** refer to issues of the **Adaptive Wall Newsletter** (published quarterly by the Experimental Techniques Branch, LaRC) in which we have published related articles.

MAGNETIC SUSPENSION AND BALANCE SYSTEMS

The first known wind tunnel Magnetic Suspension and Balance System (MSBS) was reported by ONERA in 1957. Since then 15 further systems have been constructed by 11 organizations around the world. Five systems are currently active and each will be reviewed briefly in this paper. Figure 29 highlights some milestones in MSBS development. The intense research activity in the 1960s faded due to the apparent difficulties and expense of building a large MSBS. Recent developments in the fields of large-scale applications of superconductors, advanced position and attitude sensors, and digital control systems have greatly enhanced the feasibility of a large MSBS. Research activity has therefore increased with two MSBSs operational at NASA Langley, two in England, one in Japan, and rising interest in other countries.

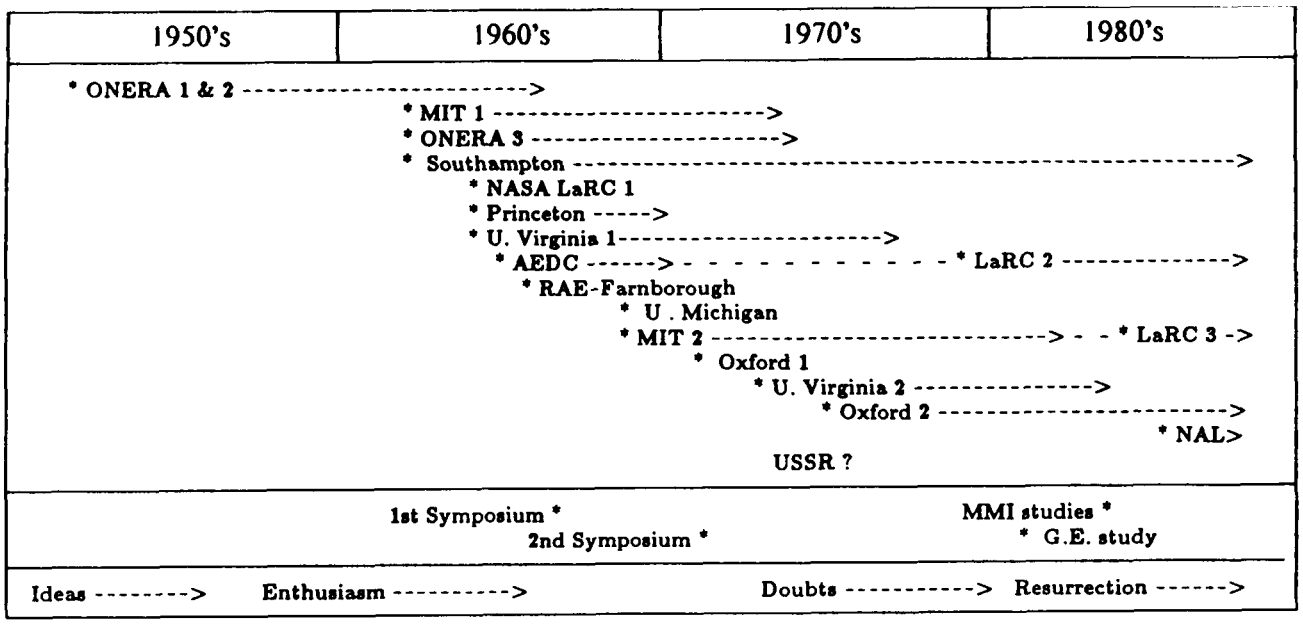

Fig. 29 - History of MSBS development.

Technical Background

The operating principles of MSBSs have been widely documented elsewhere and will not be repeated in this paper.[51] The principal attraction of MSBSs is, of course, the complete elimination of support interference. This problem, illustrated in Figure 30, can otherwise be particularly difficult in the transonic regime. Secondary benefits are the freedom to rapidly select model attitudes over a wide range and the possibility of more sophisticated and versatile dynamic testing than previously feasible.

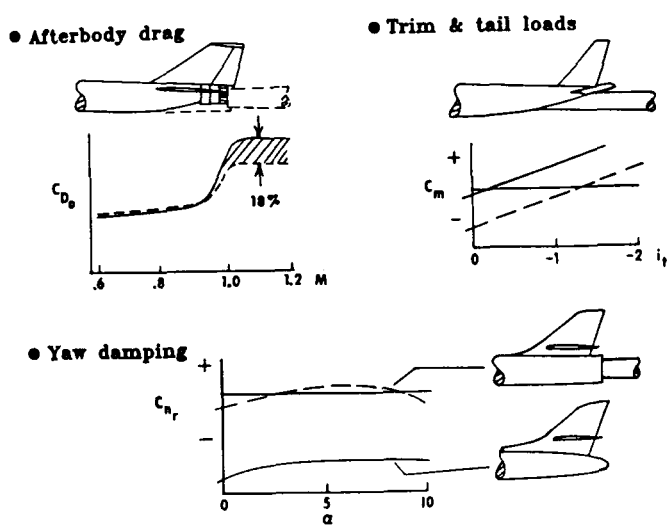

Fig. 30 - Examples of model support problems.

ORIGINAL PAGE
BLACK AND WHITE PHOTOGRAPH

United States
NASA Langley Research Center
13 inch MSBS

This system was originally built at the Arnold Engineering Development Center (AEDC) in the mid 1960s.[52] It was moved to NASA Langley in 1979 and has been progressively modified since then. In fact, of the original hardware, only the axial electromagnet and the support structure remain. The comments below relate to the present configuration.

Five electromagnets are arranged in a so-called V configuration, illustrated in Figure 31. The four vertical electromagnets are uncooled copper windings on laminated iron cores. The single water-cooled axial electromagnet is air cored. Model position and attitude is detected by an optical system based on solid-state, linear photodiode arrays. The control system is implemented with a PDP 11/73 minicomputer. Each electromagnet is fed from a bipolar thyristor power supply rated at 16kW. A low speed open circuit wind tunnel (maximum Mach 0.5) is installed. Figure 32 shows a schematic diagram of important hardware. Figure 33 shows a recent test in progress viewed from the control room.

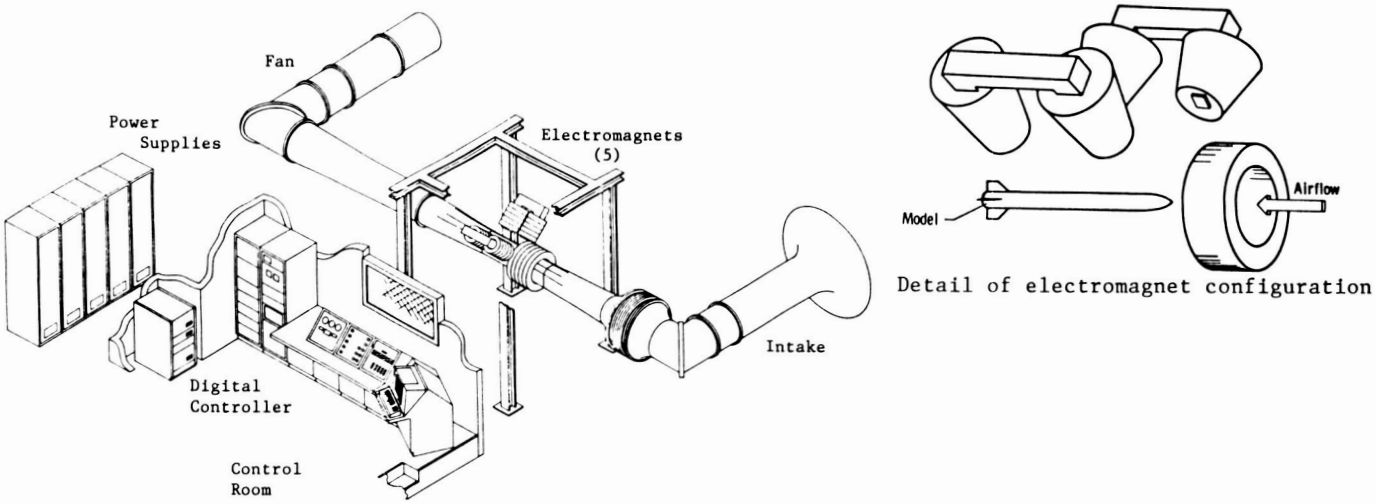

Fig. 31 - NASA Langley Research Center 13 inch MSBS.

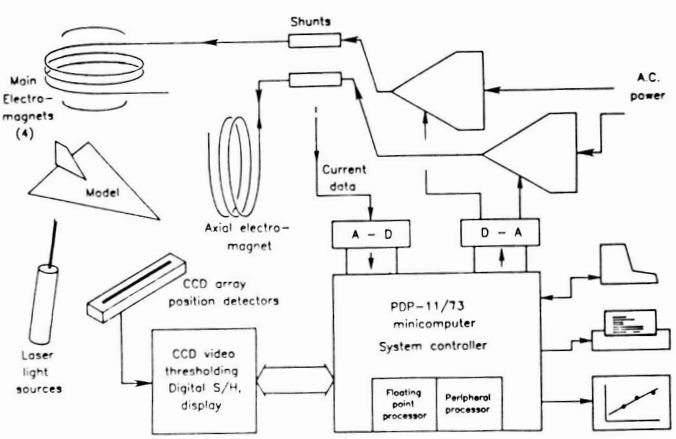

Fig. 32 - Schematic of 13 inch MSBS.

Fig. 33 - View from control room.

ORIGINAL PAGE
BLACK AND WHITE PHOTOGRAPH

NASA Langley Research Center
6 inch MSBS

This system was built at the Massachusetts Institute of Technology in the late 1960s.[51] It was moved to NASA Langley and is operational in more or less its original form, shown in Figure 34. There are 16 separate water-cooled copper electromagnets supplied from a mix of thyristor, thyratron, and motor-generator power supplies. Six-component control is possible with an AC roll control scheme. Perhaps the most notable design feature is the use of an Electromagnetic Position (and attitude) Sensor (EPS). Upgrading of EPS electronics is under way. A digital controller has been ordered and replacement of the power supplies is anticipated soon.

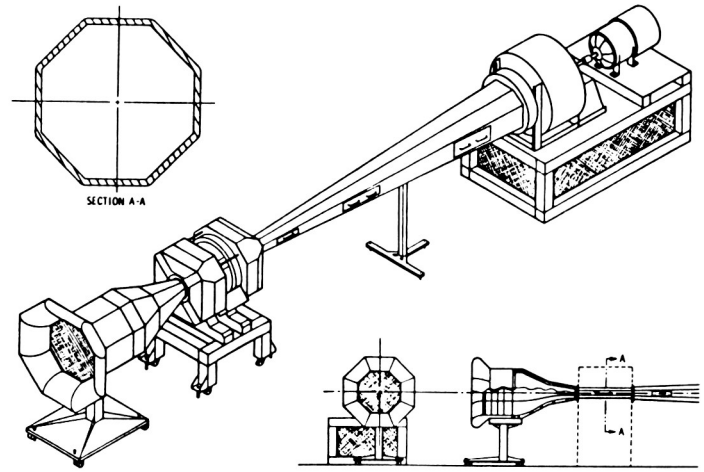

Fig. 34 - NASA Langley Research Center 6 inch MSBS.

Great Britain
University of Southampton
7 inch MSBS

Original construction of this system started in the mid 1960s. In its initial form it was used in low-speed, supersonic, and low-speed cryogenic wind tunnels. Extensive modifications were made in the early 1980s, including a fully symmetric electromagnet configuration, shown in Figure 35, and a digital controller.[53] The system is now installed in a purpose-built low-speed (M=0.3) wind tunnel. Electromagnets are uncooled copper windings, mostly using laminated iron cores, fed from bipolar transistor power supplies with a PDP 11/84 minicomputer based control system. An elaborate position sensing system, based on linear photodiode arrays, is presently installed to permit suspension up to 90° angle of attack. Previous achievements in high angle of attack suspension are shown in Figure 36.

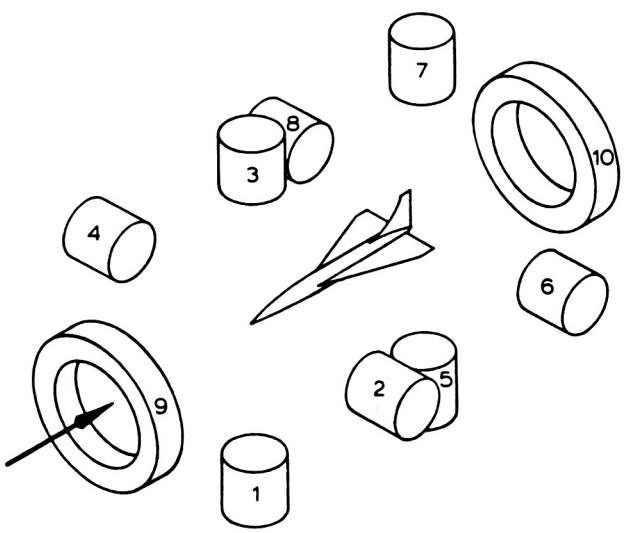

Fig. 35 - Southampton MSBS configuration.

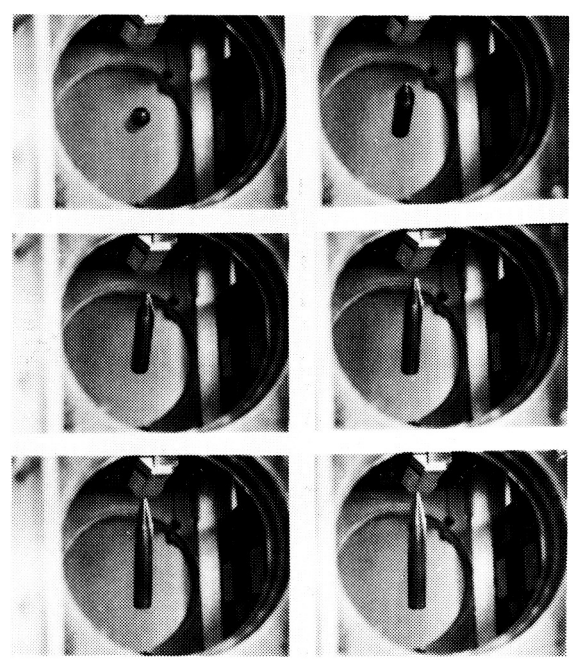

Fig. 36 - High angle of attack suspension.

ORIGINAL PAGE
BLACK AND WHITE PHOTOGRAPH

Oxford University
3 inch MSBS

For several years this MSBS has been in regular use measuring drag on small cone models in hypersonic low-density flows.[54] Figure 37 shows the system being prepared for a test. The system is simple in design, using eight water-cooled copper electromagnets for 3° of freedom control. Lateral motions are passively stabilized by special contoured pole pieces alongside the test section. An optical position sensing system and an analogue controller are used. Modifications are being studied to extend the angle of attack range for future testing.

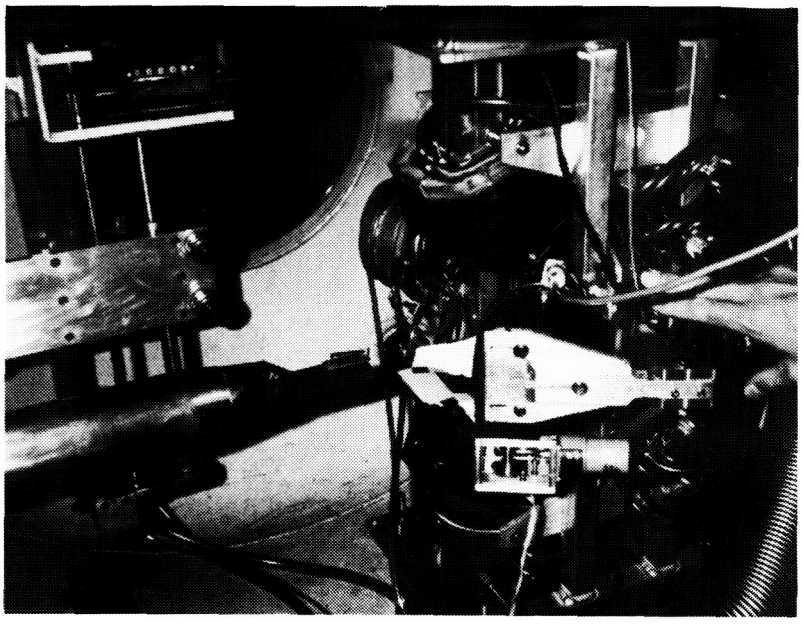

Fig. 37 - Oxford University MSBS.

Japan
National Aerospace Laboratory
4 inch MSBS

This system became operational in 1987. It is designed for 6° of freedom control but has apparently been used in 3° up to the present time. Ten electromagnets are arranged in a fairly symmetric configuration as illustrated in Figure 38. Model position and attitude sensing is carried out by a specially built camera assembly, comprising three linear photodiode arrays, illustrated in Figure 39. The camera operates in a passive mode, not requiring collimated light beams as used in other MSBSs. Current plans are to install the system in a small, transonic cryogenic wind tunnel in the near future.

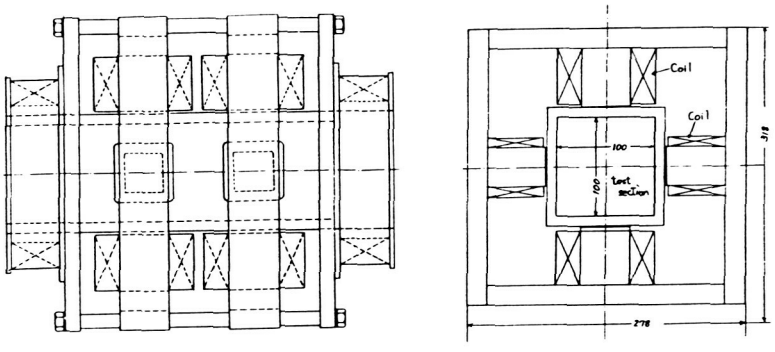

Fig. 38 - NAL MSBS configuration.

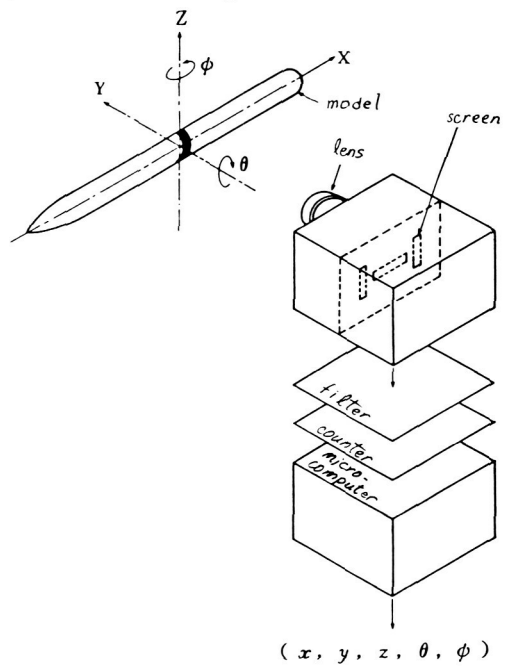

Fig. 39 - NAL position sensor.

Recent Aerodynamic Test Results

The NASA Langley 13 inch MSBS has been used for drag measurements on two laminar flow bodies of revolution (Hansen & Hoyt and Boltz). Preliminary testing of a family of slanted-base ogive cylinder models has been completed. Further tests will include sting interference assessment. The Southampton MSBS has also recently tested the Boltz body of revolution. High angle of attack tests of ogive-cylinder

ORIGINAL PAGE
BLACK AND WHITE PHOTOGRAPH

or similar models should begin at Southampton shortly. Hypersonic aerodynamic studies of cones at small angles of attack are planned at Oxford. The test program for the NAL MSBS is not known at this time. The NASA Langley 6 inch MSBS is devoted mainly to instrumentation development.

Large System Design

Three major design studies of large MSBSs have been completed.[55,56,57] Two of these are illustrated in Figure 40. All were targeted to an 8-foot, atmospheric, transonic tunnel. All studies concluded that the systems were technically feasible, though some care in design and specification is necessary to maintain reasonable costs. Latest studies indicate that the target system could be built for around $20 million. An industry survey revealed widespread support for continued MSBS development, focusing particularly on the transonic application.[58]

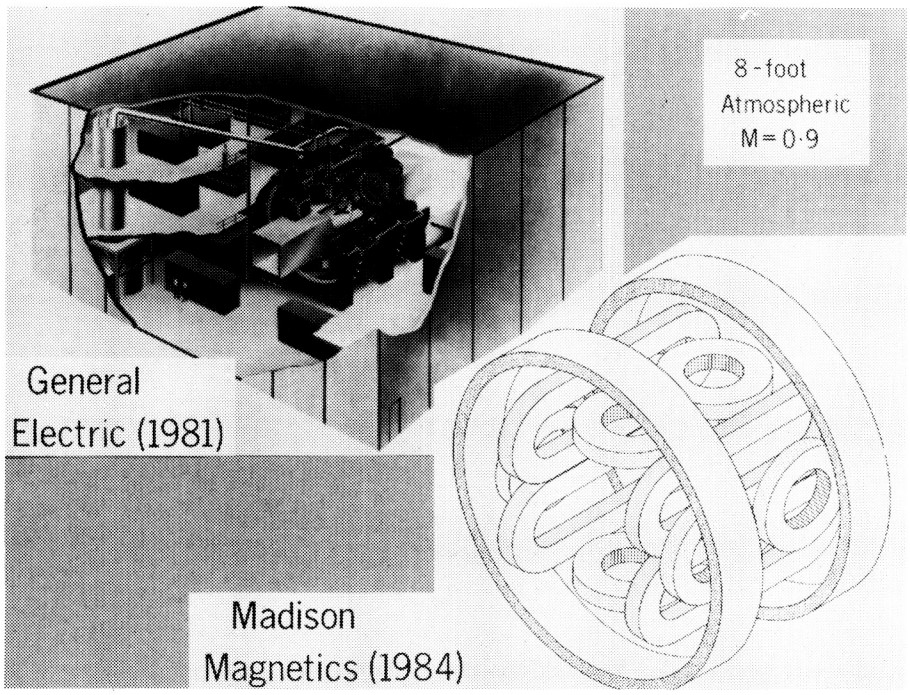

Fig. 40 - Large MSBS design studies.

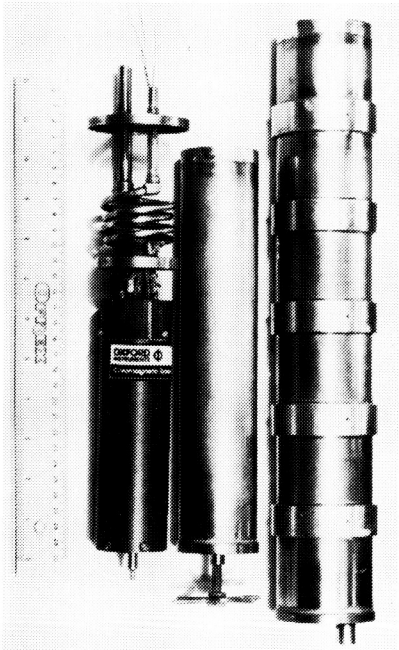

Fig. 41 - Superconducting solenoid model core.

New technology will continue to have an impact on the cost and usefulness of MSBSs. High angle of attack suspension methodology continues to advance at Southampton. Digital control systems are under widespread development.[59] The demonstration of a prototype superconducting solenoid model core, shown in Figure 41,[60] confirms the feasibility of this concept for large MSBSs where a significant reduction in electromagnet size can result from its use. New approaches to the problem of force and moment calibration are being pursued, including on-board strain-gage balance systems with data telemetry, illustrated in Figure 42.[61] High temperature superconductors may have a dramatic impact on the design and cost of a large MSBS, though it should be stressed that large MSBSs are feasible without these materials.

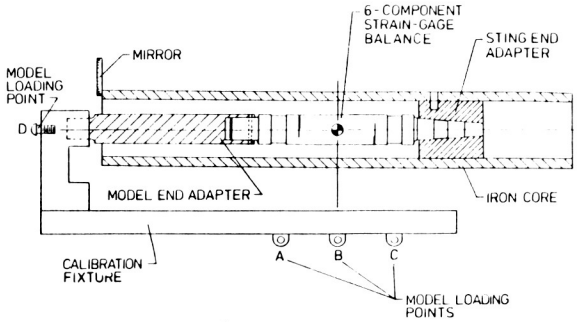

Fig. 42 - Internal strain-gage balance.

ORIGINAL PAGE
BLACK AND WHITE PHOTOGRAPH

CONCLUDING REMARKS

This survey paper covered **cryogenic wind tunnels, adaptive wall test sections,** and **magnetic suspension and balance systems** (MSBS). With a cryogenic tunnel researchers can test at flight Reynolds numbers. Having a test section with adaptive walls eliminates or greatly reduces wall interference effects. Using magnetic suspension of the model eliminates support interference effects.

Cryogenic tunnels are finding wide acceptance and use. The future for large cryogenic tunnels seems assured with the U.S. NTF and the KKK in operation and the ETW under final design.

Adaptive wall test sections are also finding wide acceptance and use. One remaining question is how complex the walls need to be for adaptation for 3-dimensional models. The next year or so will see this question resolved. Then we will see adaptive wall test sections in new wind tunnels as well as being retro-fitted in existing tunnels.

Magnetic suspension and balance systems are slower to find acceptance and application than either cryogenic tunnels or adaptive walls. One reason for this is the complexity of MSBS. Another is the limitation on size that existed before the development of so-called *ac* superconductors. The small systems now in use offer a glimpse of the tremendous potential of MSBS. The technology for building a large (8 foot or bigger) MSBS is now in hand. The building of large systems is just a matter of time.

The development of advanced test techniques is steadily moving forward. We now have the ability to test at flight Reynolds number free of both wall and support interference. The future for wind tunnel testing is bright.

REFERENCES

1. **Kilgore; Robert. A.; and Dress, David A.**: The Application of Cryogenics to High Reynolds Number Testing in Wind Tunnels. Part 1: Evolution, Theory, and Advantages. *Cryogenics*, vol. 24, pp. 395-402, 1984.

2. **Kilgore, Robert A.; and Dress, David A.**: The Application of Cryogenics to High Reynolds Number Testing in Wind Tunnels. Part 2: Development and Application of the Cryogenic Wind Tunnel Concept. *Cryogenics*, vol. 24, pp. 484-493, 1984.

3. **Dress, David A.; and Kilgore, Robert A.**: Cryogenic Wind Tunnels - a Global Perspective. *Cryogenics*, vol. 28, pp. 10-21, 1988.

4. **Law, R. D.**: Early Experiments in Using the Cryogenic Test Facility at RAE Bedford, UK. *ETW Cryogenic Technology Review Meeting*, Paper 8, NLR-Amsterdam, 1982.

5. **Goodyer, M. J.**: The 0.1m Subsonic Cryogenic Tunnel at the University of Southampton. NASA CR-145305, 1978.

6. **Kell, D. M.**: A Surface Flow Visualization Technique for Use in Cryogenic Wind Tunnels. Aeronautical Journal, vol. 82, November 1987, pp. 484-487.

7. **Goodyer, M. J.**: Engineering Changes to the 0.1m Cryogenic Wind Tunnel at Southampton University. NASA CR-172430, 1984.

8. **Owen, D.**: Development of a Mach Number Control System for Use With a Cryogenic Wind Tunnel. *Honours Project Report*, University of Southampton, UK, 1984.

9. **Britcher, C. P.; and Goodyer, M. J.**: The Southampton University Magnetic Suspension/Cryogenic Wind Tunnel Facility. *1st Int. Symp. on Cryogenic Wind Tunnels*, Paper 10, Southampton, UK, 1979.

10. **Tizard, J. A.; and Hartzuiker, J. P.**: The European Transonic Windtunnel Project ETW. AGARD R-722, Paper 12, 1985.

11. **Dor, J.-B.**: The T2 Cryogenic Induction Tunnel in Toulouse. AGARD R-722, Paper 9, 1985.

12. **Blanchard, A.; Delcourt, V.; and Plazanet, M.**: Problems Associated With Operations and Measurement in Cryogenic Wind Tunnels. Translation into English of "Problemes Lies Fonctionnement et aux Measures en Soufflerie Cryogenique." Rep. OA-13/5007-AYD DERAT-13/5007-DY, July 1981. NASA TM-88443, June 1986, 75 pp.

13. **Viehweger, G.**: The Kryo-Kanal-Köln project, KKK. AGARD R-722, Paper 11, 1985.

14. **Hefer, G.**: The Cryogenic Ludwieg Tube Tunnel at Göttingen. AGARD R-722, 1985, pp. 10-1 through 10-6.

15. **The Second Aerodynamics Division**: Construction and Performance of NAL Two-Dimensional Transonic Wind Tunnel. NAL TR-647T, 1982.

16. **Takashima, K.; Sawada, H.; Aoki, T.; and Kayaba, S.**: Trial Manufacture of NAL 0.1 m x 0.1 m Transonic Cryogenic Wind Tunnel. NAL TR-910, 1986.

17. **Adachi, T. et al**: Force and Vortex Shedding on a Circular Cylinder From Subcritical Up to Transcritical Reynolds Numbers. Bulletin of the JSME, vol. 28, no. 243, 1985.

18. **Clausing, A. M.; Clark, G. L.; and Mueller, M. H.**: The Cryogenic Heat Transfer Tunnel - A New Tool for Convective Research. *Winter Annual Meeting ASME*, San Francisco, California, 1978, pp. 73-78.

19. **Clausing, A. M.**: Experimental Studies of Forced, Natural and Combined Convective Heat Transfer at Cryogenic Temperatures. *1st International Symposium on Cryogenic Wind Tunnels*, Paper 24, Southampton, UK, April 3-5, 1979.

20. **Clausing, A. M.**: Advantages of a Cryogenic Environment for Experimental Investigations of Convective Heat Transfer. *International Journal of Heat and Mass Transfer*, vol. 25, no. 8, 1982, pp. 1255-1257.

21. **Mueller, M. H. et al**: Description of UIUC Cryogenic Wind Tunnel Including Pressure Distributions, Turbulence Measurements and Heat Transfer Data. *University of Illinois*, Tech. Rept. ME-TN-79-9180-1, 1979.

22. **Goodyer, M. J.; and Kilgore, R. A.**: High-Reynolds-Number Cryogenic Wind Tunnel. AIAA 72-995, 1972. Also, *AIAA Journal*, vol. 11, no. 5, 1973, pp. 613-619.

23. **Kilgore, Robert A. et al**: The Cryogenic Wind-Tunnel Concept for High Reynolds Number Testing. NASA TN-D-7762, 1974.

24. **Kilgore, Robert A.**: The NASA Langley 0.3-m Transonic Cryogenic Tunnel. AGARD R-722, Paper no. 13, 1985.

25. **Bruce, Walter E., Jr.**: The U.S. National Transonic Facility - I. AGARD R-722, Paper no. 14, 1985.

26. **Bruce, Walter E., Jr.**: The U.S. National Transonic Facility - II. AGARD R-722, Paper no. 15, 1985.

27. **Aldrich, J. F. L.**: Progress Report on the Douglas Four-Foot Cryogenic Wind Tunnel. *1st Int. Symp. on Cryogenic Wind Tunnels*, Paper no. 35, Southampton, UK, April 3-5, 1979.

28. **Stollery, J. L.; and Stalker, R. J.**: The Development and Use of Free Piston Wind Tunnels. *Proceedings of the 14th International Symposium on Shock Tubes and Waves*, Sydney, 1983, pp. 41-50.

29. **Pan, R.**: Cryogenic High Reynolds Number Transonic Wind Tunnel with Pre-cooled and Restricted Flow. Translated into English from Zhongguo Quiliu Dongli Xue (China), no. 2, pp. 76-92.

30. **Tuttle, Marie H.; Kilgore, Robert A.; and Cole, Karen L.**: Cryogenic Wind Tunnels - A Selected, Annotated Bibliography. NASA TM-4013, September 1987.

31. **Goodyer, M. J.**: The Self Streamlining Wind Tunnel. NASA TM-X-72699, August 1975.

32. **Wolf, S. W. D.**: The Design and Operational Development of Self-Streamlining Two-Dimensional Flexible Walled Test Sections. NASA CR-172328, March 1984, 281 pp.

33. **Bailey, A.; and Wood, S. A.**: Further Development of a High-Speed Wind Tunnel of Rectangular Cross-Section. British ARC R&M 1853, September 1938, 16 pp.

34. **Holder, D. W.**: The High-Speed Laboratory of the Aerodynamics Division, N.P.L., Parts I, II and III. Reports and Memoranda No. 2560. December 1946.

35. **Tuttle, M. H.; and Mineck, R. E.**: Adaptive Wall Wind Tunnels - A Selected, Annotated Bibliography. NASA TM-87639, August 1986.

36. **Parker, R. L., Jr.; and Erickson, J. C., Jr.**: Development of a Three-Dimensional Adaptive Wall Test Section with Perforated Walls. Presented at the 50th AGARD Fluid Dynamics Panel Specialists' Meeting on *Wall Interference in Wind Tunnels*, London, England, May 19-20, 1982, AGARD-CP-335 (N83-20957#), paper no. 17, 14 pp.

37. **Morgan, D. G.; and Lee, G.**: Construction of a 2- by 2-Foot Transonic Adaptive-Wall Test Section at the NASA Ames Research Center. *AIAA 4th Joint Fluid Mechanics, Plasma Dynamics and Laser Conference*, AIAA Paper 86-1089, Atlanta, GA, May 12-14, 1986.

38. **Heddergott, A.; Kuczka, D.; and Wedemeyer, E.**: The Adaptive Rubber Tube Test Section of the DFVLR Göttingen. *11th International Congress on Instrumentation in Aerospace Simulation Facilities*, Stanford, California, August 26-28, 1985. In: ICIASF '85 RECORD, IEEE publ. 85CH2210-3.

39. **Ganzer, U.; Igeta, Y.; and Ziemann, J.**: Design and Operation of TU-Berlin Wind Tunnel With Adaptable Walls. *14th Congress of the International Council of the Aeronautical Sciences*, Toulouse, France, September 9-14, 1984. In: Proceedings, vol. 1. (A84-44926), AIAA, 1984, pp. 52-65.

40. **Wolf, S. W. D.; Cook, I. D.; and Goodyer, M. J.**: The Status of Two- and Three-Dimensional Testing in the University of Southampton Transonic Self-Streamlining Wind Tunnel. 50th AGARD Fluid Dynamics Panel Specialists' Meeting on *Wall Interference in Wind Tunnels*, Paper no. 15, London, England, May 19-20, 1982. In: AGARD-CP-335 (N83-20957#).

41. **Blanchard, A.; Payry, M. J.; and Breil, J. F.**: Tests with Three-Dimensional Adaptations in the Rectangular Working Section of the French T2 Wind Tunnel, with a Type AS 07 Swept Wing Half Model Installed. NASA TM-88442, July 1986, 28 pp. Translation of ONERA/CERT R. T. OA 34/3075 (DERAT 12/5015 DN), November 1985, pp. 1-24.

42. **Judd, M.; Wolf, S. W. D.; and Goodyer, M. J.**: Analytical Work in Support of the Design and Operation of Two-Dimensional Self Streamlining Test Sections--Semiannual Progress Report, Oct. 1975-Mar. 1976. NASA CR-145019, July 1976, 67 pp.

43. **Wolf, S. W. D.; and Goodyer, M. J.**: Predictive Wall Adjustment Strategy for Two-Dimensional Flexible Walled Adaptive Wind Tunnel. A Detailed Description of the First One-Step Method. AASU Memo 85/12, January 1986. (NASA CR to be published.)

44. **Lamarche, L.; and Wedemeyer, E.**: Minimization of Wall Interferences for Three-Dimensional Models with Two-Dimensional Wall Adaptation. VKI TN 149 (1984).

45. **Rebstock, R.**: Procedures for Computing Transonic Flows for Control of Adaptive Wind Tunnels. Ph. D. Thesis, NASA TM-88530, January 1987.

46. **Wolf, S. W. D.**: Evaluation of a Flexible Wall Testing Technique to Minimize Wall Interferences in the NASA Langley 0.3-m Transonic Cryogenic Tunnel. *26th AIAA Aerospace Sciences Meeting*, AIAA Paper 88-0140, Reno, Nevada, January 11-14, 1988.

47. **Lewis, M. C.**: Aerofoil Testing in a Self-Streamlining Flexible Walled Wind Tunnel. Ph. D. Thesis, July 1987. NASA CR 4128.

48. **Green, L. L.; and Newman, P. A.**: Transonic Wall Interference Assessment and Corrections for Airfoil Data From the 0.3-Meter TCT Adaptive Wall Test Section. *19th AIAA Fluid Dynamics, Plasma Dynamics and Lasers Conference*, AIAA Paper 87-1431, Honolulu, Hawaii, June 8-10, 1987.

49. **Lesant Y.**: Wall Self Adaptation Process at Mach 1.2 - Final Report. ONERA-RTS-31/3075-AY-402, April 1985. In French, N86-28968#.

50. **Chevallier, J. P., Mignosi, A.; Archambaud, J. P.; and Seraudie, A.**: T2 Wind Tunnel Adaptive Walls--Design, Construction, and Some Typical Results. La Recherche Aerospatiale (English Edition), no. 4, July/August 1983, pp. 1-19.

51. **Stephens, T.**: Design, Construction and Evaluation of a Magnetic Suspension and Balance System for Wind Tunnels. NASA CR-66903, November 1969.

52. **Cortner, A. H.; and Brown, M. D.**: Design and Initial Calibration of a Magnetic Suspension and Balance System for Wind Tunnel Models at the Arnold Engineering Development Center. In: Proceedings of ARL Symposium on *Magnetic Wind Tunnel Model Suspension and Balance Systems*. ARL 66-0135, July 1966.

53. **Britcher, C. P.**: Some Aspects of Wind Tunnel Magnetic Suspension Systems with Special Application at Large Physical Scales. NASA CR-172154, September 1983.

54. **Dahlen, G. A.; and Brundin, C. L.**: Wall Temperature Effects on Rarefied Hypersonic Cone Drag. *13th International Symposium on Rarefied Gas Dynamics*, Novosibirsk, USSR, July 1982.

55. **Bloom, H. et al**: Design Concepts and Cost Studies for Magnetic Suspension and Balance Systems. NASA CR-165917, July 1982.

56. **Boom, R. W.; Eyssa, Y. M.; McIntosh, G. E.; and Abdelsalam, M. K.**: Magnetic Suspension and Balance System Study. NASA CR-3802, July 1984.

57. **Boom, R. W. et al**: Magnetic Suspension and Balance System Advanced Study. NASA CR-3937, October 1985.

58. **Martindale, W. R.; Butler, R. W.; and Starr, R. F.**: Study on Need for a Magnetic Suspension System Operating with a Transonic Wind Tunnel. NASA CR-3900, May 1985.

59. **Britcher, C. P.; Goodyer, M. J.; Eskins, J.; Parker, D.; and Halford, R. J.**: Digital Control of Wind Tunnel Magnetic Suspension and Balance Systems. *12th International Congress on Instrumentation in Aerospace Simulation Facilities*, Williamsburg, Virginia, June 1987.

60. **Britcher, C. P.; Goodyer, M. J.; Scurlock, R. G.; and Wu, Y. Y.**: A Flying Superconducting Magnet and Cryostat for Magnetic Suspension of Wind-Tunnel Models. *Cryogenics*, April 1984.

61. **Roberts, P.; and Tcheng, P.**: Strain-Gage Balance Calibration of a Magnetic Suspension and Balance System. *12th International Congress on Instrumentation in Aerospace Simulation Facilities*, Williamsburg, Virginia, June 1987.

N89-20956

AN LDA INVESTIGATION OF THREE-DIMENSIONAL NORMAL SHOCK WAVE BOUNDARY-LAYER INTERACTIONS

R.M. Chriss,
W.R. Hingst, and
A.J. Strazisar
NASA Lewis Research Center
Cleveland, Ohio

T.G. Keith, Jr.
University of Toledo
Toledo, Ohio

ABSTRACT

Nonintrusive measurements have been made of a normal shock wave/boundary-layer interaction. Two-dimensional measurements were made throughout the interaction region while three-dimensional measurements were made in the vicinity of the shock wave. The measurements were made in the corner of the test section of a continuous supersonic wind tunnel in which a normal shock wave had been stabilized. LDA,* surface pressure measurement and flow visualization techniques were employed for two freestream Mach number test cases: 1.6 and 1.3. The former contained separated flow regions and a system of shock waves. The latter was found to be far less complicated. The reported results define the flowfield structure in detail for each case.

INTRODUCTION

Normal shock wave/turbulent boundary-layer interactions occur in a number of important high-speed flow applications. These include, for example, flows within turbomachines, transonic flows over wings and external surfaces, and supersonic flows within inlet systems. The present investigation is relevant to the latter application.

It is well known that large pressure gradients associated with shock-boundary-layer interactions have the potential of producing large regions of separated flow. These, in turn, can cause a substantial degradation of inlet performance. Consequently, to design improved high-speed flow components, where normal shocks occur, a thorough understanding of the flow physics and the capability to compute the interaction is necessary. This is made more difficult by the fact that in internal flow applications with the exception of purely axisymmetric flows, normal shock-boundary-layer interactions are three-dimensional.

In this investigation a normal shock wave was stabilized in a square wind tunnel test section and was allowed to freely interact with the naturally occurring tunnel sidewall boundary layers. The emphasis was in making nonintrusive three-dimensional measurements in the corner of the test section in order to determine the flowfield associated with the interaction.

Two-dimensional measurements (of u and v) were made throughout the flowfield. The third component (w) was measured only in the corner near the the shock, where it was

*Laser-Doppler anemometry (LDA).

expected to be significant. The results will be presented in the form of Mach number contours in addition to secondary flow vector plots where the z component (w) was measured. The effect of the third component on the Mach number, where w was measured, is expected to be small due to the small flow angles encountered.

Two entirely different flow structures are known to exist for two-dimensional flows at freestream Mach numbers of 1.6 and 1.3. In addition, the Mach 1.3 flow is known to be near the limit for the onset of separation. It is thought that the ultimate test for any computational scheme which aims to provide accurate internal compressible flowfield predictive capability would be to model these two flow structures.

Previous work has been limited to two-dimensional interactions either along the center plane of rectangular flow geometries or to axisymmetric configurations, (refs. 1-15). Moreover, much of the existing data was obtained with pitot pressure probes. The sensitivity of the normal shock to these intrusive measurement techniques has limited the progress in the study of these flows.

Seddon (ref. 1), used static pressure probes to produce the benchmark model of the two-dimensional interaction shown in Fig. 1. Two-dimensional investigations by Abbiss, et al. (ref. 14) and East (ref. 15) have employed laser-Doppler anemometry (LDA). However, in addition to being two-dimensional, the scope of these investigations were limited to the interaction region only and did not describe the flowfield far downstream of the interaction.

In the following, the experimental apparatus employed, as well as the various measurements made during the course of the tests will be described. Estimates of the experimental uncertainty in the measured data are made. Finally, results from a flow visualization investigation, from surface pressure measurements and from LDA flowfield surveys are presented and discussed.

NOMENCLATURE

a_{ij}	elements of a 3 x 3 calibration matrix used to convert the measured LDA velocity components into orthogonal values.
a_t	speed of sound based on total temperature.
e	error.
k	ratio of specific heats.
M	Mach number.
N	number of LDA realizations per channel.
s	estimate of the standard deviation.
u,v,w	orthogonal time averaged, velocity components along the x,y and z directions.
z_c	confidence coefficient.
γ	flow angle in the x-y plane.
Δ	error or change appearing in the parentheses.
θ	angle in the x-y plane between the x axis and LDA channels 1 and 2.
ϕ	angle in the x-z plane between the x axis and channel 3.
subscripts	
u,v,w	refers to the x,y or z velocity components.
1,2,3	LDA channel number.

EXPERIMENTAL MEASUREMENTS AND EQUIPMENT

Facility

A normal shock wave was stabilized in the test section of the NASA Lewis Research Center's 30.5cm x 30.5cm (1 foot x 1 foot) supersonic wind tunnel, which is an open circuit, continuous-flow facility, Fig. 2. Tests were performed at nominal freestream Mach numbers of 1.6 and 1.3. The shock was established by placing a conical obstacle in the diffuser approximately 1.2 meters (4 feet) downstream of the wind tunnel test section. A schematic of the coordinate system used in the investigation is shown in Fig. 3. In both test cases, the freestream shock was maintained at x = 10cm (3.9 inches). The shock interacted with the naturally occurring tunnel wall boundary layers. The flow Reynolds number for both tests was 15 x 10^6/meter.

A preliminary schlieren investigation indicated high-frequency oscillations in the shock wave location. This was suspected from previous studies and is thought to be caused by the inherent instability of a normal shock in a constant area duct. In addition, the oscillation may be exacerbated by the turbulence of the approaching boundary layer as well as disturbances arising in the separation regions which emanate within the boundary layer throughout the interaction region. The shock position oscillated about its mean location with a magnitude of approximately ± 1 cm (0.4 inches). Its mean location could be adjusted or maintained by actuation of the cone blockage as required. These oscillations manifested themselves in the form of bimodal histograms that were obtained during LDA surveys near the shock. The mean shock location was monitored by wall surface static pressure measurements (time smoothed) in order to assure that there was no movement of the shock during the lengthy flowfield surveys.

The tunnel total pressure was maintained at 103.4 and 97.9 kPa (15.0 and 14.2 psia) for the 1.6 and 1.3 cases respectively. The total temperature varied between 10 and 20°C (50 and 70°F) throughout the tests.

Flow Visualization

Qualitative measurements of the interaction were made with schlieren and surface oil flow visualization techniques. Collectively, these two qualitative techniques provide valuable insight into the flow physics.

Floor Static Pressure Measurements

Static pressure measurements were made across the floor of the test section at 72 locations. These measurements were used to demonstrate flow symmetry as well as to monitor the shock location during the tests in addition to providing important pressure recovery information.

The Laser Anemometer

Three velocity components were obtained in this investigation: u and v in the x-y plane and w along the optical axis. A single component laser anemometer was used in off-axis forward scatter. The x and y velocity components (u and v) were obtained by rotating the beams about the optical axis. The z component (w) was obtained by rotating the entire system about the y axis. The LDA system obtained data in a nonorthogonal coordinate system depicted in Fig. 4. The LDA system employed had an angle θ of 30° and an angle ϕ of approximately 28°. The anemometer was mounted on a computer controlled 4-axis table and the measurements were monitored with a real time

graphics display that included velocity histograms. This capability is considered to be important in maintaining the accuracy of the velocity measurements.

Since the flow in the tunnel was quarter symmetric as demonstrated by examination of the wall static measurements, laser anemometer measurements were acquired in only one quadrant of the test section. The measurements were performed in the upper half of the test section due to the tendency of the seed oil to deposit on the lower half of the windows much faster than on the upper half. For clarity, however, the measured values are presented in terms of the right hand coordinate system shown in Fig. 3. The flowfields were investigated in detail by surveying along both the axial and cross section planes. Each survey plane contained on the order of 1000 individual measurement locations. The complete set of data for each freestream Mach number contained approximately 20,000 measurement locations.

The data rate was normally maintained at 1000 realizations per second. At startup with clean windows, the data rate could be adjusted up to 10,000 realizations per second without affecting the accuracy of the data. During the tests, the windows of the test section gradually became fogged with seed oil. For the Mach 1.6 tests, the tunnel could normally be run from 2 to 4 hours before the windows required cleaning. For the 1.3 case, the rate of contamination was greatly reduced so that 5 to 8 hour runs were typical.

A TSI Inc. 1990B signal processor was used, together with a PDP 11/34 Digital Computer, to aquire and record the data. The data were reduced on a VAX 11/750 computer and transferred to an IBM 3033 in order to make use of a three-dimensional graphics capability.

The Particle Generator

It is well known that in high speed flows, containing large velocity gradients, lag of the seed particles is a major experimental concern. The seed particles must be sufficiently small and bouyant enough to follow the flow closely so as to maintain accurate resolution of the data. An evaporation condensation generator (refs. 16-18) was designed and built in order to produce Dioctyl Phthalate (DOP) particles with a mean diameter of 0.8 micron. From previous investigations (refs. 19-20), it was known that this size is small enough to permit the particles to track the flow with sufficient integrity but yet large enough to produce a strong LDA signal.

The seed droplet distribution was observed in situ with a TSI, Inc. Aerodynamic Particle Sizer (APS 33), Fig. 5. The on-line LDA data provided an independent check on the seeding technique, i.e., as the shock oscillated about the probe volume while surveying near the shock, the resulting velocity histograms were distinctly bimodal, Fig. 6, indicating a monodisperse seed distribution.

ERROR AND UNCERTAINTY ANALYSIS

Error Analysis

The maximum uncertainty due to omitting the z component from the velocity and Mach number calculations can be approximated by assuming that this component has the same magnitude as the y velocity component, i.e., $w \approx v$. Thus, the flow velocity is approximated by $\sqrt{u^2 + 2v^2}$. If the w velocity component is completely ignored, the velocity would then be $\sqrt{u^2 + v^2}$. The resulting error by making this omission can be

approximately written as

$$e = 1 - \left\{ \frac{u^2 + v^2}{u^2 + 2v^2} \right\}^{1/2} = 1 - \left\{ \frac{1 + \tan^2\gamma}{1 + 2\tan^2\gamma} \right\}^{1/2} \tag{1}$$

where γ is the flow angle in the x-y plane. Outside the region where the z component (w) was measured the largest flow angle γ encountered was approximately 10° and 5° for the 1.6 and 1.3 cases respectively. With these flow angles the largest error in omitting w in the total velocity would be approximately 1.5% and 0.4% respectively.

The Mach number throughout the flowfield can be computed from

$$M^2 = (V/a_t)^2 \left\{ 1 - \frac{k-1}{2} (V/a_t)^2 \right\}^{-1} \tag{2}$$

where a_t is the speed of sound calculated at the total temperature, $V = \sqrt{u^2 + v^2 + w^2}$, and k is the ratio of specific heats. This equation is valid for thermally and calorically perfect gases undergoing adiabatic processes. Using this expression and the velocity approximations described above, the maximum error expected in the Mach number due to omitting w would be approximately 3% and 1% for the respective 1.6 and 1.3 freestream Mach number cases.

Statistical Considerations

For the coordinate system shown in Figs. 3 and 4, it can be seen that the velocity components u,v and w can be written in terms of v_1, v_2 and v_3 (the velocity components as measured by LDA channels 1,2, and 3 respectively) as follows

$$\begin{aligned} u &= \frac{v_1 + v_2}{2\cos\theta} \\ v &= \frac{v_1 - v_2}{2\sin\theta} \\ w &= -\frac{u}{\tan\phi} + \frac{v_3}{\sin\phi} \end{aligned} \tag{3}$$

where θ is the angle in the x-y plane between the x axis and channel 3. Snyder, et al. (ref. 21) have pointed out that this set of equations, for a generalized three-dimensional LDA system, can be expressed in matrix form as

$$\begin{Bmatrix} u \\ v \\ w \end{Bmatrix} = \begin{Bmatrix} a_{11} & a_{12} & a_{13} \\ a_{21} & a_{22} & a_{23} \\ a_{31} & a_{32} & a_{33} \end{Bmatrix} \begin{Bmatrix} v_1 \\ v_2 \\ v_3 \end{Bmatrix} \tag{4}$$

Thus, $a_{11} = a_{12} = (1/2)\cos\theta, a_{13} = 0$, etc.

For uncorrelated data, i.e., measurements made from different seed particles by a non-simultaneous LDA system, it has been suggested (ref. 21) that the variances associated with each of the coordinate directions x,y and z can be expressed in terms of the variances s_1^2, s_2^2 and s_3^2 of the velocity ensembles of the three LDA channels in the following manner

$$\begin{Bmatrix} s_u^2 \\ s_v^2 \\ s_w^2 \end{Bmatrix} = \begin{Bmatrix} a_{11}^2 & a_{12}^2 & a_{13}^2 \\ a_{21}^2 & a_{22}^2 & a_{23}^2 \\ a_{31}^2 & a_{32}^2 & a_{33}^2 \end{Bmatrix} \begin{Bmatrix} s_1^2 \\ s_2^2 \\ s_3^2 \end{Bmatrix} \tag{5}$$

The uncertainties due to statistical considerations in the components can be calculated from estimation theory to be

$$\begin{aligned} \Delta u &= (z_c/\sqrt{N})s_u \\ \Delta v &= (z_c/\sqrt{N})s_v \\ \Delta w &= (z_c/\sqrt{N})s_w \end{aligned} \tag{6}$$

where z_c is the confidence coefficient and N is the number of realizations per channel. For a normal distribution and a confidence level of 95%, z_c has a value of 1.96. Equations (5) and (6) allow calculation of the uncertainty in the u,v and w velocity components from the standard deviation in each of the LDA channels when N is known. Conversely, they can be used on-line in the data aquisition software to calculate the value of N which is required to yield a desired uncertainty level, by obtaining s_1, s_2 and s_3 from a preliminary sample measurement at that point.

In order to estimate the statistical uncertainty in the data presented, two components of Eq.(6) are written

$$\begin{aligned} \Delta u/u &= (z_c/\sqrt{N})s_u/u \\ \Delta v/v &= (z_c/\sqrt{N})s_v/v \end{aligned} \tag{7}$$

where s_u/u and s_v/v are the turbulence intensities along the x and y coordinate directions. Note that the third velocity component has been omitted from this consideration. Assuming isotropic turbulence, the uncertainty in V can then be approximated by

$$\Delta V/V \leq \sqrt{2/N}\,\{s_V/V\}\,z_c \tag{8}$$

with a maximum turbulence intensity of 20% in the 1.6 case and 10% in the 1.3 case and with 1000 realizations per channel the uncertainty in the velocity due to statistical considerations is computed using Eq.(8) to be approximately 2% in the 1.6 case and 1% in the 1.3 case. The resulting uncertainty in the Mach number due to statistical considerations is 3% in the 1.6 case and 1.5% in the 1.3 case.

As noted by Orloff and Snyder (ref. 22), in order to determine the matrix elements in Eq.(4) as accurately as possible, great care must be exercised in calibrating the LDA system when the angle ϕ is small. If this precaution is not observed, large systematic uncertainty can arise in the calculated z velocity component. Systematic uncertainty in the x and y velocity components is considered to be very small, and therefore has not been considered in the uncertainty analysis.

The overriding concern with an LDA system of this type (i.e., one where ϕ is small) is the uncertainty in the w component, since the uncertainty in u and v will be very small given a reasonable N. This particular problem due to LDA system geometry (being a subset of the generalized 3-D LDA system) has been investigated by Neti and Clark (ref. 23) and Yanta (ref. 24). They found the uncertainty in w to be dependent on the turbulence intensity, N, ϕ and the flow angle.

From these studies and preliminary measurements it was determined that to achieve approximately the same resolution in w, as in u and v, 8000 realizations would be required in each of the v_1 and v_3 channels and that measurements should be restricted to areas where the flow angle in the x-z plane is expected to be greater than 3°. The well behaved results tend to support this analysis.

It should also be mentioned that velocity bias was not considered for this investigation, but is expected to be very small due to the high data rates encountered in both flowfields.

The uncertainty in the Mach number from statisical considerations and from ignoring the w component in regions in which it was not measured is therefore approximately 6% and 3% for 1.6 and 1.3 cases respectively.

RESULTS AND DISCUSSION

Flow Visualization Results

For the Mach 1.6 case, schlieren photographs reveal that the shock becomes bifurcated as it approaches the boundary layer. This behavior is shown in Fig. 7 and was also observed in previous two-dimensional experiments. The photograph indicates reflections arising from the rear legs of the lambda shocks which cross near the tunnel centerline. These phenomena have not been observed in the two-dimensional case. It also shows a slip line extending downstream of the bifurcation point which arises from the air flow on either side having passed through different shock systems. The surface oil flow visualization indicates that there are large separation regions in the corners of the tunnel near the interaction region. This is shown in Fig. 8. These separated flow regions contribute to the three-dimensional nature of the interaction and impart a nozzle effect which together with the thickening of the boundary layer in the vicinity of the shock causes the reacceleration in the freestream behind the normal shock. This reacceleration region terminates at the secondary shock whereupon it reaccelerates and shocks down once more before leaving the test section.

For the Mach 1.3 case, the schlieren photographs, shown in Fig. 9, reveal a different shock structure from that found in the Mach 1.6 case. The shock degenerates as it approaches the boundary layer with no indication of a lambda shock, as in the 1.6 case. Figure 9 does indicate weak oblique shocks forward of the main shock which terminate in the boundary layer. This appears to be a precursor of the forward leg of the lambda shock that appears in the higher Mach number flows. Oil flow visualization indicates that no or very isolated corner separation occurs in the Mach 1.3 case. This is shown in Fig. 10.

Surface Static Pressure Measurements

The floor static pressure distributions for the two test cases were normalized to the upstream mid-span static pressure and are plotted in Figs. 11 and 12. These plots show the symmetry of the flow as well as a sweeping forward of the pressure gradient in the corners. This is more pronounced in the 1.6 case, indicating a sweeping forward of the front legs of the lambda as was also confirmed in the LDA results.

LDA Results

The results of the Mach 1.6 investigation show that the flow follows the one-dimensional normal shock relationships only in the center of the tunnel, and then, only immediately downstream of the shock. This flow is reaccelerated to become supersonic and then experiences a much weaker set of secondary shocks. This can be seen in Fig. 13. The growth in the boundary layer due to the adverse pressure gradient is also indicated. Just downstream of the bifurcation point a slip line can

be seen as has been indicated in previous two-dimensional investigations. The slip line is obscured further downstream due to the reacceleration in the freestream and the secondary shocks associated with the three-dimensionality of the flow.

Although LDA surveys were made near the corner, as close as 1 cm (0.4 inches) from the sidewall and floor, no reverse flow was ever detected. The lowest velocity measured in this region was approximately 100 m/s (328 fps). The cross section data for the Mach 1.6 case are plotted in Fig. 14. A sweeping forward of the front legs of the lambda shock near the corner and a sweeping back of the rear legs are evident. Just downstream of the shock, the flow is subsonic in the freestream, but remains supersonic near the corner. This region extends downstream where it interacts with the reacceleration region and the secondary shocks and then becomes indistinguishable. At this point the boundary layer has become very large. At x = 24cm (9.4 inches), the flowfield has just passed through the secondary shock, i.e., the flow in the freestream is slightly slower than that nearer the corner. At x = 30cm (11.8 inches), the flow is about to experience another weak normal shock. At x = 35cm (13.8 inches), the flow is nearly uniform in the freesteam and about to exit the test section.

The secondary flow vectors given in terms of Mach number are shown in Fig. 15 for the Mach 1.6 case. The plots show the flow turning away from the walls and corner with little or no secondary flow outside the lambda shock region. The freestream normal shock was maintained at x = 10 cm for both test cases.

The results of the Mach 1.3 investigation indicate a less dynamic, less complicated and more uniform flowfield. As expected, there is no lambda shock. Instead, weak compression waves are seen to extend from the shock into the boundary layer. Figure 16 indicates that along the tunnel centerline, the flow follows closely the one-dimensional normal shock relations. Downstream of the shock in the freestream, the flow gradually accelerates to just under sonic conditions (Mach 0.99).

There is a region of high-speed flow in the corner just downstream of the shock as in the Mach 1.6 case. This supersonic region remains isolated in the corner and becomes smaller and smaller downstream. This is shown in the series of plots in Fig. 17. At the exit of the test section, this region of supersonic flow nearly vanishes, while the remainder of the flowfield is choked.

The secondary flow plots for the 1.3 case (Fig. 18) indicate very little secondary flow relative to the 1.6 case. The plotted results indicate that the slight flow turning is near the limit of resolution for the LDA system which is a function of the flowfield turbulence and flow angle. The plots indicate a tendency of the flow to turn away from the corner as in the 1.6 case. A vortical flow is indicated in the x = 10 cm plot which is at the shock location.

CONCLUDING REMARKS

The test results reveal that the structure of the shock system, the three-dimensionality and the extent of separation are highly dependent on Mach number. The flowfield associated with the Mach 1.3 interaction is much more uniform and two-dimensional than that found in the Mach 1.6 case. Extensive separation and hence three-dimensionality (in the Mach 1.6 case) caused regions of strong acceleration downstream of the initial shock, thereby inducing a complicated secondary shock system. This causes a consequent erosion of the energy contained in the flow as well

as strong non-uniformities across the flow. Since this is generally undesirable, these tests confirm the general rule of inlet design where normal shocks are designed to occur only at Mach numbers of 1.3 and below.

Efforts are currently under way to investigate the periodic nature of the shock motion from the LDA data already obtained in addition to planning future experimental studies into the unsteady nature of the flow.

REFERENCES

1. Seddon, J., "Flow Produced by Interaction of a Turbulent Boundary Layer with a Normal Shock Wave of Strength Sufficient to Cause Separation," Brit. Aero. Res. Council, Rept. and Memo. No. 3502, March 1960.

2. Chapman,D.R.,Kuehn,D.M. and Larson,H.K., "Investigation of Separated Flows in Supersonic and Subsonic Streams with Emphasis on the Effect of Transition," NACA Rept. 1356, 1958.

3. Mateer,G.G.,Brosh,A. and Viegas,J.R., "A Normal Shock Wave Turbulent Boundary Layer Interaction at Transonic Speeds," AIAA Paper No. 76-161, January 1976.

4. Liepmann,H.W., "The Interaction Between Boundary Layers and Shock Waves in Transonic Flow," Journal of Aeronautical Sciences, Vol. 13, No. 12, 1946, pp. 623-637.

5. Ackert,J.,Feldmann,F. and Rott,N., "Investigations of Compression Shocks and Boundary Layers in Gases Moving at High Speed," NACA TM 1113, Washington,D.C., January 1947.

6. Green,J.E., "Interactions Between Shock Waves and Turbulent Boundary Layers," Royal Aircraft Establishment Technical Report 69098, May 1969.

7. Vidal,R.J.,Wittliff,C.E.,Catlin,P.A. and Sheen,B.H., "Reynolds Number Effects on the Shock Wave/Turbulent Boundary Layer Interaction at Transonic Speeds," AIAA Paper No. 73-661, 6th Fluid and Plasma Dynamics Conference, Palm Springs, California, July, 1973.

8. Klemm,W.J., A Prediction of the Interaction of a Normal Shock Wave with a Separating, Turbulent Boundary Layer, PhD Dissertation, Dartmouth College, 1978.

9. LeBlanc,R. and Goethals,R., "Study of Normal Shock Wave/ Turbulent Boundary Layer Interaction Phenomena in View of Application to Transonic Turbomachines," NASA Technical Translation F-16698, Washington, D.C., December 1975.

10. Kooi,J.W., "Experiment on Transonic Shock Wave Boundary Layer Interaction," National Aerospace Laboratory, the Netherlands, 1975.

11. Mateer,G.G. and Viegas,J.R., "Effect of Mach Number and Reynolds Number on a Normal Shock Wave/Turbulent Boundary Layer Interaction," AIAA Paper No. 79-1502, 1979.

12. Delery,J.M., "Experimental Investigation of Turbulence Properties in Transonic Shock/Boundary Layer Interactions," AIAA Journal, February 1983, p. 180.

13. Om,D., Childs, M.E. and Viegas, J.R., "An Experimental Investigation and Numerical Prediction of a Transonic Normal Shock Wave/Turbulent Boundary Layer Interaction," AIAA Paper No. 82-0990, 1982.

14. Abbiss, J.B., East, L., Nash, C., Parker, P., Pike, P., and Sawyer, W.G., "A Study of the Interaction of a Normal Shock Wave and a Turbulent Boundary Layer Using a Laser Anemometer," Royal Aircraft Establishment Technical Report 75141, Dec. 1975.

15. East, L.F., "The Application of a Laser Anemometer to the Investigation of Shock Wave Boundary Layer Interactions," Royal Aircraft Establishment Technical Memorandum Aero. 1666, February, 1976.

16. Liu, B.Y.H., Whitby, K.T. and Yu, H.H.S., "A Condensation Aerosol Generator for Producing Monodispersed Aerosols in the Size Range 0.036μm to 1.3μm," Journal de Recerches Atmospheriques, 1966.

17. Yanta, W.J., "Measurements of Aerosol Size Distributions with a Laser-Doppler Velocimeter," National Bureau of Standards Special Publication 412, May 1974.

18. Chriss, R.M., Keith, T.G. and Hingst, W.R., "An Evaporation-Condensation Aerosol Generator for LDV Seeding in a Supersonic Wind Tunnel," Particulate and Multiphase Processes, ed. Ariman, T. and Veziroglu, T.N., Vol. 2, p. 347.

19. Maxwell, B.R., Seasholtz, R.G., "Velocity Lag of Solid Particles in Oscillating Gases and in Gases Passing Through Shock Waves," NASA TN D-7490, March 1974.

20. von Stein, H.D. and Pfeifer, H.J., "Investigation of the Velocity Relaxation of Micron Sized Particles in Shock Waves Using Laser Radiation," Applied Optics, Vol. 11, No. 2, February 1972.

21. Snyder, P.K., Orloff, K.L. and Reinath, M.S., "Reduction of Flow Measurement Uncertainties in Laser Velocimeters with Nonorthogonal Channels," AIAA Journal, Vol. 22, August 1984.

22. Orloff, K.L. and Snyder, P.K., "Laser-Doppler Anemometer Measurements Using Nonorthogonal Velocity Components: Error Estimates," Applied Optics, Vol. 21, January 1982.

23. Neti, S. and Clark, W., "On-Axis Velocity Component Measurement with Laser Velocimeters," AIAA Journal, Vol. 17, No. 9, pp. 1013-1015, Sept. 1979.

24. Yanta, W.J., "The Use of the Laser Doppler Velocimeter in Aerodynamic Facilities," AIAA Paper No. 80-0435-CP, March 1980.

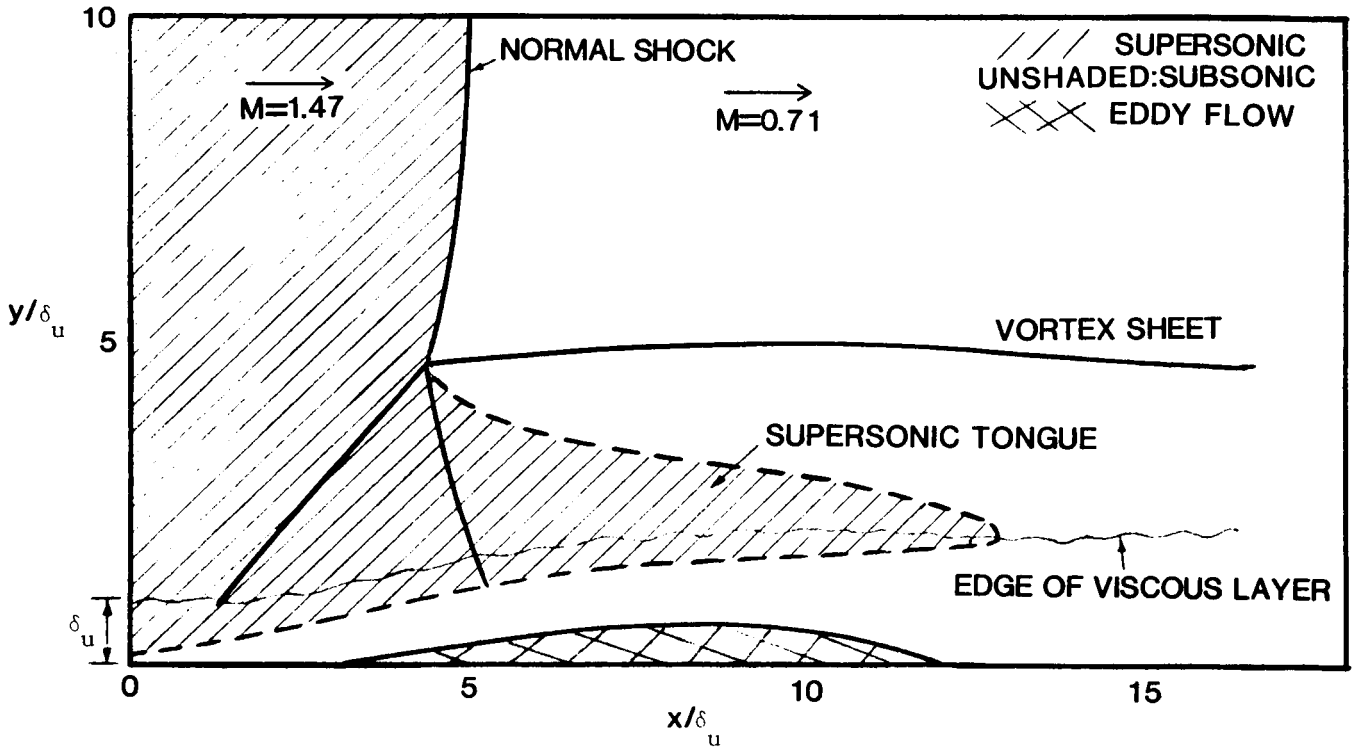

Fig. 1. Seddon's benchmark model of 2-D normal shock wave boundary-layer interaction.

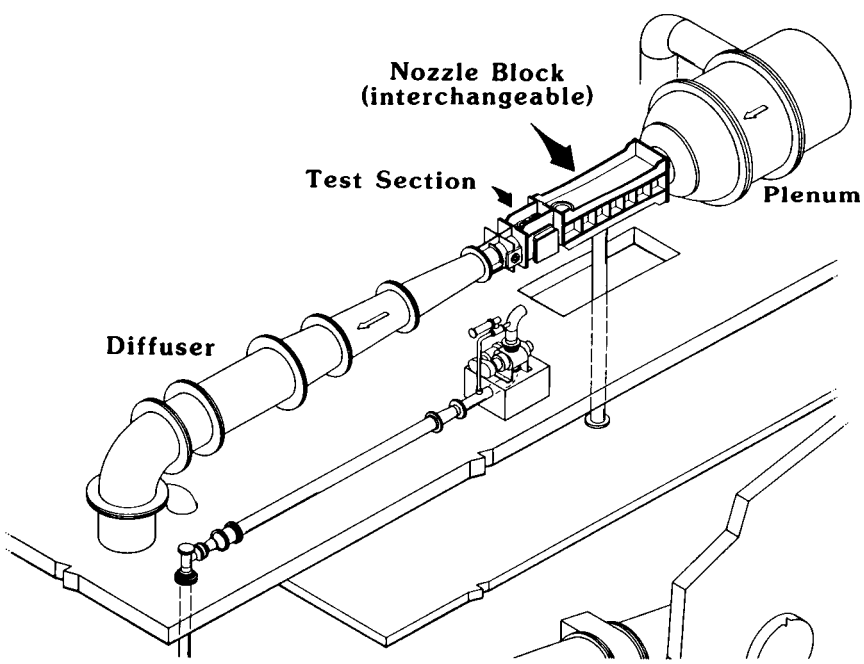

Fig. 2. NASA Lewis Research Center's 1 ft x 1 ft supersonic wind tunnel.

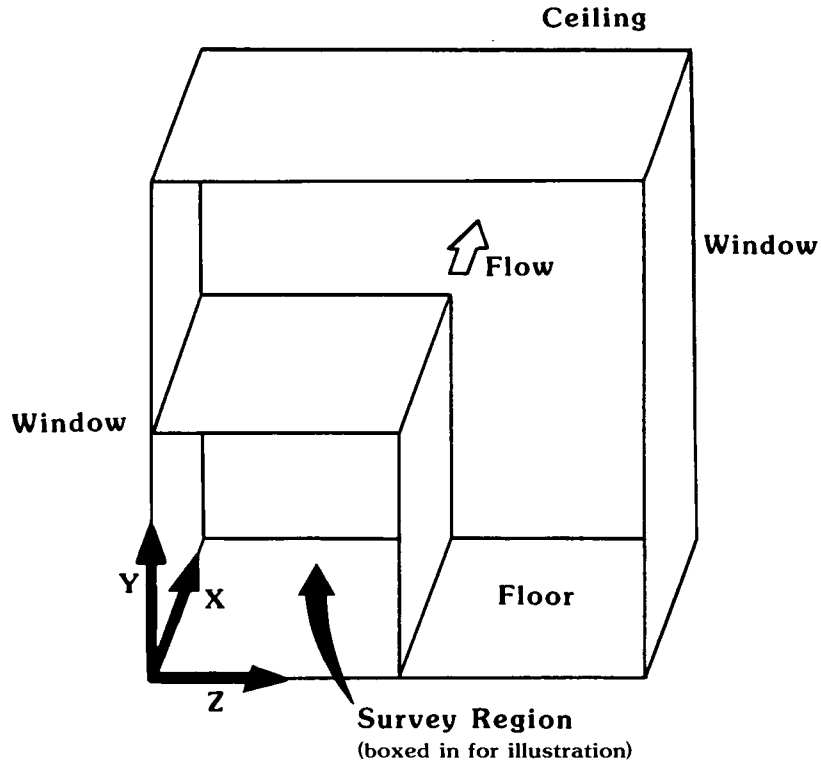

Fig. 3. Test section coordinate system.

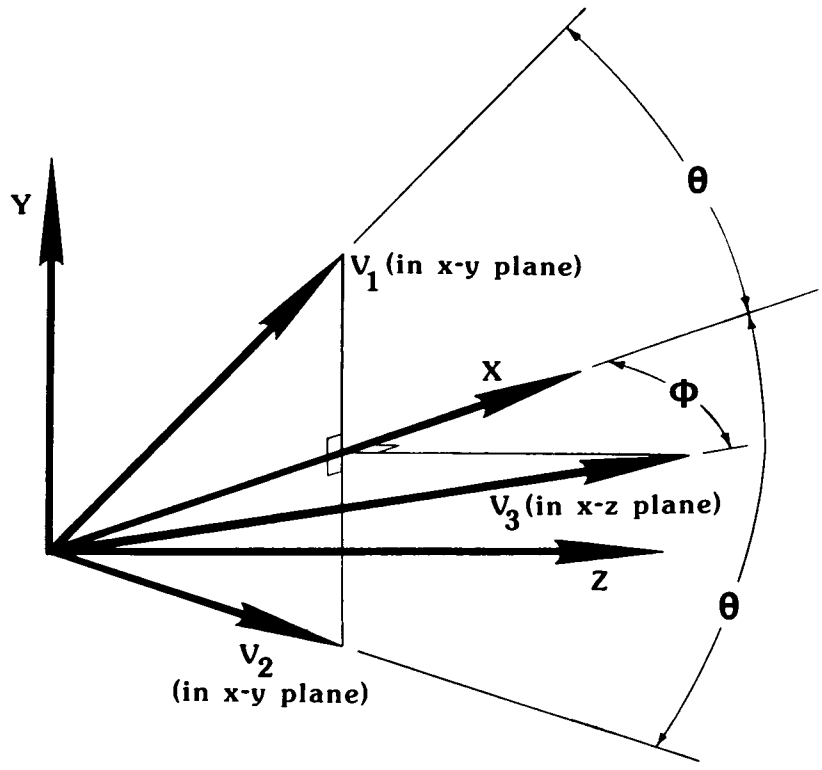

Fig. 4. Nonorthogonal LDA channels.

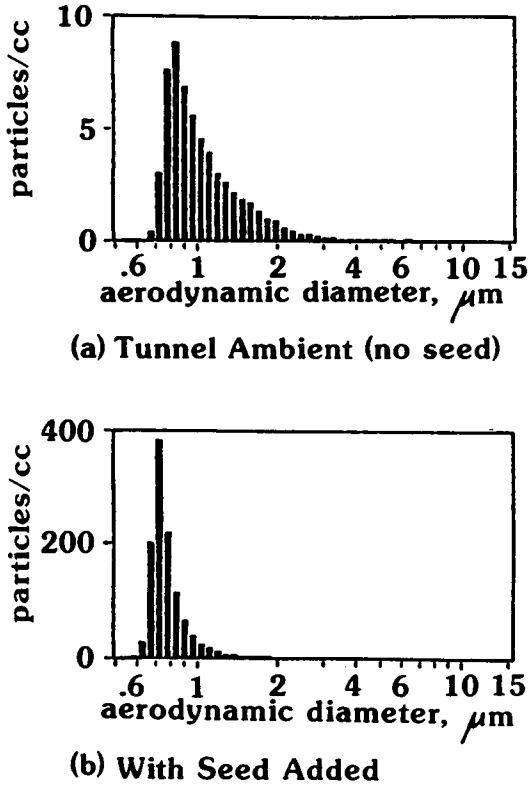

Fig. 5. Comparison of air samples taken from tunnel test section at test conditions with TSI, Inc. APS 33.

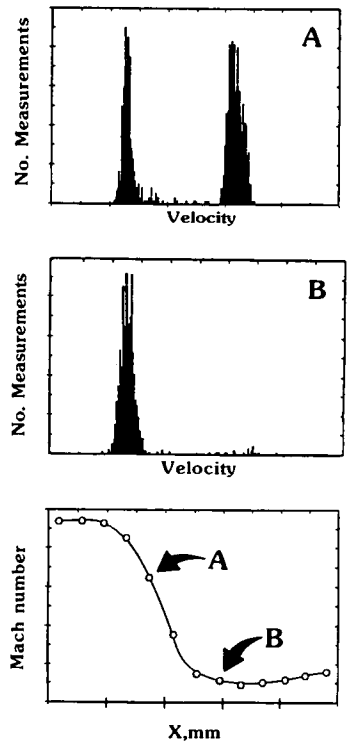

Fig. 6. Sample histograms taken as shock wave oscillates about the LDA probe volume.

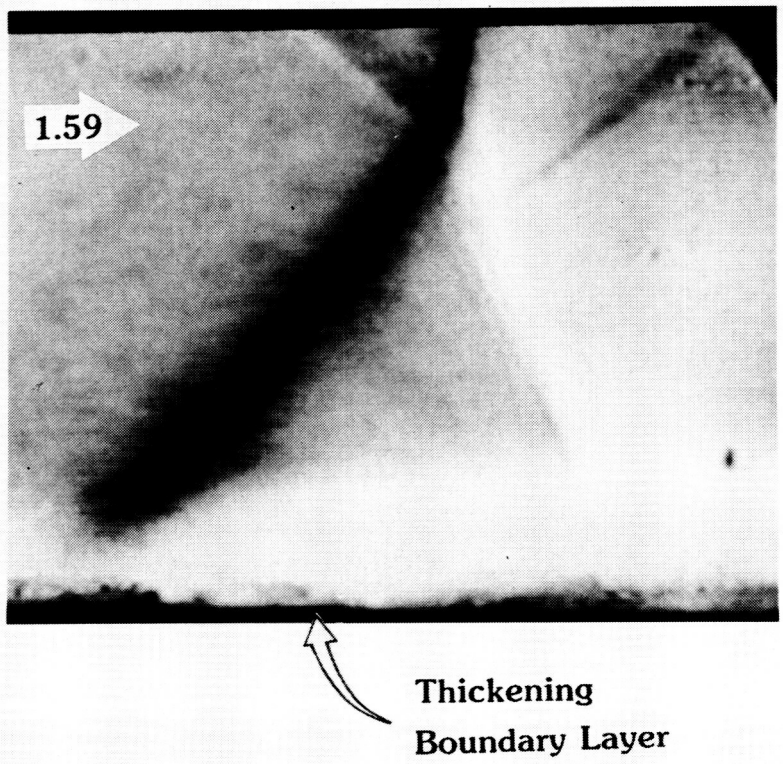

Fig. 7. Schlieren photograph taken at Mach 1.59.

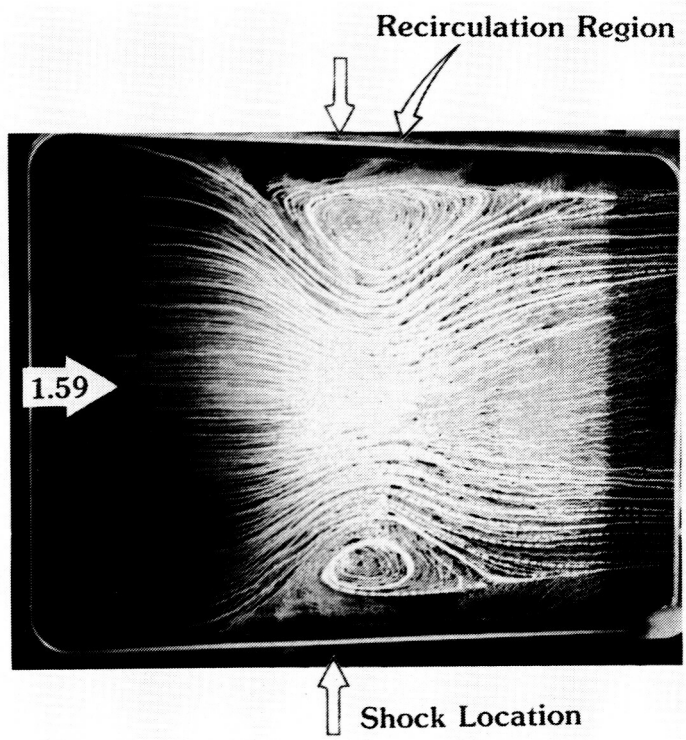

Fig. 8. Surface oil-flow pattern at Mach 1.59.

ORIGINAL PAGE
BLACK AND WHITE PHOTOGRAPH

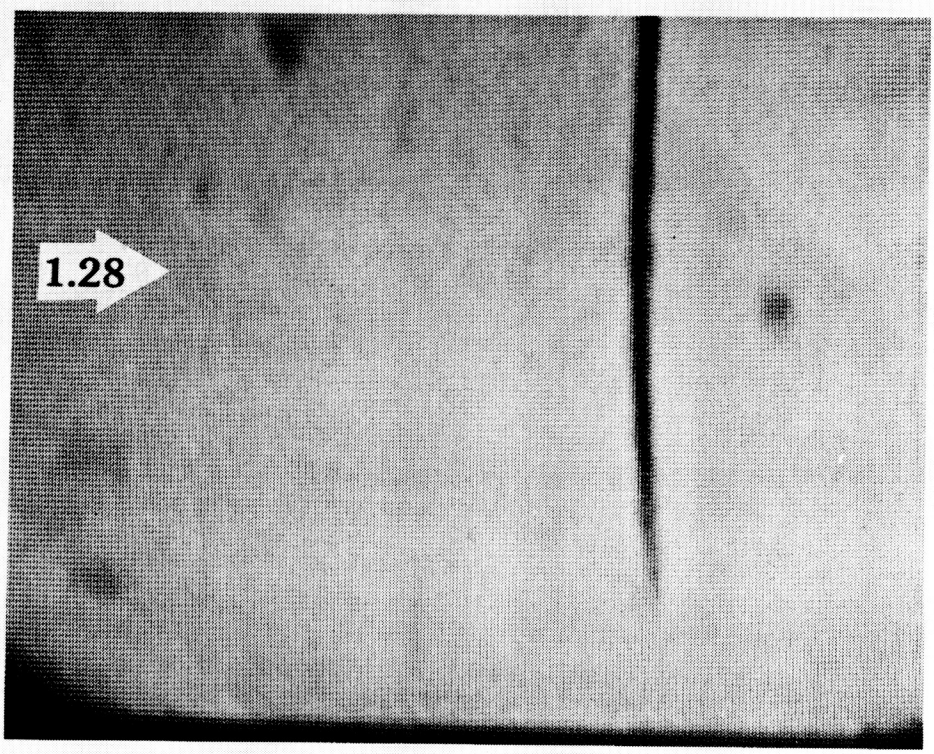

Fig. 9. Schlieren photograph taken at Mach 1.28.

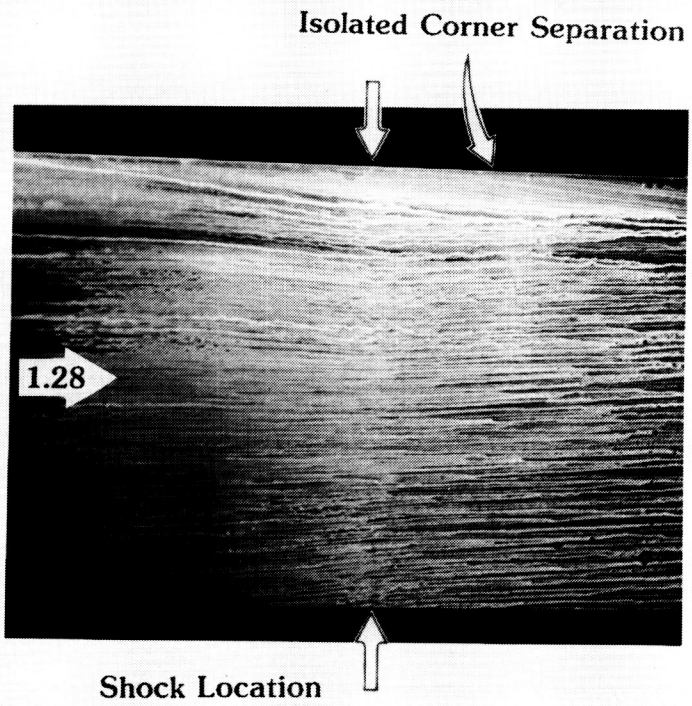

Fig. 10. Surface oil-flow pattern at Mach 1.28.

ORIGINAL PAGE
BLACK AND WHITE PHOTOGRAPH

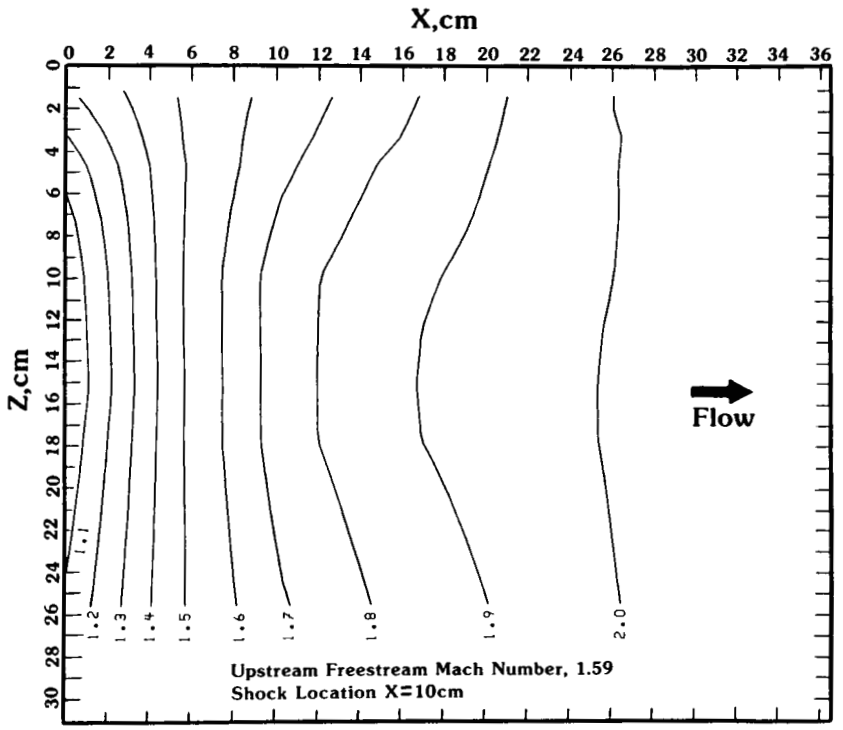

Fig. 11. Floor surface static pressure contours of the Mach 1.6 flow field, normalized to mid-span upstream static.

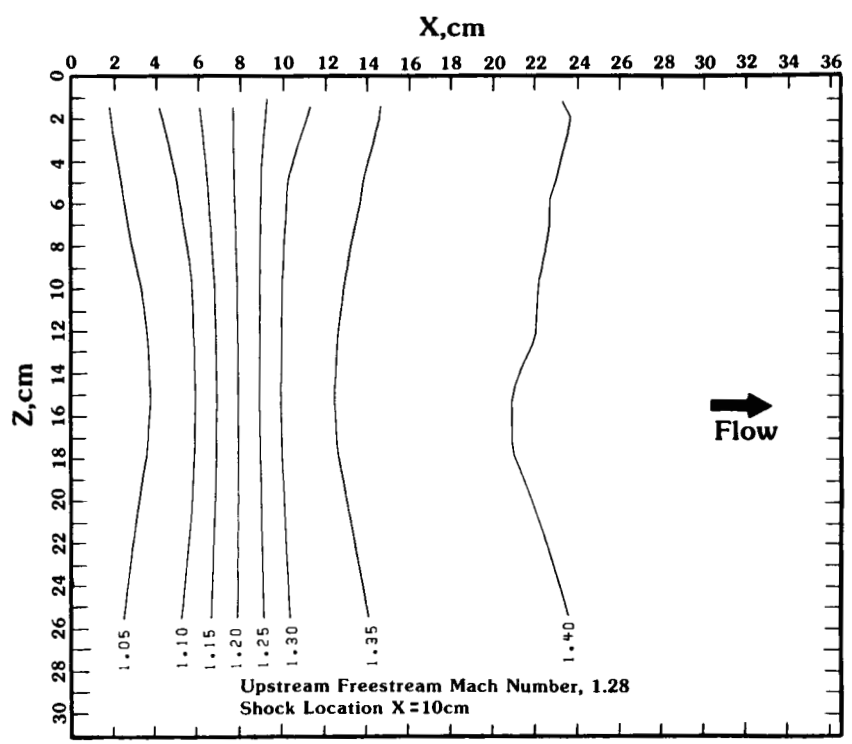

Fig. 12. Floor surface static pressure contours of the Mach 1.3 flow field, normalized to mid-span upstream static.

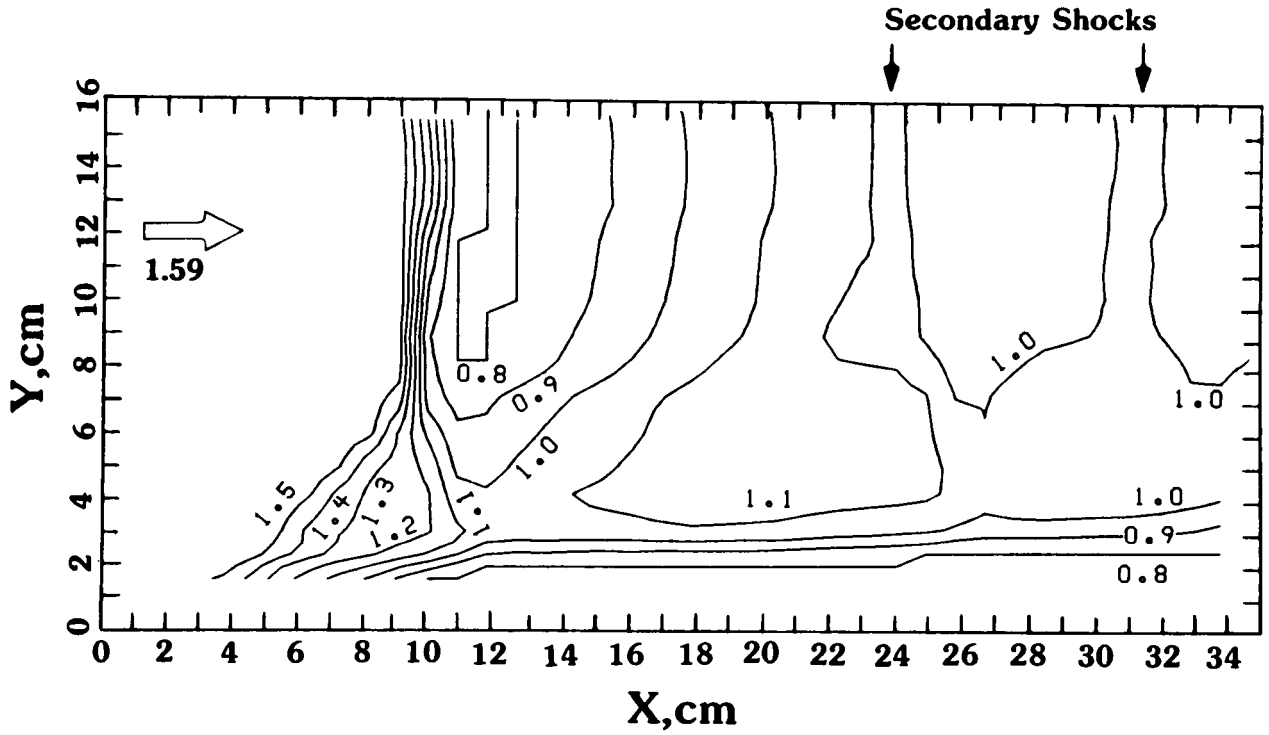

Fig. 13. LDA mid-span Mach number contours (z = 15cm) for the Mach 1.6 test case.

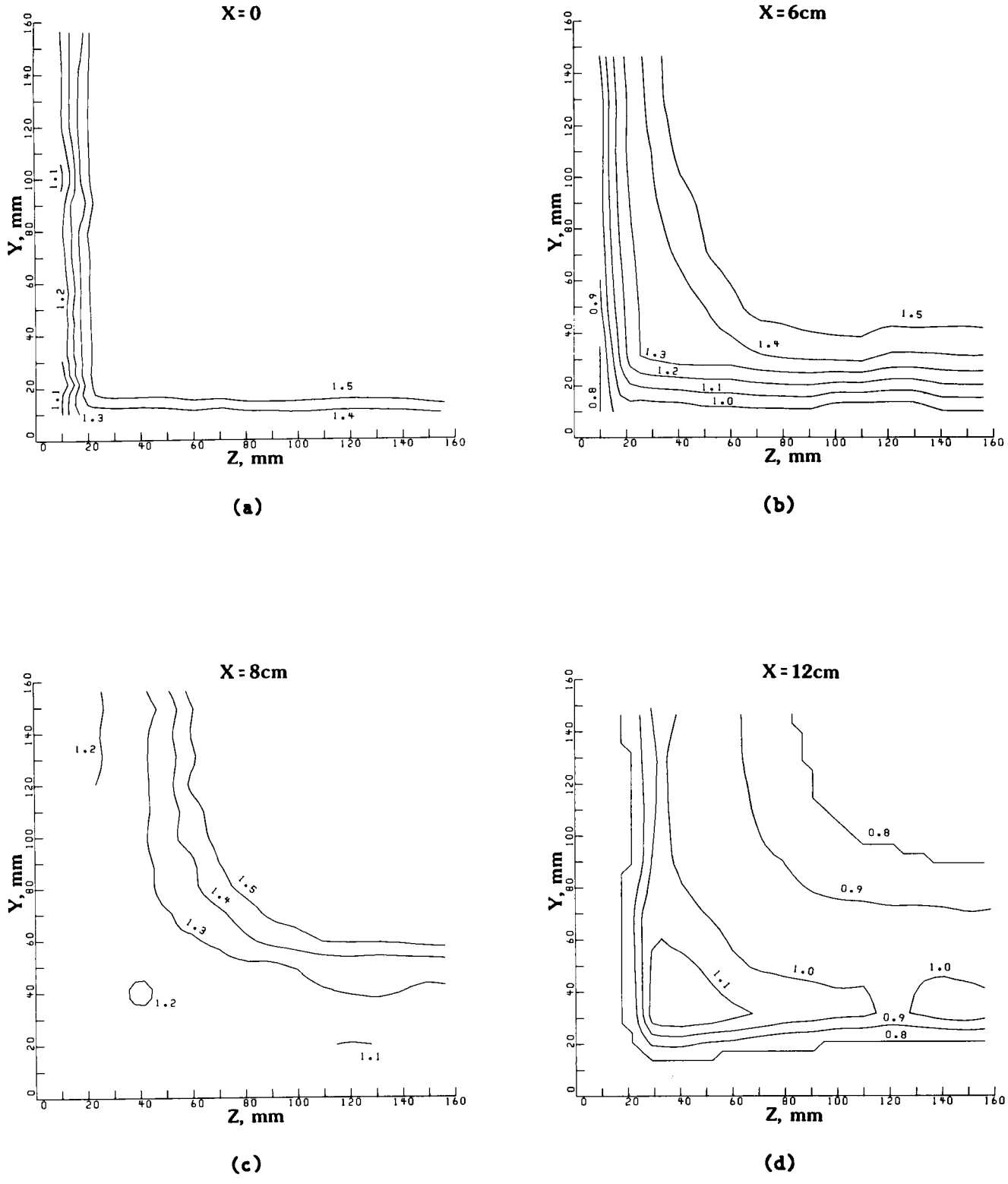

Figure 14. LDA cross-section Mach number contours for Mach 1.6 test case.

ORIGINAL PAGE IS
OF POOR QUALITY

ORIGINAL PAGE IS
OF POOR QUALITY

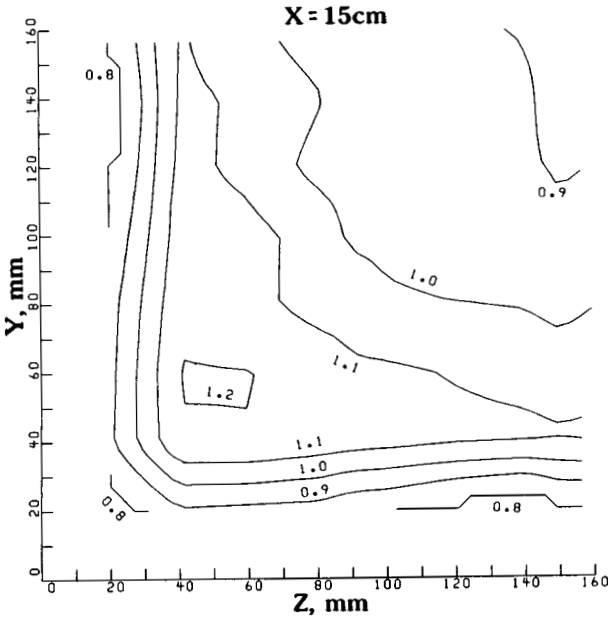

(e)

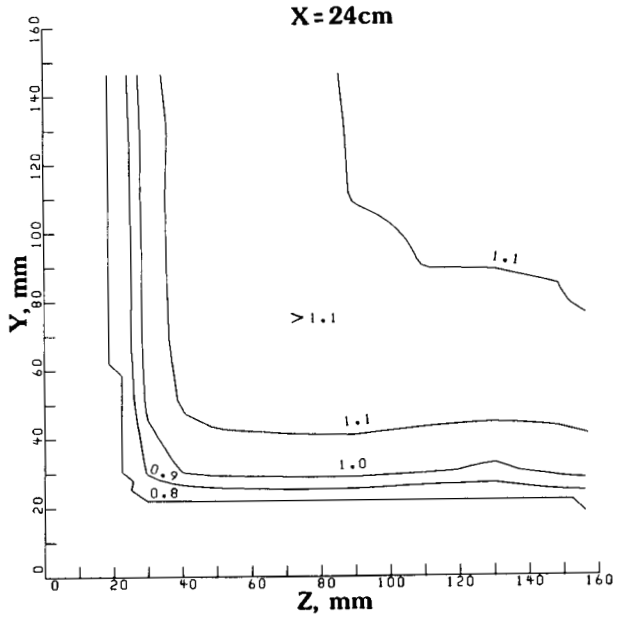

(f)

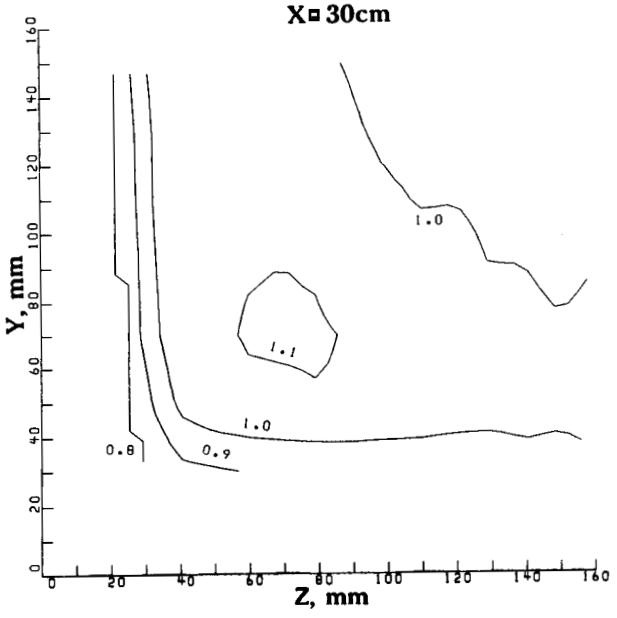

(g)

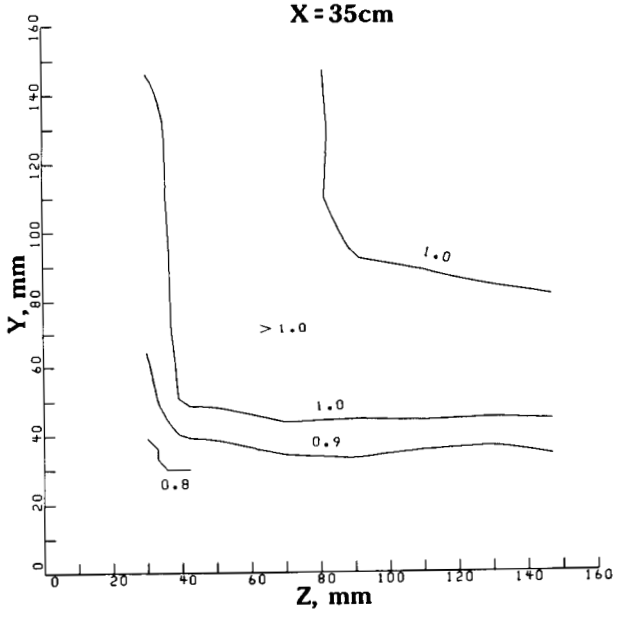

(h)

Figure 14. Concluded.

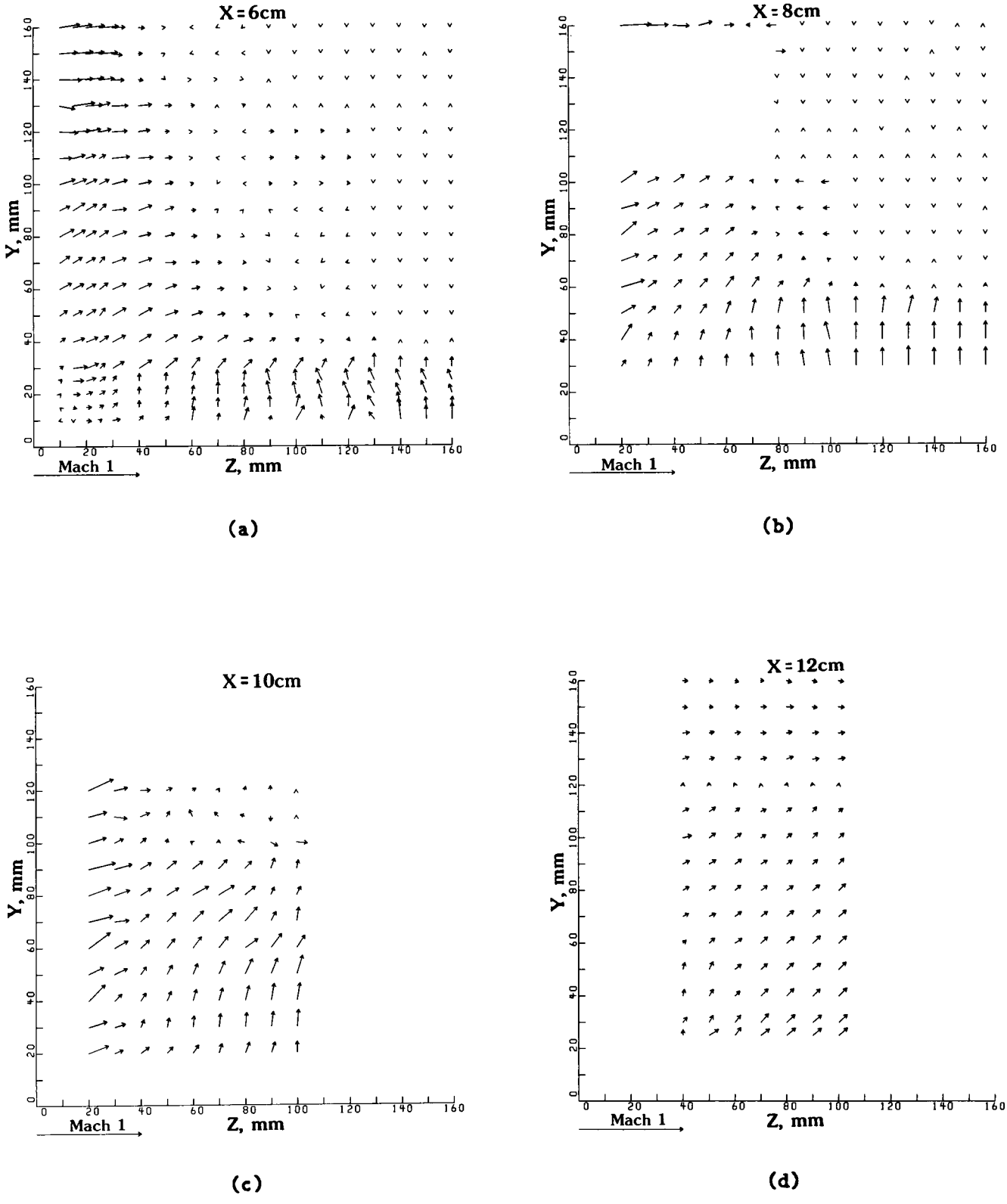

Figure 15. Secondary flow vectors for Mach 1.6 test case.

ORIGINAL PAGE IS
OF POOR QUALITY

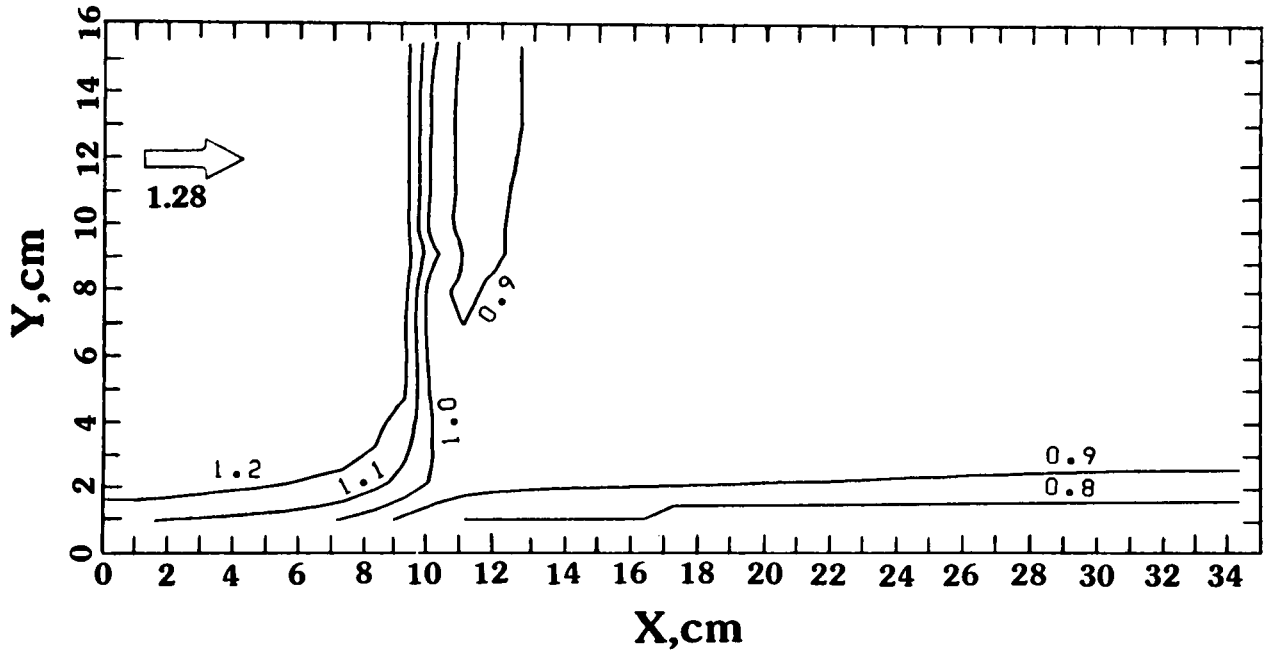

Fig. 16. LDA mid-span Mach number contours (z = 15cm) for the Mach 1.3 test case.

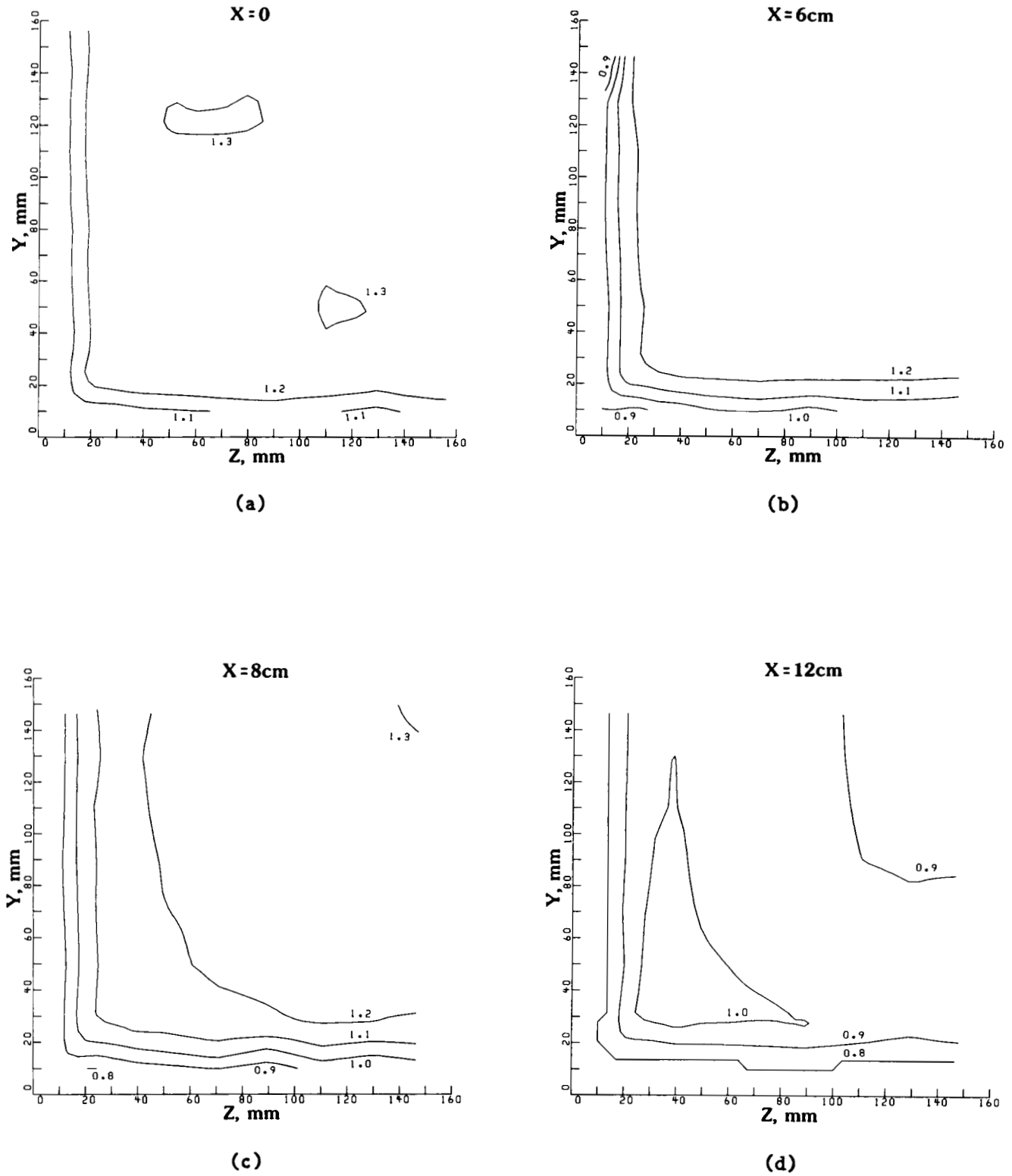

Figure 17. LDA cross-section Mach number contours for Mach 1.3 test case.

ORIGINAL PAGE IS
OF POOR QUALITY

ORIGINAL PAGE IS
OF POOR QUALITY

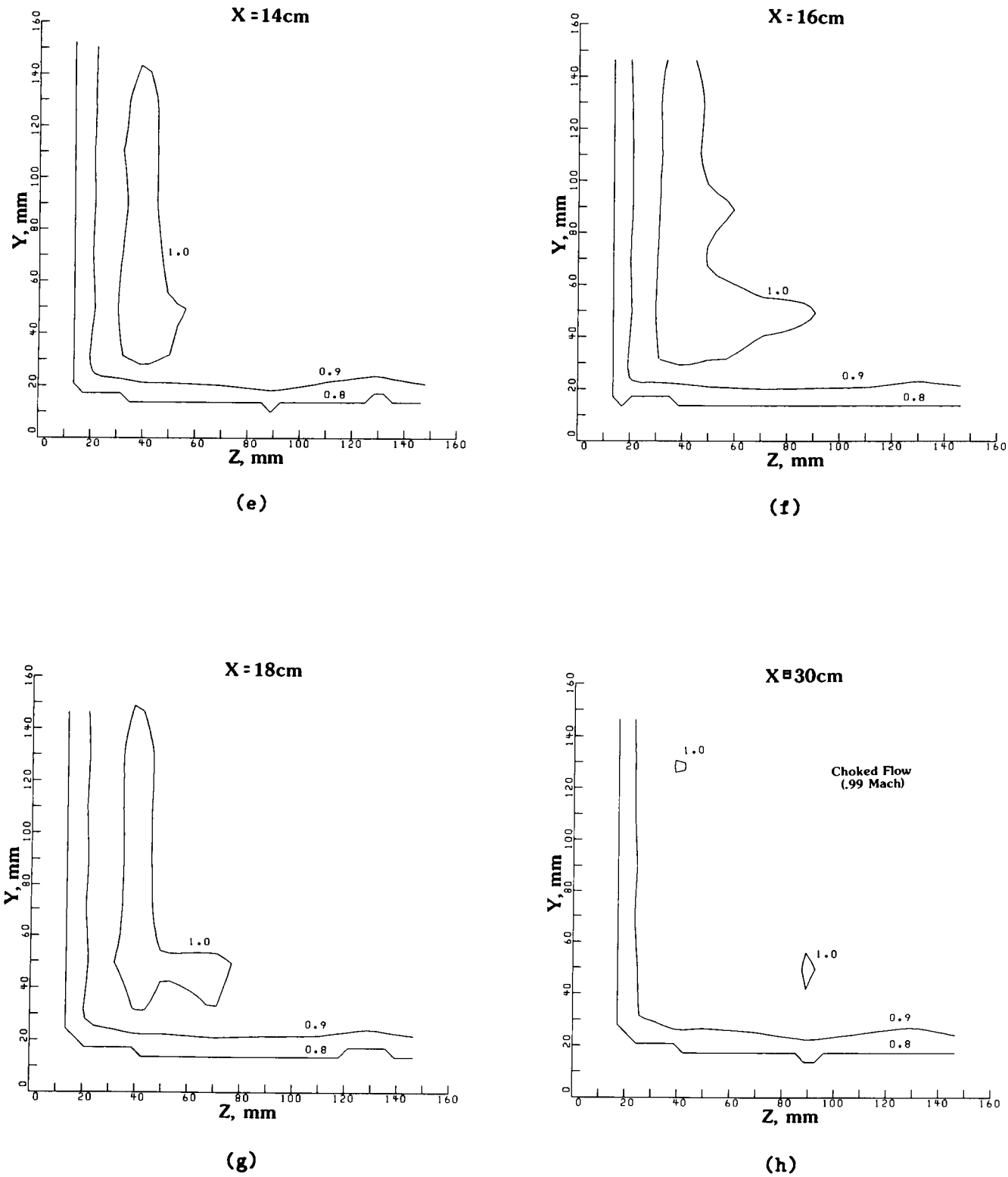

Figure 17. Concluded.

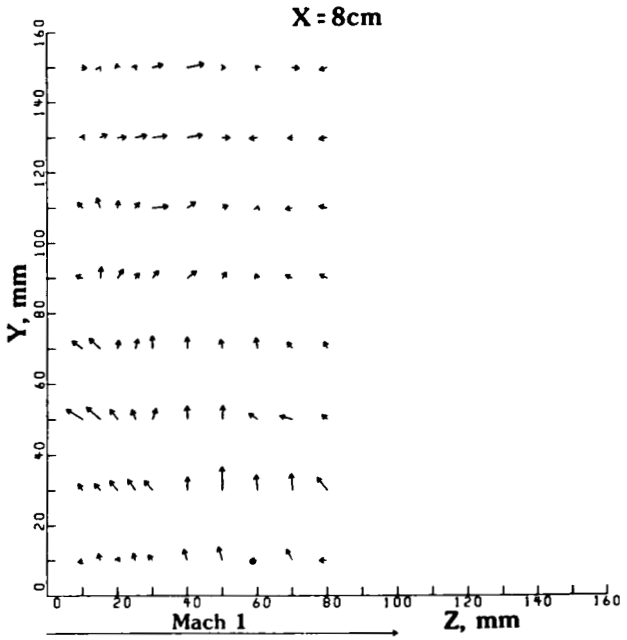

(a)

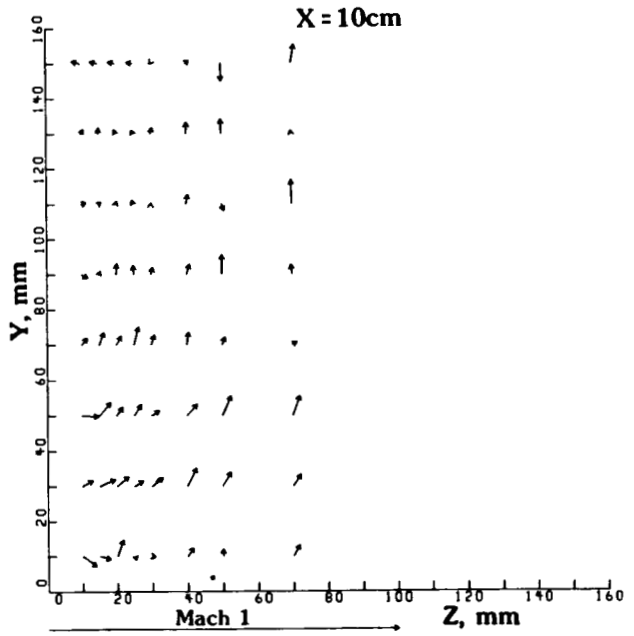

(b)

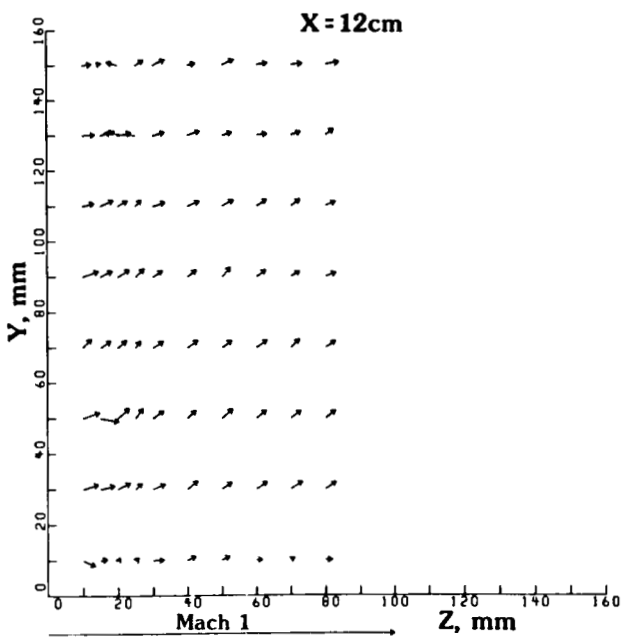

(c)

Figure 18. Secondary flow vectors for Mach 1.3 test case.

ORIGINAL PAGE IS
OF POOR QUALITY

N89-20957

INSTRUMENTATION ADVANCES FOR TRANSONIC TESTING

Percy J. Bobbitt
NASA Langley Research Center
Hampton, Virginia

SUMMARY

New and improved instrumentation, like new and improved wind tunnels, provide capabilities which stimulate innovative research and discovery. During the past few years there have been a number of instrumentation developments which have "aided and abetted" the acquisition of more accurate aerodynamic data and have led to new physical insights as well. The paper reviews some of these advances, particularly in the area of thin-film gages, hot-wire anemometry, and laser instrumentation. A description is given of the instruments and/or techniques and some sample results are shown. Finally, a few ideas for future research are described.

INTRODUCTION

There is an oft quoted statement by Ronald Smelt[1] in his Guggenheim Memorial Lecture of 1978 which reads in part "...in every aeronautical center, it is noteworthy that once the resource was available, there grew up around the facilities a group of people who knew how to use them, and use them wisely..." This observation loses very little of its accuracy if one substitutes the word "instruments" for "facilities". It may well be that he intended "facilities" to include instrumentation, for certainly they go hand in hand. Reference 2 includes both facilities and instrumentation in its list of research "drivers", which were defined as technologies or factors that stimulate research. The impact of new and improved instrumentation can be seen in nearly everything we do of an experimental nature. One can hardly attend an aerodynamics conference these days where instrumentation "breakthroughs" and innovative applications are not being displayed or discussed in some form. Therefore, it is appropriate in a conference which purports to make a statement about the state of the art of experimental transonic aerodynamics, that recent progress in instrumentation be the topic of at least one paper.

Over the past decade there has been a steady growth in the amount of diagnostic experimentation. This is being driven by the availability of new or improved instrumentation, data acquisition computers, and wind tunnel facilities as well as the ever increasing need/desire to validate fluid-dynamics computer codes. So in addition to the general benefits derived from improved or new instrumentation, code validation research will be a major benefactor.

Of particular interest in the present paper are improvements that have been made in several types of thin film gages, hot-wire anemometers, laser instrumentation, and a moving-band skin-friction gage. It will be shown that in many cases more accurate measurements can be made than just a few years ago

and, in others, measurements (or understanding) not previously possible can be acquired. The instruments will be discussed in the order just mentioned; some thoughts about future work will also be offered. Most of the research presented has been carried out or sponsored by the Langley Research Center (LaRC) Transonic Aerodynamics Division, and some was in collaboration with other LaRC organizations.

NOMENCLATURE

A	amplitude of boundary-layer disturbance
A_o	amplitude of boundary-layer disturbance at neutral stability
C_f	skin friction coefficient
C_L	lift coefficient
C_p	pressure coefficient
c	airfoil chord
E	mean voltage across hot film
e	fluctuating voltage
f	frequency
M	Mach number
m	mass flow
n	logarithmic exponent of T-S wave growth rates, $n = \ln (A/A_o)$
p	pressure
R	Reynolds number per foot, 1/ft
R_c	Reynolds number based on chord
R_θ	Reynolds number based on momentum thickness
SiO_2	Silicon Dioxide
S_{T_t}	$\left(\frac{\partial \log E}{\partial \log T_t}\right)_{u,\ \rho,\ T_w}$ or $\left(\frac{\partial \log E}{\partial \log T_t}\right)_{m,\ T_w}$
S_u	$\left(\frac{\partial \log E}{\partial \log u}\right)_{\rho,\ T_t,\ T_w}$

S_ρ	$\left(\frac{\partial \log E}{\partial \log \rho}\right)_{u,\ T_t,\ T_w}$
T	mean temperature
u	velocity in flow direction
v	velocity in vertical direction
w	velocity in horizontal direction
x	chordwise distance from leading edge of airfoil
α	angle of attack, degrees
δ_f	trailing-edge flap deflection
γ	ratio of specific heats
ρ	density
°R	degrees Rankine

Abbreviations:

Å	angstrom (10^{-10} meters)
COSAL	name of compressible boundary-layer stability code
Hz	Hertz, cycles/sec
IRD	Langley Research Center, Instrument Research Division
L	laminar
LDV	Laser doppler velocimeter
LTPT	Low-Turbulence Pressure Tunnel
mv	milli-volt
NAE	Canadian Natural Aeronautical Establishment
NLF	natural laminar flow
NTF	National Transonic Facility
SALLY	name of incompressible boundary-layer stability code
T	turbulent
TCT	Transonic Cryogenic Tunnel
T-S	Tollmien-Schlichting

Superscripts:

~	root-mean square value
-	mean value
'	instantaneous value

Subscripts:

aw	adiabatic wall
max	maximum value
T	end of transition
t	total condition also start of transition
tr	value at transition
w	wall
∞	free-stream conditions

THIN-FILM SENSORS

The use of thin-film (or hot-film) sensors spans a number of decades with application to both heat transfer and transition. In recent years the increase in the amount of laminar-flow experimentation has resulted in a corresponding increase in the use of thin-film sensors. Tests of laminar-flow airfoils and wings are greatly enhanced if they include a determination of where transition takes place. Of nearly equal importance is the identification of the most amplified frequency since it is this quantity that determines transition as predicted by classical stability theory. In the subsequent sections a variety of thin-film gages will be discussed with some sample data to indicate the type of information that one can extract using these gages.

Patch Thin-Film Gages

Transition detection has been accomplished using stick-on or patch gages individually or in arrays. The latter permits the mapping of transition zones or the monitoring of the movement of transition as flow conditions change. A row of patch gages on a laminar-flow airfoil model in the Low-Turbulence Pressure Tunnel (LTPT) and on a laminar-flow wing (Cessna 210 with laminar glove) are shown in figures 1(a) and 2, respectively. Figure 1(b) shows an enlarged photograph of the patch gages on the airfoil model in the LTPT and the trailing flexible leads connected to terminal blocks. Each thin-film patch gage will cause transition; consequently, downstream gages must be displaced laterally to make an uncontaminated measurement.

Normally, one looks at the amplitude and character of the output signals to make a determination if the flow is laminar, transitional, or turbulent. This was done in both the wind tunnel and flight experiments, and transition was easily detected. Transition-location results from these investigations are plotted in figure 3 including several points determined from sublimating chemicals in flight. When these data are compared with each other and to calculated results from incompressible stability theory, it is evident that they all agree quite well.

The LTPT test mentioned above had an additional significance since it was during the course of this investigation that J. P. Stack[3] showed for the first time that these gages were sensitive enough to enable the detection of the most amplified frequency. Figure 4 gives the spectrum from one of the patch gages of the LTPT tests and clearly shows that a Tollmein-Schlichting wave of 1.4 KHz was the most amplified frequency. Stability calculations carried out for the same conditions as the test (right side of figure 4) also indicated that the most amplified frequency was in the vicinity of 1500 Hz and added credibility to the discovery.

Patch gages have also been employed in flight tests[4] and produced results similar to those obtained in the wind tunnel except they are for a higher Mach number (M = 0.79). The experiments were carried out on the top side of the wing of a Lear 28/29 as pictured in figure 5. Several gages were located at a number of chordwise locations but most of the data were obtained at the 30 and 40 percent chord locations. Power spectra obtained at these two locations are shown in figure 6 and, as in the wind tunnel tests (figure 4), the most amplified frequencies are easily seen. These frequencies, however, are in the range of 4 to 5.5 thousand, which are much higher than those encountered at low speed. Another noteworthy feature of the data of figure 6 is the amplification in the range of 8.35 to 11.10k Hz.

Stability calculations were carried out with both incompressible and compressible codes using the measured distribution and the results displayed in reference 4. Figure 7, taken from this reference, shows the experimental pressure distribution and the wave amplification ratio (n factor) for a range of frequencies up to 7000 Hz, calculated using the SALLY incompressible code. The most amplified frequency is 5600 Hz which is in good agreement with the thin-film data; the corresponding n factor is approximately 8.3. Compressible calculations using the COSAL code indicate an n factor of 3.9 at transition which is much lower than most would expect.

Plug Thin-Film Gages

Plug type gages can be used in the same way as patch gages[5] but have the added advantage that they are flush with the surface and, unlike the patch gages, do not cause transition. Consequently, one gage can be placed directly downstream of another. Their disadvantage is that they are more difficult to install. The laminar-flow control (LFC) airfoil experiment in the 8' TPT utilizes plug gages[6,7] to determine the regions where the flow is laminar or turbulent. Figure 8 shows an enlarged picture of a plug-gage installation where the plug gages are made of quartz with a diameter of 0.06 in. A map of the surface of the LFC airfoil with the letters L and T at the various gage locations to indicate the state of the flow for a particular test is given on

the left side of figure 9. On the right of figure 9 are typical time traces of the voltage output from gages as one moves from the laminar region (bottom of figure) through the transitional zone and finally (top of figure) to the turbulent flow near the trailing edge. These gage outputs are monitored in real time as an aid in adjusting the suction distribution on the airfoil. In addition, the signals are electronically analyzed to determine the state of the boundary layer at each gage for recording.

Surface Deposited Thin-Film-Gage Arrays

For wing or airfoil models with chords of just a few inches, neither patch or plug gages are appropriate. However, there are several gage, or sensor, array concepts that have been invented which are quite capable of "filling the bill." One of these is the McDonnell-Douglas developed vapor deposited hot-film gages and gold leads all on an epoxy dielectric substrate (see figure 10). A photograph of an airfoil model equipped with these films installed in the Langley 0.3-Meter TCT is given in figure 11(a) in which the gold leads are clearly visible; the sensor itself can be seen in the enlarged picture in figure 11(b). Of course, some means of carrying the electrical signals from the gold leads to the anemometer cables must be provided. Figure 12 shows a picture of the end of the airfoil model where the contact points are labeled and the anemometer leads can be easily seen.

Typical results from the 0.3-M TCT are presented in figure 13 taken from reference 8. Shown in figure 13(a) is a typical pressure distribution for a Mach number of 0.6, R_c of 7.5×10^6, and angle of attack of -4°. Figure 13(b) gives, for the same free-stream conditions, the normalized RMS voltages for eight sensors along the chord of the supercritical airfoil at adiabatic wall conditions. The fluctuating voltages from each of these gages is also given. The gage nearest the leading edge indicates a very low amplitude oscillation indicative of laminar flow while the second indicates short periods of laminar flow followed by turbulent bursts (large voltage spikes). At an x/c of 0.2, the location of the forth gage, the flow has become fully turbulent. Data for several Mach numbers and T_w/T_t ratios are given in reference 8 and clearly demonstrate the viability of the vapor deposited sensors.

Despite the success of the 0.3-M TCT tests, a large number of gages were lost and it was clear that some improvements to the gage system were desirable. After considerable effort and numerous trials, a new metalization process was formulated[9]. It has a 0.0003 inch dielectric substrate of parylene C, which also serves as a strain isolation pad, covered by an even thinner layer of silicon dioxide SiO_2 (see figure 14). The hot-film sensor and leads are deposited on the SiO_2 and are composed of nickel and aluminum, respectively. Aluminum is used instead of gold because it adhears to the SiO_2 much better than gold.

Proof of concept tests were carried out in the NTF with a sidewall mounted model as shown in figure 15 and in a small calibration tunnel with the model shown in figure 16. The NTF model used a 20% thick symmetric airfoil with an 8 inch span mounted on the tunnel side wall. Tests of this model showed that the new hot film and substrate materials worked well together at both ambient and cryogenic temperatures (down to -247° F).

The model used in the low speed calibration tunnel, shown in figure 17, had a NACA 0012 airfoil section, a 12-inch chord, and a 12-inch span. A slot was cut in the upper surface for a 3-in. by 10-in. aluminum insert on which 30 hot-film gages were deposited (figure 18). Normalized RMS voltages from a number of sensors along the chord of this model are plotted in figure 19. Free-stream conditions are $M_\infty = 0.122$ and an angle of attack of zero degrees ($R_c = 0.86 \times 10^6$). Also shown in figure 19 are time traces of the voltage output to indicate the signal differences that go with laminar, transitional, and turbulent flow. Spectral analysis of three of these signals near the onset of transition yield the curves in figure 20. Of particular note here is the peak near 2.5 KHz which was the frequency predicted to be the most amplified.

In summary, a technique has been developed to deposit a dielectric, hot-film gages and leads on a model surface, which will function at cryogenic temperatures and has the potential for providing much needed transition data at high Reynolds numbers at transonic speeds. However, tests on wings on complete aircraft models in a cryogenic wind tunnel are still required to firmly establish this form of thin film technology.

Thin-Film-Gage Arrays on Polyimide Substrate

Another thin-film array concept which is being developed consists of a number of individual nickel films electron-beam evaporated on a thin (0.05 mm) polyimide substrate (figure 21).[10] Each sensor consists of a Nickel film 0.9-mm long and 0.15-mm wide with 50 micron copper-coated nickel leads routed to the attachment point of the anemometer leads. The films may be positioned very close together in a single row or a number of rows, and they can be aligned either with the chord or on a diagonal. One of the first arrays using the very small spacing is shown in the photograph of figure 22 where 30 sensors are mounted at 0.1-inch intervals. It was bonded to a low-speed natural laminar-flow (NLF) airfoil with a chord of 15 cm and with the sensors positioned in the streamwise direction on the top surface. The first sensor is located at 0.45 c and the last at 0.95 c.

The leads of the sensors shown in figure 22 run to the trailing edge where they are taken out to the anemometer. Clearly, this arrangement was not meant to provide definitive force and moment data but to prove the sensor-array concept and investigate the characteristics of the gage outputs. The 30 gages in the array were scanned in groups of 8 since only 8 anemomenters were available. A multichannel switch was used to connect the desired sensor group to the constant temperature anemometers which simultaneously heated the film to a nominal 50°C (122°F) above recovery temperature. This required only a small amount of heat and the heated thin films cause little disturbance to the shear layer or to each other. This was established by heating each sensor individually and in groups, with the downstream sensor maintained at a cold temperature. The sensor signals were amplified by an A-C coupled amplifier and recorded on an analog tape recorder. Signals from the amplifier were also provided to an array of oscilloscopes to provide on-line time-history traces.

The NLF airfoil used in the test is designated LRN(1)-1010 and was chosen because of its known laminar separation characteristics at low Reynolds number. Pressure distribution on this airfoil obtained in a low-speed tunnel at a Mach

number of 0.06 and a Reynolds number of 200,000 are plotted in figure 23. A separation bubble exists at all angles of attack plotted in the vicinity of 0.70c.

Typical time histories from the thin-film gages at different locations along the chord of the airfoil are shown in figure 24 beginning with the "laminar-flow" signal at x/c = 0.467. Time traces are given for a location further downstream, just past separation (x/c = 0.667), at the beginning of transition (x/c = 0.717), at peak separation (x/c = 0.750), and finally at reattachment (x/c = 0.883). An interesting discovery reported in reference 10 was that if only the low frequency components (< 20 H_z) of the signals are retained, one can see a clear phase reversal of the signals from gages on either side of separation. Figure 25 shows this effect where the signals ahead of and downstream of x/c = 0.65, the separation point, are out of phase. The same type of signal reversal occurs at reattachment.

An analysis of the spectra of a signal trace from a gage near the onset of transition has been carried out to demonstrate that the present sensors also have the sensitivity to detect the most amplified T-S frequencies which lead to transition. Figure 26 shows the auto correlation of the thin-film signals of the gage at x/c = 0.6 and the results from a boundary-layer stability calculation using the SALLY code. Clearly the most amplified frequencies from the experiment are in the range of 1000 to 2200 Hz; the theoretical frequencies are in the same range.

Tests of an improved gage array on the polyimide substrate were carried out in the Langley Low-Turbulence Pressure Tunnel (LTPT).[11] The multielement sensor leads in this test ran spanwise (see figure 27) so that the anemometer leads were connected at the tunnel wall and, consequently, the flow was not distorted at the trailing edge as was the case for the prototype configuration. Another difference of these tests was the airfoil model, which had an Eppler 387 section and a 6-inch chord. The results obtained in the LTPT test were similar to those described previously; separation and reattachment were easily detected. Figure 28 showing filtered and unfiltered signals in the vicinity of reattachment shows the low energy signal at reattachment, x/c = 0.687, and the signal reversal on either side. Phase correlations of the signals from the gages on either side of reattachment and separation confirm the reversals.

The tests of the polyimide based thin-film gages described preivously have all been low speed. High-subsonic speed tests have also been carried out in the 0.3-M TCT to look not only at separation and reattachment but to explore the possibility that new diagonostic information related to the supersonic zone and shock interaction could be obtained from the thin-film signals. Films were bonded on both the top and bottom surface of the airfoil depicted in figure 29(a) but, for a number of reasons, only a few of the gages on the upper surface were operative throughout the tests. Gages on the lower suface yielded some interesting results; a sample is described below.

A test was run with the airfoil of figure 29(a) at an angle of attack of -1.0° and a Mach number of 0.7 ($R_c = 6 \times 10^6$). The resulting lower surface pressure distribution is plotted in figure 29(b) and shows a shock in the vicinity of x/c = 0.33; resolution does not permit a precise determination. If one looks at the gage outputs in this region (see figure 30) and phase

correlations between successive gages (figure 31), it is clear that there is a small separation bubble beneath the foot of the shock. The separation point is somewhere between x/c of 0.326 and 0.343 (see phase reversal in figure 31(c)), and reattachment occurs between x/c = of 0.343 and 0.359 (see phase reversal in figure 31(d)). A close look at the time traces for a long period of time indicated that there is shock unsteadiness and bubble movement. Even though data reduction and analysis of the present test results have just begun, it is clear that more tests are needed at transonic speed including, if possible, some complimentary flow visualization activity.

The development of multielement dynamic shear stress sensors and the discovery of the phase reversal phenomenon at flow separation and reattachment have opened up new avenues for studying surface shear-flow characteristics in ways that were considered impossible until recently. It should now be possible to obtain detailed surface flow characteristics in such hard-to-reach locations as turbomachinery blades and junctures as well as on very thin surfaces. In view of the ability to make simultaneous measurements, the new technique can be used with equal ease for steady as well as unsteady flow conditions and has enormous potential for both ground and flight test applications. Since the entire surface flow field can be mapped, with the right equipment, in "one fell swoop," the time required to conduct an experiment is remarkably small compared to all other existing techniques which are more cumbersome and time-consuming.

Another possible application of thin-film arrays is to determine the direction of the most amplified wave. This is an important quantity at transonic speeds where stability theory predicts that waves propagating at up to 50° or 60° from the stream direction are the most amplified. A gage array with perhaps 5 or 6 rows and twenty sensors on a row could yield the necessary solutions.

HOT-WIRE ANEMOMETRY

Through the 1950's and 60's progress in hot-wire anemometry was aided by advances in computers and electronic equipment, but improvement in the accuracy of results was hindered by assumptions in the data reduction methodlogy. It was the consensus that the problems due to these assumptions were confined to compressible subsonic and transonic flows where mean flow measurements indicated that the voltage measured across a heated wire oriented normal to the flow was a function of velocity, density, and total temperature.[12-17] Several papers were published in the mid seventies by Rose, McDaid, and Horstman[18,19] which reported on results which indicated that the mean voltage across a heated wire was only a function of mass flow and total temperature. Assuming this to be true, they formulated a two probe technique for temperature and mass fluctuations which made the determination of the velocity, mass flow, and density fluctuations tractable.

In 1980 Stainback[20] outlined a new technique utilizing a three wire probe (see figure 32), each with different overheats and a solution technique accounting for sensitivities to velocity, density, and total temperature. For a constant temperature hot-wire anemometer the equation for the instantaneous voltage ratioed to the mean is given by[20]

$$\frac{e'}{E} = S_u\left(\frac{u'}{u}\right) + S_\rho\left(\frac{\rho'}{\rho}\right) + S_{T_t}\left(\frac{T_t'}{T_t}\right)$$

where S_u, S_ρ, S_{T_t} are the sensitivity coefficients. Stainback's approach is to solve equation (1) for the instantaneous value of u, ρ, and T_t. Sensitivity coefficients are obtained from a mean flow calibration and curve fitting techniques; e and E are measured. Solution of the sensitivity-coefficient matrix is abetted by operating the three wires at different overheats provided the heat transfer characteristics of the wires are similar. Additional details of the method and error sources are given in references 20 and 21.

Some results of applying the "3-wire" technique to flow quality measurements in the Langley 0.3-Meter Transonic Cryogenic Tunnel are given in reference 20. It was shown that the sensitivity coefficients for density and velocity are not the same, as often assumed in the past, with that for density generally being higher than that for velocity. It was also demonstrated in reference 22 that mass flow fluctuations were very much less than the velocity fluctuations due to the fact that at high subsonic Mach numbers most of the disturbances are moving upstream from the diffuser. Because of this, u'/u and ρ'/ρ are anti-correlated and the mass flow fluctuations are reduced. Thus, the use of mass flow fluctuations as an indicator of tunnel disturbance levels was shown to be inappropriate.

In the past few months, a flow-quality survey of the Langley 8-foot Transonic Pressure Tunnel has been made utilizing 3-wire and single wire probes and associated data reduction techniques. Data were obtained in the test section using 3-wire probes and in the settling chamber using single wires. Probes were located in a number of locations in the test section but the location which was thought to give flow-quality data that was most representative of that seen by the "laminar" test region on the laminar flow control (LFC) airfoil was one that was ahead of the airfoil 2 1/2 feet off the side wall and 3 feet above the floor. Figure 33 shows this installation with the LFC airfoil downstream of the probe holder.

A 3-wire probe was calibrated on this rake by holding pressure and temperature constant and varying Mach number then changing pressure at the same temperature and repeating the Mach sweep. Temperature was then changed and the process repeated. Data for four pressure levels at a fixed temperature and three temperatures at a fixed density was obtained. Example plots for one of the wires for the variation of S_u, S_{T_t}, and S_ρ with $\log(\rho)$, $\log(u)$, and $\log(T_t)$ respectively are given in figure 34(a). These plots were obtained using a curve fit technique and can be inserted in equation (1) along with those for the other two wires and a 3- by 3-matrix solved for the instantaneous values of ρ, u, T_t, with the voltage from each of the three wires for input. Subsidiary equations allow for the determination of m and p as well.

There are a number of different approaches for using a single wire for the determination of $\tilde{u}/u$. Most require the assumption that the sensitivity of the wire to density and velocity be the same. In one approach, calibrations are done with mass flow and a single sensitivity curve that grossly approximates the points obtained by varying pressure (if one uses a pressure tunnel) and u. This type of approximation is labeled Method I on figure 34(b) and works best at very low Mach numbers where the data tends to collapse on a single line.

A second approach (Method II) uses the slope of the data in the vicinity of the Mach number and pressure of the test. Figure 34(b) shows this approximation for a pressure of 710 psf. This gives a representation of the log(E) dependence on log(ρu) that is quite good for Mach numbers below 0.6. If one takes the slope of the data at $M_\infty = 0.65$ where log(E) is a maximum, then the sensitivity will be zero and the Method will yield ridiculous values of u'. Results for the 3-wire technique and both Method I and II for single wires are discussed below.

Using the 3-wire sensitivity coefficients just described, the RMS values of $\tilde{u}/u$, $\tilde{\rho}/\rho$, $\tilde{T}_t/T_t$, $\tilde{m}/m$, and $\tilde{p}/p$ have been determined for Mach numbers for 0.4 to 0.82. Values of these quantities for a probe location discussed previously (see figure 33) are given in Table I. If one of the wires is treated as a single wire using single-wire data-reduction assumptions, the sensitivity coefficient of Method I and

$$\frac{\tilde{u}}{u} = \frac{\sqrt{\overline{(m'/m)^2} + \overline{(p'/p)^2}}}{[1 + (\gamma - 1) M_\infty^2]}$$

then the values for $\tilde{u}/u$ and $\tilde{m}/m$ labeled 1-wire are obtained. Finally, in the last column of Table I are values of $\tilde{p}/p$ obtained from a microphone in the probe.

Several things stand out in Table I. One is the large differences in the values of $\tilde{u}/u$ and $\tilde{m}/m$ between the 3-wire and single wire results. Another is large differences between the 3-wire $\tilde{p}/p$ and that of the microphone. It must be remembered in looking at these data that most of our thinking relative to what constitutes good flow quality is based on single wire and microphone data. If, in this case, we were to use single-wire thinking in interpreting the single wire data, we would conclude that we have "pretty good" flow quality. On the other hand, if we use single-wire thinking and the 3-wire data we would say we have poor flow quality. The fact is that a whole new set of standards has to be created to decide what is good and bad flow quality when using the 3-wire data.

Another look at single wire data is afforded by figure 35 where $\tilde{u}/u$ and $\tilde{m}/m$ from Method I and II are plotted as a function of free-stream Mach number along with $\tilde{p}/p$. The levels are what one would expect in a good flow quality tunnel and, at the highest Mach numbers where the test section is choked ($M > 0.75$), the levels from Method I are outstanding. The large effect of the "choke" on the levels is clear and, indeed, what most would expect.

Values of $\tilde{u}/u$ from Method II are quite a bit higher than those of Method I but are still an order of magnitude lower than those produced by the 3-wire techniques. A quite different picture emerges if we examine the 3-wire $\tilde{u}/u$ data plotted in figure 36. It is obvious that 3-wire levels are 3 to 4 times higher than those of the single wire and that the choke is less effective. The drop in magnitude of $\tilde{u}/u$ is about the same in each case but the 3-wire level is so high that the relative effect of the choke is much smaller.

Only a few flows have been examined using the 3-wire hot-wire probe. A much larger data base must be created to provide the understanding that will enable the formulation of new standards. One contribution to this understanding will come from an experiment in the Basic Aerodynamic Research Facility to be described later. In this experiment a 3-component LDV will be used along with a 3-wire probe to provide two independent measurements of u/u.

LASER INSTRUMENTATION

Laser velocimeters have been in use for over 2 decades in fluid flow research starting with the work of Yeh and Cummin in 1964.[23] Most of the systems producing data since that time have been 2-component systems and used primarily for mean-flow velocity measurements. Some systems employed forward scatter, others back scatter and within these two-categories a number of different techniques/systems were developed. At Langley 2-component systems have been installed in the 14- by 22-Foot Subsonic Tunnel for helicopter and turboprop flow-field research, in the Vortex Facility for trailing vortex diagnostics and in the 16-Foot Transonic Tunnel for flow-field surveys.

In this section several types of 3-component LDV systems that have been used at LaRC for flow-field surveys will be discussed followed by a description of a laser interferometer being developed for transition measurements. Finally, a short section is included to show some recent results from the use of a laser vapor screen.

3-Component Single Axis LDV

The first use of a 3-D LDV used at this Center for 3-component mean and fluctuating flow-field data was in the LTPT for a juncture-flow investigation.[24,25,26] The system used was a single axis, five-beam optical configuration and is shown in the photograph in figure 37. Optical access was only through a side window in the tunnel test section and precluded the use of an off-axis system. The data obtained from the juncture-flow experiment was highly accurate on the u and v axis but less so on the w axis due to the small beam angle.[27]

A second application of the LDV system of figure 37 was in a study of Taylor-Görtler instabilities in a concave region of the airfoil pictured in figure 38.[28] The airfoil model was equipped with a suction panel in the concave region and patch transition gages just beyond the suction panel. A small sample of the laser results obtained are plotted in color-coded contours in figure 39. Shown in this figure are the mean (top of figure) and fluctuating (bottom of figure) components of the horizontal velocity measured adjacent to the surface in, and just beyond, the concave region. The periodic nature of the vortex spacing is very clear in the LDV measurements and further substantiated by the sublimating-chemical flow visualization pictured in figure 40. Wavelength data from both of these sources (flow visualization and laser) are plotted in figure 41 as a function of unit Reynolds number. Also shown for comparison is the theoretical prediction of Floyan.[29] The figure indicates that the theory agrees with both the laser and flow visualization measurements.

Orthogonal 3-Component LDV

The angle betweem the beams yielding the w, or lateral, velocity component should be made as large as the optical access will permit[28] with an orthogonal arrangement such as that pictured in the photograph of figure 42 yielding the best accuracy. This figure shows the LDV system which has been installed in the transonic Basic Aerodynamic Research Facility (BARF) during its laboratory checkout. Figure 43 shows the same system wrapped around the glass-walled test section of BARF. A better view of the test section is afforded by the photograph in figure 44(a) where the test section with a wall interference model mounted on a sting is shown. Both side walls and the top of the test section are glass; the cross section is 18-in. x 18-in and the length is 55-in. Figure 44(b) gives a sketch of the main components of the BARF including the contraction, test section, plenum, and high-speed diffuser.

The BARF was specifically modified to make 3-D LDV measurements with a system as accurate as technology permits in order to compare LDV measurements with those obtained by multiwire hot-wire anemometers at transonic speeds.[30] A variety of basic attached and separated flows will be "measured" and accuracy relation judgments made where possible. In this connection it is anticipated that high order viscous flow calculations will be an equal partner in many of the accuracy assessments.

The first measurements made in the BARF were of the "free-stream" flow quality in the test section. Some selected data for the RMS unsteady component of the longitudinal velocity are plotted in figure 45 and are preliminary in the truest sense of the word (they were otained just a few days ago). Transients in the tunnel circuit, uniformity of seeding, and the effects of the tunnel vibration and acoustic environments still need to be investigated. The scatter in the LDV data at Mach numbers of 0.4, 0.45, and 0.5 are much larger than one can attribute to instrument accuracy. Repeatability at Mach numbers of 0.1 and 0.2 was excellent; each of the plotted points represents several test points.

The reason for presenting this preliminary data is to make a comparison of the LDV data with that of the 3-wire and 1-wire anemometers. Clearly the LDV and 3-wire measurements of $\tilde{u}/u$ agree quite well in level. Both are at variance with the single wire results obtained using Method I. It should be noted that mean values of the longitudinal velocity obtained by the LDV are in excellent agreement with the values obtained from the pressure system used to determine Mach number in the test section. Further experimentation in this facility will, no doubt, lead to a better understanding of both the laser and 3-wire results.

Laser Interferometer for Transition Measurement

Responding to the need for measurements of boundary-layer transition during wind tunnel experiments, NASA Langley has developed under contract an optical interferometer to nonintrusively detect transition in compressible boundary layers. The device is a highly sensitive differential interferometer capable of detecting optical path-length differences of less than one-thousandth of the wavelength of the laser light.

The interferometer uses a 5-mW helium-neon laser for its light source (see figure 46). The beam is passed through a polarizing plate and then into a Pockels cell, which is aligned 45° from the direction of original polarization and effectively produces two orthogonally polarized beams. In addition, the Pockels cell provides a means of creating a phase difference between the two beams so that the instrument operates at its greatest sensitivity (see reference 31). The beam expander and lens provide a collimated beam to the beam splitter and Wollaston (1). Wollaston (1) acts as a prism that deflects one of the two orthogonally polarized beams by a predetermined angle. The two beams then pass through the boundary layer on the model (see figure 47) at different locations. Differences in density fluctuations in the boundary layer at the two model locations manifest themselves as optical path length differences.

Light reflecting back from the model surface returns through the lens and Wollaston (1) and is directed by the beam splitter to Wollaston (2) and the two photodetectors. The photodetectors generate the signal voltage, which is a function of optical path length differences between the two beams, and also provide information back to the Pockels cell for adjusting the relative phase between the two beams for optimal interferometer performance. On the basis of the thin-film data previously discussed and traversing pitot pressure probe studies by Dougherty in reference 32, the fluctuations in voltage signal are expected to be minimal for a laminar region, to reach a maximum in the transitional region, and fall again to a lower level in the fully turbulent region.

An important evaluation of the instrument occurred during June of 1986 when it was tested in the Boeing Model Transonic Wind Tunnel at a Mach number of 0.7. As seen in figure 48, the instrument was set up on an optical bench next to the tunnel and the beams entered the tunnel normal to the test section sidewall. A 6-inch NACA 66-006 airfoil was mounted between the bottom and top walls so that the beams struck the airfoil in a direction approximately normal to its surface. As seen in figure 49(a), the RMS output signal values vary as expected for natural transition along the airfoil. Its value is initially minimal near 3.5-inches from the leading edge, where laminar flow is expected to be present. However, as transition begins to take place in the boundary layer, the level of fluctuations increases until a maximum magnitude is reached near 5-inches, which is assumed to be the location of greatest unsteadiness in the transitional region. Further downstream at 5.75-inches, where the flow is becoming fully turbulent, the RMS level has dropped below its maximum value and appears to be approaching an intermediate level.

For comparison purposes, a separate flow visualization run was done with sublimating chemicals and the beginning of the scrubbed region was found to coincide, within experimental error, with the location of the maximum signal RMS of the interferometer (see figure 49(b)). Even though there may be no fundamental reason why these two positions should coincide, the instrument is recording peak activity in the same region that sublimating chemicals would suggest transition occurs.

Finally, this promising technique for unobstrusive measurement of boundary-layer transition will be further investigated at the Langley Research Center during 1988 as part of an assessment of boundary-layer transition measurement techniques to be conducted in the Unitary Plan Wind Tunnel at supersonic speeds. The results of the optical interferometer will be compared, during the same test, to techniques such as liquid crystals, infrared photography, and hot-film anemometers.

Laser Vapor Screen for Flow Visualization

Another application of laser technology to diagnostic measurements is the vapor screen. The vapor screen technique is a simple, yet effective, flow visualization tool used to study the off-body flows about aerodynamic shapes at subsonic, transonic, and supersonic speeds. In recent years, this technique has frequently been employed in wind tunnel experiments to improve the understanding of the vortices shed from the slender bodies of missiles and the fuselage forebodies and wings of fighter aircraft at high angles of attack. The technique features the injection of water into the tunnel circuit to create a uniform fog in the test section and a laser generated intense sheet of light that can be oriented in any selected plane relative to the test model. The light is scattered as the water particles pass through the sheet, which enables the off-body flow to be visualized.

Figures 50 and 51 show representative results from a NASA experiment that were obtained using a laser vapor screen technique in the David Taylor Research Center's (DTRC) 7- by 10-Foot Transonic Tunnel. The model is a general research fighter configuration having a 55° cropped delta wing and slender, sharp-edged forebody chines, or strakes. A beam of coherent light generated by an 18-watt argon-ion laser was directed to a set of optics located in a window in the right side of the test section. The beam passed through a line generator, or cylindrical lens, and the resultant sheet of light "sliced" through a model cross-plane located approximately 75 percent of the distance along the wing centerline chord measured from the apex. This position coincided with a spanwise row of upper surface static pressure orifices on the right wing. Figure 50 illustrates the cross flow as observed from a three-quarter right rear view, corresponding to an angle of attack of 30° and a free-stream Mach number of 0.95. The laser light sheet illuminates the vortex pair generated by the forebody chines. The dark areas within the donut-shaped structures define the location of the vortex centers, which are essentially devoid of water particles. The wing leading-edge vortices are also present, but are not well-illuminated due to the side-scatter orientation. Figure 51 shows the flow structure in the same cross-plane at an angle of attack of 20° and a free-stream Mach number of 1.10. The 35-mm still camera was positioned in a three-quarter left-rear view. The vortex pair from the forebody chines is again depicted. Due to forward scatter, the right wing leading-edge vortex is now clearly visible as a flat, elliptically-shaped region within which water particles are noticeably absent. The left wing vortex is not seen since it is located in the shadow created by the center fuselage.

Articulation of the laser-system platform or the optics has been used in some investigations to look at the entire flow field.

MOVING BELT SKIN FRICTION BALANCE CONCEPT

The principal of operation of the moving belt skin friction balance developed, under Langley grant, by the University of Tennessee Space Institute (UTSI) can be illustrated with the aid of figure 52. The balance is mounted such that the belt is flush with the surface to be investigated. The two drums that support the belt are, in turn, supported by flexures. When the belt experiences force due to the shear of a passing fluid, it rotates the drums against the restoring force of the flexures. The stiffness of the flexures is

selected to allow a maximum of 3° of rotation for the expected forces. Strain gages are attached to the flexures to produce a voltage proportional to, and linear with, the torque produced by the belt rotating the drums. Since the small gaps that are open to the flow do not change with this rotation, there is no need for a closed-loop nulling device to center the measuring element as there is in the floating element type balances. Further details are available in reference 33.

The moving belt gage has been used to make measurements in several wind tunnels to determine it capabilities. One such test was carried out in the 0.3-M TCT on the test section sidewall as part of an investigation designed to evaluate the performance of several skin friction measurement devices in a cryogenic, transonic environment. To insure a minimum of disturbance during these tests there was no model mounted in the tunnel. Special care was taken in mounting the gage to minimize boundary-layer disturbances; however, the data exhibits a rough wall trend, i.e., very little change in C_f with increasing Reynolds number. It is instructive to consider the distributed-wall roughness height which would be required to "fit" the observed data. Plotted in figure 53 are curves representing a range of values for roughness height; values in the range from 0.005 to 0.02 mm (0.0002 to 0.0008 inches) are typical of the data. The figure serves to demonstrate the severe effects of small roughness heights in a turbulent boundary layer, and that an equivalent roughness height of only 0.02mm is sufficient to match the data.

The approximate formula for rough flat plate flow used to generate the curves was

$$C_f = (2.87 + 1.58\log(x/\varepsilon))^{-2.5}$$

where ε is the roughness height and x is distance from the leading edge.[34] Reference 35 discusses the details of applying this formula to a test section wall boundary layer, by calculating an equivalent flat plate length. The curve labeled smooth in figure 53 was calculated from the relation

$$C_f = 0.027/(Re_x)^{1/7}$$

also from reference 34.

Current plans call for further testing of UTSI balances on a large flat plate in the NTF. Floating element balances as well as other types of skin friction measuring devices will also be tested for comparison. The surface finish will be carefully controlled and extensive boundary-layer profile surveys will be conducted. The result will be for a boundary layer much better understood than the test section sidewall cases just discussed.

The basic feasibiliy of the UTSI balance to operate in cryogenic conditions has been demonstrated, but carefully controlled testing is required to establish limits on accuracy. Work to be undertaken in the near future will include the use of fiber optics to read the movement of the belt rather than strain gages. A bench setup using fiber optics is described in reference 36. This

technique is expected to be less sensitive to temperature changes, thus simplifying balance calibration and use at cryogenic temperatures. Also electrical noise and error due to gage heat will be eliminated. Finally, eliminating the strain gage removes the primary barrier to miniaturization.

A concurrent effort is also under way to fabricate these balances using the relatively new wire-cut method (electron discharge machining using a wire for an electrode). The use of the wire-cut technique has the potential to lower the cost of the balances by reducing the part count and simplifying the assembly procedure. This technique also enhances miniaturization. The combination of the wire-cut technique and the use of fiber optics may significantly reduce the cost per balance. Reference 37 speculates on the installation of many balances on a single airfoil configuration. A typical layout is shown in figure 54 on a 14-percent thick, 10-inch chord airfoil. Each balance would be contoured to match the airfoil surface. This would simplify measurement of the location of transition separation and transonic shocks.

CONCLUDING REMARKS

The quality and pace of experimental research in aerodynamics is very much dependent on the capabilities of the instrumentation available. So our pursuit of new insights into the behavior of complex fluid flows should always be accompanied by an effort to improve the accuracy and "range" of our measurements. The validity of this statement was demonstrated in a number of instances in the present paper where new or improved instrumentation were shown to provide not only more accurate results but frequently yield new truths as well. Thin-film-gage arrays and 3-D laser instrumentation are just starting to pay dividends while multiwire hot-wire anemometers are yielding data much different from "current" techniques and offering new opportunities for unsteady flow measurements. There are several new techniuqes for skin friction measurement being investigated, one example, a compact skin-friction gage, was discussed.

REFERENCES

1. Smelt, R.: The Role of Wind Tunnels in Future Aircraft Development. Florence Guggenheim Memorial Lecture. Lisbon, Portugal, September 1978.

2. Bobbitt, Percy J.: Modern Fluid Dynamics of Subsonic and Transonic Flight. AIAA Paper 80-0861, May 1980.

3. Stack, John P.; Yeaton, Robert B.; and Dagenhart, J. R.: Research in Natural Laminar Flow and Laminar-Flow Control - Predicted and Hot-Film Measured Tollmien-Schlichting Wave Characteristics. NASA CP-2487, Part 2, 1987, pp. 377-380.

4. Croom, Cynthia C.; Manuel, Gregory S.; and Stack, John P.: In-Flight Detection of Tollmien-Schlichting Instabilities in Laminar Flow. SAE Paper 871016, April 1987.

5. Rubesin, M. W.; Okuno, A. T.; Mateer, G. G.; and Brosh, A.: A Hot-Wire Surface Gage for Skin Friction Measurements and Separation Detection. NASA TMX 62-465, 1975.

6. Harvey, W. D.; Stainback, P. C.; and Owen, F. K.: Evaluation of Flow Quality in Two Large Wind Tunnels at Transonic Speeds. NASA TP-1737, December 1980.

7. Bobbitt, P. J.; Waggoner, E. G.; Harvey, W. D.; and Dagenhart, J. R.: A Faster "Transition" to Laminar Flow. SAE Paper 851855, 1985.

8. Johnson, C. B.; Carraway, D. L.; Stainback, P. C.; and Fancher, M. F.: A Transition Detection Study Using a Cryogenic Hot Film System in the Langley 0.3-Meter Transonic Cryogenic Tunnel. AIAA Paper 87-0049, January 1987.

9. Johnson, Charles B.; Carraway, Debra L.; Hopson, Purnell, Jr.; and Tran, Sang Q.: Status of a Specialized Boundary Layer Transition Detection System for Use in the U.S. National Transonic Facility. Presented at the 12th International Congress on Instrumentation in Aerospace Simulation Facilities, Williamsburg, Virginia, June 22-25, 1987.

10. Stack, J. P.; Mangalam, S. M.; and Berry, S. A.: A Unique Measurement Technique to Study Laminar-Separation Bubble Characteristis on an Airfoil. AIAA Paper 87-1271, June 1987.

11. Stack, John P.; Mangalam, Siva M.; and Kalburgi, Vijay: The Phase Reversal Phenomenon at Flow Separation and Reattachment. AIAA Paper 88-0408, January 11-14, 1988.

12. Spangenberg, W. G.: Heat-Loss Characteristics of Hot-Wire Anemometers at Various Densities in Transonic and Supersonic Flow. NACA TN-3381, May 1955.

13. Winovich, W.; and Stine, H. A.: Measurement of the Nonlinear Variation with Temperature of Heat-Transfer Rate from Hot Wires in Transonic and Supersonic Flow: NACA TN-3965, April 1957.

14. Lowell, H. H.: Design and Applications of Hot-Wire Anemometer for Steady-State Measurements at Transonic and Supersonic Airspeed. NASA TN-2117, 1950.

15. Baldwin, L. V.: Slip-Flow Heat Transfer from Cylinders in Subsonic Airstream. NACA TN-4369, September 1958.

16. Laurence, J. C.; and Lander, L. G.: Auxiliary Equipment and Techniques for Adapting the Constant-Temperature Hot-Wire Anemometer to Specific Problems in Air-Flow Measurements. NACA TN-2843, 1952.

17. Sanborn, V. A.; and Laurence, J. C.: Heat Loss from Yawed Hot Wires at Subsonic Mach Numbers. NACA TN-3563, 1955.

18. Rose, W. C.; and McDaid, E. P.: Turbulence Measurements in Transonic Flow. AIAA 9th Aerodynamic Testing Conference, Arlington, Texas, June 7-9, 1976, pp. 267-271.

19. Horstman, C. C.; and Rose, W. C.: Hot Wire Anemometery in Transonic Flow. AIAA Journal, Vol. 15, No. 3, March 1977, pp. 375-401.

20. Stainback, P. C.; Johnson, C. B.; and Basnett, C. B.: Preliminary Measurements of Velocity, Density, and Total Temperature Fluctuation in Compressible Subsonic Flow. AIAA Paper 83-0384, AIAA 21st Aerospace Sciences Meeting, Reno, Nevada, June 10-14, 1983.

21. Stainback, P. C.: A Review of Hot Wire, Anemometery in Transonic Flows. Presented at the Eleventh International Congress on Instrumentation in Aerospace Simulation Facilities, Stanford, California, August 26-28, 1985.

22. Stainback, P. C.; and Johnson, C. B.: Flow Quality Measurements in Compressible Subsonic Flows. NASA CP-2487, Part 2, pp. 345-357.

23. Yeh, Y.; and Cummins, H. Z.: Localized Fluid Flow Measurements with an He-Ne Laser Sepctrameter Applied Physics. Letters, Vol. 4, pp. 176-178, May 1964.

24. Scheiman, J.; and Kubendian, L. R.: Juncture Flow Measurements Using Laser Velocimetry. AIAA Paper 85-1612.

25. Meyers, James F.; and Hepner, Timothy E.: Velocity Vector Analysis of a Juncture Flow Using a Three Component Laser Velocimeter. Second International Symposium on Application of Laser Anemometry to Fluid Mechanics, Lisbon, July 1984.

26. Meyers, James F.: The Elusive Third Component. Proceedings of the Symposium on Laser Anamometery, ASME 1985 Winter Annual Meeting, Miami, Florida, November 1985, pp. 247-254.

27. Scheiman, J.; and Kubendran, L. R.: Laser Velocimeter Measurements in a Wing-Fuselage Type Juncture. NASA TM-100588, April 1988.

28. Mangalam, S. M.; Dagenhart, J. R.; Hepner, T. E.; and Meyers, J. F.: The GortlerInstability on an Airfoil. AIAA Paper 85-0491, January 1985.

29. Floryan, J. M.: Stability of Boundary-Layer Flows Over Curved Walls. Ph.D. Thesis, Virginia Polytechnic Institute and State University, Blacksburg, Virginia, January 1980.

30. Jones, G. S.; Gartrell, L. R.; Sewall, W. G.; and Stainback, P. C.: Designing Transonic Wind-Tunnel Test Sections for Flow Diagnostics and Laser Velocimeter Applications. AIAA Paper 87-1434, June 1987.

31. Azzazy, M; Modarress, D.; and Hall, R.: Optical Boundary-Layer Transition Detection in a Transonic Wind Tunnel. AIAA Paper 87-1430, June 1987.

32. Dougherty, N. Sam, Jr.: Influence of Wind Tunnel Noise on the Location of Boundary-Layer Transition on a Slender Cone at Mach Numbers from 0.2 to 5.5. Volume I: Experimental Methods and Summary of Results. AEDC-TR-78-44, March 1980.

33. Vakili, A. D.; and Wu, J. M.: A New Instrument for Direct Measurement of Wall Shear Stress. Proceedings of the 28th International Instrumentation Symposium, Instrument Society of America, Vol. 19, part one, pp. 147-152, May 1982.

34. White, Frank M.: Viscous Fluid Flow. McGraw Hill Book Company, 1974.

35. Vakili, A. D.; Wu, J. M.; and Lawing, Pierce L.: Wall Shear Stress Measurements Using A New Transducer. AIAA Paper 86-1092, May 1986.

36. Vakili, A. D.; and Wu, J.M.: Direct Measurement of Skin Friction with a New Instrument. Proceedings of the Interational Symposium of Fluid Control and Measurement, Tokoyo, Japan, paper no. F43, FLUCOME 85, Pergammon Press, 1985.

37. Lawing, Pierce L.; Vakili, A. D.; and Wu, J. M.: Experience at LaRC with a UTSI Skin Friction Balance. Symposium on Natural Laminar Flow and Laminar Flow Control Research. Langley Research Center, Hampton, Virginia, March 16-19, 1987.

ACKNOWLEDGMENTS

The author gratefully acknowledges the beneficial discussions with, and material obtained from, the following individuals of the Langley Research Center Staff: Charles D. Harris, William D. Harvey, J. Pete Stack, Sivaramakrishnan M. Mangalam*, Charles B. Johnson, Debra L. Carraway, James F. Meyers, Gregory S. Jones, Luther R. Gartrell, Pierce L. Lawing, Robert M. Hall, P. Calvin Stainback**, Gary F. Erickson, Cynthia C. Lee, and Robert A. Kilgore.

* Analytical Services and Materials, Inc.
** Complere

ORIGINAL PAGE IS
OF POOR QUALITY

TABLE I. - COMPARISON OF FLOW QUALITY DATA FOR 8-FOOT TPT FROM 3-WIRE AND 1-WIRE TECHNIQUES
- p_t = 710 psf, T_t = 540°R -

	3-Wire					1-Wire Method I		
Mach No.	$\tilde{u}/u$	$\tilde{\rho}/\rho$	$\tilde{T}/T_t$	$\tilde{m}/m$	$\tilde{p}/p$	$\tilde{u}/u$	$\tilde{m}/m$	$\tilde{p}/p$
0.40	0.830	0.306	0.026	0.528	0.334	0.039	0.033	0.026
0.75	2.963	0.946	0.0581	2.019	1.507	0.118	0.063	0.130
0.82	2.643	0.781	0.052	1.864	1.399	0.050	0.055	0.033

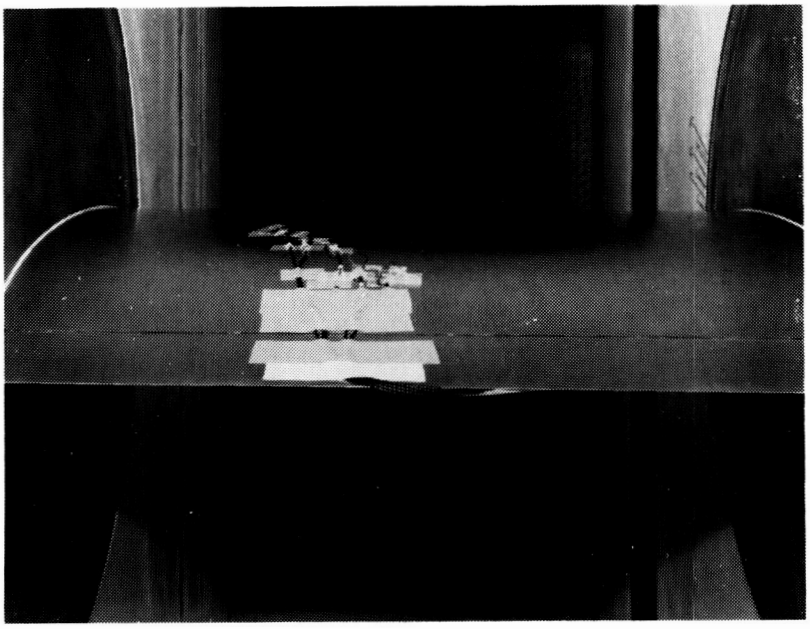

(a) Photograph of thin-film patch gages on NASA NLF(1)-0414F Airfoil installed in NASA Langley Low-Turbulence Pressure Tunnel.

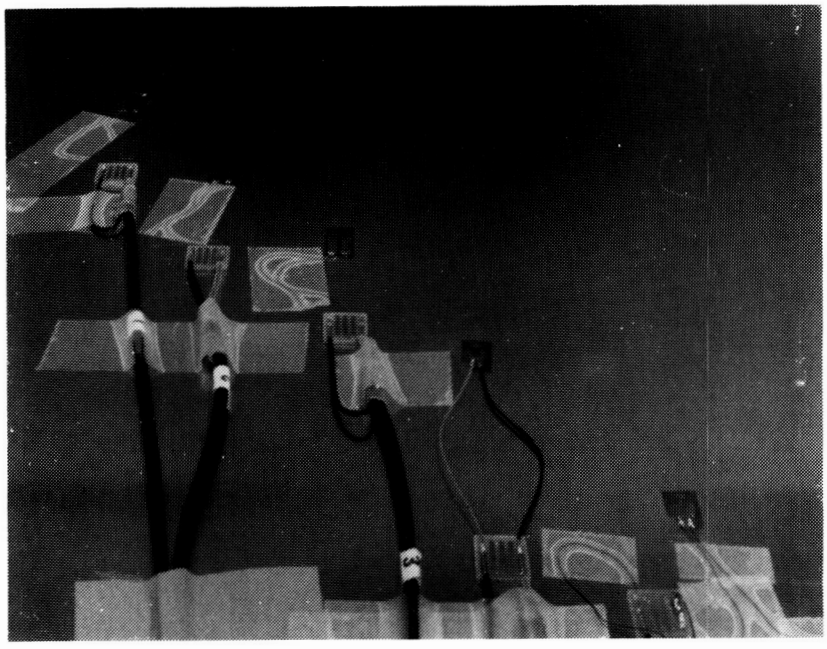

(b) Enlarged photograph of patch-gage installation showing hot-film sensors and terminal blocks for anemometer leads.

Figure 1. Patch gage installation in LTPT airfoil tests.

ORIGINAL PAGE
BLACK AND WHITE PHOTOGRAPH

ORIGINAL PAGE
BLACK AND WHITE PHOTOGRAPH

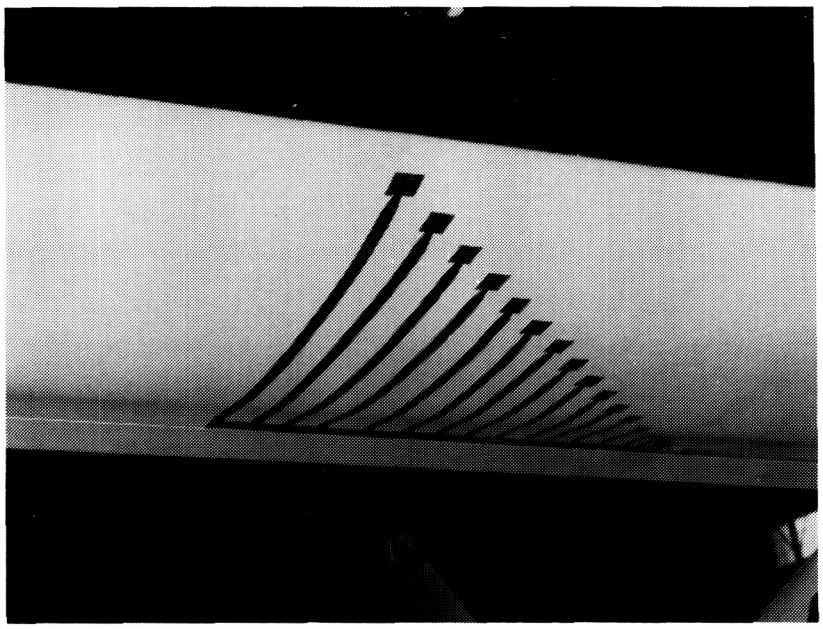

Figure 2. Photograph of an array of thin-film gages installed on the Cessna 210 with a NASA NLF(1)-0414F Airfoil glove. Photograph is taken from upstream.

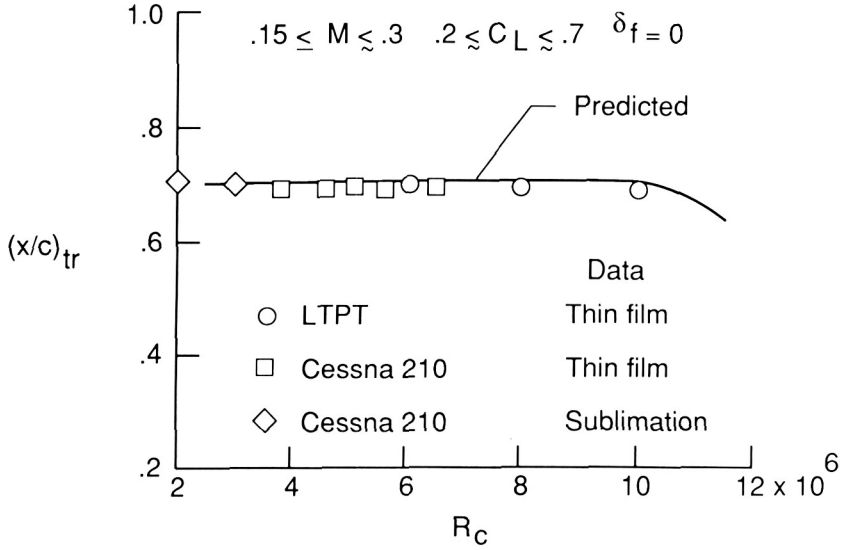

Figure 3. Comparison of wind tunnel and flight transition measurements.

ORIGINAL PAGE
BLACK AND WHITE PHOTOGRAPH

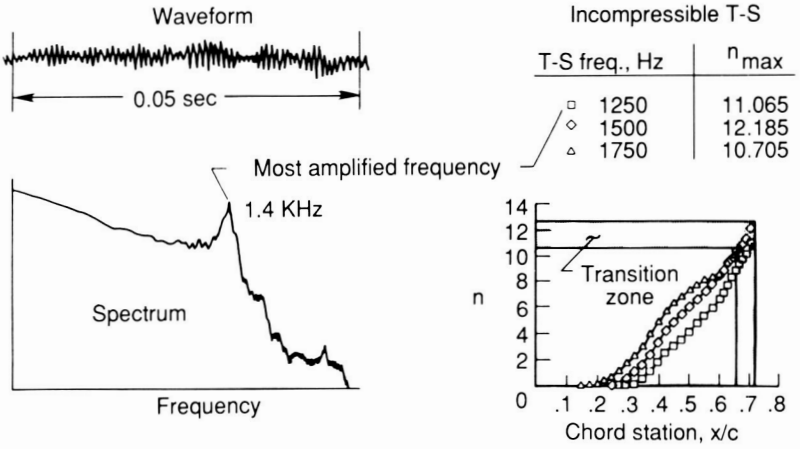

Figure 4. Predicted and measured Tollmien-Schlichting wave characteristics.

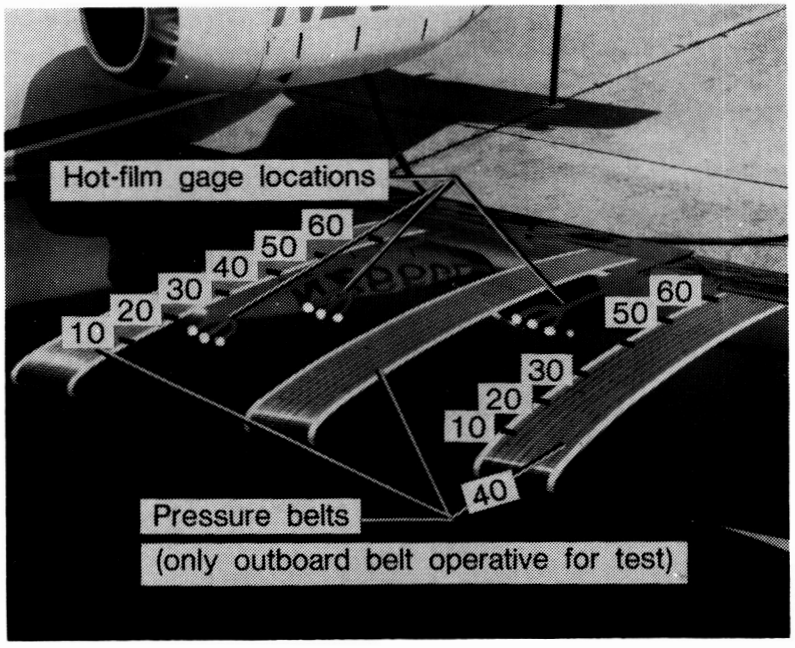

Figure 5. Lear 28/29 instrumentation for T-S instability detection test.

ORIGINAL PAGE
BLACK AND WHITE PHOTOGRAPH

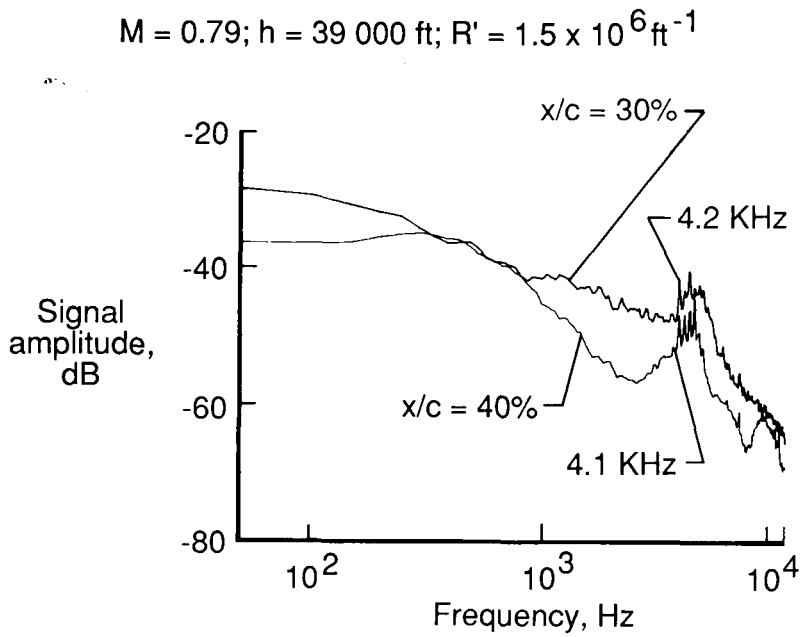

Figure 6. Power spectral density analysis of hot-film signals at 30- and 40-percent chord. $M_\infty = 0.79$, $h = 39{,}000$ ft, $R = 1.5 \times 10^6$/ft.

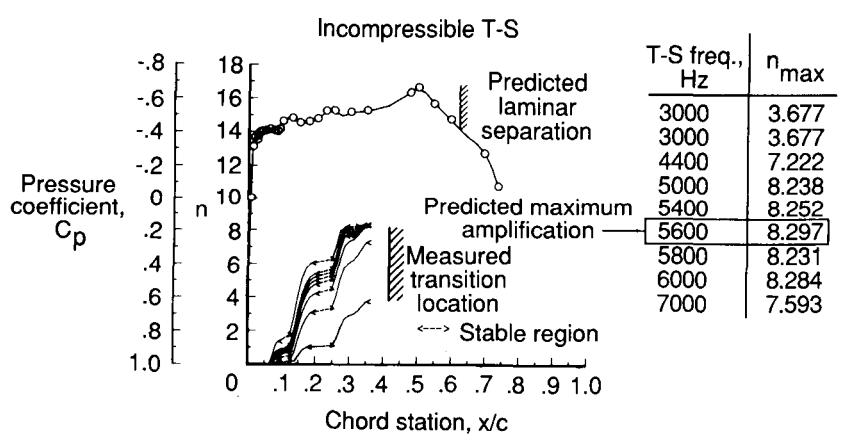

Figure 7. Incompressible prediction of T-S amplification ratios for measured pressure distribution. $M_\infty = 0.79$, $h = 39{,}000$ ft, $R = 1.5 \times 10^6$/ft.

ORIGINAL PAGE
BLACK AND WHITE PHOTOGRAPH

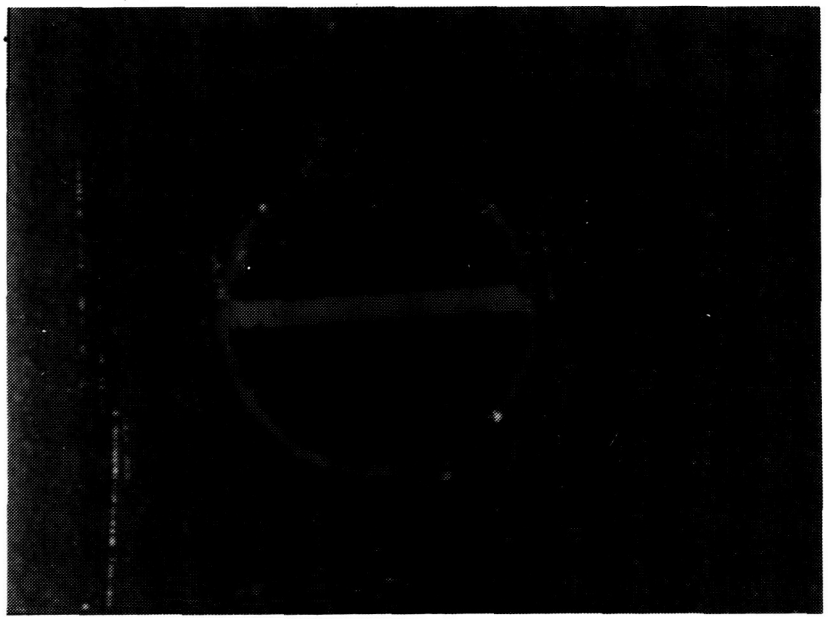

Figure 8. Enlarged photo of a thin-film plug gage installed on the 7-foot chord Laminar Flow Control (LFC) Airfoil. Diameter of plug is 0.0625 in.

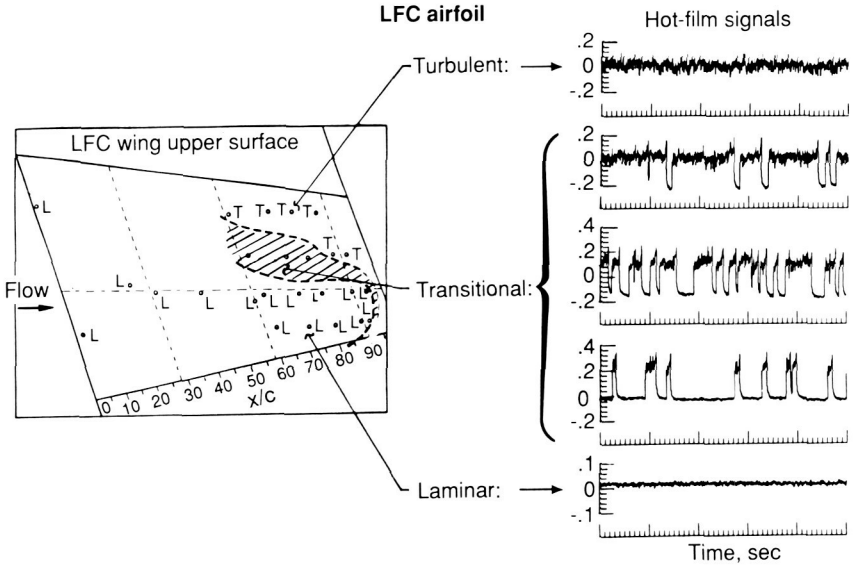

Figure 9. Sketch showing the location of the thin-film plug gages on the LFC airfoil and the state of the boundary layer at each location (L for laminar, T for turbulent).

ORIGINAL PAGE
BLACK AND WHITE PHOTOGRAPH

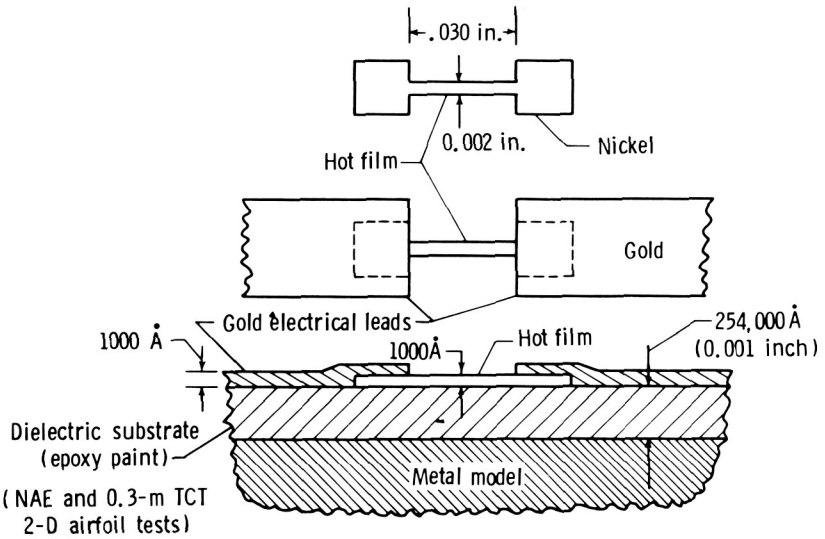

Figure 10. Sketch showing the construction of the McDonnell-Douglas hot-film gages, leads, and substrate.

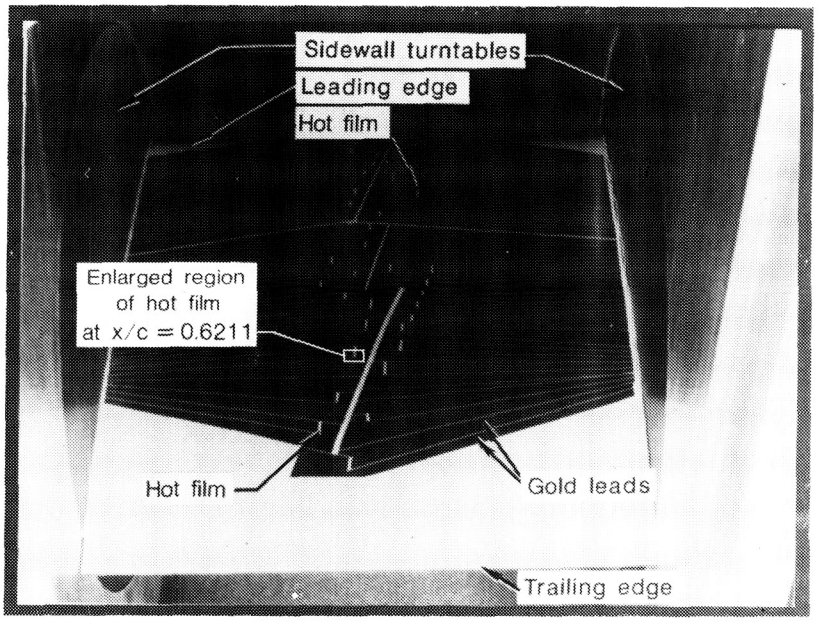

Figure 11(a). Photograph of the supercritical airfoil model installed in the 0.3-M TCT showing the vapor-deposited gold hot-film leads.

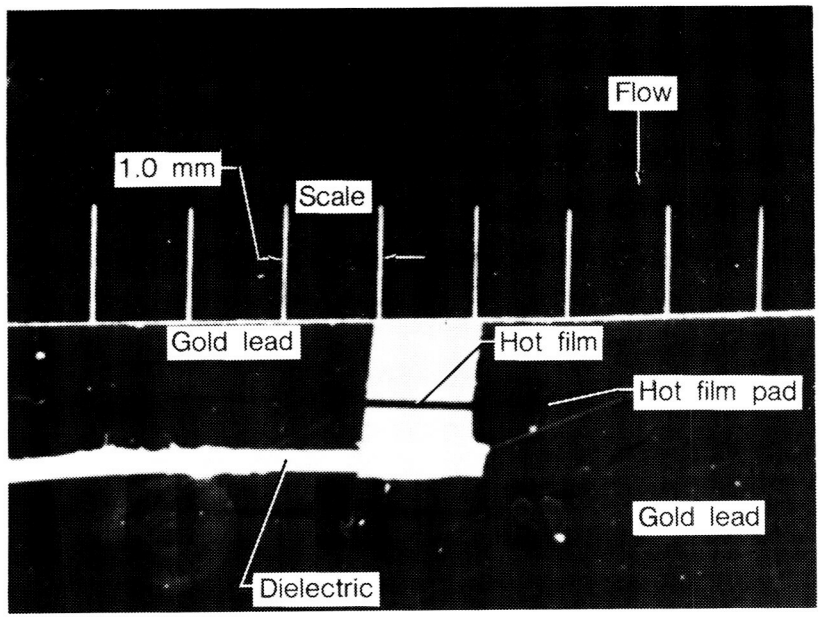

(b) Enlarged photographs of hot-film sensor, gold leads, and dielectric substrate.

Figure 11. Photographs of a supercritical airfoil model with hot-film gage installation.

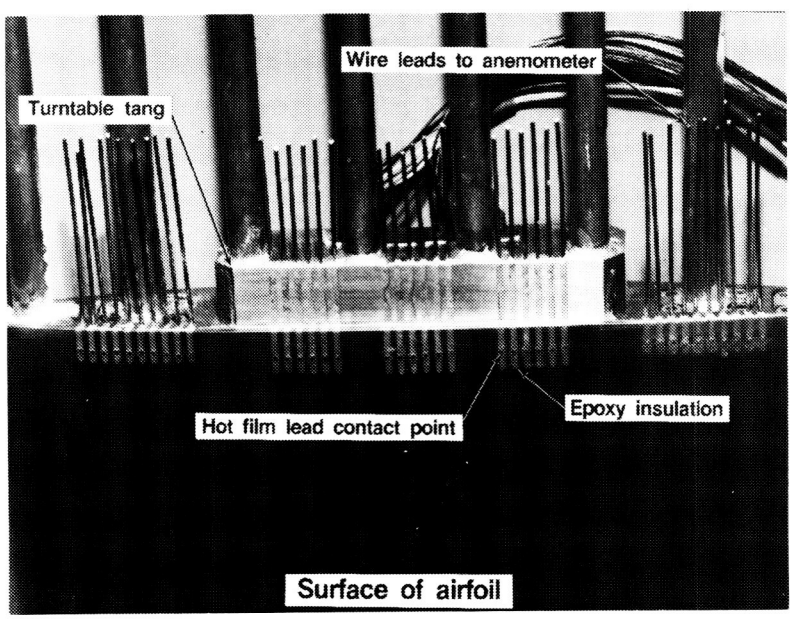

Figure 12. Photograph of end of supercritical airfoil model showing hot-film-lead contacts and anemometer leads.

ORIGINAL PAGE
BLACK AND WHITE PHOTOGRAPH

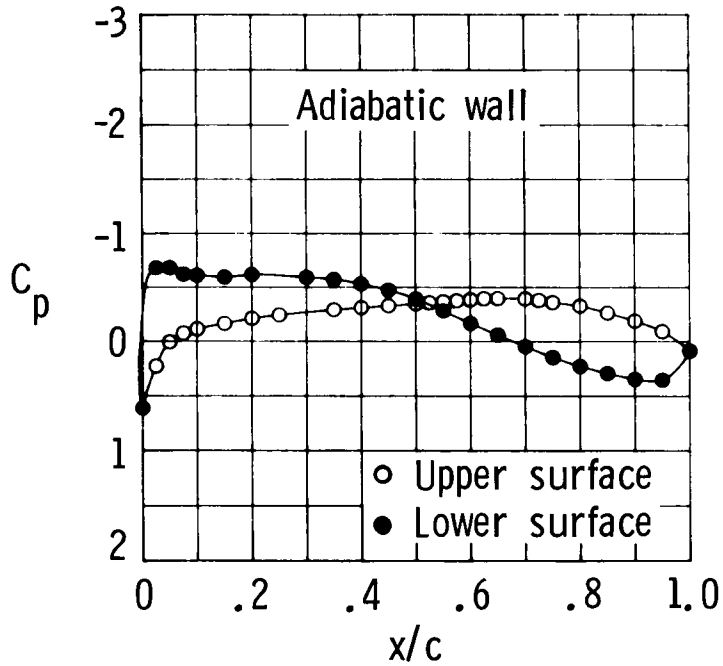

(a) Airfoil pressure distribution.

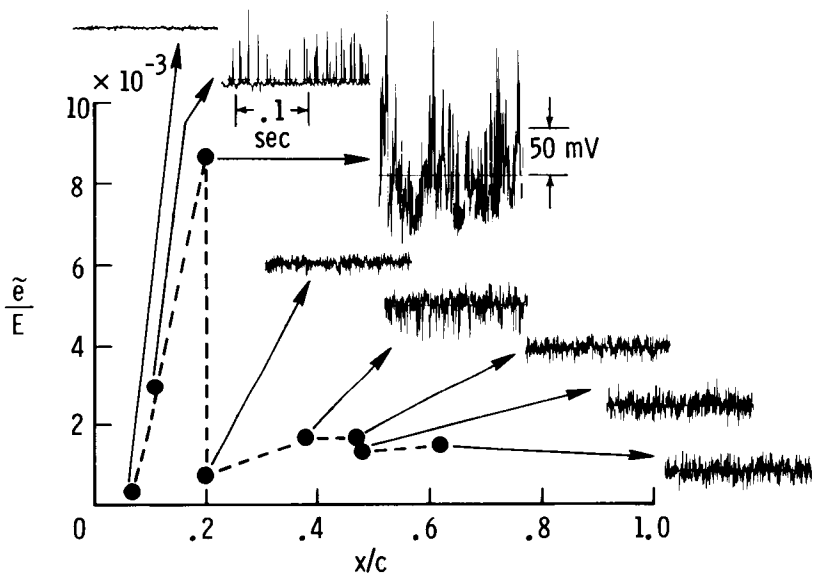

(b) Normalized RMS flucuating voltages for a number of chordwise locations.

Figure 13. A typical airfoil pressure distribution and normalized RMS flucuating voltages from the 0.3-M TCT hot film tests. Adiabatic wall, $M_\infty = 0.6$, $R_c = 7.5 \times 10^6$, $\alpha = 4.0^0$, $T_t = 360°R$.

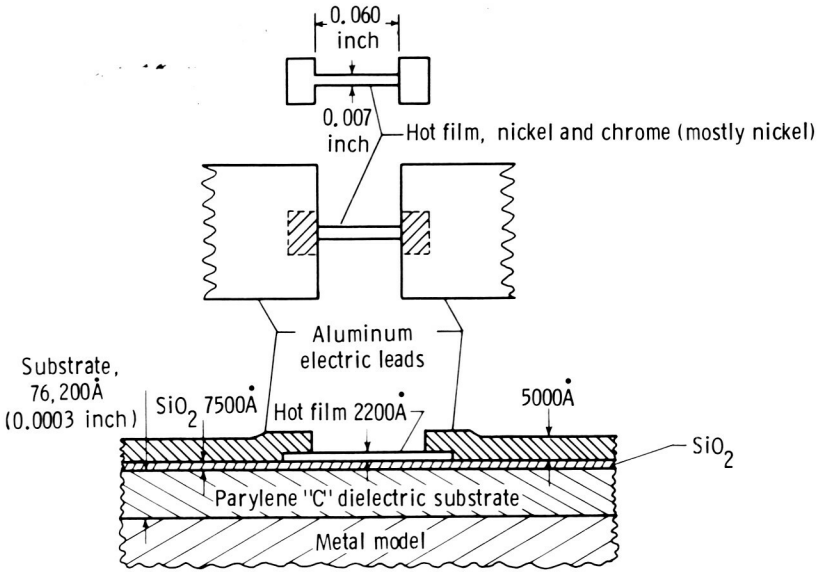

Figure 14. Sketch showing the construction of the Langley developed scheme of hot-film deposition.

Figure 15. Airfoil mounted on the sidewall of the NTF for tests of the hot-film dielectric.

ORIGINAL PAGE
BLACK AND WHITE PHOTOGRAPH

ORIGINAL PAGE
BLACK AND WHITE PHOTOGRAPH

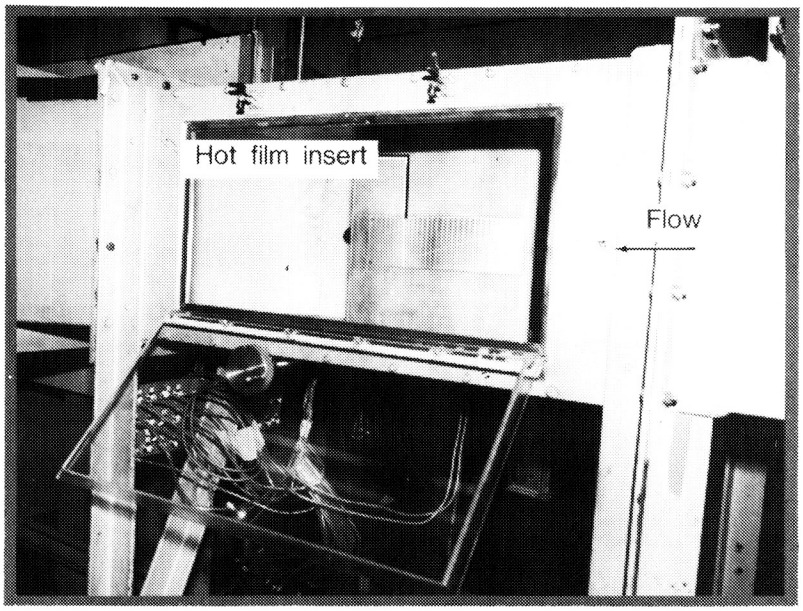

Figure 16. NACA 0012 Airfoil model installed in test section of IRD small calibration facility.

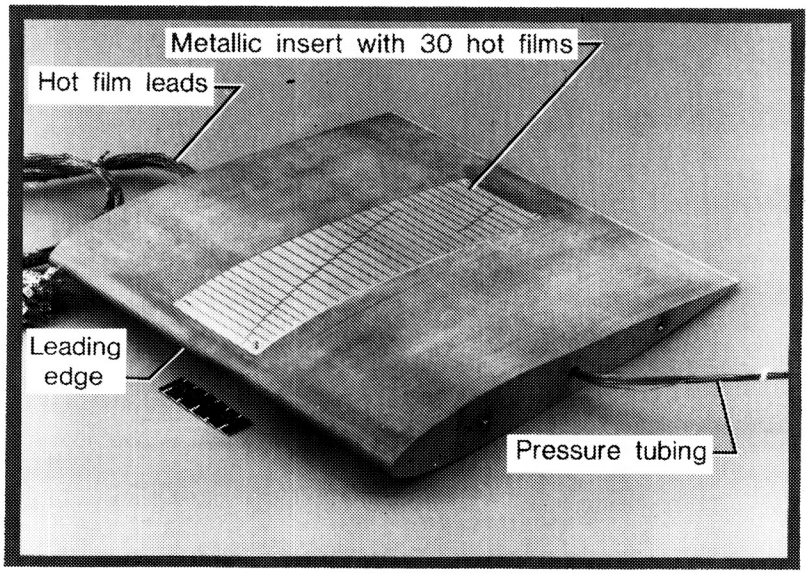

Figure 17. 2-D airfoil with hot-film insert used to demonstrate on-line transition detection with cryogenic hot-film system. NASA 0012 Airfoil c = 12 in., 12-in. span.

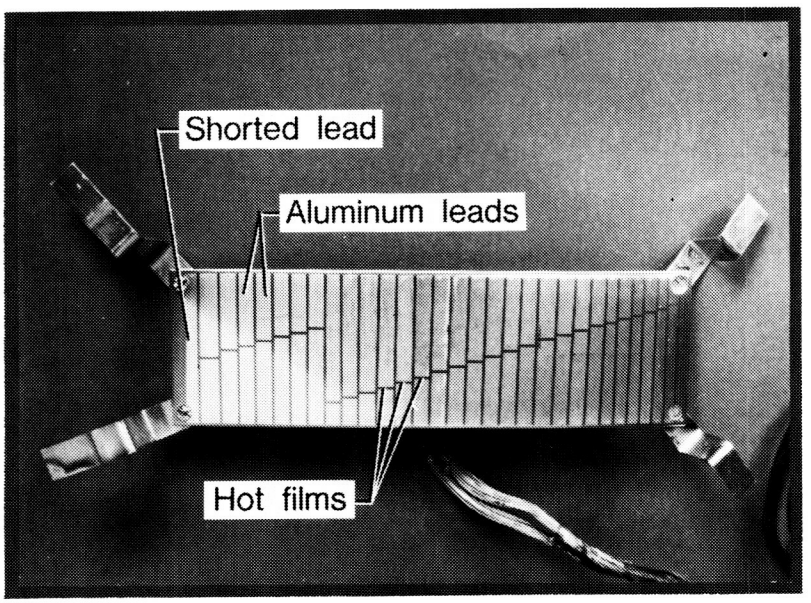

Figure 18. Metallic insert with 30 Langley developed cryogenic hot-film sensors.

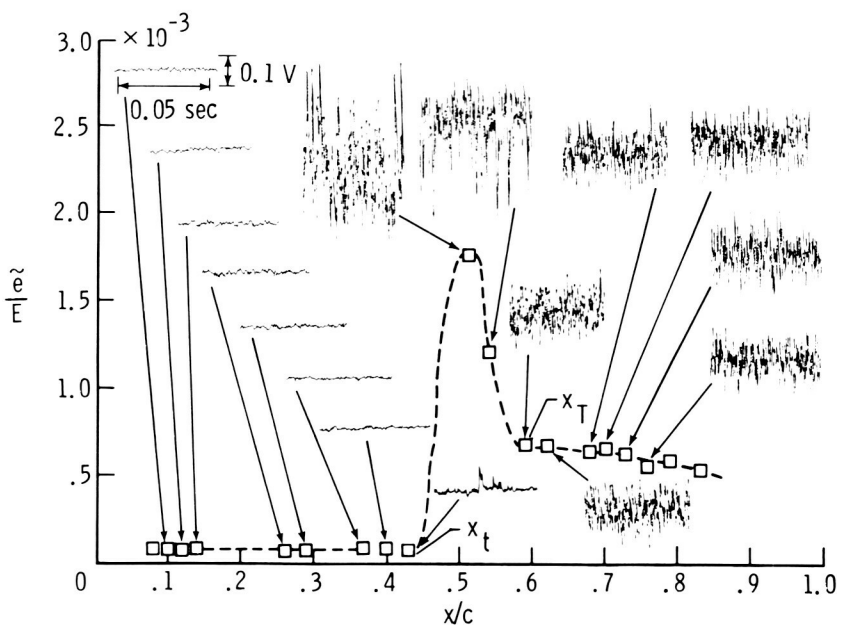

Figure 19. Normalized RMS fluctuating voltages for a number of chordwise locations. $\alpha = 0^0$, $M_\infty = 0.122$, $R_c = 0.86 \times 10^6$, c = 12 in.

ORIGINAL PAGE
BLACK AND WHITE PHOTOGRAPH

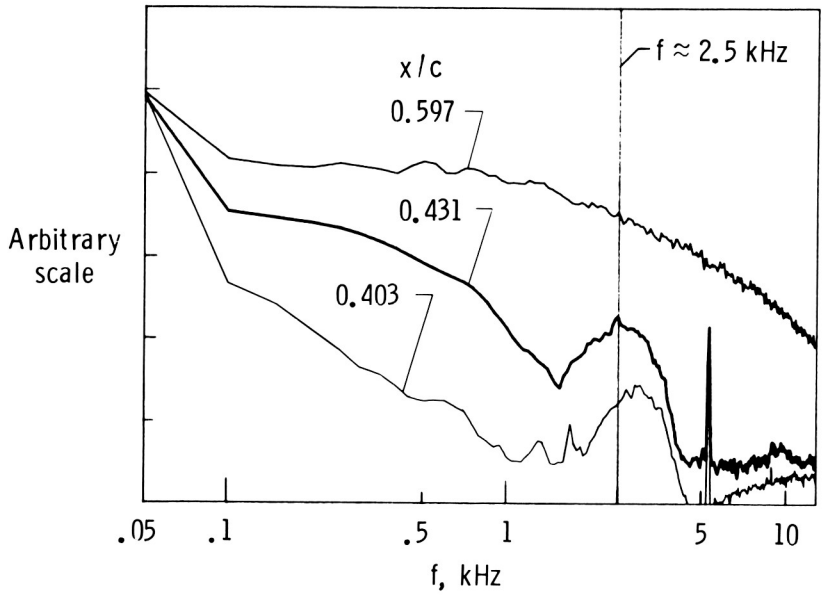

Figure 20. Spectra at three chordwise locations showing amplification of T-S waves in vicinity of 2.5 KH_z. $\alpha = 0^0$ $M_\infty = 0.122$, $R_c = 0.86 \times 10^6$.

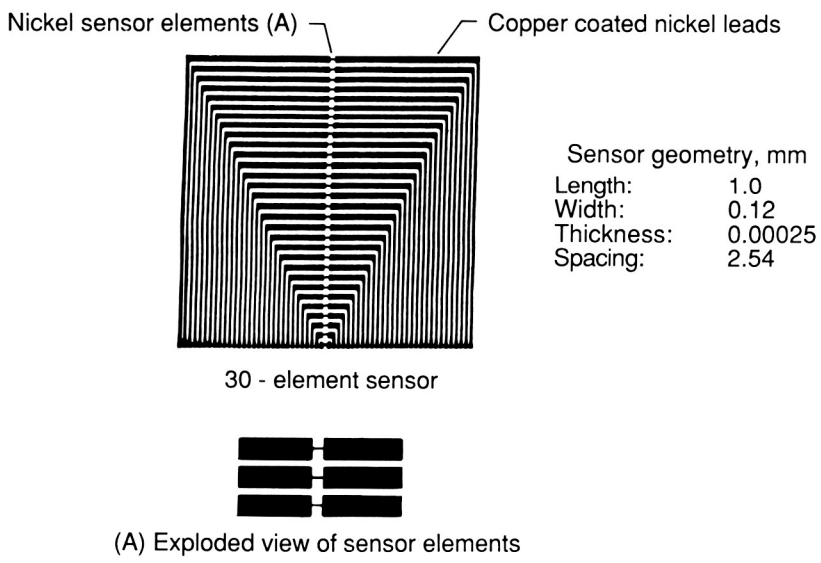

Figure 21. Prototype hot-film sensor array.

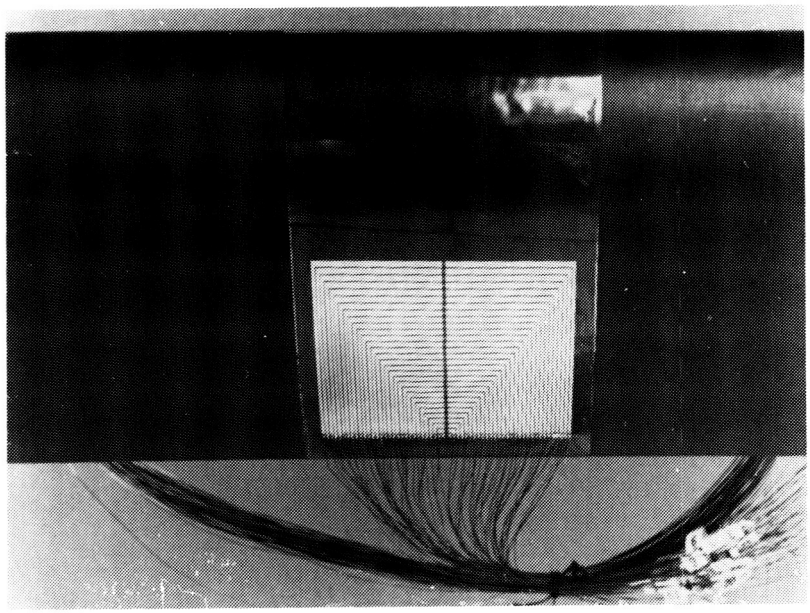

Figure 22. Photograph of prototype hot-film sensor array of polyimide substrate bonded to LRN(1)-1010 airfoil model. 15-cm chord, 30.48-cm span.

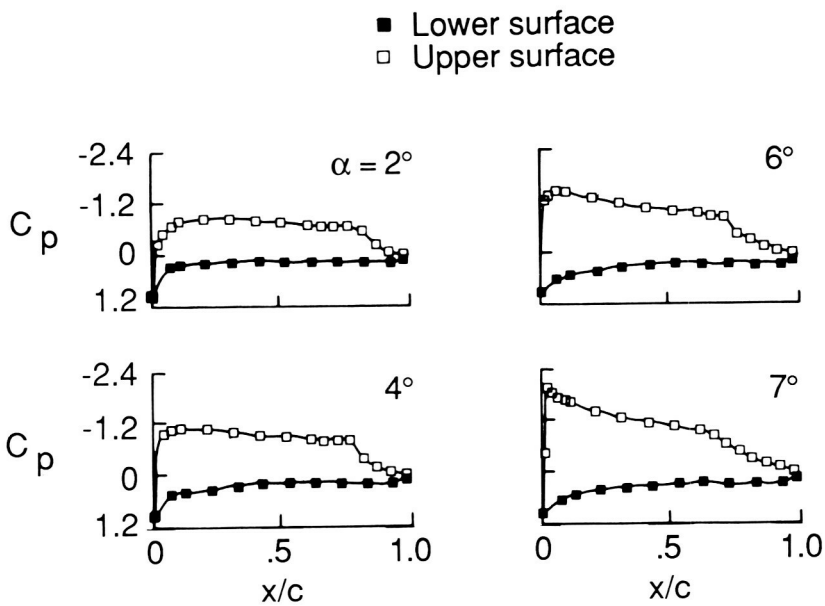

Figure 23. Pressure distribution for various angles of attack of LRN(1) 1010 airfoil. $R_c = 0.200 \times 10^6$, $M_\infty = 0.06$.

ORIGINAL PAGE
BLACK AND WHITE PHOTOGRAPH

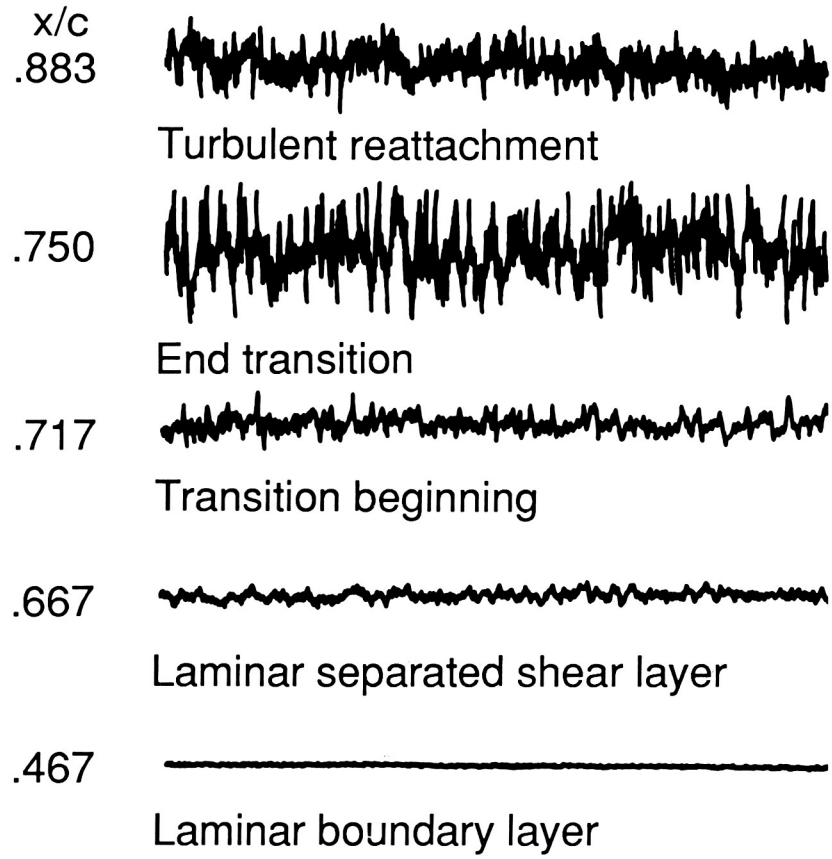

Figure 24. Time history of signals from hot films at five chord locations. R_c = 199,900, $\alpha = 5^0$, M_∞ = 0.06.

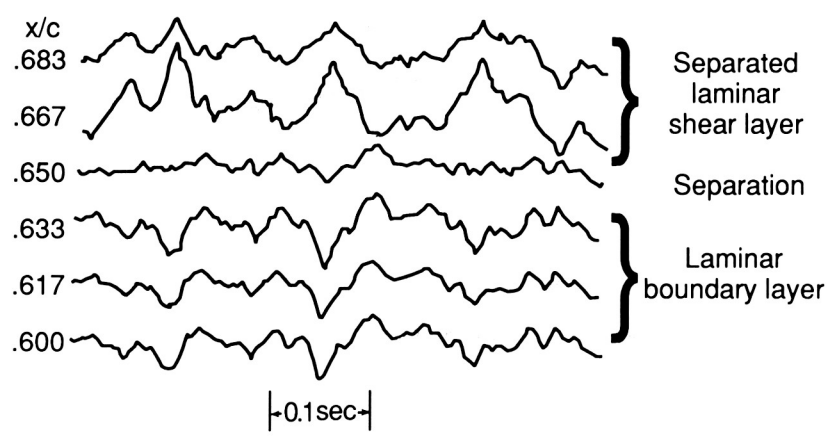

Figure 25. Time history of signals from gages in laminar separation region.

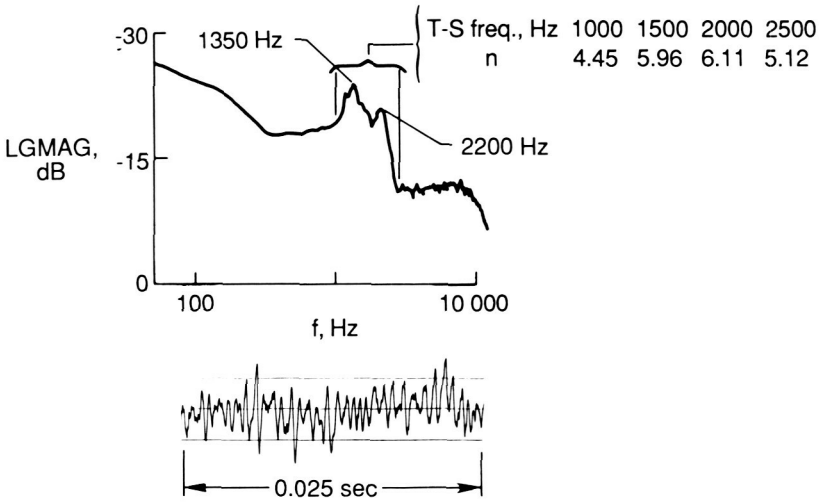

Figure 26. Auto correlation of hot-film signals and comparison of most amplified T-S frequencies with stability theory. A typical time history plot of output signal is given in the lower part of the picture. $\alpha = 7.25^0$, $R_c = 0.222 \times 10^6$, $x/c = 0.6$.

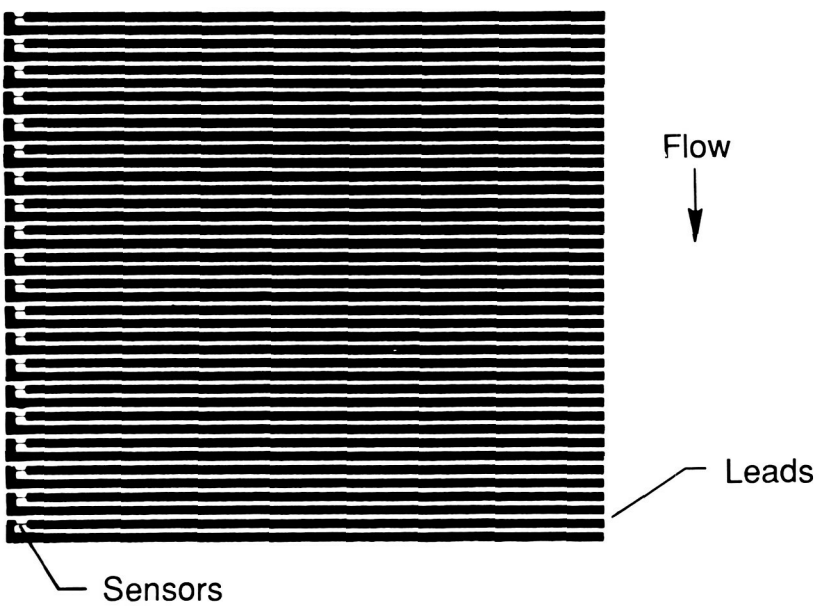

Figure 27. Improved multi-element sensor configuration.

ORIGINAL PAGE
BLACK AND WHITE PHOTOGRAPH

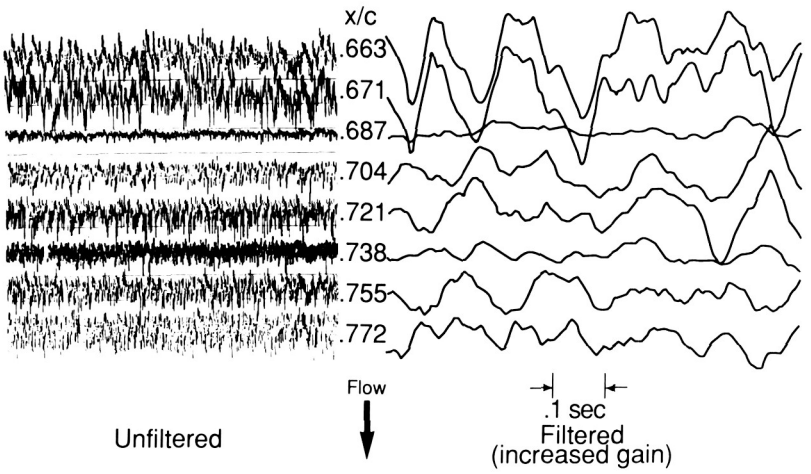

Figure 28. Time history of signals in the laminar reattachment region on Eppler-387 airfoil at R_c = 200,000, $\alpha = 2^0$, $M_\infty = 0.06$

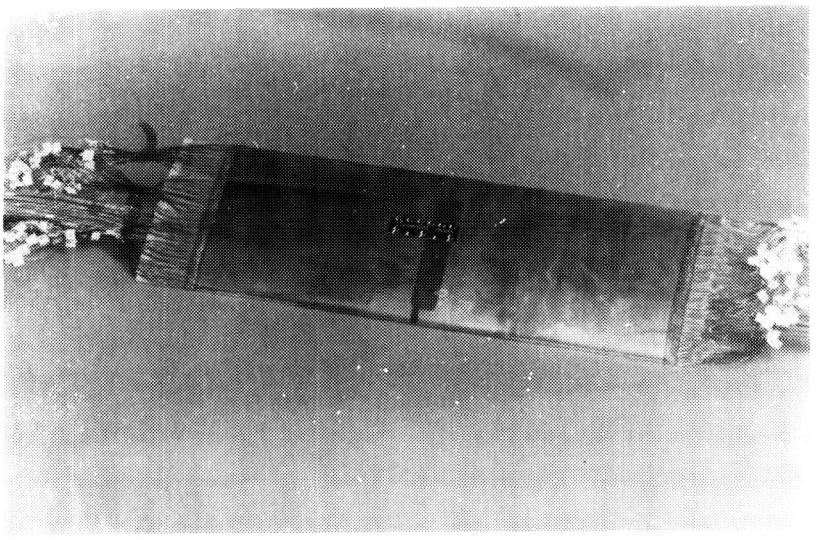

Figure 29(a). Photograph of airfoil model, with thin-film arrays bonded to the surface, that was used in the 0.3-M TCT tests.

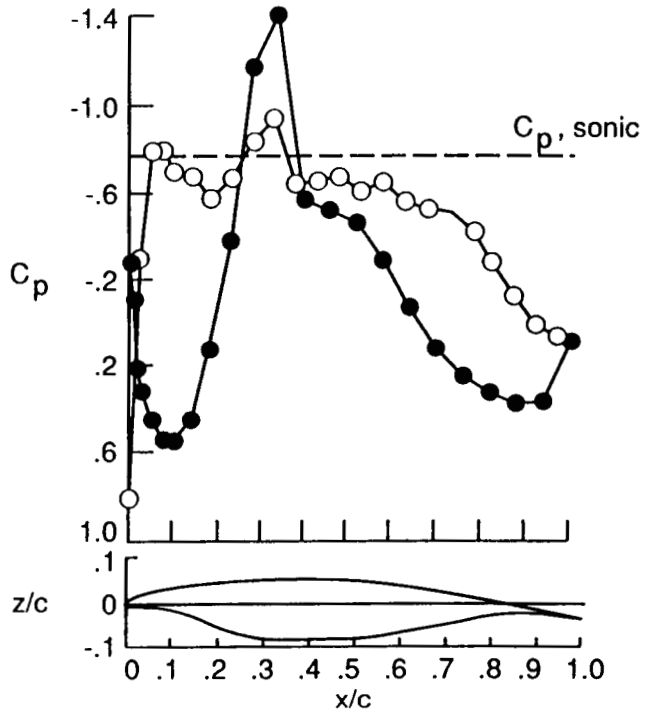

(b) Pressure distribution on airfoil model. $\alpha = -1.02^0$, $M_\infty = 0.70$, $R_c = 6 \times 10^6$.

Figure 29. Airfoil model tested in 0.3-M TCT and an example of pressure distribution.

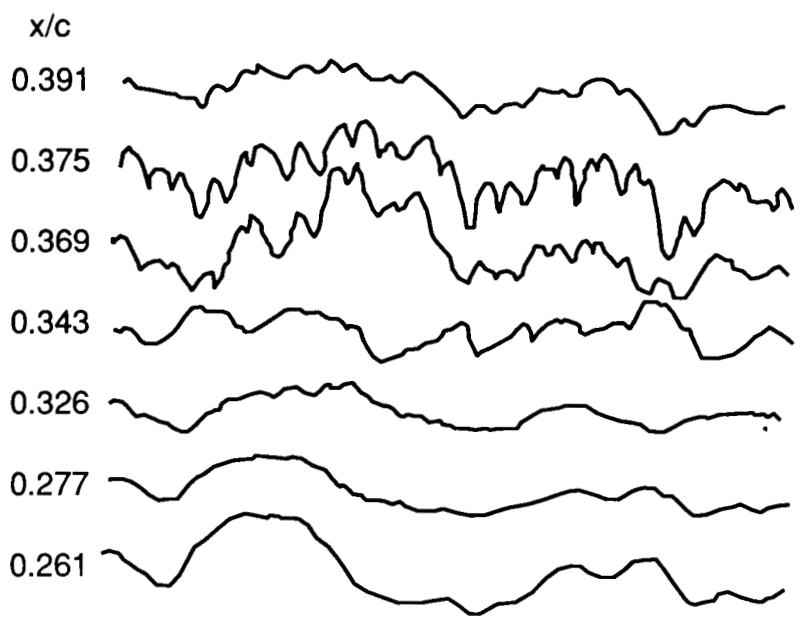

Figure 30. Time traces of voltage outputs from gages in the vicinity of shock on the lower surface of the airfoil.

ORIGINAL PAGE
BLACK AND WHITE PHOTOGRAPH

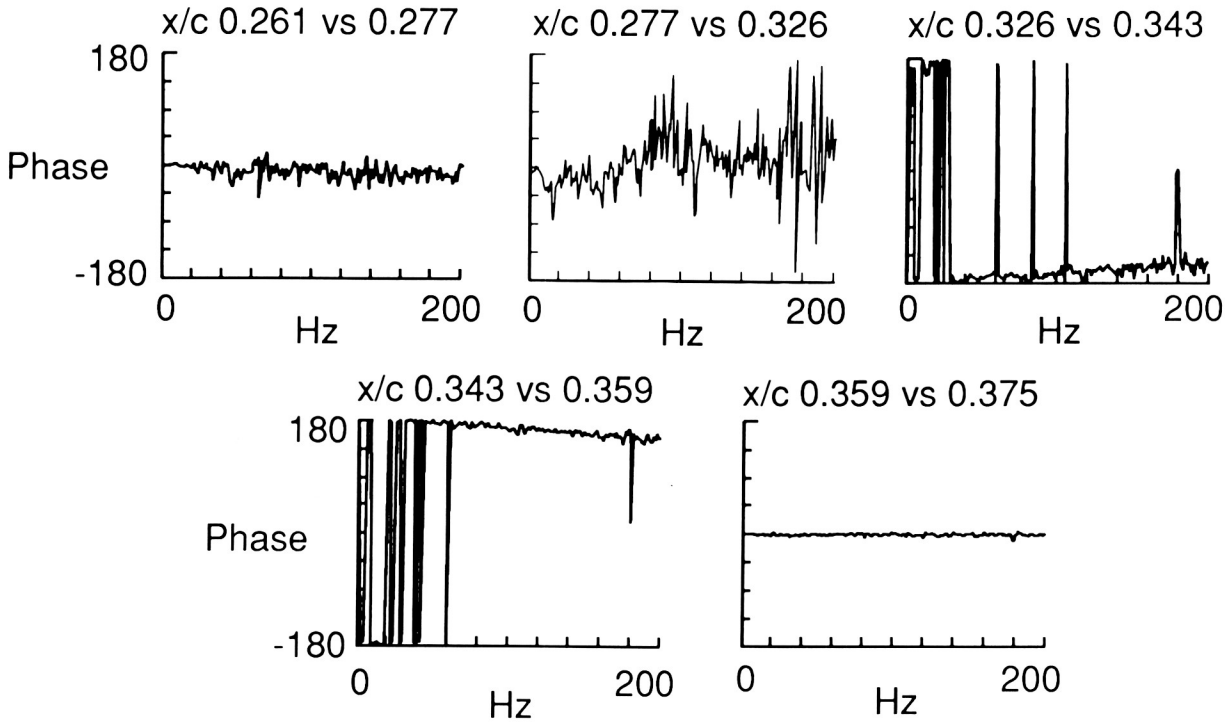

Figure 31. Phase correlation between successive gages showing phase reversals at separation and reattachment.

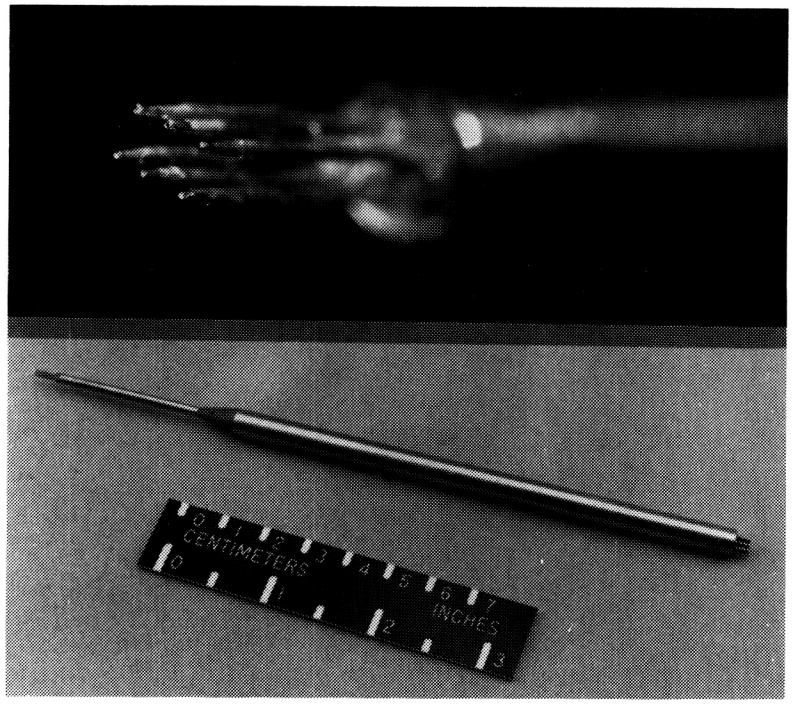

Figure 32. Enlarged photograph of a three-wire, hot-wire probe.

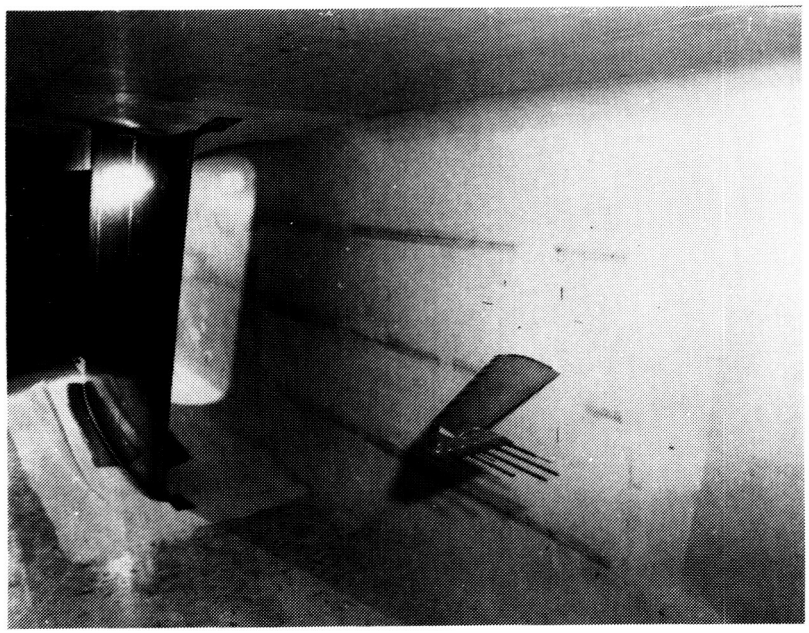

Figure 33. Photographs of probe-rake installation in LaRC 8-Foot Transonic Pressure Tunnel.

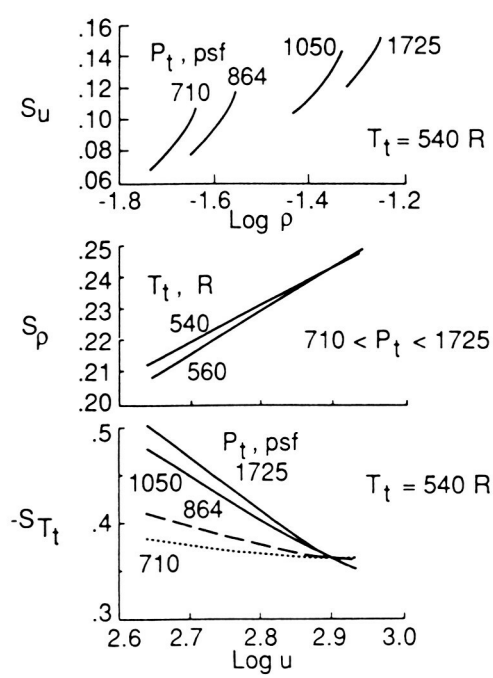

(a) 3-wire sensitivity coefficients S_u, S_{T_t}, and S_ρ .

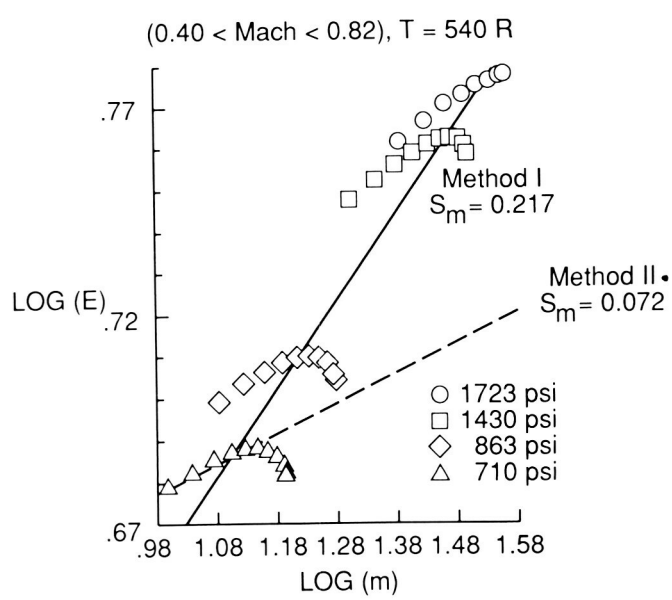

(b) Single wire variations of log(E) with log (m) and the associated sensitivities for Method I and II.

Figure 34. Single and 3-wire sensitivity coefficients.

ORIGINAL PAGE
BLACK AND WHITE PHOTOGRAPH

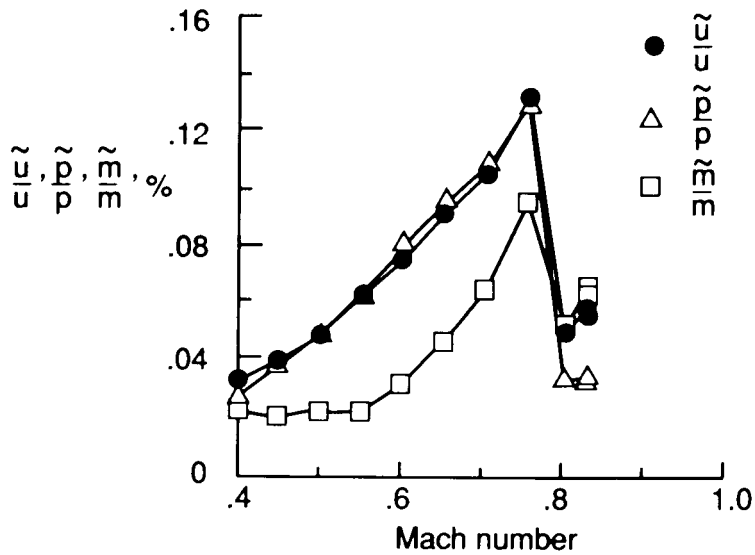

Figure 35. The variation of $\tilde{u}/u$, $\tilde{p}/p$, and $\tilde{m}/m$ with Mach number as determined from a single-wire hot-wire anemometer and microphone in the LaRC 8'TPT. p_t = 710 psf.

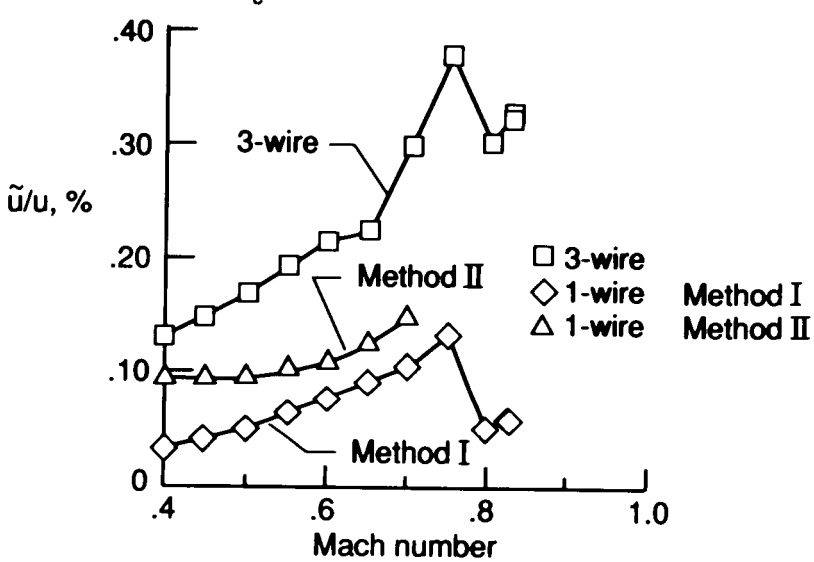

Figure 36. The variation of $\tilde{u}/u$ with Mach number for both single and 3-wire anemometers. p_t = 710 psf.

ORIGINAL PAGE
BLACK AND WHITE PHOTOGRAPH

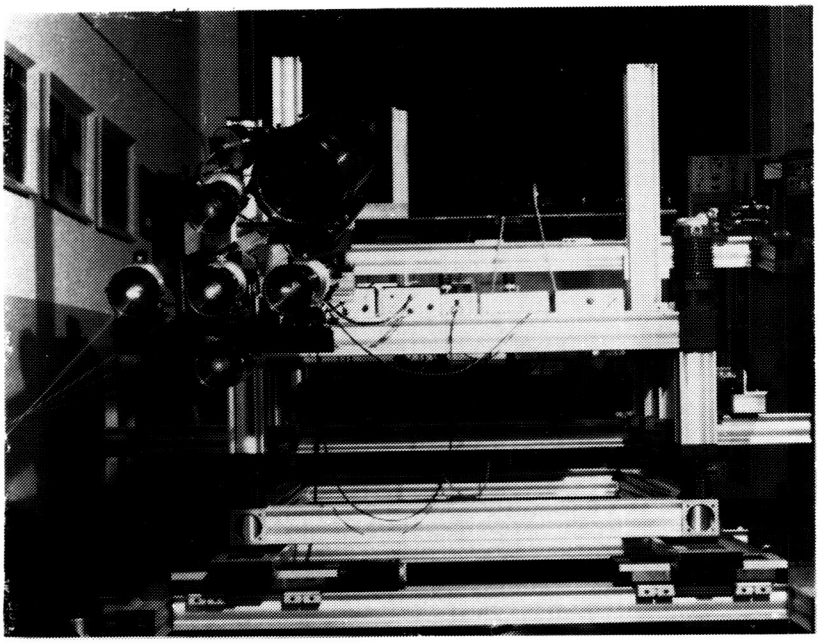

Figure 37. Photograph of the signal axis, 5-beam, 3-component LDV system used in LTPT Taylor-Gortler instability and juncture-flow investigations.

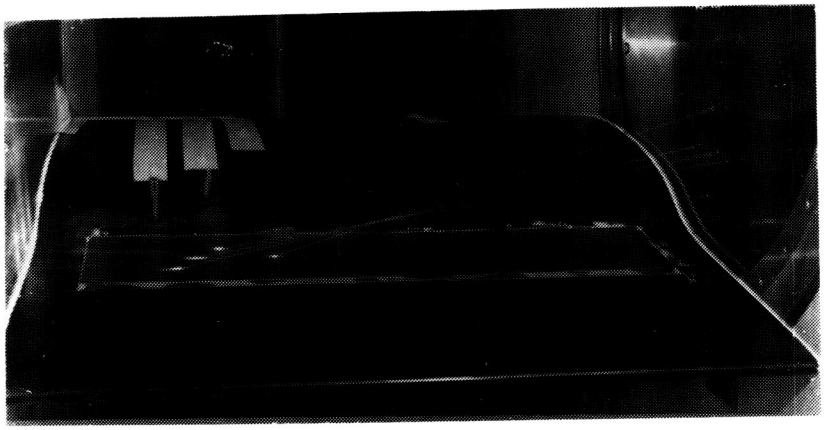

Figure 38. Photograph of airfoil with concave surface used in Taylor-Gortler instability investigation.

ORIGINAL PAGE
BLACK AND WHITE PHOTOGRAPH

ORIGINAL PAGE
COLOR PHOTOGRAPH

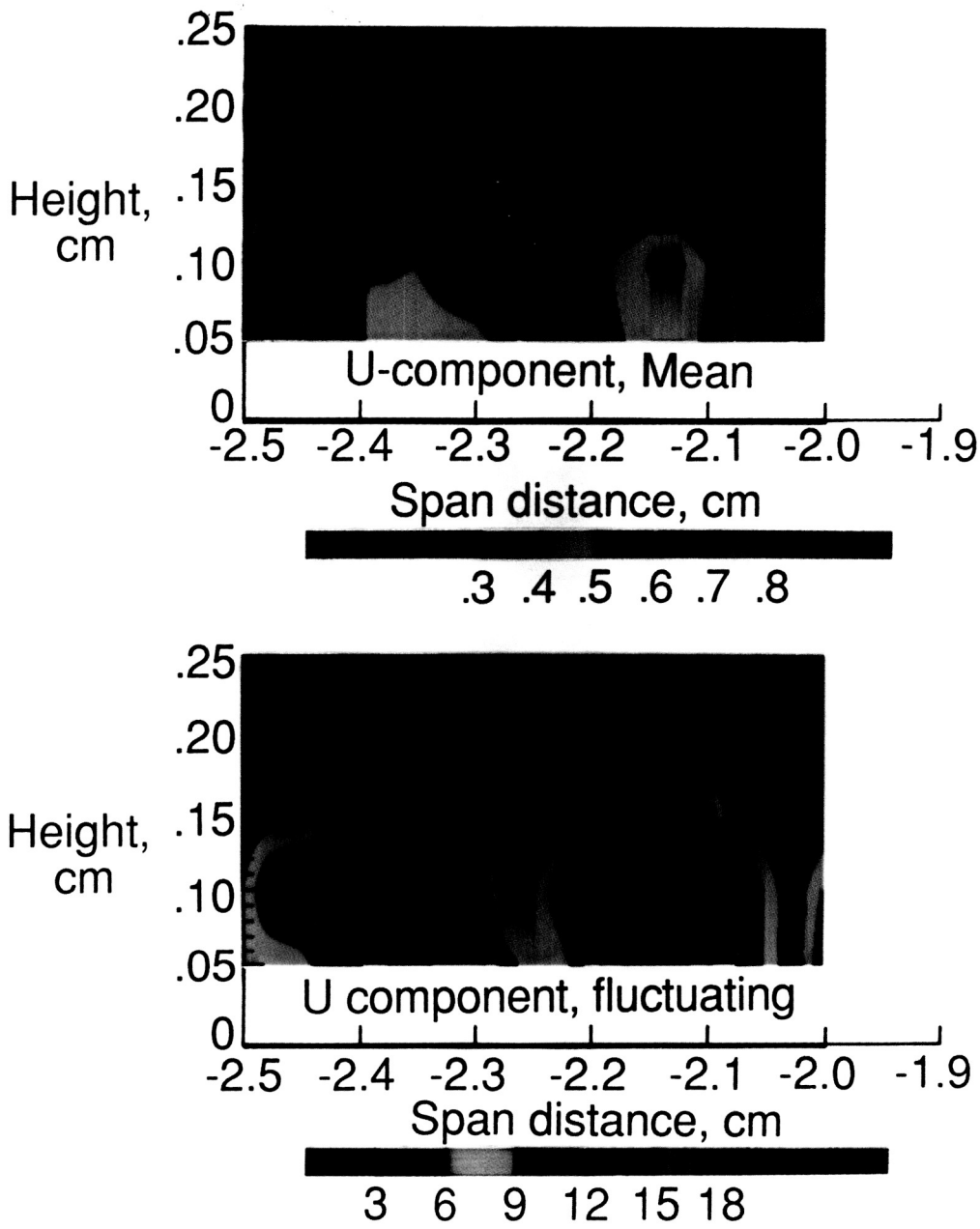

Figure 39. Contour plots of mean and fluctuating u components of velocity field obtained by 3-component LDV showing structure of Taylor-Gortler vortices.

Figure 40. Flow-visualization picture of Taylor-Gortler vortices in airfoil concave region looking downstream.

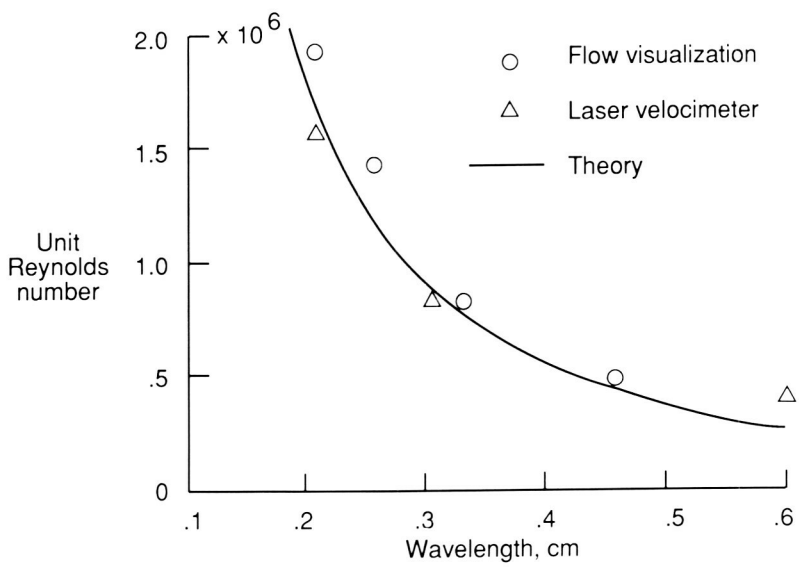

Figure 41. Comparison of theoretical and experimental data on Taylor-Gortler vortex spacing.

ORIGINAL PAGE
BLACK AND WHITE PHOTOGRAPH

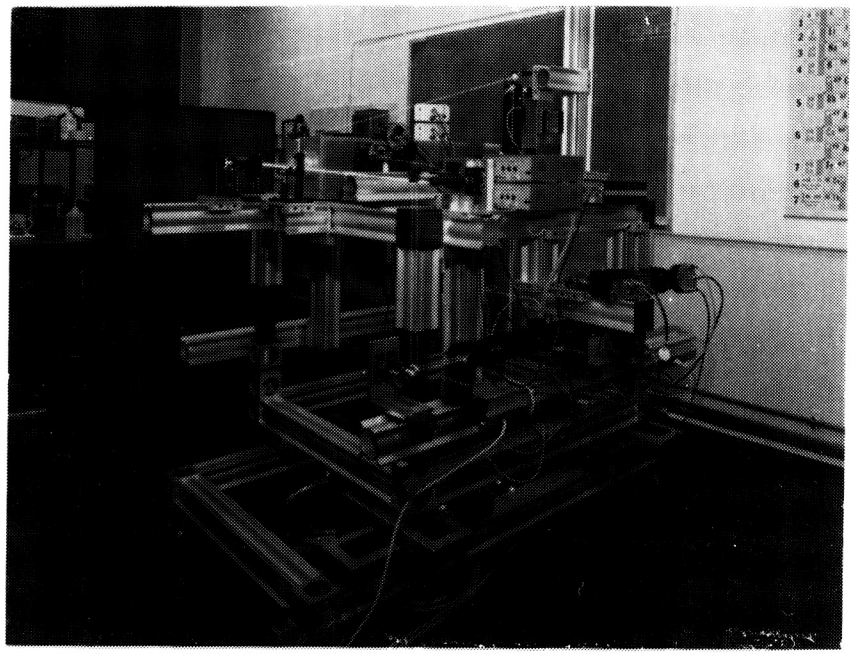

Figure 42. Photograph of orthogonal 3-component LDV system set up in laboratory to measure pipe flow.

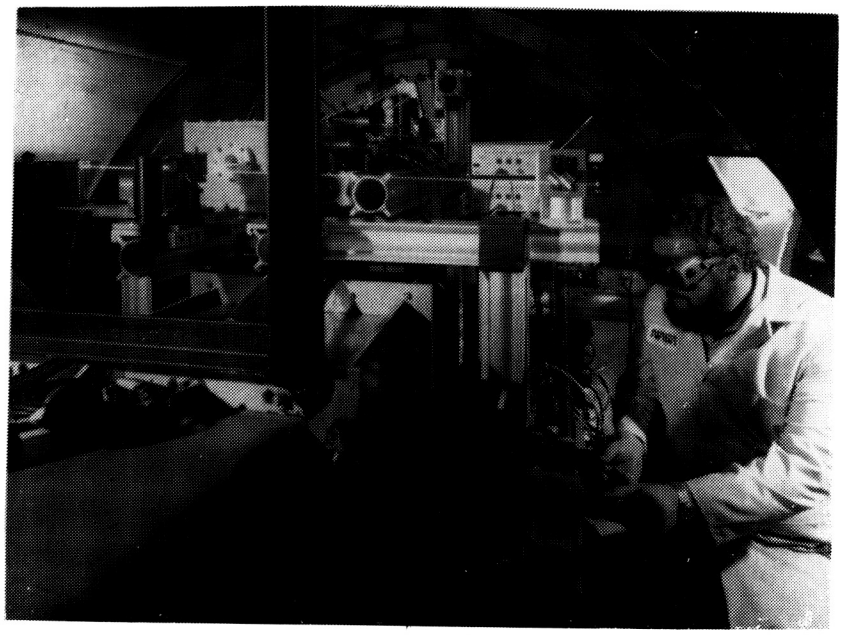

Figure 43. Photograph of an orthogonal 3-component LDV system installed in the Basic Aerodynamics Research Facility.

ORIGINAL PAGE
BLACK AND WHITE PHOTOGRAPH

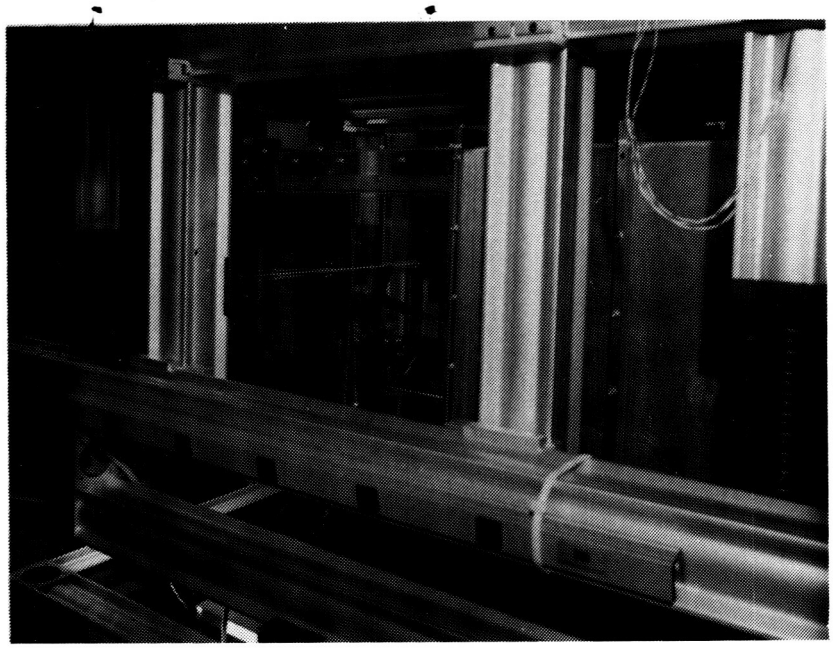

(a) Photograph of glass-walled test section with wall-interference model mounted on sting.

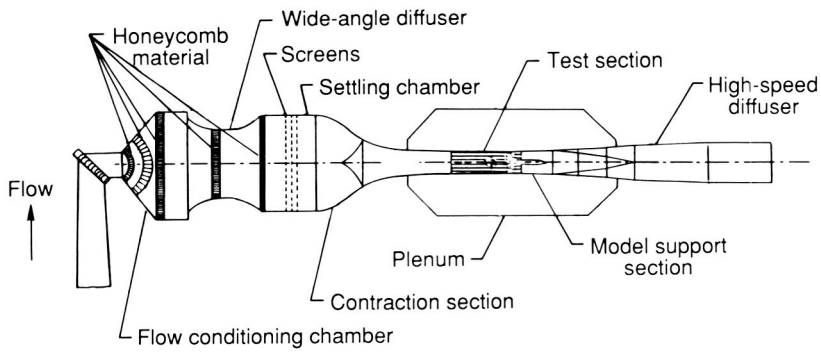

(b) Sketch of Basic Aerodynamics Research Facility showing contraction, test-section, plenum, and high speed diffuser.

Figure 44. Features of Basic Aerodynamics Research Facility.

ORIGINAL PAGE
BLACK AND WHITE PHOTOGRAPH

ORIGINAL PAGE IS
OF POOR QUALITY

ORIGINAL PAGE
~~COLOR PHOTOGRAPH~~

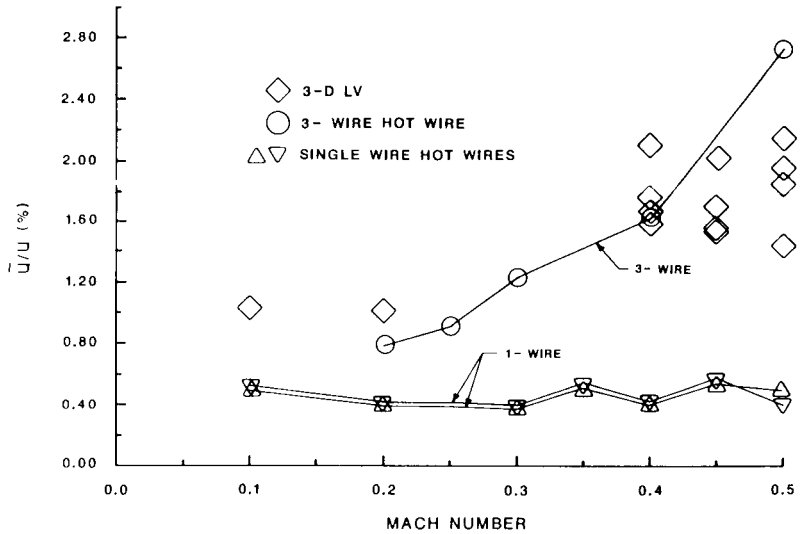

Figure 45. Comparison of hot-wire and LDV measurements for u/u in BARF.

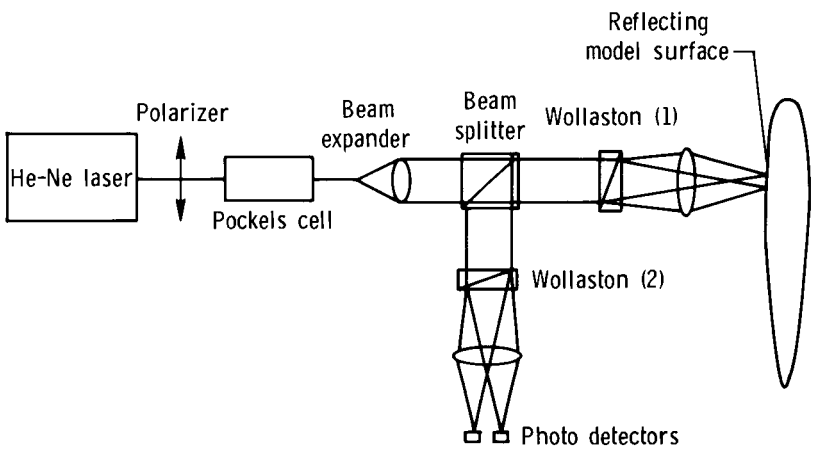

Figure 46. Schematic of laser interferometer system.

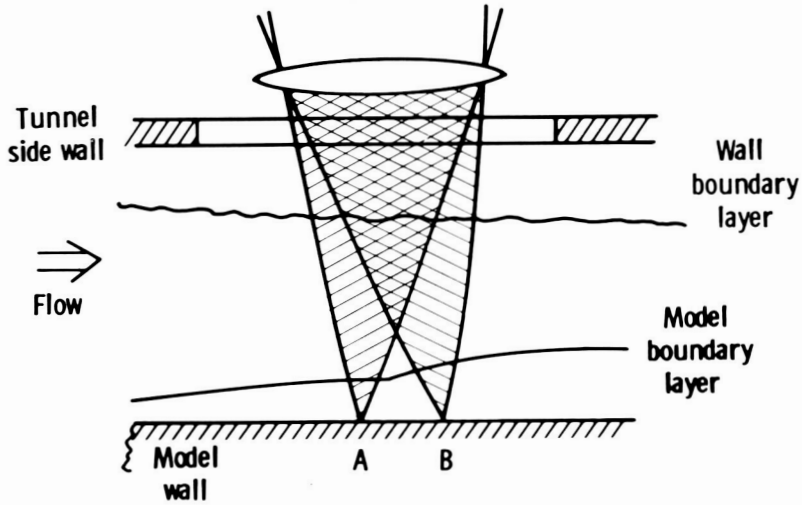

Figure 47. Sketch showing optical paths near model.

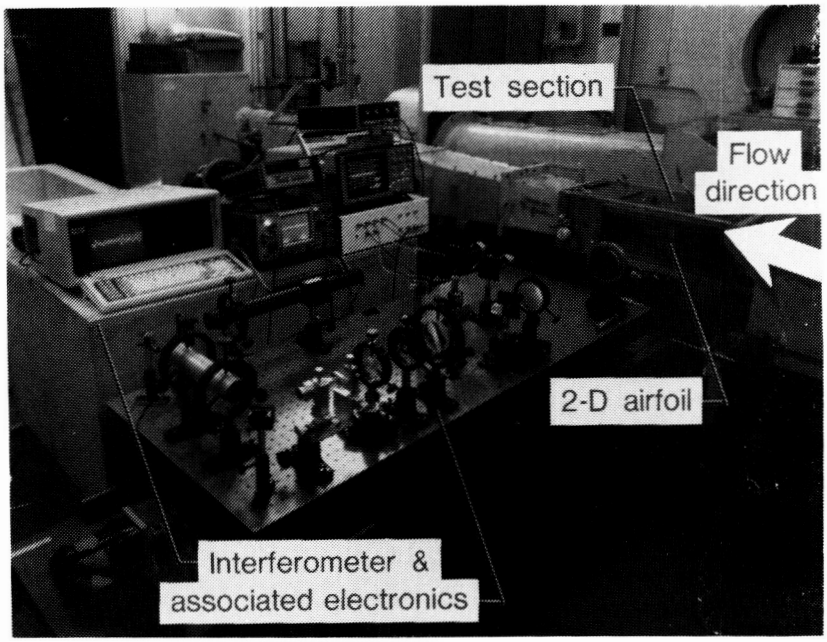

Figure 48. Photograph showing transition detection system (interferometer) installed in the Boeing Model Transonic Wind Tunnel.

ORIGINAL PAGE
BLACK AND WHITE PHOTOGRAPH

ORIGINAL PAGE
BLACK AND WHITE PHOTOGRAPH

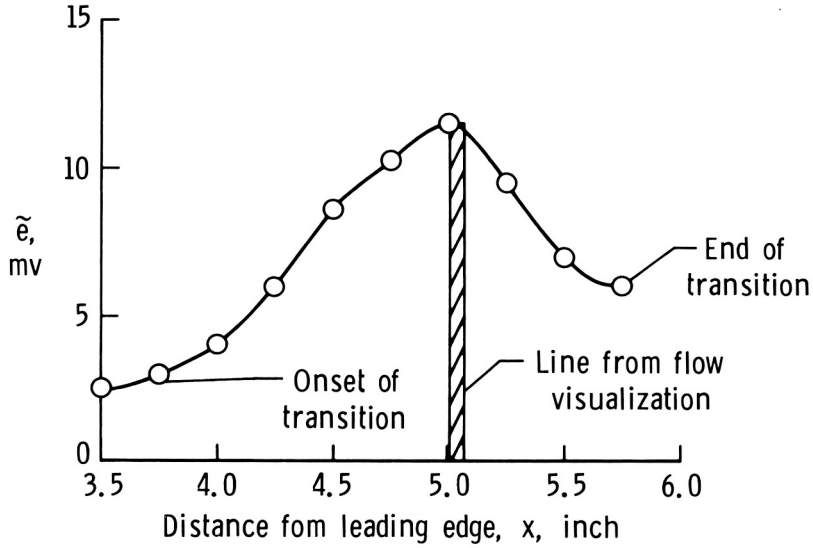

(a) RMS interferometer signal compared to beginning of scrubbed region in the sublimating chemical flow visualization. NACA 66-066, $M_\infty = 0.70$, $R_c = 2 \times 10^6$.

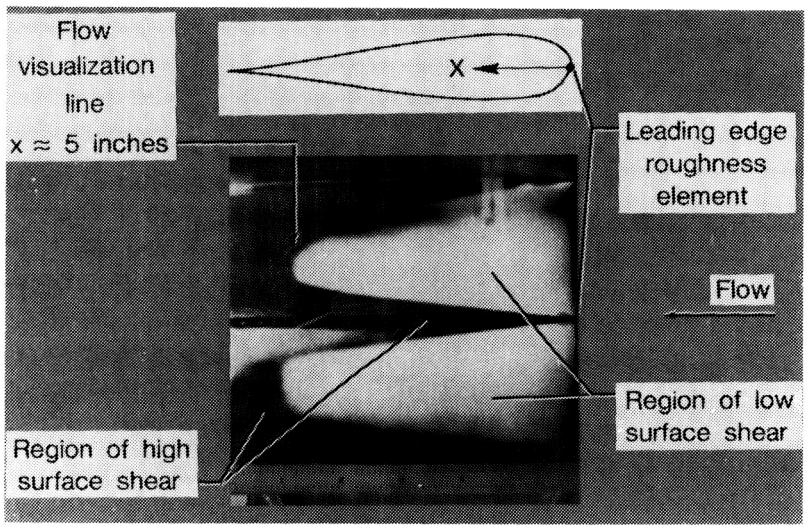

(b) Flow visualization picture showing-transition.

Figure 49. RMS interferometer signal variation through transition region and flow visualization picture showing transition location.

ORIGINAL PAGE
BLACK AND WHITE PHOTOGRAPH

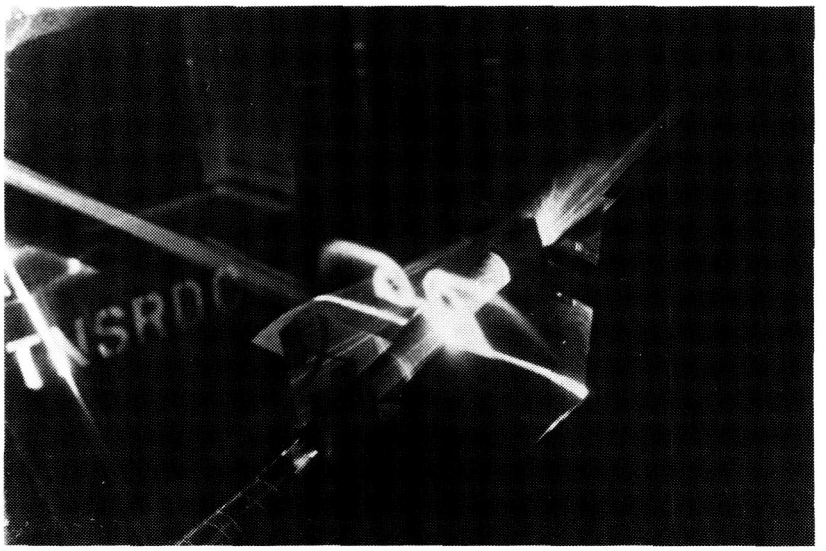

Figure 50. Laser vapor screen photograph as observed from a three-quarter right rear view. $M_\infty = 0.95$, $\alpha = 30^0$.

Figure 51. Laser vapor screen photograph as observed from a three-quarter left rear view. $M_\infty = 1.10$, $\alpha = 20^0$.

ORIGINAL PAGE
BLACK AND WHITE PHOTOGRAPH

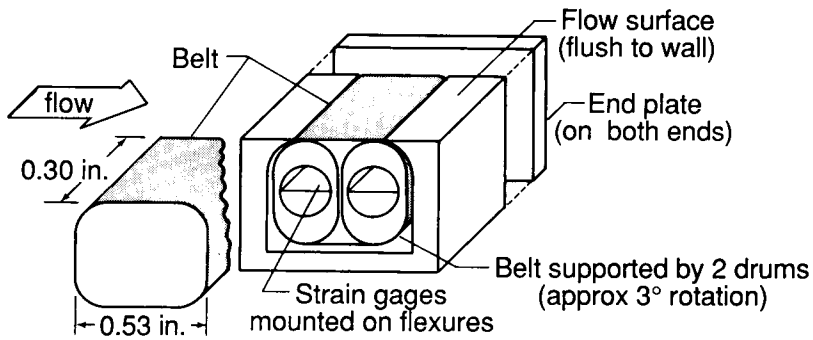

Figure 52. Sketch of the moving belt skin-friction gage showing its principal features.

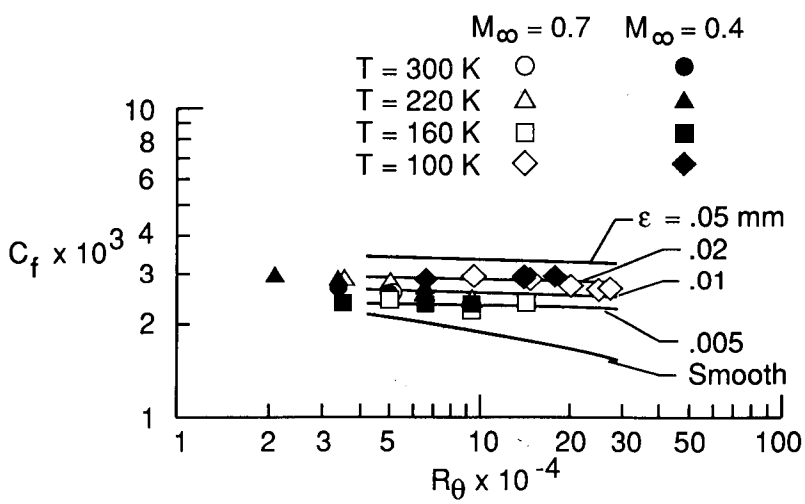

Figure 53. Plot of the variation of skin friction with Reynolds number based on momentum thickness.

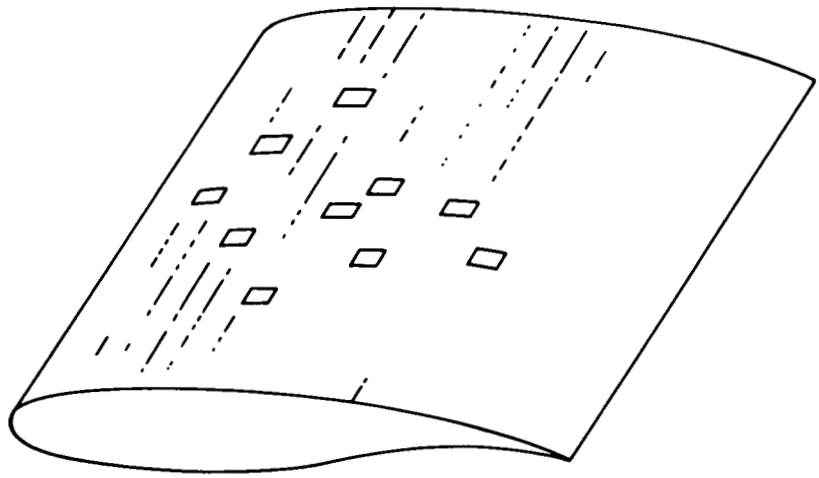

Figure 54. Sketch of an airfoil model with multiple skin-friction gages installed.

N89-20958

WALL INTERFERENCE ASSESSMENT AND CORRECTIONS

P. A. Newman
NASA Langley Research Center
Hampton, Virginia

W. B. Kemp, Jr. and J. A. Garriz
Vigyan Research Associates, Inc.
Hampton, Virginia

SUMMARY

Wind-tunnel-wall interference assessment and correction (WIAC) concepts, applications, and typical results are discussed in terms of several nonlinear transonic codes and one panel method code developed for and being implemented at NASA Langley Research Center. Contrasts between 2-D and 3-D transonic testing factors which affect WIAC procedures are illustrated using airfoil data from the 0.3-m Transonic Cryogenic Tunnel (TCT) and Pathfinder I data from the National Transonic Facility (NTF). Initial results from the 3-D WIAC codes are encouraging; research on and implementation of WIAC concepts will continue.

INTRODUCTION

The technology of wind-tunnel-wall interference was first formulated about 1919 by Prandtl (refs. 1-3), and its continued development, refinement, and extension parallels that of the wind tunnel. The classical theory, taken to mean that based upon boundary value problems for the linearized potential flow equation subject to linearized tunnel-wall boundary conditions, predicted wall interference satisfactorily in the open-jet and solid-wall wind tunnels used for subsonic testing. Furthermore, this theory pointed to the partially open test section as a possibility for minimizing wall interference, prompting the introduction of a slotted wall about 1948 (refs. 4-6). The ventilated wall allowed for tunnel testing through the transonic range without choking; however, for the sensitive high-speed flow and ventilated walls at the test section boundary, flow linearity and homogeneity became suspect. The evolution of this classical wall-interference theory and applications can be traced through a few sample works, listed herein as references 7 to 13.

The introduction of practical high-speed digital computers during the 1960's opened the door to computational aerodynamics. It permitted rapid systematic recalculations of the linear theory wall-interference parameters, particularly those for several formulations of the ventilated-wall boundary conditions (refs. 14, 15). However, interest in obtaining accurate results for the high subsonic speed regime led to the numerical solution of nonlinear partial differential equations. Demonstration of a method for making practical transonic aerodynamic calculations occurred about 1970 (ref. 16) and spawned applications within several years to rather complex geometric configurations and also for more realistic field equation sets. Numerical experiments related to tunnel-wall effects could be performed without the linearization restriction on either the

field equation or the wall boundary condition; it became evident that somewhere in the transonic flow regime linear superposition did not remain valid (ref. 17). During this same time frame, it was realized that ventilated tunnel-wall flow characteristics (from which the wall boundary conditions are obtained) were very nonlinear at transonic flow conditions and dependent upon the model pressure field (ref. 18). Many attempts to obtain satisfactory ventilated-wall boundary conditions have been and still continue to be made (ref. 19, 20); the early history of tunnel-wall boundary conditions can also be traced through the several works listed as references 7 to 13.

The concept of actively adapting the test section wall shape or flow condition in order to eliminate or minimize the interference as the test proceeds was put forward around 1973 (refs. 21, 22). The various procedures for implementing these concepts required hardware complexity in two forms: additional instrumentation for making flow property measurements near (or on) the walls; and, automatically variable geometry for iteratively adapting the test section at each data point. The feasibility of having instrumentation for routinely measuring flow data at or near the walls, as in the adaptive tunnel, also led to reformulations of the classical wall-interference ideas where various measured data were used in lieu of tunnel-wall and/or model boundary conditions. Two such posttest wall-interference-assessment formulations for 2-D subsonic and transonic flow were given in references 23 and 24, respectively; in these two, only measured pressures are used in the boundary conditions. Most posttest wall-interference-assessment/correction (WIAC) procedures were formulated by the early 1980's and are based upon linear field equations. However, since this is a transonic symposium, the present discussion of WIAC emphasizes the nonlinear transonic procedures. Progress in developing and applying WIAC methods from the mid-1970's to the present can be traced through the topical conference proceedings and summary papers listed as references 25 to 35.

In this paper, WIAC concepts, applications, and typical results are discussed in terms of several nonlinear transonic codes (refs. 23, 24, 36-48) and one panel method code (refs. 49-51) developed for and being implemented at NASA Langley Research Center. Contrasts between 2-D and 3-D transonic testing factors which affect WIAC procedures are illustrated using airfoil data from the 0.3-m Transonic Cryogenic Tunnel (TCT) and Pathfinder I data from the National Transonic Facility (NTF). In addition, both 2-D and 3-D Euler equation method WIAC codes have been developed (refs. 52, 53) but not yet implemented into a procedure nor used on real wind-tunnel data; the 3-D code is briefly discussed. The nonlinear procedures discussed herein are truly representative of what is currently available; only five other nonlinear code procedures have been published and apparently none of them has been used very much. Of these latter procedures, three are for 2-D flow (refs. 54-56), another is for axisymmetric flow (ref. 57), and the last is a two-variable procedure for 3-D flow (ref. 19). Note that reference 56, which discusses the latter of these 2-D nonlinear procedures, is the following paper in these proceedings. The 2-D WIAC procedures are pretty mature; a few sample results are shown and general observations about applications are made. Results from application of 3-D nonlinear transonic WIAC procedures to real wind-tunnel data have not yet been published; however, limited initial results for the Pathfinder I model tested in the NTF are given herein. Other research groups in government and industry have contributed to developing and testing the nonlinear WIAC procedures which are discussed.

SYMBOLS

arabic

b	wing or airfoil semispan
c	airfoil chord
$\bar{c}$	wing mean chord
C_d	2-D or section drag coefficient
C_ℓ	2-D or section lift coefficient
C_L	3-D configuration lift coefficient
C_m	2-D or section moment coefficient
C_n	2-D or section normal force coefficient
C_p	pressure coefficient
h	tunnel half-height
M	Mach number
Re	Reynolds number
Re_c	Reynolds number based on chord
u,v,w	velocity components parallel to x,y,z
v_{up}	vertical velocity at upstream end of test section
x, y, z	Cartesian coordinates, x streamwise

subscripts

c, corr	corrected condition or at corrected conditions
ref	reference condition or at reference condition
t	tail
w	wing
T	tunnel condition
WI	classical wall interference correction
WIAC	wall interference assessment/correction
o	calibration condition

greek

α	angle of attack
ΔC_p	pressure coefficient difference
ΔM	Mach number correction, $= M_{corr} - M_{ref}$
$\Delta\alpha$	angle-of-attack correction, $= \alpha_{corr} - \alpha_{ref}$
$\Delta C_{p_{wall}}$	scatter in wall pressure coefficient measurements
$\Delta C_{p_{gauge}}$	error due to pressure gauge accuracy
θ	flow angularity, $= v/u$
τ	airfoil thickness to chord ratio

abbreviations

AR	Model Aspect Ratio
AW, AWTS	Adaptive-Wall Test Section
BC	Boundary Condition
CFD	Computational Fluid Dynamics
DFVLR	Deutsche Forschungs- und Versuchsanstalt für Luft- und Raumfahrt
EUCOR3D	3-D Euler Equation WIAC code
NACA	National Advisory Committee for Aeronautics
NASA	National Aeronautics and Space Administration
NTF	National Transonic Facility
PANCOR	3-D Panel Method WIAC code
SW, SWTS	Slotted-Wall Test Section
SWBL	Sidewall Boundary Layer
TUNCOR	3-D TSDE Method WIAC code
TCT	Transonic Cryogenic Tunnel
TS	Test Section

TSDE	Transonic Small Disturbance Equation
VLOR	Vertical Line Over-Relaxation
WBT	Wing-Body-Tail Configuration
WIAC	Wall Interference Assessment/Correction
1-D	One-dimensional
2-D	Two-dimensional
3-D	Three-dimensional

WIAC CONCEPT, METHODS AND VALIDATION

WIAC concepts and applications draw upon ideas and capabilities from classical wall-interference theory, computational fluid dynamics (CFD) capabilities, and adaptive-wall technology. Briefly stated, the WIAC concept is to determine the wall interference which exists in conventional or partially adapted wind-tunnel data by making use of measurements made during the test, generally at or near the test-section walls. WIAC is, therefore, a posttest technique. The various applications or realizations of it depend upon the amount and type of data taken, the fluid flow equation approximations used in the analysis, the tunnel geometry and capabilities, as well as the timeliness, costliness, and accuracy desired in the result. It is not expected that all test data can be corrected; an assessment procedure should give some indication of the measure of goodness for the corrections which are obtained. When one considers the trade-offs between computational complexity versus wind-tunnel complexity, the two extremes being complete 3-D Navier-Stokes CFD solutions and 3-D adaptive-wall wind-tunnel data, respectively, then WIAC techniques lie between those extremes, hopefully making good use of the best practical aspects of both computational and wind-tunnel simulations.

Traditionally, transonic testing of both 2-D airfoil and 3-D configuration models has been carried out in wind tunnels with ventilated-wall test sections. As already noted, the flow interactions at these finite length walls are generally neither homogeneous nor linear and can be greatly influenced by the model flow field. Thus it is not surprising that the classical linear theories were found to be inadequate. For wind-tunnel data taken in most 3-D transonic facilities with ventilated-wall test sections, no wall-interference corrections were made. The renewed interest and effort in transonic wall-interference corrections here at NASA Langley commenced about 1974 in order to support the NTF. In this facility where both Mach and Reynolds numbers of free flight could be simulated (ref. 58, the first paper in this proceedings), wall interference would be a prime candidate for uncertainty in the test data. A conventional slotted-wall test section (with some capability to vary test-section divergence angle, reentry flap angle and step height, and diffuser entrance angle) was chosen since the 3-D adaptive wall concept had not yet been demonstrated to be feasible. Reference 59, a prior paper in this proceedings, discusses the history and current status of adaptive wall wind-tunnel technology. The total wall-

interference assessment/reduction effort at Langley which resulted from this renewed interest sparked by NTF was summarized in reference 33.

The elements involved in establishing the corrected test conditions in conventional transonic wind tunnels are depicted in Table I. Calibration runs and flow-angle surveys will have been made to determine the tunnel-empty Mach number and angle-of-attack offsets at the model location (ΔM_o, $\Delta\alpha_o$) which are to be applied in the data reduction process to reference conditions (M_{ref}, α_{ref}) for each test-data point in order to obtain the tunnel test conditions (M_T, α_T). Wall interference corrections in the conventional sense (ΔM_{WI}, $\Delta\alpha_{WI}$) are then determined by some procedure or analysis and applied to obtain the corrected flow conditions (M_c, α_c). As previously noted, this latter step is frequently not taken with ventilated transonic tunnel data. WIAC was developed and pursued in order to be able either to perform this latter step in a consistent and meaningful way or to indicate that it might not be possible. However, it should be pointed out that WIAC is not limited to application at only the latter step, as will be shown subsequently. The last entry in Table I is intended to indicate that the WIAC quantities (ΔM_{WIAC}, $\Delta\alpha_{WIAC}$) may be obtained with or without regard to a tunnel calibration and applied to whatever flow conditions ($M_?$, $\alpha_?$) were quoted as belonging to (i.e., used to reduce) the test data. In fact, application of WIAC procedures to calibration run data provides information about the tunnel-empty flow and effects due to variable tunnel-geometry parameters (ref. 51). For adapted-wall or partially adapted-wall tunnels, it is not clear what meaning should be attached to the tunnel-empty calibration. The WIAC procedure can be constructed to model (account for) tunnel geometry other than just the constraining walls (i.e., sting, sting support, etc.); the corrections obtained are then more properly called tunnel-interference rather than simply wall-interference corrections.

Transonic Concept

As previously noted, the possibility of routinely measuring flow data at or near the test-section walls (as required in the adaptive-wall tunnel) led to reformulations of the classical wall-interference ideas for 2-D airfoil tunnel data at subsonic (ref. 23) and transonic (ref. 24) flow conditions. A schematic of the WIAC concept where pressure measurements are made on both the top and bottom test-section walls as well as on both model surfaces is shown in Figure 1. As shown on the left side, the tunnel is instrumented to make the additional wall measurements. As shown on the right side, one now solves at least two fluid flow problems. The first is an equivalent inviscid tunnel flow simulation where pressure measurements on the walls and the model are specified boundary values with the measured lift and drag forces constrained (i.e., also used or matched). Since this is an inverse (or design-like) problem, the equivalent inviscid model shape is obtained as its solution. This shape is then used as the internal boundary condition in the second problem, with external boundary conditions appropriate to unbounded flow (free air). In this solution, the far-field Mach number, M, and angle of attack, α, required to minimize the error in local velocity (squared) or Mach number over the airfoil surface between these two calculated solutions are determined. The adjustments to far-field Mach number and angle of attack so determined define the corrections to tunnel conditions and the value of the error which was minimized is a measure of the residual interference.

In Figure 2, the upper half-plane of a Cartesian grid used in the transonic 2-D WIAC (ref. 24) is shown. The wind-tunnel grid (outlined by the inner bold lines) is used in the first problem discussed above; it is a proper subset of the free-air grid used in the second problem. The top and bottom wall boundary conditions are derived from the measured tunnel-wall pressure coefficients, C_p, and enforced along grid lines at the (mean) tunnel-wall location. Lift and, indirectly, drag enter the downstream outflow boundary condition, whereas it was assumed that the upstream upwash velocity components v_{up} near the walls would be measured and used in the inflow boundary condition. However, it was found (ref. 38) that these upwash components could be obtained iteratively by successive passes through the WIAC code if they were not measured. The airfoil boundary conditions, C_p for the in-tunnel calculation and equivalent inviscid airfoil shape for the free-air calculation, are applied along the slit as noted on Figure 2. For the free-air calculation, the grid extends outward in all directions from the tunnel grid, and approximate free-air far-field boundary conditions are imposed.

Classification of Methods

Kraft (ref. 60) has categorized WIAC procedures in terms of the number of measured data arrays used in the boundary conditions. The zero (0) measured-data array procedures are, therefore, pretest procedures and include the classical wall-interference correction methods as well as a number of more recent CFD code analyses which implement the tunnel-wall boundary condition in some functional (or empirical) form. The one (1) measured-data array procedures utilize one flow-variable array (C_p or θ or u or v) measured along an interface near (or on) the wall as outer boundary data. The two (2) measured-data array procedures utilize either two flow-variable arrays (C_p and θ or u and v) measured along an interface near (or on) the wall or one flow-variable array measured along two interfaces or boundaries. For 2-D WIAC procedures, these arrays of measured data are 1-D whereas for 3-D WIAC procedures the arrays are 2-D on each interface.

The concept outlined on Figures 1 and 2 applies to the 2-D transonic small disturbance equation (TSDE) WIAC procedures developed (refs. 23, 24, 36-44) and used to obtain the sample results to be presented herein; it is seen to be one type of the two-measured flow-variable array procedures. Another of this type, but using θ rather than C_p, was described by Schairer (ref. 61). Other 2-D WIAC procedures utilizing the two measured-variable arrays on one surface for boundary specification have been described by Ashill and Weeks (ref. 62), by Kraft and Dahm (ref. 63), and, at this symposium, by Lo and Sickles (ref. 56). These methods need no a priori definition of either the test model or the tunnel-wall characteristics. The 2-D WIAC procedures utilizing one measured-variable array at the walls (e.g., static pressure) plus a model representation based on known model geometry and aerodynamic loads have been given by Capelier, Chevallier, and Bouniol (ref. 64), Sawada (ref. 65), Mokry and Ohman (ref. 66), and Smith (ref. 67). Methods using either of the above boundary types require the assumption of linear superposition of model and tunnel influences to quantify the tunnel interference and, therefore, are strictly applicable only to purely subsonic flows. They are probably suitable, however, for low transonic cases where the outer boundary flow is fully subsonic. A review of most of these 2-D procedures is given in reference 31.

Both of the 3-D WIAC procedures developed (refs. 45-51) and used to obtain the sample results to be presented herein are one measured flow-variable array procedures. Measured tunnel-wall C_p data are used in the outer-wall boundary condition but the model is defined by its real geometry. For the 3-D TSDE WIAC procedure, TUNCOR, the inner model boundary condition for both the in-tunnel and free-air calculations is the model shape. With this one important exception, the TUNCOR concept and method are 3-D analogs of that outlined in Figures 1 and 2. For the 3-D panel method WIAC procedure, PANCOR, the measured wall C_p data are used in conjunction with geometric data (related to the slotted wall, plenum, and reentry flaps) to define the complete outer-wall boundary condition, as will be discussed later. The Euler equation based WIAC code (ref. 53) mentioned later is also a one measured-variable array method utilizing C_p in the outer boundary condition. Other 3-D one measured-variable array linear procedures have been developed by Rizk and Smithmeyer (ref. 68), Mokry (ref. 69), Schulz (ref. 70), Labrujere (ref. 71), Moses (ref. 72), and Crites (ref. 73), for example. Two 3-D two measured-variable array procedures have been discussed by Schairer (ref. 74) and Kraft, et al. (ref. 19). The classification by Kraft (ref. 60) does not distinguish those procedures which have been formulated to include the nonlinear flow equations; in fact, many of the WIAC procedures rely on linear superposition and are, therefore, not strictly appropriate for flows with extensive regions of supercritical flow. The nonlinear procedures to be discussed and others which are available have been identified in the Introduction section of this paper.

Validation Procedure

Validation or verification of the WIAC procedure results (or, for that matter, those obtained by any means) must depend upon the mutual agreement or consistency of results from all viable means of obtaining the answer. Since the WIAC is both an assessment and correction procedure, it is natural to assume that all test data contain some wall interference. Operating from this premise then, one would expect to obtain consistent corrected results for data from separate tests of a common model shape if the WIAC procedure were valid in accounting for all pertinent aspects of the interference. That is, test data on the same model in different tunnels/test sections, or test data from different size models in the same facility should collapse to a common curve, result, etc. A second variation of this theme is to make independent free-air flow-field calculations with the best available CFD codes at both uncorrected (M_T, α_T) and corrected (M_{corr}, α_{corr}) flow conditions. Comparison of calculated detail results (such as model surface C_p, lift-curve slope, drag-rise Mach number, etc.) with the experimental data and the experimental data renormalized to the corrected conditions, respectively, allows one to ascertain whether or not the corrections are valid or, perhaps, the range of validity.

WIAC APPLICATIONS TO AIRFOIL (2-D) DATA

Initial applications of WIAC were to airfoil tunnel data where, to good approximation, the flow is 2-D. Most of the procedures, both linear and nonlinear, have been discussed in reference 31. The techniques are relatively mature, but questions still remain concerning the tunnel sidewall boundary-layer (SWBL) interaction, particularly at transonic flow conditions. In this section,

test techniques which affect WIAC for 2-D transonic airfoil tunnel data are discussed so that a comparison can be made with the 3-D case. Then, recent results from application of nonlinear WIAC to sample data from the 0.3m TCT are given to illustrate several points.

2-D Test Techniques Affecting WIAC

Table II gives the transonic testing factors affecting 2-D WIAC. For routine testing, the airfoil chord, c, is typically the order of 1/2 to 1/4 of the tunnel half-height, h, resulting in solid blockage ratios, $\tau/(2h/c)$, of several percent. The measured model data generally includes 1-D pressure data, C_p, with good resolution which can be integrated to produce good values for the normal force coefficient, C_n, and moment coefficient, C_m. The drag coefficient, C_d, is normally deduced from measurements of the wake momentum deficit, taken on a wake rake. It is deemed to be more accurate than the value obtained using the axial force from integrated model pressures along with α_T and C_n. Measured field data on an interface near (or on) the upper and lower walls are needed for WIAC. These 1-D arrays are taken very near the center of the walls; C_p data can be obtained with good resolution and signal (to noise) strength. Figure 3 shows distributions of C_p (negative up) on the airfoil and tunnel walls. These data were from the 0.3-m TCT slotted-wall test section with a nominally sized (h/c = 2.0) supercritical model at transonic flow conditions. The vertical scale is given as the pressure coefficient difference, ΔC_p, over the vertical length of the chord, c. It can be seen that both on the model and wall the pressure signal (to noise) strength is good.

Measurements of 1-D data arrays of the flow angularity, θ, or upwash velocity, v, are more difficult near the walls of the ventilated-wall test sections used for transonic testing. In the case of the solid-wall adaptive tunnels, this information (within the local viscous effect) is given by the wall location. With all WIAC procedures using one-variable arrays of C_p or u, one flow angularity or upwash velocity measurement is required; it is needed by WIAC as an integration constant. In the present 2-D nonlinear WIAC procedures, this requirement has been circumvented in second and succeeding WIAC passes by using the front portion of the airfoil as a flow angle probe; procedures using two measured-variable arrays on a single interface should not require the additional θ measurement.

In airfoil testing, models are mounted between the two sidewalls on turntables in order to provide angle-of-attack changes. The boundary layers on these two sidewalls (SWBL) are subjected to the model pressure field which includes severe adverse pressure gradients (for the flow approaching the model leading and trailing edges and at shock waves) and rapid favorable gradients (behind the model leading and trailing edges). These SWBL interactions become so severe at transonic high-lift conditions that the flow is no longer 2-D. In fact, there are always some manifestations of 3-D flow near the sidewalls. This present 2-D nonlinear WIAC procedure incorporates several simple means for approximating the subsonic attached-flow SWBL interaction due to Barnwell and Sewall (ref. 75) and Murthy (ref. 76). Transonic 2-D WIAC procedures must include some accounting for the SWBL interaction; i.e., a 4-wall correction.

The test section design of ventilated-wall airfoil tunnels is generally near the classical-theory minimum blockage condition; this is required in order to be able to test without choking or extremely large blockage (Mach number) corrections. The test sections are ventilated, either by means of holes (perforated) or longitudinal slots. The minimum blockage condition, however, does mean that large angle-of-attack corrections are to be expected according to classical wall-interference theory. Adaptive-wall test sections have been used now for about a decade (ref. 59) in pilot-size (less than 1-ft diameter) and small (~2-ft diameter) airfoil tunnels. In these facilities, the wall adaptation attempts to minimize all aspects of the wall interference. The present adaptive-wall nonlinear 2-D WIAC procedure is deemed to assess and correct for the residual interferences.

Sample Results for 0.3-m TCT Data

A number of results obtained from various versions of the nonlinear 2-D airfoil WIAC codes have been presented over the last few years in references 23, 24, and 36-44. These results have been for data obtained in the NASA Langley 0.3-m TCT (ref. 77) for several different airfoil shapes tested during the Advanced Technology Airfoil Test Program (ref. 78) and later cooperative agreements with industry and foreign government laboratories. WIAC results have been obtained for both slotted- and adaptive-wall test sections. The technology is mature, and several findings have evolved from the work. These are briefly summarized as follows:

(a) For all of the airfoil data assessed to date, some wall interference appears to be present according to the WIAC procedure.
(b) The SWBL interaction effects appear to be part of (sometimes dominating) this wall interference and must be accounted for in WIAC.
(c) For test conditions near and above the transonic drag rise for aft-loaded supercritical airfoils at moderate to high lift, the simple approximate SWBL interaction models are inadequate (which is not surprising since these models are based upon subsonic attached-flow theories).
(d) Multiple passes (2 or 3) through the WIAC procedure are required to properly assess the unmeasured upstream flow angularity which directly influences the angle-of-attack correction.
(e) WIAC results for both ΔM and $\Delta\alpha$ are smaller for the adapted-wall test section than those for the slotted-wall test section.
(f) Independent transonic free-air CFD code solutions from both conservative full-potential with interacted boundary-layer (ref. 79) and Navier-Stokes (ref. 80) tend to confirm the WIAC results, except as noted in (c) above.
(g) Corrected data for common airfoils tested at different size and in different test sections tend to collapse to a common curve; i.e., the corrected data correlates.
(h) Not all test data are correctable by WIAC; for some cases the code solutions may not be obtained and for others, there may not be a good correspondence with any free-air result. Quantitative interpretation of the WIAC measure of error still appears to be elusive.

Some of the findings summarized above concerning application of the 2-D nonlinear WIAC are illustrated on the next several figures using transonic data for two different airfoils. Sample data and WIAC results for NACA 0012 airfoils of three chord lengths and CAST 10-2/DOA 2 airfoils of two chord lengths are discussed. The relative sizes of the models with respect to the test sections in which they were tested are given in Table III; also indicated are tunnel half-height to chord ratios, model aspect ratios, model thickness ratios, and references for both the data and WIAC results. As indicated earlier in discussing the present transonic WIAC concept, both the measured lift and drag are constrained; therefore, corrections to Mach number and angle-of-attack generally produce only small changes (due to the dynamic pressure rescaling) in C_ℓ and C_d, C_d being measured via the wake rake. Thus, the angle-of-attack correction, $\Delta\alpha$, is seen on a lift curve plot (C_ℓ versus α) as an α shift at almost constant C_ℓ whereas the Mach number correction, ΔM, is seen on a drag rise plot (C_d versus M) as an M shift at almost constant C_d. For a ventilated 2-D airfoil tunnel designed at near minimum classical blockage, the Mach number correction is generally small up to near the drag rise Mach number and above unless the contribution from the SWBL effect is large.

Shown in Figure 4 are the results of applying the 2-D WIAC to data from the adaptive-wall 0.3-m TCT for two different size models. The data shown were obtained during the adaptation sequence from unadapted to fully-adapted. These are lift curve plots and therefore illustrate the corrections to angle-of-attack at the nominal test conditions of M_T=0.65, $\alpha_T = 2^\circ$, and $Re_c = 9\times10^6$ on two different size NACA 0012 airfoils, h/c = 1.0 and h/c = 0.5. Data are shown as symbols for seven different model/tunnel configurations (though not all distinguishable at this scale) and these represent seven different tunnel wall interferences. The uncorrected data are shown in the upper left hand plot, having different C_ℓ at the same nominal test α. The solid curve, shown on all plots in this figure, is the free-air Navier-Stokes solution obtained from the code of Swanson and Turkel (ref. 80). The first application of WIAC (1st pass) assumes that the far upstream flow direction at the upper and lower wall positions is known and is used in the upstream boundary condition. As can be seen in the upper right hand plot, the angle-of-attack correction makes the lift-curve slopes for the two models approximately the same, but the curves themselves appear to have been displaced from one another. Successive applications of the WIAC procedure (passes) with improving estimates of the upstream flow direction (as deduced from the alignment of the computed and real model camber lines) produce angle-of-attack corrections which tend to collapse the two sets of data around the Navier-Stokes free-air solution. The interference and thus corrections were greatest for the larger model (h/c = 0.5, the 13" chord model in the 13" high AWTS) at the highest lift level; three WIAC passes were required to produce an acceptable correction.

The results of applying the 2-D WIAC to data from the slotted-wall test section of the 0.3-m TCT for two different size CAST 10-2/DOA 2 airfoils are shown in Figure 5. These are drag-rise curves and thus illustrate the Mach number corrections which are directly related to the SWBL interference and our approximation of it. The uncorrected data, plotted at the left, shows distinctly different drag-rise Mach numbers for the two different size models. Application of WIAC with the Barnwell-Sewall (ref. 75) SWBL approximation produces Mach number corrections which tend to spread, rather than collapse the curves at the drag rise as shown in the center plot. The Murthy (ref. 76) SWBL approximation includes a model aspect-ratio factor and reduces to the Barnwell-Sewall

approximation in the limit AR → 0, a narrow tunnel. It can be seen in the plot at the right that the knee of the drag-rise curves are most nearly collapsed, tending to define the same drag-rise Mach number.

Shown in Figure 6 are the results of applying the 2-D WIAC to data for the NACA 0012 airfoil in several sizes from both slotted-wall and fully adapted-wall test sections of the 0.3-m TCT. Both uncorrected and corrected data for lift curves (C_ℓ vs. α) and drag-rise curves (C_d vs. M) are shown in Figures 6a and 6b, respectively. The free-air Navier-Stokes results shown as the solid line are obtained from the code described in reference 80. The WIAC results utilized the SWBL approximation of Murthy (ref. 76). Again, the corrected data are collapsed and correlate well with the free-air result at the corrected conditions. Note also that the angle-of-attack and Mach number corrections are larger for the slotted-wall data.

WIAC APPLICATIONS TO CONFIGURATION (3-D) DATA

There are several fundamental differences between 2-D and 3-D transonic testing techniques and practices which have important implications for the WIAC procedures. Two of these differences are the amount of data measured and the means of model support. These will be discussed for the 3-D case in the following section and contrasted with the 2-D case discussed previously.

As already mentioned, several applications of linear WIAC procedures to 3-D tunnel data have appeared in the literature. The 3-D nonlinear WIAC results shown in the last section here, for the Pathfinder I in the NTF, are the first such results, as far as we know, to be published.

3-D Test Techniques Affecting WIAC

Table IV gives the testing factors affecting 3-D WIAC. Typical model sizes for transonic testing are generally governed by the model wing span, 2b, lift level, or body length. This results in solid blockage ratios of 1/2 to 1 percent; i.e., much less than 2-D airfoil tunnels. Thus, wing-section chord lengths are less than those in 2-D tunnels, and even when pressure distributions are measured, the resolution is not as good. Furthermore, there are seldom more than a few chordwise rows of pressure taps so that the resulting 2-D C_p arrays on the model are indeed very sparse. In fact, for many tests no model surface pressures are taken. For most tests, force balances are installed in the model or sting mount so that model aerodynamic forces are available. Thus, most 3-D WIAC procedures are constructed assuming that model pressures will not be available to be used as an inverse internal boundary condition. The model description must come from its geometry and the measured forces if it is required by the WIAC procedure. Figure 7a shows typical wing pressure coefficient data from the Pathfinder I model in the NTF. The dashed lines in the C_p distribution indicate missing data at the leading and trailing edges. Where data are taken, on six spanwise wing stations in this case, as indicated at the left, the signal (to noise) strength is good.

Measured 2-D field data arrays on interfaces near (or on) all walls are generally required by the 3-D WIAC procedures. Such large amounts of data are not going to be taken routinely and even those data which are taken generally have small signal (to noise) strength. This is illustrated in Figure 7b, where NTF wall pressure data, taken for a Pathfinder I test point, are shown along the top, bottom, and sidewall centerlines. As indicated at the left, the top and bottom wall data are taken on the centerlines of three slats, whereas the two sidewall pressure tap rows off the centerline are in the solid blanks covering the region reserved for the sidewall slots. The 2-D data arrays are indeed sparse, and the "noise" is evident; more will be said about this aspect later.

Measurement of 2-D arrays of the flow angularity, Θ, or boundary interface normal velocities near the walls is extremely difficult. The small blockage coupled with the 3-D relief effect implies very small signal strength. Thus the present 3-D WIAC procedures do not rely on such arrays of flow data. However, several simultaneous flow angularity measurements or frequent model inverted runs may be required in order to properly assess the upstream flow angularity which effectively appears in the boundary data or as integration constants.

The model support effects and resulting interference in 3-D testing are varied, depending on both the facility and test data desired. In semispan model testing there is generally one SWBL interaction at the root station. For transonic flow conditions where shock waves impinge upon this SWBL, the true 3-D effects are modified. In the WIAC procedure, measured C_p data, rather than a symmetry condition, should be used for the mounting-wall boundary condition. The usual means for supporting full-span models is a sting at the rear of the model generally through the fuselage. The model support can also be done via blade mount into the fuselage bottom or from the top at the vertical tail. These latter two arrangements, as well as some high angle-of-attack testing, require more complicated bent stings. The support interference can thus differ from test to test and, even though not generally considered to be wall interference, is certainly part of the tunnel environment interference. At transonic flow speeds, one may not be able to decompose or separately account for all of the individual interferences; therefore, the concept of tunnel interference may be the most proper.

Design criteria for 3-D transonic test sections vary even though most of the conventional ones are now ventilated. Again the relatively small blockage and 3-D relief effects make the classical minimum blockage criteria of lesser importance than in the airfoil tunnel. Adaptive-wall test sections specifically designed for 3-D testing have been at the pilot-size, with the one exception being the "rubber-wall" subsonic tunnel of the DFVLR (ref. 59). Several 2-D adaptive-wall tunnels have been used for testing 3-D models (ref. 59), and the criterion to which the 2-D wall is adapted varies. In these latter facilities, there will surely be residual interference, for which one needs a 3-D WIAC procedure. The two measured-variable array WIAC procedures may be better suited for this task. The last paper in this symposium (ref. 85) gives results for a semi-span wing tested in the 2-D AWTS of the 0.3-m TCT.

Description of 3-D Codes

Some features of the 3-D WIAC codes being developed for use in the NTF and to be discussed here are given in Table V. The left column lists the code

characteristics to be covered whereas the next three columns give those characteristics for the WIAC codes PANCOR, TUNCOR, and EUCOR3D respectively. PANCOR is based on linear-theory panel methods whereas TUNCOR and EUCOR3D are based on nonlinear flow equations.

The PANCOR code was developed by Kemp (refs. 49-51) in order to simulate the slotted-wall boundary flow features better than would be possible by using only the sparsely measured C_p distributions alone. Figure 8 depicts the types of singularity panels and networks used in PANCOR for the tunnel boundaries. It can be seen that the finite length, discrete, segmented source lines are used to simulate the slots; their strength is governed by the sparsely measured slotted-wall C_p distributions. Panel representations are used to simulate the solid surfaces (slats between the slots, sidewalls, and reentry flaps) as well as to enforce unperturbed outer flow and flow through the end planes of the test section. In addition, other tunnel features such as variable wall divergence, reentry flap settings, model sting, and sting support sector are also treated in PANCOR. Sample results from the application of this code to NTF data are shown later.

The TUNCOR code was developed by Rizk, et al (refs. 45-48) in order to provide a (nonlinear) transonic WIAC capability for the NTF. As indicated in Table V, this code is based upon numerical vertical line overrelaxation (VLOR) solutions of 3-D TSDE's, analogous to the 2-D procedure previously discussed. The grid and boundary conditions are the 3-D extensions of those depicted for the 2-D WIAC in Figure 2. The sparsely measured C_p distribution data on all of the walls are enriched and interpolated onto the outer boundary grid for the tunnel flow calculation in the WIAC procedure. Sample results from the application of this code to NTF data are also shown later.

The EUCOR3D code was also developed by Rizk et al (refs. 52, 53) in order to overcome some of the approximations inherent in the TSDE formulation of TUNCOR and to provide benchmark corrections against which more approximate WIAC codes could be evaluated. As indicated in the right column of Table V, EUCOR3D is based upon the Euler equations which are solved by an efficient numerical algorithm on an H-H body fitted grid. Figure 9 depicts this grid for a wing-body configuration; both symmetry plane and spanwise section cuts through the grid near the model are shown; the final shearing transformations to the outer flat tunnel-wall boundaries have not been included here. This code is still being debugged and adapted into a partially automated procedure; it has not yet been applied to real tunnel data.

Sample Results for NTF Data

WIAC results relevant to the NTF which are discussed here include numerical simulations of the Pathfinder I model in NTF-sized ideal tunnels, assessment of the "tunnel-empty" interference using NTF calibration data, and initial corrections of Pathfinder I data taken in the NTF. The size of the Pathfinder I model with respect to the NTF was that of a typical transport configuration for testing at high-subsonic speeds with little wall interference according to conventional guidelines. It was a 0.5% solid-blockage model. The only data published to date for both the NTF calibration and Pathfinder I tests are given in reference 58, the first talk in this symposium.

Numerically Simulated Pathfinder I in Ideal Tunnels

Numerical simulation of the Pathfinder I model in NTF-size ideal tunnels was performed in order to bracket and size the wall-interference corrections to be expected in the NTF. The open-jet and solid-wall outer boundary conditions represent the two extremes of a slotted-wall and, according to classical 3-D wall interference theory, produce corrections ΔM and $\Delta\alpha$ which bracket those for the ideal slotted wall. The numerical simulations were carried out using various options of the TUNCOR 3-D WIAC procedure; values of ΔM and $\Delta\alpha$ which were obtained are given in Table VI. The NTF test section design criterion was to eliminate lift interference with all four walls slotted, according to an empirically correlated ideal slotted-wall theory (ref. 86). Currently, the NTF sidewall slots are closed; therefore, the current configuration should appear to be somewhat closed. It can be seen from Table VI that the numerically simulated open-jet and solid-wall test section results bound those for the NTF slotted-wall configuration which were obtained from classical theory. This classical theory calculation also shows the present NTF configuration to be somewhat closed.

Figure 10 illustrates the effect of the WIAC corrections for these ideal open-jet and solid-wall tunnel results, in particular, those for the flow parameters C_L and the size of the embedded region of supersonic flow above the wing. The simulated test conditions are $M_T = 0.82$ and $\alpha_T = 1.93^\circ$. The lift curve, shown in Figure 10(a), is not sensitive to the Mach number correction, ΔM, so the effect of the angle-of-attack correction, $\Delta\alpha$, is readily seen. The baseline free-air curve, over approximately a 0.6° range, is established by the three open circles connected by the solid line; the open-jet and solid-wall tunnel solutions at the nominal α_T are seen to lie below and above the free-air curve, respectively. When the WIAC is applied, these results are shifted by $\Delta\alpha$ as indicated and lie very near the free-air curve. Figure 10(b) is more complicated since the size of the embedded supersonic flow region (bubble) depends upon both M and α (ΔM and $\Delta\alpha$). The free-air solution surface for this parameter versus M and α is denoted by the five open circles connected by solid lines, traces for $M = M_T$ (with α variable) and $\alpha = \alpha_T$ (with M variable). At the nominal tunnel conditions, M_T and α_T, the open-jet and solid-wall tunnel results lie below and above the free-air surface respectively. Upon correction by the WIAC procedure, the results are seen to closely approach the free-air surface from below and above, respectively.

Typical NTF Calibration Data

Recall from the earlier discussion on the WIAC concept that calibration tests are performed to assess the "tunnel-empty" Mach number, ΔM_o, and flow angularity, $\Delta\alpha_o$, offsets (corrections) which must be applied to the reference values deduced from the measured data in order to arrive at the test conditions, M_T and α_T. Conventional wall-interference corrections, ΔM_{WI} and $\Delta\alpha_{WI}$, are then deemed to be those attributable to the wall <u>after</u> consideration of the calibration offsets. The WIAC procedure can be applied with or without the calibration; however, some subtle differences need to be considered. Kemp (ref. 51) has discussed the philosophy of WIAC without regard to needing the tunnel calibration, structured the PANCOR procedure accordingly and, thus, obtains tunnel corrections (or more properly, interference fields) which correspond to ΔM_{WI} and $\Delta\alpha_{WI}$ <u>plus</u> the effect of calibration offsets.

In the NTF, test-section wall-divergence (convergence) angles can be varied in order to provide the capability for maintaining zero Mach number gradient through the "empty" test section over the wide range of Mach and Reynolds numbers achievable. Typical wall-angle settings for uniform tunnel-empty Mach number through the test section as well as the Mach number offsets (corrections) from the reference values are determined in the tunnel calibration as a function of M and Re. During this calibration, wall pressure data were taken so that the WIAC codes could be used to assess the calibration. Application of WIAC procedures to calibration data provides information about the tunnel-empty flow and effects due to variable tunnel-geometry parameters. Such studies have been made using the PANCOR code and are reported in reference 51. An example of the PANCOR WIAC analysis for two sample NTF calibration points is shown in Figure 11. The distribution of flow angle along the tunnel centerline is shown. The upstream test-section flow angularity was assumed to be zero and, according to the WIAC code, a downwash is being produced which amounts to about 0.1° at the nominal model location. This occurs for both M_T = 0.6 and 0.8.

Results from both TUNCOR and PANCOR WIAC analyses of calibration data from the NTF for nominal tunnel Mach numbers of 0.6 and 0.8 at a Reynolds number of 4×10^6/ft are given in Table VII. Here, the WIAC results are compared with the experimental values of ΔM from the tunnel calibration and $\Delta\alpha$ obtained from lifting models tested in both the upright and inverted positions (ref. 58). The first row of results (where the upstream upwash velocity, v_{up}, is set to zero) is from the first pass. Both WIAC codes assess, from the measured wall-pressure signatures used in the boundary conditions, that the upstream part of the test section is generating about 0.1° downwash, indicating either (a) that value at the model position, or (b) a non-zero upwash at the upstream end of the test section. As can be seen from the model upright and inverted tests, the flow angularity in the vicinity of the model location is about 0.01° upwash. When an upwash equal to the negative of that at the model location obtained from the first pass is used as the upstream value in the second pass (i.e., $v_{up} = -\Delta\alpha_1$) then the second pass WIAC assessments show zero or small positive upwash at the model. Without an independently measured flow angularity somewhere in the test section during the test, this second pass through WIAC cannot be any more meaningful than the first pass; a flow angle criterion must be satisfied somewhere in the test section in order to have properly aligned the flow and deduce an angle-of-attack correction. These calibration points, using the upright and inverted model data, give the "zero-lift" value for this upstream flow angularity; it should be measured during the tunnel run for each data point.

Typical NTF Pathfinder I Data

The NTF Pathfinder I data used here for assessment by the WIAC procedures had been reduced before the tunnel calibration had been included in the tunnel data-reduction process. Thus, the reference values of static pressure and corresponding values of Mach number and dynamic pressure were used to compute C_p, etc. in the data reduction. This is evident in Figure 12, where tunnel sidewall centerline C_p data are shown. It can be seen that the far upstream values of the C_p from the model wall-pressure signature, denoted by the solid symbols, do not vanish. In addition, these model signature C_p data show a scatter estimated to be about ±0.003 which is larger than the indicated gauge accuracy and therefore due perhaps to local wall or pressure tap imperfections. When the calibration run ("tunnel-empty") wall-pressure signature at the same tunnel M and Re is

subtracted (as a tare) from the model wall-pressure signature, the data denoted by the open symbols (model-no model) are obtained. It can be seen in taking such a tare correction of the wall C_p data, that one must make a corresponding Mach number correction or accounting and also (perhaps) an unknown flow angularity correction.

The WIAC codes have been run with both tared and untared data in the outer boundary condition. The formulation of the PANCOR code was made assuming that one should not make such tare corrections since one is in effect subtracting out part of the tunnel interference present in the test data point. On the other hand, boundary conditions presently in the TUNCOR code seem to be more appropriate, particularly at the upstream and downstream ends of the test section, to properties exhibited by the tared wall-pressure signature. Details and conclusions relating to this matter are still being investigated in both WIAC codes. As has been seen, both codes give very good assessment of the tunnel calibration, where one must use the untared signature.

Sample PANCOR code results for ΔM are presented as a contour plot in the wing-plane on Figure 13. The data were taken at $M_T = 0.6$, $\alpha_T = 4.3^\circ$, and $Re_{\bar{c}} = 2x10^6$ and the WIAC results are for no tare correction of the tunnel wall C_p signature. It can be seen that the principal part of the correction is that due to the tunnel calibration, -0.0037, as previously quoted in Table VII. The ΔM deviations from this value over the model are seen to be an order of magnitude smaller, tending to confirm the NTF slotted-wall test section design results given in Table VI.

Sample TUNCOR code results showing the influence of $\Delta\alpha$ on the lift curves at M = 0.6 and 0.8 for $Re_{\bar{c}} = 2x10^6$ are given in Figure 14. The tunnel-wall C_p signature used in the WIAC boundary condition is that "tared" using the corresponding calibration wall signature. It can be seen that the angle-of-attack corrections are indeed small and positive for positive C_L. This also agrees with the NTF slotted-wall tunnel design estimates based on classical theory and given in Table VI. However, the small size of these corrections does not necessarily mean that they are of no concern or consequence. The sensitivity of the supercritical flow on the Pathfinder I wing to such small changes in the tunnel Mach number and angle of attack was demonstrated in reference 58.

CONCLUSIONS

Several general conclusions are drawn here for the WIAC applications to both 2-D and 3-D transonic wind-tunnel data. Recall that a number of specific findings (conclusions) for the 2-D nonlinear WIAC have already been given in the section of this paper concerning application to the 0.3-m TCT airfoil data.

General conclusions with respect to the 2-D airfoil-tunnel WIAC are:

(a) The nonlinear, 4-wall, posttest WIAC procedures offer a means for assessing and correcting transonic wind-tunnel data to accuracies approaching present-day requirements for airfoil test results.

(b) At transonic flow conditions with very large regions of supercritical flow, the complicated 3-D sidewall boundary-layer interaction is inadequately modelled by simple approximations; further work is required for this aspect.

General conclusions with respect to the 3-D configuration-tunnel WIAC are:

(a) A high degree of quality is needed in the wall C_p signature data since the signal (to noise) is small relative to that from 2-D airfoil tunnels.

(b) For one measured-data, C_p, array WIAC procedures, some flow angle data, taken during the model test runs, is also required.

(c) The nonlinear 3-D WIAC is just now being applied to real 3-D transonic data while the transonic limits of applicability of the linear 3-D WIAC are still being investigated; initial results from both procedures are encouraging.

REFERENCES

1. Prandtl, L.: Tragflügeltheorie, Part II. Nachrichten der K. Gesellschaft der Wissenschaften zu Göttingen, 1919.

2. Prandtl, L.; and Tietjens, O. G.: Applied Hydro- and Aerodynamics, Dover, NY, 1957.

3. Prandtl, L.: Tragflügeltheorie II. Ludwig Prandtl gesammelte Abhandlunge, Springer-Verlag, 1961, pp. 346-372.

4. Wright, Ray H.; and Ward, Vernon G.: NACA Transonic Wind-Tunnel Test Sections. NACA Report 1231, 1955.

5. Becker, John W.: The High-Speed Frontier - Case Histories of Four NACA Programs, 1920-1950. NASA SP-445, 1980, pp. 61-118.

6. Hansen, James R.: Engineer in Charge: A History of the Langley Aeronautical Laboratory, 1917-1958. NASA SP-4305, 1987, pp. 311-331.

7. Theodorsen, T.: The Theory of Wind-Tunnel Wall Interference. NACA Report No. 410, 1931.

8. Allen, H. Julian; and Vincenti, Walter G.: Wall Interference in a Two-Dimensional-Flow Wind Tunnel, With Consideration of the Effect of Compressibility. NACA Report No. 782, 1944.

9. Goethert, B. H.: Transonic Wind Tunnel Testing. Edited by W. C. Nelson. AGARDograph 49. Pergamon Press, 1961.

10. Pope, Alan; and Harper, John J.: Low-Speed Wind Tunnel Testing. John Wiley & Sons, Inc., 1966, Chapter 6, Wind Tunnel Boundary Conditions.

11. Pankhurst, R. C.; and Holder, D. W.: Wind-Tunnel Technique, An Account of Experimental Methods in Low- and High-Speed Wind Tunnels. Sir Isaac Pitman & Sons, LTD., 1952 (reprinted with corrections 1965), Chapter 8, Tunnel Interference Effects.

12. Garner, H. C.; Rogers, E. W. E.; Acum, W. E. A.; and Maskell, E. C.: Subsonic Wind Tunnel Wall Corrections. AGARDograph 109, 1966.

13. Pindzola, M.; and Lo, C. F.: Boundary Interference at Subsonic Speeds in Wind Tunnels with Ventilated Walls. AEDC TR-69-47, 1969.

14. Keller, J. D.; and Wright, R. H.: A Numerical Method of Calculating the Boundary-Induced Interferences in Slotted or Perforated Wind Tunnels of Rectangular Cross Section. NASA TR R-379, 1971.

15. Keller, J. D.: Numerical Calculation of Boundary-Induced Interference in Slotted or Perforated Wind Tunnels Including Viscous Effects in Slots. NASA TN D-6871, 1971.

16. Murman, Earll M.; and Cole, Julian D.: Calculation of Plane Steady Transonic Flows. AIAA J., vol. 9, Jan. 1971, pp. 114-121.

17. Murman, Earll M.: Computation of Wall Effects in Ventilated Transonic Wind Tunnels. AIAA Paper 72-1007, 1972.

18. Jacocks, J. L.: An Investigation of the Aerodynamic Characteristics of Ventilated Test Section Walls for Transonic Wind Tunnels. Ph.D. Dissertation, University of Tennessee, December 1976. (Also available as AEDC-TR-77-61, 1977.)

19. Kraft, E. M.; Ritter, A.; and Laster, M. L.: Advances at AEDC in Treating Transonic Wind Tunnel Wall Interference. 15th Congress, International Council of the Aeronautical Sciences, London, U.K., Sept. 7-12, 1986. Proceedings, Vol. 2, 1986, pp. 748-769. (ICAS-86-1.6.1).

20. Everhart, Joel L.: Theoretical and Experimental Studies of the Transonic Flow Field and Associated Boundary Conditions Near a Longitudinally-Slotted Wind-Tunnel Wall. D.Sc. Dissertation, George Washington University, Feb., 1988.

21. Ferri, A.; and Baronti, P.: A Method for Transonic Wind-Tunnel Corrections. AIAA J., vol. 11, Jan. 1973, pp. 63-66.

22. Sears, W. R.: Self Correcting Wind Tunnels. The Aeronautical Journal, vol. 78, Feb./Mar. 1974, pp. 80-89.

23. Kemp, William B., Jr.: Toward the Correctable-Interference Transonic Wind Tunnel. AIAA Ninth Aerodynamic Testing Conference, June 1976, pp. 31-38.

24. Kemp, W. B.: Transonic Assessment of Two-Dimensional Wind Tunnel Wall Interference Using Measured Wall Pressures. NASA CP-2045, 1978, pp. 473-486.

25. AGARD: Wind Tunnel Design and Testing Techniques. Proceedings of the Fluid Dynamics Panel Symposium, London, Oct. 6-8, 1975, AGARD-CP-174, 1976.

26. Elsenaar, A. (Editor): Two-Dimensional Transonic Testing Methods, Final Report. NLR-TR-83086, GARTEUR/TP-011 (work completed July 1981).

27. AGARD: Windtunnel Capability Related to Test Sections, Cryogenics, and Computer-Windtunnel Integration. Report of The Windtunnel Testing Techniques Sub-Committee of the AGARD Fluid Dynamics Panel, AGARD-AR-174, 1982.

28. AGARD: Wall Interference in Wind Tunnels. 50th Fluid Dynamics Panel Specialists' Meeting, London, England, May 19-20, 1982, AGARD-CP-335.

29. Newman, P. A.; and Barnwell, R. W., editors: Wind Tunnel Wall Interference Assessment/Correction, 1983. A workshop held at NASA Langley Research Center, Hampton, VA., Jan. 25-26, 1983. NASA CP-2319, 1984.

30. AGARD: Wind Tunnel & Testing Techniques. Symposium, Cesme, Turkey, Sept. 26-29, 1983, AGARD-CP-348.

31. Mokry, M.; Chan, Y. Y.; and Jones, D. J.; Edited by Ohman, L. H.: Two-Dimensional Wind Tunnel Wall Interference. AGARD AG-281, 1983.

32. Hornung, H.; and Stanewsky, E. (editors): Adaptive Wall Wind Tunnels and Wall Interference Correction Methods. Oct. 15-17, 1984, Rep. no. DFVLR-IB-222-84-A-37, 1984.

33. Newman, P. A.; Mineck, R. E.; Barnwell, R. W.; and Kemp, W. B., Jr.: Wind Tunnel Wall Interference. Langley Symposium on Aerodynamics, Vol. I, NASA CP-2397, 1986, pp. 225-260.

34. AGARD: Aerodynamic Data Accuracy and Quality: Requirements and Capabilities in Wind Tunnel Testing. AGARD Fluid Dynamics Panel Symposium, Naples, Italy, Sept. 28 - Oct. 1, 1987. (AGARD CP-429, 1988.)

35. Tuttle, M. H.; and Cole, K. L.: Wind Tunnel Wall Interference (Jan. 1980 - May 1988) - A Selected, Annotated Bibliography. NASA TM-4061, 1988.

36. Kemp, W. B., Jr.: TWINTAN: A Program for Transonic Wall Interference Assessment in Two-Dimensional Wind Tunnels. NASA TM-81819, 1980.

37. Kemp, W. B., Jr.; and Adcock, J. B.: Combined Four-Wall Interference Assessment in Two-Dimensional Airfoil Tests. AIAA Paper 82-0586, 1982. (AIAA J., Vol. 21, 1983, pp. 1353-1359).

38. Gumbert, C. R.; Newman, P. A.; Kemp, W. B., Jr.; and Adcock, J. B.: Adaptation of a Four-Wall Interference Assessment/Correction Procedure for Airfoil Tests in the 0.3-m TCT, pp. 393-414 of reference 29.

39. Kemp, W. B., Jr.: TWINTN4: A Program for Transonic Four-Wall Interference Assessment in Two-Dimensional Wind Tunnels. NASA CR-3777, 1984.

40. Gumbert, C. R.; and Newman, P. A.: Validation of a Wall Interference Assessment/Correction Procedure for Airfoil Tests in the Langley 0.3-m Transonic Cryogenic Tunnel. AIAA Paper 84-2151, 1984.

41. Gumbert, C. R.: User Manual for 0.3-m TCT Wall-Interference Assessment/Correction Procedure: 8- by 24-Inch Airfoil Test Section. NASA TM-87582, 1985.

42. Green, L. L.; and Newman, P. A.: Transonic Wall Interference Assessment and Corrections for Airfoil Data from the 0.3-m TCT Adaptive Wall Test Section. AIAA Paper 87-1431, 1987.

43. Green, L. L. R.: Wall Interference Assessment and Corrections for Transonic Adaptive Wall Airfoil Data. M.S. Thesis, George Washington University, April 1988.

44. Gumbert, C. R.: Wall Interference Assessment/Correction of Data from Tests of a CAST 10-2/DOA 2 Airfoil in the Langley 0.3-m Transonic Cryogenic Tunnel. M.S. Thesis, George Washington University, May 1988.

45. Rizk, M. H.; Hafez, M.; Murman, E. M.; and Lovell, D.: Transonic Wind Tunnel Wall Interference Corrections for Three-Dimensional Models. AIAA Paper 82-0588, 1982.

46. Rizk, M. H.; and Murman, E. M.: Wind Tunnel Wall Interference Corrections for Aircraft Models in the Transonic Regime. J. of Aircraft, Vol. 21, Jan. 1984, pp. 54-61.

47. Rizk, M. H.; Smithmeyer, M. G.; and Murman, E. M.: Wind Tunnel Wall Interference Corrections for Aircraft Models, pp. 301-322 of reference 29.

48. Rizk, M. H.: Improvements in Code TUNCOR for Calculating Wall Interference Corrections in the Transonic Regime. AEDC-TR-86-6, 1986.

49. Kemp, W. B., Jr.: A Slotted Test Section Numerical Model for Interference Assessment. J. of Aircraft, Vol. 22, Mar. 1985, pp. 216-222.

50. Kemp, W. B., Jr.: Computer Simulation of a Wind Tunnel Test Section with Discrete Finite-Length Wall Slots. NASA CR-3948, 1986.

51. Kemp, W. B., Jr.: A Panel Method Procedure for Interference Assessment in Slotted-Wall Wind Tunnels. AIAA Paper 88-2537, 1988.

52. Rizk, M. H.; and Lovell, D. R.: Two-Dimensional Transonic Wind Tunnel Wall Interference Corrections Based on the Euler Equations. AIAA Paper 86-0124, 1986.

53. Rizk, M. H.; Lovell, D. R.; and Baker, T. J.: A Procedure Based on the Euler Equations for Correcting Transonic Wind Tunnel Wall Interference. AIAA Paper 88-0141, 1988.

54. Murman, E. M.: A Correction Method for Transonic Wind Tunnel Wall Interference. AIAA Paper 79-1533, 1979.

55. Zhang, Q.: Two-Dimensional Subsonic and Transonic Wind Tunnel Wall Interference Corrections for Varied Walls. Acta Aerodynamic Sinica, Vol. 5, June 1987, pp. 132-140 (in Chinese).

56. Lo, C. F.; and Sickles, W. L.: Two-Measured Variable Method for Wall Interference Assessment/Correction. Transonic Symposium, NASA CP-3020, vol. I, 1989, pp. 853-866.

57. Stahara, S. S.; and Spreiter, J. R.: A Transonic Wind Tunnel Interference Assessment: Axisymmetric Flows. AIAA J., Vol. 18, Jan. 1980, pp. 63-71.

58. McKinney, L. W.; Bruce, W. E., Jr.; and Gloss, B. B.: National Transonic Facility Status. Transonic Symposium, NASA CP-3020, 1989. (Paper 1, vol. II.)

59. Kilgore, R. A.; Dress, D.A.; Wolf, S. W. D.; and Britcher, C. P.: Test Techniques - A Survey Paper on Cryogenic Tunnels, Adaptive Wall Test Sections, and Magnetic Suspension and Balance Systems. Transonic Symposium, NASA CP-3020, vol. I, 1989, pp. 705-741.

60. Kraft, E. M.: An Overview of Approaches and Issues for Wall Interference Assessment/Correction, pp. 3-20 of reference 29.

61. Schairer, E. T.: Two-Dimensional Wind Tunnel Interference from Measurements on Two Contours. J. of Aircraft, Vol. 21, June 1984, pp. 414-419.

62. Ashill, P. R.; and Weeks, D. J.: A Method for Determining Wall-Interference Corrections in Solid-Wall Tunnels from Measurements of Static Pressure at the Walls. Paper No. 1 in reference 28.

63. Kraft, E. M.; and Dahm, W. J. A.: Direct Assessment of Wall Interference in a Two-Dimensional Subsonic Wind Tunnel. AIAA Paper 82-0187, 1982.

64. Capelier, C.; Chevallier, J. P.; and Bouniol, F.: Nouvelle Methode de Correction des Effets de Parois en Courant Plan. La Recherche Aerospatiale, Jan./Feb. 1978, pp. 1-11.

65. Sawada, H.: A General Correction Method of the Interference in Two-Dimensional Wind Tunnels with Ventilated Walls. Transactions of the Japan Society for Aeronautical and Space Sciences, Vol. 21, Aug. 1978, pp. 57-68.

66. Mokry, M.; and Ohman, L. H.: Application of the Fast Fourier Transform to Two-Dimensional Wind-Tunnel Wall Interference. J. of Aircraft, Vol. 17, June 1980, pp. 402-408.

67. Smith, J.: A Method for Determining 2D Wall Interference on an Aerofoil from Measured Pressure Distributions near the Walls and on the Model. NLR TR 81016 U, 1981.

68. Rizk, M. H.; and Smithmeyer, M. G.: Wind Tunnel Wall Interference Corrections for Three-Dimensional Flows. J. of Aircraft, Vol. 19, June 1982, pp. 465-472.

69. Mokry, M.: Subsonic Wall Interference Corrections for Half-Model Tests Using Sparse Wall Pressure Data. Euromech Colloquium No. 187, Gottingen, FRG, Oct. 15-17, 1984. Report No. LR-616; NRC-25132, DCAF F002839, Nov. 1985.

70. Schulz, G.: A Universal 3-Dimensional Wall Pressure Correction Method for Closed Rectangular Subsonic Wind Tunnel Test Sections (Displacement, Downwash, Streamline Curvature). ESA-TT-800, June 1983, (translation of DFVLR-FB-82-19).

71. Labrujere, T. E.: Correction for Wall-Interference by Means of a Measured Boundary Condition Method. Rep. No. NLR-TR-84114-U, B8671294, ETN-86-98650, Nov. 21, 1984.

72. Moses, D. F.: Wind Tunnel Wall Corrections Deduced by Iterating From Measured Wall Static Pressure. AIAA J., Vol. 21, Dec. 1983, pp. 1667-1673.

73. Crites, R. A.: Transonic Wind Tunnel Boundary Interference - A Correction Procedure. AGARD Fluid Dynamics Panel Symposium on Aerodynamic Data Accuracy and Quality: Requirements and Capabilities in Wind Tunnel Testing, Naples, Italy, Sept. 28 - Oct. 1, 1987. Paper #15 of ref. 34.

74. Schairer, E. T.: Assessment of Lift- and Blockage-Induced Wall Interference in a Three-Dimensional Adaptive-Wall Wind Tunnel, pp. 89-100 of reference 29.

75. Barnwell, R. W.; and Sewall, W. G.: Similarity Rules for Effects of Sidewall Boundary Layer in Two-Dimensional Wind Tunnels. Paper No. 3 in reference 28.

76. Murthy, A. V.: Effect of Aspect Ratio on Sidewall Boundary-Layer Influences in Two-Dimensional Airfoil Testing. NASA CR-4008, 1986.

77. Ladson, C. L.; and Ray, E. J.: Evolution, Calibration, and Operational Characteristics of the Two-Dimensional Test Section of the Langley 0.3-Meter Transonic Cryogenic Tunnel. NASA TP-2749, 1987.

78. Ray, E. J.; and Ladson, C. L.: Review of the Advanced Technology Airfoil Test (ATAT) Program in the 0.3-m TCT, pp. 361-374 in reference 29.

79. Melnik, R. E.; Mead, N. R.; and Jameson, A.: A Multi-Grid Method for the Computation of Viscid/Inviscid Interaction on Airfoils, AIAA Paper 83-0234, 1983.

80. Swanson, R. C.; and Turkel, Eli: A Multistage Time-Stepping Scheme for the Navier-Stokes Equations. AIAA Paper 85-0035, 1985.

81. Ladson, C. L.; Hill, A. S.; and Johnson, W. G., Jr.: Pressure Distributions from High Reynolds Number Transonic Tests of an NACA 0012 Airfoil in the Langley 0.3-Meter Transonic Cryogenic Tunnel. NASA TM 100526, 1987.

82. Ladson, C. L.; and Hill, A. S.: High Reynolds Number Transonic Tests of an NACA 0012 Airfoil in the Langley 0.3-Meter Transonic Cryogenic Tunnel. NASA TM 100527, 1987.

83. Dress, D. A.; Johnson, C. B.; McGuire, P. D.; Stanewsky, E.; and Ray, E. J.: High Reynolds Number Tests of the CAST 10-2/DOA 2 Airfoil in the Langley 0.3-Meter Transonic Cryogenic Tunnel - Phase I. NASA TM-84620, 1983.

84. Dress, D. A.; Stanewsky, E.; McGuire, P. D.; and Ray, E. J.: High Reynolds Number Tests of the CAST 10-2/DOA 2 Airfoil in the Langley 0.3-Meter Transonic Cryogenic Tunnel - Phase II. NASA TM-86273, 1984.

85. Rebstock, R; and Lee, E. E., Jr.: Capabilities of Wind Tunnels with Two Adaptive Walls to Minimize Boundary Interference in 3-D Model Testing. Transonic Symposium, NASA CP- , 19 . (Paper of this compilation.)

86. Barnwell, R. W.: Design and Performance Evaluation of Slotted Walls for Two-Dimensional Wind Tunnels. NASA TM-78648, 1978.

Table I. Approaches to Establishing Corrected Transonic Wind Tunnel Test Conditions

CONVENTIONAL TUNNEL	
Test Data Point:	M_{ref}, α_{ref}
Mach Number Calibration:	$\Delta M_o \rightarrow M_T = M_{ref} + \Delta M_o$
Flow Angle Survey OR Model Upright/Inverted:	$\Delta\alpha_o \rightarrow \alpha_T = \alpha_{ref} + \Delta\alpha_o$
Wall Interference: (model/wall interaction)	$\Delta M_{WI} \rightarrow M_c = M_T + \Delta M_{WI}$ $\Delta\alpha_{WI} \rightarrow \alpha_c = \alpha_T + \Delta\alpha_{WI}$
WIAC	
Tunnel Interference:	$\Delta M_{WIAC} \rightarrow M_c = M_? + \Delta M_{WIAC}$ $\Delta\alpha_{WIAC} \rightarrow \alpha_c = \alpha_? + \Delta\alpha_{WIAC}$

Table II. Transonic Testing Factors Affecting WIAC for 2-D Airfoil Tunnel

MEASURED MODEL DATA

- 1-D C_p arrays with good resolution
- Drag rake for C_d

MEASURED FIELD DATA

- 1-D C_p arrays with good resolution and signal
- 1-D θ arrays are difficult to measure
- One θ required with C_p array

MODEL SUPPORT EFFECT

- Two SWBL interactions
- Flow may not be 2-D

TEST SECTION DESIGN

- Ventilated, generally near minimum blockage
- Adaptive

Table III. Relative Sizes of 0.3-m TCT Test Sections and Airfoil Models Used for Sample 2-D Results

Airfoil Section	chord length	thickness to chord τ	test section		half-height to chord (h/c)	model AR (2b/c)	Data ref.	WIAC ref.
			size	type				
NACA 0012	6"	.12	8"x 24"	SW	2.0	1.33	81, 82	40
	6.5"	.12	13"x 13"	AW	1.0	2.00		42, 43
	13"	.12	13"x 13"	AW	0.5	1.00		42, 43
CAST 10-2/DOA 2	3"	.121	8"x 24"	SW	4.0	2.67	84	40, 44
	6"	.121	8"x 24"	SW	2.0	1.33	83	40, 44

Table IV. Transonic Testing Factors Affecting WIAC for 3-D Configuration Tunnel

MEASURED MODEL DATA

- 2-D C_p arrays with sparse resolution OR none
- Force balances

MEASURED FIELD DATA

- 2-D C_p arrays w/ sparse resolution and small signal
- 2-D θ arrays are very difficult to measure
- Several θ's required with C_p array

MODEL SUPPORT EFFECT

- One SWBL interaction for semi-span models
- Sting/sector interference

TEST SECTION DESIGN

- Ventilated, criterion varies
- Pilot adaptive

Table V. Description of 3-D WIAC Codes

CODE CHARACTERISTICS	PANCOR	TUNCOR	EUCOR3D
Tunnel Type	Rectangular, slotted	Rectangular or circular	Rectangular
Flow Equation	Prandtl-Glauert	TSDE	Euler
Computational Mesh	Paneled Boundaries	Cartesian or cylindrical	H-H Body-fitted
Solution Method	Gaussian elimination	VLOR	Multi-grid, time stepping
Test Model	Distributed singularities based on C_L, C_D, C_M & approx. WBT shape	Small dist. shape BC for WBT α_w, α_t to match C_L, C_M	Exact shape BC for WBT α_w to match C_L 2-D strip boundary layer
Test Section Boundary singularities	Panels for solid walls, slats, reentry region, end planes & unperturbed outer flow Line sources for discrete slots	— —	— —
Boundary data	Wall shape, slot Kutta condition, Measured C_p rows	Measured C_p interpolated to computational mesh	Measured C_p interpolated to computational mesh
Other components	Distributed singularities for sting and sting support based on shape	None	None
Status	Validating on real data	Validating on real data	Code delivered, being debugged
Developed by	W. B. Kemp	M. H. Rizk, et al	M. H. Rizk, et al

Table VI. Numerically Simulated Wall Corrections for the Pathfinder I Model in NTF-Size Ideal Tunnels; $M_T = 0.82$, $\alpha_T = 1.93^\circ$, $C_L = 0.452$

TUNNEL	CORRECTIONS	
	ΔM	$\Delta\alpha$
open-jet	-0.00063	-0.12693
solid-wall	+0.00127	+0.20445
classical theory for NTF Slot design*	+0.00030	+0.00612
finite TS length	+0.00050	+0.00612

*NTF test section design criterion was zero lift interference with all four walls slotted. Currently, sidewall slots are closed.

Table VII. WIAC Results for Two NTF Calibration Data Points at $Re = 4 \times 10^6$/ft.

CONDITIONS		TUNCOR		PANCOR		EXP.	
M_T	v_{up}	ΔM	$\Delta\alpha$	ΔM	$\Delta\alpha$	ΔM	$\Delta\alpha$*
0.6	0	-0.0035	-0.1328	-0.0037	-0.0866	-0.0034	≈+0.01
	$-\Delta\alpha_1$	-0.0034	+0.0177	-0.0037	0		
0.8	0	-0.0038	-0.1117	-0.0042	-0.1016	-0.0038	≈+0.01
	$-\Delta\alpha_1$	-0.0039	+0.0153	-0.0042	0		

*obtained from model upright and inverted tests

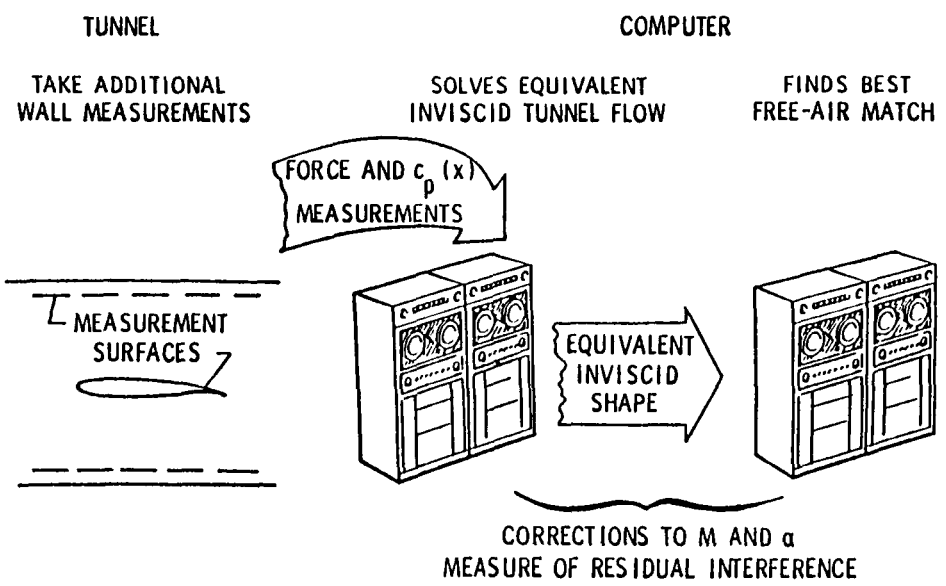

Figure 1. - Schematic of 2-D transonic WIAC concept.

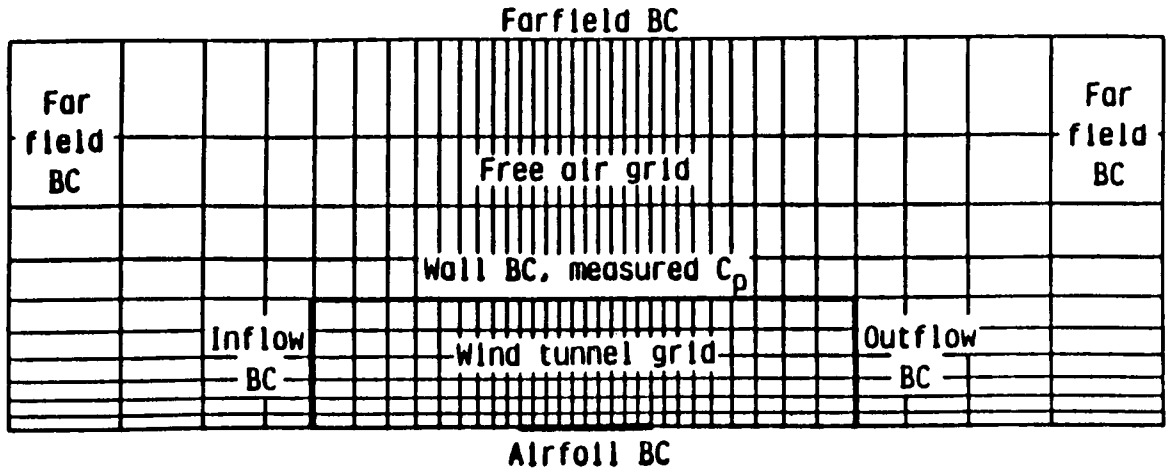

Figure 2. - Upper half-plane of Cartesian grid for 2-D TSDE WIAC code.

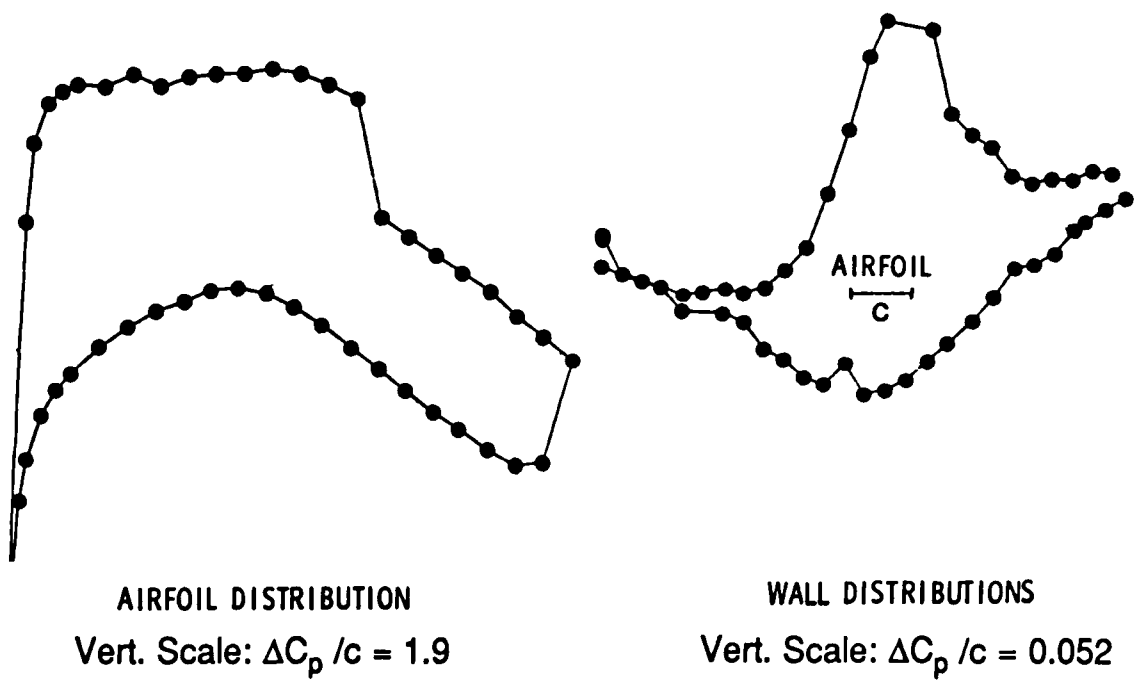

Figure 3. - Sample 0.3-m TCT slotted-wall and airfoil C_p distributions; $M_T = 0.765$, $\alpha_T = 2^\circ$, c = 6", $Re_c = 6 \times 10^6$.

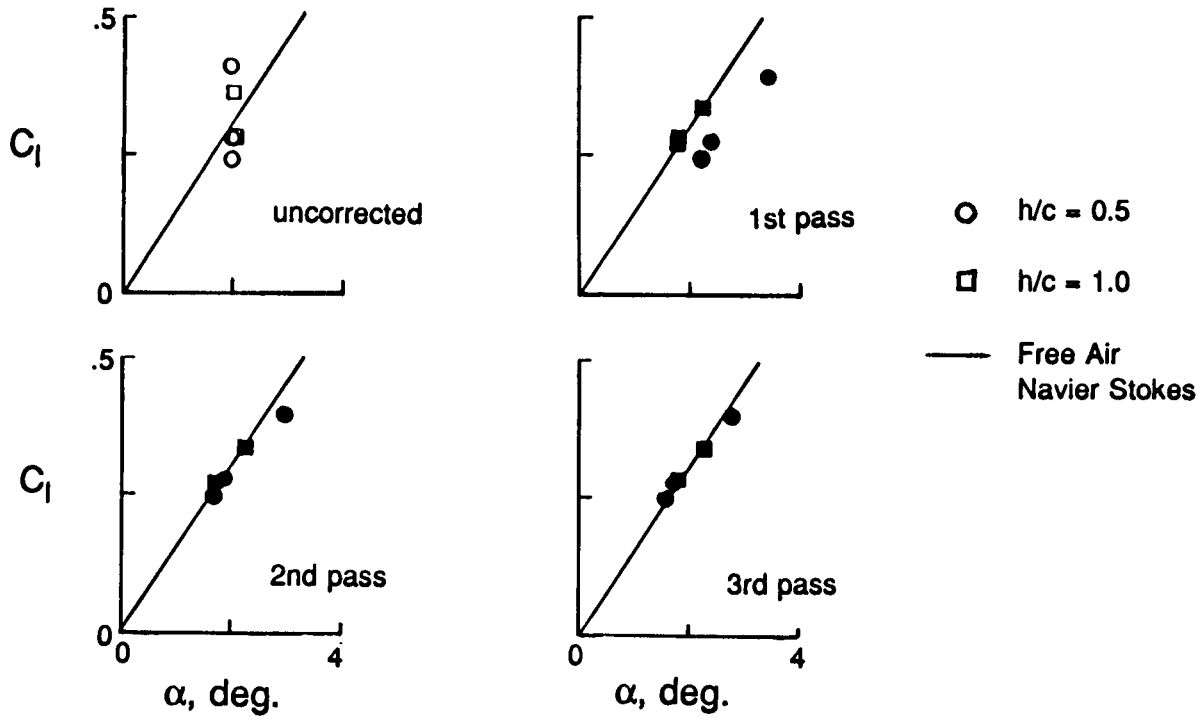

Figure 4. - Sample results for 2-D TSDE WIAC application to NACA 0012 airfoil data from the 0.3-m TCT with partially adapted walls; Lift curves at $M_T = 0.65$, $\alpha_T = 2^o$, $Re_c = 9x10^6$.

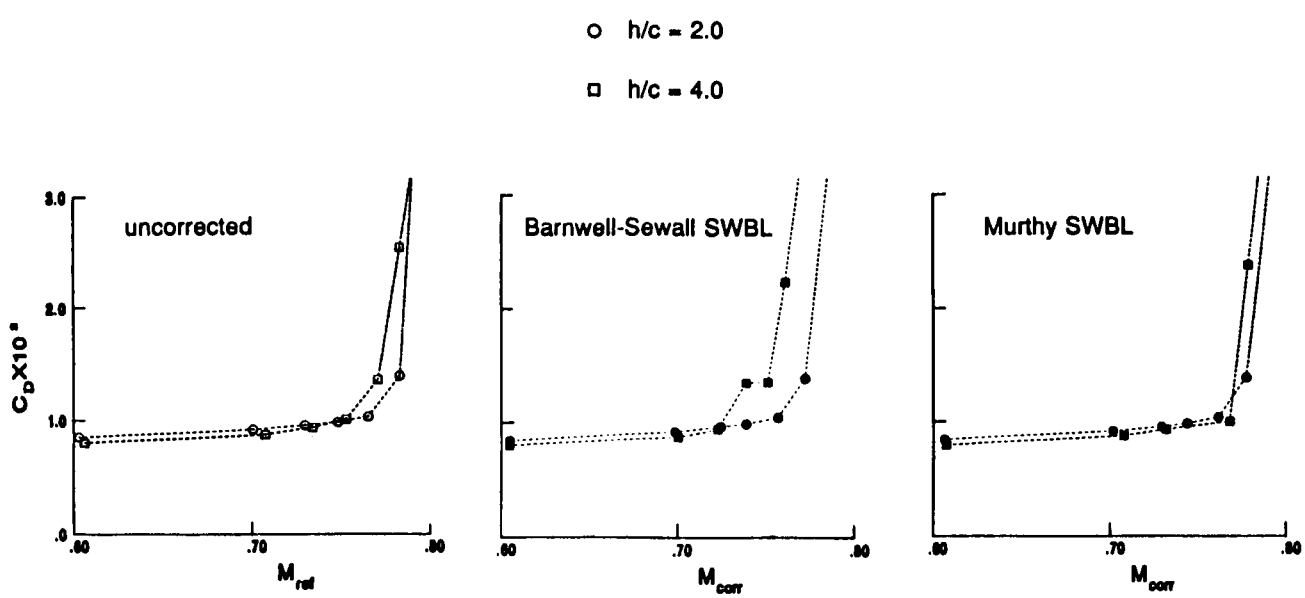

Figure 5. - Sample results for 2-D TSDE WIAC application to CAST 10-2/DOA 2 airfoil data from the 0.3-m TCT with slotted walls; Drag-rise curves at $C_\ell = 0.5$, $Re_c = 15x10^6$.

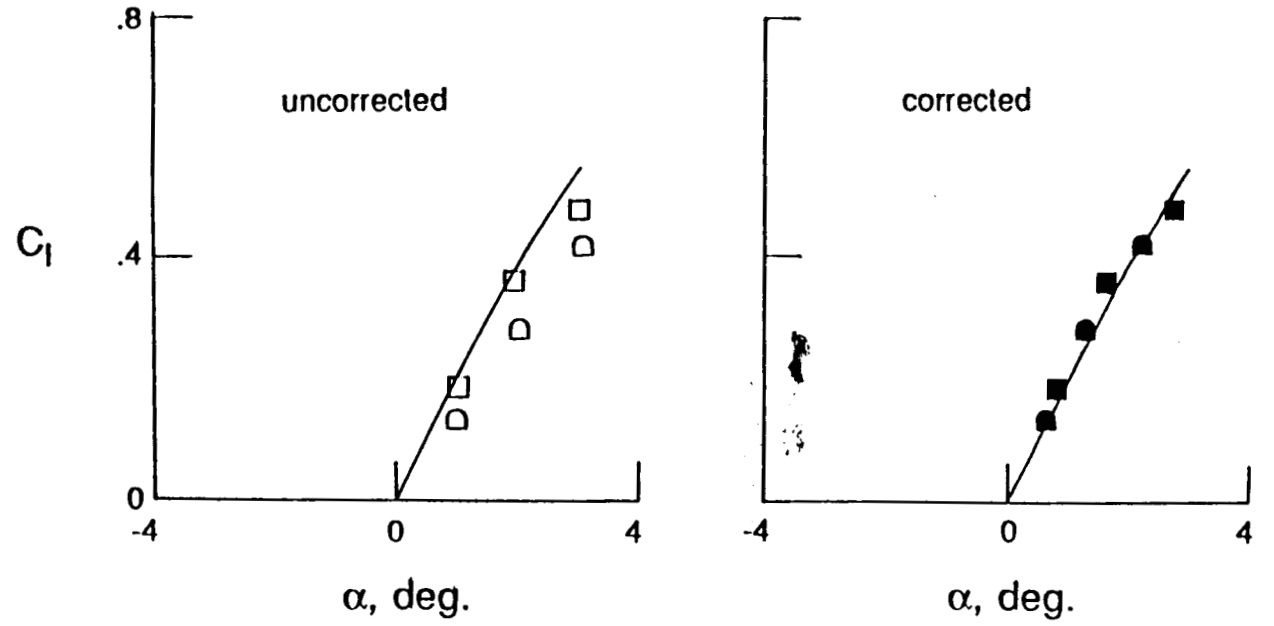

(a) Lift curves at M_T = 0.76.

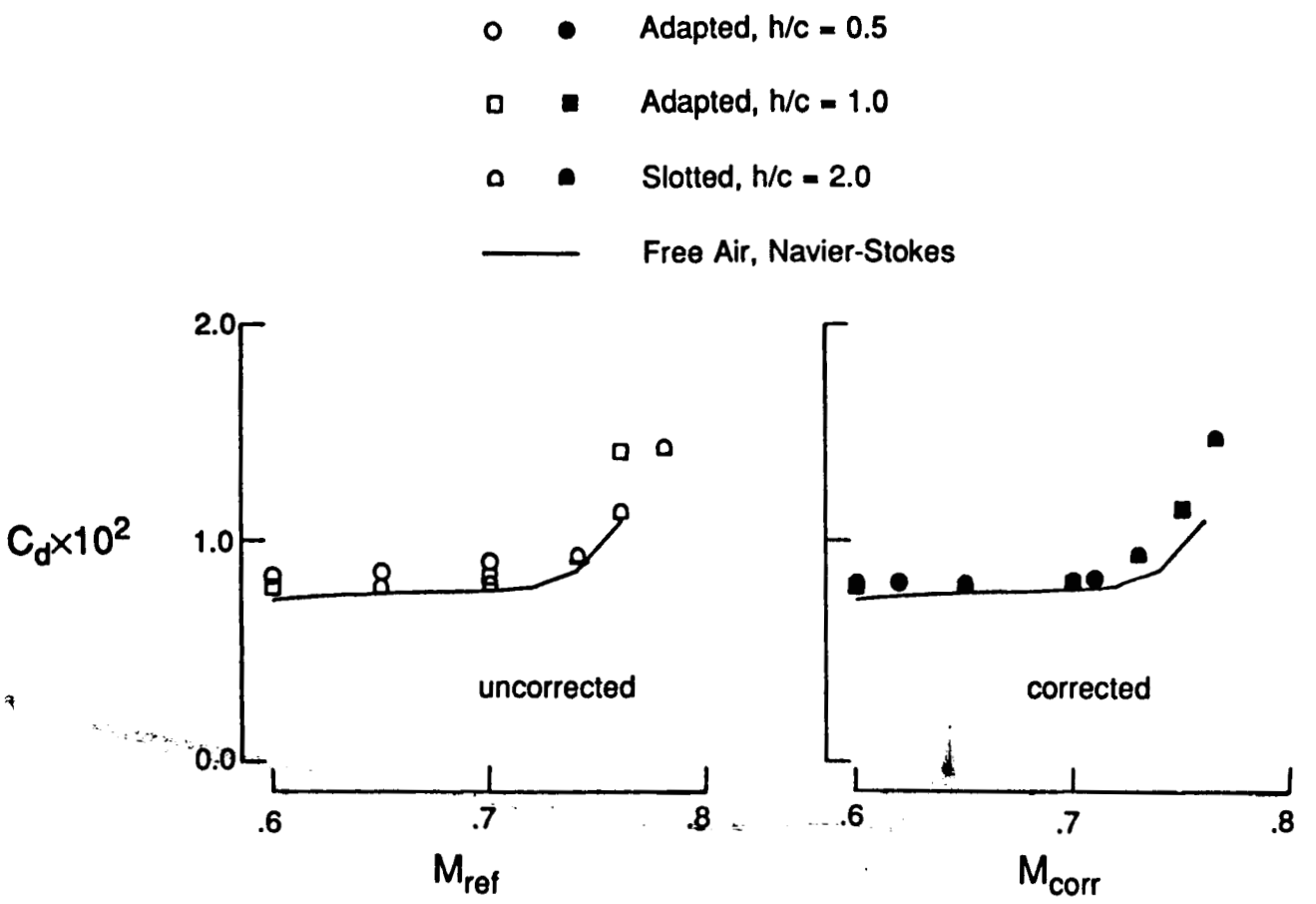

(b) Drag-rise curves at C_ℓ = 0.2.

Figure 6. - Sample results for 2-D TSDE WIAC application to NACA 0012 airfoil data from the 0.3m TCT with slotted and fully-adapted walls at $Re_c = 9 \times 10^6$.

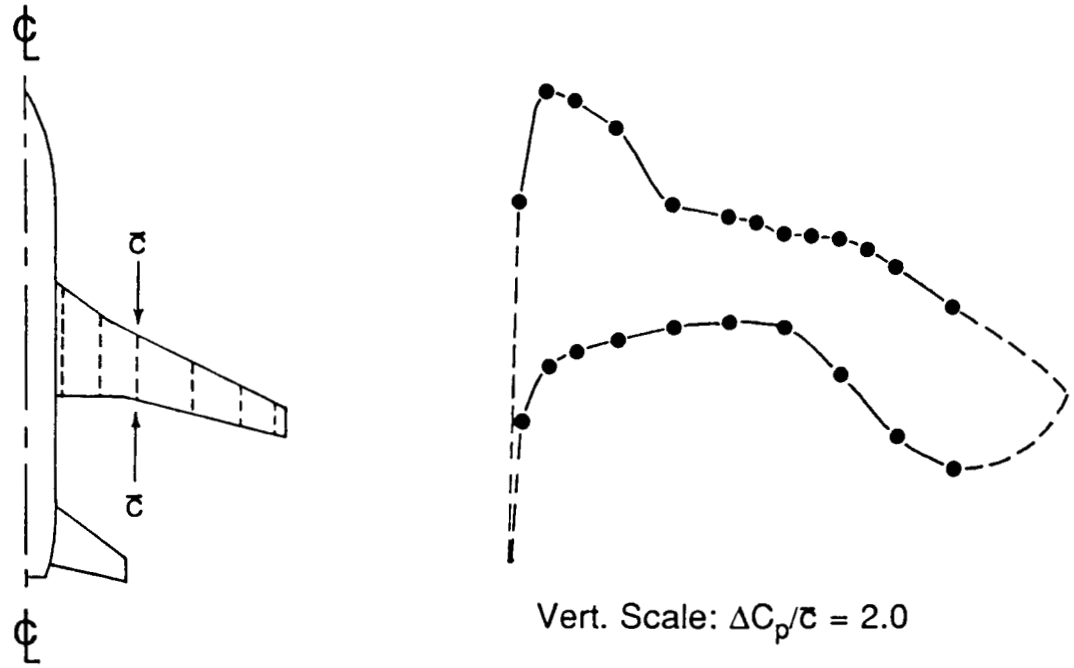

(a) Model wing C_p distribution

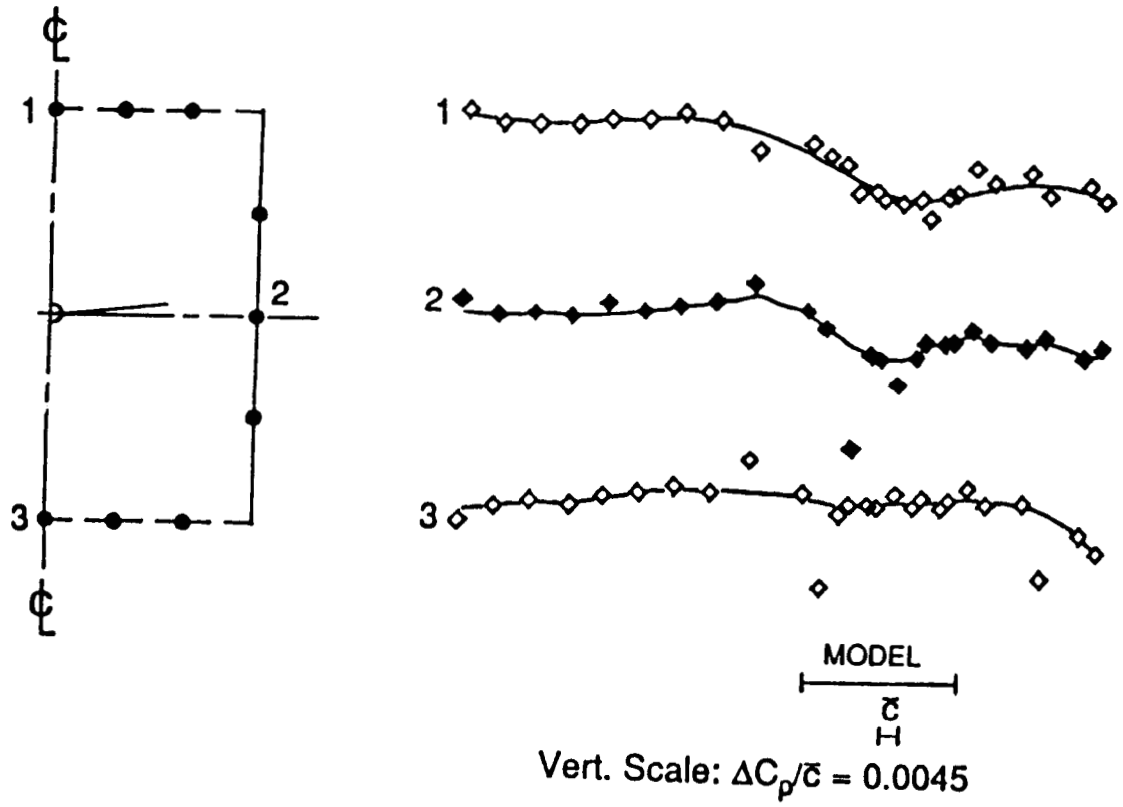

(b) Tunnel wall centerline C_p distributions

Figure 7. - Sample NTF slotted-wall and model C_p distributions; $M_T = 0.8$, $\alpha_T = 2.2^\circ$, $\bar{c} = 5.74"$, $b = 53.08"$, $Re_{\bar{c}} = 2 \times 10^6$.

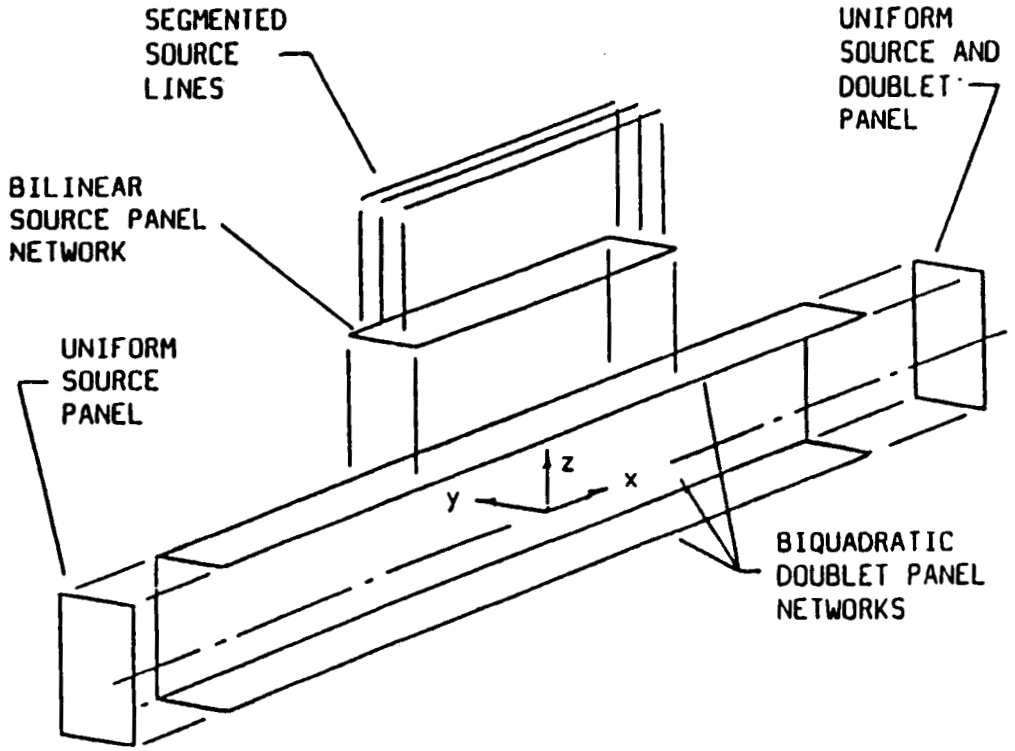

Figure 8. - Singularities representing the tunnel boundaries in the 3-D panel method WIAC code PANCOR.

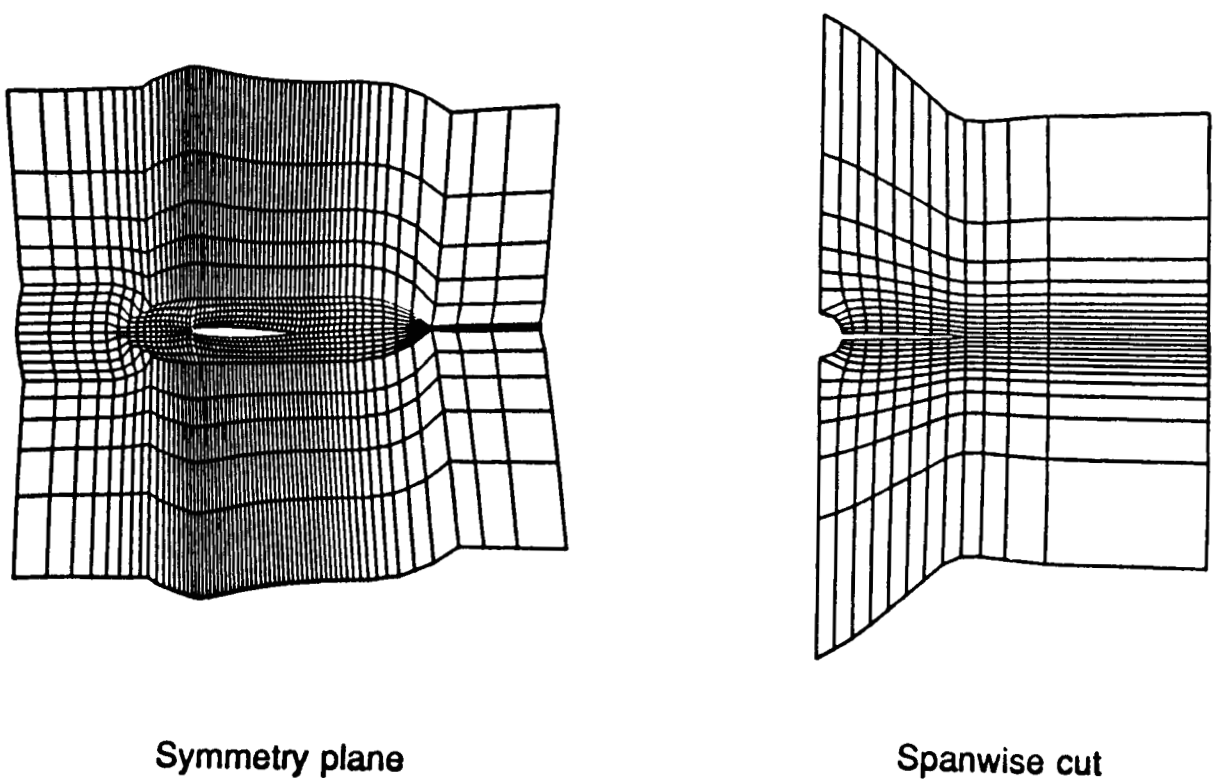

Figure 9. - Body-fitted H-H grid about wing-body configuration for the 3-D Euler equation WIAC code EUCOR3D.

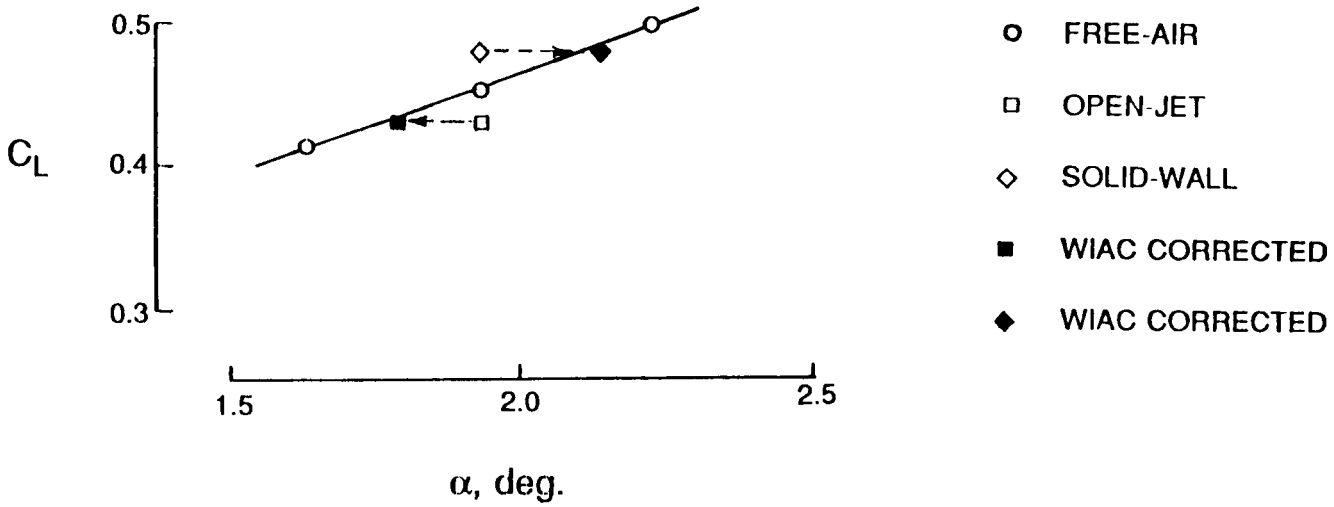

(a) Lift curve, C_L versus α.

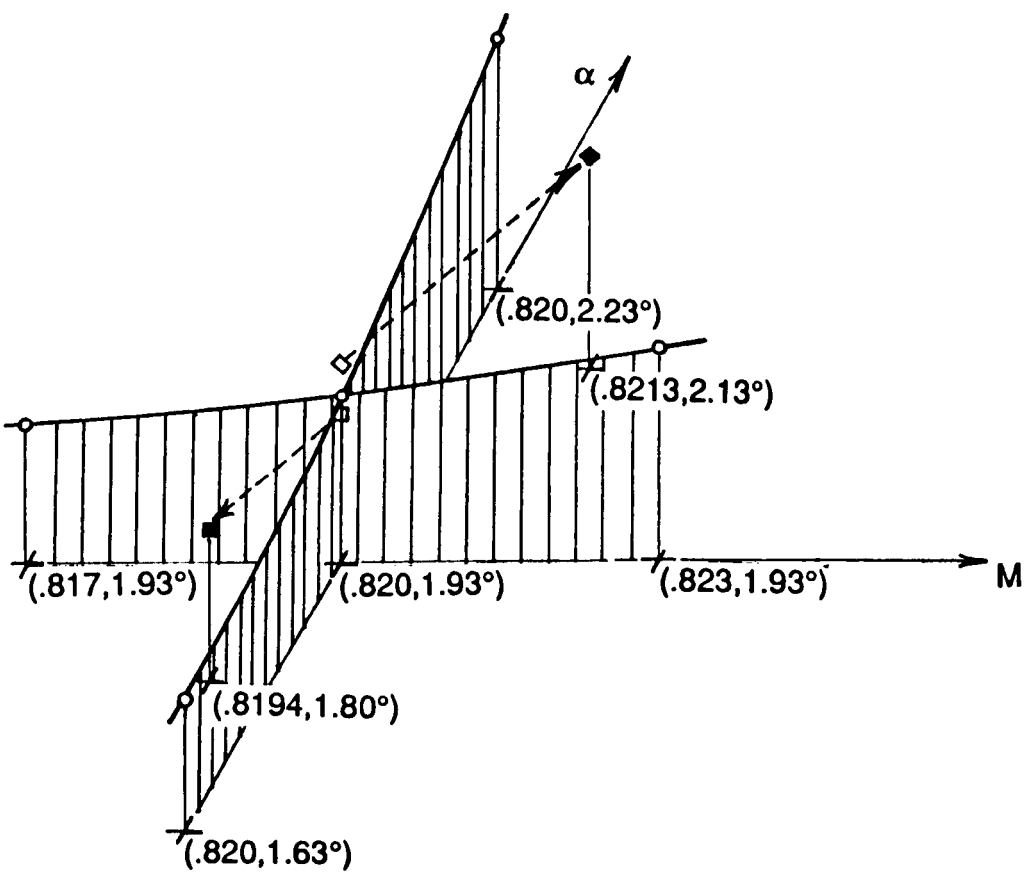

(b) Size of embedded supersonic flow region versus M and α.

Figure 10. - Numerically simulated wall corrections for the Pathfinder I model in NTF-size ideal tunnels; $M_T = 0.82$, $\alpha_T = 1.93^\circ$, $C_L = 0.452$.

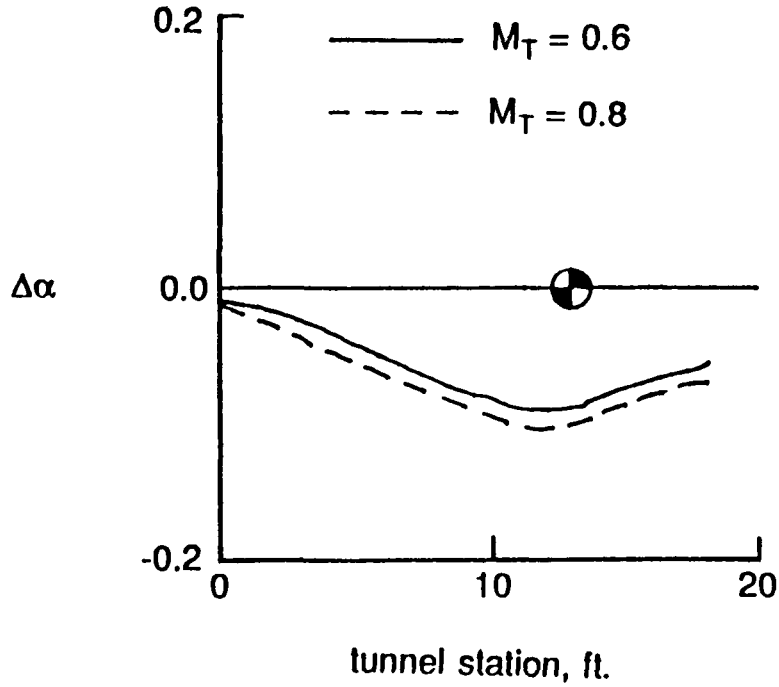

Figure 11. - Sample results for 3-D PANCOR WIAC application to calibration data from the NTF; Distribution of flow angularity along the tunnel centerline at Re = 4×10^6/ft.

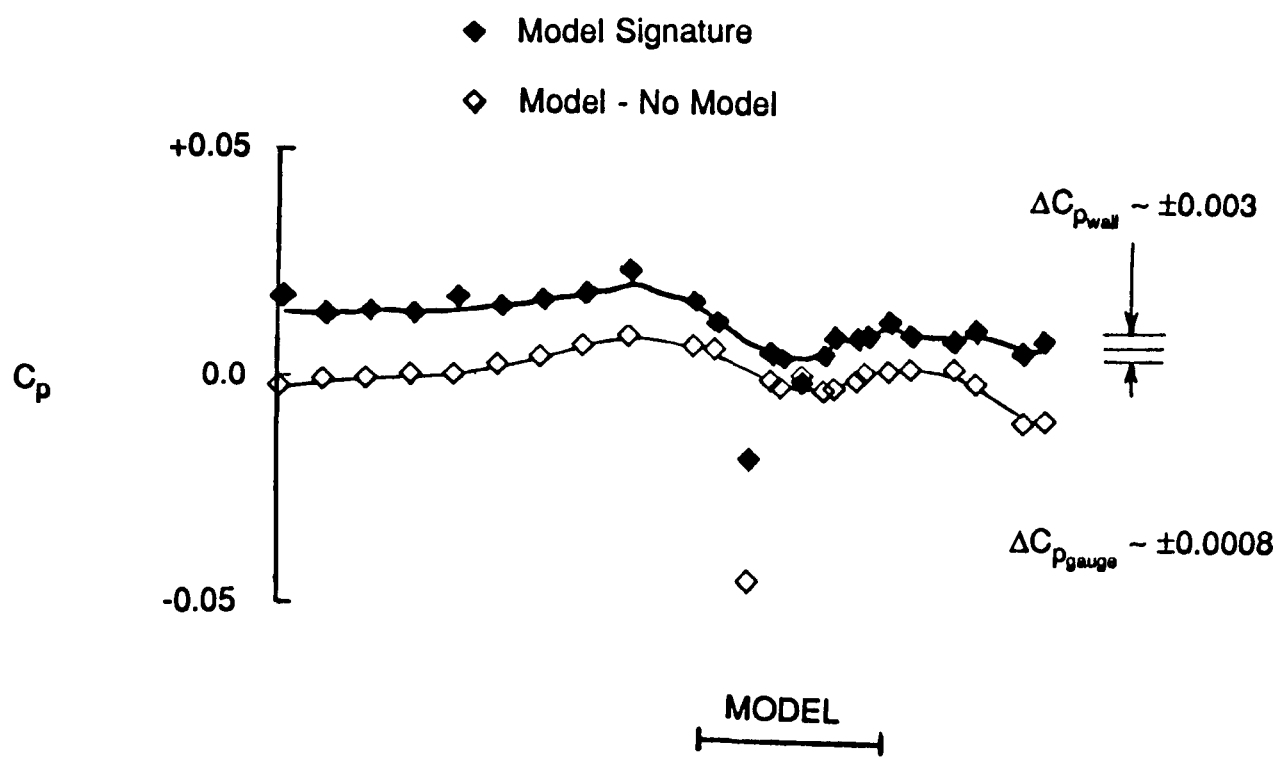

Figure 12. - Sample NTF sidewall centerline C_p distribution for the Pathfinder I model, with and without calibration data as tare; $M_T = 0.8$, $\alpha_T = 2.2^\circ$, $Re_{\bar{c}} = 2 \times 10^6$.

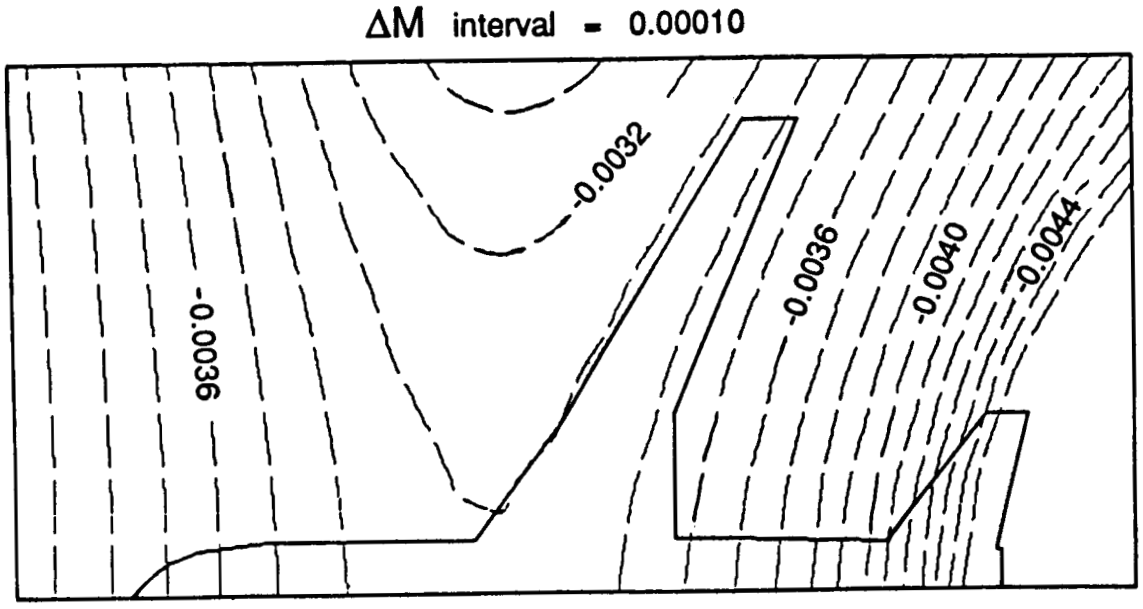

Figure 13. - Sample results for 3-D PANCOR WIAC application to Pathfinder I data from the NTF; Contour plot of ΔM at $M_T = 0.6$, $\alpha_T = 4.3^\circ$, $Re_{\bar{c}} = 2 \times 10^6$.

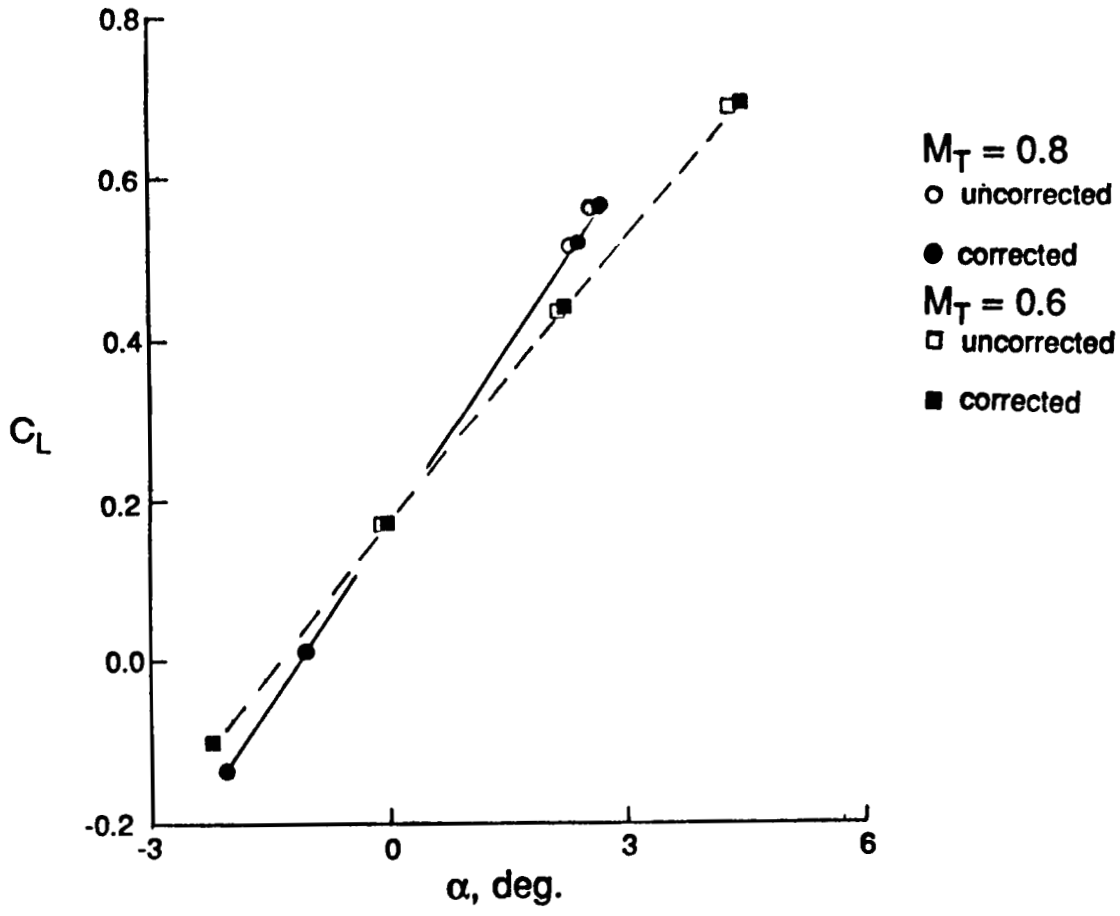

Figure 14. - Sample results for 3-D TUNCOR WIAC application to Pathfinder I data from the NTF; Lift curves at $M_T = 0.6$ and 0.8, $Re_{\bar{c}} = 2 \times 10^6$.

N89-20959

TWO-MEASURED VARIABLE METHOD FOR WALL INTERFERENCE ASSESSMENT/CORRECTION

C. F. Lo and W. L. Sickles
Calspan Corporation/AEDC Division
Arnold Air Force Station, Tennessee

Summary

An iterative method for wall interference assessment and/or correction is presented specifically for transonic flow conditions in wind tunnels equipped with two-component velocity measurements on a single interface. The iterative method does not require modeling of the test article and tunnel wall boundary conditions. Analytical proof for the convergence and stability of the iterative method is shown in the subsonic flow regime. The numerical solutions are given for both two-dimensional and axisymmetrical cases at transonic speeds with the application of global Mach number correction.

Introduction

The recognition of the shortcomings of the classical methods for determining wall interference has demanded that a variety of flow measurements near or on the tunnel wall be made to assess wall interference. For example, Arnold Engineering Development Center has designed an interface measurement system for the 4-foot Transonic Tunnel and the wall pressure measurement system is being planned for installation in the current 12-ft Wind Tunnel restoration project at NASA/Ames Research Center. It is well known that classical methods require a mathematical modeling of the wall boundary condition which is a difficult task, in particular, for a ventilated wall. The characteristics of a ventilated wall are not precisely known and generally vary with Mach number, model geometry, Reynolds number and wall configuration. Another shortcoming is the necessity to accurately represent the test article beyond the simplified representation used in the classical approach.

Furthermore, the development of an adaptive wall tunnel requires that the boundary flow measurements be an integral part of the procedure. The boundary measurements are designed to determine adaptive-wall setting for free-air or noninterference condition. Techniques using only the measurements to assess the level of interference will complement the adaptive-wall process by determining if a noninterference wall setting has been achieved or by correcting for residual interference. Therefore, several wall interference methods based solely on the measured flow boundary condition have been developed for different kinds of measurements, such as two velocity components at a single interface (Refs. 1-4) or one velocity component at two interfaces (Ref. 5). However, all methods are limited to subsonic flow.

PRECEDING PAGE BLANK NOT FILMED

The purpose of this paper is to present a method for assessing wall interference for subsonic as well as transonic flow regimes based only on two velocity distributions measured on a single interface and no knowledge of the test article. This method as shown in Fig. 1 is divided into two tasks. The first task is the determination of the effective (equivalent) shape of the model from the two-measured variables by an iterative procedure. The second task is to predict the wall interference, such as a global Mach number correction, based on the effective shape predicted from Task 1.

In the presentation of the paper, a proposed iterative procedure to accomplish Task 1 is described and convergence analytically proved for subsonic flow. Numerical validation is demonstrated for two-dimensional and axisymmetrical transonic flows using a transonic small disturbance equation, and the global Mach number corrections are determined for Task 2.

Iterative Procedure of Effective Shape

To accomplish Task 1, an iterative procedure using two measured distributions of velocity near the wall has been developed and is shown in Fig. 2. The procedure consists of two basic steps in which each step involves obtaining a solution for the region between a measurement interface ($y=h$) and an effective shape line ($y=y_1$) near the model. In the first step, the velocity component, $u^o(y_1)$, is obtained from a solution of the region where the boundary conditions are provided by an initial guess of the effective shape $v^o(y_1)$, and the measured velocity component $u_t(h)$. With the result, $u^o(y_1)$, the second step obtains the solution $v^1(y_1)$ in the same region using the measured boundary condition $v_t(h)$. These two steps are repeated until convergence has been achieved and the effective shape, $v(y_1)$, determined.

Defining a merit function for the difference, $v^{n+1}(y_1) - v^n(y_1)$, one can relax the effective shape between iterations by the form of

$$v^{n+1}(y_1) = \omega v^{n+1}(y_1) + (1-\omega) v^n(y_1)$$

with ω as a relaxation factor. An updated effective shape, $v(y_1)$, is yielded by repeating Steps 1 and 2 with this relaxed form of velocity as input until the given criterion of merit function is satisfied.

Predicted Effective Shape

The iterative procedure for determining the effective shape is extremely flexible and can be applied to a variety of tunnel flow conditions. Depending on the flow condition, the region between the two surfaces could be analytically or numerically solved for the appropriate fluid equations, such as the Prandtl-Glauert equation, transonic small disturbance equation, full potential equation, or Euler equations. To illustrate the validity of the iterative procedure, it is applied to the two-dimensional, subsonic, Prandtl-Glauert equation. For this linear problem the solution for each iterative step can be determined analytically. The analytical expressions of the iterative solutions were derived by the Fourier transform technique as

$$u^n(x,y_1) = \frac{1}{2\beta(h-y_1)} \int_{-\infty}^{\infty} \frac{u_t(\xi,h)}{cosh\left(\frac{\pi(\xi-x)}{2\beta(h-y_1)}\right)}$$

$$- \frac{1}{2\beta^2(h-y_1)} \oint_{-\infty}^{\infty} \frac{v^n(\xi,y_1)}{sinh\left(\frac{\pi(\xi-x)}{2\beta(h-y_1)}\right)} d\xi \tag{1}$$

$$v^{n+1}(x,y_1) = \frac{1}{2\beta(h-y_1)} \int_{-\infty}^{\infty} \frac{v_t(\xi,h)}{cosh\left(\frac{\pi\xi-x)}{2\beta(h-y_1)}\right)} d\xi$$

$$+ \frac{1}{2(h-y_1)} \oint_{-\infty}^{\infty} \frac{u^n(\xi,y_1)}{sinh\left(\frac{\pi(\xi-x)}{2\beta(h-y_1)}\right)} d\xi \tag{2}$$

The convergence and stability of these iterative procedures has been proved analytically in Appendix A and Appendix B, respectively. The results for a NACA0012 airfoil at M = 0.6 in an open-jet tunnel are shown in Fig. 3. It can be seen that the predicted effective shape compares well with an independent reference calculation from the original airfoil profile.

For transonic flow, the numerical solution of the transonic small disturbance equation was solved for the procedure as shown in Fig. 4. The results for a two-dimensional 12% parabolic airfoil at M = 0.8 and an axisymmetrical body of revolution of a 10% parabolic arc profile at M = 0.975 are given in Figs. 5 and 6, respectively. For both two-dimensional and axisymmetrical cases, the agreement between the predicted effective shape and the reference calculation are very good. Now that effective shape has been determined, the next task is to determine the correction.

Global Mach Number Correction

The concept of global Mach number correction assumes that there exists an equivalent Mach number in free air where the calculated pressure distribution at a corrected Mach number will match the tunnel pressure distribution on the model or in a surface near the model as on the current procedure and simulation. This equivalent or corrected Mach number (M_C) is computed using the effective shape determined from the iterative procedure. Setting the free-air Mach number equal to the tunnel

Mach number ($M_f = M_t$), free-air calculations are performed exterior to the surface near the model. Comparisons of the pressure distribution for the axisymmetric case are shown in Fig. 7. Correcting the free-air Mach number from $M_f = 0.975$ to $M_c = 0.925$ resulted in a very good match between the free-air pressure distribution determined at M_c and the tunnel pressure distribution determined from the iterative procedure as shown in Fig. 7. Therefore, these tunnel data at $M = 0.975$ correspond to those in free air at $M = 0.925$.

Concluding Remarks

A method of the wall interference assessment/correction for transonic flow conditions has been developed using a two-component measured flow boundary condition approach successfully. The method avoids the difficulty of modeling the test article and the tunnel wall boundary conditions. The prediction of interferences includes subsonic and transonic flow regimes without the limitation on the selection of equations.

References

1. Lo, C. F., "Tunnel Interference Assessment by Boundary Measurements," AIAA Journal, April 1978.

2. Lo, C. F. and Sickles, W. L., "The Adaptive Wall Method for Two-Dimensional and Axisymmetrical Wind Tunnel," AEDC-TR-79-55, November 1979.

3. Kraft, E. M. and Dahm, W.J.F., "Direct Assessment Wall Interference in a Two-Dimensional Subsonic Wind Tunnel," AIAA Paper No. 82-0187, January 1982.

4. Mokry, M., Chan, Y. Y., and Jones, D. J., "Two-Dimensional Wind Tunnel Wall Interference," AGARDograph No. 281, November 1983.

5. Schairer, E. T., "Two-Dimensional Wind Tunnel Interference from Measurements on Two Contours," Journal of Aircraft, June 1984.

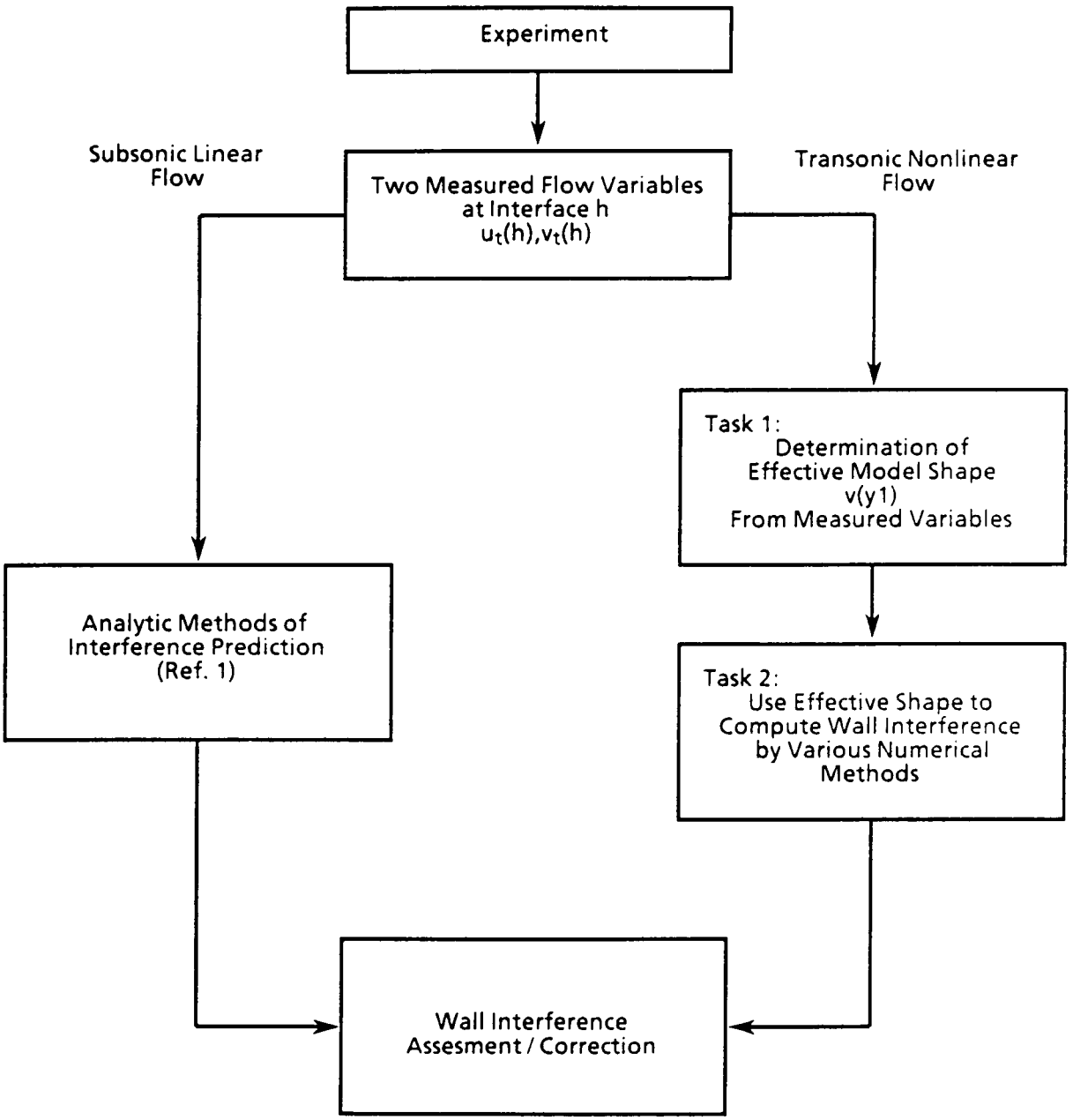

Figure 1. Prediction methods of wall interference assessment/correction using two measured variables at interface.

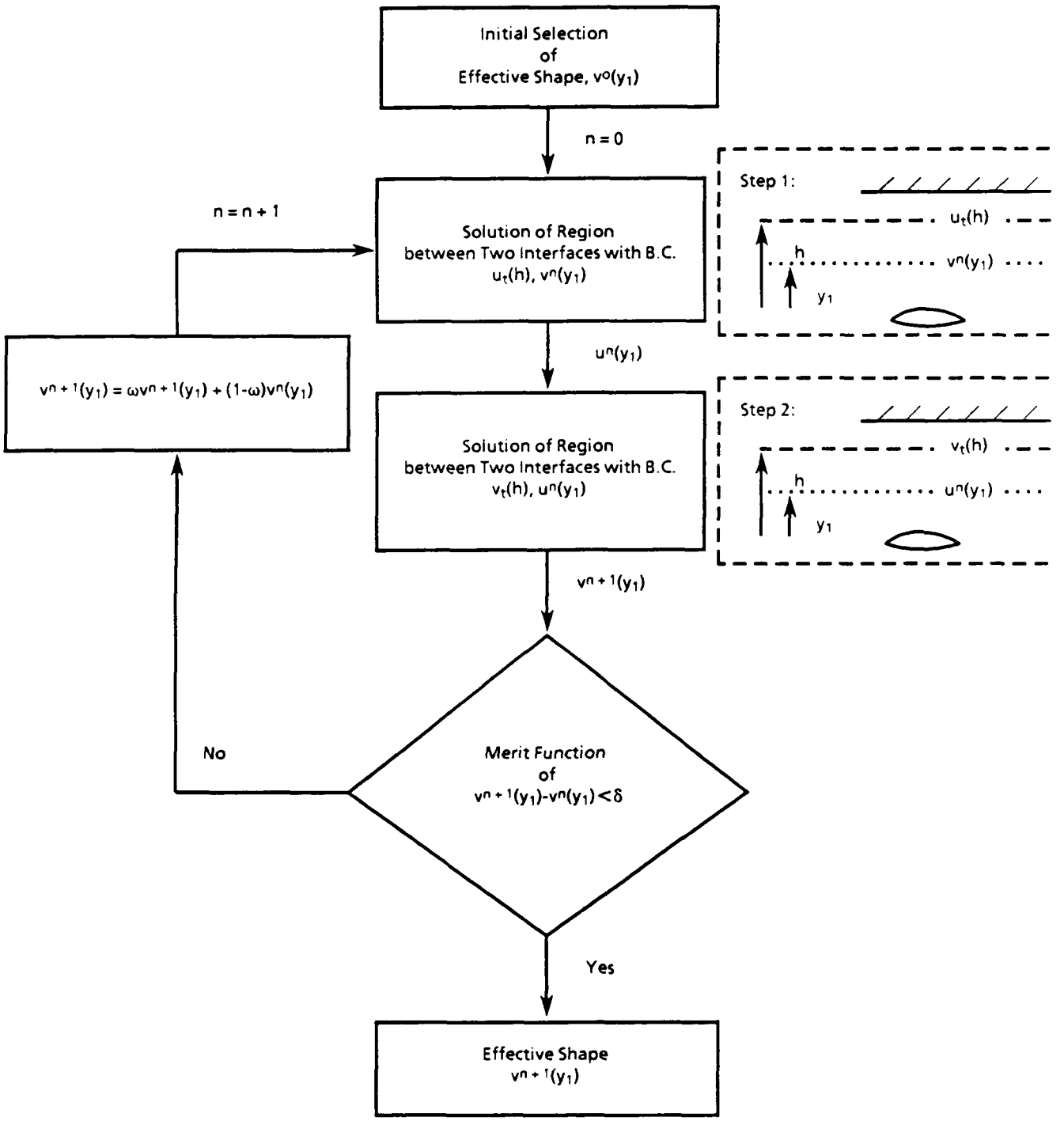

Figure 2. Iterative procedure for obtaining effective flow shape at $y = y_1$ by using measured variables, $u_t(h)$ and $v_t(h)$.

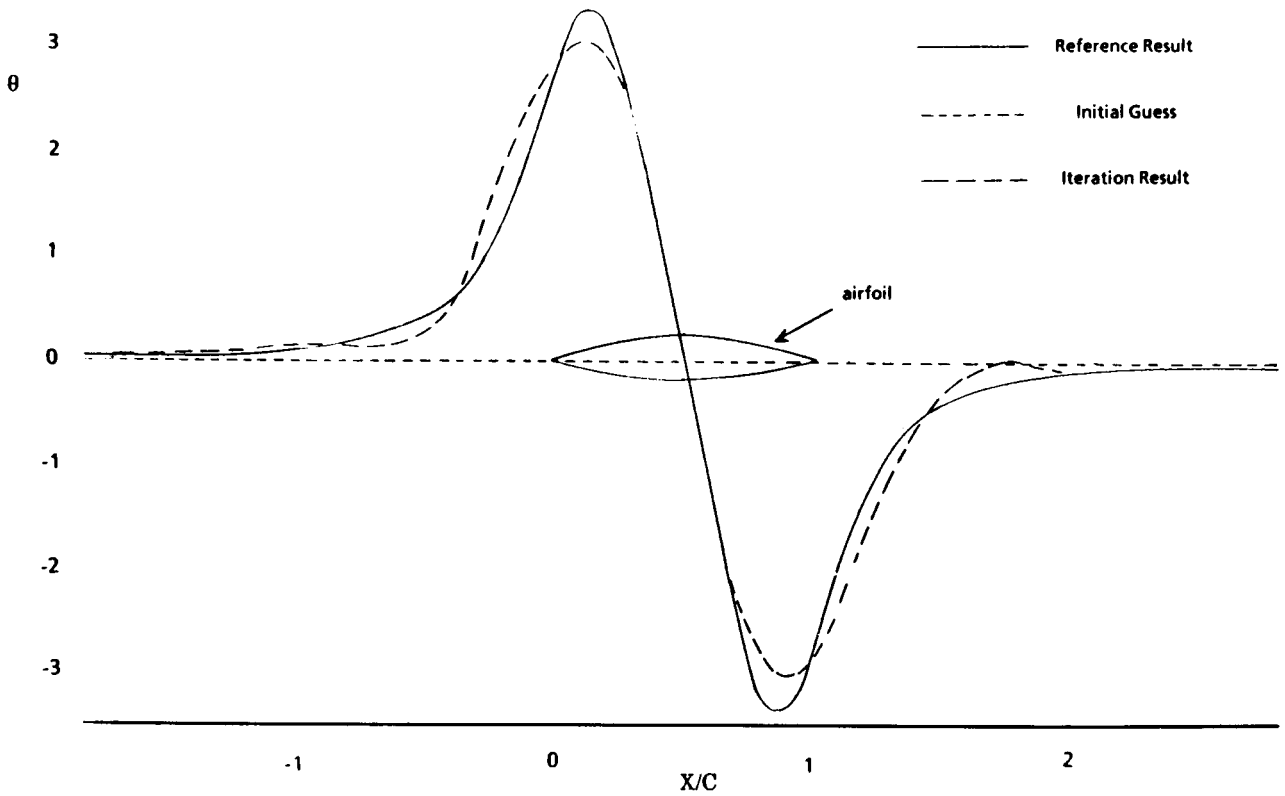

Figure 3. Comparison of results between iterative procedure with analytic expressions and reference calculation for NACA 0012, M = 0.6.

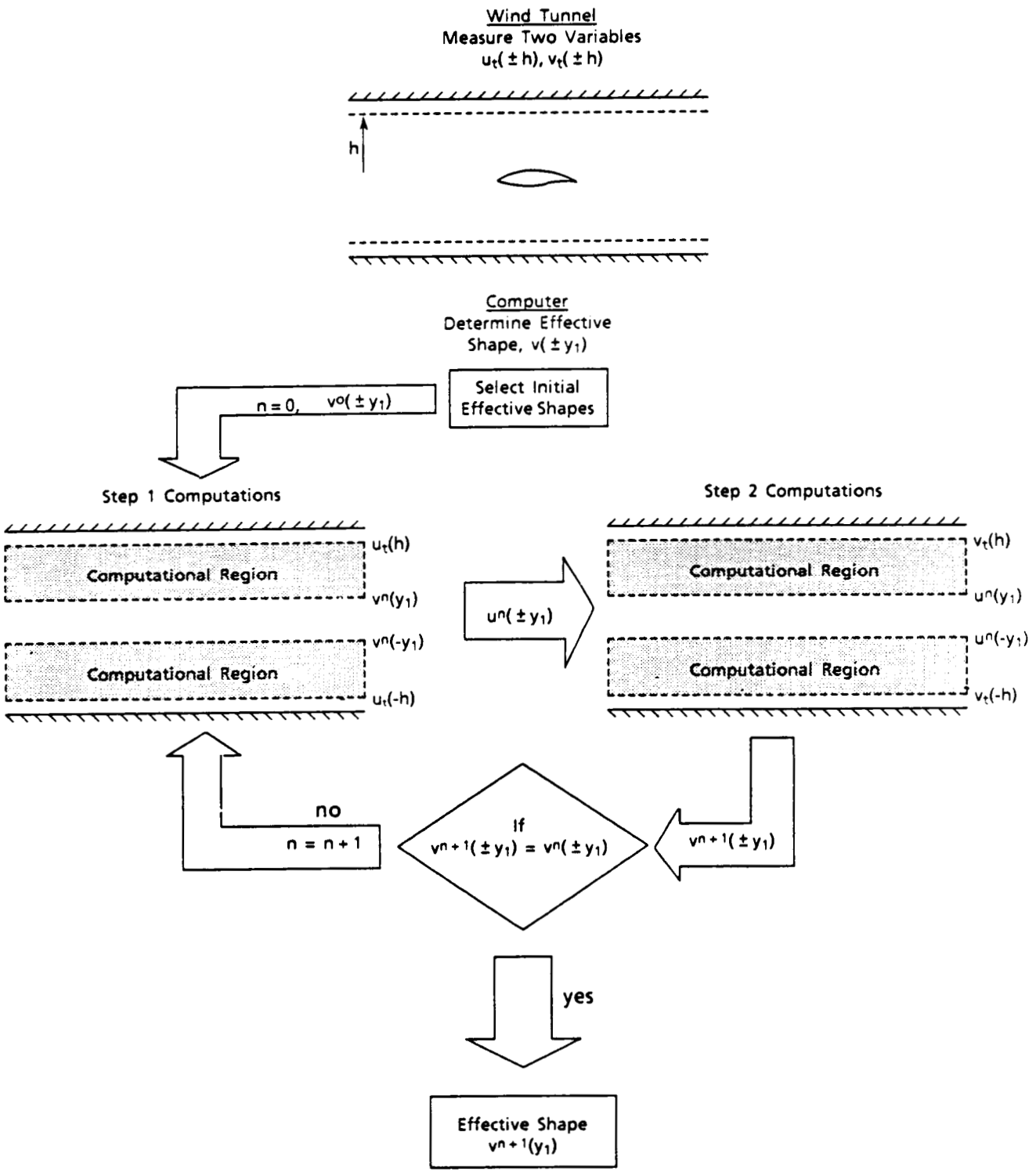

Figure 4. Two-variable numerical procedure to determine effective shape.

ORIGINAL PAGE IS
OF POOR QUALITY

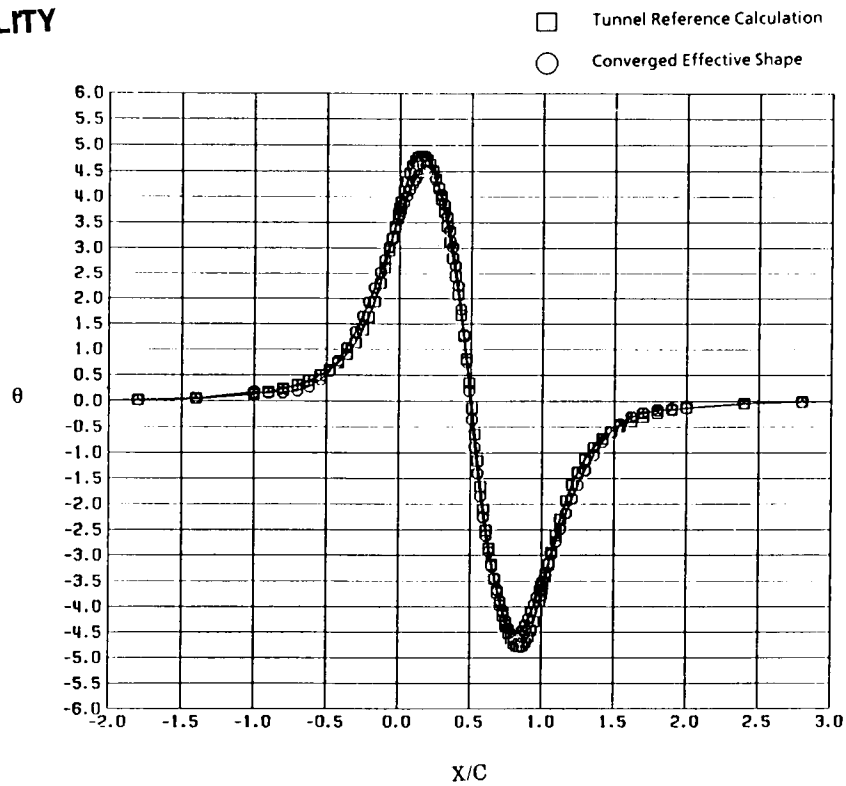

Figure 5. Predicted effective shape for two-dimensional case over 12% parabolic airfoil at $M_t = 0.8$, $\alpha = 0$, $y_1 = 0.3$, $h = 1$, $v^o = (x,y_1) = 0$, open jet tunnel.

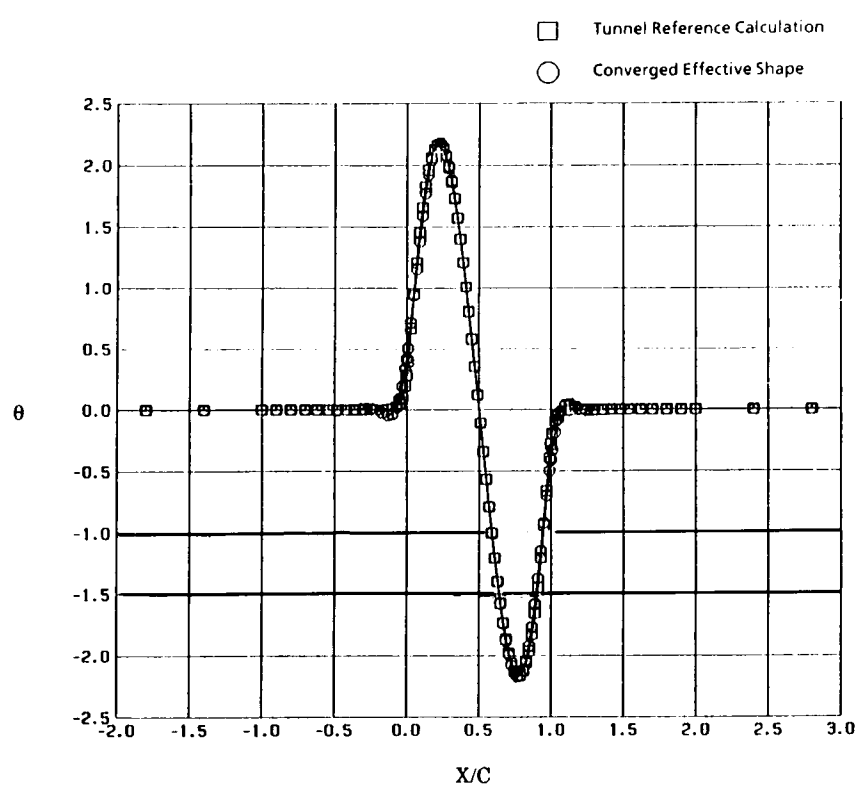

Figure 6. Predicted equivalent shape for axisymmetric case over 10% parabolic arc body at $M_t = 0.975$, $r_1 = 0.1$, $h = 0.5$, $v^o(x,r_1) = 0$, open jet tunnel.

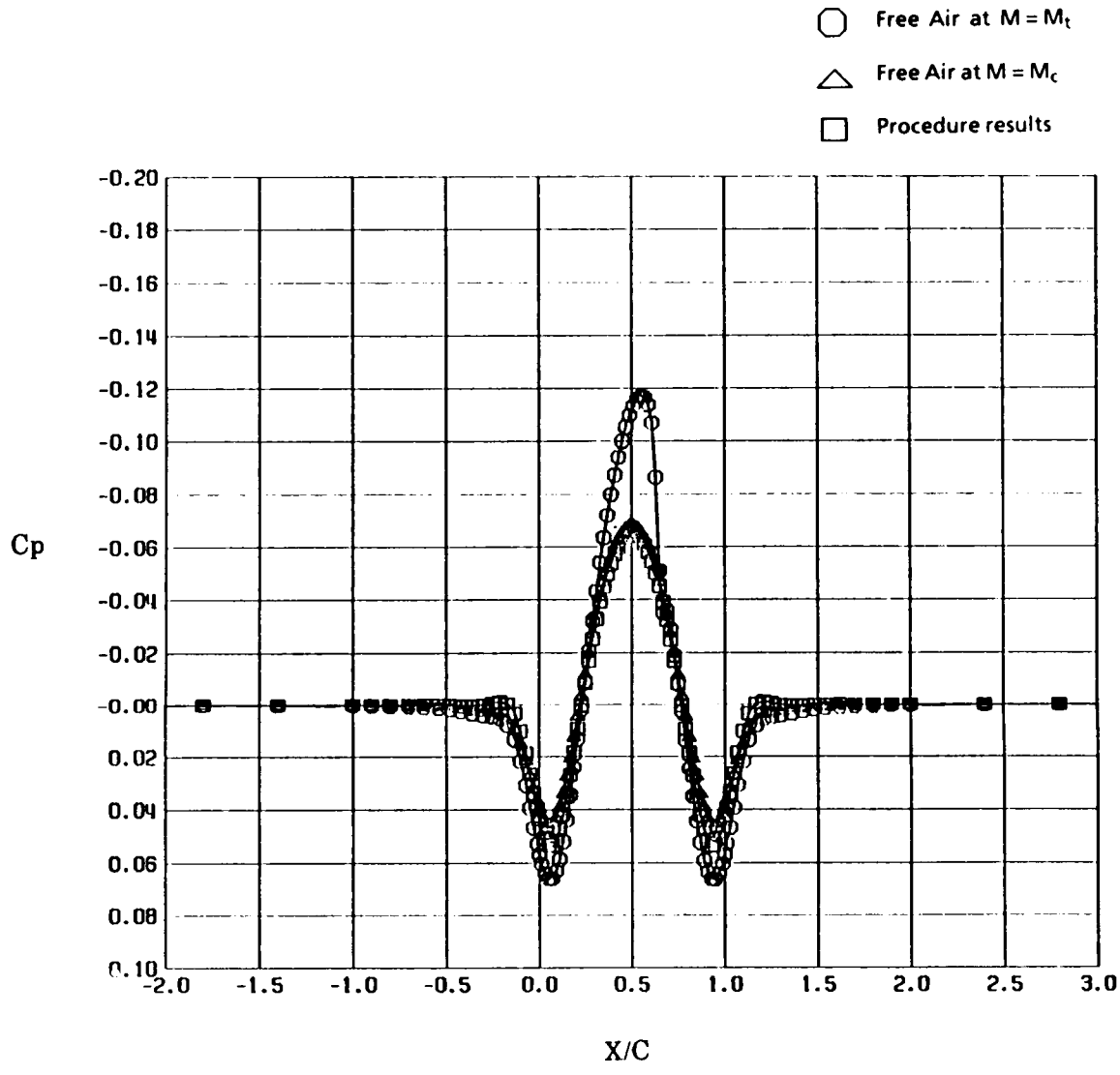

Figure 7. Pressure distributions for tunnel flow at M_t = 0.975 and free flight flow at M_c = 0.925.

Appendix A. Convergence of the Iterative Procedure

For the convenience of mathematical manipulation, the Fourier Transform technique is applied to prove the convergence of the iterative procedure. In the transform plane, the solution for $u(y_1)$ at $y = y_1$ for Step 1 in Eq. (1) is of the form

$$\bar{u}^{(n)}(p,y_1) = \frac{\bar{u}_t(p,h)}{\cosh p\beta(h-y_1)} - \frac{i}{\beta}\,\bar{v}^{(n)}(p,y_1)\tanh p\beta(h-y_1) \tag{A-1}$$

The boundary conditions applied to obtain the solution $u^{(n)}(y_1)$ are $u_t(h)$ measured and $v^{(n)}(y_1)$ selected. For Step 2, the solution for $v(y_1)$ of Eq. (2) can be expressed in the transform plane as

$$\bar{v}^{(n+1)}(p,y_1) = \frac{\bar{v}_t(p,h)}{\cosh p\beta(h-y_1)} - i\beta\,\bar{u}^{(n)}(p,y_1)\tanh p\beta(h-y_1) \tag{A-2}$$

where $u^{(n)}(y_1)$ is obtained from Eq. (A-1) of step 1 and $v_t(h_1)$ is measured.

Substituting $u^{(n)}(y_1)$ from Eq. (A-1) into Eq. (A-2), one obtains a single expression which can be used to start the iterative procedure as described in the previous section

$$\begin{aligned}\bar{v}^{(n+1)}(p,y_1) = {} & \frac{\bar{v}_t(p,h)}{\cosh p\beta(h-y_1)} - i\beta\,\bar{u}_t(p,h)\frac{\sinh p\beta(h-y_1)}{\cosh^2 p\beta(h-y_1)} \\ & + \bar{v}^{(n)}(p,y_1)\tanh^2 p\beta(h-y_1)\end{aligned} \tag{A-3}$$

This single expression, Eq. (A-3), can be utilized to prove the convergence of the iterative procedure. For simplicity the iterative expression, Eq. (A-3) is written in the following function form,

$$\bar{v}^{(n+1)} = G(\bar{u}_t, \bar{v}_t) + K\,\bar{v}^{(n)} \tag{A-3a}$$

where

$$G(u_t,v_t) = \frac{\bar{v}_t(p,h)}{\cosh p\beta(h-y_1)} - i\beta\,\bar{u}_t(p,h)\frac{\sinh p\beta(h-y_1)}{\cosh^2 p\beta(h-y_1)} \tag{A-3b}$$

and

$$K = \tanh^2 p\beta(h-y_1)$$

Before carrying successive substitution of each iteration, we can obtain the converged solution directily from Eq. (A-3a) as $v^{(n+1)} = v^{(n)} = v$

$$\bar{v} = G\frac{1}{1-K} \tag{A-4}$$

It should be noted that the solution of Eq. (A-4) in the physical plane is an integral equation of the first kind which is unstable and difficult to solve (see Appendix B). Thus, we choose Eq. (A-3) to obtain the present solution in an iterative fashion.

Let the initial guess be $V^{(o)}(y_1)$, the n-th iteration gives

$$\bar{v}^{(n)} = G + GK + GK^2 + \ldots + GK^{n-1} + \bar{v}^{(o)}K^n = G\,\frac{1-K^n}{1-K} + \bar{v}^{(o)}K^n \tag{A-5}$$

Since $K = \tanh^2 p\beta\,(h-y1) < 1$,

$$\lim_{n\to\infty} \bar{v}^{(n)} = G\,\frac{1}{1-K}\,.$$

which converges to Eq. (A-4) as we wish to prove.

Appendix B. Stability of the Iterative Procedure

Before examining the stability of the iterative procedure, we investigate the explicit solution Eq. (A-4) in the physical plane. Equation (A-4) in the physical plane can be expressed as an integral equation of the first kind

$$\oint_{-\infty}^{\infty} = \frac{\bar{v}(\zeta)d\zeta}{\cosh\frac{\pi(\zeta-x)}{2\beta h}} = 2\beta h\, v_t(x,h) + \beta \oint_{-\infty}^{\infty} \frac{u_t(\zeta,h)d\zeta}{\sinh\frac{\pi(\zeta-x)}{2\beta h}} \tag{B-1}$$

The effects of measurement errors of u_t, v_t on the effective shape will be evaluated by the following assumed errors

$$v_{t_{err}}(x,h) = \frac{1}{a}\sin ax \tag{B-2}$$

where a is a parameter. The measurement error will vanish as a approaches infinity.

The result of effective shape due to $v_{t_{err}}$ of Eq. (B-2) obtained from Eq. (B-1) is

$$v_{err}(x) = \frac{1}{a}\sin ax \cdot \cosh a\beta h \tag{B-3}$$

As the $v_{t_{err}}$ decreases to the vanishing small as $a \to \infty$, the error of effective shape is magnified to an arbitrarily large value

$$Max\left|v_{err}(x)\right| = \left|\frac{1}{a}\cosh a\beta h\right| \to \infty \text{ as } a \to \infty \tag{B-4}$$

This demonstrates that the formulation of Eq. (B-1) is not stable, since a small measurement error in the boundary flow quantities will result in the effective shape of Eq. (B-4) growing to an arbitrarily large amount. On the other hand, we will demonstrate that the iterative procedure is stable as follows.

We assume that the measurement error of v_t and u_t of the forms

$$v_{t_{err}}(x,h) = \frac{1}{a}\cos ax \tag{B-5}$$

$$u_{t_{err}}(x,h) = \frac{1}{a}\cos ax$$

The error of the effective shape obtained from Eqs. (1) and (2) is:

$$v_{t_{err}}(x) = \frac{\cos ax}{a}\,\frac{1}{\cosh a\beta h} - \beta\,\frac{\sin ax}{a}\,\frac{\tanh a\beta h}{\cosh a\beta h} \tag{B-6}$$

when the measured error vanishes as $a \to \infty$, the error of effective shape Eq. (B-6) will also vanish. This indicates that the iterative procedure is stable as the measured input is perturbed.

N89-20960

COMPARISON OF AIRFOIL RESULTS FROM AN ADAPTIVE WALL TEST SECTION AND A POROUS WALL TEST SECTION

Raymond E. Mineck
NASA Langley Research Center
Hampton, Virginia

SUMMARY

Two wind tunnel investigations have been conducted to assess two different wall interference alleviation/correction techniques: adaptive test section walls and classical analytical corrections. The same airfoil model has been tested in the adaptive wall test section of the NASA Langley 0.3-Meter Transonic Cryogenic Tunnel (TCT) and in the National Aeronautical Establishment (NAE) High Reynolds Number Two-Dimensional Facility. The model has a 9-inch chord and a CAST 10-2/DOA 2 airfoil section. The 0.3-m TCT adaptive wall test section has four solid walls with flexible top and bottom walls. The test section is 13 inches by 13 inches at the entrance. The ratio of the TCT test section height to the model chord is 1.4. The NAE test section has porous top and bottom walls and solid side walls. It is 15 inches wide and 60 inches tall. The ratio of the NAE test section height to model chord is 6.7.

This report compares the aerodynamic results corrected for top and bottom wall interference at Mach numbers from 0.3 to 0.8 at a Reynolds number of 10×10^6. Movement of the adaptive walls was used to alleviate the top and bottom wall interference in the test results from the NASA tunnel. Classical analytical techniques were used to correct the test results from NAE tunnel for top and bottom wall interference. Selected chordwise pressure distributions and the integrated force and moment coefficients are presented for common test conditions. A comparison of the slope of the normal force curves, the drag rise characteristics, and the upper surface shock locations is also included. A portion of the results has been corrected for sidewall interference. These experimental results are then compared with analytically predicted free air results.

The shock locations were in very good agreement. The slopes of the normal force curves and the drag levels were in reasonable agreement except at the highest Mach numbers. The adaptive wall used for the NASA tests alleviated the top and bottom wall interference to produce results in reasonable agreement with the analytically corrected results from the NAE tests.

INTRODUCTION

The interference of test section walls on the flow field around a model introduces an error in the measurements from wind tunnel tests. In two-dimensional airfoil tests, different types of interference arise from the top and bottom walls and from the sidewalls. Corrections are applied to wind tunnel test results to account for the wall interference. These corrections are relatively simple for tests in closed test sections at low subsonic speeds. However, the corrections become more complex and difficult to apply for tests in ventilated test sections at high subsonic speeds. The difficulties involve mathematically modeling and experimentally measuring the flow field at the wall. The digital computer has aided the development of sophisticated wall correction techniques for ventilated test sections at high subsonic speeds. These techniques often depend on extensive measurements taken on or

near the test section boundaries. Several examples of these techniques used for two-dimensional testing are presented in reference 1. The digital computer has also aided the development of adaptive wall test sections which have the potential of removing the wall interference at its source. Free air results can be approached using a post-test wall correction technique, a real-time adaptive wall test section technique, or some combination of the two techniques.

The National Aeronautical Establishment (NAE) of Canada and the National Aeronautics and Space Administration (NASA) have a cooperative agreement to develop and validate methods to correct or alleviate wall interference in transonic two-dimensional wind tunnel testing at high Reynolds number. Both organizations desired to verify wall interference correction methods for data obtained at high subsonic speeds and high Reynolds numbers. The same model was tested in both wind tunnels. The corrected results could then be compared to assess each correction technique. The NAE used an analytical wall correction technique for airfoil data from its High Reynolds Number Two-Dimensional Facility. NASA used an adaptive wall test section technique for airfoil data from its 0.3-m Transonic Cryogenic Tunnel (TCT).

Under the cooperative agreement, the NAE designed and fabricated a CAST 10-2/DOA 2 airfoil model with a 9-inch chord. This airfoil profile was chosen because it has aerodynamic characteristics sensitive to changes in Mach number and Reynolds number. The model was tested in both tunnels at Mach numbers from 0.3 to 0.8 at chord Reynolds numbers of 10, 15, and 20 x 10^6. The angle of attack varied from about -2° to stall. The airfoil model was first tested in the NAE High Reynolds Number Two-Dimensional Facility. This tunnel, described in references 2 and 3, has a 15-inch by 60-inch test section with perforated top and bottom walls. The ratio of the NAE test section height to the model chord was 6.7 for this test. The relatively large ratio was expected to lead to moderate levels of wall interference. The results from the NAE tests, presented in reference 4, were corrected for top and bottom wall interference using the method of reference 5.

The same model was then tested in the NASA Langley 0.3-m TCT with the two-dimensional, adaptive wall test section. Details of the tunnel may be found in reference 6. A description of the test section may be found in reference 7. The 13-inch by 13-inch test section has four solid walls with flexible top and bottom walls. The ratio of TCT test section height to model chord was 1.4. This small ratio would be expected to lead to large levels of wall interference unless the flexible walls were properly positioned. The results from the 0.3-m TCT tests, presented in reference 7, were corrected for top and bottom wall interference by the movement of the adaptive walls. The wall adaptation technique used for this test is described in reference 8.

This report compares the aerodynamic results corrected for top and bottom wall interference at a Reynolds number of 10 x 10^6. Selected chordwise pressure distributions and the integrated force and moment coefficients are presented for common test conditions. A comparison of the slope of the normal force curves, the drag rise characteristics, and the upper surface shock locations is also included. A selected portion of both sets of results has been corrected for sidewall interference. These experimental results are compared with analytically predicted free air results.

SYMBOLS

c	model chord, inches
c_d	section drag coefficient, measured on tunnel centerline

C-6

c_m	section pitching moment coefficient, resolved about the 0.25c
c_n	section normal force coefficient
$c_{n,c}$	section normal force coefficient corrected for sidewall interference
c_{n_α}	slope of section normal force coefficient curve, deg^{-1}
$c_{d,c}$	section drag coefficient corrected for sidewall interference
c_{n,c_α}	slope of section normal force coefficient curve corrected for sidewall interference, deg^{-1}
C_p	local pressure coefficient
M_∞	free stream Mach number
$\bar{M}_\infty$	average free stream Mach number for a set of data
$M_{\infty,c}$	free stream Mach number corrected for sidewall interference
NAE	NAE Two-Dimensional High Reynolds Number Facility
NASA	NASA Langley 0.3-Meter Transonic Cryogenic Tunnel
R_c	free stream Reynolds number based on model chord
Tun	Tunnel used for experiments
u	non-dimensional disturbance velocity in x direction due to test section walls
u_c	non-dimensional computed disturbance velocity in x direction
u_m	non-dimensional measured disturbance velocity in x direction
v	non-dimensional disturbance velocity in y direction due to test section walls
v_c	non-dimensional computed disturbance velocity in y direction
x	chordwise position, measured aft from leading edge, inches
x_s	chordwise position of shock on upper surface, measured aft from leading edge
y	adaptive wall displacement or distance normal to free stream direction
z	model vertical ordinate, positive up
α	geometric angle of attack, degrees
β	Prandtl-Glauert compressibility factor, $\sqrt{1 - M_\infty^2}$
γ	ratio of specific heats

Γ	strength of vortex
Δy	change in adaptive wall displacement
$\Delta y'$	change in slope of adaptive wall
$\Delta\alpha$	Correction to angle of attack due to top and bottom wall interference
ΔM_∞	Correction to Mach number due to top and bottom wall interference
μ	strength of doublet
η	transformed co-ordinate in y direction
ξ	transformed co-ordinate in x direction or dummy variable of integration
φ	disturbance potential
φ_m	disturbance potential from model boundary
φ_w	disturbance potential from wall boundary

WIND TUNNELS

NASA Langley 0.3-Meter Transonic Cryogenic Tunnel

The NASA tests used the Langley 0.3-m TCT with the adaptive wall test section. The 0.3-m TCT is a fan-driven, cryogenic pressure tunnel which uses gaseous nitrogen as the test gas. It is capable of continuous operation at stagnation temperatures from about 80K to 327K and at stagnation pressures from 1.2 atmospheres to 6.0 atmospheres. The fan speed is variable so that the empty test section Mach number can be varied from about 0.20 to 0.95. This combination of test conditions provides a test envelope of chord Reynolds numbers up to about 100×10^6 based on a model chord of 12 inches. Additional details of the tunnel may be found in reference 6.

A sketch of the adaptive wall test section with the test section plenum wall removed is presented in figure 1. The test section is 13 inches by 13 inches in cross section at the entrance. All four walls are solid. The sidewalls are rigid and parallel. The top and bottom walls are flexible and movable. The test section portion of the flexible wall is 55.8 inches long. The flexible walls are anchored at the upstream end. The shape of each wall is determined by 21 independent jacks. Pressure orifices are located at each jack position on each flexible wall centerline. The model is supported between two turntables centered 30.7 inches downstream of the test section entrance. The sidewall boundary layer removal system, shown in figure 1, was not used in this test. Further details of this test section may be found in reference 7.

A total head probe rake was installed 17.5 inches downstream of the center of the turntable. This location was 1.2 chords downstream of the model trailing edge. The rake had 6 total pressure probes positioned across the left half of the test section. The drag data presented in this report was computed from the data from the probe on the test section centerline.

No traditional model upright and inverted tests of flow angularity and no empty test section tests with a flow angularity probe have been conducted in the adaptive wall test section. Therefore, no corrections for flow angularity have been made to the angle of attack, α.

NAE Two-Dimensional High Reynolds Number Facility

The NAE tests used the 5-ft x 5-ft Blowdown Wind Tunnel with the Two-Dimensional High Reynolds Number Facility test section. Details of the tunnel and the test section may be found in references 2 and 3. The tunnel with the two-dimensional test section typically operates at stagnation pressures up to about 10 atmospheres and at stagnation temperatures near room temperature. The test section Mach number can be varied from about 0.10 to 0.95. These test conditions provide a test envelope of chord Reynolds number up to 50×10^6 based on a model chord of 12 inches. The air storage system provides run times from 5 to 60 seconds depending on the test conditions.

A sketch of the two-dimensional test section is presented in figure 2. The test section is 15 inches wide and 60 inches high at the entrance and is 141 inches long. The sidewalls are solid and parallel. The porous top and bottom walls are also parallel. The porous walls are covered with a 30 mesh, 40.8-percent open screen to reduce the edgetone noise. The resulting overall porosity of the walls is 8.4 percent. A 1-inch diameter static pressure tube is mounted on the centerline of the top wall and the bottom wall. There are 40 static pressure taps on the tube. The pressure orifice locations extend from 80.9 inches upstream to 47.1 inches downstream of the model center of rotation. The center of rotation is located on the centerline, 94 inches downstream of the start of the test section. The model is mounted on a porous turntable within an 18-inch by 24-inch porous panel covered with a woven wire sheet. The porous panel is connected to a suction box to control the boundary layer in the vicinity of the model. The suction is intended to control the adverse growth of the boundary layer from the pressure signature imposed on the sidewall by the model. It is not intended to remove completely the boundary layer. A suction velocity (nondimensionalized by the free stream velocity) of 0.0085 was chosen for these tests. Previous tests have shown that this value is sufficient to prevent premature separation of the sidewall boundary layer in the region of adverse pressure gradients.

A total head probe rake is mounted 21 inches downstream of the center of the turntable. For the 9-inch chord airfoil used in this test, this location corresponds to 1.78 chords downstream of the trailing edge. The rake had four total head probes. The drag data presented in this report was computed from the data from the probe on the test section centerline.

The flow angularity in the NAE test section is very small. Measurements taken before the latest improvements to the tunnel indicate a downwash of about 0.05°. The current flow angularity is expected to be even smaller. No correction to the angle of attack for test section flow angularity has been applied to the results.

MODEL

The model used in these tests has a 9-inch chord and a CAST 10-2/DOA 2 airfoil section which is 12.2 percent thick. The design and measured airfoil ordinates are presented in table 1. A photograph of the model is given in figure 3. The model has a 15-inch span to fit the NAE test section. Since the 0.3-m TCT test section is 13 inches wide, the outer 1 inch on each end of the model extended into the model mounting blocks as shown. With this arrangement, the model centerline and the test section centerline coincided for both tests.

The model chord line was defined as the line passing from the center of the leading to the center of the trailing edge. This line is rotated 0.88° nose up relative to the reference line used to define the airfoil shape. For these tests, α was referenced to the model chord line. Care is needed when comparing these CAST 10-2/DOA 2 airfoil results to other CAST 10-2/DOA 2 results because some tests have referenced α to the line $z = 0$ used to define the airfoil shape.

The model is equipped with 45 pressure orifices in a chordwise row on the upper surface and 23 orifices in a chordwise row on the lower surface. Two spanwise rows of 6 orifices were installed. One row was on the upper surface. The other row was on the lower surface. The orifices in the chordwise row are staggered about the model centerline to minimize interference on the neighboring orifices. The orifices from the leading edge back to the 22-percent chord are 0.010 inches in diameter. All other orifices are .014 inches in diameter. Smaller orifices are used over the forward portion of the airfoil to reduce any orifice size effects where the pressure gradients could be large.

TEST PROGRAM

The test program was designed to assess test section wall interference alleviation and correction techniques in an adaptive wall tunnel and a passive wall tunnel. The test program was not intended to determine airfoil performance. Previous tests of a CAST 10-2/DOA 2 airfoil section in the ONERA T2 adaptive wall tunnel show the shock locations differ significantly for fixed and free transition at a chord Reynolds number of 13×10^6 (reference 9). At the Reynolds numbers planned for these tests, tunnel turbulence levels could influence the boundary layer characteristics and the shock location. Since the primary purpose of these tests was to evaluate two wall interference alleviation and correction techniques using two different tunnels, the effect of tunnel turbulence on transition and shock location had to be removed from the experiments. Therefore, both tests were conducted with transition strips on both surfaces of the model. The grit size was determined using the method of reference 10 for a Reynolds number of 10×10^6. Carborundum grit no. 320 with average grit size of .0011-inches was used for both tests. The 0.1-inch wide transition strip was located at the 5-percent chord.

The range of Mach numbers was from 0.3 to 0.8 at chord Reynolds numbers of 10, 15, and 20×10^6. The range of α was from about -2° through stall. The wall positioning hardware in the NASA 0.3-m TCT could not reach the required displacement for successful wall adaptation for some of the higher α's. The NASA tests do not include results up to the stall angle for many of the test conditions. The α's chosen for the NASA tests were selected to obtain data at the same normal force coefficients achieved in the NAE tests.

INTERFERENCE ALLEVIATION AND CORRECTION TECHNIQUES

Wall Adaptation Technique for the NASA Tests

This section presents a summary of the wall adaptation technique used to alleviate the interference of the top and bottom walls of the NASA results. The alleviation is achieved by proper movement of the top and bottom flexible walls. Further details of the method may be found in reference 8. As shown in figure 4, the flow field is split into two regions: a real flow field inside a control surface near the test section walls and an imaginary flow field extending from the control surface to infinity in both directions. The control surface, or the effective wall position, is the physical wall position plus the displacement thickness of the boundary layer.

Finding the proper flexible wall position is an iterative process. The wall position and the wall static pressure are measured at each jack station. The tangential perturbation velocity at the control surface is determined from the measured pressure coefficient. The wall position and the tangential velocity are converted to the incompressible equivalent, $y(x)$ and $u_m(x)$, using the Prandlt-Glauert compressibility factor. The wall shape for the imaginary flow field is set to the measured incompressible wall shape and the potential flow over this wall shape is computed. The potential flow solution is used to compute the horizontal perturbation velocity, $u_c(x)$. The wall slope is assumed to be small. Therefore, the computed perturbation $u_c(x)$ is assumed to be parallel to the control surface. The difference between the measured, u_m, and the computed ,u_c, velocity perturbations can be treated as a vortex sheet.

$$\Gamma(x) = u_m(x) - u_c(x)$$

For small wall slopes, the downwash, $v_c(x)$, induced by the vortex sheet can be determined by integration as follows

$$v_c(x) = \frac{1}{2\pi}\int_{-\infty}^{\infty}\frac{\Gamma(\xi)}{x-\xi}\,d\xi$$

The wall shape will be a streamline if the downwash is zero (no normal flow). This can be done by redirecting the free stream through the appropriate angle to cancel the computed downwash. For small wall slopes, the angle is the non-dimensional vertical perturbation velocity.

$$\Delta y'(x) = -v_c(x)$$

The change in wall displacement is found by integration from the wall anchor point.

$$\Delta y(x) = \int_0^x \Delta y'(\xi)\,d\xi$$

The change in wall displacement is converted to the compressible equivalent and the wall positioned to the new shape. This process is repeated until a set of convergence criteria are satisfied. The convergence criteria are presented in table 2. Once the convergence criteria are satisfied, the data are recorded.

The wall adaptation technique determines the wall position from wall pressures measured on the centerline of the top and bottom walls. No pressures are measured off the centerline. The flow field in the test section can be three dimensional and successful adaptation can still take place.

Analytical Correction Technique for the NAE Tests

This section presents a summary of the analytical technique used to correct the NAE results for interference from the top and bottom walls only. Details of the technique may be found in reference 5. The NAE correction technique assumes the flow field at the test section boundaries can be represented by potential flow theory with linearized compressibility effects. This type of flow can reasonably be expected for the long length and large ratio of test section height to model chord for the NAE test section and the typical airfoil test Mach numbers. An axis system is defined with the origin located at the quarter chord of the model. A rectangular control surface, shown in figure 5, is defined with the corners at the most upstream and downstream pressure orifices on the top wall and bottom wall static pipes. If this control surface is far from the model, the compressible potential equation can be used to represent the flow field near the control surface.

$$\beta^2\varphi_{xx}(x,y) + \varphi_{yy}(x,y) = 0$$

The disturbance potential can be decomposed into two parts, one part due to the wall and the other part due to the model.

$$\varphi(x,y) = \varphi_w(x,y) + \varphi_m(x,y)$$

The part due to the model can be represented by a series of singularities representing the model lift, blockage, and wake. The model lift is represented by a vortex, the blockage by a doublet, and the wake by a source. The wake is assumed to be small because attached flow on the model is assumed. If there was massive separation and a large wake, two dimensional flow would not be expected and the data would be questionable. Therefore, the source term is ignored. The resulting series for the perturbation potential of the model is

$$\varphi_m(x,y) = -\frac{\Gamma}{2\Pi}\tan^{-1}\frac{\beta y}{x} + \frac{\mu}{\Pi\beta}\frac{x}{x^2 + (\beta y)^2}$$

The strength of the vortex is determined from the model lift coefficient. The strength of the doublet is determined from the model cross-sectional area. By stretching the x co-ordinate by $1/\beta$, the governing equation is transformed into the Laplace equation in a new (ξ,η) coordinate system.

$$\varphi_{\xi\xi}(\xi,\eta) + \varphi_{\eta\eta}(\xi,\eta) = 0$$

$$\text{where: } \xi = \frac{x}{\beta}$$

$$\eta = y$$

The derivatives of solutions of Laplace are also solutions to Laplace's equation. Thus, the perturbation velocity in the x direction also satisfies Laplace's equation.

$$u_{\xi\xi}(\xi,\eta) + u_{\eta\eta}(\xi,\eta) = 0$$

$$\text{where: } u(\xi,\eta) = \varphi_{w_\xi}(\xi,\eta) = \beta\varphi_{w_x}(\xi,\eta)$$

The boundary condition is obtained from

$$u(\xi,\eta) = -\beta\left(\tfrac{1}{2}C_p(x,y) - \varphi_{m_x}(x,y)\right)$$

The perturbation potential from the model is known from the integrated lift coefficient and the model cross-sectional area. The pressure coefficient is measured on the top and bottom sides of the control surface. No measurements of the pressure coefficient on the upstream and downstream faces of the control surface are available. If these faces are far enough from the model, the missing measured pressures can be approximated by linearly interpolating between the measured values at the corners. Thus, the Laplace equation for the perturbation velocity and the boundary conditions on all sides of control surface form a Dirichlet problem that can be solved by the Fast Fourier Transform method. The solution for the perturbation velocity take the form of a Fourier sine series with coefficients determined from the boundary conditions. The correction to the Mach number is

$$\Delta M_\infty = \left(1 + \frac{\gamma - 1}{2} M_\infty{}^2 \right) \varphi_{w_x} = \left(1 + \frac{\gamma - 1}{2} M_\infty{}^2 \right) M_\infty \quad u$$

The perturbation velocity, u, is evaluated at the quarter chord point on the model. The correction to α is

$$\Delta\alpha = v(\xi,\eta) = \varphi_{w_y}$$

The vertical interference velocity can be obtained by integrating as follows

$$v(\xi,\eta) = \int u_\eta(\xi,\eta)\ d\eta = -\int u_\xi(\xi,\eta)\ d\eta$$

The integral is evaluated from some reference point to the model quarter chord. The resulting constant of integration is a function of the location of the chosen reference point and the flow direction at that point with the tunnel empty.

The applied corrections to α and the Mach number have been plotted in figure 6. The correction to α increases with normal force coefficient and is a weak function of Mach number. The correction to the Mach number is dependent on both the Mach number and the normal force coefficient. As expected from the large test section height to model chord ratio, the magnitude of these corrections is moderate. The level of uncertainty in the results after these corrections have been applied should be only a fraction of the correction.

DISCUSSION OF RESULTS

Results Corrected for Top and Bottom Wall Interference

The measured aerodynamic data consisted of chordwise static pressure distributions on the airfoil model and loss of momentum in the model wake. Many of the chordwise pressure distributions from the two tests have been compared. Two samples are presented in figure 7. These samples represent the worst and best agreement of the results. The agreement is very good even for the worst case. The small discrepancies can easily be explained. The small discontinuity near the 5-percent chord location is caused by the presence of the boundary layer transition strip. The pressure orifice at the 41-percent chord on the upper surface leaked during the NASA tests. It is possible similar problems occurred during the NAE tests.

The chordwise shock location is sensitive to wall interference. It is a useful gauge to assess the agreement of the results, especially when the test conditions differ slightly. Different methods have been used to define shock location. A

sketch showing the method used is presented in figure 8a. A straight line was drawn through the pressure distribution in the area just ahead of the shock, through the shock, and just behind the shock. The intersection of the line upstream of the shock and the line through the shock defined the upstream limit of the shock region. Similarly, the intersection of the line downstream of the shock and the line through the shock defined the downstream limit of the shock region. The average shock location, x_s, corresponded to the mid-point of the shock region. The variation of the shock location with normal force coefficient is presented in figure 8b. The shock locations are in excellent agreement with each other, seldom differing by more than 2 percent chord.

The model chordwise pressure distributions and the momentum loss in the wake were integrated to obtain the section normal force, drag, and pitching moment coefficients. Two samples of these results are presented in figure 9. The drag coefficient was measured on the tunnel centerline. No corrections for the effect of flow angularity or for the interference from the sidewall boundary layer have been applied to these results. The pitching moment data are in very good agreement except near the stall. The drag coefficient at a given normal force coefficient is less for the NASA tests than for the NAE tests. Only a limited number of the NASA tests reached the stall. Of these results, the maximum normal force coefficient measured in the NASA tests is greater in all cases except one. Examination of the spanwise distribution of the drag coefficient shows the flow in the wake is not two-dimensional for many of the test conditions near the stall.

The slopes of the fairings of the section normal force curves have been calculated at $c_n = 0.2$, $c_n = 0.4$, and $c_n = 0.6$. The slope of the section normal force curve, c_{n_α}, should vary linearly with β^{-1}, the reciprocal of the Prandtl-Glauert compressibility factor, over the range of Mach numbers where linear aerodynamic theory is valid. The slopes have been plotted against β^{-1} rather than M_∞ for two reasons. At the smaller values of M_∞ (and β^{-1}), deviation from a linear relationship would indicate a problem in the results. At the larger values of M_∞ (and β^{-1}), the data would be spread out on the abscissa to permit closer inspection of the results for small Mach number changes. The calculated slopes are presented in figure 10. The level of agreement is reasonable. Except for the NAE results at $\beta^{-1} = 1.05$, (M_∞=0.30), the slopes vary linearly at the lower normal force coefficients and Mach numbers. The slope measured in the NASA tests is greater and the difference increases with Mach number. Both sets of results show the dramatic loss in slope at about the same Mach number.

The section drag coefficient has been cross-plotted against Mach number at constant values of section normal force coefficient. The results are plotted in figure 11. As noted previously, the drag at a given normal force is slightly less in the NASA tests. The difference in c_d is only 0.0004 over most of the Mach number range. The drag rise Mach number is difficult to determine because of non-uniformities in the curves. The drag rise appears to occur at a Mach number 0.01 lower in the NAE results.

Results Corrected for Sidewall Interference

The test section top and bottom walls and the sidewalls produce wall interference. The top and bottom wall interference has been accounted for in both the NAE and NASA results. Both sets of results contain residual interference, including that from the sidewalls. The model pressure distribution will lead to a local thinning and thickening of the sidewall boundary layer. The change in the sidewall boundary layer displacement thickness changes the blockage present in the

empty test section calibration. Murthy has developed a correction method for this sidewall interference in conventional two-dimensional wind tunnels. This method, described in reference 11, is not directly applicable to an adaptive wall test section. In an adaptive wall test section, part of the blockage change from the sidewalls is felt in the pressures measured on the top and bottom walls. The wall adaptation scheme will compensate for that part of the blockage when it finds the proper wall shape. What portion of Murthy's correction needs to be applied has not yet been determined.

The results from both tests must be corrected for sidewall interference. The Murthy method, as implemented in the computer program of reference 12, was used to correct both sets of data for sidewall interference. Since the portion of the correction needed for the NASA results was unknown, the whole correction was applied as a limiting case. The slopes of the corrected normal force curves were computed at $c_n = 0.4$. The results are presented in figure 12. The corrected slopes are still in reasonable agreement. Both curves have been shifted slightly upward and to the left. The corrected drag coefficients have been crossplotted against the corrected Mach number at $c_n = 0.4$. The results are presented in figure 13. These results are also in reasonable agreement.

Comparison with Analytical Free Air Results

The results still differ slightly after corrections for the sidewall interference. A set of free air results is needed to determine the level of residual interference remaining in each set of data. Experiments to determine free air airfoil results at the desired Reynolds number and Mach number are not practical. For this study, analytical results will be used to approximate free air results. A coupled inviscid/viscid airfoil program, GRUMFOIL, was used to generate free air results. This program is described in reference 13. The results are presented in figure 13. The computed level of drag agrees more closely with the NASA results at the lower Mach numbers. The Grumfoil computed drag rise agrees more closely with the NAE results.

The adaptive wall alleviated the wall interference from the top and bottom walls. Correcting the data for sidewall interference improves the agreement with the analytical free air results. Some residual errors remain in one or both sets of data.

CONCLUDING REMARKS

A two-dimensional airfoil model has been tested in the adaptive wall test section of the NASA Langley 0.3-Meter Transonic Cryogenic Tunnel and in the National Aeronautical Establishment High Reynolds Number Two-Dimensional Facility. The primary goal of the tests was to assess two different wall interference alleviation and correction techniques: adaptive test section walls and classical analytical corrections. The wall interference in the NASA tests has been alleviated by the movement of the top and bottom walls. The wall interference in the NAE tests has been corrected by classical analytical techniques. The results can be summarized as follows:

1. The shock locations are in excellent agreement.

2. The NASA results had a lower drag coefficient at a given normal force coefficient. The drag rise for the NASA results occurs at a higher Mach number.

3. The slopes of the normal force curves were in reasonable agreement where linear aerodynamic theory is valid. At the higher Mach numbers, the NASA slopes were slightly greater.

4. Correcting the results for sidewall interference improves the agreement of the results with the analytical results.

5. The adaptive wall was successful in alleviating the top and bottom wall interference. Corrections for the effects of the sidewall interference are needed to approach free air results.

ACKNOWLEDGMENTS

I would like to express my appreciation to the staff of the NAE High Speed Aerodynamics Laboratory. Their assistance and cooperation in all aspects of the tests insured a successful test program. Special thanks are extended to Dr. Louis Chan of the NAE for the thorough tests at the NAE and his assistance during the tests at NASA. I would like to thank Mr. Edward Ray of the Experimental Techniques Branch at NASA for his technical review of this paper.

REFERENCES

1. Two-Dimensional Wind Tunnel Wall Interference, AGARD-AG-281, November 1983.

2. Brown D.: Information for Users of the National Research Council's 5 ft x 5 ft Blowdown Wind Tunnel at the National Aeronautical Establishment. NRC/NAE LTR-HA-6, Third edition, September 1977.

3. Ohman, L. H.: The NAE High Reynolds number 15 in. x 60 in. Two-Dimensional Test Facility. Part 1. General Information NRC/NAE Laboratory Technical Report LTR-HA-4, April 1970.

4. Chan, Y. Y.: Wind Tunnel Investigation of the CAST-10-2/DOA-2 12% Supercritical Airfoil Model. NAE Laboratory Technical Report LTR-HA-5x5/0162. May 1986.

5. Mokry, M.; and Ohman, L. H.: Application of Fast Fourier Transform to Two-Dimensional Wind Tunnel Wall Interference. Journal of Aircraft, Vol. 17, No. 6, June 1980, pp.402-408.

6. Ladson, Charles L.; and Ray, Edward J.: Evolution, Calibration, and Operational Characteristics of the Two-dimensional Test Section of the 0.3-Meter Transonic Cryogenic Tunnel. NASA TP 2947, September 1987.

7. Mineck, Raymond E.: Wall Interference Tests of a CAST 10-2/DOA 2 Airfoil in an Adaptive-Wall Test Section. NASA TM 4015, November, 1987.

8. Judd, M.; Wolf, S. W. D.; and Goodyer, M. J.: Analytical Work in Support of the Design and Operation of Two Dimensional Self-Streamlining Test Sections. NASA CR-145019. 1976.

9. Seraudie, A.; Blanchard, A.; Briel, J. F.: Rapport d'essais du Profil CAST 10 en Transition Declenchee Effectues dans la Soufflerie Transsonique Cryogenique T2 en Presence de Parois Auto-adaptables. ONERA R.T. OA 63/1685 AND. 1985.

10. Braslow, A. L.; and Knox, E. C.: Simplified Method for Determination of Critical Height of Distributed Roughness Particles for Boundary Layer Transition at Mach Numbers from 0 to 5. NASA TN 4363. 1958.

11. Murthy, A. V.: Effect of Aspect Ratio on Sidewall Boundary Layer Influence in Two-Dimensional Airfoil Testing. NASA CR 4008. September 1986.

12. Murthy, A. V.: A Simplified Fourwall Interference Assessment Procedure for Airfoil Data Obtained in the Lamgley 0.3-Meter Transonic Cryogenic Tunnel. NASA CR 4042. January 1987.

13. Melnik, R. E.; Chow, R. R.; Mead, H. R.; and Jameson, A.: An Improved Viscid/Inviscid Interaction Procedure for Transonic Flow Over Airfoils. NASA CR-3805. October 1985.

TABLE 1

Airfoil Model Ordinates

Upper Surface			Lower Surface		
x/c	z/c design	z/c measured	x/c	z/c design	z/c measured
.0000	.0034	.0034	.0001	.0034	.0034
.0003	.0062	.0063	.0004	.0004	.0004
.0015	.0094	.0093	.0014	-.0021	-.0021
.0033	.0124	.0123	.0031	-.0043	-.0043
.0063	.0159	.0158	.0061	-.0066	-.0065
.0140	.0217	.0217	.0096	-.0081	-.0081
.0195	.0250	.0251	.0153	-.0099	-.0099
.0247	.0279	.0279	.0273	-.0127	-.0128
.0356	.0331	.0332	.0339	-.0141	-.0142
.0470	.0376	.0377	.0470	-.0169	-.0169
.0654	.0432	.0433	.0673	-.0205	-.0206
.0846	.0478	.0478	.0874	-.0238	-.0238
.1179	.0536	.0536	.1148	-.0277	-.0277
.1519	.0580	.0580	.1562	-.0328	-.0329
.2139	.0633	.0633	.2741	-.0446	-.0447
.2764	.0665	.0665	.3366	-.0492	-.0492
.3321	.0681	.0681	.3919	-.0520	-.0520
.3949	.0689	.0689	.4539	-.0532	-.0532
.4576	.0686	.0685	.5161	-.0520	-.0520
.5132	.0673	.0672	.5714	-.0489	-.0488
.5757	.0645	.0644	.6340	-.0436	-.0436
.6376	.0601	.0600	.6967	-.0373	-.0374
.6925	.0542	.0541	.7525	-.0316	-.0317
.7539	.0453	.0452	.8149	-.0255	-.0257
.8152	.0338	.0337	.8775	-.0204	-.0206
.8763	.0203	.0202	.9189	-.0177	-.0178
.9172	.0106	.0105	.9468	-.0162	-.0164
.9511	.0024	.0024	.9743	-.0151	-.0152
.9782	-.0042	-.0042	1.0000	-.0145	-.0146
1.0000	-.0095	-.0095			

TABLE 2

Adaptive Wall Method Convergence Criteria

1	Average C_p error, top wall	Less than 0.01
2	Average C_p error, bottom wall	Less than 0.01
3	Induced angle of attack	Less than $.015^{\circ}$
4	Induced camber	Less than .07
5	Average C_p error along model chord	Less than .007

ORIGINAL PAGE IS
OF POOR QUALITY

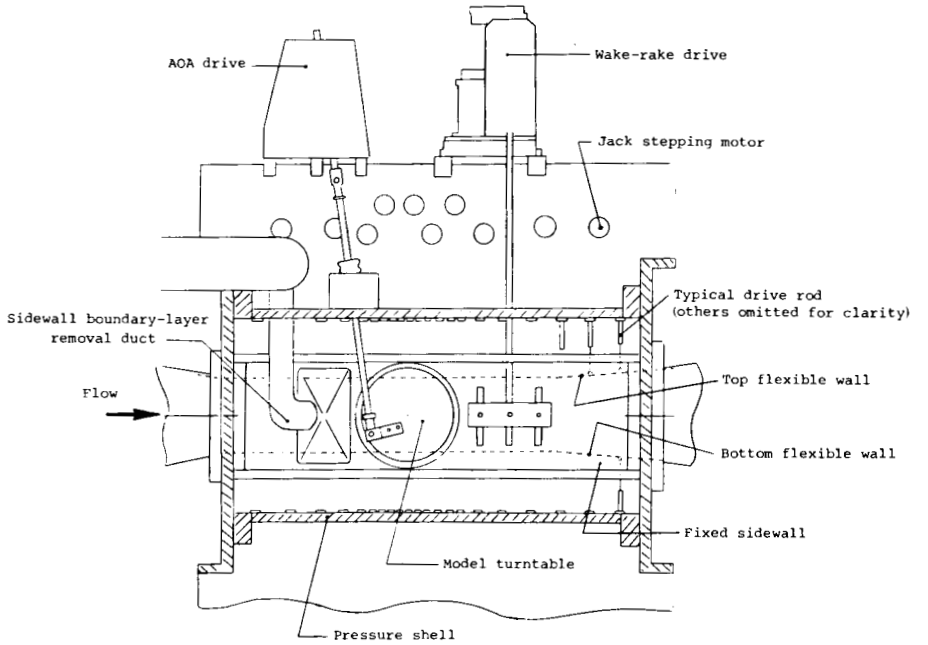

Figure 1. Details of the NASA Langley 13 inch by 13 inch adaptive wall test section. (Plenum sidewall removed).

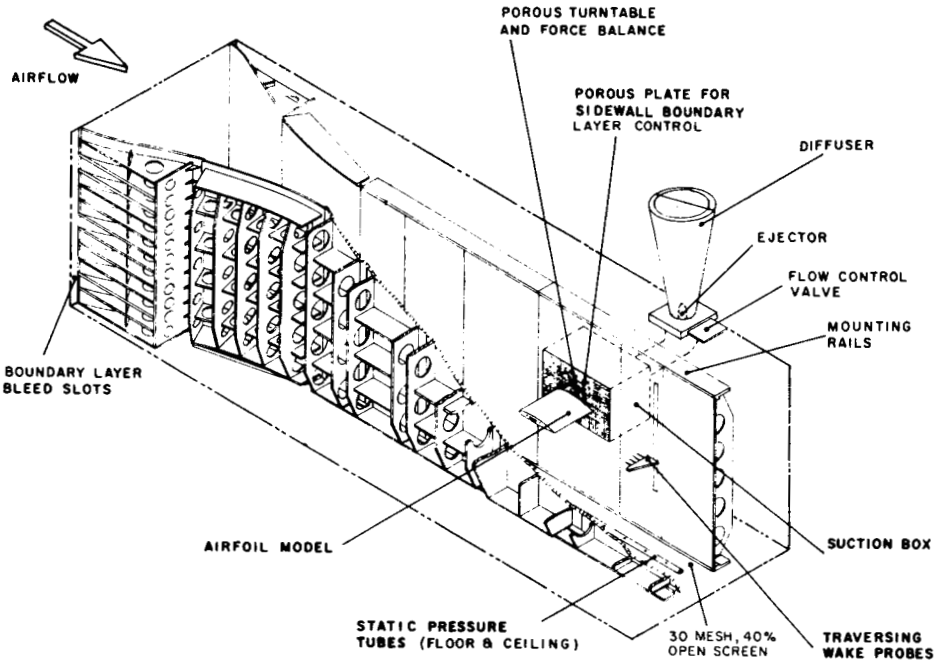

Figure 2. Details of the NAE 15 inch by 60 inch Two-dimensional High Reynolds Number Facility.

ORIGINAL PAGE IS
OF POOR QUALITY

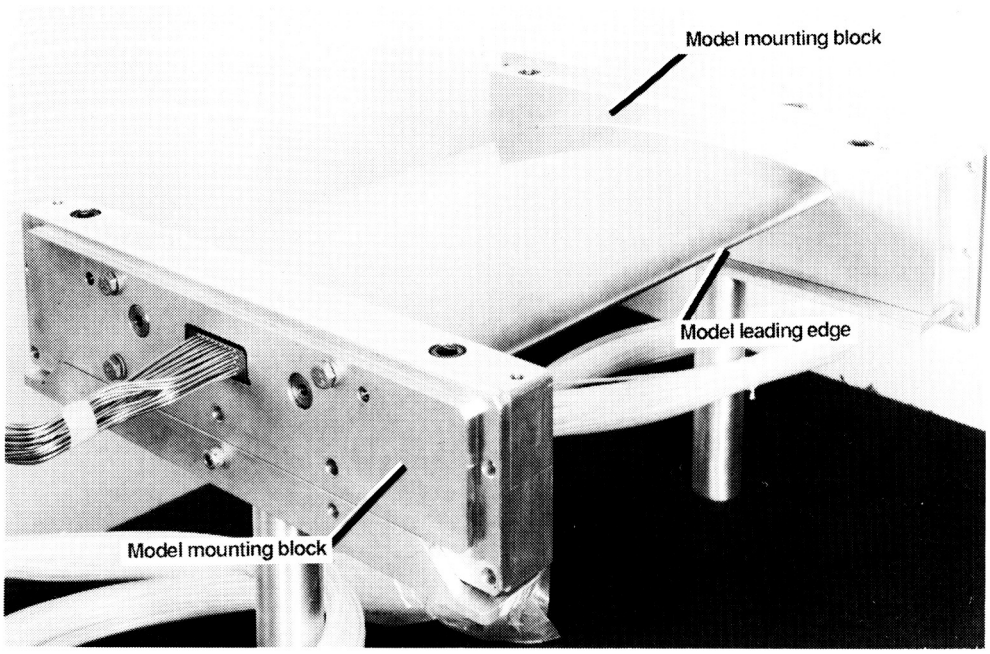

Figure 3. CAST 10-2/DOA 2 airfoil model with the model mounting blocks for the NASA tests.

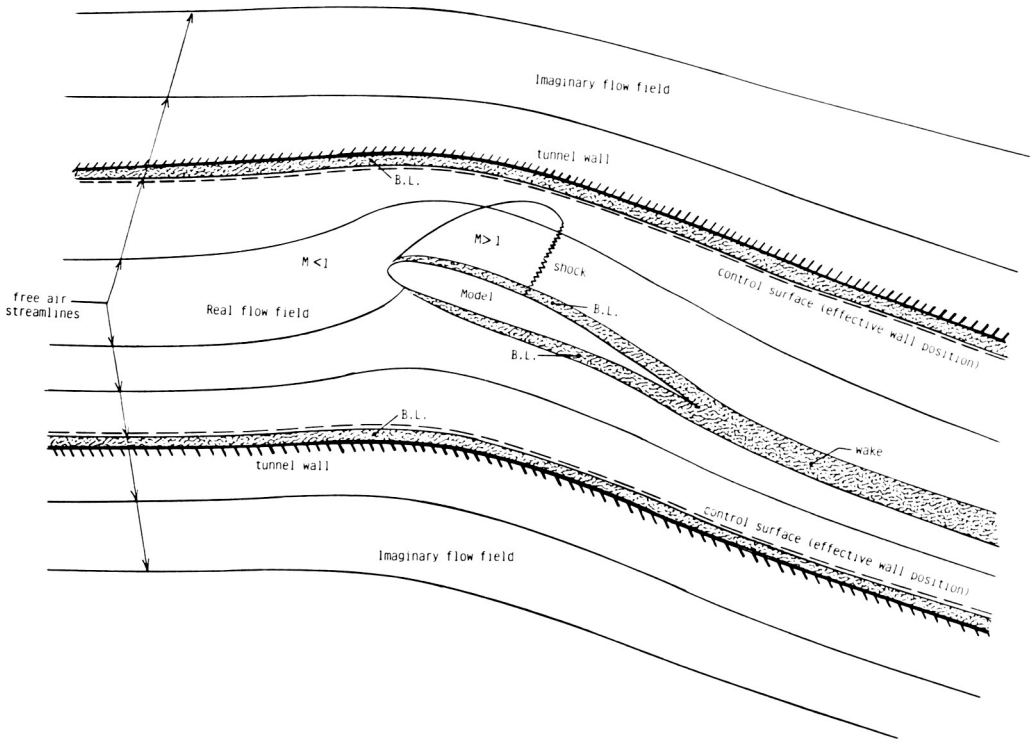

Figure 4. Diagram of the flowfield assumed for the adaptive wall technique.

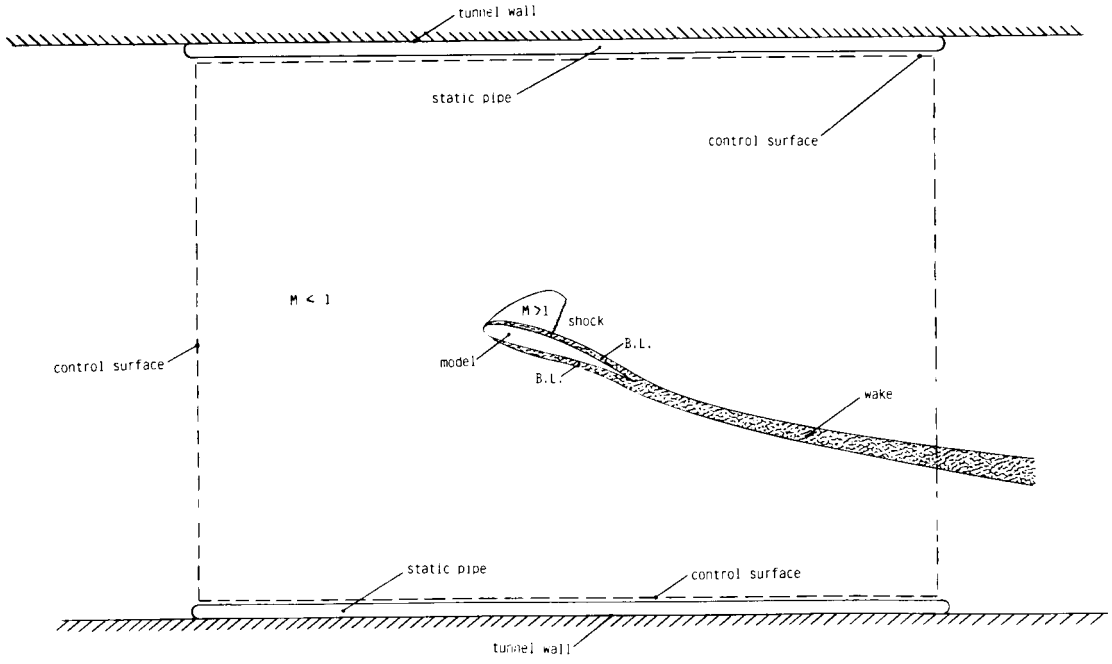

Figure 5. Diagram of the flowfield assumed for the NAE wall interference correction technique.

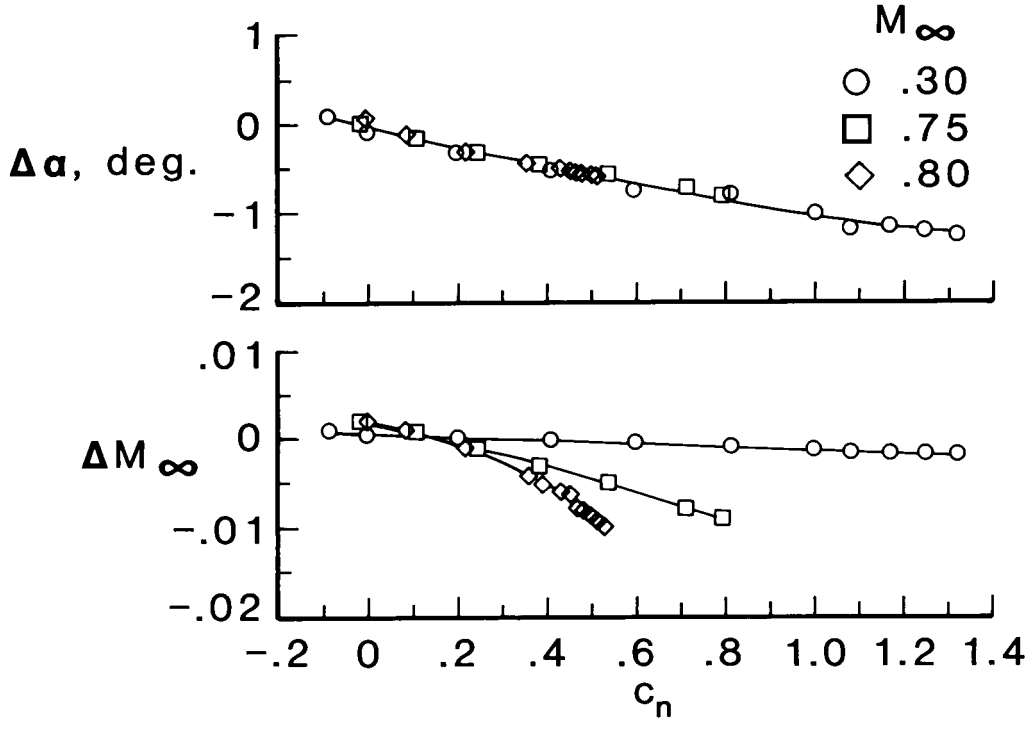

Figure 6. Corrections applied to NAE data for top and bottom wall interference. $R_c = 10 \times 10^6$.

ORIGINAL PAGE IS
OF POOR QUALITY

ORIGINAL PAGE IS
OF POOR QUALITY

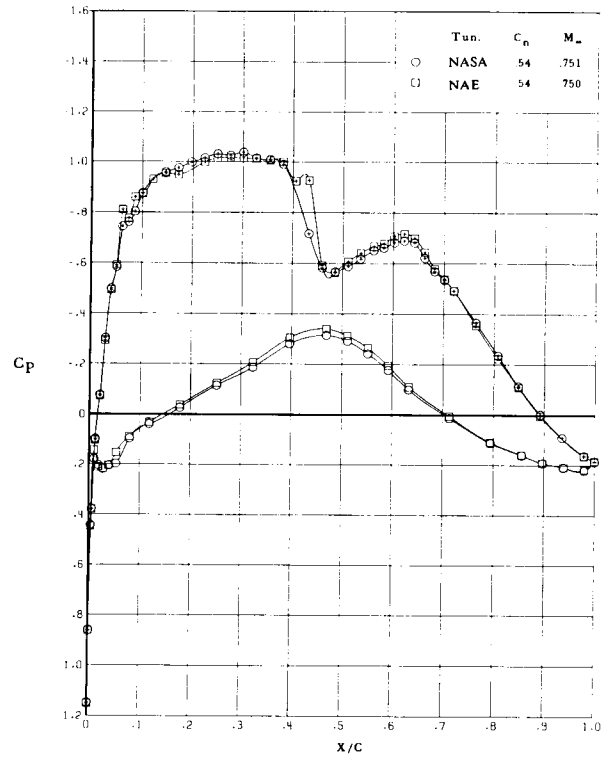

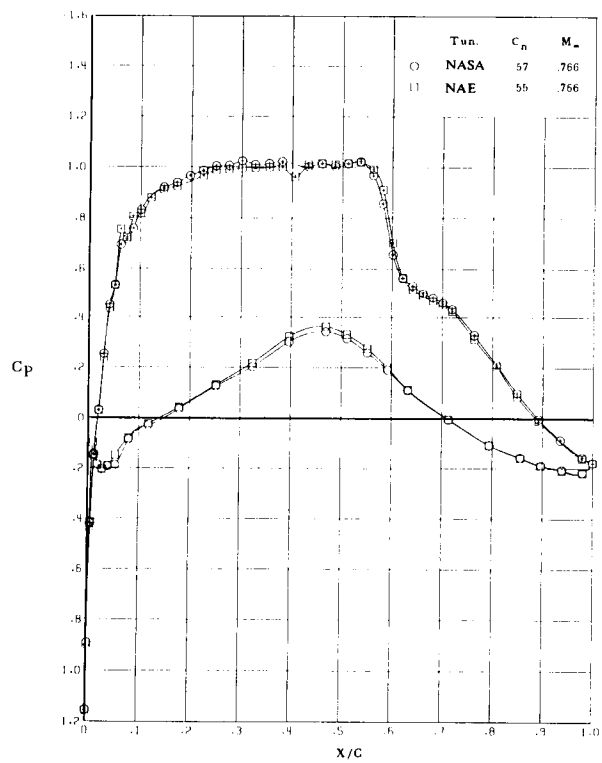

Figure 7. Comparison of the chordwise pressure distributions. $R_c = 10 \times 10^6$.

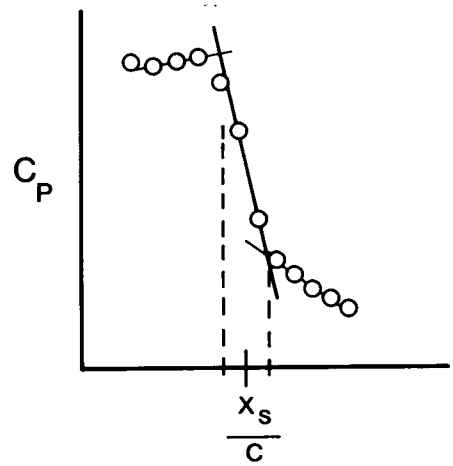

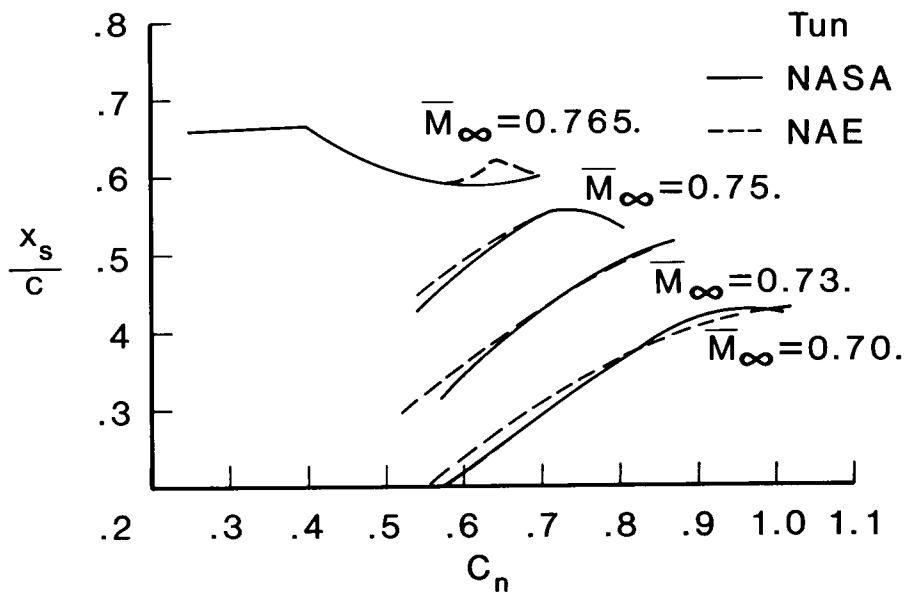

Figure 8. Comparison of the shock position. $R_c = 10 \times 10^6$.

ORIGINAL PAGE IS
OF POOR QUALITY

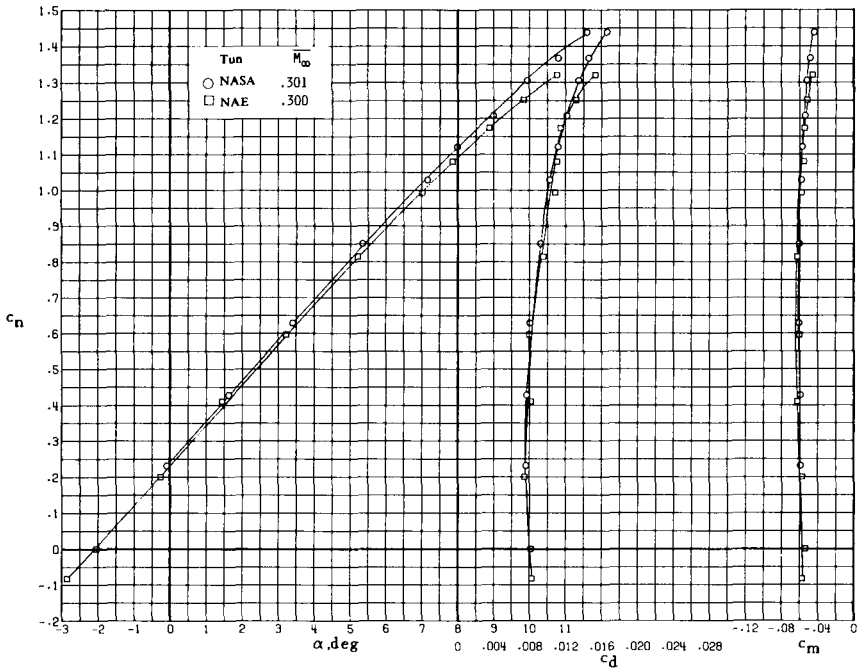

(a) $M_\infty = 0.30$.

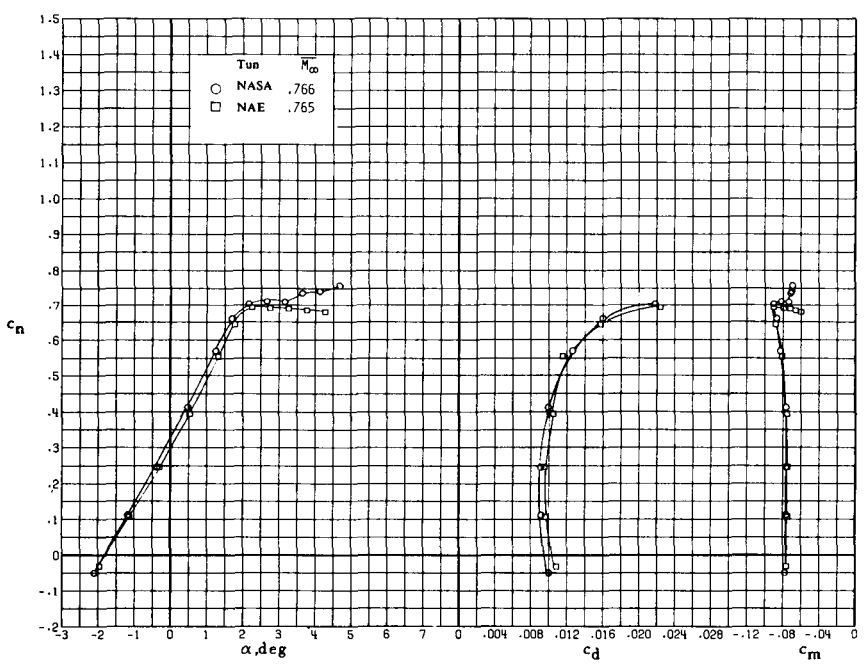

(b) $M_\infty = 0.765$.

Figure 9. Comparison of the integrated forces and moments. $R_c = 10 \times 10^6$.

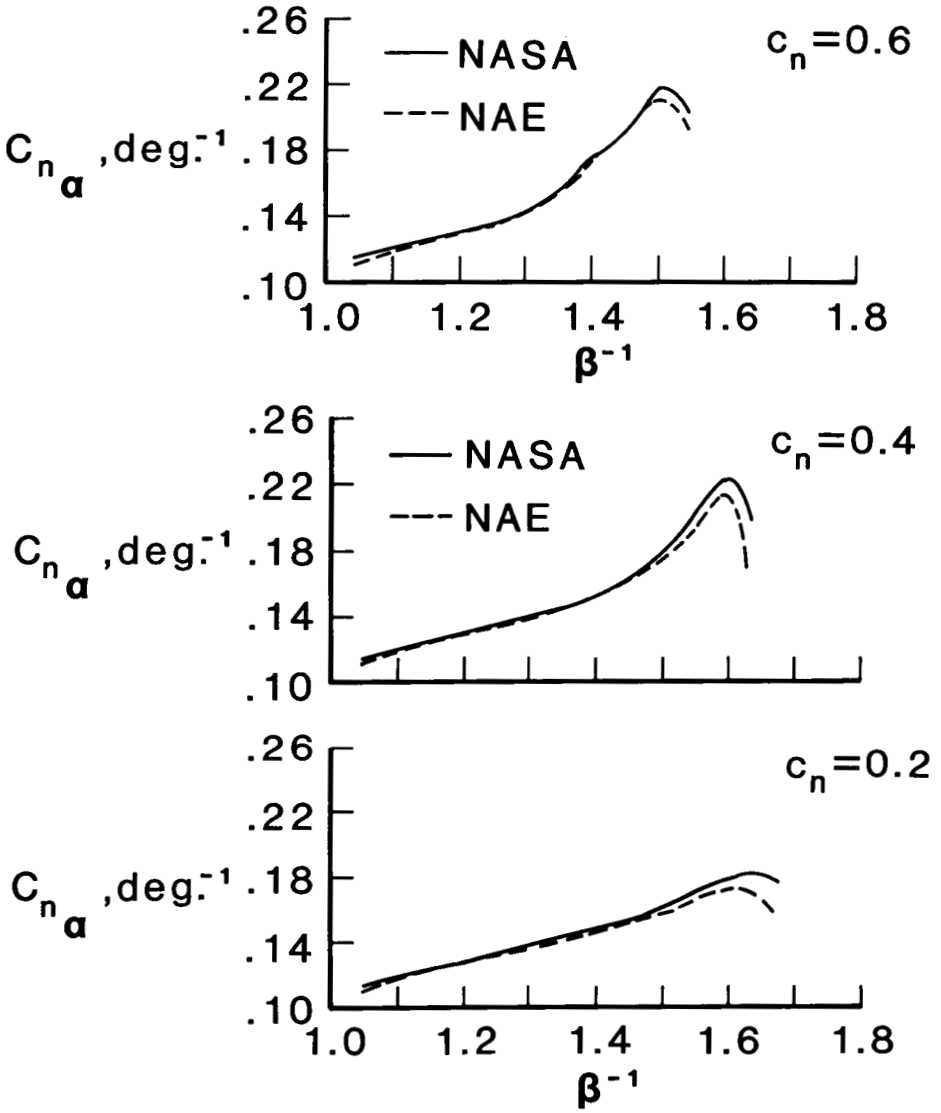

Figure 10. Comparison of the slopes of the normal force curves. $R_c = 10 \times 10^6$.

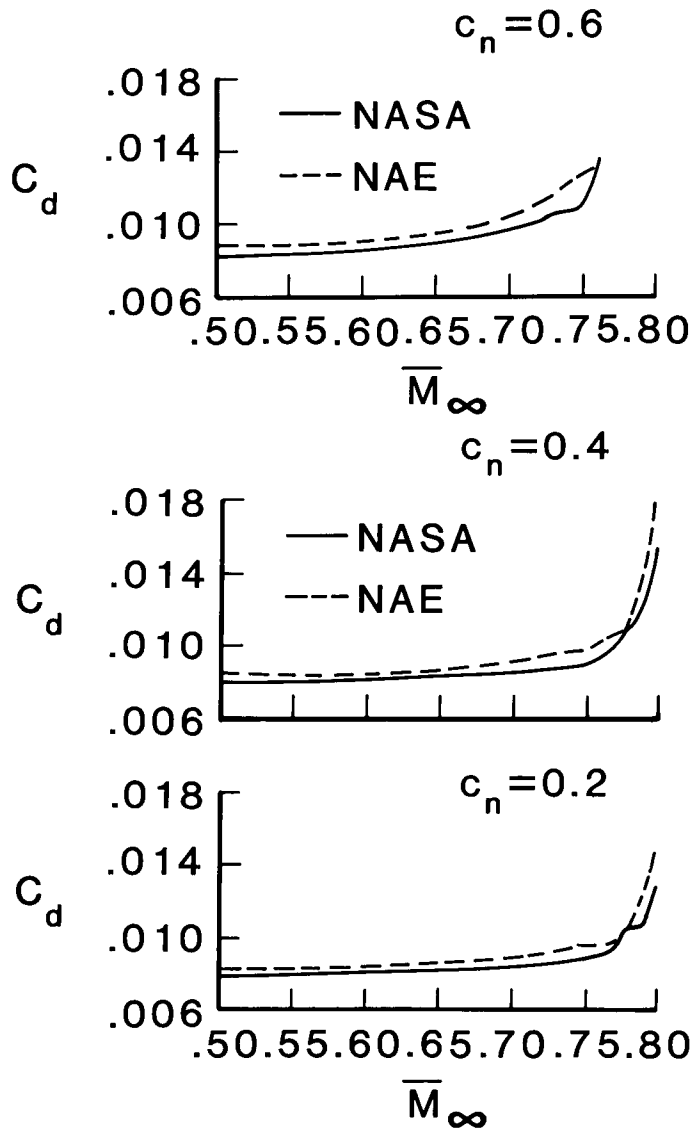

Figure 11. Comparison of the drag rise characteristics. $R_c = 10 \times 10^6$.

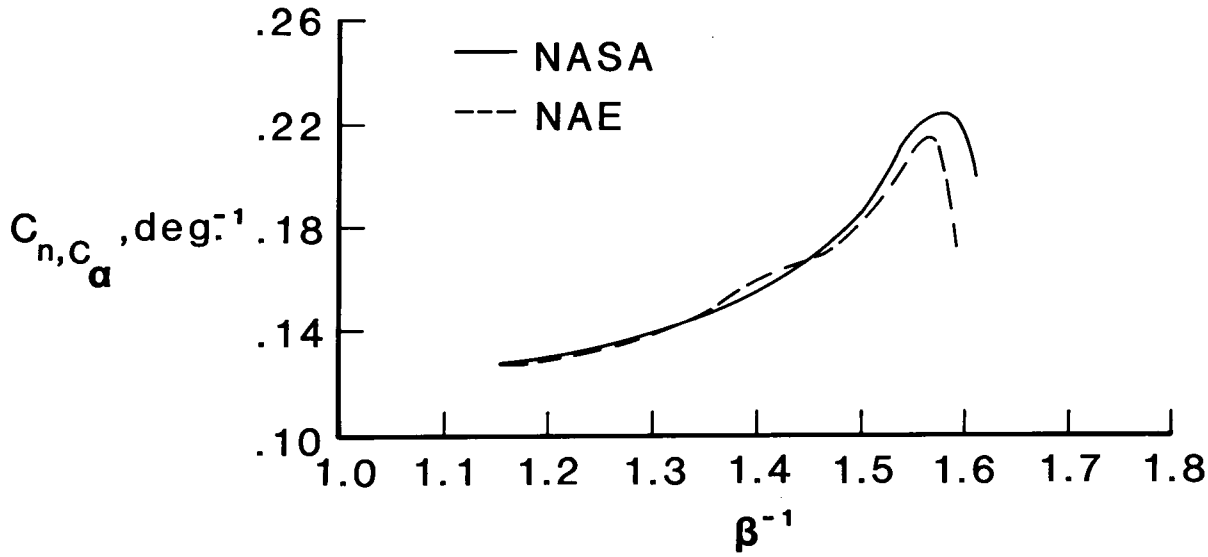

Figure 12. Comparison of slopes of the normal force curves corrected for sidewall interference with theory. $R_c = 10 \times 10^6$.

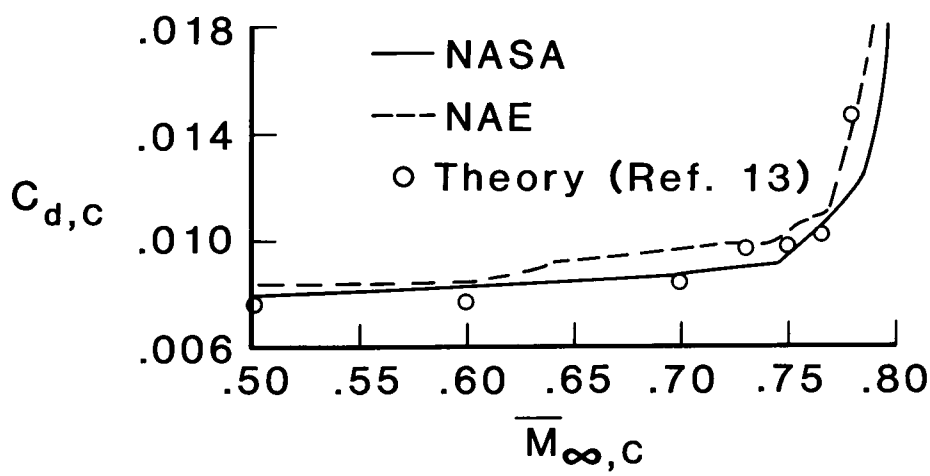

Figure 13. Comparison of the drag rise characteristics corrected for sidewall interference with theory. $R_c = 10 \times 10^6$.

N89-20961

CAPABILITIES OF WIND TUNNELS WITH TWO ADAPTIVE WALLS TO MINIMIZE BOUNDARY INTERFERENCE IN 3-D MODEL TESTING*

Rainer Rebstock and Edwin E. Lee, Jr.
Experimental Techniques Branch
NASA Langley Research Center
Hampton, VA

SUMMARY

An initial wind tunnel test was made to validate a new wall adaptation method for 3-D models in test sections with two adaptive walls. The model tested was an unswept semi-span wing. It was mounted on one sidewall of NASA's 0.3-m Transonic Cryogenic Tunnel, which is fitted with flexible top and bottom walls (semispan/tunnel height = 0.51). The vertical position of the wing in the test section could be changed to increase the wall interference. The experiments were conducted at freestream Mach numbers of 0.7, 0.8 and 0.85 and model angles-of-attack between 0 and 7°. Model forces and moments were measured with a five-component balance.

First part of the adaptation strategy is an on-line assessment of wall interference at the model position. The wall-induced blockage was very small at all test conditions. Noticeable lift interference occurred at higher angles of attack with the walls set aerodynamically straight. The induced upwash varied considerably in the chordwise as well as in the spanwise direction.

The adaptation of the top and bottom tunnel walls is aimed at achieving a correctable flow condition. The deflections are calculated to exactly eliminate the upwash gradient and the blockage velocity along one straight line in the test section. The location of this target line can be chosen with respect to the actual interference at the model.

The blockage was virtually zero throughout the wing planform after the wall adjustment. The upwash velocity was small and nearly constant in chordwise direction. However, a spanwise gradient remained, even after a second wall adaptation. The induced angle of attack at the mean aerodynamic chord of the wing was chosen as correction to the freestream velocity vector.

The lift curve measured with the walls adapted agreed very well with interference free-data for $M_\infty = 0.7$, regardless of the vertical position of the wing in the test section. However, noticeable discrepancies remained at $M_\infty = 0.85$ and high model angles of attack. This deviation was probably caused by an inaccurate wall interference assessment due to an insufficient number of pressure readings at the tunnel boundary.

The 2-D wall adaptation can significantly improve the correctability of 3-D model data. Nevertheless, residual spanwise variations of wall interference are inevitable. This may restrict the usable model span. Further tests with different configurations are needed to clarify this point.

---

*This work was done while the first author held a National Research Council - NASA Research Associateship

INTRODUCTION

Wall interference can be eliminated by adjusting the flow at the test section boundary. The idea is to provide a streamtube that is the same as in free-air.

This concept is relatively easy to apply in 2-D airfoil testing. Only the top and bottom walls of the test section need to be flexible or ventilated. The side walls can be solid. A practical algorithm for streamlining the walls was devised by Sears in 1973 (ref. 1). Effectively interference-free data have been obtained in these "2-D adaptive" test sections for both conventional and supercritical airfoils. References 2, 3, 4 and 5 provide more details.

The use of adaptive walls is less obvious for testing 3-D models. A simulation of free-air conditions requires active flow control along the whole test section boundary. The three facilities built so far therefore almost inevitably suffer from increased mechanical and operational complexity (refs. 3 and 4).

A simpler approach for transonic 3-D testing has been outlined by Kemp (ref. 6). His idea is to provide only the amount of wall control necessary to achieve a correctable flow condition. An on-line interference assessment method would be used to categorize the disturbances at the model as negligible, correctable or uncorrectable according to the required data accuracy.

The practical implications of this concept were independently studied by Harney and Wedemeyer. Harney shows experimentally that a 2-D wall adaptation has the potential to substantially reduce the interference velocities in the region of the tested model (ref. 7). In other words, a 2-D adaptive-wall test section may also be adequate for testing 3-D models.

Wedemeyer develops a wall adaptation technique for this purpose (ref. 8). Assuming linear potential flow, he calculates wall deflections that would lead to interference-free flow at the tunnel centerline. (The method is also applicable, in principle, if the top and bottom walls of the test section are ventilated rather than flexible.) The interference velocities (blockage and upwash) are deduced from the slope of the two flexible walls and their centerline pressure distributions. No explicit information about the tested model is needed.

A computer program of the adaptation method was developed in cooperation with Lamarche (refs. 9 and 10). Wind tunnel experiments at TU Berlin and ONERA/CERT demonstrated the soundness of this concept. References 3 and 10 contain a detailed analysis of the test results.

The Wedemeyer-Lamarche technique uses the same few wall pressure measurements as in airfoil testing. This makes it easy to apply, but seems to preclude an accurate interference assessment, at least in half-model tests. Consequently, no "figure-of-merit" has been defined (see ref. 4). The convergence of the wall adjustments is the only criterion to estimate the progress of the adaptation. This may lead to more iterations than necessary to achieve a correctable condition. Moreover, a separate method is needed to determine the residual interference at the model (ref. 11).

In this paper, an improved wall adaptation strategy for 3-D models in 2-D adaptive wind tunnels is described. Its essential features are:

(1) accurate on-line wall interference assessment based on flow measurements at the tunnel boundary ("two-variable method")
(2) elimination of wall interference at a user defined straight line in the test section
(3) evaluation of residual interference in terms of a Mach number and angle-of-attack correction

Initial validation tests have been performed with a semi-span wing in NASA Langley's 0.3-m TCT with flexible top and bottom walls. The model forces measured with the tunnel walls adapted are generally in good agreement with interference-free values.

ASSESSMENT OF WALL INTERFERENCE

Wall interference in the test section is deduced from the pressure distribution and the no-flux condition at the four test section walls (or equivalent measurements). A representation of the tested model is not required. Reference 12 provides a detailed description of the technique. The essential steps are as follows:

The disturbance velocities induced by the tunnel boundary are assumed to be small and irrotational. Their potential ϕ_W fulfills the linear differential equation

$$\beta^2\partial^2\phi_W/\partial X_P^2 + \partial^2\phi_W/\partial Y_P^2 + \partial^2\phi_W/\partial Z_P^2 = 0$$

$$\beta = (1-M_\infty^2)^{1/2} \tag{1}$$

throughout the test section as long as the flow around the model is dominantly subcritical.

We seek a solution of (1) in form of a source potential

$$\phi_W(P) = -1/4\pi\int_S \sigma_W(Q)g(P,Q)dQ$$

with

$$g(P,Q) = \{(X_P-X_Q)^2+\beta^2(Y_P-Y_Q)^2+\beta^2(Z_P-Z_Q)^2\}^{-1/2} \tag{2}$$

The sources $\sigma_W(Q)$ are distributed at a control surface S enclosing the model. We choose the cylindrical streamtube formed by the non-deflected test section walls.

Equation 2 represents the wall constraint as a source-sink distribution. The goal is to determine the local strength $\sigma_W(Q)$ from the flow condition at the tunnel boundary.

The measured wall pressures are first transformed into axial disturbance velocities u_I and the local wall slope into disturbance velocities v_I normal to the control surface S. The number of pressure measurements should be large enough to allow a precise interpolation both in streamwise and cross-stream direction (see APPARATUS).

The following analysis is a direct application of Sears' adaptive wall concept (refs. 1 and 4). The essential idea is to extend the experimental flow field in the

test section to infinity by adding a computed exterior flow. This fictitious flow satisfies the appropriate (farfield) differential equations and the condition of vanishing disturbances at infinity. One of the two measured distributions, say u_I, serves as inner boundary condition. If the flow field in the test section is interference-free, it matches perfectly with the computed outer flow at the control surface. In this case, the combined flow fields simply represent the unconfined flow around the model. The computed (v_E) and measured v-distributions (and all other flow variables) are the same at the control surface.

However, if a mismatch occurs, $v_E - v_I \neq 0$ at S, the experimental flow field is not consistent with the farfield boundary conditions. Indeed, the discontinuity in the v-component completely defines the wall interference in the test section. We can see this as follows:

For subsonic freestream Mach numbers, the flow in the farfield fulfills the linearized potential equation (1). The exterior flow field computation thus becomes a Dirichlet problem for the infinite region beyond the tunnel boundary. We can construct the solution in terms of a source-sink distribution at the control surface. The resulting surface integral is similar to equation (2), but the field point P now lies in the exterior region. The potential generated within the test section has no physical significance.

$$\phi_E(P) = -1/4\pi \int_S \sigma_E(Q) g(P,Q) dQ \qquad (3)$$

The unknown singularity strength σ_E is uniquely defined by the inner boundary condition. In fact, streamwise integration of the prescribed u_I-distribution determines the potential at the control surface

$$\phi_E(P) = \int_{-\infty}^{X_P} u_I(T, Y_P, Z_P) dT \quad , \quad P \in S \qquad (4)$$

The integration upstream of the test section can usually be ignored in practice. However, an extrapolation of u_I in downstream direction is often required.

A combination of (3) and (4) leads to an integral equation of the first kind for σ_E. We can solve it by approximating the surface integral with a suitable quadrature formula.

Differentiation of the solution in normal direction finally yields the desired outer v-component v_E at S

$$v_E(P) = \partial\phi_E/\partial n_E(P) \quad , \quad P \in S \qquad (5)$$

If a jump in the normal velocity occurs, $v_E - v_I \neq 0$ at S, the experimental flow field is not interference-free. However, this discontinuity can be removed by putting sources and sinks at the control surface that exactly compensate the local flux imbalance. The required singularity strength is given by Gauss' flux theorem as

$$\sigma(P) = v_I(P) - v_E(P) \qquad (6)$$

The added singularities modify both the flow field in the test section and the computed exterior flow. The resulting flow field is continuous at the control surface and still fulfills the boundary condition of vanishing disturbances at

infinity. In other words, the modified flow field is interference-free. The source layer $\sigma(P)$ generates velocity perturbations within the test section that exactly cancel the wall interference.

Consequently, the singularity distribution that represents the tunnel walls is given by

$$\sigma_W(P) = - \sigma(P) = v_E(P) - v_I(P) \tag{7}$$

Insertion of (7) into (2) defines the wall interference potential everywhere in the test section. The wall-induced velocities follow by differentiation.

CALCULATION OF ADAPTED WALL SHAPES

A deflection of the top and bottom walls of the test section changes the blockage and upwash interference experienced by the model. The perturbations caused by small contour changes are governed by the linear potential equation

$$\beta^2\phi_{XX} + \phi_{ZZ} = 0 \tag{8}$$

The cross-stream component is zero, since the wall deflections are constant across the tunnel width.

The existence of a flow potential allows us to calculate the induced velocities

$$\begin{aligned} u(X,Z) &= \phi_X(X,Z) \\ w(X,Z) &= \phi_Z(X,Z) \end{aligned} \tag{9}$$

everywhere in the test section.

An adjustment of the wall contours is, of course, aimed at minimizing the wall interference in the region of the tested model. The blockage and upwash velocities for the given wall shape are known from the wall interference potential (equation 2)

$$\begin{aligned} u_W(P) &= \partial\phi_W(P)/\partial X_P \\ w_W(P) &= \partial\phi_W(P)/\partial Z_P \end{aligned} \tag{10}$$

We disregard the cross-stream component since it cannot be reduced by a 2-D wall adaptation.

The physical condition for the wall adaptation therefore reads

$$\begin{aligned} (u + u_W)_{Model} &= Min \\ (w + w_W)_{Model} &= Min \end{aligned} \tag{11}$$

As we can see, the determination of the required deflections is an <u>inverse</u> problem. We need to simplify it in order to find a solution. A reasonable compromise is as follows:

We pick the vertical plane $Y = Y_0$ in the test section where the wall interference is worst. Within this plane we define a straight target line Z_0 = const. that passes through the model region.

An easy-to-impose boundary condition for the wall adaptation is

$$\begin{aligned} u(X,Z_0) + u_W(X,Y_0,Z_0) &= 0 \\ w(X,Z_0) + w_W(X,Y_0,Z_0) &= 0 \end{aligned} \tag{12}$$

In other words, it is feasible to exactly cancel the blockage and upwash interference along the target line. (However, it is often more practical to just eliminate the upwash-gradient and include the remaining constant value in the angle-of-attack correction. See RESULTS AND DISCUSSION.) The residual interference in the model region can be accounted for as corrections to the freestream velocity vector.

To find the desired deflections Δh_u (upper wall) and Δh_l (lower wall), we take advantage of the linearity of the potential equation (8). Basically, we expand Δh_u and Δh_l in Fourier series, calculate the induced disturbance velocities, and then determine the unknown series coefficients by imposing the boundary condition (12):

$$\Delta h_l(X) = a_0 X + \sum_{n=1}^{\infty} a_n \sin(\lambda_n X)$$

$$\Delta h_u(X) = c_0 X + \sum_{n=1}^{\infty} c_n \sin(\lambda_n X) \tag{13}$$

$$\lambda_n = n\pi/L, \ L = \text{test section length}$$

The linear divergence terms are added to allow non-zero deflections at the test section end (allowance for model wake).

The calculation of the induced disturbance velocities is easier in terms of the stream function ψ rather than the potential ϕ. The two functions are related through the (Cauchy-Riemann) differential equations

$$\psi_\xi = -\phi'_\eta \ , \ \psi_\eta = \phi'_\xi \tag{14}$$

where $\phi'(\xi,\eta)$ denotes the incompressible potential obtained from the Prandtl-Glauert transformation

$$X = \xi \ , \ Z = \eta/\beta \ , \ \phi(X,Z) = \phi'(\xi,\eta)/\beta \tag{15}$$

The boundary-value problem for the stream function follows from (13), (14) and (15) as

$$\begin{aligned} \psi_{\xi\xi} + \psi_{\eta\eta} &= 0 \\ \psi(\xi,-\beta H/2) &= -\Delta h_l(\xi) \ , \ 0 \le \xi \le L \\ \psi(\xi,\beta H/2) &= -\Delta h_u(\xi) \ , \ 0 \le \xi \le L \end{aligned} \tag{16}$$

$$(H = \text{test section height})$$

The solution consists of two parts

$$\psi(\xi,\eta) = \psi_1(\xi,\eta) + \psi_2(\xi,\eta)$$

$$\psi_1(\xi,\eta) = -\{(a_0+c_0)/2 + (c_0-a_0)\eta/\beta H\}\xi \tag{17}$$

$$\psi_2(\xi,\eta) = \sum_{n=1}^{\infty}\{a_n\sinh[\lambda_n(\eta-\beta H/2)] - c_n\sinh[\lambda_n(\eta+\beta H/2)]\}\ \sin(\lambda_n\xi)/\sinh(\lambda_n\beta H)$$

ψ_1 represents the disturbances caused by a linear divergence of the top and bottom walls. The Fourier solution ψ_2 can be derived by a separation of the independent variables. Ref. 13 describes this technique in detail.

The velocities induced at the target line Z_0 = const., result from (9), (14) and (15)

$$u(X,Z_0) = \psi_\eta(\xi,\beta Z_0)/\beta$$

$$w(X,Z_0) = -\psi_\xi(\xi,\beta Z_0) \tag{18}$$

We develop the upwash and blockage interference at the target line into Fourier series compatible with (18)

$$u_W(X) = u_W(L)X/L + \sum_{n=1}^{\infty} r_n\sin(\lambda_n X)$$

$$w_W(X) = s_0/2 + \sum_{n=1}^{\infty} s_n\cos(\lambda_n X) \tag{19}$$

with the coefficients

$$r_n = 2/L \int_0^L \{u_W(X)-u_W(L)X/L\}\ \sin(\lambda_n X)dX\ ,\ n=1,2,...$$

$$s_n = 2/L \int_0^L w_W(X)\cos(\lambda_n X)dX\ ,\ n=0,1,... \tag{20}$$

Imposition of the boundary condition (12) finally leads (after some straightforward calculations) to the following expressions for the series coefficients in (13)

$$a_0 = -s_0/2 - \beta^2 u_W(L)(H+2Z_0)/2L$$

$$a_n = -1/\lambda_n\ \{\beta r_n\sinh[\lambda_n\beta(Z_0+H/2)] + s_n\cosh[\lambda_n\beta(Z_0+H/2)]\}$$

$$c_0 = -s_0/2 + \beta^2 u_W(L)(H-2Z_0)/2L \tag{21}$$

$$c_n = -1/\lambda_n\ \{\beta r_n\sinh[\lambda_n\beta(Z_0-H/2)] + s_n\cosh[\lambda_n\beta(Z_0-H/2)]\}$$

As we can see, the determination of the adapted wall shape involves three steps. First, computation of the Fourier coefficients r_n and s_n (eq. 20). Since the blockage and upwash velocities are very smooth, both sets of coefficients rapidly go

to zero with increasing frequency n. Typically, the lowest 8 to 12 frequencies provide enough resolution. We pick $N = 16$ ($= 2^4$) in order to apply the very efficient FFT-method. This requires an even distribution of the input values $u_W(X_i)$ and $w_W(X_i)$, $i=1,\ldots,N$ along the target line. Reference 14 provides more details on FFT and contains a suitable computer program. The subsequent evaluation of the algebraic equations (21) is straightforward. The coefficients a_n and c_n, $n=0,\ldots,N-1$ determine the wall deflections (eq. 13). We can compute the finite sums (inverse Fourier transform) with the same FFT computer program as in step 1. All three steps combined require very little execution time, even on a small computer.

APPARATUS

We conducted the experiment in NASA Langley's 0.3-M Transonic Cryogenic Tunnel. An adaptive test section with flexible top and bottom walls was installed in the tunnel circuit in 1985. It is nominally 33cm (13 inches) square and has an effective length of 1.42m (55.8 inches). Reference 5 describes the facility in more detail.

The model was a scaled-up (1.6 times) replica of a semi-span wing tested at Langley Research Center in 1951 (ref. 15). It was selected for the experiment because of the essentially free-air data available from this test. We measured the forces and moments on the model with a five-component strain gauge balance. Figure 1 shows the apparatus in detail, including the model turntable, which was installed in the right sidewall of the test section. We could mount the wing at two vertical positions; the tunnel centerline and halfway between the center and the top wall. Figure 2 shows the wing in the center position.

The blockage ratio of the model in the TCT adaptive wall test section was 0.79% and the semi-span to tunnel width ratio was 0.51. Table 1 provides more information about the wing geometry and summarizes the test conditions. As in the early Langley test, all experiments were performed without a boundary-layer trip.

Recording of the static pressure distribution at the tunnel walls provided some difficulty. The test section was only equipped with pressure orifices at the centerline of the top- and bottom walls, which is adequate for airfoil testing. On the other hand, three rows of orifices above and below the model and one row at one sidewall are typically required for an accurate wall interference assessment in 3-D flows (ref. 16).

However, it was too time-consuming to add orifices on the flexible walls. Instead, we installed two rows at the right sidewall of the test section, as close to the flex walls as possible. The orifices drilled in the model turntable show the exact location of the two rows (see figure 1). Their displacement for non-zero angle-of-attack was ignored in the wall interference computations. The opposite sidewall was equipped with 14 pressure taps, concentrated in the model region.

The inaccurate representation of the wall pressure distribution is probably responsible for the noticeable residual interference at higher Mach numbers and angles-of-attack (see RESULTS AND DISCUSSION).

RESULTS AND DISCUSSION

In the following, we will illustrate the wall adaptation procedure for the typical flow case $M_\infty = 0.7$ and $\alpha = 7°$. The wing is in the high position, 3.25 inches above the tunnel centerline. A flow chart of the algorithm is presented in figure 3.

The first step is an assessment of the wall interference at the model position. Figures 4,5 and 6 show the induced Mach number and angle of attack at three spanwise locations with the tunnel walls set to aerodynamically straight. The blockage interference is small and constant at the wing planform. However, the induced upwash varies considerably, in chordwise as well as in spanwise direction. At the wing root, for example, $\Delta\alpha$ increases from 0.3° at the leading edge to 1.7° at the trailing edge. A similar behavior occurs at the location of the mean aerodynamic chord (figure 5) and the wing tip (figure 6).

Figure 7 summarizes the wall interference experienced by the model. This plot appears on the control monitor of the wind tunnel computer during the test. It indicates the progress of the adaptation and helps the researcher to position the target line for the wall shape calculation (equation 12). The calculated Mach number increment ΔM at each spanwise location simply is an average value across the respective chord. The lift interference across the span is represented by the induced <u>absolute</u> angle-of-attack (ref. 17):

$$\Delta\alpha_{abs}(Y) = -1/\pi \int_0^\pi \partial\phi_W/\partial Z(\Theta,Y,Z_0)(\cos\Theta-1)d\Theta \qquad (22)$$

In this way, the induced camber at each spanwise section is properly taken into account.

Interference is highest at the wing root and we position the target line accordingly. The wall interference assessment method then calculates the blockage and upwash along this line. In other words, the previously computed interference velocities at the selected wing location are extended upstream and downstream.

The next step is to determine improved wall shapes. It is possible to completely eliminate the blockage and lift interference at the target line. The necessary deflections are calculated in eq. (21). However, the required constant downward wall slope downstream of the model may result in jack movements beyond the 2-D design limits. It is therefore more practical to eliminate the upwash <u>gradient</u>. We simply achieve this by setting $s_0 = 0$ in (21), that is by ignoring the constant part in the induced upwash distribution. The resulting wall shape appears to be rotated about the anchor points compared with the 'fully' adapted contours. Figure 8 shows this schematically.

Figure 9 presents the actual wall contours after the first iteration. The largest deflection of about 0.65 inches occurs in the region of the model. These rather small displacements are quite feasible in a 2-D adaptive test section. For example, the 0.3-m adaptive wall test section allows a maximum jack movement of 3 inches upward and 1 inch downward.

The residual interference after the wall adjustment is shown in figure 10 for the wing root. The induced angle of attack is virtually constant across the chord, as expected. The remaining Mach number deviation is beyond measurement accuracy.

The upwash and blockage interference at the other spanwise locations is, of course, simultaneously reduced. Figure 11 summarizes the results.

However, the induced angle of attack still varies across the wing span. This residual spanwise gradient is an inevitable limitation of a 2-D wall adjustment (deflections constant across the tunnel width). In practise, we may need to reduce the span of the tested model to achieve the required accuracy. However, conclusions are difficult to draw at this point. The model aspect ratio will undoubtedly play an important role. Numerical simulations done by Smith provide some insight into this problem (ref. 18).

The remaining wall interference had no significant effect on the measured model data in this test. We can see this on figure 12 for $M_\infty = 0.7$ and the wing in the high position. The model lift measured with the flexible walls set to aerodynamically straight (fig. 9) is larger than the 7x10 (interference-free) values. However, a linear correction based on the induced angle-of-attack at the mean aerodynamic chord of the wing ($2y/b = 0.42$, see figure 7) is generally sufficient in this case. Only for the highest angle of attack, do we actually need to deflect the walls to achieve correctability. As expected, a second wall adjustment has little effect on the model measurements.

Figure 13 shows a similar comparison for the wing in the center position. Again, the model lift in the adapted test section agrees well with the interference-free data throughout the whole angle-of-attack range.

However, noticeable discrepancies remained for $M_\infty = 0.85$. Figure 14 presents the results obtained with the wing centered. Adapting the walls reduces the wing lift as it should, but not to the extent necessary to simulate free-air conditions. This defect may be partly caused by a Reynolds number mismatch ($Re = 1.5 \times 10^6$ compared with 0.73×10^6 in the 7x10 test, ref. 15). Another contributing factor undoubtedly was the inaccurate interference assessment due to an insufficient number of wall pressure orifices.

CONCLUDING REMARKS

Although a 2-D adaptive-wall test section cannot precisely simulate interference-free flow around a 3-D model, it can improve the correctability of the test data to a considerable extent. However, some residual spanwise variation of wall interference is inevitable. The required wall deflections are feasible within 2-D design limits.

ACKNOWLEDGMENT

The authors wish to thank the adaptive wall research team, headed by Edward J. Ray, for the outstanding support of the research project.

REFERENCES

1. Sears, W. R.: Self-Correcting Wind Tunnels. Calspan Report No. RK-5070-A-2, July 1973. Also: Aeronautical Journal, Vol 78, 1974.

2. Tuttle, M. H. , Mineck, R. E.: Adaptive Wall Wind Tunnels - A Selected, Annotated Bibliography. NASA TM 87639, August 1986.

3. Ganzer, U.: A Review of Adaptive Wall Wind Tunnels. Prog. Aerospace Sci., Vol. 22, pp. 81-111, 1985.

4. Sears, W. R. , Erickson, J. C.: Adaptive Wind Tunnels. Ann. Rev. Fluid Mech., Vol. 20, 1988.

5. Wolf, S. W. D, Ray, E. J.: Highlights of Experience with a Flexible Walled Test Section in the NASA Langley 0.3-Meter Transonic Cryogenic Tunnel. Paper 88-2036, presented at AIAA 15th Aerodynamic Testing Conference in San Diego, May 18-20, 1988.

6. Kemp, W. B.: Toward the Correctable-Interference Transonic Wind Tunnel. Paper presented at AIAA 9th Aerodynamic Testing Conference in Arlington, Texas, June 7-9, 1976.

7. Harney, D. J.: Three-Dimensional Testing in a Flexible-Wall Wind Tunnel. AIAA-Paper 84-0623.

8. Wedemeyer, E.: Wind Tunnel Testing of Three-Dimensional Models in Wind Tunnels with Two Adaptive Walls, VKI Preprint 1982-36, Sept. 1982.

9. Lamarche, L., Wedemeyer, E.: Two-dimensional Wall Adaptation for Three-dimensional Flows, VKI Preprint 1984-34, Sept. 1984.

10 Lamarche, L.: Reduction of Wall Interference for Three-dimensional Models with Two-dimensional Wall Adaptation. Ph.D. Thesis, University of Brussels, Dec. 1986.

11. Archambaud, J. P., Mignosi, A.: Two-Dimensional and Three-Dimensional Adaptation at the T2 Transonic Wind Tunnel of ONERA/CERT. Paper presented at AIAA 15th Aerodynamic Testing Conference in San Diego, May 18-20, 1988.

12. Rebstock, R.: Procedures for Computing Transonic Flows for Control of Adaptive Wind Tunnels. NASA TM-88530, Jan. 1987.

13. Powers, D. L.: Boundary Value Problems. Academic Press, New York 1972.

14. Press, W. H., Flannery, B. P., Teukolsky, S. A., Vetterling, W. T.: Numerical Recipes. Cambridge University Press 1986

15. Sleeman, W. C. Jr., Klevatt, P. L., Linsley, E. L.: Comparison of Transonic Characteristics of Lifting Wings from Experiments in a Small Slotted Tunnel and the Langley High-Speed 7- by 10- Foot Tunnel. NACA RM L51F14, 1951.

16. Mokry, M.: Subsonic Wall Interference Corrections for Half-Model Tests Using Sparse Wall Pressure Data. NAE Aeronautical Report LR-616, Nov. 1985.

17. Kuethe, A. M., Chow, C.: Foundations of Aerodynamics. Fourth Edition, John Wiley & Sons, 1986.

18. Smith, J.: A Theoretical Exploration of the Capabilities of 2-D Flexible Wall Test Sections for 3-D Testing. NLR Rep. MP 84018 U, Feb. 1984.

TABLE 1. Three-Dimensional Semispan Adaptation Test

- **Unswept wing model**

Aspect ratio	4.0
Taper ratio	0.6
Airfoil section	NACA 65A006
Semispan/width	0.51
Reference data	LRC 7' x 10' tunnel - 1951

- **Test conditions**

Mach number	0.7 - 0.85
Angle of attack	0° to 7°

- **Test configurations** — Wing centered and high

- **Measurements** — Model forces; wall pressures and deflections

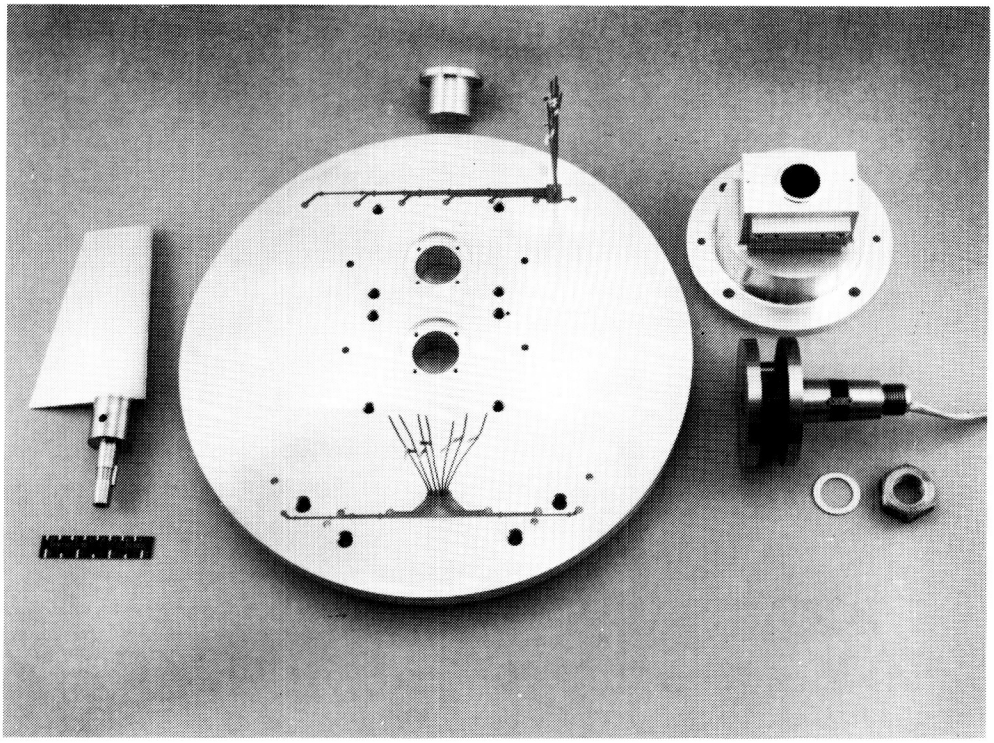

Figure 1. Semispan force-model apparatus.

ORIGINAL PAGE
BLACK AND WHITE PHOTOGRAPH

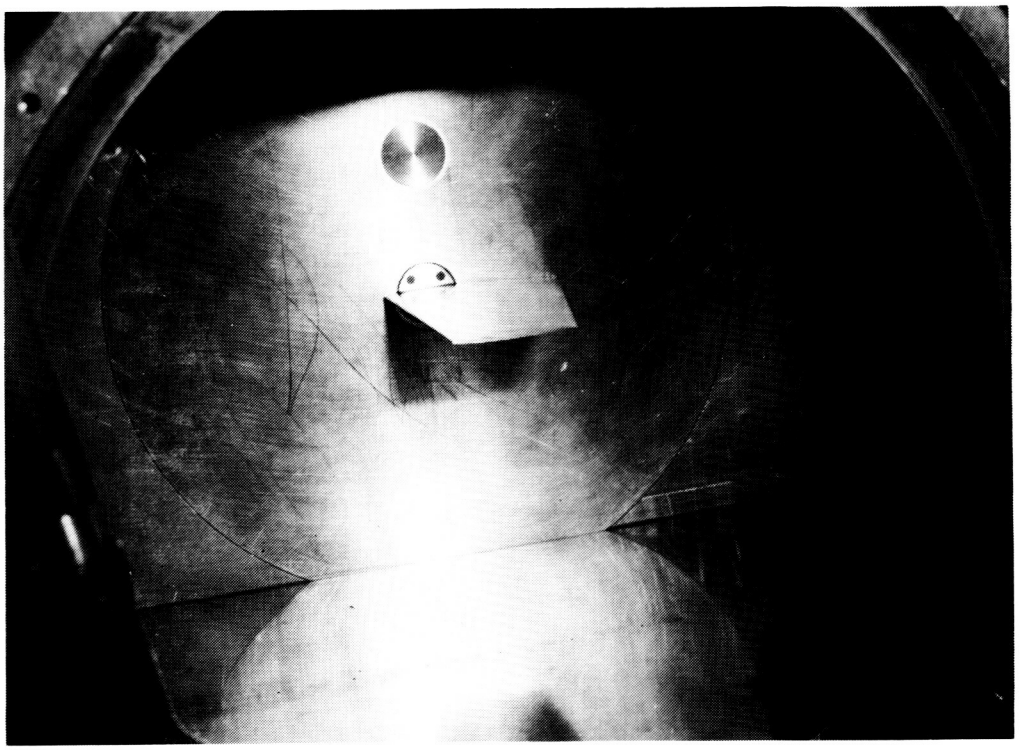

Figure 2. Model installed in Langley 0.3-m Transonic Cryogenic Tunnel.

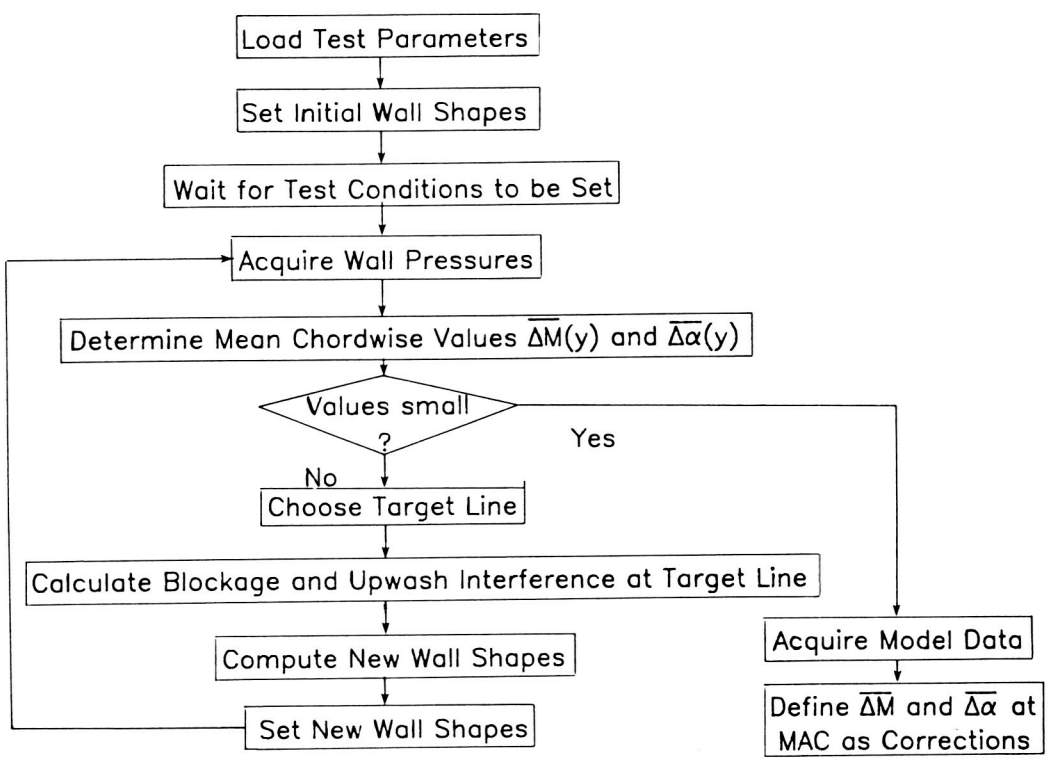

Figure 3. Wall adaptation flow chart.

ORIGINAL PAGE
BLACK AND WHITE PHOTOGRAPH

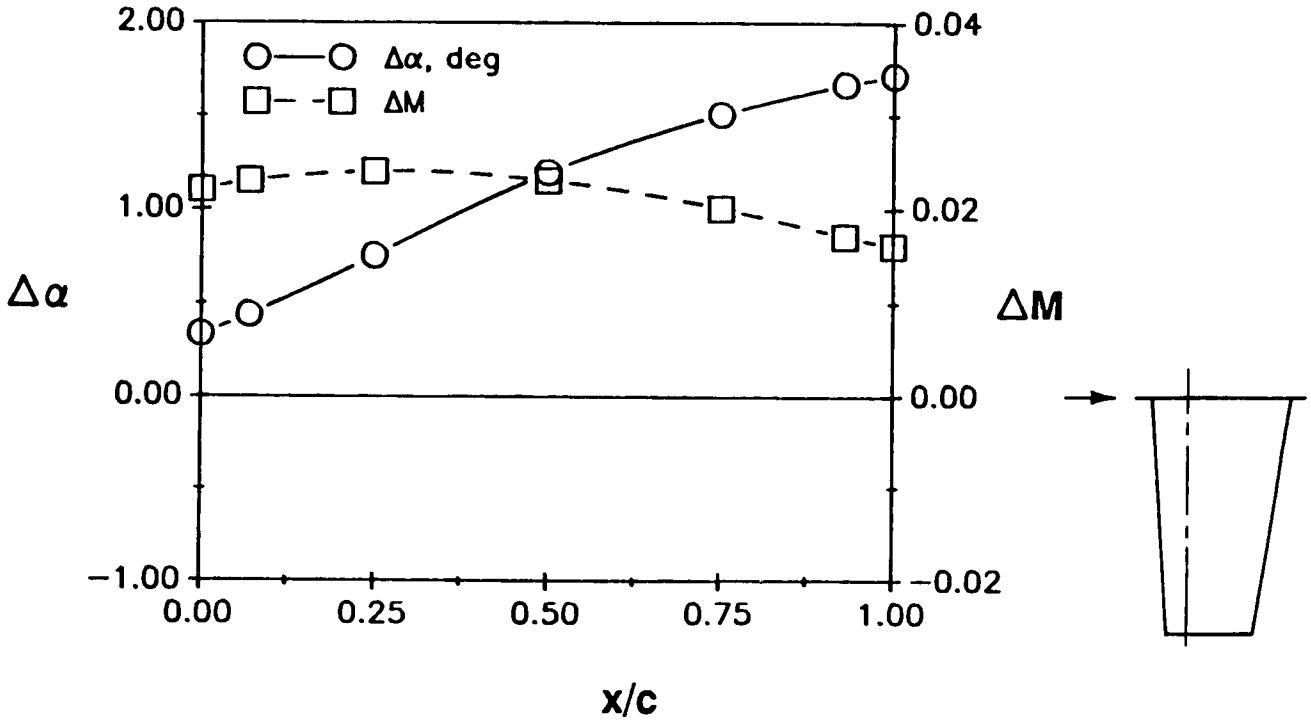

Figure 4. Chordwise variation of wall interference, walls straight, $M_\infty = 0.7$, $\alpha = 7^\circ$, wing high.

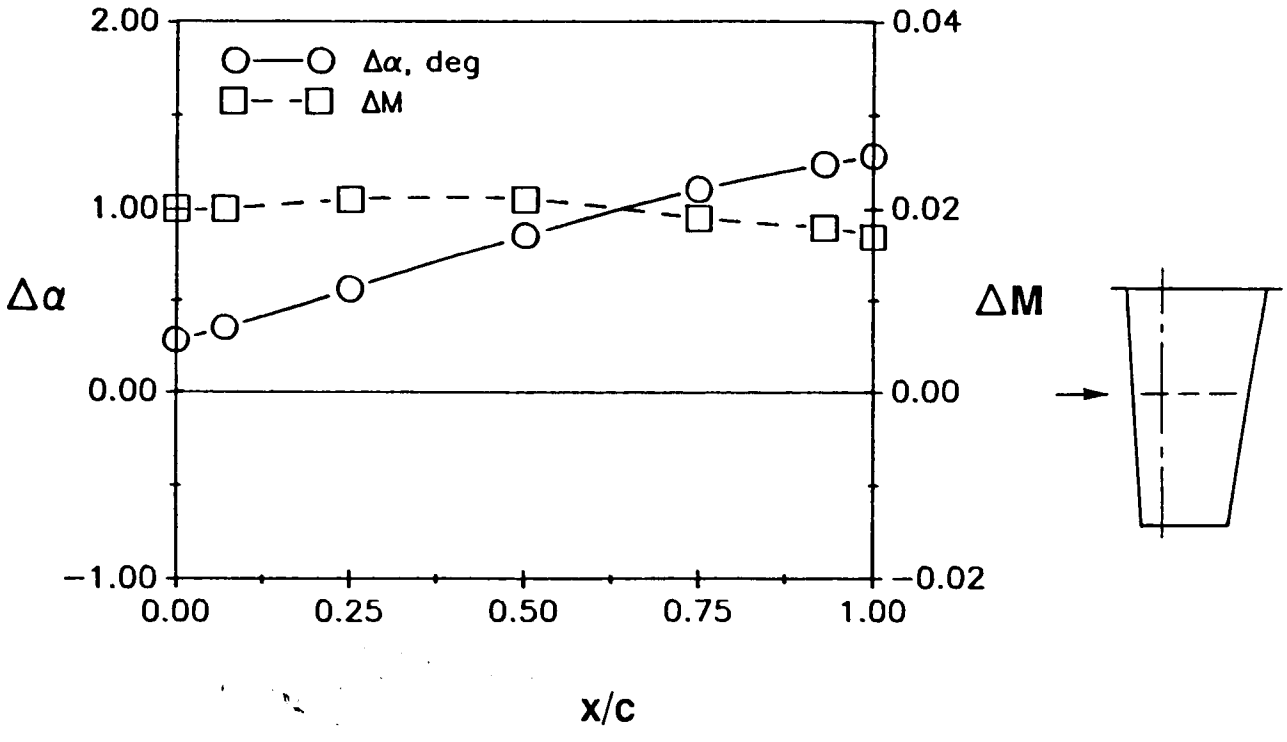

Figure 5. Chordwise variation of wall interference, walls straight, $M_\infty = 0.7$, $\alpha = 7^\circ$, wing high.

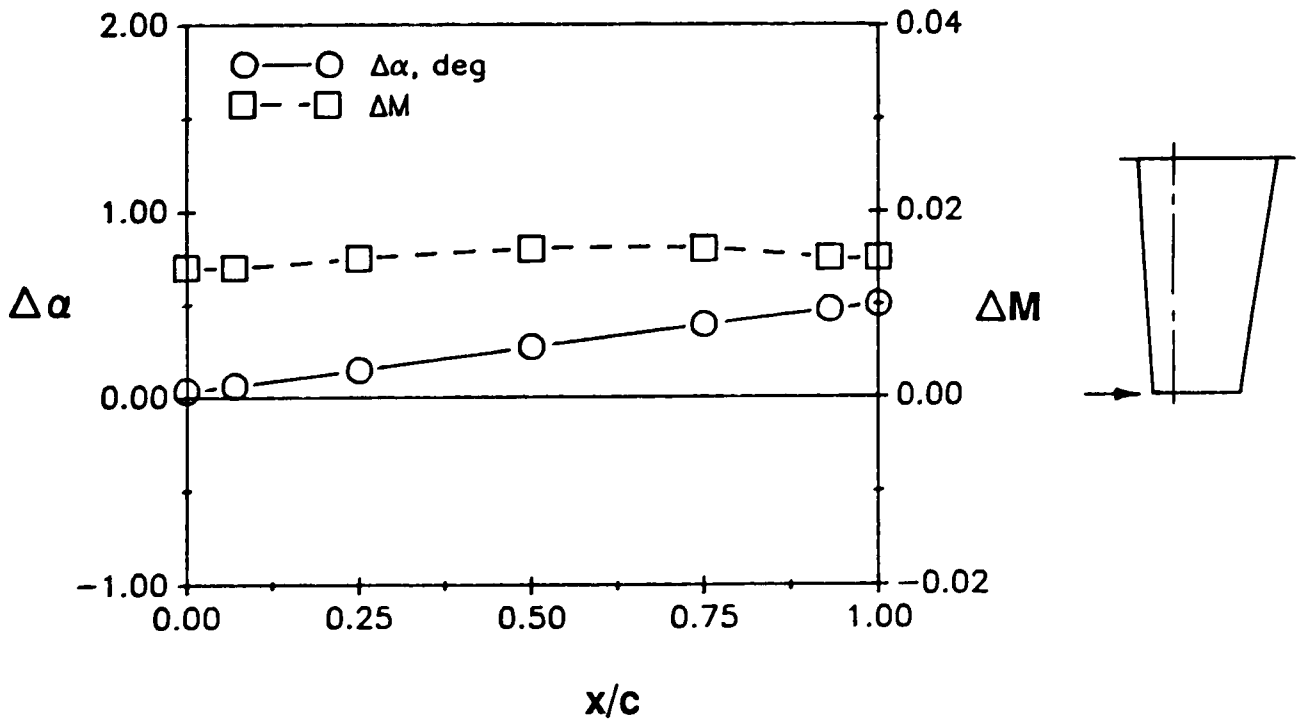

Figure 6. Chordwise variation of wall interference, walls straight, $M_\infty = 0.7$, $\alpha = 7^\circ$, wing high.

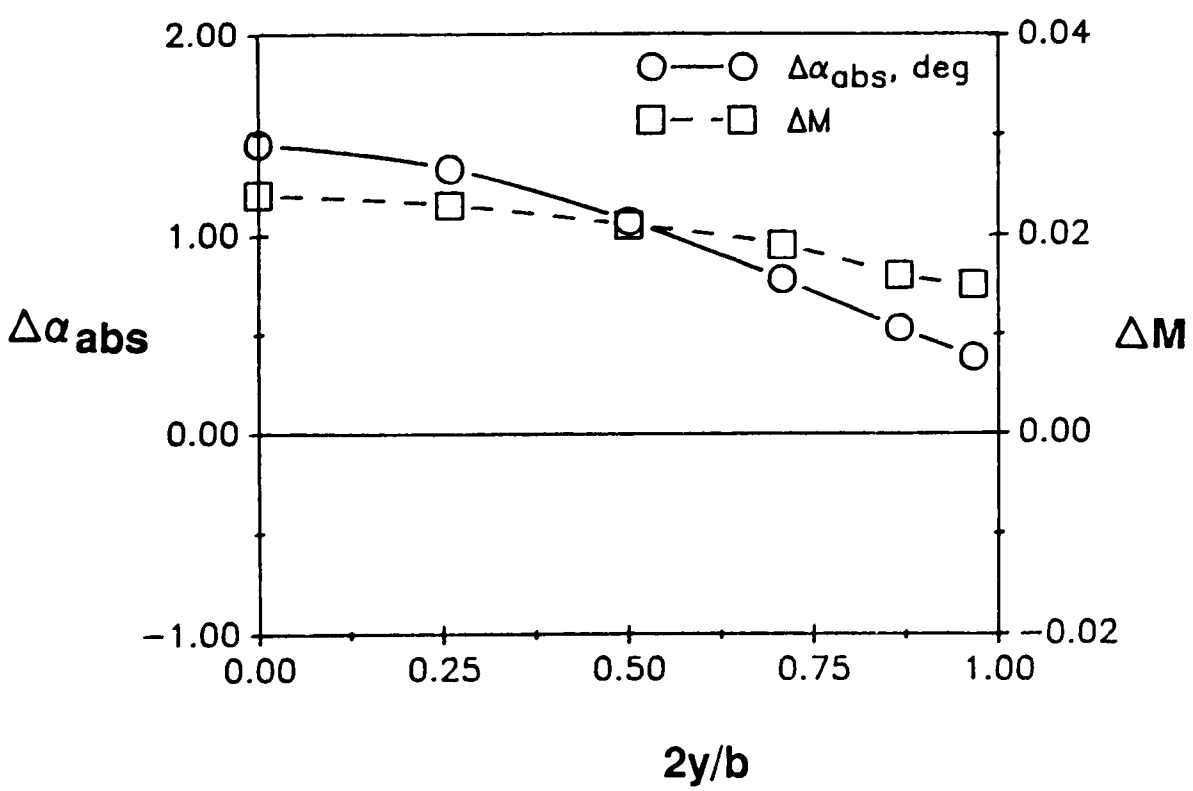

Figure 7. Summary of wall interference along the wing span, walls straight, $M_\infty = 0.7$, $\alpha = 7^\circ$, wing high.

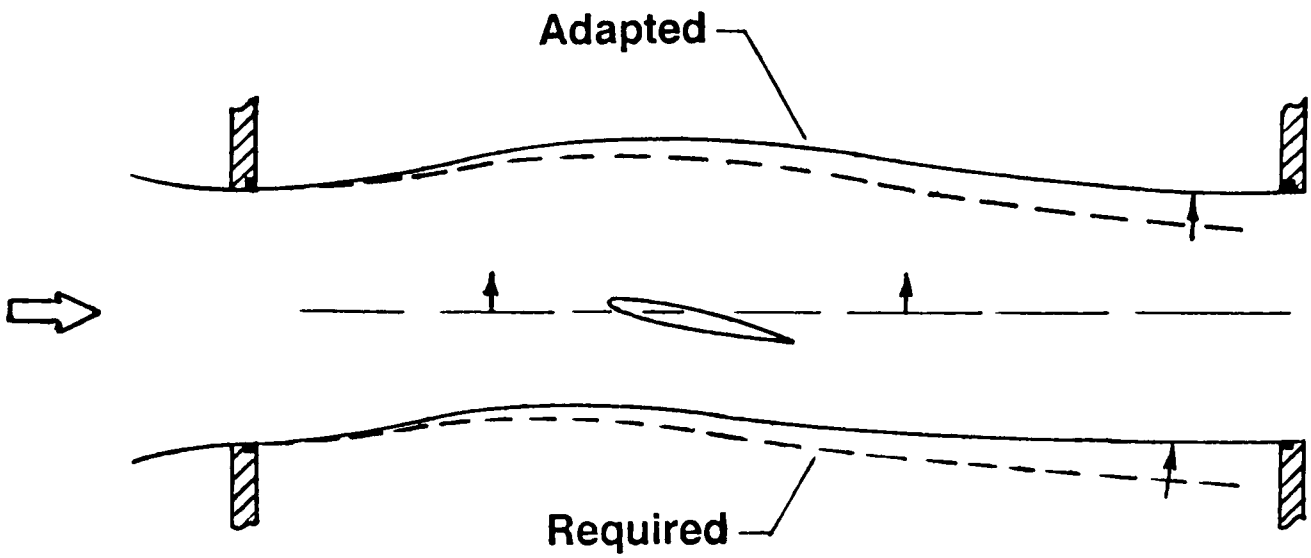

Figure 8. Flow field rotation.

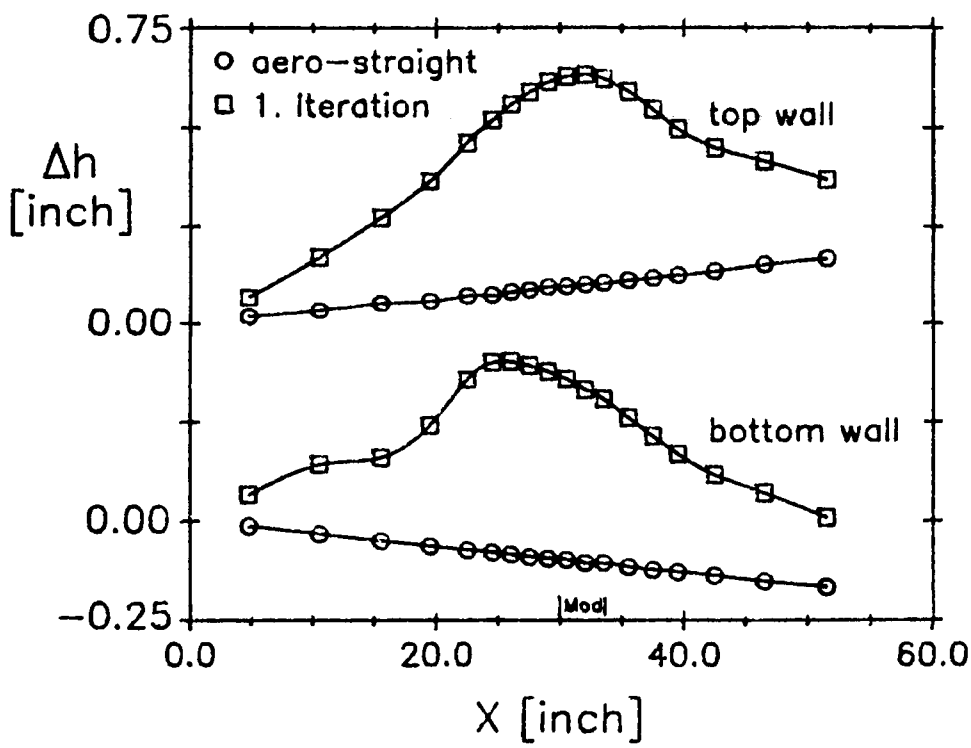

Figure 9. Wall deflections, $M_\infty = 0.7$, $\alpha = 7^o$, wing high.

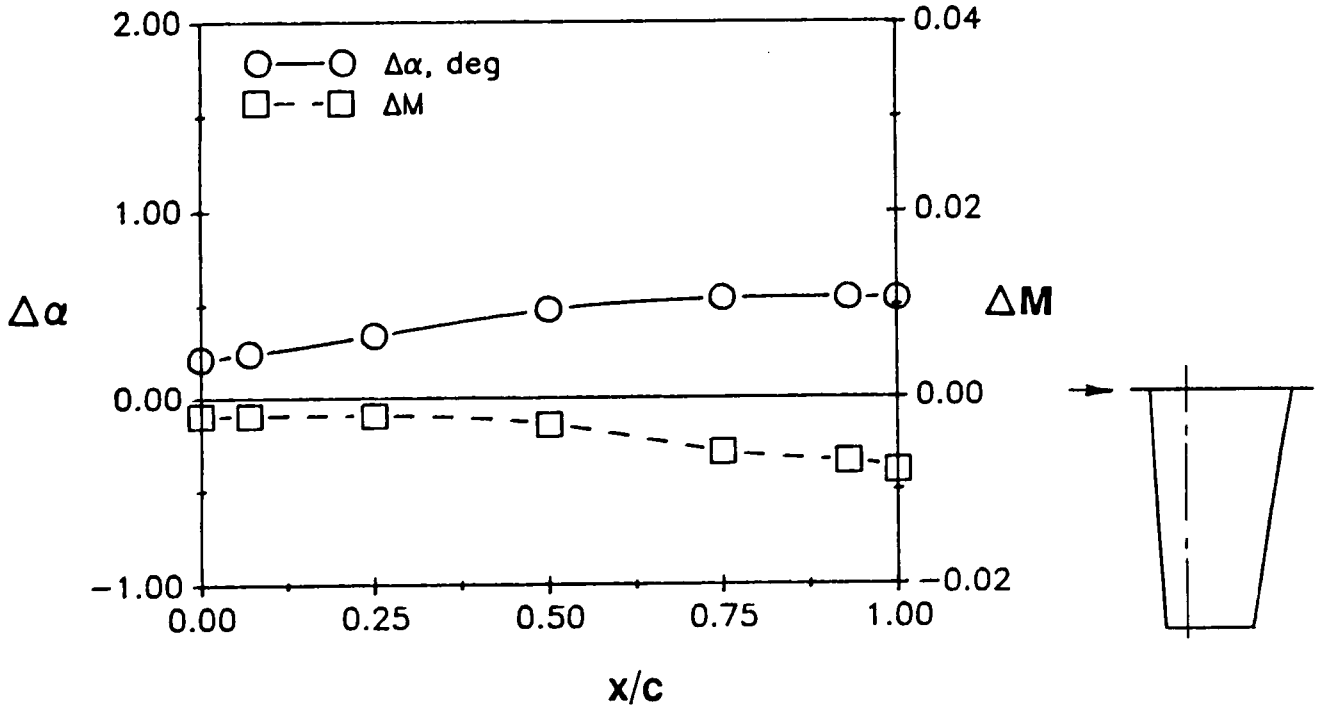

Figure 10. Chordwise variation of wall interference, first iteration, $M_\infty = 0.7$, $\alpha = 7^\circ$, wing high.

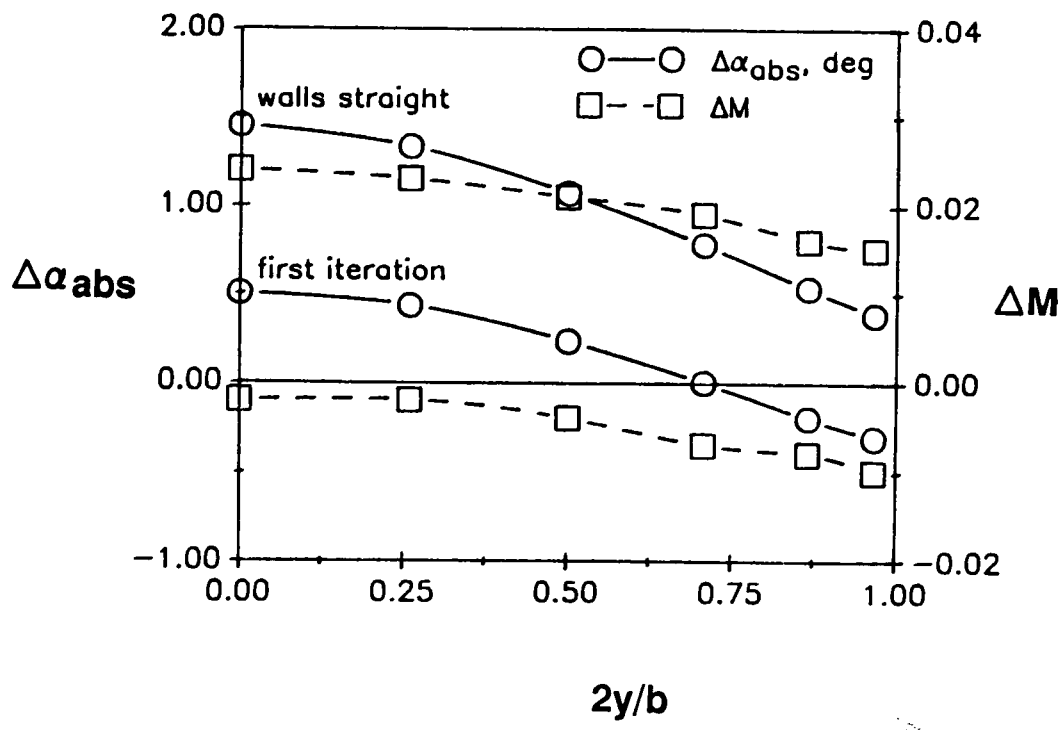

Figure 11. Interference at wing after first wall adjustment, $M_\infty = 0.7$, $\alpha = 7^\circ$, wing high.

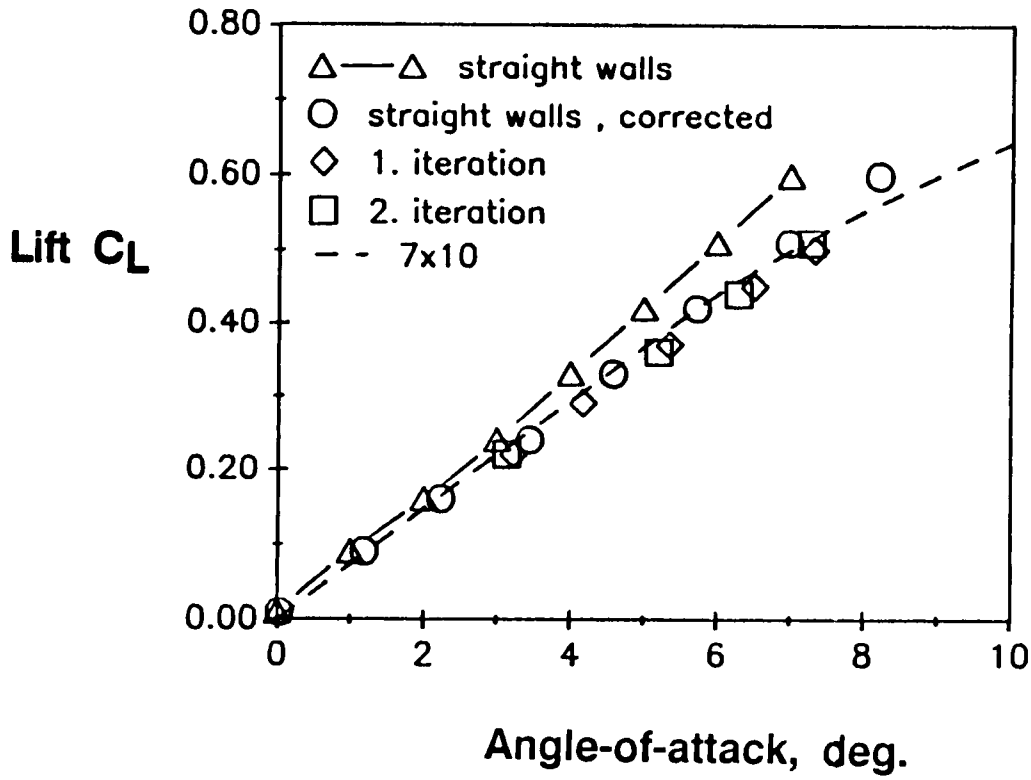

Figure 12. Measured wing lift versus interference-free data, $M_\infty = 0.7$, wing high.

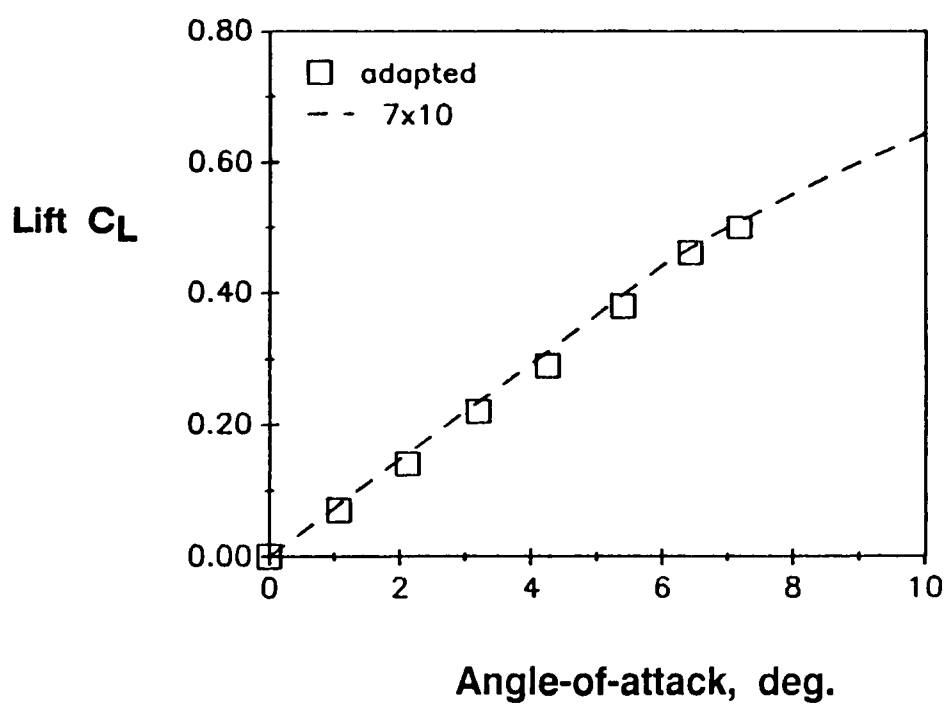

Figure 13. Measured wing lift versus interference-free data, $M_\infty = 0.7$, wing centered.

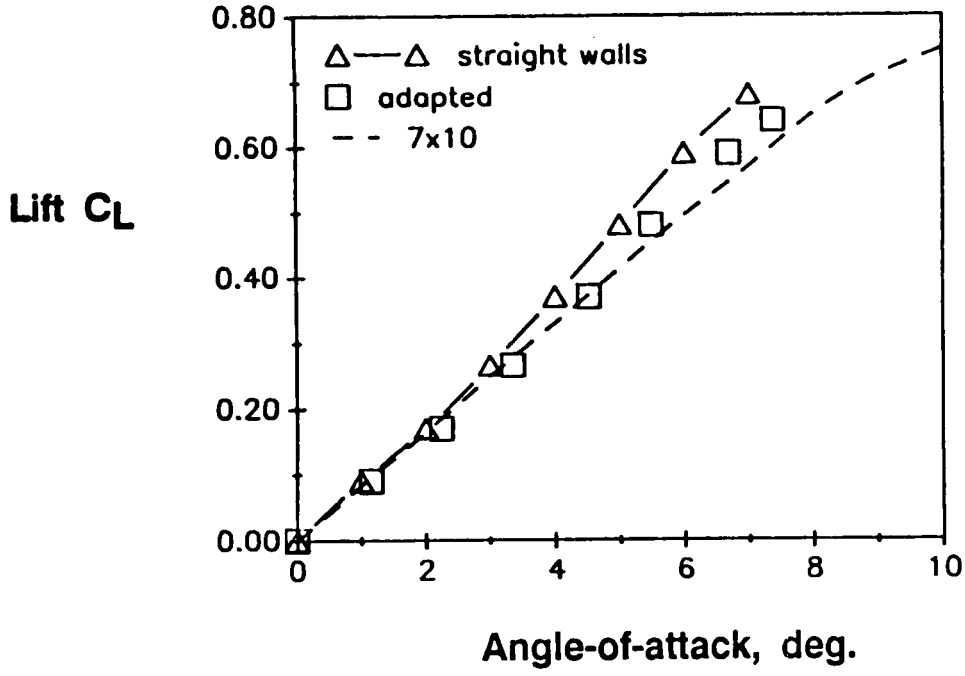

Figure 14. Measured wing lift versus interference-free data, $M_\infty = 0.85$, wing centered.

NASA
National Aeronautics and Space Administration

Report Documentation Page

1. Report No.	2. Government Accession No.	3. Recipient's Catalog No.
NASA CP-3020, Vol. I, Part 2		

4. Title and Subtitle	5. Report Date
Transonic Symposium: Theory, Application, and Experiment	March 1989
	6. Performing Organization Code
7. Author(s)	8. Performing Organization Report No.
Jerome T. Foughner, Jr., Compiler	L-16501
	10. Work Unit No.
	505-60-11-01
9. Performing Organization Name and Address	11. Contract or Grant No.
NASA Langley Research Center Hampton, VA 23665-5225	
	13. Type of Report and Period Covered
12. Sponsoring Agency Name and Address	Conference Publication
National Aeronautics and Space Administration Washington, DC 20546-0001	14. Sponsoring Agency Code

15. Supplementary Notes

16. Abstract

In order to assess the state of the art in transonic flow disciplines and to glimpse at future directions, the NASA Langley Research Center held a Transonic Symposium on April 19-21, 1988. Emphasis was placed on steady, three-dimensional external, transonic flow and its simulation, both numerically and experimentally.

Papers were presented by researchers from NASA, industry, and universities. The symposium included technical sessions on wind tunnel and flight experiments; computational fluid dynamics applications (industry overviews and configuration analysis design); inviscid methods and grid generation; viscous methods and boundary-layer stability; and wind tunnel techniques and wall interference.

The proceedings are published in two volumes as follows because of the range of classifications: Volume I, Unclassified (Parts 1 and 2); and Volume II, Unclassified, FEDD Restricted.

17. Key Words (Suggested by Author(s))	18. Distribution Statement
Aerodynamics External transonic flow Numerical simulation Experimental simulation	Unclassified - Unlimited Subject Category 02

19. Security Classif. (of this report)	20. Security Classif. (of this page)	21. No. of pages	22. Price
Unclassified	Unclassified	516	A22

NASA FORM 1626 OCT 86

NASA-Langley, 1989

For sale by the National Technical Information Service, Springfield, Virginia 22161-2171